MiCon 78:
OPTIMIZATION OF PROCESSING, PROPERTIES, AND SERVICE PERFORMANCE THROUGH MICROSTRUCTURAL CONTROL

Abrams/Maniar/Nail/Solomon
editors

ASTM STP 672

AMERICAN SOCIETY FOR
TESTING AND MATERIALS

MiCon 78: OPTIMIZATION OF PROCESSING, PROPERTIES, AND SERVICE PERFORMANCE THROUGH MICROSTRUCTURAL CONTROL

A symposium
sponsored by ASTM
Committee E-4 on
Metallography
AMERICAN SOCIETY FOR
TESTING AND MATERIALS
Houston, Tex., 3-5 April 1978

ASTM SPECIAL TECHNICAL PUBLICATION 672
Halle Abrams, Bethlehem Steel Corp.
G. N. Maniar, Carpenter Technology Corp.
D. A. Nail, Cameron Iron Works
H. D. Solomon, General Electric Co.
editors

List price $53.50
04-672000-28

AMERICAN SOCIETY FOR TESTING AND MATERIALS
1916 Race Street, Philadelphia, Pa. 19103

Library of Congress Catalog Card Number: 78-74560

Printed in Baltimore, Md.
July 1979

Foreword

The symposium on MiCon 78: Optimization of Processing, Properties, and Service Performance Through Microstructural Control was held in Houston, Texas, 3-5 April 1978. Sponsored by Committee E-4 on Metallography of the American Society for Testing and Materials, the symposium was also cosponsored by The Metallurgical Society of the American Institute of Mining, Metallurgical, and Petroleum Engineers, the International Metallographic Society, and the Houston Chapter of the American Society for Metals. Dr. Halle Abrams, Bethlehem Steel Corporation, G. N. Maniar, Carpenter Technology Corporation, D. A. Nail, Cameron Iron Works, and Dr. H. D. Solomon, General Electric Company are editors of this publication.

The success of the First MiCon Symposium, on which this ASTM special technical publication is based, was the outgrowth of two years of effort on the part of several individuals and technical societies. The MiCon Organizing Committee was the driving force behind this undertaking, and thanks are due to members of this committee, in particular to Dr. Charles Hays, General Chairman of MiCon 78, J. A. Richardson, IMS Liaison, and J. D. Blanchard, ASM Houston Liaison. Thanks are also due to P. S. Gupton, ASM Houston Chapter, Dr. A. G. Gray, ASM, J. J. Palmer, ASTM, R. J. Gray, IMS, and Dr. Kinrad Kundig, TMS/AIME. Finally, an expression of appreciation goes to Dr. Dan Albrecht, IMS, for his invaluable help in the formative stage of MiCon.

MiCon symposia are the responsibility of the MiCon Organizing Committee. The members of the committee for MiCon 78 and their responsibilities were:

- Dr. Halle Abrams, Bethlehem Steel Corporation, Chairman, Steels Session
- James D. Blanchard, Rolled Alloys Inc., ASM Houston Liaison
- Dr. William D. Forgeng, Jr., U.S. Steel Corporation, ASTM Committee E-4 Liaison
- Dr. Charles Hays, Dept. of Mechanical Technology, University of Houston, General Chairman
- Gunvant N. Maniar, Carpenter Technology Corporation, Chairman, High Temperature Alloys Session
- Don A. Nail, Cameron Iron Works, Technical Chairman and Organizing Committee Chairman
- James H. Richardson, The Aerospace Corporation, IMS Liaison and Organizing Committee Secretary
- Dr. Harvey D. Solomon, General Electric Company, Chairman, Stainless Steels Session and TMS/AIME Liaison
- Dr. Martin G. H. Wells, Colt Industries

The MiCon Organizing Committee is deeply appreciative of the support of MiCon 78 by the following corporations:

AVCO Corporation
Buehler, Ltd.
Cameron Iron Works, Inc.
Carpenter Technology Corp.
Cooper Industries, Cooper Energy Services Division
Deere and Company
General Electric Company,
  Corporate Research and Development Center
Houston Lighting and Power
Ladish Company
Shell Development Company
Sun Petroleum Products Company
Universal-Cyclops
  Cyclops Corporation
Wyman-Gordon Company

Related ASTM Publications

Unified Numbering System for Metals and Alloys, DS 56A (1977), $49.00, 05-056001-01

Quantitative Surface Analysis of Materials, STP 643 (1978), $21.50, 04-643000-39

Surface Analysis Techniques for Metallurgical Applications, STP 596 (1976), $15.00, 04-596000-28

Bearing Steels: The Rating of Nonmetallic Inclusion, STP 575 (1975), $22.25, 04-575000-02

Metallography—A Practical Tool for Correlating the Structure and Properties of Materials, STP 557 (1974), $24.25, 04-557000-28

Temper Embrittlement of Alloy Steels, STP 499 (1972), $10.00, 04-499000-02

Introduction to Today's Ultrahigh-Strength Structural Steels, STP 498 (1971), $3.75, 04-498000-02

A Note of Appreciation to Reviewers

This publication is made possible by the authors and, also, the unheralded efforts of the reviewers. This body of technical experts whose dedication, sacrifice of time and effort, and collective wisdom in reviewing the papers must be acknowledged. The quality level of ASTM publications is a direct function of their respected opinions. On behalf of ASTM we acknowledge with appreciation their contribution.

ASTM Committee on Publications

Editorial Staff

Contents

STEELS

STAINLESS STEELS

HIGH-TEMPERATURE ALLOYS

Introduction

This symposium was organized under the egis of the E-4, Metallography Committee of the American Society for Testing and Materials and was cosponsored by the Houston Chapter of the American Society for Metals, the International Metallographic Society, and the Metallurgical Society of the American Institute of Mining, Metallurgy, and Petroleum Engineers.

The E-4 Metallography Committee is concerned with the microstructural aspects of materials. Its members recognized the importance of microstructural control to the processing, properties, and service performance of materials; hence, their desire to hold a symposium devoted to this topic.

No problem is more central to metallurgy than the relationship of microstructure to properties. The symposium was organized to provide a forum for discussing new results in this important area of study. Since the topic of microstructure and properties is so broad, it was decided to narrow it down a bit by focusing on materials used for a specific type of application—in this case, materials for energy generation. Future symposia may deal with materials for land or sea transportation, or with aerospace or electronic materials.

The symposium brought together about 150 participants from universities, producers of materials for energy generation, and users of such materials. There was a lively discussion of many aspects of the relationship of microstructures and properties. The discussion together with the papers presented at this symposium are included in this special technical publication. It is hoped that these proceedings will be of value to those who use the alloys discussed here, to those who produce them, and to those of the research community who study them. Some care was taken to balance the presenters among these three areas. The resulting set of papers therefore covers a spectrum of viewpoints, from those who must produce a material to those who must use it, and a spectrum of approaches to the problem, from the fundamental to the more applied.

Halle Abrams
Homer Research Laboratories, Bethlehem Steel Corp., Bethlehem, Pa., editor.

G. N. Maniar
Research & Development Center, Carpenter Technology Corp., Reading, Pa., editor.

D. A. Nail
Technical Department, Cameron Iron Works, Inc., Houston, Tex., editor.

H. D. Solomon
Research and Development Center, General Electric Co., Schenectady, N. Y., editor.

Steels

Summary—Steels Session

The papers for the Steels Session of MiCon 78 were chosen to be consistent with the objectives of MiCon and to emphasize the theme of the symposium, namely, energy generation and related applications. The Steels Session had ten invited papers, of which six addressed the subject of high-strength low-alloy (HSLA) steels for Arctic linepipe application. The papers were complementary to one another in terms of the overall theme, and each one dealt with specific topics such as: alloy composition and processing, microstructural control, stress corrosion cracking and hydrogen embrittlement, accelerated cooling, and regression analysis and prediction of plate and pipe mechanical properties. The keynote paper discussed the need for improved wear- and abrasion-resistant steels for components in advanced fossil energy conversion systems such as coal gasification plants. In the area of turbine materials, which are susceptible to temper embrittlement at the operating temperatures involved, Viswanathan's paper reviewed the most common steels used for this application (Cr-Mo, Cr-Mo-V, Ni-Cr-Mo-V) and provided an insight into the role of microstructure in interpreting the embrittlement susceptibility as effected by transformation product and strength level. In the area of pressure vessel steels, the Swift and Smith paper considered A533-B steel and describes a procedure for predicting the microstructure of heavy-gage plates as a function of carbon equivalent and cooling rate. The final paper by Diesburg considered the problems of drilling large-diameter deep oil wells and, because of the high stresses involved, the need for rolling-cutter rock bits having high levels of hardenability.

The intent of this summary is not to abstract each of the papers presented, but rather to comment on how their salient highlights fit into the overall theme of the symposium. In Prof. Zackay's keynote paper, he described the utilization of composition control to provide the desired combination of mechanical properties required in advanced fossil energy conversion systems. In this context, high hot strength up to 593°C (1100°F) with adequate room temperature toughness is required for screw feeders. Secondary hardening alloys with combinations of up to 3Si and 3Al retard the tempering reactions, and optimum improvement in room temperature toughness is obtained by combining 1.5Al and 1.5Si. However, additions of more than 2Si cause intragranular fracture after tempering at 550°C.

Cohen and Hansen's paper, "Microstructural Control in Microalloyed Steels," was based on the premise that a fine ferritic grain size is essential to develop the best strength toughness combination in microalloyed steels. Structural refinement of the ferrite was shown to depend on control of the austenite structure during rolling, coupled with control of the austenite-to-ferrite transformation kinetics. The finest ferritic grain sizes evolve on transformation from unrecrystallized austenite, and the mechanism and control of the austenite recrystallization reaction were discussed. The subsequent transformation of unrecrystallized austenite was followed, and it was stressed that any structural refinement gained during rolling may be further maximized by appropriate control of the transformation kinetics via alloying or process controls.

The paper, "Evaluation of Steels for Arctic Line Pipe," by Abrams and Roe was a practical demonstration of microstructural control to improve the strength and toughness properties described by Cohen and Hansen. Extensive property data were presented from seven full-scale mill trials, which were used to predict the plate and pipe properties based on chemistry and processing. The improved strength and toughness properties are associated with a fine ferrite grain size and a high percent of fine-grain ferrite patches (fgfp). Specifically, for a vanadium-columbium (VCb) grade, to assure an 85 percent shear fracture appearance below −23°C (−10°F) in the pipe, the control-rolled plate must have a grain size number greater than ASTM 11 and a percent fgfp value greater than 75 percent. Lower slab reheating temperatures reduce the amount of duplex ferrite microstructure common to severely control-rolled steels and provide further improvement in toughness as characterized by the Battelle Drop Weight Tear Test.

In the paper, "The Control of Microstructure by Processing Parameters and Chemistry in Arctic Line Pipe Steels," by Ouchi et al, the authors evaluated a series of columbium (0.02 to 0.05 percent) and vanadium (0.03 to 0.09 percent) steels and studied the effects of controlled rolling and quench and temper heat treatment (after rolling) on microstructure and mechanical properties. In the control-rolled condition, these steels exhibit ferrite/pearlite or acicular ferrite microstructures and develop yield strengths of 70 to 75 ksi. Accelerated cooling after control-rolling increased the yield strength to 80 to 85 ksi due to a more refined structure consisting of ferrite and bainite. The quench and temper heat treatment by induction heating of pipe produces a ferrite-bainite-martensite microstructure, retaining a fine grain size and further increasing the yield strength to 100 ksi. This heat treatment eliminates variations in toughness across the heat-affected zone (HAZ) and results in improved resistance to hydrogen-induced cracking and H_2S stress corrosion cracking.

The role of hydrogen-induced cracking of microalloyed steels in the 40 to 100 ksi strength range was described in detail by Malcolm Gray, who presented the paper, "High-Strength Microalloyed Pipe Steels Resistant to Hydrogen-Induced Failures," by Parrini and DeVito of Italsider. The susceptibility to H_2S stress corrosion cracking was found to increase with increasing tensile strength. Above 120 ksi tensile strength, the failure was always intragranular, whereas below 80 ksi tensile strength, the failure was always ductile. This susceptibility was also related to steel cleanliness and the degree of inclusion elongation. Lower levels of MnS via desulfurization and higher finish-rolling temperatures reduced the degree of cracking, but the major improvement was associated with rare earth additions. Another approach to the hydrogen cracking problem in sour gas environments was to make the weld metal cathodic with respect to the HAZ, thereby preferentially attracting the hydrogen to the weld metal. This cathodic protection was accomplished by additions of 0.5Mo and 0.4Cr to the welding rod.

Processing, mechanical properties, and microstructure interrelationships for an acicular ferrite steel containing Mn-Mo-Cb were described in the Stelco paper, "Controlled Processing of Molybdenum Bearing Line Pipe Steels," by Delvecchio, Hood, and McCutcheon. The acicular ferrite grades are attractive for Arctic line pipe because in the plate form the yield strength is relatively low, about 60 ksi, which upon forming to pipe and hydraulic expansion achieves X70 to X80 levels due to the continuous yielding behavior and appreciable strain hardening. However, these grades typically are very low-carbon and high-manganese and offer the disadvantage of BOF melting problems and added alloy costs. Delvecchio and co-workers found that both the low- and high-manganese grades are suitable for X70 Arctic applications. However, at the more economical 0.2Mo level, the higher manganese grades consistently provided higher yield strengths and required less low-temperature rolling.

Coldren et al reported on their laboratory study of Mn-Mo-Cb steels finish-rolled moderately below Ar_3. In this study, they rolled 19 mm (3/4 in.) plate into the two-phase region to determine the relative effects of ferrite grain refinement, dislocation substructure and Cb (C, N) precipitation strengthening on the strength and toughness. They found that stress-assisted precipitation and dislocation substructure can effectively increase the strength without adversely affecting the toughness, and these mechanisms were most efficient in plates with 30 to 40 percent deformed ferrite that was given a 20 percent reduction on the last pass. Increasing the molybdenum content from 0.2 to 0.4 percent reduced the yield point elongation, and in plates with as little as 11 percent deformed ferrite, there was continuous yielding. This behavior, as mentioned previously, offers the capability of making an X75/X80 expanded line pipe from a molybdenum-containing alloy grade. However, the effect of this work hardening on notch toughness at these high-strength levels would have to be more fully studied before an X80 grade could be exploited.

One of the many factors that influence toughness is reversible temper embrittlement, which manifests itself as an increase in the ductile-to-brittle transition temperature of the steel. The problem has assumed even greater importance in recent years in view of the findings that the susceptibility of steels to cracking in hydrogen and stress corrosion attack is also increased due to prior temper embrittlement. The critical temperature range over which embrittlement occurs often coincides with the operational or heat treatment temperature for many of the steels used by the petrochemical and other energy-related industries. Results have recently been reported relating microstructural variations produced by varying the transformation product and/or the tensile strength level to embrittlement susceptibility and in turn to the susceptibility of cracking in adverse environments. In his paper, "Influence of Microstructure on the Temper Embrittlement of Some Low-Alloy Steels," Viswanathan provides a critical review and interpretation of the results for Cr-Mo-V, Ni-Cr-Mo-V, and 2.25Cr-1Mo steels.

The mechanical properties of heavy-gage plate for pressure vessels is determined by the microstructure and tempering parameters. The microstructure is in turn controlled by the hardenability and post-austenitizing cooling rate. Using the carbon equivalent to account for the hardenability effects of the steel chemistry, Swift and Smith studied the effects of composition and cooling rate on the microstructure of A533-B steel. Equations were developed from the experimental data to predict the microstructures, and comparison with the microstructures to commercial heats showed that the predictions were in good agreement.

In view of the energy shortage and its increasing cost, it is now economical to recover oil and gas from known deep reserves, which require large-diameter shafts. The replacement of worn or broken rock bits during the drilling of these deep shafts is obviously undesirable from the standpoint of cost and productivity. Accordingly, the rolling-cutter rock bit is an integral part of making the drilling operation efficient. In most instances, the best combination of properties for these rock bits is obtained by carburizing and quenching and tempering. In his paper, "High Hardenability Carburizing Steels for Rock Bits," Diesburg describes the excellent performance of EX55 (0.87Mn, 0.58Cr, 1.85Ni, 0.75Mo) in impact fatigue, high-cycle fatigue, impact fracture stress, and plane strain fracture toughness tests. Comparison of EX55 grades with high-nickel SAE 4800 grades indicates that the improved hardenability of the EX55 grades would be suitable for rolling-cutter rock bits for deep shaft drilling.

In conclusion, I would like to stress the excellent participation of the authors and others attending the symposium. The knowledge and enthusiasm of the authors were apparent in their papers, some of which represent years of experimental work. In addition to the value of the papers themselves, there are the fine points and interplay of ideas in the discussions, which have been grouped together and appended to the volume of Steels Session papers.

I would also like to take this opportunity to thank each of the authors, reviewers, and participants for making the Steel Session of MiCon 78 such a rewarding experience for all of us.

Halle Abrams
Homer Research Laboratories, Bethlehem Steel Corporation, Bethlehem, Pa., session chairman.

V. F. Zackay[1]

Design of High Hardness, Tough Steels for Energy-Related Applications

REFERENCE: Zackay, V. F., "**Design of High Hardness, Tough Steels for Energy-Related Applications,**" *MiCon 78: Optimization of Processing, Properties, and Service Performance Through Microstructural Control, ASTM STP 672*, Halle Abrams, G. N. Maniar, D. A. Nail, and H. D. Solomon, Eds., American Society for Testing and Materials, 1979, pp. 10–33.

ABSTRACT: The need for improved wear and abrasion resistant steels for components in advanced fossil energy conversion systems is described. Desirable combinations of mechanical properties for these components are enumerated. A critical component, coal feeders, in coal gasification plants requires adequate room temperature toughness and high strength at both room and moderately elevated temperatures. Through modification of both composition and heat treatment, it has been shown that commercial secondary hardening *matrix* steels are promising candidates for this application. It is further shown that improvements can be achieved by the synthesis of new secondary hardening steels. A key feature of the design of these steels is the suppression, by composition control, of solid-state tempering reactions that (in commercial secondary hardening steels) lead to inadequate toughness. In other components for advanced coal technology, hot strength is not required but hardness and impact strength are. Modified medium-alloy, ultra-high-strength steels are described with combinations of strength and toughness achievable only in the high-alloy (and expensive) maraging steels.

KEY WORDS: steels, microstructure, high-strength steels, secondary hardening steels, coal gasification, abrasion resistance

The widespread recognition of the diminishing supply of certain fossil fuels, notably oil and natural gas, has resulted in the initiation of research and development programs in advanced energy conversion systems throughout the world. While many of these systems are in an early stage of planning, others have advanced sufficiently to enable designers to specify performance criteria and to suggest materials of construction. While it is economically desirable to utilize commercially-available materials for these advanced systems, it is not always possible to do so. In

---

[1] Professor of Metallurgy, University of California, Berkeley, Calif. 94720.

these latter instances, it becomes necessary to design new materials that will have the specified combination of chemical and mechanical properties. The Fossil Energy Research and Nuclear Research Groups, Energy Technology, Department of Energy, have recently initiated projects at the University of California, Berkeley, to address some of these alloy design problems. For example, a major interdisciplinary research effort is being made to build devices utilizing metals as energy absorbers. These devices are intended to enhance the safety of nuclear reactor piping systems under cyclical (seismic) and impact (water hammer) loading.

A major feature of the national energy plan is a doubling of the use of coal as a source of energy [*1,2*].[2] The execution of this plan will pose many challenges to the engineer and scientist and, in particular, to those in the field of materials. Major forthcoming materials problems have been identified in the mining, transporting, and processing of coal. Some of these problems are a direct consequence of the massive materials handling aspects of new technologies such as large-scale coal gasification and liquefaction. Although the present program at Berkeley is primarily concerned with coal handling equipment, some of the results are relevant to mining and earthmoving equipment.

The mining, sizing, and transporting of large tonnages of coal call for materials with improved wear and abrasion resistance. In some of these applications, unusual combinations of mechanical properties are often required. For example, high hardness and toughness at room temperature as well as strength at elevated temperatures may be specified. Where existing commercial steels are not adequate, new steels have to be designed, tested, and introduced into the technology. This paper discusses the preliminary results obtained in a study of the design of alloys for improved wear and abrasion resistance.

Materials Requirements

The wear and abrasion resistant alloys being investigated are intended for use in the following: (1) coal feeders; (2) coal moving equipment, such as chutes and loader shovels; and (3) coal crushing and milling equipment. The operating conditions of such components are different and, in the case of the coal feeder, not completely established. However, sufficient information is available in all instances for the initial formulation of desirable alloy compositions, mechanical property requirements, and wear test procedures.

An evaluation of the various designs of dry coal feeders and expected performances was made recently [*3*]. Certain types of feeders were selected for further study and development. One type, the screw feeder,

---

[2] The italic numbers in brackets refer to the list of references appended to this paper.

was judged to have the highest probability of eventual commercialization. Preliminary tests with laboratory-size feeders revealed that severe wear could be expected at several places, namely, at the outer edges of the screw tips, where the velocity of the feed material is high, and at the exit end, because of the high pressure and velocity in this region [*4*,*5*]. It was concluded [*5*] that the abrasive wear observed was due to high stress, dry, three-body abrasion (that is, coal particles, 6.35 mm (1/4-in.) in diameter or less, being wedged between two metal surfaces, namely, barrel and screw). A study of the performance of screw feeders in injection molding machines [*6*,*7*] revealed that adhesive wear also occurs due to such factors as misalignment, uneven feeding, and nonuniform heating, although under normal operating conditions the screw is expected to *float* in the center of the barrel. A critical feature of the screw feeder in the coal gasifier is the temperature of operation. Depending on the particular design, the device may operate at temperatures of 538°C, (1000°F) or it may be subject to a temperature gradient, that is, only that part of the device nearest to the gasifier vessel may be heated.

An analysis of the performance criteria for screw feeders suggests that an unusual combination of mechanical properties is desirable. These include hardness and adequate toughness from room to the maximum operating temperature. In addition, enough hot strength at the maximum operating temperature is required to resist plastic deformation caused either by the abrading particles or by the unit loads on the sliding metal parts.

The materials requirements for coal handling equipment, such as chutes and loader shovels, are better known than for coal feeders and are less demanding. These components are subject to relatively low-stress dry abrasion of a two-body type (contact between two materials having relative motion) with the abrading material varying widely in size, shape, and hardness. These components are also subject to the multiple impacts of falling rock and coal. Alloys for parts exposed to these conditions must have adequate hardness, toughness, and, in some instances, impact fatigue resistance. Because they are used in large volumes and must be replaced periodically, economy of manufacture is also essential.

The components of coal crushing and milling equipment are subjected to wear and environmental factors that include dry abrasion and impact. Therefore, the properties desired are adequate hardness, impact fatigue resistance, and toughness.

It is emphasized that the *optimum* combination of mechanical properties of an alloy for any wear application, regardless of its nature, is unpredictable. Although there is no consensus among experts as to the precise combination of mechanical properties that control the different types of wear, there is general agreement that microstructure is an important variable [*8*–*15*]. Most, if not all, of the design for wear and abrasion resistant alloys involves dependence on simulated wear tests in the laboratory, plus field evaluation [*16–18*]. The laboratory testing and field evaluation aspects of the current program are still in an early stage and will be described in more detail in later publications.

Feeder Components

Alloy Design Criteria

The distinguishing metallurgical feature of materials used in screw feeders is the requirement for both hot strength and adequate room-temperature toughness. Either static (compact tension) or dynamic (notched Charpy impact) tests can be used to measure the toughness of metals. The applications of concern, that is, coal handling, screw feeders, etc., involve dynamic loading and, for this reason, the Charpy impact test has been used as the criterion of toughness in the *initial* phase of these studies. The compact tension test (characterized by static loading in the presence of a sharp crack) will also be used in the latter phases of the research program to obtain the fracture toughness of selected alloys. Secondary hardening steels have been used in certain manufacturing industries for many years because of their ability to retain their strength to moderately elevated temperatures, that is, 538 to 593°C (1000 to 1100°F). However, at the optimum tempering temperature for hot strength (and peak hardness), the room-temperature toughness is discouragingly low. In fact, the toughness of these steels is characteristically so poor that it is often not reported. The usual relationship between strength (hardness) and toughness is revealed in a study of 5Cr-Mo-V steel by Contractor et al [*19*]. As shown in Fig. 1, the maximum in room-temperature hardness and the minimum in room-temperature toughness occur at the same tempering temperature, 538°C (1000°F). At a tempering temperature less than 538°C, (1000°F), the steel would not have its maximum hot strength. The composition-microstructure-mechanical property relationships of these steels will be described later.

In contrast to the secondary hardening steels, many low- and medium-alloy quenched and tempered steels are known to possess excellent combinations of strength and toughness through microstructural control. These ultra-high-strength steels are widely used in the aerospace, transportation, and manufacturing industries. However, it is unlikely that these steels can be used at temperatures exceeding about 482°C (900°F), because a pronounced degradation of properties, especially hardness, almost invariably occurs above this temperature.

The first objective of the alloy design program was, therefore, to establish whether this inverse relationship of high strength and low toughness in secondary hardening steels could be overcome. Before

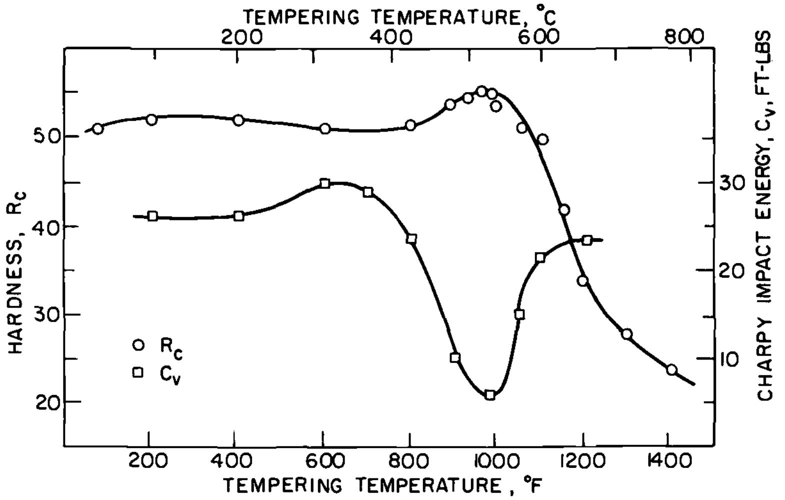

FIG. 1—*Hardness and impact strength versus tempering temperature relationships for a 5Cr-Mo-V steel from Ref.* 19.

describing the experimental program, it is useful to examine both the tempering sequence of secondary hardening steels and the basic factors contributing to the enhancement of toughness in ultra-high-strength steels.

Speich [*20*], among others, has established the sequence and chemistry of solid-state reactions occurring in steels containing only iron (Fe) and carbon (C). Briefly, for steels having greater than 0.2 C, a transition carbide, called epsilon-carbide, first forms as a decomposition product of martensite. Epsilon-carbide forms at temperatures up to 200°C (392°F). Above 250°C (482°F), Fe_3C precipitates are formed at lath boundaries and at former austenite grain boundaries. The cementite also precipitates within the laths initially as plates that grow and spheriodize rapidly at higher temperatures. Also, any retained austenite that is present will decompose into ferrite and cementite in the temperature range of 230 to 280°C (446 to 536°F). From 400°C (752°F) to 600°C (1112°F), recovery of the martensite defect structure occurs. The hardness drops continuously following tempering at temperatures above about 200°C (392°F) to 300°C (572°F), and this decrease is often associated with the formation of iron carbides in the martensite lath boundaries [*21–24*].

The hardness versus tempering relationship and the associated solid-state reactions in a highly alloyed, secondary hardening steel are similar to those of the plain carbon or low-alloy steels for temperatures below about 450°C (842°F). Above this temperature, any highly alloyed retained austenite that is present decomposes to form low-alloy retained austenite and complex carbides. Also, at this temperature, some of the iron atoms in the precipitated Fe_3C are replaced by transition elements such as chromium to form complex iron carbides. At about 540°C (972°F), finely dispersed complex refractory element carbides such as $(MoW)_6C$ form, completely replacing the complex iron carbides. The formation of these carbides and the resultant increase in hardness is referred to as secondary hardening. At a sufficiently high temperature, these refractory carbides grow, the hardness drops, and the steel is said to be overtempered.

Goolsby [*21*] and Tom [*25*] attempted to relate the various features of the tempering temperature versus toughness relationship to microstructural features. The relationships between tempering temperature and hardness, Fig. 2*a*, and toughness, Fig. 2*b*, in a 0.3C-5Mo secondary hardening steel, are taken from Goolsby [*21*]. He ascribed the first drop in toughness, between 225°C (437°F) and 300°C (572°F), to the precipitation of iron carbides at martensite lath boundaries. He attributed the second drop, at about 600°C (1112°F) to the precipitation of refractory carbides at the same sites. Clearly, the minimization of deleterious solid-state chemical reactions during the tempering operation is desirable. The precipitation of brittle compounds at heterogeneous nucleation sites, such as lath or grain boundaries, is obviously a major reason for the lack of toughness in secondary hardening steels.

Goolsby [*21*] also listed some of the factors that might account for the high toughness of the martensite tempered at low temperatures. These were: (1) the microstructure was relatively free of minor amounts of weak and ductile phases such as ferrite or retained austenite; (2) there were no extensive lath or grain boundary precipitates; (3) there were no undissolved carbides, that is, carbides not dissolved during austenitization and embedded in the martensite after quenching. Tom [*25*] has also shown that there is a threshold size for these undissolved carbides above which the fracture toughness abruptly decreases for a given strength level.

To these results might be added the well-known fact that an excessively large prior austenite grain size can degrade impact toughness. The temperature of austenitization is therefore a very important factor in the heat treatment of secondary hardening steels. The temperature must be sufficiently high to remove undissolved carbides, or at least to minimize the number of such particles, and also it should be below that which causes excessive grain coarsening.

The relationship between toughness and austenitizing temperature may also vary according to the type of toughness test, as shown by Ritchie et al [*26*]. In recent work, Ritchie and Horn [*27*] have shown that an austenitizing temperature intermediate between a conventional and a high (grain-coarsening) one results in an increase in the fracture toughness without a concomitant decrease in the Charpy impact strength.

These considerations and others, which will be discussed later, provide

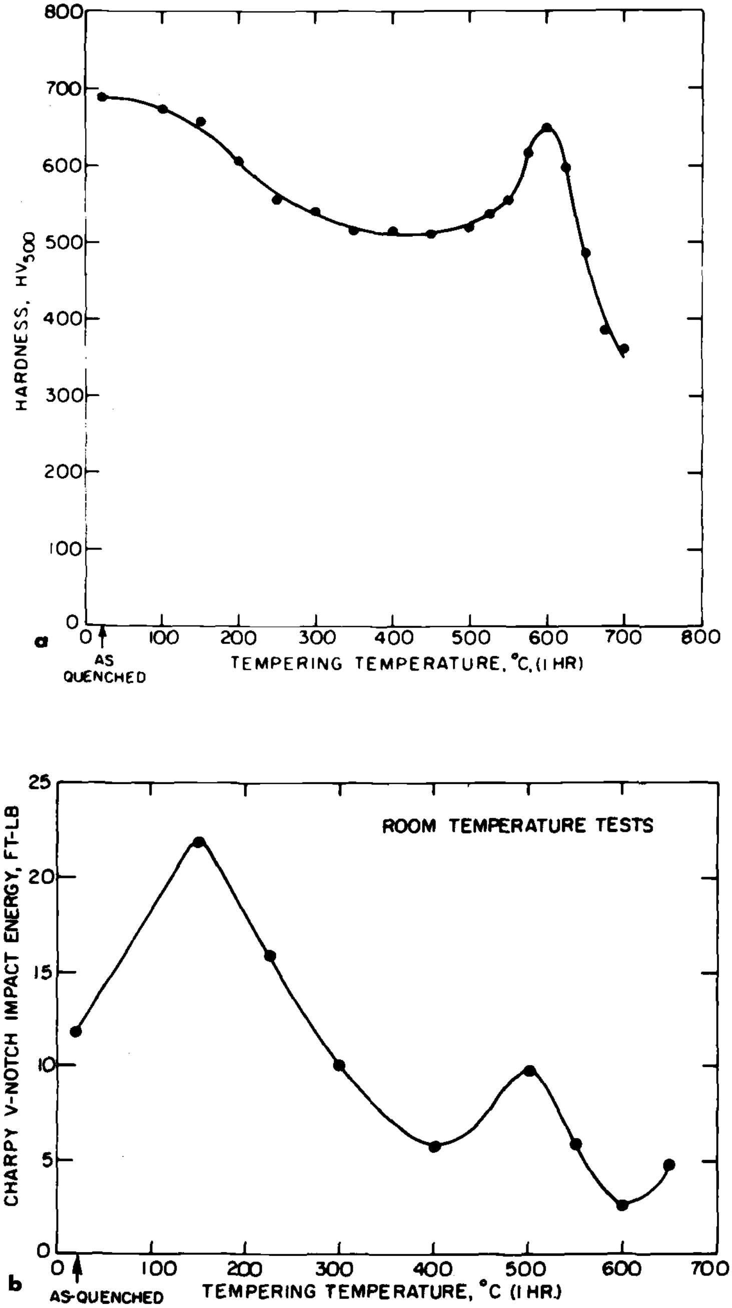

FIG. 2—(a) *Microhardness versus tempering temperature curve for the tempering of a 0.3C-5Mo steel* [21]. (b) *The variation of Charpy impact energy with tempering temperature for a 0.3C-5Mo steel* [21].

the basis for either the appropriate modification of commercially available steels or the design of new alloys. These two paths of research were both explored and are described in the following sections.

Modified Commercial Matrix Alloys

Early in the research program, a commercially available steel (Vasco-MA), having a composition and microstructure that appeared to meet some of the basic requirements, was selected. This steel is one of a family of *matrix steels* whose matrix is that of the popular M-2 tool steel. The composition of M-2 and the recommended heat treatment have been adjusted to minimize the volume fraction of primary carbides. The relative absence of large brittle primary carbides is purported to confer enhanced toughness and high hardness on these secondary hardening steels.

The hardness and impact strength of Vasco-MA were measured, and the relatively poor toughness (about 8.13 J (6 ft · 1 lb) at 56 HRC) suggested that, contrary to expectation, the matrix was not free of large primary carbides. This was confirmed by metallographic and fracture surface examination of specimens austenitized over a wide range of temperatures, 900 to 1200°C (1652 to 2192°F). Large, undissolved primary carbides are clearly shown in Fig. 3, in a specimen austenitized at 1000°C (1832°F). Scanning electron microscopic (SEM) examination, in conjunction with energy-dispersive X-ray analysis, established that tungsten was the major, and vanadium and molybdenum were the minor, alloy constituents of these carbides.

The observations formed the basis of a program encompassing one of the two approaches mentioned earlier, that is, modification of an existing commercial steel. A series of steels whose compositions are shown in Table 1 was made based on the base composition on the Vasco-MA steel, designated B1 in the table. The analysis consisted of chemical determinations (using energy-dispersive X-ray analysis) of the complex alloy carbides after each of several austenitization treatments. The analyses provided the guidance for the formulation of new matrix compositions that might possess better combinations of hardness and toughness than those of the base Vasco-MA steel.

The results of studies to date are presented in Figs. 4 through 7. Useful information can be obtained by qualitative comparisons of the hardness versus austenitizing and hardness versus tempering temperature curves of the several steels. The hardness versus austenitizing temperature curves of the three steels, B1 (2 W), B4 (1 W), and B6 (0.5 W) are shown in Fig. 4. The significantly higher hardness of B4 and B6, at temperatures between 1000°C (1832°F) and 1100°C (2012°F) suggests that (prior to reaching a temperature of 1200°C (2192°F)) the tungsten carbides in these steels

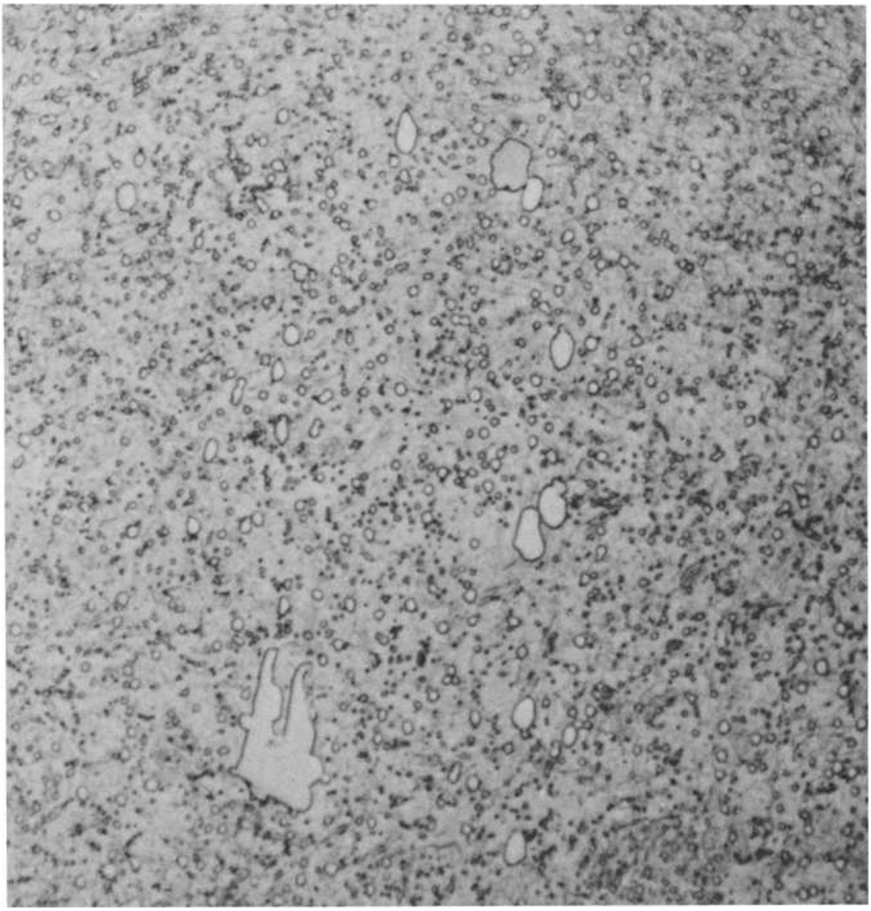

FIG. 3—*Optical micrograph showing large undissolved primary carbides in a B1 steel specimen austenitized at 1000°C (1832°F).*

TABLE 1—*Nominal composition of matrix-type steels.*

	Composition, weight %						
Alloy No.	C	Si	Cr	Mo	V	W	Fe
B1	0.5	0.2	4.5	2.8	1	2	balance
B4	0.5	0.2	4.5	2.8	1	1	balance
B5	0.5	0.2	4.5	2.8	0.5	2	balance
B6	0.5	0.2	4.5	2.8	1	0.5	balance
B9	0 5	0.2	3.5	2.8	1	2	balance
B10	0.5	0.2	2.5	2.8	1	2	balance

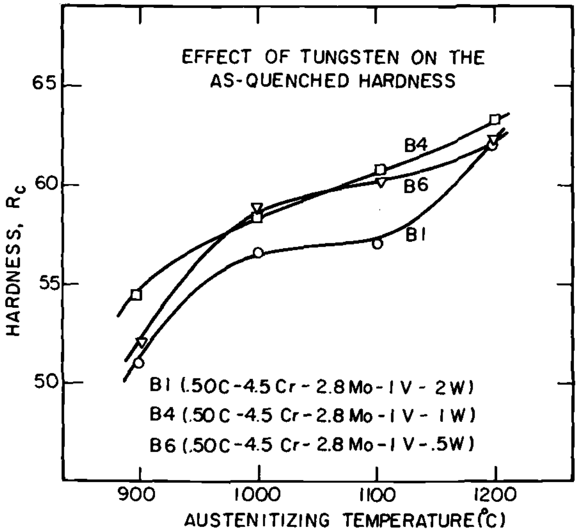

FIG. 4—*The variation of hardness with austenitization temperature for Steels B1, B4, and B6.*

have largely gone into solution while those in Steel B1 have not. The hardness and Charpy impact energy versus tempering temperature data for these three steels, austenitized at 1000°C (1832°F), is shown in Fig. 5*a* and *b*, respectively, in the tempering range of 450°C (842°F) to 650°C (1202°F). From Fig. 5*a*, it is observed that Steel B4 hardened to a greater extent than the base steel, B1. However, Steel B6 with only 0.5 W had lower hardnesses than the Steel B1.

The secondary hardening peak of all three steels is at a tempering temperature of about 550°C (1022°F). In Steels B4 and B6, the Charpy impact energy, associated with the peak hardness, is either a maximum (B6) or at a plateau (B4) with tempering temperature, as shown in Fig. 5*b*. Steels B4 and B6 possessed much higher Charpy impact toughness than the base steel, B1. The combinations of hardness and Charpy impact toughness for these steels at the peak hardness, that is, 52 HRC and 27.1 J (20 ft · lb) for Steel B6, and 54 HRC and 20.3 J (15.50 ft · lb) for Steel B4, are far superior to those of the commercial steel, B1.

A similar comparison of the influence of vanadium on mechanical properties can be made by comparing Steels B1 (1 W) and B5 (0.5 W), as shown in Fig. 6*a* and *b*. The flatness (and position) of the hardness versus austenitizing temperature curve for Steel B5, Fig. 6*a*, indicates that most of the carbides are in solution above about 1000°C (1832°F). The higher hardness on tempering this steel in the 450 to 650°C (842 to 1202°F) range, as shown in Fig. 6*b*, substantiates this conclusion. In Fig. 7, the Charpy impact energy of Steels B1, B4, and B5 are plotted as a function of

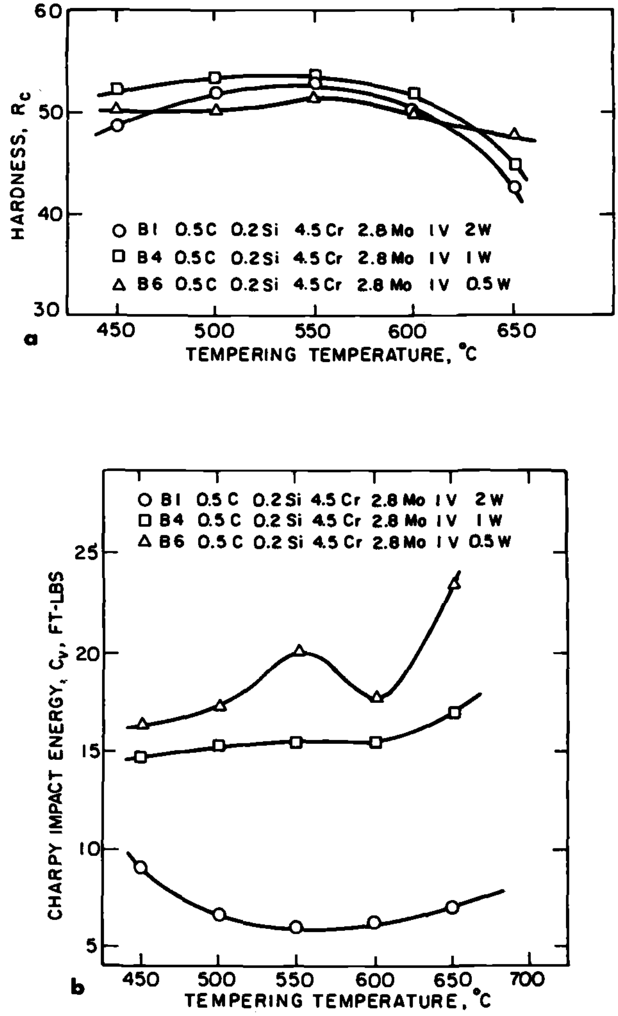

FIG. 5—(a) *The variation of hardness with tempering temperature for Steels B1, B4, and B6, austenitized at 1000°C (1832°F).* (b) *The variation of Charpy impact energy with tempering temperature for Steels B1, B4, and B6, austenitized at 1000°C (1832°F).*

tempering temperature. It is seen that Steel B5, with the lower vanadium content, had a higher Charpy impact toughness than Steel B1. Both the lower tungsten (B4) and lower vanadium (B5) steels showed an increase in *both* the hardness *and* toughness as compared with Steel B1, supporting the conclusions mentioned previously. From a study of Steels B9 and B10, it appeared that at least 4.5 Cr is desirable in these steels for obtaining a sufficient secondary hardening response [*4*].

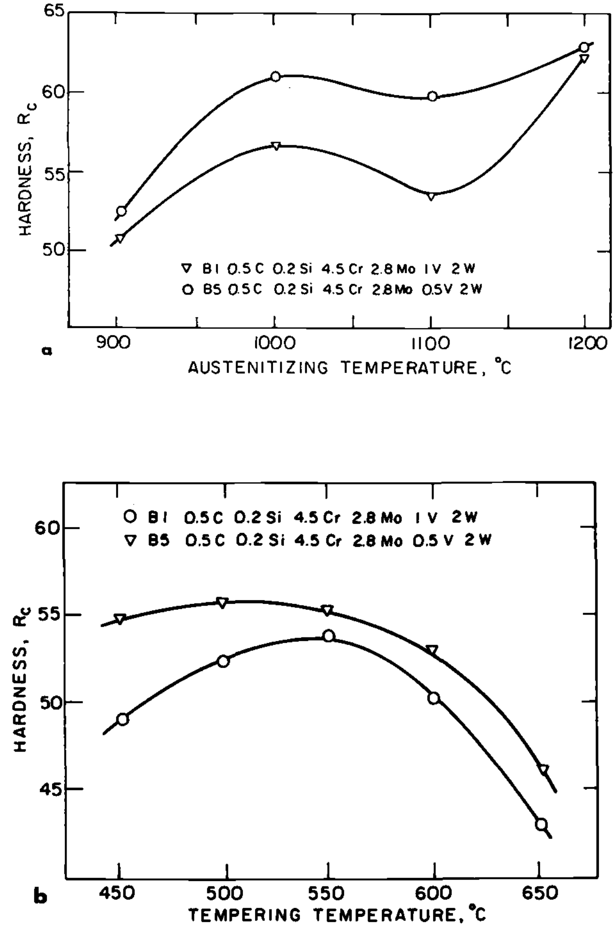

FIG. 6—(a) *The variation of hardness with austenitizing temperature for Steels B1 and B5.* (b) *The variation of hardness with tempering temperature for Steels B1 and B5.*

The best hardness and toughness combinations obtained for this first group of steels are shown plotted in Fig. 8. The results of this initial study suggest that one of the research objectives, that is, a secondary hardening steel with a hardness of 55 HRC and a Charpy impact energy of at least 20.3 J (15 ft · lb) is attainable.

New Secondary Hardening Alloys

Encouraging as the results on the modified commercial matrix alloys were, scanning and transmission electron micrographs of fracture surfaces of those steels with the best combinations of hardness and tough-

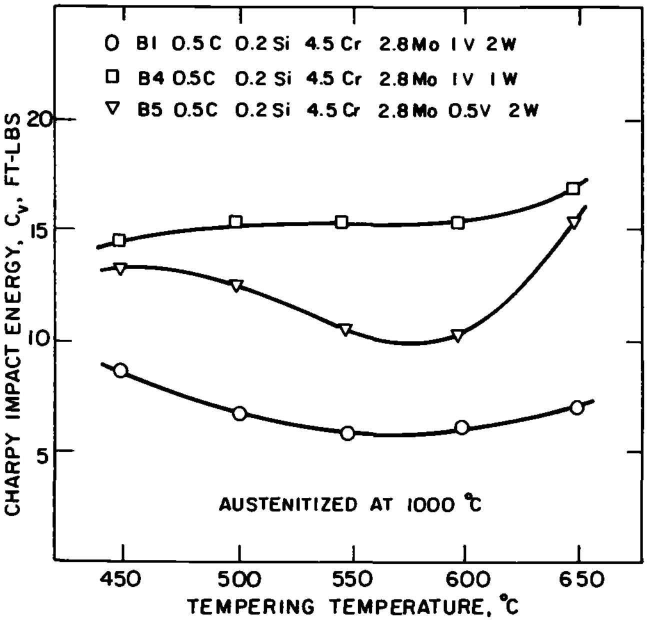

FIG. 7—*The variation of Charpy impact energy with tempering temperature for Steels B1, B4, and B5.*

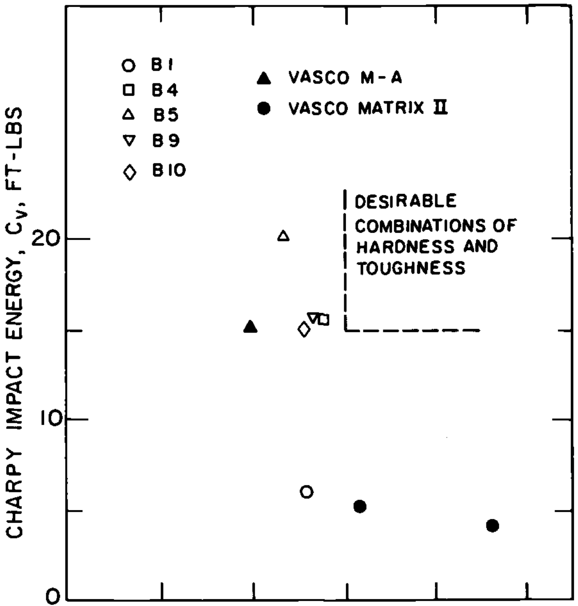

FIG. 8—*Representative combinations of hardness and Charpy impact energy for several secondary hardening steels.*

ness revealed some microstructural deficiencies. For example, grain boundary precipitates and precipitate-free zones were observed in Steel B4, as shown in Fig. 9. The fracture of this steel was complex, involving intergranular, quasi-cleavage, and dimpled rupture modes. Some undissolved primary carbides were also observed in Steels B4 and B5. As shown in Fig. 10, these fine carbides were often associated with the dimpled rupture facets of the fracture. These and other observations strongly suggested that new balanced compositions should be formulated.

One intent in the design of the new steels is to explore the possibility of minimizing those solid-state reactions that lead either to embrittlement or to marked decreases in hardness. As mentioned earlier, these undesirable reactions usually involved the formation of Fe_3C at intermediate tempering temperatures. The subsequent precipitation of Fe_3C in grain and lath boundaries inevitably leads to a degradation of mechanical properties.

Independent studies in this laboratory and others have convincingly demonstrated that silicon, and especially silicon plus aluminum additions can alter the kinetics of formation of Fe_3C from epsilon-carbide [*9,16,28,29*]. Bhat [*28*] observed that the softening that normally occurs on tempering AISI 4340 steels beyond 200°C (392°F) was retarded by the additions of aluminum or combinations of aluminum and silicon, with the combined additions being more effective. The tempering behavior of some of these steels is shown in Fig. 11 from which it is observed that the tempering was retarded to temperatures as high as 400°C (752°F).

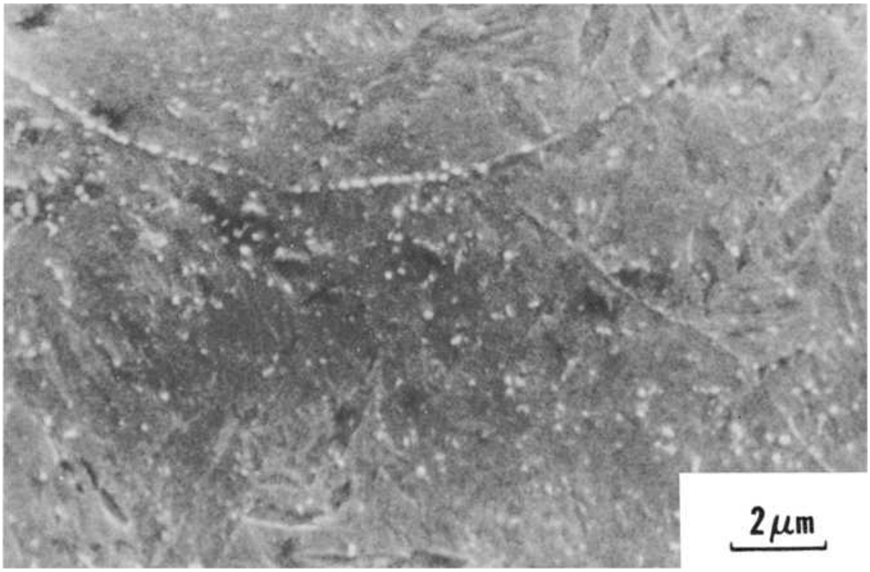

FIG. 9—*Scanning electron micrograph of Steel B4, austenitized for 1 h at 1000°C (1832°F).*

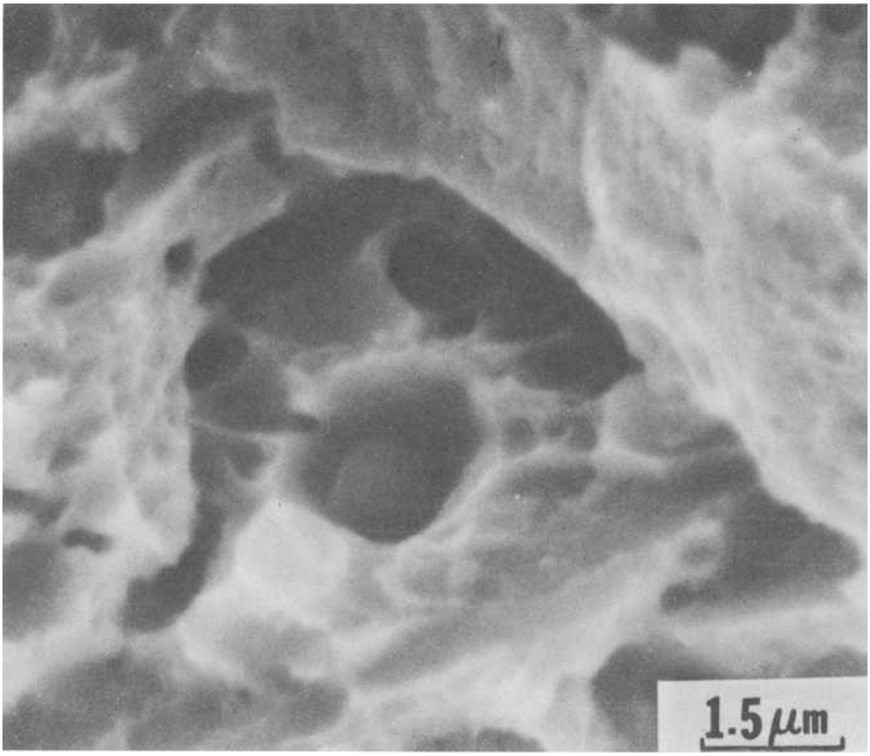

FIG. 10—*High magnification scanning electron fractograph of Steel B4, showing carbides associated with dimples.*

Even beyond this temperature, the modified steels maintained higher hardness, presumably due to lower growth rates of carbides in the presence of silicon and aluminum [*28*]. From an investigation of the tempering response and the microstructure, at the electron optical level, of these steels, it was concluded that additions of aluminum and combinations of aluminum and silicon to AISI 4340 steel resulted in: (*a*) the extension of the first stage of tempering to higher tempering temperatures, (*b*) an increase in the temperature for the second stage of tempering, (*c*) the retardation of the third stage of tempering to temperatures greater than about 350 to 400°C (662 to 752°F) depending upon the alloy content, and (*d*) an inhibition of the growth rate of carbides.

Figure 12 shows a comparison of one of the experimental steels with base AISI 4340 steel showing the following effects: (*a*) an increase in strength, (*b*) an increase in toughness, and (*c*) a shift in the tempered martensite embrittlement range to higher temperatures. Optimum yield strength and fracture toughness combinations of 245 ksi and 80 ksi$\sqrt{\text{in.}}$,

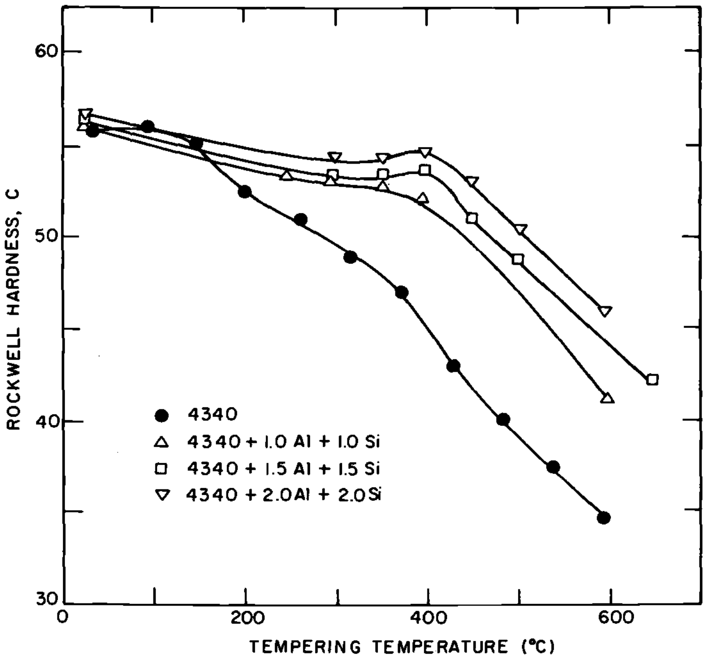

FIG. 11—*The influence of aluminum and silicon additions on the tempering behavior of AISI 4340 steel.*

significantly higher than those achievable in commercial low-alloy, ultra-high-strength steels, were attained.

The microstructural study of the modified steels led to the conclusion that optimum combinations of strength and toughness are obtained in the presence of: (*a*) fine dispersions of carbides in dislocated martensite, (*b*) retained austenite films at lath boundaries that are stable to stress/strain, and (*c*) smaller prior austenite grain sizes.

The study of the possible influence of silicon and aluminum on the tempering response of secondary hardening steels was an objective in the design of the new steels. Another intent in the design of the new steels was to achieve balanced compositions with respect to the austenitic and ferritic alloying elements. The carbide-forming elements, such as chromium, molybdenum, and vanadium, and the noncarbide formers, silicon and aluminum, are all strong ferrite stabilizers. The desirable composition of a secondary hardening steel is one that provides a large enough austenite phase field at solutionizing temperatures to dissolve all the carbides present, and that also has enough carbon and carbide-forming elements to provide the desired hardness.

The steels listed in Table 2 represent an initial attempt to achieve the

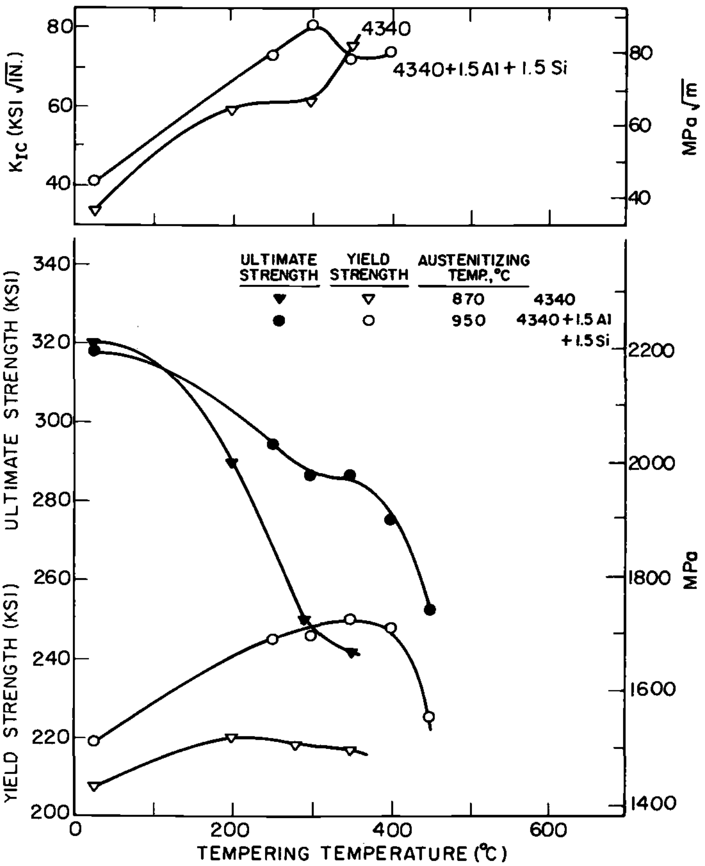

FIG. 12—*Plots of yield strength, ultimate tensile strength, and fracture toughness versus tempering temperature for AISI 4340 and modified AISI 4340 steels* [28].

TABLE 2—*Nominal compositions of new steels.*

	Composition, weight %								
Designation	C[a]	Mn	Mo	V	Cr	Ni	Al	Si	Fe
A10	0.35	0.5	2	0.4	1.0	3	1.5	1.5	balance
A14	0.28	0.5	2	. . .	1	3	. . .	. . .	balance
A15	0.35	0.5	2	. . .	1	3	. . .	1	balance
A16	0.29	0.5	2	. . .	1	3	. . .	2	balance
A17	0.31	0.5	2	. . .	1	3	. . .	3	balance
A18	0.35	0.5	2	. . .	1	3	1	. . .	balance
A19	0.34	0.5	2	. . .	1	3	1	1	balance
A20	0.33	0.5	2	0.25	1	3	. . .	. . .	balance
A21	0.36	0.5	2	0.25	1	3	1	1	balance

[a] Weight % of carbon was obtained by chemical analysis.

balance and to establish whether the addition of silicon and aluminum would be helpful in secondary hardening steels.

The influence of silicon content on the tempering behavior of several molybdenum-nickel-chromium steels is shown in Fig. 13. The hardness of the non-silicon steel (A14) decreases continuously to about 400°C (752°F) followed by a flattening of hardness curve occurring around 500 to 600°C (932 to 1112°F) indicating some secondary carbide precipitation. The hardness of Steel A16 (2 Si) is nearly constant with tempering temperature to 500°C (932°F) with a nearly imperceptible minimum at 400°C (752°F). The analogous curve for Steel A17 (3 Si) is displaced to a higher hardness and exhibits a dip in hardness at 200°C (392°F) for reasons probably related to the higher carbon content (relative to A14 and A16). The tempering behavior of Steel A15 (1 Si) is consistent with the trends shown for A14, A16, and A17, but is not plotted in Fig. 13.

Bhat's [*28*] studies with low- and medium-alloy, ultra-high-strength steels revealed that a combination of aluminum and silicon was more effective in enhancing the strength (hardness) and toughness than either aluminum or silicon alone. The tempering behavior of a steel containing combined additions of aluminum and silicon is compared with that of a steel containing no aluminum or silicon in Fig. 14. The effect of the combined aluminum plus silicon addition on the level and shape of the hardness curve, especially above 200°C (392°F) is striking. The effect of a combined aluminum plus silicon addition on the tempering behavior of a steel (A21) containing small amounts of another carbide former (vana-

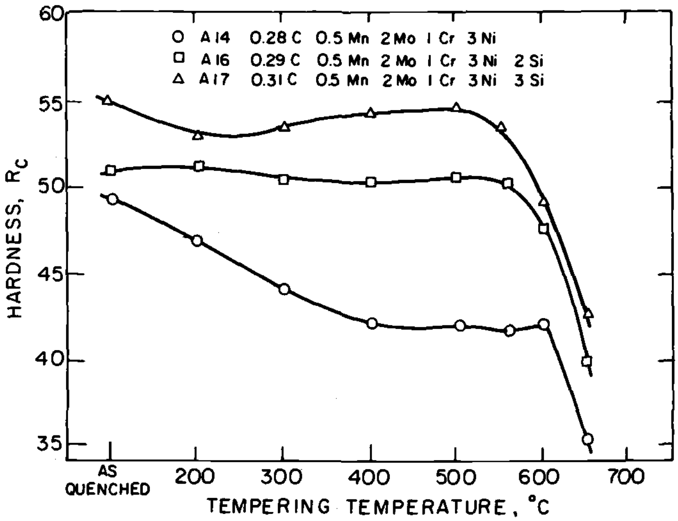

FIG. 13—*The variations of hardness with tempering temperature for Steels A14, A16, and A17, austenitized at 1100°C (2012°F).*

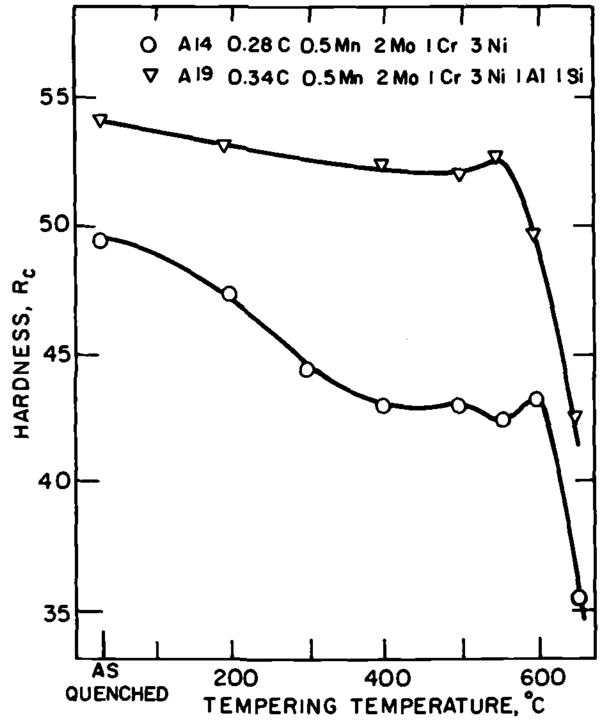

FIG. 14—*The variation of hardness with tempering temperature for Steels A14 and A19, austenitized at 1100°C (2012°F).*

dium) is similar, as shown in Fig. 15. It is well known that the element vanadium increases the temperature at which the hardness drops. The dip in the hardness versus tempering temperature curve at intermediate temperatures is not always eliminated by the combined aluminum plus silicon addition. However, the minimum hardness is invariably raised.

The hardness and toughness combinations of the new steels have not yet been completely determined, but a few selected measurements have been made and the properties of Steel A10 are worthy of comment. This chromium-nickel-molybdenum-vanadium-aluminum-silicon steel has a relatively high hardness versus tempering temperature curve, as shown in Fig. 16. At the secondary hardening temperature, 550°C (1022°F), it has a hardness of about 58 HRC and a measured room-temperature Charpy-impact energy of 20.3 J (15 ft · lb). Although these data are from small ingots and from single rather than multi-specimen tests, the attainment of these properties suggests that the combination of hardness and toughness specified for the feeder components will eventually be met.

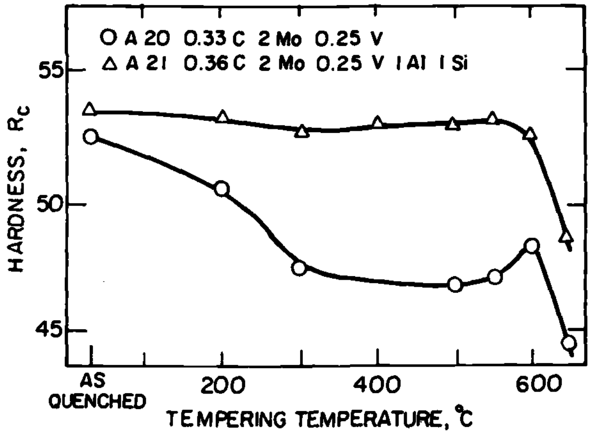

FIG. 15—*The variation of hardness with tempering temperature for vanadium-containing Steels A20 and A21, austenitized at 1100°C (2012°F).*

Coal Handling and Moving Equipment

Modified Commercial Alloys

In the section on materials requirements, it was stated that the combination of mechanical properties thought to be required for components in coal handling and moving equipment consisted of adequate hardness, toughness, and in all probability, impact fatigue resistance. The elimination of hot strength as a requisite property in these components considerably lessens the difficulties in the design of these steels.

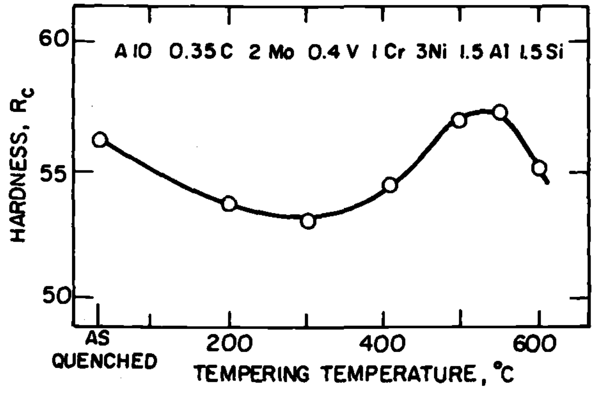

FIG. 16—*The variation of hardness with tempering temperature for Steel A10, austenitized at 1100°C (2012°F).*

Certain builders and users of earth (and coal) moving equipment have established a minimum of Charpy impact toughness for structural wear and abrasion resistant alloys as (20.3 J) (15 ft · lb) at −40°C (−40°F) [5]. Currently-used alloys meeting this minimum toughness have a maximum hardness in the 50 to 52 HRC range. In this study, a hardness goal of 54 to 55 HRC has been set at the (20.3 J) (15 ft · lb) Charpy level. It is noted, however, that combinations of toughness and hardness below the 54 to 55 HRC level that are superior to those in currently-available commercial steels would undoubtedly be welcome for many less severe applications.

As previously mentioned, it has been shown that the addition of aluminum and silicon to the popular, ultra-high-strength steel, AISI 4340, can enhance both its strength and toughness [28]. In this study, the modified AISI 4340 steel was used as a base in a series in which the carbon, silicon, and aluminum contents were varied, as shown in Table 3.

The tempering response of the first three modified steels, C1, C2, and C3, is shown in Fig. 17. The steels with higher carbon contents, C2 and C3, appear to have a slight peak in hardness at about 300°C (572°F). The variation of Charpy impact energy with tempering temperature for Steels C1 and C2 is shown in Figs. 18 and 19. The values of hardness and toughness of Steel C1 closely approximate those observed in an earlier investigation [28]. The best combination of hardness versus impact energy obtained was 54 HRC at (27.1 J) (20 ft · lb). For the Steel C2, which had a higher carbon content, the best combination of mechanical properties obtained was 56 HRC at (19.6 J) (14.5 ft · lb). The toughness values for Steel C3 (not plotted) were relatively low at all tempering temperatures. It appears that combined additions of aluminum and silicon greater than about 3 percent are not desirable. These studies suggest that with further refinements in composition and heat treatment, the desired properties should be attainable in medium-alloy steels whose technology is well known to the steel industry.

Acknowledgments

The author wishes to express his gratitude to Dr. M. Bhat, project leader, and graduate students Warren Garrison, Tom Lechtenberg, and

TABLE 3—*Nominal compositions of modified AISI 4340 steels.*

	Composition, weight %							
Designation	C	Mn	Si	Al	Cr	Mo	Ni	Fe
C1	0.4	0.7	1.8	1.5	0.8	0.3	1.8	balance
C2	0.5	0.7	1.8	1.5	0.8	0.3	1.8	balance
C3	0.5	0.7	2.3	2.0	0.8	0.3	1.8	balance

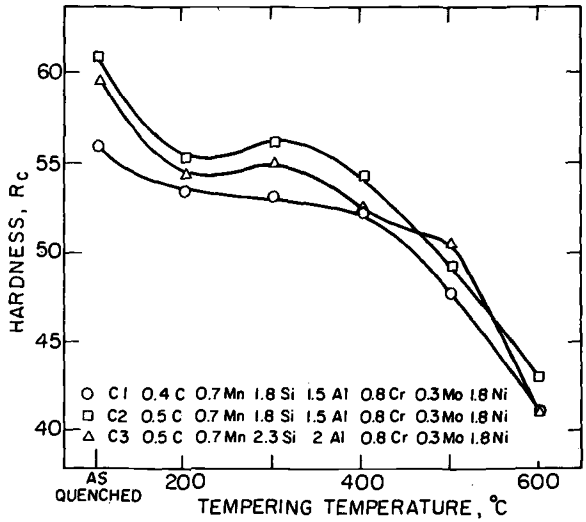

FIG. 17—*The variation of hardness with tempering temperature of Steels C1, C2, and C3.*

Naresh Kar for the use of their unpublished data. He also thanks his friend and colleague, Prof. Earl Parker, and Drs. Bhat and Horn for their detailed critique of the manuscript, and R. B. Mundhe for his assistance in the preparation of the manuscript.

The author is especially grateful to Wate Bakker and Dr. Tom Cox, Energy Technology, Department of Energy, for their constant support, encouragement, and guidance of this effort over the past two years.

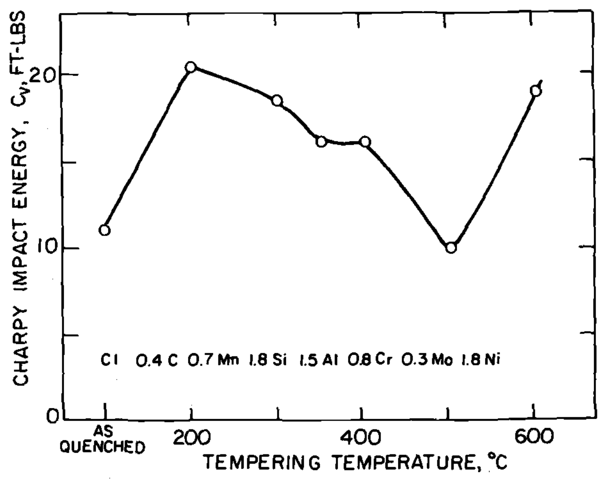

FIG. 18—*The variation of Charpy impact energy with tempering temperature of Steel C1, austenitized at 1000°C (1832°F).*

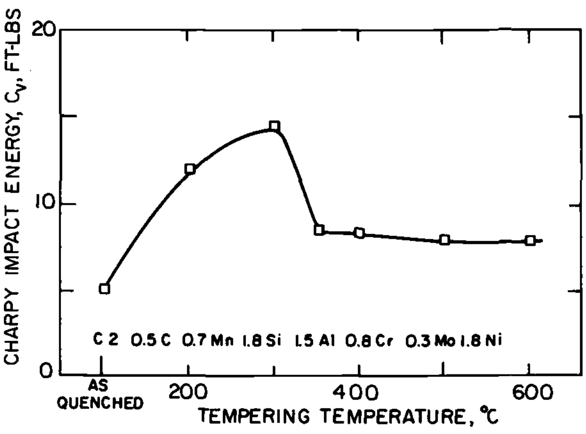

FIG. 19—*The variation of Charpy impact energy with tempering temperature of Steel C2, austenitized at 950°C (1742°F).*

References

[1] "A National Plan for Energy Research, Development and Demonstration: Creating Energy Choices for the Future," ERDA-76-1, Vol. 1, 1976.

[2] Fossil Energy Program Report, ERDA, 76–10, 1975–1976.

[3] Phen, R. L., Lucklow, W. K., Mattson, L., Otth, D., and Tsou, P., *Proceedings*, Conference on Coal Feeding Systems, Pasadena, 21–23 June 1977, JPL Publication 77–55, Jet Propulsion Laboratory, Pasadena, Calif. p. 324.

[4] Fields, S. F., *Proceedings*, Conference on Coal Feeding Systems, Pasadena, 21–23 June 1977, JPL Publication 77–55, Jet Propulsion Laboratory, Pasadena, Calif. p. 359.

[5] Bhat, M. S., Zackay, V. F., and Parker, E. R., "Wear Resistant Alloys for Coal Handling Equipment," Progress Report, 1 Jan. to 30 Sept. 1977, Materials and Molecular Research Div., Lawrence Berkeley Laboratory, University of California, Berkeley, Calif.

[6] Saltzman, G. A., *Plastics Design and Processing*, Dec. 1973, p. 9.

[7] Saltzman, G. A., *Proceedings*, International Conference on Wear of Materials, St. Louis, Mo., April 1977, W. A. Glaeser, K. C. Ludema, and S. K. Rhee, Eds., The American Society of Mechanical Engineers, New York, p. 217.

[8] Hurricks, P. L., *Wear*, Vol. 26, 1973, p. 285.

[9] Muscara, J. and Sinnot, M. J., *Metals Engineering Quarterly*, Vol. 12, No. 2, 1972, p. 21.

[10] Borik, F. and Schalz, W. G., *Journal of Materials*, Vol. 6, No. 3, 1971, p. 576.

[11] Diesburg, D. E. and Borik, F., "Materials for the Mining Industry," Climax Molybdenum Co. 1974, p. 15.

[12] Bhansali, K. J. and Silence, W. L., *Metals Progress*, Vol. 112, No. 6, 1977, p. 39.

[13] Silence, W. L., *Proceedings*, International Conference on Wear of Materials, St. Louis, Mo., April 1977, W. A. Glaeser, K. C. Ludema, and S. K. Rhee, Eds., The American Society of Mechanical Engineers, p. 77.

[14] Budinski, K. G., *Proceedings*, International Conference on Wear of Materials, St. Louis, Mo., April 1977, W. A. Glaeser, K. C. Ludema, and S. K. Rhee, Eds., The American Society of Mechanical Engineers, p. 100.

[15] Kruschov, M. M., *Wear*, Vol. 28, 1974, p. 69.

[16] *A Catalog of Friction and Wear Devices*, 2nd ed. American Society of Lubrication Engineers, Park Ridge, Ill., 1972.

[17] Borik, F., *Metals Engineering Quarterly*, Vol. 12, No. 2, 1972, p. 33.

[18] Blickensderfer, R., Deardorff, D. K., and Kelley, J. E., Report of Investigations 7930, U.S. Department of the Interior, Bureau of Mines, Albany Metallurgical Research Center, Albany, Ore., 1974.
[19] Contractor, G. P., Schempp, E. G., and Morgan, W. A., *Transactions,* American Society of Metallurgists, Vol. 54, 1961, p. 208.
[20] Speich, G. R., *Transactions,* Metallurgical Society, American Institute of Mining, Metallurgy, and Petroleum Engineers, Vol. 245, Dec. 1969, p. 2553.
[21] Goolsby, R. D., Ph.D. thesis, LBL-405, Lawrence Berkeley Laboratory, University of California, Berkeley, preprint, Nov. 1971.
[22] Horn, R. M., and Ritchie, R. O., LBL-6607, Lawrence Berkeley Laboratory, University of California, Berkeley, preprint, Nov. 1977.
[23] Thomas, G., LBL-5732, Lawrence Berkeley Laboratory, University of California, Berkeley, preprint, Oct. 1977.
[24] Speich, G. R., and Leslie, W. C., *Metallurgical Transactions*, Vol. 3, 1972, p. 1043.
[25] Tom, T., D. Eng. thesis, LBL-1856, Lawrence Berkeley Laboratory, University of California, Berkeley, preprint, Sept. 1973.
[26] Ritchie, R. O., Francis, B., and Server, W. L., *Metallurgical Transactions A,* Vol. 7A, 1976, p. 831.
[27] Ritchie, R. O. and Horn, R. M., *Metallurgical Transactions A,* Vol. 9A, 1978 (in press).
[28] Bhat, M. S., Ph.D. thesis, LBL-6046, Lawrence Berkeley Laboratory, University of California, Berkeley, preprint, Feb. 1977.
[29] W. S. Owen, *Transactions,* American Society of Metallurgists, Vol. 46, 1954, p. 812.

Morris Cohen[1] *and S. S. Hansen*[2]

Microstructural Control in Microalloyed Steels*

REFERENCE: Cohen, Morris and Hansen, S. S., "**Microstructural Control in Microalloyed Steels,**" *MiCon 78: Optimization of Processing, Properties, and Service Performance Through Microstructural Control, ASTM STP 672,* Halle Abrams, G. N. Maniar, D. A. Nail, and H. D. Solomon, Eds., American Society for Testing and Materials, 1979, pp. 34–52.

ABSTRACT: High-strength low-alloy (HSLA) steels constitute a classic metallurgical development in which alloying additions and thermomechanical processing have been brought together effectively to attain desired combinations of engineering properties through microstructural control. Moreover, the microstructural control is relatively inexpensive because the alloying elements are used only in small concentrations as carbide-formers, and the associated thermomechanical processing is introduced merely as a modification of the final hot-rolling operation. A key feature of the resulting microstructure is the small ferritic grain size that provides a favorable balance of strength and toughness in the as-rolled steel.

Here, we examine the interactions in columbium-treated HSLA steels among austenite chemistry, plastic deformation, strain-induced carbonitride precipitation, recrystallization characteristics, and the subsequent transformation of the thermomechanically-processed or *conditioned* austenite to the final ferrite-based structures. The latter transformations are studied in order to relate the ferrite nucleation and growth as well as its ultimate morphology to the state of the prior austenite.

KEY WORDS: steels, microstructure, HSLA steels, carbonitride precipitation, austenite recrystallization, austenite transformation, ferritic grain refinement, structural control

Over the past decade, high-strength low-alloy (HSLA) steels have emerged as cost-effective, relatively high strength-to-weight engineering materials for increasingly energy-efficient designs. Appropriate compositional and processing control can develop yield strengths typically in the range of 350 to 700 MPa (50 to 100 ksi), thus doubling the corresponding

---

* Part of the new results reported in this paper are taken from a Doctor of Science degree thesis by S. S. Hansen at the Massachusetts Institute of Technology, February 1978.

[1] Institute Professor Emeritus, Department of Materials Science and Engineering, Massachusetts Institute of Technology, Cambridge, Mass. 02139.

[2] Associated with the Research Department, Bethlehem Steel Corporation, Bethlehem, Pa. 18016.

strength levels of mild steels. At the same time, the associated toughness and weldability have paved the way for applications in transportation, pipe line, construction, and pressure-vessel technologies.

Today's commercial HSLA steels are predominantly low in carbon (0.05 to 0.15C) and alloyed with small quantities of strong carbide-forming elements such as columbium, vanadium, or titanium [*1,2*].[3] These steels are essentially ferritic as used, with minor amounts of pearlite, although low-carbon bainitic (or acicular ferritic) steels[4] have been introduced [*4*]. For the most part, the microalloying is intended to contribute to enhanced combinations of mechanical properties primarily through ferritic grain refinement, often supplemented by precipitation or substructural (dislocation) strengthening or both.

As we shall see, the effectiveness of microalloying is closely linked to the thermomechanical processing of the austenite prior to its transformation on cooling to the ambient. In this connection, considerable attention has been directed to controlled rolling [*5*] as a feasible alternative to the conventional hot rolling and controlled cooling [*6*] after rolling, for the purpose of beneficially modifying the final ferritic structure. Such continuing developments have led to the introduction of HSLA steels as a new class of ferrous materials in which the chemistry, thermomechanical processing, and the ensuing structure/property relationships have become a tightly coupled system.

Structure/Property Relationships in HSLA Steels

Comprehensive reviews dealing with the dependence of properties on the microstructure of microalloyed steels are available [*7–9*]. In the present context, we need only highlight the following points concerning the relevant mechanisms of strengthening, illustrated by Fig. 1.

Grain Refinement

Grain refinement of the ferrite is a major mode of strengthening in HSLA steels. Based on the Hall-Petch type of strengthening increments [*10*] as in Fig. 1, a decrease of ferritic grain size from ASTM 6–8 (typical of hot-rolled mild steels) to ASTM 12–13 (typical of HSLA steels) is accompanied by an increase in yield strength of about 210 MPa (30 ksi).

---

[3] The italic numbers in brackets refer to the list of references appended to this paper.

[4] In this paper, we shall concentrate on the principles of microstructural control for polygonal ferrite (plus pearlite) structures in microalloyed steels. Acicular structures and the still more recent *dual phase* steels [*3*], although important in themselves, will not be treated here.

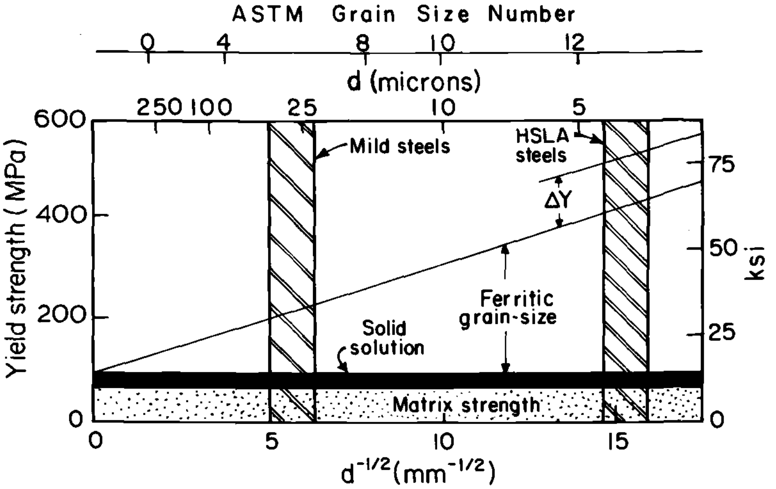

FIG. 1—*Schematic diagram illustrating possible strengthening mechanisms operative in low-carbon steels (adapted from Ref* 10).

Precipitation and Substructural Strengthening

Precipitation and substructural strengthening, indicated by the increment ΔY in Fig. 1, can provide substantial strengthening. In microalloyed steels, the precipitation strengthening may range up to 175 MPa (25 ksi) due to the formation of fine alloy carbides, nitrides, or carbonitrides (all such precipitates are collectively referred to as carbonitrides in this paper). Comparable strengthening additions can be obtained by rolling the austenite into the two-phase ($\alpha + \gamma$) region where the ferrite acquires substructural features due to strain hardening.

An important aspect of the preceding strengthening mechanisms is their influence on toughness, and this is portrayed in Fig. 2 [7]. Here, strength/toughness vectors are shown, comparing the effects of grain refinement, precipitation, and substructural strengthening on the impact transition temperature (ITT) of HSLA steels. Clearly, grain refinement has special significance, because it is the only mechanism that improves the strength and toughness concurrently. Therefore, if the other mechanisms are employed to raise the strength level, attaining the finest practicable ferritic grain size is still an overriding objective in order to compensate for the loss of toughness that would otherwise be introduced.

Factors Influencing the Ferritic Grain Size

The development of a fine ferritic grain size in as-rolled HSLA steels requires microstructural control of the austenite during rolling, and of the

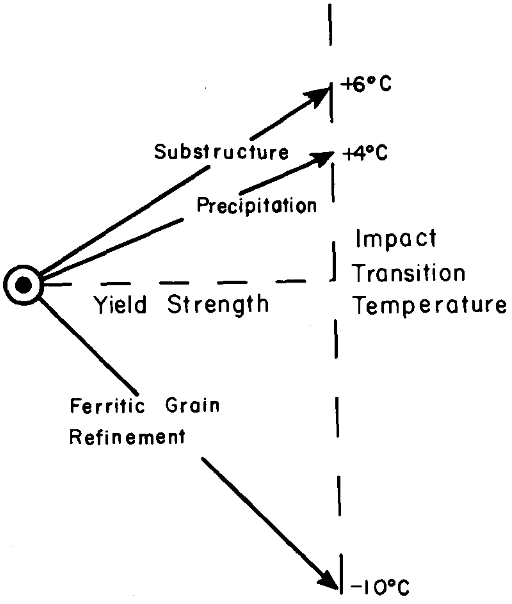

FIG. 2—*Factors affecting yield strength and impact transition temperature. Numbers indicate the change in transition temperature per 15 MPa (2.25 ksi) increase in yield strength* [7].

ferrite during transformation. The influence of various aspects of the hot-rolling process on the significant microstructural variables are illustrated in Fig. 3. The hot-rolled microstructure and properties resulting therefrom are a direct consequence of the austenite morphology prior to transformation, and of the austenite-to-ferrite ($\gamma \rightarrow \alpha$) transformation characteristics.

The austenite morphology prior to transformation is determined by the austenite recrystallization and grain-growth rates, both of which are affected by (*a*) temperature, (*b*) the amount of deformation, and (*c*) the microalloying elements in solid solution or precipitated as carbonitrides. The ferritic grain size, in turn, is governed by the prior austenite morphology, and the ferrite nucleation and growth rates. These rates are influenced by the prior austenite and precipitate morphologies as well as by the alloying elements and process variables (for example, cooling rate or coiling temperature) that determine the temperature range over which the $\gamma \rightarrow \alpha$ transformation occurs.

We will now consider each of these aspects of microstructural control in more detail.

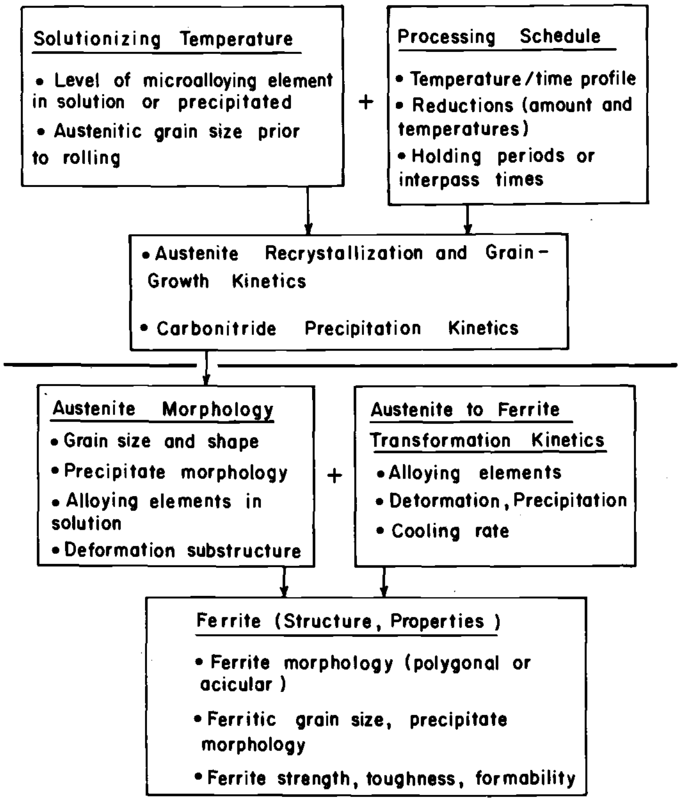

FIG. 3—*Interactions between process and compositional variables during hot-rolling of HSLA steel.*

Microstructural Control of the Austenite During Rolling

Austenites in HSLA steels are *conditioned* by appropriate thermomechanical processing that typically involves the solution and precipitation of carbonitrides during such processing. This type of microstructural control may also bring about refinement of the austenitic grain size prior to hot-rolling or the retardation of austenite recrystallization and grain growth during or after the hot deformation or both. From the standpoint of austenite recrystallization and grain growth, the hot-rolling of HSLA steels can be divided into four stages [*11*], as illustrated in Fig. 4.

Stage I rolling comprises high-temperature deformation (usually above 1000°C for commercial HSLA steels), followed by rapid austenite recrystallization after each pass. Subsequent grain growth at these high temperatures may allow only minimal structural refinement after rolling, but

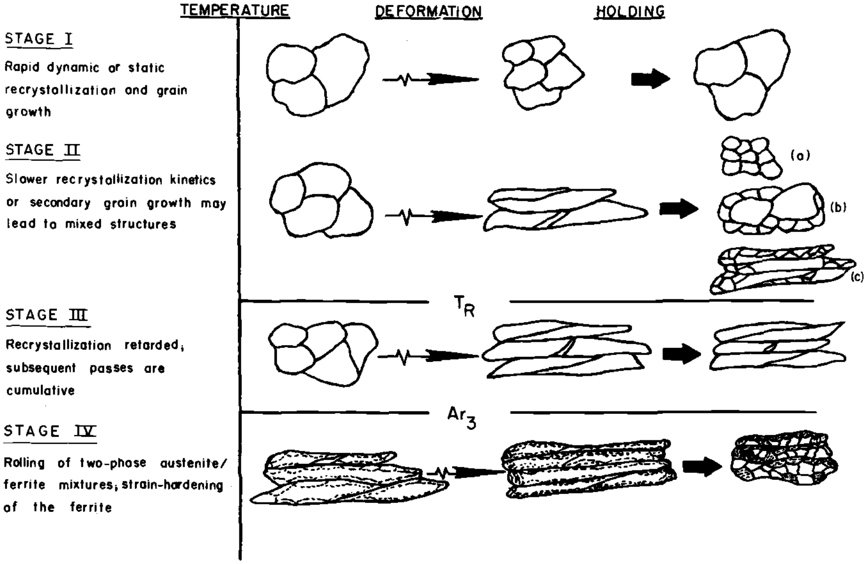

FIG. 4—*Four stages of hot rolling in the thermomechanical processing of HSLA steel.* T_R *is the rolling temperature below which a critical degree of carbonitride supersaturation is reached to inhibit austenite recrystallization by carbonitride precipitation.*

some grain-size control can be retained in the presence of a finely dispersed second phase [*12*].

At somewhat lower hot-rolling temperatures (Stage II), complete recrystallization and minimal grain growth of the austenite may lead to grain refinement (Case a); alternatively, partial recrystallization (Case c) or discontinuous coarsening after recrystallization (Case b) may take place, resulting in mixed structures.

In the lower austenitic regime of hot-rolling (Stage III), down to Ar_3, austenite recrystallization is retarded. Here, subsequent passes are *cumulative* in the sense that the austenitic grains become more and more pancaked in shape prior to their transformation on cooling.

Finally, Stage IV involves rolling below Ar_3, that is, deformation of austenite-ferrite mixtures. The ferrite becomes strain-hardened and may develop a dislocation substructure as well as a texture [*13*]. These changes result in higher strength, via substructural strengthening, but with poorer impact properties.

Thus, thermomechanical processing of the austenite leads to a wide variety of possible austenite morphologies. Such structural evolution becomes important to understand, because there is then a significant effect on the subsequent transformation. Naturally, the temperature regimes over which these changes occur (that is, Stages I to IV) vary with steel composition and, in particular, with the microalloying additions.

Under typical hot-rolling conditions (>950°C), austenite recrystallization follows each rolling pass. Successive passes may tend to produce some further grain refinement, but there seems to be a limit to the degree of structural refinement that can be achieved by repeated recrystallization. Data plotted in Fig. 5 [*14*] for simulated plate rolling of a columbium-treated HSLA steel indicate an *asymptotic* recrystallized austenitic grain size approaching 20 μm. A similar limiting trend is shown compared to the austenitic grain size *prior* to deformation (Fig. 6). It will be noted that the degree (ratio) of austenitic refinement due to recrystallization in these columbium steels decreases progressively with decreasing initial grain size, down to a minimum of about 20 μm for the recrystallized grain size. These findings suggest that, realistically, in order to obtain still finer austenitic grain sizes, recrystallization must be avoided, and this is

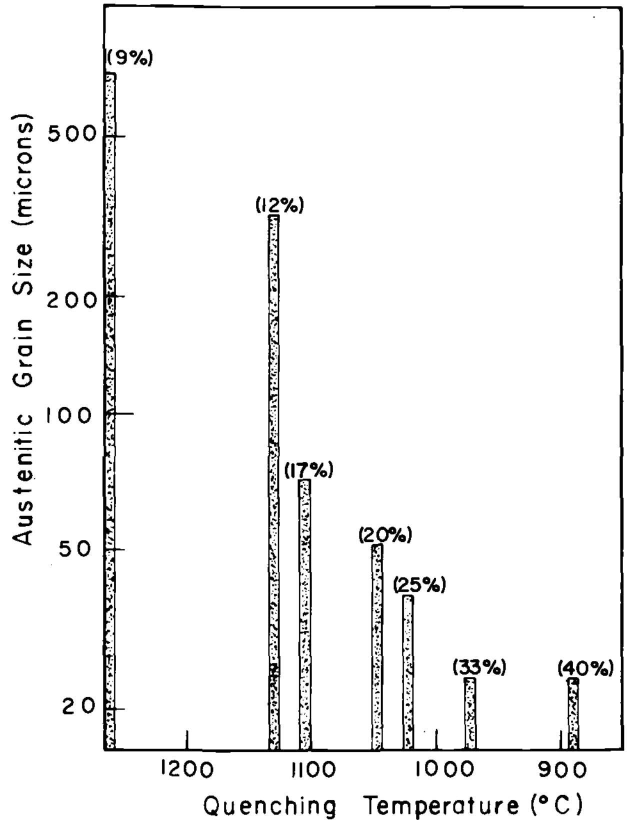

FIG. 5—*Progressive austenitic grain refinement via recrystallization during simulated plate rolling of a 0.1C-1.4Mn-0.05Cb steel. The austenite was reduced at the indicated temperature by the amount shown in parentheses and quenched 7 s after deformation* [14].

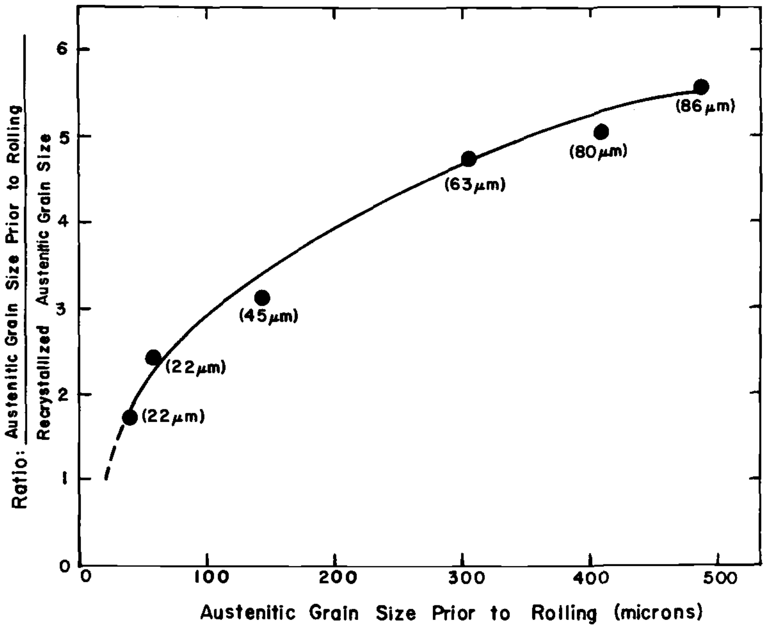

FIG. 6—*Degree of austenitic grain refinement in a series of columbium-treated HSLA steels achieved via recrystallization after a 50 percent reduction, as a function of the initial austenitic grain size. As-recrystallized grain sizes are shown in parentheses.*

why alloying elements that inhibit austenite recrystallization (during and after hot rolling) are needed. Since subsequent rolling passes are then cumulative in continuing to flatten the grains, the effective refinement of the austenite can be carried to extremely small lateral dimensions prior to the eventual transformation. Accordingly, the mechanism and control of the recrystallization retardation become key factors in HSLA steel processing.

Retardation of Austenite Recrystallization

Numerous investigations have shown that under suitable conditions, vanadium, titanium, and columbium can retard austenite recrystallization during and after hot rolling. Although columbium has received the most attention to date in this respect, nevertheless, the precise nature of its effect on austenite recrystallization has not been established. The operative mechanism has been variously ascribed to *solute drag*, or more frequently to *precipitate pinning*. Recent work has attempted to answer this question [*15–17*], but the data are conflicting and leave the problem unresolved.

More recently, we have studied austenite recrystallization in a series of

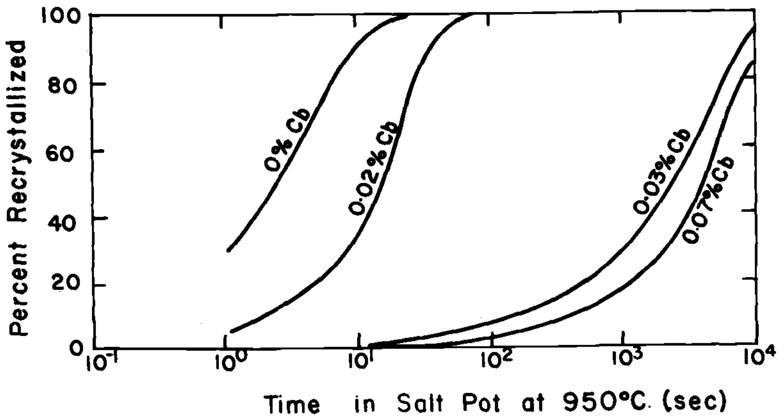

FIG. 7—*Austenite recrystallization kinetics at 950°C for the indicated levels of columbium in solid solution prior to 50 percent deformation at 950°C.*

columbium steels by quantitative metallography[5], and have also monitored the Cb(C,N) precipitation by carbide-extraction replicas. Typical recrystallization curves are given in Fig. 7 for different levels of columbium in solid solution prior to hot rolling.[6] The recrystallization process is seen to be retarded as a function of increasing columbium in solid solution before the deformation; although there is a detectable effect due to 0.02Cb, the major change between the 0.02 and 0.03Cb levels is particularly striking. There are also two noteworthy effects at the 0.03 and 0.07Cb levels: (1) a definite incubation period for the initiation of recrystallization; and (2) a slow recrystallization growth rate, once recrystallization is underway.

The concomitant Cb(C,N) precipitation reaction in the unrecrystallized austenite takes place in two stages (Fig. 8). There is an initial precipitation along austenitic grain boundaries and deformation bands[7] (Fig. 8*a*). This precipitation occurs very rapidly after rolling, and the particles coarsen rather quickly on further holding. In the second stage, a more general Cb(C,N) precipitation sets in, mainly on prior austenitic subboundaries

---

[5] The austenite in HSLA steels cannot be observed directly, due to its transformation on cooling to room temperature. Therefore, the prior austenitic structure was delineated in the as-quenched martensitic matrix by hot-etching at 50 to 60°C in a solution of saturated aqueous picric acid plus 1 percent (by volume) of sodium alkyl sulphonate.

[6] The solubility calculations were based on the equation of Irvine et al [*2*]:

$$\log_{10}([\%\text{Cb}]\cdot[\%\text{C}+\frac{12}{14}\%\text{N}]) = 2.26 - \frac{6770}{\text{T(K)}}.$$

[7] On quenching from the austenitic phase field, a trace amount of ferrite forms at prior austenitic boundaries. Hence, on the replicas, the boundaries can be distinguished from the grain interiors by the contrast between the ferrite (F) and the martensite (M).

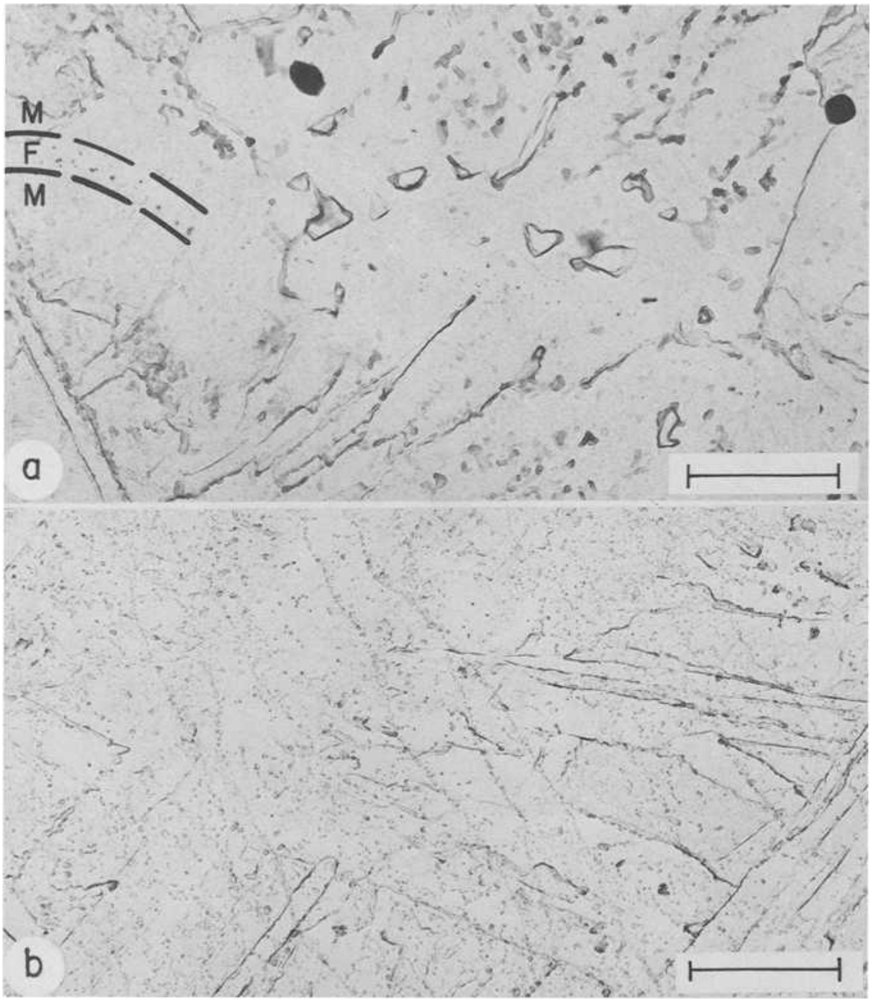

FIG. 8—*Extraction replicas showing (*a*) Cb(C,N) precipitation at a prior austenitic grain boundary and (*b*) Cb(C,N) precipitation on prior austenitic substructure. Scale mark indicates 1 μm.*

(Fig. 8*b*). The latter precipitate morphology has been observed previously (for example, in Ref *18*), and used as evidence for the *precipitate pinning* of subboundaries.

The precipitate size distribution and the areal density of precipitates can be combined to define a parameter (*K*), such that [*19*]:

$$K = N_s' (\bar{x}_A^2 + \sigma_A^2)$$

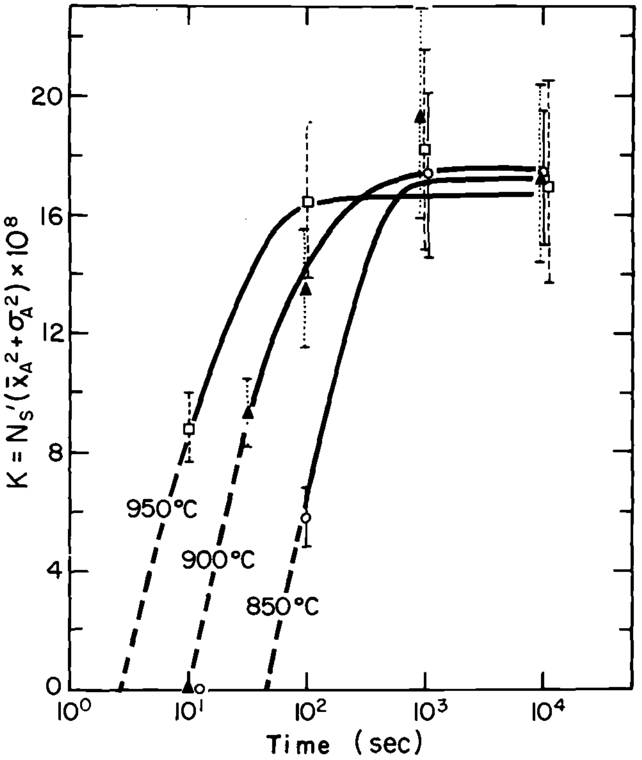

FIG. 9—*Plot of the* K *parameter, as an index of precipitate volume fraction in a 0.1C-1.3Mn-0.095Cb steel after 50 percent deformation of austenite at 950°C, and holding for various time/temperature combinations. Error bars represent two times the standard deviation of the average.*

where

N_s' = measured number of precipitate particles per unit area on the replica,
$\bar{x}_A$ = arithmetic mean of particle diameters, and
σ_A = standard deviation from the mean.

Following Ashby and Ebeling [*19*], K is proportional to the precipitate volume fraction if the extraction efficiency (that is, the fraction of the existing precipitated particles that are extracted and retained on the replica) is the same from replica to replica. Typical results for a 0.095Cb steel are shown in Fig. 9. The Cb(C,N) precipitation rate obviously decreases with decreasing temperature in the austenitic range, indicating that 950°C is below the nose of the precipitation C-curve for this steel.

Such recrystallization and precipitation kinetics can be assembled in the form of recrystallization/precipitation/time/temperature (RPTT) diagrams, as in Fig. 10. In this example, wherein austenite recrystallization is found to be significantly retarded (Fig. 7), the Cb(C,N) precipitation precedes the start of recrystallization at all temperatures, and the major retardation occurs after the precipitation reaction is complete. Hence, *solute drag* arguments are clearly inadequate since there is essentially no columbium left in solution over the time when the inhibition of recrystallization is most pronounced.

Order-of-magnitude calculations show that the Cb(C,N) precipitation on the austenitic substructure is sufficient to provide a pinning force comparable to the driving force for recrystallization. Furthermore, the recrystallization growth rates are observed to decrease with increasing volume fraction and decreasing particle size of the Cb(C,N) particles, just as expected from precipitate pinning. However, austenite recrystallization is not appreciably affected by Cb(C,N) precipitates existing *prior* to rolling [*15*] (that is, solution of the carbonitrides before rolling is necessary).

Not only does precipitation subsequent to hot rolling impede recrystallization, but the precipitation is accelerated by the deformation (being very rapid in deformed, unrecrystallized austenite and very slow in unstrained or recrystallized austenite [*20*]). At the same time, we have

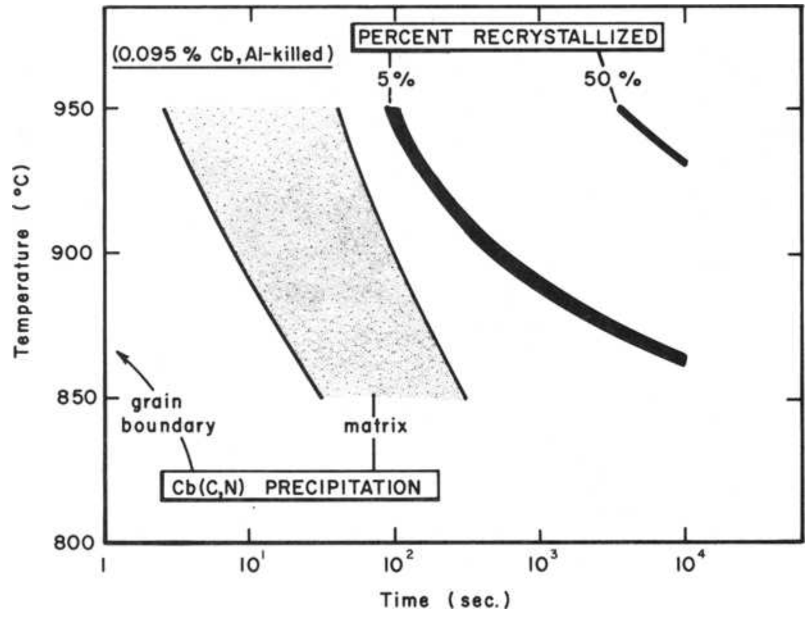

FIG. 10—*Recrystallization/precipitation/time/temperature diagram for a 0.1C-1.3Mn-0.095Cb steel, following 50 percent deformation of austenite at 950°C.*

seen that the recrystallization itself is inhibited if it is preceded by precipitation. Consequently, the condition necessary for an effective interaction between precipitation and recrystallization is that the precipitation must be rapid enough to precede austenite recrystallization, that is, a sufficient Cb(C,N) supersaturation must exist at the rolling temperature so that *strain-induced* precipitation will precede austenite recrystallization. Evidently, at 950°C, 0.03Cb in solution provides the required supersaturation, while 0.02Cb does not. This means that the critical supersaturation ratio in these steels lies between 5 and 7.5.[8]

The results of such investigations can be summarized with respect to the recrystallization/precipitation interaction as follows:

(*a*) There is substantial retardation of austenite recrystallization if Cb(C,N) precipitation occurs prior to or during the early stages of the recrystallization. However, if austenite recrystallization precedes such precipitation, there may still be a small retardation of the recrystallization, presumably attributable to solute drag.

(*b*) There is a two-way interaction between austenite recrystallization and Cb(C,N) precipitation, inasmuch as the precipitation reaction is accelerated in an unrecrystallized austenite, and the recrystallization reaction is retarded by Cb(C,N) precipitation on austenite subboundaries.

(*c*) The criterion for an effective precipitation/recrystallization interaction appears to be the degree of Cb(C,N) supersaturation at the rolling temperature.

It is suspected that a similar criterion may be applicable to titanium and vanadium HSLA steels, and may explain why commercial vanadium (0.1V) and low titanium additions (0.03Ti) have been reported as ineffective in retarding austenite recrystallization [*2*]. In fact, higher vanadium [*21*] or higher titanium [*6*] concentrations in solution do become effective. On this basis, a recrystallization temperature (T_R) can be estimated for various HSLA steel compositions, defined as that rolling temperature below which austenite recrystallization is essentially inhibited via carbonitride-precipitate pinning because a critical degree of supersaturation is then reached. Stage III rolling in Fig. 4 would then extend from T_R to Ar_3, but would be nonexistent if $T_R < Ar_3$.

We are now ready to consider the transformation, particularly to ferrite, of the recrystallization-inhibited austenite.

Transformation of Conditioned Austenites

As detailed previously, various thermomechanical or *conditioning* treatments can result in a variety of austenite morphologies prior to

---

[8] The supersaturation ratio is defined as:

$$\frac{[\mathrm{Cb}]_{\mathrm{solution}}[\mathrm{C} + 12/14\ \mathrm{N}]_{\mathrm{solution}}}{\mathrm{Cb(C,N)\ solubility\ product\ at\ the\ rolling\ temperature}}$$

transformation. However, in terms of ferritic grain refinement, the principal structures are recrystallized polygonal versus unrecrystallized pancaked austenites. Although austenitic grain refinement via recrystallization is usually reflected in a finer ferritic grain size on transformation, this type of structural control appears to have its limits, as we have observed, even with repeated rolling-recrystallization cycles of the austenite. This means there is also a limiting *ferritic* grain size that can result on transformation from recrystallized austenites.

The limiting ferritic grain size can be approximated by considering the case in which ferrite-nucleation sites (that is, austenitic grain boundaries) are effectively saturated; the average ferrite-growth distance, and hence the ferritic grain size, is then about one half the prior austenitic grain diameter. In columbium steels, we have found that the smallest recrystallized austenitic grain size is about 20 μm (ASTM 8) (Figs. 5 and 6), thus leading to a ferritic grain size of about 10 μm (ASTM 10). This represents a useful degree of ferritic grain refinement, but is not exceptional.

On transformation from unrecrystallized pancaked austenites, however, the potential minimum ferritic grain size is governed by the thickness of the deformed austenitic grains. This parameter depends on the austenitic grain size prior to Stage III deformation, but more importantly on the rolling reduction below T_R. The latter low-temperature deformation increases the effective surface-to-volume (S_v) ratio of the austenitic grains by increasing the grain aspect ratio, and also results in the introduction of numerous deformation bands within the austenite, which likewise provide ferrite-nucleation sites (Fig. 11). The deformation-band density increases with the extent of rolling in Stage III but is insensitive to the grain size or rolling temperature in this range (Fig.

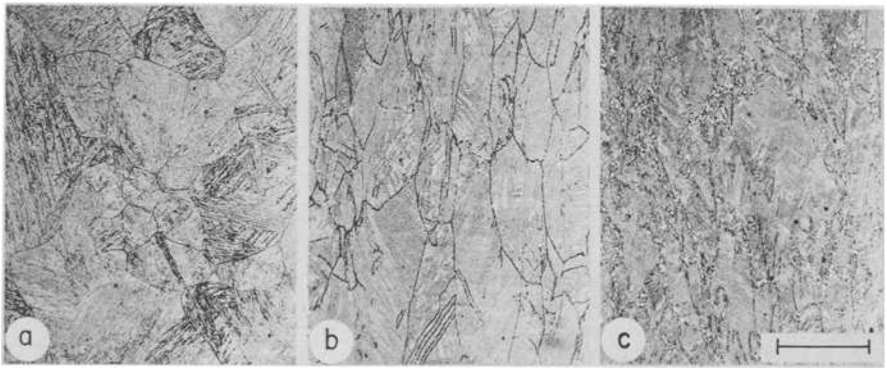

FIG. 11—*Series of micrographs of a 0.1C-1.3Mn-0.095Cb steel that was solutionized (1250°C for 1 h), deformed 50 percent at 950°C, and partially transformed (800°C for 10 000 s), showing:* (a) *structure prior to deformation,* (b) *deformed structure, and* (c) *partially transformed structure. Scale mark indicates 200 μm.*

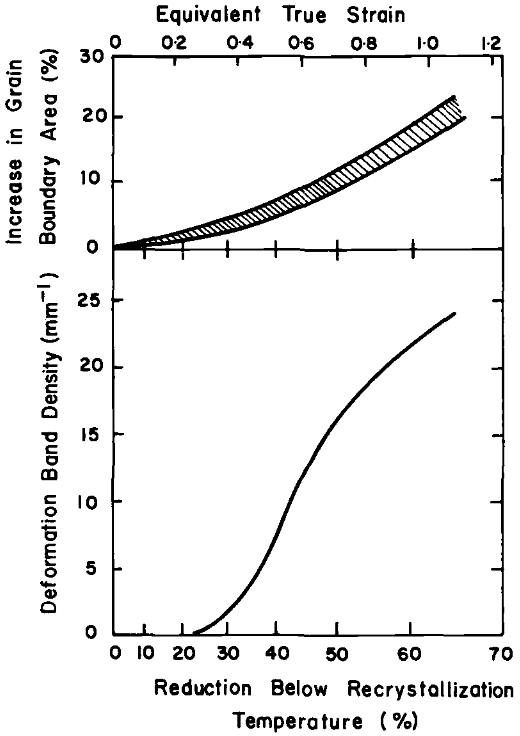

FIG. 12—*Increase in austenitic grain-boundary area and in deformation-band density with increasing deformation below* T_R. *The rolling temperature varied from 800 to 900°C, and the austenitic grain size prior to rolling from ASTM 1.6 to ASTM 4.8* [22].

12) [22]; the generation of deformation bands appears to approach a practical limit beyond about 65 percent reduction. In any event, it is evident that finer ferritic grain sizes may be expected in the limit from unrecrystallized austenites than from recrystallized austenites. For example, if a 20 μm (ASTM 8) austenitic grain size exists just prior to Stage III rolling, and a cumulative reduction of 80 percent is applied below T_R, then on transformation, the ferritic grain size may be smaller than 2 μm (ASTM 14–15). This degree of grain refinement, compared to the ferritic grain size obtainable from the finest recrystallized austenitic grain size, corresponds to a strengthening increment of 280 MPa (40 ksi). Therefore, we see that the transformation characteristics of unrecrystallized austenites warrant particular attention.

A typical transformation sequence in an unrecrystallized austenite on continuous cooling (~0.2°C/s)[9] is illustrated in Fig. 13. Trace amounts of

---

[9] This cooling rate is calculated on the basis of time spent between 750 and 450°C, and is roughly equivalent to that at the center of an air-cooled 2-in. plate.

ferrite are evident at 750°C, and by 700°C, considerable transformation has taken place. At this point, all prior austenitic grain boundaries are covered by ferrite, and appreciable intragranular nucleation has also occurred. Ferrite formation is almost complete at 650°C, while on further cooling, most of the remaining austenite transforms to pearlite. The duplex ferritic grain size in the fully transformed structure is typical of controlled-rolled steels. The finest ferritic grains are associated with prior austenitic grain boundaries and deformation bands, their continued growth being stopped mainly by impingement against other ferrite grains (arrows in Fig. 13). Because fine-grained ferrite is desirable, it is advantageous to have a fine austenitic grain size prior to Stage III deformation and to increase the amount of this deformation [*23*]. Nevertheless, in view of the heterogeneous nature of the rolling process, some coarser-grained ferrite may ultimately result, even after heavy Stage III reductions.

Aside from the morphology of the *conditioned* austenite, the finest ferritic grain sizes require control of the austenite-to-ferrite transformation range. Alloying elements such as manganese or molybdenum act to retard the transformation to ferrite; the austenite decomposition then

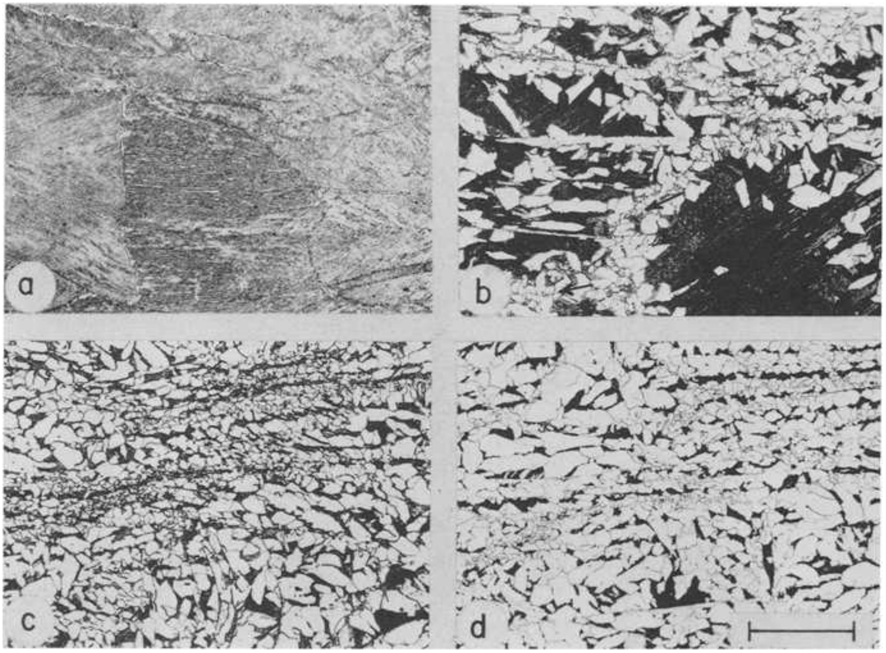

FIG. 13—*Stages of transformation of a 0.1C-1.3Mn-0.03Cb unrecrystallized austenite on cooling at 0.2°C/s. The samples were solutionized (1250°C for 1 h), deformed 50 percent at 950°C, and then cooled continuously, being quenched from the indicated temperatures:* (a) *750°C,* (b) *700°C,* (c) *650°C, and* (d) *550°C. Scale mark indicates 200 μm.*

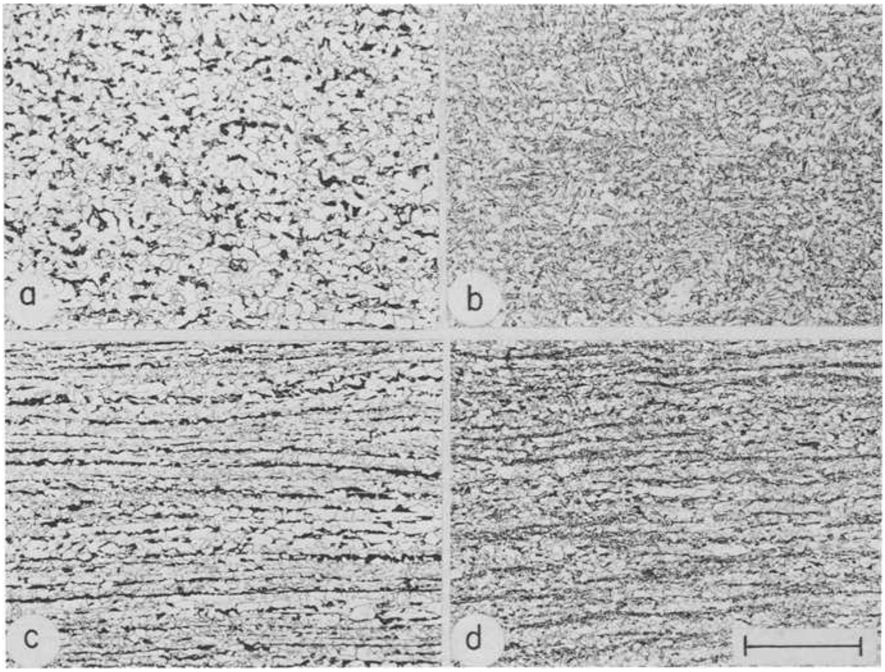

FIG. 14—*Effect of manganese level and processing schedule on the as-rolled microstructure of 0.1C-0.03Cb steel.* (a) *1.3Mn hot-rolled,* (b) *1.9Mn hot-rolled,* (c) *1.3 Mn controlled-rolled, and* (d) *1.9Mn controlled-rolled. Scale mark indicates 200 μm.*

occurs at lower temperatures, and the corresponding faster ferrite-nucleation and slower ferrite-growth rates act to produce finer ferritic grain sizes. Processing control, such as accelerated cooling after rolling to lower coiling temperatures, may be employed for hot-mill sheet rolling in order to lower the transformation range, but such procedures are not practical for plate rolling. Hence, in plate processing, where the cooling rate is dictated by the thickness, a judicious balance between the alloying level and attainable cooling rate must be established to obtain the appropriate transformation temperature range.

Of course, if the cooling rate is too fast or the alloying level is too high, undesirable transformation products may result, and so the alloying chemistry and processing parameters have to be considered simultaneously to achieve microstructural optimization.

The practical implications of the structural control of the austenite during rolling and of the austenite-to-ferrite transformation range subsequent to rolling can be illustrated with the aid of Fig. 14. Here, two simulated rolling schedules and two levels of manganese have been employed as the independent variables to demonstrate their combined effects on the final transformation product. The hot-rolling schedule produces equiaxed austenite prior to transformation, and leads, at both levels of manganese, to an equiaxed transformation product. The higher manganese steel has a finer ferritic grain size due to the effect of manganese in retarding the decomposition to ferrite, but the added hardenability also results in the formation of considerable bainite. Controlled-rolling (involving 80 percent reduction below T_R) causes significant ferritic grain refinement in both cases, accentuated pearlite banding, and a duplex ferritic grain size. The higher manganese steel still possesses a fine ferritic grain size, but the unrecrystallized austenitic grain shape prior to transformation effectively counteracts the added hardenability due to the higher manganese content and is manifested by the much smaller volume fraction of bainite compared to the hot-rolled structure.

Summary

We can now summarize certain guidelines for microstructural control in microalloyed steels.

Hot deformation of HSLA steels can be divided into various stages, each characterized by the development of a particular austenite morphology.

For typical hot-rolling practices, where the austenite recrystallizes after each pass, there is a limiting austenitic grain size, and hence a limiting ferritic grain size that can be achieved on transformation.

Carbide-forming elements (titanium, vanadium, and columbium) can be added to retard austenite recrystallization, and then the rolling schedule can be designed to maximize the cumulative deformation below an effective recrystallization temperature, T_R, which depends on the alloying addition and the prior solution treatment. Transformation from unrecrystallized austenites results in the finest ferritic grain sizes practicable in HSLA steels.

Appropriate control of the austenite-to-ferrite transformation range should be used to maximize the ferrite-nucleation rate and minimize the ferrite-growth rate, while avoiding undesirable transformation products. This may include alloying additions (for example, manganese or molybdenum) or process control (for example, accelerated cooling or low coiling temperature).

Acknowledgments

The authors are indebted to the Bethlehem Steel Corporation for a research grant and valuable technical assistance in connection with studies at the Massachusetts Institute of Technology on the physical metallurgy of columbium-treated HSLA steels.

References

[1] Duckworth, W. E., Phillips, R., and Chapman, J. A., *Journal*, Iron and Steel Institute, Vol. 203, 1965, p. 1108.

[2] Irvine, K. J., Pickering, F. B., and Gladman, T., *Journal*, Iron and Steel Institute, Vol. 205, 1967, p. 161.

[3] Rashid, M. L., "GM980X: A Unique High Strength Steel with Superior Formability," Society of Automotive Engineers, Paper 760206, 1976.

[4] Cryderman, R. L., Coldren, A. P., and Mihelich, J. L., "The Development of a High-Strength, Hot-Rolled, Mn-Mo-Cb Steel," 10th Mechanical Working and Steel Processing Conference, Chicago, Jan. 1972.

[5] Irvine, K. J., Gladman, T., Orr, J., and Pickering, F. B., *Journal*, Iron and Steel Institute, Vol. 208, 1970, p. 717.

[6] Korchynsky, M. and Stuart, H., *Proceedings*, Symposium on Low-Alloy, High-Strength Steels, Nuremberg, The Metallurg Companies, 1970, p. 17.

[7] Pickering, F. B., *Proceedings*, Microalloying 75, Union Carbide Corporation, 1977, p. 9.

[8] Gladman, T., Dulieu, D., and McIvor, I. D., *Proceedings*, Microalloying 75, Union Carbide Corporation, 1977, p. 32.

[9] Meyer, L., Heisterkamp, F., and Mueschenborn, W., *Proceedings*, Microalloying 75, Union Carbide Corporation, 1977, p. 153.

[10] Baird, J. D. and Preston, R. R. in *Processing and Properties of Low Carbon Steel*, J. M. Gray, Ed., The Metallurgical Society of American Institute of Mining, Metallurgical, and Petroleum Engineers, 1973, p. 1.

[11] Cohen, M. and Owen, W. S., *Proceedings*, Microalloying 75, Union Carbide Corporation, 1977, p. 2.

[12] Gladman, T., *Proceedings*, The Royal Society, Vol. A294, 1966, p. 298.

[13] Tanaka, T., Tabata, N., Hatomura, T., and Shiga, C., *Proceedings*, Microalloying 75, Union Carbide Corporation, 1977, p. 107.

[14] Sekine, H. and Maruyama, T., *Proceedings*, 3rd International Conference on the Strength of Metals and Alloys, London, Iron and Steel Institute, 1973, p. 85.

[15] LeBon, A., Rofes-Vernis, J., and Rossard, C., *Metal Science*, Vol. 9, 1975, p. 36.

[16] Hoogendoorn, T. M. and Spanraft, M. J., *Proceedings*, Microalloying 75, Union Carbide Corporation, 1977, p. 75.

[17] Davenport, A. T., Miner, R. E., and Kot, R. A. in *The Hot Deformation of Austenite*, J. B. Ballance, Ed., The Metallurgical Society of American Institute of Mining, Metallurgical, and Petroleum Engineers, 1977, p. 186.

[18] Jones, J. D. and Rothwell, A. B., Publication 108, Iron and Steel Institute, 1968, p. 78.

[19] Ashby, M. F. and Ebeling, R., *Transactions*, American Institute of Mining, Metallurgical, and Petroleum Engineers, Vol. 236, 1966, p. 1396.

[20] Watanabe, H., Smith, Y. E., and Pehlke, R. D. in *The Hot Deformation of Austenite*, J. B. Ballance, Ed., The Metallurgical Society of American Institute of Mining, Metallurgical, and Petroleum Engineers, 1977, p. 140.

[21] White, M., S.M. thesis, Massachusetts Institute of Technology, Sept. 1977.

[22] Kozasu, I., Ouchi, C., Sampei, T., and Okita, T., *Proceedings*, Microalloying 75, Union Carbide Corporation, 1977, p. 120.

[23] Fukuda, M., Hashimoto, T., and Kunishige, K., *The Sumitomo Search*, Vol. 9, 1973, p. 8.

C. Parrini[1] *and A. DeVito*[1]

High-Strength Microalloyed Pipe Steels Resistant to Hydrogen-Induced Failures

---

REFERENCE: Parrini, C. and DeVito, A., "**High-Strength Microalloyed Pipe Steels Resistant to Hydrogen-Induced Failures,**" *MiCon 78: Optimization of Processing, Properties, and Service Performance Through Microstructural Control, ASTM STP 672,* Halle Abrams, G. N. Maniar, D. A. Nail, and H. D. Solomon, Eds., American Society for Testing and Materials, 1979, pp. 53–72.

ABSTRACT: The continuing increase in oil and natural gas prices has made the utilization of *sour* gas reserves more and more economical. In addition, *sweet* gas may in time turn sour due to the action of bacteria carried in by injected seawater. Thus, future pipeline steels must be increasingly resistant to hydrogen sulfide and hydrogen-induced cracking (HIC). The present investigation on the susceptibility of steels to HIC covers pipe diameters from ~50 to 142 cm (20 to 56 in.) and steel grades from X42 to X80. The influence of the alloying elements carbon, manganese, sulfur, chromium, molybdenum, copper, nickel, niobium, and the rare earth metals was investigated. Hydrogen effects were evaluated by means of sulfide stress corrosion (SSC) and British Petroleum (BP) tests on base metal and U-bend tests on welded joints. The effects of inclusion shape, control rolling practices and cold deformation on hydrogen susceptibility were also studied. A new welding method, able to produce joints fully resistant to HIC, was developed. Large diameter, cold expanded, submerged arc welded pipes not susceptible to hydrogen cracking have been produced.

KEY WORDS: steels, microstructure, alloys

In a wet environment, the presence of hydrogen sulfide (H_2S) in natural gas pipelines may cause several problems, the most important of which being hydrogen-induced cracking (HIC) and sulfide stress corrosion cracking (SSCC). Both of these phenomena may occur on baseplate as well as in welded joints in high-strength steels.

Hydrogen sulfide may be present in the gas as a natural impurity or as the product of the reduction of sulfate ions by the bacterium, *desulfo-*

---

[1] Coordinator and assistant coordinator, respectively, Research and Development, Taranto Works, Italsider, S.p.A., Taranto, Italy.

vibrio desulfuricans. These organisms normally live in seawater and can be introduced into pipelines either during hydrostatic testing [*1,2*][2] or after water is pumped into submarine gas reservoirs during secondary recovery operations.

Hydrogen-induced cracking (HIC) derives from the atomic hydrogen liberated during corrosion. Entry of this hydrogen into the steel is aided by the catalytic *poisoning* action of absorbed HS^- ions [*3*]. Thus,

$$Fe \rightarrow Fe^{++} + 2e$$

$$H^+ + e \rightarrow H$$

$$H \xrightarrow{HS^-} (H)$$

The atomic hydrogen will recombine to H_2 in microtraps mostly existing as voids between the steel matrix and nonmetallic inclusions (NMI). The high pressure resulting from this phenomenon, together with the hydrogen embrittlement of the steel matrix itself, results in the formation of cracks such as shown in Fig. 1. Obviously, as these defects grow, they will eventually compromise the integrity of the pipeline at its operating pressure. If the cracks form near the surface, they may be accompanied by visible macroscopic blisters, hence the name often given to this type of damage.

It is believed that the most important factor affecting HIC is the presence of highly deformable NMI, particularly those of the Type II manganese sulfide (MnS) variety. With respect to SSCC, laboratory studies [*4,5*] and practical experience have confirmed that the heat affected zone (HAZ) of welded joints is much more susceptible to attack than is the base material.

In spite of the successful use of inhibitors against SSCC (which result in large increases in pipeline operating costs), we believe that a better solution to the problem lies in improving the resistance of pipeline steels to hydrogen and H_2S-related damage. With this in mind, we have undertaken a number of research programs aimed at understanding the parameters that control the influence of hydrogen in several commercial high-strength low-alloy (HSLA) steels, both in the form of plates and as (submerged arc welded) SAW plus cold expanded pipes. Our end result was the full-scale production of pipes suitable for sour gas transmission, having a very high resistance to HIC and SSCC in the base metal, HAZ, and welds.

Sulfide Stress Corrosion Cracking (SSCC)

Results obtained from the wide range of laboratory experiments (Appendix I) carried out by Italsider in collaboration with the C.S.M.

---

[2] The italic numbers in brackets refer to the list of references appended to this paper.

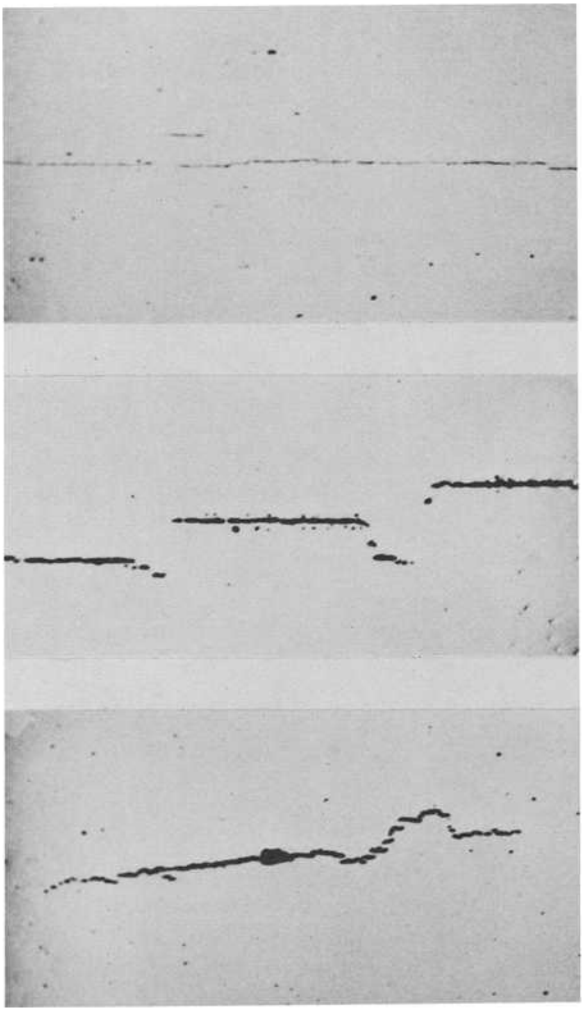

FIG. 1—*Examples of hydrogen-induced cracks (HIC).*

(Centro Sperimentale Metallurgico) of Rome [*6–12*] confirmed that the susceptibility to SSCC greatly depends upon the tensile properties of the steel(s) in question. It has been confirmed that for steels with an ultimate tensile strength (UTS) lower than 60 kg/mm^2 (85.3 ksi), there is generally a ductile fracture. Hydrogen simply concentrates in microvoids at NMI/matrix interfaces, at such similar defects as segregation bands, large carbides, and at severe structural inhomogeneities caused by erroneous heat treating or welding techniques, localized cold deformations, etc.

If the hydrogenating conditions are particularly severe, blistering may

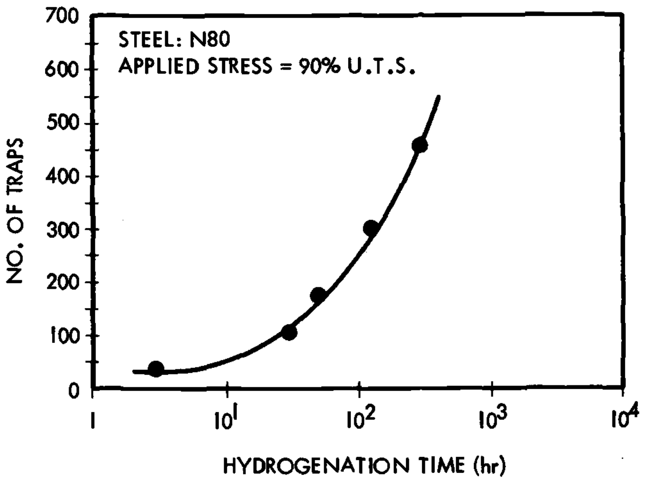

FIG. 2—*Increase in number of traps with increase in exposure time (after C.S.M.).*

occur; that is, molecular hydrogen concentration at metal/NMI interfaces or in internal voids reaches the point where internal pressures generated produce stresses exceeding the metal's yield strength. As a result, the voids expand, often to macroscopic dimensions.

When the steel's UTS is greater than 60 kg/mm^2 (85.3 ksi), but remains below a limit of about 100 kg/mm^2 (140 ksi) for low-alloy steels, susceptibility to SSCC depends on several factors:

Quantity and Shape of the NMI

This influence increases with their number and with the extent to which they exist as long stringers, the sharp tips of which can act as stress concentrators. By experimentation, a quantitative correlation was found between the measured number of active traps and the hydrogenation time for the same material at constant load (Fig. 2). Fractured surface examination confirmed that each trap was a nonmetallic inclusion.

Matrix Structure

It has been determined that, for equivalent mechanical properties, different microstructures may have different sensitivity to hydrogen. Based on our experiments, we have ascertained the following order of increasing susceptibility:

Upper Bainite
Lower Bainite
Tempered Martensite
Ferrite/Pearlite

This classification should not be taken to mean that a quenched and tempered steel always behaves better than a ferrite/pearlite one; in the case of welded joints, for example, we have found that—for the same welding process—quenched and tempered steels produce HAZ structural conditions much more sensitive than those in ferrite/pearlite steels [*13*].

Alloying Elements

In the ranges studied, these have the following effects:

Element	Experimental Range	Effect
Silicon	0.3 to 0.9%	beneficial
Manganese	0.3 to 1.5	detrimental
Copper	0.5 maximum	detrimental
Chromium	1.0 maximum	beneficial
Nickel	0.8 maximum	detrimental
Molybdenum	0.5 maximum	none
Niobium/Vanadium	0.1 maximum	none
Aluminum	0.5 maximum	beneficial

The effect of alloying elements on the steels' sensitivity to SSCC can be explained in terms of induced structural effects as well as in variations in electrochemical conditions on the steels' surfaces.

At tensile strengths greater than 100 kg/mm^2 (140 ksi), the embrittlement phenomenon cannot easily be controlled by microstructural parameters, because fracture tends to be intergranular (Fig. 3). The mechanism by which the fracture mode changes is not completely explained. Perhaps, because these strength levels are generally obtained from quenched and tempered structures, susceptibility to SSCC is strongly affected by (*a*) the exact nature of the microstructure present, (*b*) the level of (reduced) toughness available, and (*c*) the increased number of defects taking part in the fracture process.[3]

As a producer of HSLA pipeline steels, we have naturally paid greater attention to those materials having tensile strengths in the range 50 to 70 kg/mm^2 (70 to 100 ksi), obtained by microalloying and controlled rolling or normalizing.

---

[3] The critical dimensions of such inclusions are inversely proportional to the UTS. For a commercially clean steel, the density of inclusions with diameters ~1000 Å is approximately 10^7/mm^3 [*14*].

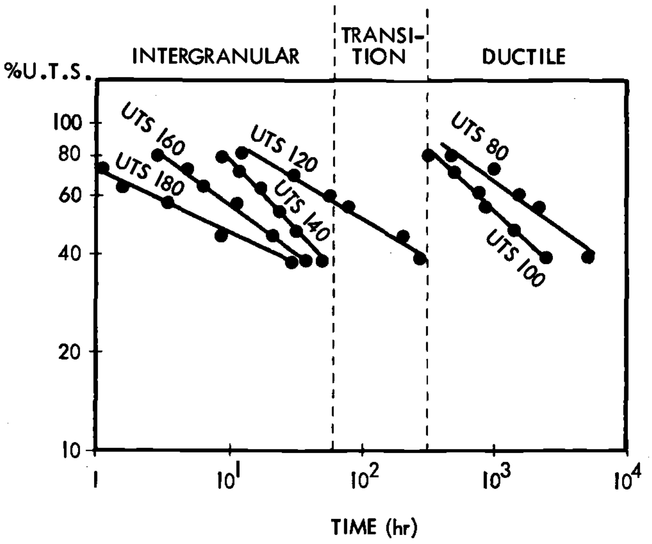

FIG. 3—*Effect of yield strength on fracture mode (after C.S.M.).*

Conventional SSCC tests have been used to evaluate failure times in commercial line pipe steels [*15*] (see Fig. 4 and Table 1). There is no apparent difference among the ferrite/pearlite structures found in normalized steels (CORTEN B and ASA 52), the control rolled (×60), and as-rolled plain carbon steels (Fe42). The worst SSCC behavior, found in steels with a *mixed acicular structure* (×70 and ×80, control rolled), could

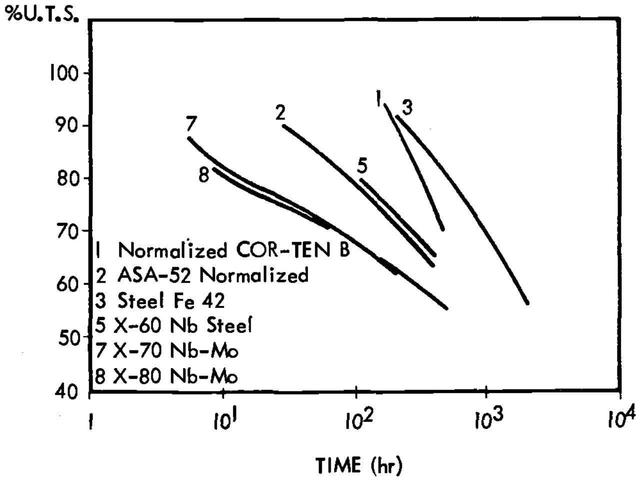

FIG. 4—*Stress corrosion cracking of various steels (after C.S.M.).*

TABLE 1—*Chemical analysis and mechanical properties of steels tested for SSCC resistance.*

	Steel	C	Mn	P	S	Si	Cr	V	Cu	Mo	Nb	Al	Ce(tot.)	Yield Strength, kg/mm²	Ultimate Tensile Strength, kg/mm²	Elongation, %
1	Corten B	0.12	1.15	0.018	0.018	0.25	0.54	0.08	0.35	. . .	. . .	. . .	. . .	46.4	65.1	. . .
2	ASA 52	0.18	1.26	0.019	0.015	0.25	. . .	. . .	. . .	. . .	0.039	. . .	. . .	38.4	55.6	. . .
3	Fe 42	0.24	1.14	0.019	0.011	0.19	. . .	. . .	. . .	. . .	0.010	. . .	. . .	33.3	56.6	28
4	×60	0.14	1.46	0.008	0.015	0.24	. . .	. . .	. . .	. . .	0.040	0.027	. . .	43.2	56.7	27
5	×60	0.16	1.40	0.013	0.004	0.23	. . .	. . .	. . .	. . .	0.037	0.028	. . .	48.3	63.4	26
6	×60	0.14	1.35	0.015	0.006	0.26	. . .	. . .	. . .	. . .	0.040	0.022	0.027	45.0	59.9	27
7	×70	0.05	1.73	0.015	0.004	0.34	. . .	. . .	. . .	0.30	0.041	0.033	. . .	50.1	61.5	27
8	×80	0.07	2.07	0.012	0.004	0.33	. . .	. . .	. . .	0.44	0.080	0.038	. . .	61.1	80.5	26

be explained mainly by means of microstructural effects; in fact, the structure generally denoted *acicular ferrite* or *new structural ferrite* is a mixture of structures [*16*] such as:

1. polygonal ferrite,
2. upper bainite,
3. lower bainite,
4. autotempered martensite, and
5. untempered martensite with retained austenite.

We believe the islands of untempered martensite are the most susceptible to hydrogen embrittlement among all microstructures. Since these martensitic areas disappear after aging or tempering, we shall be able to test this hypothesis. Experiments are currently under way to do so.

Figure 4 and Table 1 also show some influence of the dispersoid strengthening elements (niobium and vanadium) in increasing the SSCC susceptibility in normalized and control-rolled steels, compared with plain carbon steels having similar structures and ultimate tensile strengths. Most probably, what we see here is the effect of increased yield strength brought about by the precipitation hardening. In fact, we can exclude, based on our previous tests, any specific chemical effect of the alloying elements when their concentration is less than 0.10 percent.

The importance of the role that nonmetallic inclusions play in this problem has once again been confirmed. Examining particularly the ×60 curves in Fig. 4 and Table 1, we can see that, for the same mechanical properties, microstructures, and chemical analyses, failure times in SSCC tests are significantly influenced by the amount and morphology of MnS inclusions. The highest SSCC resistance was demonstrated by rare earth metals (REM) treated steels. Further work obviously needs to be done in this field, and we shall try to extend our understanding of the observations made thus far.

Hydrogen Induced Cracking (HIC)

With regard to the phenomenon measured in the British Petroleum (BP) test (Appendix II), we have studied the effects of chemical composition, inclusion content and morphology and rolling conditions in control-rolled steels. Table 2 gives the compositions and mechanical properties of the steels studied; they have been produced in 350 ton BOF converters and were poured as 28 to 36 ton ingots.

The U-bend test method was used to study the SSCC in the HAZ: SAW joints were produced for these specimens, using both conventional wires and fluxes and special wires whose chemical compositions were designed to control SSCC in the HAZ electrochemically. Our aim in setting the weld metal composition was to concentrate the cathodic reaction far from

TABLE 2—*Chemical analysis and mechanical properties of steels tested for hydrogen-induced cracking.*

	C	Mn	Si	P	S	Cr	Ni	Cu	Mo	Al	V	Nb	Rare Earth (Misch Metal), kg/ton	Carbon Equivalent	Thickness, mm	Yield Strength, 0.2 kg/mm²[a]	Tensile Strength, kg/mm²	Elongation 2 in. %	Shelf Energy kg/cm²	FATT °C
A	0.13	1.40	0.28	0.021	0.018	. . .	. . .	. . .	. . .	0.024	. . .	0.040	. . .	0.36	12.7	43.0	56.0	30	3.5	–60
B	0.14	1.08	0.29	0.009	0.004	. . .	. . .	. . .	. . .	0.028	. . .	. . .	. . .	0.32	7.2	44.0	57.0	32	10.0	–50
C	0.10	1.46	0.27	0.011	0.006	. . .	. . .	. . .	. . .	0.022	. . .	0.034	. . .	0.34	12.0	44.8	56.8	38	9.5	–40
D	0.10	1.42	0.26	0.012	0.005	. . .	. . .	. . .	. . .	0.020	. . .	0.033	0.7	0.34	15.0	44.5	56.4	41	16.2	–40
E	0.14	1.20	0.24	0.015	0.005	. . .	. . .	. . .	. . .	0.028	. . .	0.038	0.7	0.34	12.7	41.0	53.0	40	17.0	–40
F	0.19	1.30	0.22	0.015	0.010	. . .	. . .	. . .	. . .	0.030	. . .	0.040	1.7	0.41	12.0	45.0	58.5	36	12.5	–30
G	0.11	1.48	0.24	0.012	0.005	. . .	. . .	. . .	. . .	0.030	. . .	0.040	1.7	0.36	12.0	43.5	56.0	34	18.0	–35
H	0.15	1.35	0.23	0.012	0.007	. . .	. . .	. . .	. . .	0.030	0.07	. . .	1.7	0.39	12.0	42.8	57.5	34	15.0	–10
I	0.06	1.50	0.23	0.013	0.004	. . .	0.38	0.22	. . .	0.024	. . .	0.032	. . .	0.35	16.8	48.4	60.0	34	13.4	–50
L	0.06	1.46	0.24	0.016	0.004	. . .	0.32	0.26	. . .	0.030	. . .	0.035	. . .	0.34	16.8	48.1	59.5	36	13.0	–50
M	0.10	1.35	0.23	0.016	0.008	. . .	0.26	0.25	. . .	0.025	. . .	0.042	. . .	0.36	12.0	47.5	57.3	36	7.0	–60
N	0.10	1.40	0.23	0.024	0.004	. . .	0.26	0.27	. . .	0.020	. . .	0.041	0.7	0.37	15.0	43.4	56.5	40	12.5	–50
O	0.07	1.55	0.26	0.014	0.004	. . .	. . .	. . .	0.32	0.025	. . .	0.050	0.7	0.39	12.7	51.0	63.0	38	13.5	–40
P	0.16	1.37	0.30	0.015	0.003	0.32	. . .	0.11	. . .	0.034	. . .	0.032	1.7	0.46	12.7	49.5	64.3	28	11.5	–40
Q	0.12	1.21	0.28	0.021	0.006	0.40	. . .	. . .	. . .	0.050	. . .	. . .	1.7	0.40	12.7	43.7	56.1	40	13.0	–30
R	0.10	1.22	0.27	0.017	0.004	0.38	. . .	. . .	. . .	0.009	. . .	. . .	. . .	0.38	18.0	33.4	50.6	40	6.0	–20

[a] 1 kg/mm² = 1421.8 psi.

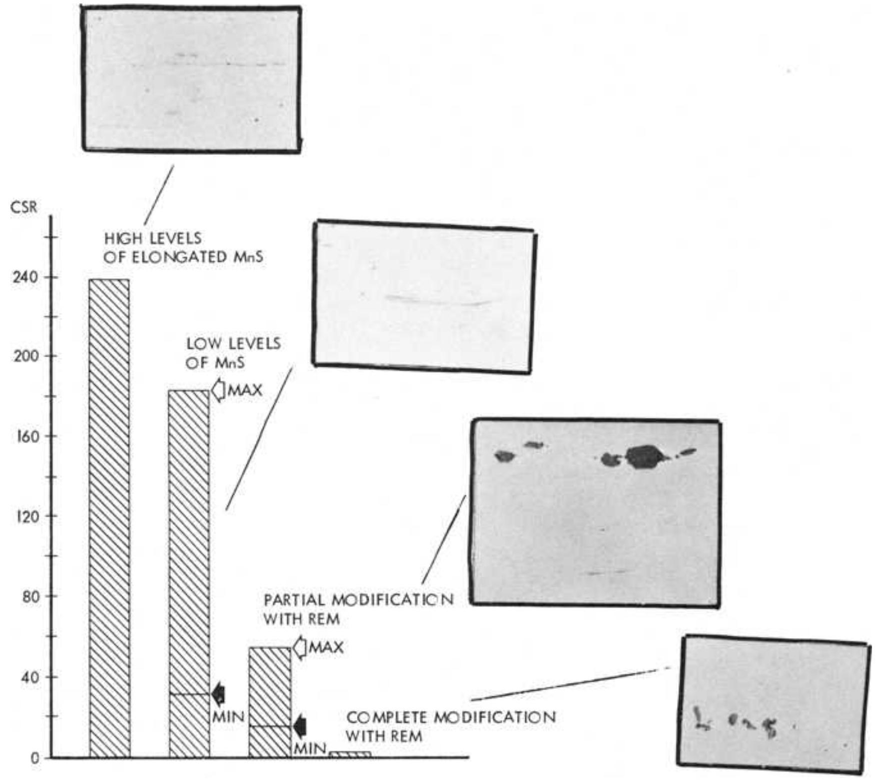

FIG. 5—*Effect of sulfide inclusion shape on cracking behavior.*

the hydrogen-sensitive HAZ. Our compositions are covered by an Italsider patent.

Thus, for the compositions chosen, the fusion zone (FZ) is cathodic and more noble than the adjacent HAZ (anodic). SSCC resistance of the hydrogen-rich FZ has been improved through the addition of such elements as chromium and molybdenum.

HIC Results on Base Metal

Results of the BP test for our steels show that inclusion shape control—through REM or other suitable treatment (Table 3 and Fig. 5)—is very beneficial in improving resistance to HIC. From Fig. 6, it appears that high finishing temperatures are also helpful, probably because of their effect on inclusion shape. Moreover, there appears to be little or no influence of copper in amounts greater than 0.25 percent [*17,18*] while additions of chromium are very effective (Fig. 7).

TABLE 3—*Results of BP test for hydrogen-induced cracks.*

	Finishing Rolling Temperature,°C	Hydrogen Diffusion, cm³/100g	Extent of Blister	Crack Length Ratio,[a] %	Stepwise Cracking,[b] %	Cracking Sensitivity Ratio[c]
A	780	4.0	E	80.0	34.5	239.3
B	780	3.9	E	44.5	31.9	183.3
C	780	4.0	E	29.0	5.4	57.5
C	830	3.2	M	25.0	5.0	47.0
C	900	1.4	S	11.0	0	9.2
D	780	4.0	S	37.0	8.0	55.2
D	830	0.6	S	24.0	0	16.0
D	900	0.3	S	8.0	0	5.3
E	780	3.5	M	23.5	7.4	51.4
F	780	0.2	O	0	0	0
G	780	0.7	O	0	0	0
H	780	0.2	O	0	0	0
I	780	1.9	S	77.5	7.5	83.0
I	830	1.3	S	24.5	2.0	24.0
I	900	0.9	S	5.0	0	3.0
L	780	2.0	S	29.7	2.9	30.7
M	780	2.3	E	26.3	6.1	58.6
N	780	4.0	M	25.0	0	16.7
O	780	2.3	E	19.0	0	15.0
P	780	0.4	O	0	0	0
P	830	0.3	O	0	0	0
P	900	0.5	O	0	0	0
Q	780	0.3	O	0	0	0
R	780	0.5	O	0	0	0

[a]

$$\frac{\sum_{J=1}^{N}\sum_{i=1}^{n} l\,i\,J}{20\times N}\times 100$$

[b]

$$\frac{\sum_{J=1}^{N}\sum_{i=1}^{n} h\,i\,J}{t\times N}\times 100$$

[c]

$$\frac{\sum_{J=1}^{N}\sum_{i=1}^{n}\times h\,i\,J}{\sum_{J=1}^{N}(20\times t)J}\times 1000$$

where:

N = sections number,
n = cracks number for each section,
t = coupon thickness,
h = crack stepwise, and
l = crack length.

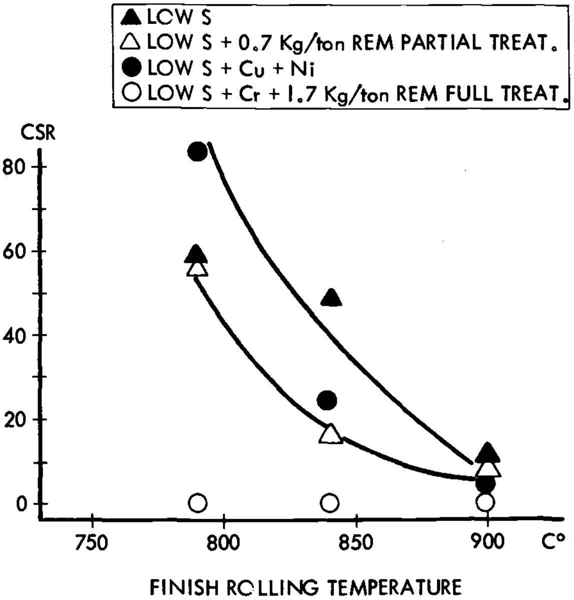

FIG. 6—*Influence of finish rolling temperature on cracking susceptibility.*

SSCC Results in the HAZ

Figure 8 compares the results of U-bend tests on the two types of welds studied after 15 days immersion in a sulfidic solution (CH_3COOH + Na_2S, pH = 4.0). A deep crack marks the HAZ perimeter on the traditionally welded sample. In the sample welded according to the described criterion, on the other hand, no cracks were observed in the HAZ, even after immersion for 30 days. The macrostructure of both joints is shown in Fig. 9. (Note that it is possible to observe blistering and related HIC phenomena in the base metal of the conventionally produced weld.) In order to identify the galvanic current that arises between the various parts of the welded joint, we measured the surface potential along the pertinent section of the two welds studied. This was done by means of a capillary electrode probe, filled with a test solution and held against the specimens while they were immersed in the sulfide solution. The probe contained a reference electrode and was translated horizontally across the weld joint by means of a micrometer screw. Results are shown in Fig. 10.

Discussion

Based on the proposed mechanisms [*19–22*] and our experimental results, we can state that HIC occurs even in the absence of an applied external stress. In the presence of elongated inclusions, hydrogen mi-

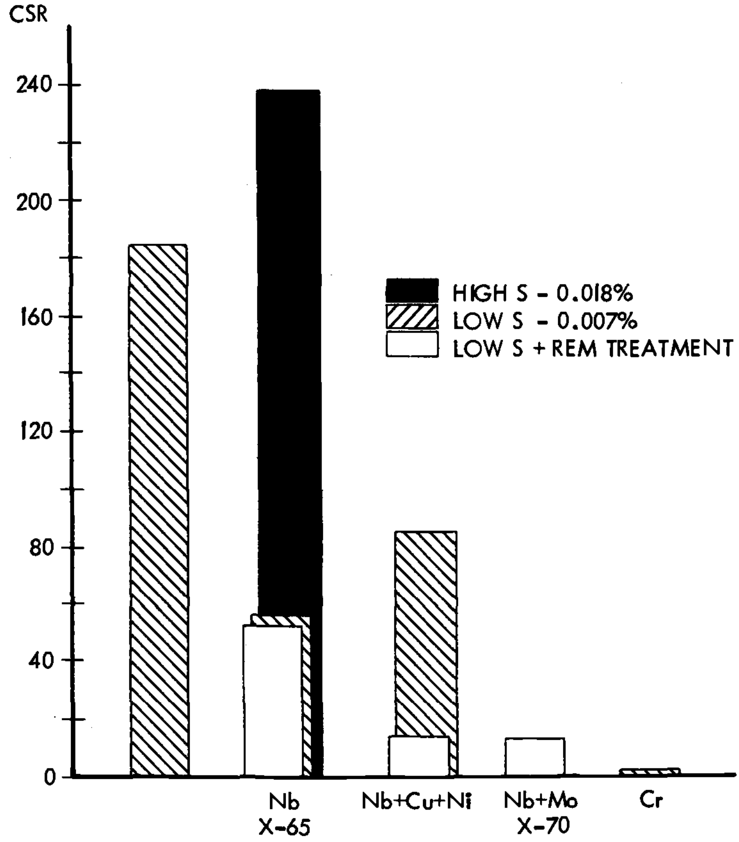

FIG. 7—*Effect of steel composition on cracking behavior.*

grates to the inclusion-matrix interfaces. As it recombines to molecular hydrogen at these sites, it creates an internal pressure that in turn generates stress fields around the inclusion tips that are high enough to exceed the matrix yield strength. The end result is the typical SCC/ hydrogen embrittlement phenomenon.

Our experimental experience leads us to consider two cases:

(1) As in the case of the BP test conditions, the steel matrix is saturated with hydrogen; that is, there is as much hydrogen present as the inclusions and the surrounding metal are able to contain. Clearly, there is enough hydrogen present to provide for the observed embrittlement and the results, in terms of crack formation, are directly proportional to the quantity and morphology of the inclusions present

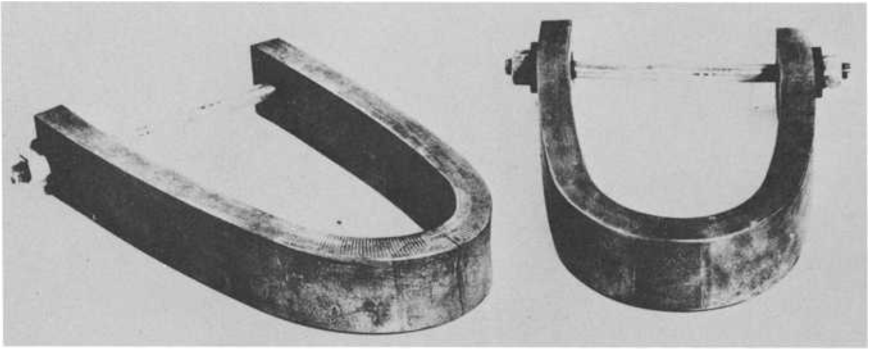

FIG. 8—*Bend test samples of welded joints.*

(considering also, of course, those factors emphasized by other researchers).

(2) The case in which the matrix contains less than the saturation amount of hydrogen, in this case, the hydrogen may concentrate at the NMI, while the amount dissolved in the matrix may not be sufficient to cause embrittlement. Under these conditions, the inclusions/voids will eventually generate cracks, the dimensions of which will be determined by the pressure exerted by the gaseous hydrogen, H_2, being arrested in the still ductile matrix. One can therefore understand that, under these conditions, cracking can be reduced by *increasing* the number of traps (inclusions), thereby dispersing the available hydrogen and effectively reducing its pressure within the available voids.

Generally, we must assume that a material, even under conditions generating hydrogen at a moderate rate, will eventually reach saturation—excluding, of course, short-term effects such as the hydrogen generated during welding. Consequently, the solution to the HIC problem must eventually lie in avoiding entry of hydrogen into a sensitive material, or through improving the material's resistance to hydrogen damage, and that through control of the nonmetallic inclusions.

The first remedy can be obtained by controlling the external environment (for example, through the use of inhibitors), by protecting the steel surfaces or by means of suitable alloying to relocate, electrochemically, the H^+ discharge reaction to a region where it can do no harm.

The latter condition can be obtained by means of alloying with elements capable of modifying the morphology of the inclusions or of decreasing their number or both. The beneficial effect of chromium as an alloying element in our experiments can be explained in terms of (*a*) a decreasing solubility of hydrogen with increasing chromium content; and (*b*) the hypothesis that chromium alters the electrochemical conditions on the

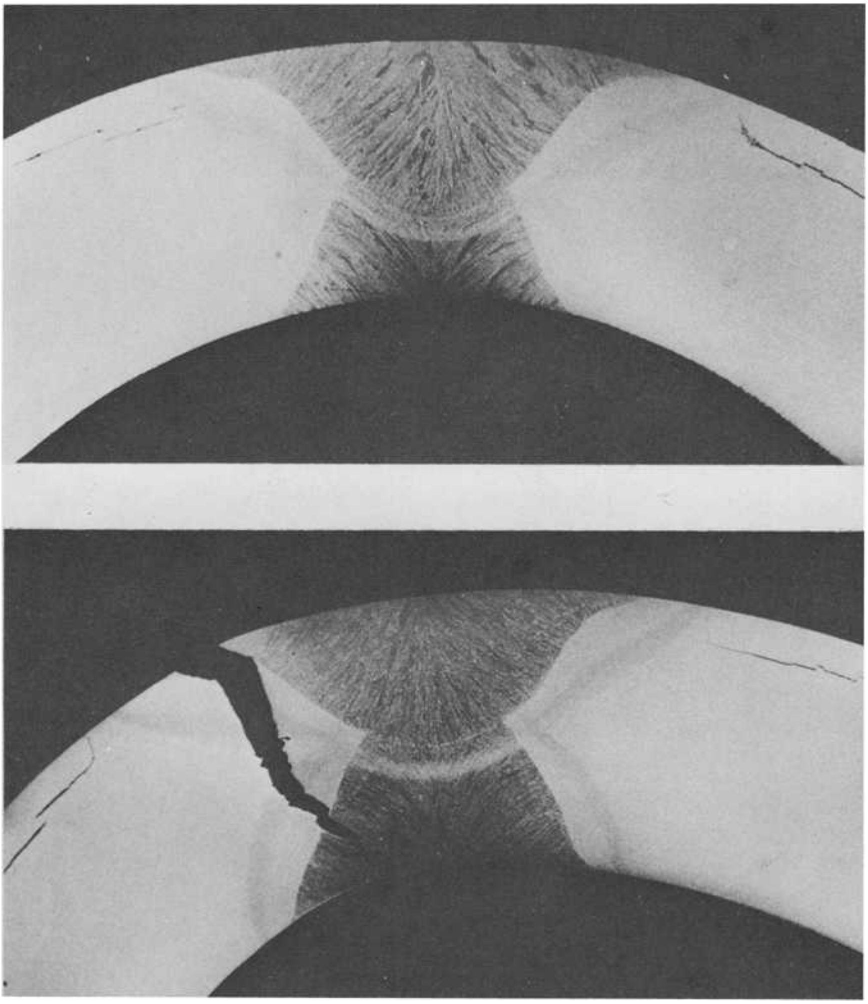

FIG. 9—*Comparison of modified and unmodified weld metal after exposure to sulfidic environment.*

steel's surface, depressing the activity of HS^- ions, enhancing the oxidation of sulfur or depressing adsorption of atomic hydrogen.

In addition to the base metal, we must also consider the welding process in order to ensure the reliability of the final product in the sulfide-bearing environment. The positive results from industrial-scale welding of our pipe confirm the theoretical approach: that a galvanic system (couple) at the welded joint is able to protect the HAZ from the discharge of hydrogen and thus avoid embrittlement. With suitable modifications, this principle is applicable to circumferential welds made

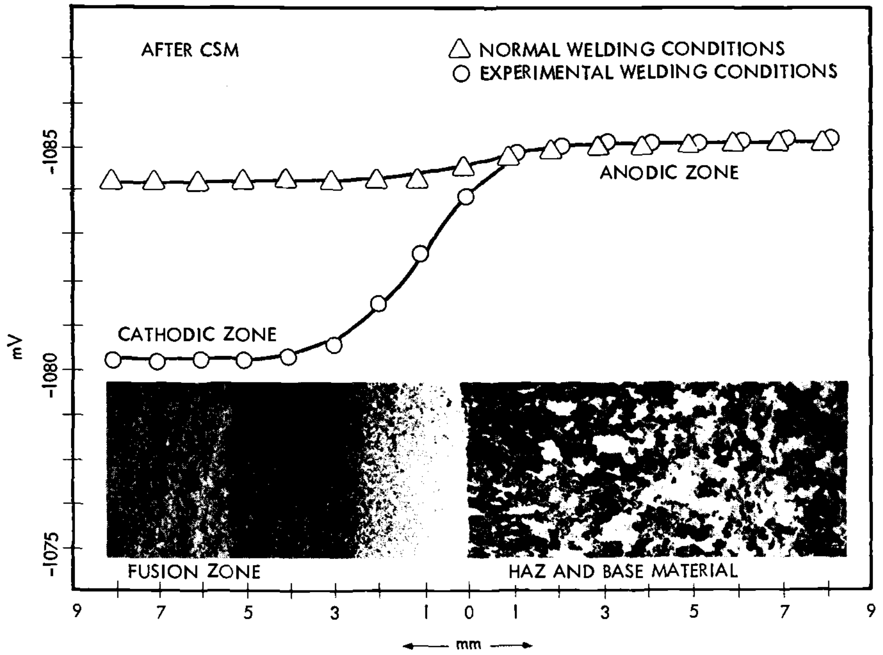

FIG. 10—*Traverse across modified and unmodified weld using capillary electrode probe.*

during pipeline fabrication or, for that matter, any weld containing filler metals subjected to corrosive environments.

Conclusions

Hydrogen, absorbed into steel products from the service environment can cause severe cracking by means of the HIC mechanism; lowering the sulfur content (sulfur ≤ 0.010 percent) is a necessary but not sufficient means for improving hydrogen resistance, inasmuch as the shape of the inclusions—as much or more that their quantity—is a most important factor.

The morphology of the inclusions can be altered in such a way as to make them less dangerous by adopting higher finishing temperatures, thus producing less deformation of the Type II MnS inclusions during rolling. Much more effective is the utilization of sulfide shape control through the use of REM, calcium, zirconium, magnesium, or similar treatments.

Among alloying elements, chromium (at around 0.30 percent) seems to be the most beneficial of all those examined. It is possible that low sulfur steel containing sufficient chromium and properly rolled would not need any inclusion shape control in order to resist the HIC mechanism.

Our tests of the SSCC mechanism lead us to the following conclusions:

(*a*) The SSCC mechanism is strongly influenced by the steel's tensile properties (yield point and UTS).

(*b*) Microstructures have the following decreasing order of resistance to SSCC: upper bainite, lower bainite, tempered martensite, ferrite/pearlite, and—probably least—untempered martensite.

(*c*) In terms of composition, chromium, silicon, and aluminum are beneficial; manganese, copper, and nickel are detrimental, probably due to their influence on substructure or their effect on surface electrochemical potential in the presence of a damaging environment.

(*d*) There is no difference between as-rolled, control-rolled, or normalized products providing they have the same microstructures (ferrite/pearlite). The dispersion-strengthening elements, niobium and vanadium, appear to have a detrimental influence explainable by Point *a*.

(*e*) There is a strong influence of inclusion quantity and morphology, confirming that inclusions should play a very important role in influencing the effect of tensile properties on SSCC mechanisms. In fact, it is known that increasing the allowable applied stress decreases the size of inclusions potentially able to take part in the fracture mechanism. In *clean* steels, there are about 10^7 inclusions per/mm^3 with dimensions around 1000 Å. The effect of the NMI implies as well that the SSCC problem can be related to the toughness anisotropy of flat-rolled products.

(*f*) It is possible to protect the HAZ from SSCC by means of a galvanic couple induced through the proper selection of weld metal composition. This is a fundamental prerequisite to obtaining a SAW pipe having high resistance to hydrogen.

Our laboratory tests and full-scale industrial trials have enabled the Taranto Works to initiate the production of HYRES pipes with guaranteed properties for sour gas transmission pipelines. To date, 13 000 tons of finished pipes (×60 grade, ~ 106 by 1.2 cm (42 by ½ in.)) have been produced and have passed the BP test, fully confirming our experimental results.

APPENDIX I

SSCC Test Methodology

The HS^-anion-containing environment, combined with electrochemical potential gradients on a metal surface (localized anodes and cathodes), can lead to very severe corrosive attack. This can lead to crack nucleation at such sites as dislocations, inclusions, grain boundaries, and areas coated by various corrosion products (concentration cells), that is, highly active local cells. The specimen used for testing in this environment, unnotched, is shown in Fig. 11.

Measurement of time to failure, using the specimen in Fig. 11, is made in a solution buffered to pH = 4 consisting of $CH_3COOH + Na_2S$. This will give the

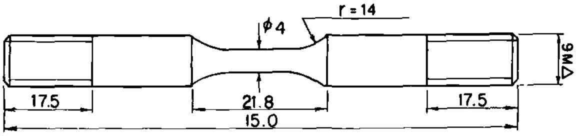

FIG. 11—*Specimen for SSCC test.*

maximum concentration of HS^- ions [*28*]. The specimen axis is oriented parallel to the rolling direction in order to minimize the detrimental effect of inclusions on the fracture mechanism.

APPENDIX II

British Petroleum (BP) Test for Evaluation of Hydrogen-Induced Cracking

For each test, three samples are cut from the pipe parent metal according to Fig. 12.

Samples are machined and surfaces ground with 320-grade silicon carbide paper. Samples are then placed in a solution of synthetic seawater prepared in accordance with ASTM Specification for Substitute Ocean Water (D1141–75) that had previously been deaerated by bubbling nitrogen (100 cm^3/liter/min, 1 h) through it. The specific volume of the brine must be in the range 3 to 6 cm^3/cm^2,

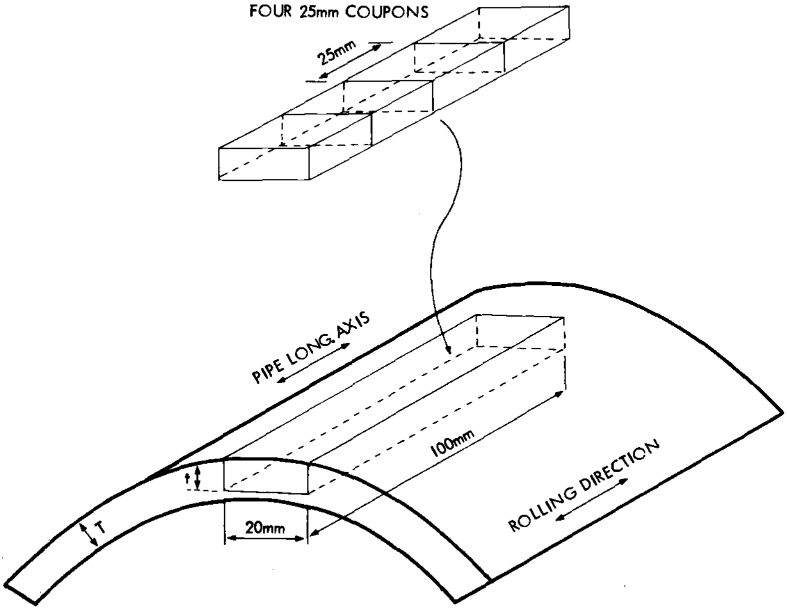

FIG. 12—*Test coupons for BP test.*

and its pH adjusted to 8.2. Specimen side surfaces exposed by the machining operations are coated to prevent contact with H_2S.

The solution is saturated with H_2S flowing at 4 litres/min. After 1 h (saturation), flow rate is reduced to 50 cm^3/min (cell capacity: 5 litres) and maintained for 96 h.

Test conditions:

Temperature	25°C ± 3°C
H_2S concentration	2300 to 3500 ppm
pH	approximately 4.8

After testing, the specimens are removed from the solution, rinsed in flowing water, wire brushed to remove loose deposits, washed in acetone, and dried in petroleum ether and cold air. The sample is then placed in a glass cell and the evolved hydrogen is collected over glycerine at 45°C for 72 h.

The coupons are then sectioned at three planes perpendicular to their long axis to determine the extent of cracking, as shown in Fig. 13.

Data to be collected include: (1) diffusable hydrogen, ml/100 g of steel; (2) photos of coupons, showing any blisters; and (3) results of crack detection, with photos.

APPENDIX III

U-Bend Test

Because it offers a better simulation of the stress conditions in an actual pipe, the U-bend test, ASTM Recommended Practice for Making and Using U-Bend Stress Corrosion Test Specimens (G 30–72), is employed.

Samples taken from the pipe are 25 mm wide, full pipe wall thickness, oriented across the weld seam. Bend diameter is 75 mm. Free ends are held with stainless steel screws.

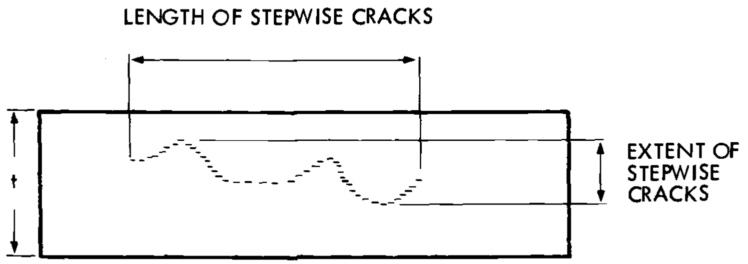

$$CSR = \frac{AC}{TA} \times 1000$$

AC = total cracked area
TA = total area of sectioned coupon faces examined

FIG. 13—*Definition of crack length and extent of stepwise propagation* [24].

The samples are immersed in a sulfidic solution ($CH_3COOH+Na_2S$, pH=4) and checked daily for visible cracks for a maximum of 30 days.

References

[1] Bush, H. E. and Beasley, A. E., *Pipeline and Gas Journal,* Nov. 1975, pp. 36–56.

[2] Tamba, A., Technical Report No. 2728, Centro Sperimentale Metallurgico Rome, June 1977.

[3] Le Boucher, B., *Proceedings,* NACE 47th International Conference on Metallic Corrosion, Amsterdam (1969), Houston (1970), N.E. Hamner, Ed., pp. 550–555.

[4] Bates, J. F., *Material Protection and Performance,* Vol. 70, No. 8, 1969, p. 33.

[5] Sarracino, M. and Lannaioli, A., Technical Report No. 2057R, Centro Sperimentale Metallurgico, Rome, Jan. 1975.

[6] Sarracino, M. and Giuliani, L., Technical Report No. 1316R, Centro Sperimentale Metallurgico, Rome, June 1972.

[7] Sarracino, M. and Giuliani, L., Technical Report No. 1646R, Centro Sperimentale Metallurgico, Rome, June 1973.

[8] Sarracino, M. and Giuliani, L., Technical Report No. 1744R, Centro Sperimentale Metallurgico, Rome, Nov. 1973.

[9] Sarracino, M. and Giuliani, L., Technical Report No. 1888R, Rome, May 1974.

[10] Lannaioli, A. and Sarracino, M., Technical Report No. 2158R, Centro Sperimentale Metallurgico, Rome, May 1975.

[11] Lannaioli, A. and Sarracino, M., Technical Report No. 2239R, Centro Sperimentale Metallurgico, Rome, Sept. 1975.

[12] Sarracino, M., Technical Report No. 430, Centro Sperimentale Metallurgico, Rome, April 1976.

[13] Civallero, M. et al, "Experience in the Development and Welding of Large Diameter Pipes," WRC Bulletin 201, Dec. 1974.

[14] Faccenda, V. et al, Technical Report No. 2736R, Centro Sperimentale Metallurgico, Rome, June, 1977.

[15] Bruno, R. and Lannaioli, A., Technical Report No. 2793R, Centro Sperimentale Metallurgico, Rome, Sept. 1977.

[16] Biss, V., "Characterization of Transformation Products and Precipitates in 19-mm Plate of Italsider Molytar X70," Climax Molybdenum Company, Technical Report J-4195-01, Jan. 1977.

[17] Miyoshi, E. et al, "Hydrogen-Induced Cracking of Steels Under Wet Hydrogen Sulfide Environment," American Society of Mechanical Engineers Conference, Tulsa, Paper No. 75, Sept. 1975.

[18] Ikeda, A. et al, "On the Hydrogen Induced Cracking of Line Pipe Steels Under Wet Hydrogen Sulfide Environments," 2nd International Conference on Hydrogen in Metals, Paris, 1977.

[19] De Kazinczy, F., *Journal,* The Iron and Steel Institute, May 1954, pp. 85–92.

[20] Troiano, A. R., "The Role of Hydrogen and Other Interstitials in the Mechanical Behavior of Metals," *Transactions,* American Society of Metals, 1960.

[21] Snape, E., "Sulfide Stress Corrosion of some Medium and Low Alloy Steels," *NACE Corrosion,* June 1967, pp. 154–172.

[22] Savage, W. F., "Sulfide Inclusions in Steel," American Society of Metals Meeting, Port Chester, N.Y., Nov. 1974.

[23] Giuliani, L. and Sarracino, M., Technical Report No. 1595R, Centro Sperimentale Metallurgico, Rome, May, 1973.

[24] Moore, E. M. and Warga, J. J., Factors Influencing the Hydrogen Cracking Sensitivity of Pipeline Steels, The International Corrosion Forum, Houston, Paper No. 144, 1976.

Halle Abrams[1] *and G. J. Roe*[1]

Evaluation of Steels for Arctic Line Pipe

REFERENCE: Abrams, Halle and Roe, G. J., "**Evaluation of Steels for Arctic Line Pipe,**" *MiCon 78: Optimization of Processing, Properties, and Service Performance Through Microstructural Control, ASTM STP 672,* Halle Abrams, G. N. Maniar, D. A. Nail, and H. D. Solomon, Eds., American Society for Testing and Materials, 1979, pp. 73–104.

ABSTRACT: Line pipe for transporting gas from Arctic fields is subjected to the conditions of an extremely hostile environment. Bethlehem Steel has been conducting an extensive program to evaluate the materials and processes that can produce the property requirements for Arctic-grade line pipe. In the course of the program, several alloy combinations were evaluated. The paper describes each of these, but concentrates on the vanadium-columbium (V-Cb) alloy grade, which we feel is the most practical and economical to produce. The critical aspects, from steelmaking to plate rolling and testing, are described. A regression analysis correlation of chemistry and processing to microstructure and properties is presented. This correlation permits the prediction of plate and pipe properties on the basis of the chemistry and processing. The dependence of properties on a number of specific microstructural features is illustrated by metallographic studies.

KEY WORDS: steels, microstructure, microalloys, controlled rolling, regression analysis, line pipe

Various specifications have been proposed for Arctic line pipe for transportation of gas from the Alaskan fields. Although a final decision has not yet been reached, the final specifications will probably include: (*a*) a yield strength of 450 to 480 MPa (65 to 70 ksi); (*b*) a minimum of 41 J (30 ft·lb) transverse Charpy energy at the design temperature −20 to −5°C (−10 to +25°F); and (*c*) an 85 percent shear fracture appearance for the Battelle Drop-Weight Tear Test (BDWTT) at the design temperature, −20 to −5°C (−10 to +25°F).

In our experimental studies, the basic approach for meeting these demanding property requirements has been the control of both the alloy chemistry and the processing steps. Following are the chemistry and

---

[1] Research engineers, Research Department, Bethlehem Steel Corporation, Bethlehem, Pa. 18016.

processing parameters that have the most significant effect on properties [*1*–*5*].[2]

Chemistry +	Processing →	Properties
Low carbon	Slab-heating temperatures	Strength required
Low sulfur	Percent reduction <900°C (1650°F)	Charpy energy required
Microalloys: vanadium, columbium, titanium	Finishing temperatures	BDWTT required
Silicon-aluminum (Si-Al) killed	Finished plate gage	

For evaluating the effect of chemistry and processing on properties and microstructure and the interrelationships among these factors, 26 laboratory heats and nine full-size basic oxygen furnace (BOF) heats were melted and processed to various gage plates in accordance with the proposed Arctic specifications. Data were accumulated on tensile, impact, and other properties as well as on metallographic features, including grain size, percent secondary phase, microcleanliness, and the degree of microstructural homogeneity.

Experimental Procedure

The experimental work was conducted in two phases. First, detailed laboratory plate evaluations, and second, full-scale mill trials, which included the melting of BOF heats followed by controlled plate rolling and U-ring (U) and O-ring (O) pipe fabrications.

Throughout both the laboratory and mill phases, a comprehensive metallographic evaluation was conducted. This microstructure study included grain-size determination, the rating of structure duplexity (for example, mixture of coarse and fine ferrite), the determination of volume fraction of secondary phase (either pearlite or lower transformation products), as well as selective scanning electron microscope, microprobe, and transmission electron microscope work. Transverse mechanical property evaluations included tension tests, full-curve Charpy V-notch (CV) data for which selected values were used to characterize the notch toughness (for example, CV$_{15}$ transition temperature (20.5 J (15 ft · lb)), 50 percent fracture appearance transition temperature (FATT), 100 percent

---

[2] The italic numbers in brackets refer to the list of references appended to this paper.

shear, energy absorbed at −45, −20, and 0°C (−50, −10, and +32°F), and BDWTT studies.

Results and Discussion

The first part of the discussion deals with mechanical properties, demonstrating the range of obtainable results. To provide a basis for subsequent correlations, key microstructural features are discussed. Finally, regression analyses are used to interrelate processing variations, properties, and microstructure.

Mechanical Properties

For each strength and gage level investigated, both a laboratory and mill study were conducted. The laboratory work was preliminary to mill trials in order to evaluate compositions, processing, and properties. For example, 26 laboratory heats of various vanadium-columbium (V-Cb), columbium (Cb), columbium-molybdenum (Cb-Mo), and titanium (Ti) chemistries were made to optimize compositions and rolling practices for 19-mm (0.750-in.) gage plate before proceeding to the full-scale mill trials.

Laboratory Heats

For possible use as 19-mm (0.750-in.) gage Arctic material, the following range of laboratory compositions were rolled and tested:

V-Cb Steels

C	Mn	S	Si	Al	V	Cb	Ni	Cu	Cr	Mo
0.03	1.39	0.006	0.22	0.032	0.040	0.032	0.03	0.01	0.01	0.01
↓	↓		↓	↓	↓	↓	↓	↓	↓	↓
0.14	1.80	max	0.46	0.054	0.094	0.045	0.30	0.22	0.20	0.12

Cb and Cb-Mo Steels

C	Mn	S	Si	Al	Cb	Mo
0.04	1.37	0.006	0.11	0.043	0.036	0.01
↓	↓		↓	↓	↓	↓
0.09	1.73	max	0.61	0.085	0.160	0.33

Ti Steels

C	Mn	S	Si	Al	Ti	Ni	Cr
0.09	1.29	0.006	0.34	0.035	0.10	0.01	0.01
↓	↓		↓	↓	↓	↓	↓
0.10	1.49	max	0.37	0.045	0.13	0.26	0.29

These laboratory compositions were processed as follows:

Slab Heating	% Reduction Below 900°C (1650°F)	% TCR[3] Below 900°C (1650°F)	Plate Finishing
1230 to 1040°C (2250 to 1900°F)	43 to 82	63 to 182	690 to 760°C (1270 to 1400°F)

The laboratory 19-mm (0.750-in.) gage transverse plate properties are summarized in Figs. 1 and 2. As these figures show, the laboratory plates were generally rolled to produce a yield strength between 450 to 480 MPa (65 to 75 ksi), a tensile strength of about 515 to 620 MPa (75 to 90 ksi), with a minimum transverse Charpy energy of 68 J at −20°C (50 ft · lb at −10°F), and 85 percent shear in the BDWTT below −5°C (+25°F).

These laboratory results pointed to the following requirements and precautions for the subsequent mill trials:

1. Close control would have to be maintained to prevent roughing- and finishing-stand mill overloads during severe controlled rolling.
2. Three different microalloy systems, V-Cb, Cb-Mo, and Ti, could give similar plate properties, provided that rolling practices were tailored for each alloy type.
3. To obtain 85 percent shear in the BDWTT at low temperatures, very severe plate-rolling practices would be required. A further restriction would be low-temperature slab heating to achieve requirements below −20°C (0°F).
4. Detailed quantitative metallography would be needed to determine microstructural changes responsible for property variations obtained from severe controlled-rolling practices.

Laboratory work was also conducted on 16-mm (0.630-in.) gage plate to establish combinations of chemistry and processing that would consistently produce desired strength-toughness requirements while maintaining the processing conditions within the capabilities of production facilities.

BOF Heats

After a thorough evaluation of laboratory plate rollings, full-scale mill trials were conducted. For the V-Cb grade, three initial BOF heats were made and evaluated before four more heats were made. One Cb-Mo heat and one titanium heat were also melted. With laboratory compositional ranges as a guide, the following BOF heat chemistries were made:

---

[3] TCR, percent total cumulative reduction, for example, 10 reduction passes, each of 15 percent, equals 150 percent TCR.

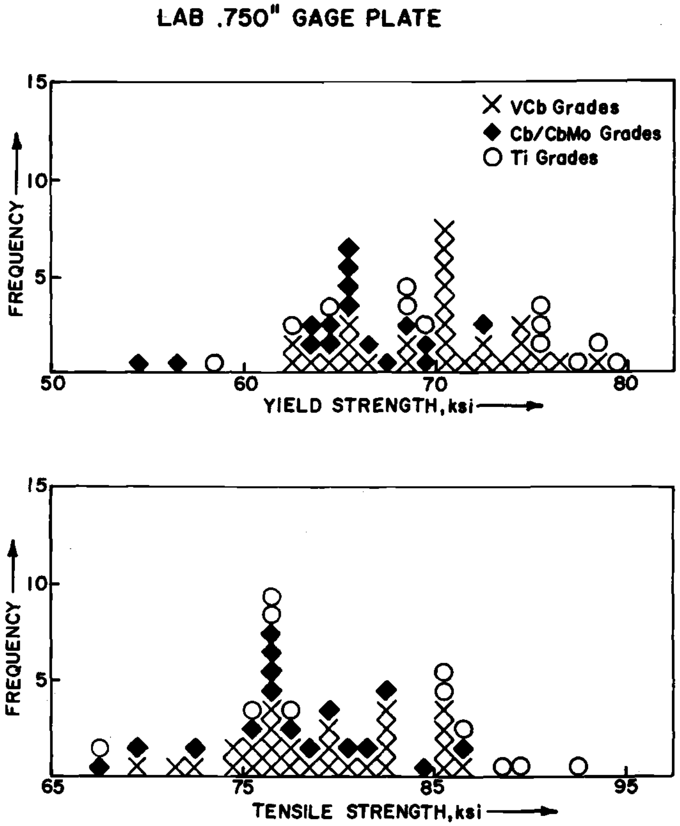

FIG. 1—*Distribution of strength for 19-mm (0.750-in.) laboratory plates.*

V-Cb Steels

C	Mn	S	Si	Al	V	Cb
0.08	1.44	0.002	0.06	0.042	0.047	0.031
↓	↓	↓	↓	↓	↓	↓
0.13	1.70	0.012	0.48	0.064	0.075	0.036

Cb-Mo Steel

C	Mn	S	Si	Al	Cb	Mo	Ni
0.07	1.81	0.005	0.34	0.058	0.058	0.28	0.25

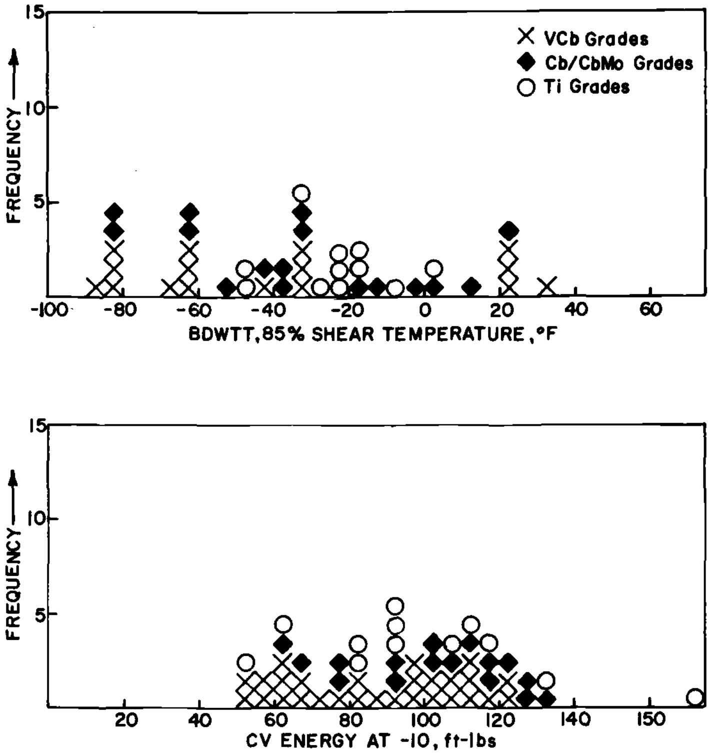

FIG. 2—*Distribution of impact properties for 19-mm (0.750-in.) laboratory plates.*

Ti Steel

C	Mn	S	Si	Al	Ti
0.08	1.45	0.008	0.46	0.049	0.10

For 19-mm (0.750-in.) gage, these BOF heats were rolled to the following 4064-mm (160-in.) plate mill practices:

Slab Heating	% Reduction Below 900°C (1650°F)	% TCR 900°C (1650°F)	Plate Finishing
1315 to 1040°C (2400 to 1900°F)	60 to 81	81 to 156	700 to 770°C (1290 to 1420°F)

Figures 3 and 4 summarize the physical properties of the 19-mm (0.750-in.) gage mill trials. The final processing steps in the mill trial consisted of U and O pipe fabrications, followed by an approxiately 1-1/4 percent cold expansion. After pipe fabrication, extensive pipe property testing was conducted. A more complete discussion of pipe properties is given later in the section on regression analysis.

In all cases—laboratory plate, mill plate, and the resulting line pipe—there was a large range of properties associated with compositional and processing variations. For various strength-toughness levels, quantitative metallography provided information relating microstructural features to property variations.

Microstructure Characteristics

The microstructural evaluation included quantitative optical metallography, electron microprobe analysis, and scanning and transmission electron microscopy.

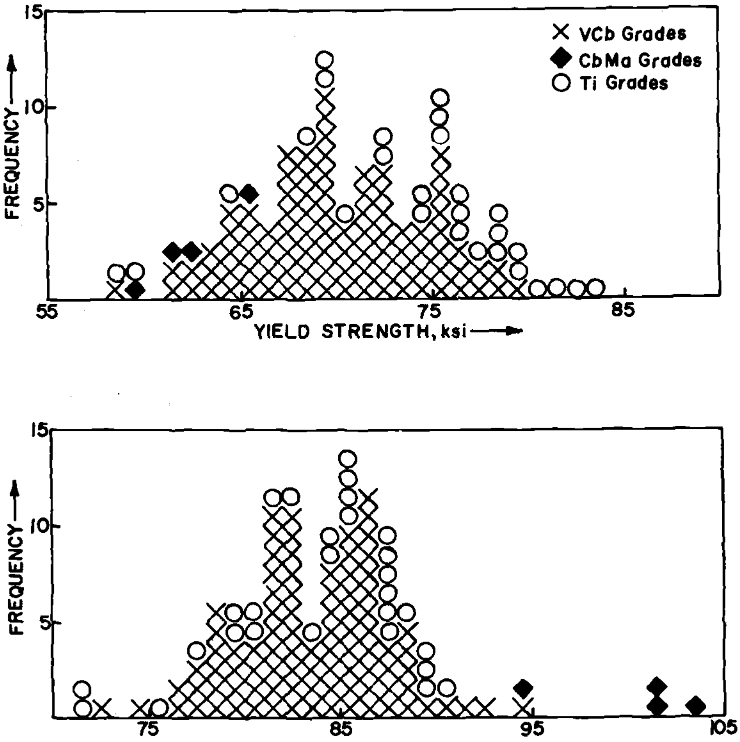

FIG. 3—*Distribution of strength for 19-mm (0.750-in.) mill plates.*

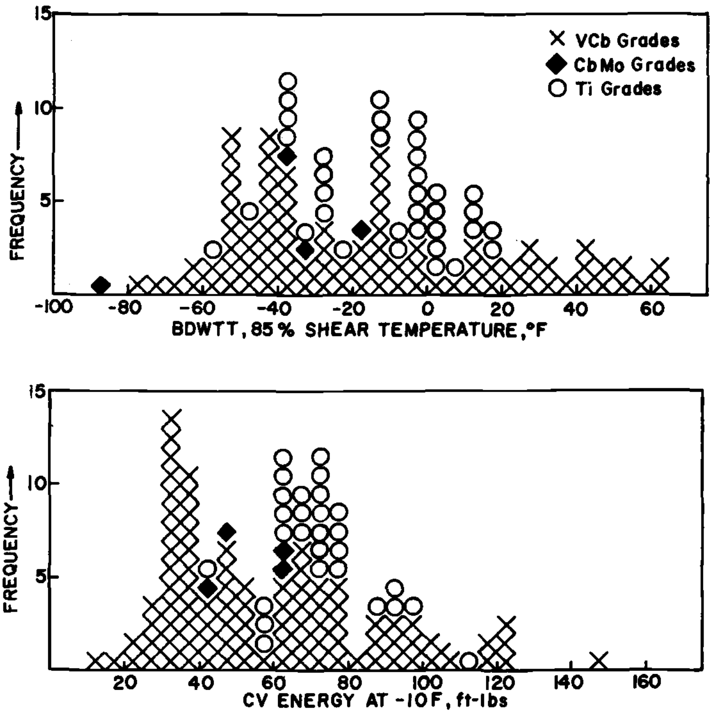

FIG. 4—*Distribution of impact properties for 19-mm (0.750-in.) mill plates.*

Grain Size—Because of the extremely fine ferrite generated in these steels, an intercept method of grain-size measurement was employed. The specific intercept technique utilized a 50-cm (ASTM Method for Estimating the Average Grain Size of Metals E 112-77) total-length circular pattern consisting of three concentric circles whose radii obey an arithmetic progression [*6*]. For these line pipe steels a magnification of × 1000 was needed to obtain the desired accuracy.

For the 19 mm (0.750-in.) gage mill trials, the range of ASTM grain size was 10.5 to 13.0. The grain-size measurements were useful for qualitatively evaluating the effects of various rolling practices, including changes in slab heating and percent of reduction below 900°C (1650°F). For example, on V-Cb mill plates the following results were obtained:

Plate	Slab Heating	Rolling Practice	Average Grain Size ASTM No.
0.750	1315°C (2400°F)	60% below 900°C (1650°F)	11.0
	1150°C (2100°F)	60% below 900°C (1650°F)	11.7
	1200°C (2200°F)	80% below 900°C (1650°F)	12.4

As these results illustrate, both a reduction in slab heating temperature and a more severe rolling practice below 900°C (1650°F) produce a finer grain size.

The grain-size measurements could be directly related to the mechanical properties. However, there was a significant scatter in these results, as seen in Fig. 5, which compares grain size and BDWTT fracture appearance for 19-mm (0.750-in.) gage V-Cb mill plates. Indeed, although ferrite grain size is clearly a dominant influence on the percent shear rating, the fact that there is significant scatter at any given grain size points to the existence of other influences, such as the amount of duplex structure. Both laboratory and mill rolling results presented examples where the same average grain size provided a wide range of BDWTT fracture-appearance results. For example, as shown in Fig. 6, the 1315°C (2400°F) slab heating produced a greater amount of duplex structure—in

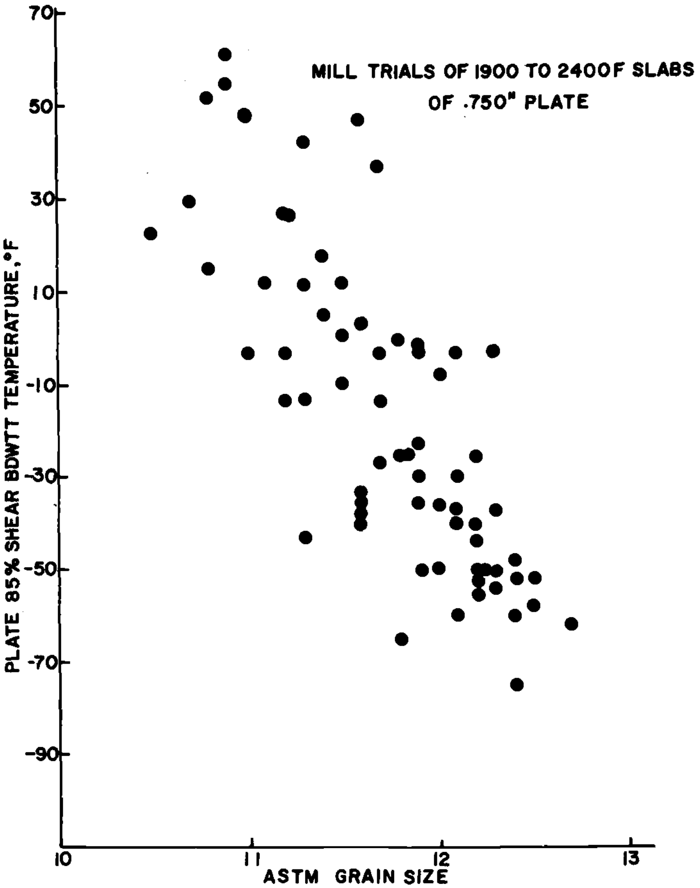

FIG. 5—*Relationship between ASTM grain size and plate 85 percent shear temperature.*

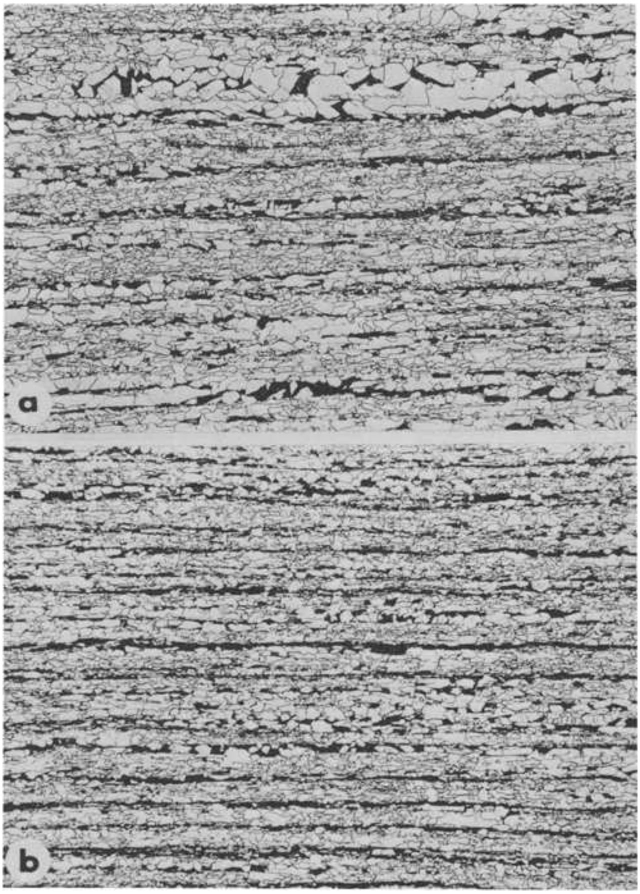

FIG. 6—*Variation of microstructure with slab reheating temperature, V-Cb grade at ×200 original magnification.* (a) *1315°C (2400°F) slab heating, ASTM grain size 12.7, plate BDWTT 85 percent shear −4°C (−42°F); and* (b) *1150°C (2100°F) slab heating, ASTM grain size 12.7, plate BDWTT 85 percent shear <−65°C (<−85°F).*

this case, a mixture of coarse and fine ferrite—than did the 1150°C (2100°F) slab heating. Thus, although the grain sizes were equivalent, the large difference in BDWTT 85 percent shear temperature could be explained by the presence of the duplex structure.

Percent Fine-Grain Ferrite Patches (%fgfp)—To further quantitatively define the duplex ferrite, we used a rating of observed fine-grain ferrite patches. This rating was obtained by utilizing a 100-point grid on ten fields at a magnification that gave approximately one point per ferrite patch. For the control-rolled steels examined in this study, ×100 to ×200 was normally used.

As in the case of grain size, the % fgfp was directly related to plate mill heating and rolling variables. The following table illustrates the trend of % fgfp for V-Cb production plates. The significance of this trend is that greater structural uniformity can be achieved either by going to lower slab-heating temperatures or increasing the rolling reductions at lower temperatures.

Plate Gage	Slab Heating	Rolling Practice	% fgfp
0.750	1315°C (2400°F)	60% below 900°C (1650°F)	39.0
	1150°C (2100°F)	60% below 900°C (1650°F)	71.0
	1090°C (2000°F)	60% below 900°C (1650°F)	79.5
	1040°C (1900°F)	60% below 900°C (1650°F)	81.5
	1200°C (2200°F)	81% below 870°C (1600°F)	82.5

The coupling of grain size and % fgfp data was useful in developing structure-property correlations, as demonstrated in the section on Regression Analysis.

Percent Pearlite/Lower Transformation Product—The titanium steel and the V-Cb steels showed a secondary phase consisting essentially of pearlite, whereas the Cb-Mo material had no pearlite. Only an occasional isolated area of lower transformation product (martensite/bainite) was observed on some V-Cb plates. For the V-Cb grades, the percent pearlite was directly tied to the carbon content, with percent pearlite ranging from 11 to 30 percent for the steel examined.

The BOF Cb-Mo heat produced a polygonal/acicular ferrite microstructure that is quite different from the polygonal ferrite generally observed in V-Cb line pipe grades. An example of the Cb-Mo microstructure is shown in Fig. 7. The structure was examined at various magnifications from ×200 to ×60 000 by means of optical, scanning, and transmission electron microscopy. The unusual structural features of the Cb-Mo grade are as follows: (*a*) optically, a polygonal/acicular ferrite structure plus an unresolved secondary phase are observed (Fig. 7*a*); (*b*) scanning microscopy resolves the secondary phase into what appears to be martensite and bainite patches (Fig. 7*b*); and (*c*) transmission electron microscopy reveals the presence of lath martensite (Fig. 7*c*).

The martensite/bainite product of this Cb-Mo heat constituted about 7 percent of the microstructure.

Microcleanliness—In general, all steels exhibited good cleanliness because of both the low sulfur contents and the addition of rare earths for sulfide shape control. Hence, these line pipe steels were devoid of large sulfide stringers. For nonmetallic cleanliness ratings, the total volume fraction of nonmetallics was established by examining 300 fields at ×1000

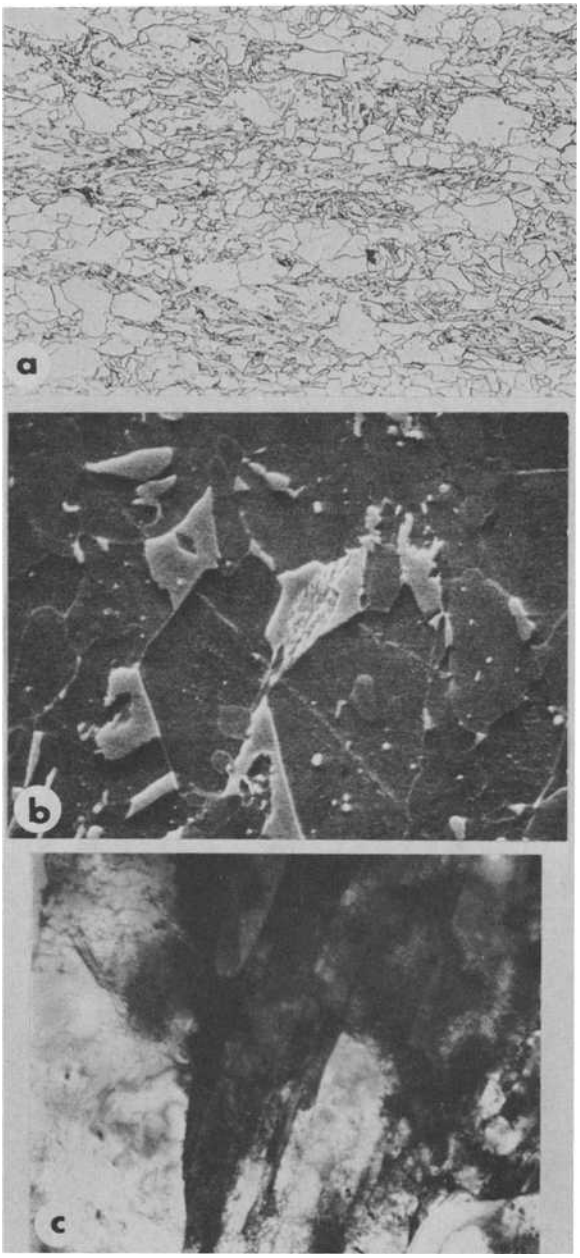

FIG. 7—*Representative microstructures of the Mo-Cb grade.* (a) *Original magnification ×500, optical, ASTM grain size 11.9;* (b) *original magnification ×2000, scanning electron microscopy; and* (c) *original magnification ×20 000, transmission electron microscopy.*

per sample. For the mill samples evaluated, the percent total volume fraction of nonmetallics ranged from 0.084 to 0.192 percent, with most of the nonmetallics being extremely fine oxides or oxysulfides, under 6 μm.

Regression Analysis

Both the laboratory and the mill-trials data were subjected to statistical analysis. Since the results of both sets of analyses were quite similar, the discussion will be limited to the mill-trial-based regression analysis of: (*a*) chemistry and processing on microstructure for the V-Cb grades, (*b*) chemistry and processing on mechanical properties for the V-Cb grades, and (*c*) plate-to-pipe mechanical property relationships for all the grades.

Regression Analysis of Chemistry and Processing on Microstructure

Four microstructural parameters were classified as dependent variables in the regression analysis based on 12 independent chemistry and processing variables. The variables pertinent to the regression were:

Chemistry Variables	Processing Variables	Microstructural Variables
Carbon	% TCR < 900°C (1650°F)	Grain size, μm
Manganese	Average will load < 900°C (1650°F)	ASTM No.
Vanadium	TCR ratio	Volume % pearlite
Columbium	Slab reheat temperature (SRT)	% fgfp
Nitrogen	Finish temperature	
Sulfur	Gage	

The chemistry variables are self-explanatory. The processing variables were selected to represent the time, temperature, deformation interactions that characterize the controlled-rolling practice. The % TCR< 900°C (1650°F) is a means of characterizing the above interactions designed for the rolling and is an indirect measure of the recovery, recrystallization, and grain growth occurring during processing. The average mill load (ML) < 900°C (1650°F) provides an indication of the severity of the controlled rolling. The TCR ratio describes the transfer intermediate gage relative to the finish gage. The slab reheat temperature (SRT) influences the starting austenite grain size and precipitate re-solution as well as the duplex nature of the microstructure. The finish temperature influences the recovery and recrystallization behavior. Finally, the plate gage strongly influences properties and accordingly is considered as a significant variable affecting microstructure. The microstructural parameters and their measurement were previously described. Table 1 lists each variable and its range.

The computer regression program employed for the analysis was capable of specifying first- and second-level variables that controlled the sequence in which they were entered into the regression equation.

TABLE 1—*Microstructural regression variables and their range.*

Variable	Average	Minimum	Maximum
Processing			
% TCR <1650°F	132.7	92.2	174.9
ML <1650°F, $\frac{\text{k-lb}}{\text{in.}}$	50.0	38.4	60.3
TCR ratio	4.43	3.47	6.56
Finish temperature, °F	1335	1250	1410
SRT, °F	2288	1900	2400
Gage, in.	0.681	0.587	0.777
Chemistry			
C	0.10	0.07	0.15
Mn	1.57	1.38	1.74
V	0.061	0.043	0.080
Cb	0.034	0.027	0.038
N	0.0094	0.0065	0.013
S	0.0062	0.002	0.013
Microstructure			
Grain size, μm	5.20	3.45	8.20
ASTM No.	11.9	10.5	13.0
Volume % pearlite	16.9	8.6	22.7
% fgfp	53.8	32.8	100.0

However, for the microstructural and mechanical property analysis, this option did not provide any significant benefit. Furthermore, all the independent variables were classed as level one and the program entered them sequentially into the regression based on the maximum F value, that is, the variable that best explained the regression. It should be noted that there were strong first-order interactions between some of the independent variables; and although good correlations were obtained, these interactions caused some inconsistencies in the results. These inconsistencies and the effect of interactions are discussed more fully in the mechanical-property regression section of this paper. The results of the regression analysis are summarized in Table 2.

As expected, the grain size and ASTM number produced almost identical results. (However, they cannot produce an identical result, because grain size and ASTM number are not linearly related. Furthermore, when converting grain size to ASTM number, we rounded off to the nearest tenth of an ASTM number, thereby introducing some minor variation.) The arrows in Table 2 indicate whether the independent variable should be increased (↑) or decreased (↓) to cause the direction of change indicated for the corresponding dependent variable. For example, to achieve a fine grain size a lower slab reheat temperature should be used, and this empirical result is consistent with the finer austenite grain size that would be obtained at lower slab reheating temperatures. Simi-

TABLE 2—*Regression analysis of chemistry and processing on microstructure.*

Dependent Variable	Number	Multiple Correlation Coefficient	Standard Error of the Estimate, ±1σ	Independent Variables Explaining Regression in Order of Importance[a]
↓Grain Size, μm	50	0.781	±0.73 μ	↑C, ↓SRT, ↓Mn, ↓V, ↓ML <1650, ↓gage, ↓Cb, ↓TCR ratio
↑ASTM No.	50	0.795	±0.36	↑C, ↓SRT, ↓Mn, ↓Cb, ↓gage, ↓TCR ratio, ↓ML <1650
↓Volume % pearlite	50	0.631	±2.6%	↓C, ↓gage, ↓V, ↓Mn, ↑Cb, ↓SRT
↑% fgfp	41	0.860	±8.9%	↓SRT, ↓Mn, ↓ML <1650, ↓TCR ratio, ↑TCR <1650, ↑finish temperature

[a] The sign ↑ indicates the need to increase and ↓ the need to decrease the independent variable to cause the direction of change indicated for the corresponding dependent variable.

larly, one could increase the % fgfp by the required changes listed in the independent-variables line in Table 2. (For reasons noted later, there are exceptions, for example, in the case of manganese.) As will be shown later in the paper, the grain size and % fgfp correlate with the mechanical properties, specifically the 85 percent shear BDWTT temperature. Figures 8 shows the predicted versus measured grain size results based on the regression analysis. Figure 9 shows a similar plot for the % fgfp.

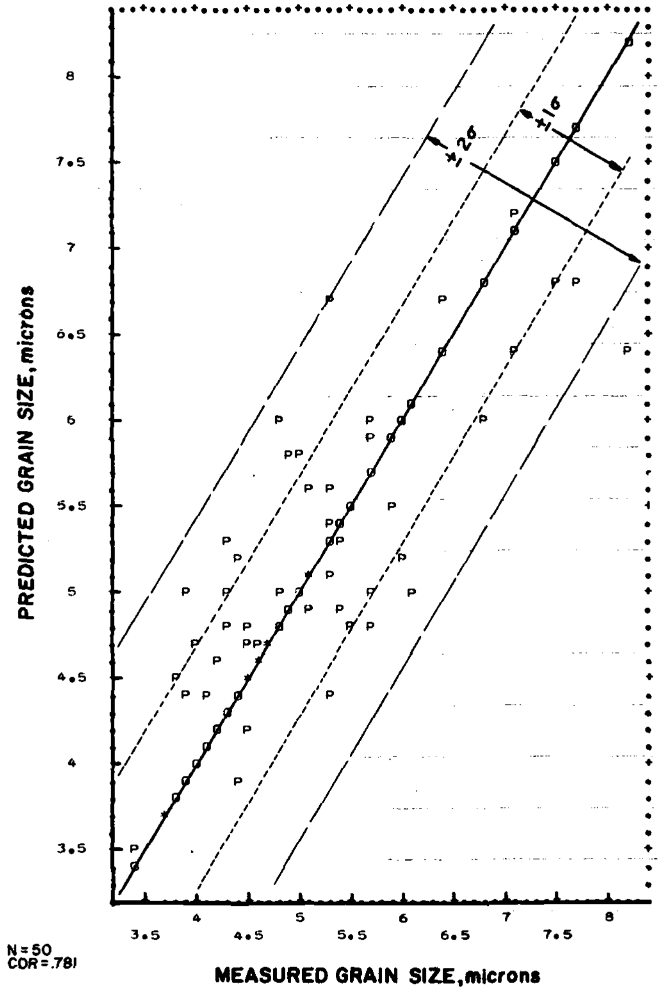

FIG. 8—*Computer plot showing the predicted grain size based on the regression analysis and the measured grain size.*

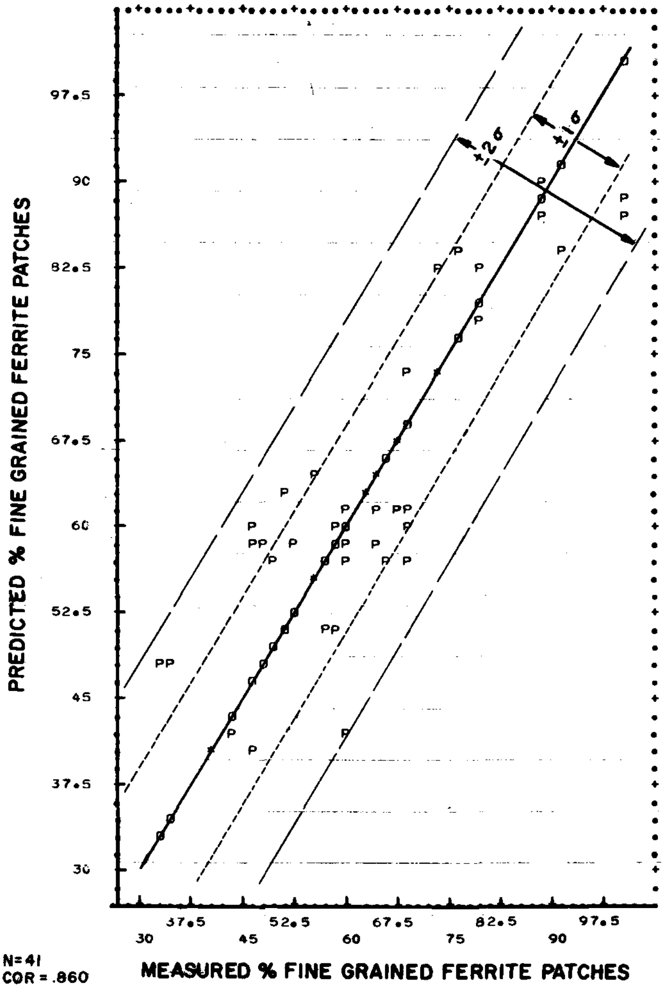

FIG. 9—*Computer plot showing the predicted percent fine grain ferrite patches (% fgfp) based on the regression analysis and the measured % fgfp.*

Regression Analysis of Chemistry and Processing on Mechanical Properties

Although the correlation of chemistry and processing on microstructure is important from the standpoint of design, a more useful regression analysis is obtained by determining the influence of chemistry and processing on mechanical properties. These regressions can then be used for predictive purposes.

The transverse mechanical properties used in the regression were: 0.2 percent offset yield strength, tensile strength, CV_{15} transition temperature, CV 50 percent FATT, CV 100 percent shear temperature, CV energy absorbed at −45°C (−50°F), and the BDWTT 85 percent shear temperature. Table 3 summarizes the results of this regression where the major chemistry and processing variables were introduced into the regression as level-one factors based on F value. Referring to Table 3, the arrows alongside the dependent variables indicate the direction (↑) to increase strength and the direction (↓) to increase toughness in the plate, and the arrows next to the independent variables indicate the corresponding directions to achieve these desired improvements. It would not be practical to consider each of these chemistry and processing factors relative to the dependent variables. However, for those interested in the methodology, it will be useful to provide at least two key examples—the CV energy at −45°C (−50°F) and the 85 percent shear BDWTT temperature. Before discussing the examples, it should be pointed up that the data from Tables 2 and 3 are being treated in a somewhat qualitative way in that the regression coefficients for each factor have not been presented. This omission was intentional, since the regression coefficients obtained will change with the number of data sets until a sufficiently large number is available. Thus, although 50 data sets is sufficient for the analysis presented, a final set of regression coefficients would probably require 500 or more data sets.

In designing the controlled-rolling practice to obtain an increase in the energy absorbed at −45°C (−50°F), the regression analysis in Table 3 indicates one should increase the total cumulative reduction below 1650°F (TCR <1650), average finishing stand mill load below 1650°F (ML <1650), finish temperature, and manganese, and decrease the SRT and gage. All of these factors are consistent with the influence on the microstructure to achieve the very fine grain size and high percent of fgfp that would provide the desired result.

However, where obtaining a decrease in the 85 percent shear BDWTT temperature is concerned, the regression analysis produced two inconsistencies. Namely, the average ML <1650 should be decreased and the carbon should be increased. These inconsistencies are explainable as follows. The average ML <1650 has a first order interaction with the TCR <1650, and the increase in the TCR <1650 accounts for the wrong-way influence of the average ML <1650. The effect of carbon is quite small, since its regression coefficient is −1.432, and changes as much as 10 points in carbon content would cause less than a 39°C (2°F) change in the 85 percent BDWTT shear temperature.

Since yield strength and BDWTT 85 percent shear temperature are two of the mechanical-property requirements usually specified for pipe applications, the computer plot of predicted versus measured results for both of these dependent variables, based on the regression results in Table 3, is shown in Figs. 10 and 11, respectively. Similar plots were obtained for

TABLE 3—*Regression analysis of chemistry and processing on properties.*

Dependent Variable	Number	Multiple Correlation Coefficient	Standard Error of the Estimate ± 1σ	Independent Variables Explaining Regression in Order of Importance
↑ Yield strength, ksi	50	0.869	3.90	↓ finish temperature, ↓ gage, ↑ V
↑ Tensile strength, ksi	50	0.825	3.42	↓ finish temperature, ↑ SRT, ↓ gage
↓ CV_{15}, °F	51	0.878	17.7	↑ ML <1650, ↓ SRT, ↓ gage
↓ FATT 50, °F	51	0.831	24.1	↑ TCR <1650, ↓ TCR ratio, ↓ finish temperature, ↓ SRT, ↓ gage, ↑ C
↓ CV 100% shear, °F	51	0.712	36.9	↑ TCR <1650, ↓ TCR ratio, ↓ finish temperature, ↓ SRT, ↓ gage, ↑ V
↑ CV energy at −50°F, ft·lb	50	0.815	15.7	↑ TCR <1650, ↑ ML <1650, ↑ finish temperature, ↓ SRT, ↓ gage, ↑ Mn
↓ 85% shear BDWTT temperature, °F	53	0.777	20.2	↑ TCR <1650, ↓ ML <1650, ↓ finish temperature, ↓ SRT, ↓ gage, ↑ C

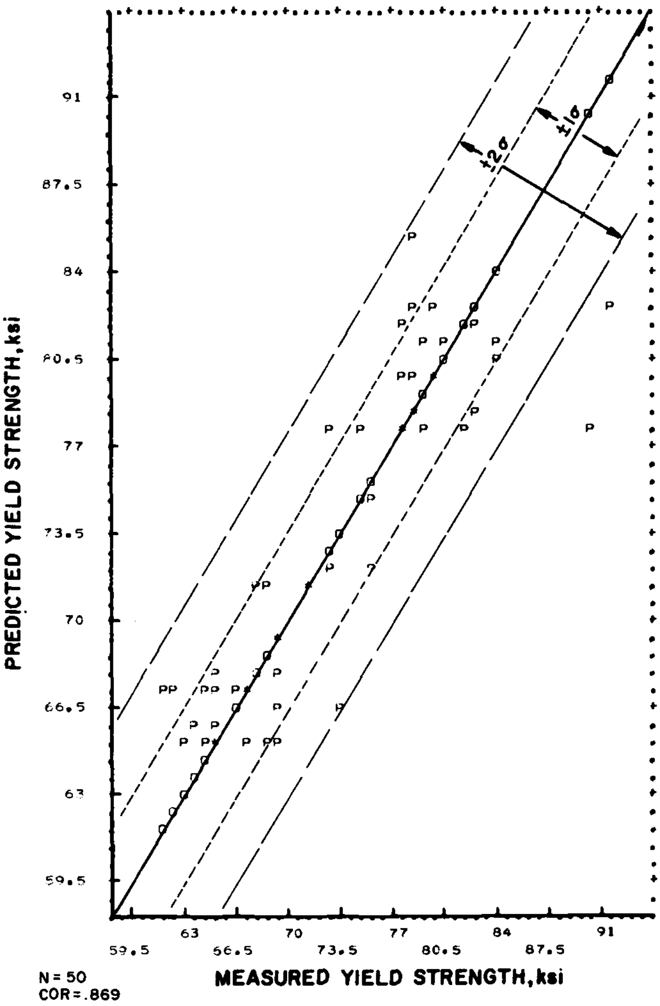

FIG. 10—*Computer plot showing the predicted yield strength based on the regression analysis and the measured yield strength.*

each of the mechanical property variables previously mentioned, and the regression equations were then utilized to predict the plate properties for a second full-scale mill trial conducted at our Sparrows Point and Burns Harbor plants.

At Sparrows Point, normal slab reheating of 1315°C (2400°F) was employed and a rolling practice described previously was used to obtain plates of nominal 16-mm (0.630-in.) gage. Table 4 lists the predicted and measured mechanical properties for two 220-ton BOF heats that provided

23 double-patterned plates that were subsequently fabricated into forty-six 1065-mm (42-in.) outside diameter line pipes.

As the results in Table 4 indicate, the regression analysis provided an excellent tool for predicting the plate properties based on chemistry and processing. A similar analysis was performed for a 300-ton heat melted at Burns Harbor and rolled to nominal 19-mm (0.750-in.) gage plate using a reduced slab-reheating temperature of 1200°C (2200°F). Twelve double-patterned plates were obtained, which were fabricated into twenty-four 1065-mm (42-in.) outside diameter line pipes, and the predicted and measured mechanical properties are listed in Table 5.

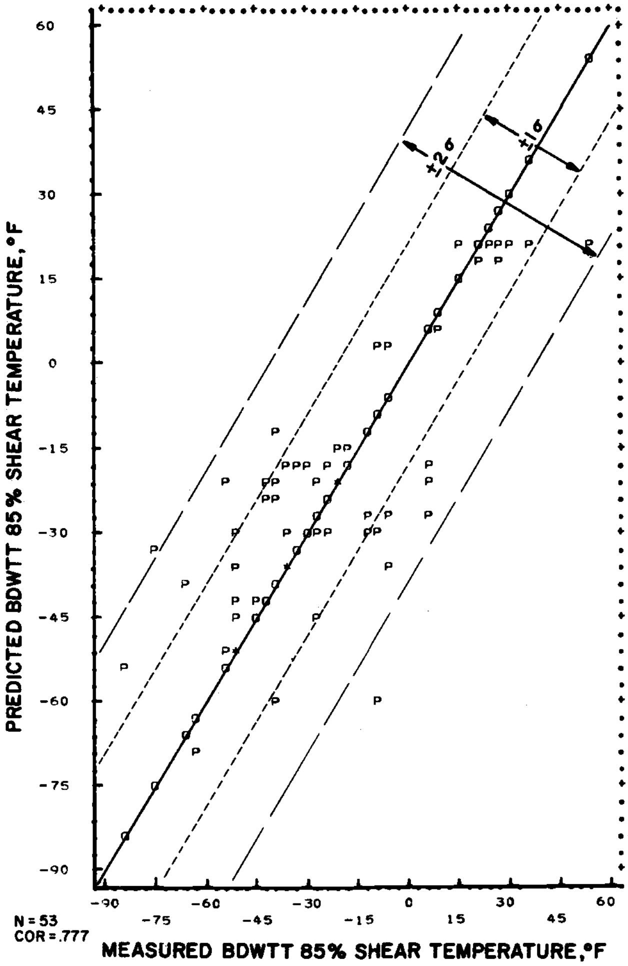

FIG. 11—*Computer plot showing the predicted BDWTT 85 percent shear temperature based on the regression analysis and the measured BDWTT 85 percent shear temperature.*

TABLE 4—*Comparison of predicted and measured mechanical properties for 0.630-in. gage plate.*

Mechanical Property	Predicted Value	Average Measured Value
Yield strength, ksi	79.6	80.5
Tensile strength, ksi	94.0	93.1
CV_{15} transition temperature, °F	−96	−100
CV 50% FATT, °F	−108	−102
CV 100% shear temperature, °F	−58	−49
CV energy at −50°F, ft·lb	35	40
85% shear BDWTT temperature, °F	−30	−20

As the results in Table 5 indicate, although they were not as accurate as those for the Sparrows Point rolling, the regression analysis provided a good tool for predicting the plate properties based on chemistry and processing.

The discussion on regression analysis has thus far considered the relationship between chemistry, processing, and microstructure and those between chemistry, processing, and mechanical properties. The more usual approach to structure-property studies would, of course, be regression analysis of mechanical properties and microstructure. To illustrate a regression analysis of this type, we have chosen the 85 percent shear BDWTT temperature, a requirement that is critical for Arctic line pipe applications. All of the plate data for the different grades and gages as previously described were grouped, but each grade was given its own plot symbol as shown in Fig. 12. A regression analysis was performed using the microstructural parameters listed in Table 2. The best fit for this wide range of chemistries and processing was obtained using a microstructural parameter that included the grain size and % fgfp. As shown in Fig. 12, for 91 data sets a correlation coefficient of 0.760 and a standard error of

TABLE 5—*Comparisons of predicted and measured mechanical properties for 0.750-in. gage plate.*

Mechanical Property	Predicted Value	Average Measured Value
Yield strength, ksi	76.9	75.7
Tensile strength, ksi	91.5	86.7
CV_{15} transition temperature, °F	−116	−138
CV 50% FATT, °F	−120	−130
CV 100% shear temperature, °F	−66	−93
CV energy at −50°F, ft·lb	44	67
85% shear BDWTT temperature, °F	−49	−51

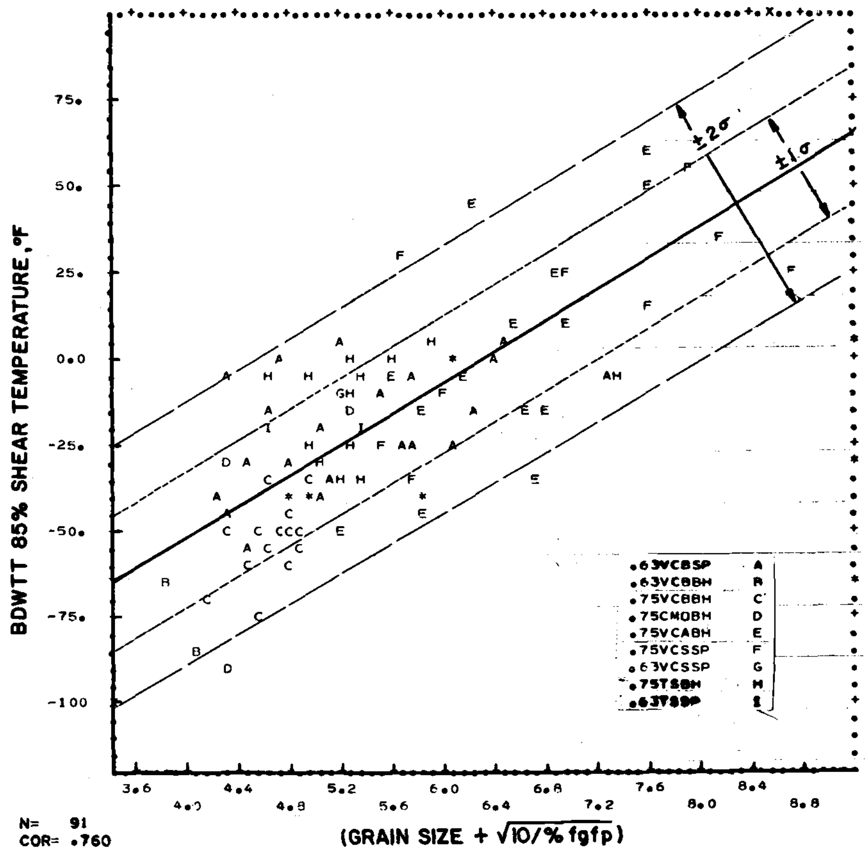

FIG. 12—*Computer plot showing the dependence of the BDWTT 85 percent shear temperature on the microstructural parameter (grain size +* $\sqrt{10/\%\ fgfp}$*); grain size in microns.*

±9.4°C (±19.9°F) was obtained. Given the wide range of chemistry and processing, this agreement is quite good.

Regression Analysis of Plate-to-Pipe Shift in Properties

The 85 pipes comprising the second mill trial study provided a common base of approximately 50 data sets for evaluating the observed plate-to-pipe property variations. Table 6 summarizes the average change observed going from plate to pipe. With the exception of the CV energy, for the V-Cb grade the changes observed were relatively independent of wall thickness. Comparison of the average change with the first mill trial (Columns 4 and 5) shows that there was a significant difference for the strap yield strength and the toughness as measured by CV_{15}, FATT 50, CV 100, and BDWTT 85 percent shear temperature. Since the last trial

TABLE 6—*Average Δ observed plate to pipe. (Numbers in parentheses indicate number of tests.)*

Transverse Mechanical Property	Sparrows Point 16-mm (0.630-in.) Wall, V-Cb	Burns Harbor 19-mm (0.750-in.) Wall, V-Cb	Burns Harbor 19-mm (0.750-in.) Wall, Mn-Mo-Cb	All Data, V-Cb	All Data, First Mill Trial
Ring yield strength, ksi	(20) + 0.4	(23) + 0.7	(7) +25.4	(48) + 0.4	+ 2.2
Strap yield strength, ksi	(20) −10.4	(23) − 8.9	(7) +10.0	(48) − 9.7	− 2.5
Tensile strength, ksi	(20) − 4.0	(23) + 0.8	(7) − 0.5	(48) − 1.4	+ 1.6
CV_{15} transition temperature, °F	(25) +16	(23) +17	(7) +33	(53) +16	+54
CV 50% FATT, °F	(24) +16	(23) 14	(7) + 6	(52) +16	+53
CV 100% shear, °F	(23) + 2	(23) 10	(7) −11	(51) + 6	+47
CV energy at −10°F, ft · lb	(24) −17	(23) − 4	(23) − 15	(52) − 9	−15
CV energy at +32°F, ft · lb	(25) −22	(23) − 7	(23) − 12	(53) −13	−12
BDWTT 85% shear, °F	(25) +12	(23) +16	(23) +13	(53) +14	+31

included four different grades and four different slab reheating temperatures, the changes observed for this trial are considered to be more representative of a production order. The changes tabulated in Column 4 are very similar to those reported by Yamaguchi et al [2] for a V-Cb grade with additions of copper, nickel, and chromium. The results also document the positive plate-to-pipe shift in strength for the manganese-molybdenum-columbium (Mn-Mo-Cb) composition.

To determine the effect of the changes in properties associated with the pipe fabrication processes relative to the minimum pipe-property requirements, regression analysis was performed on the plate-pipe data set. Linear, polynomial, and logarithmic models were fitted to the data. The most consistent model that explained all of the data was the linear model. Table 7 summarizes the results of the linear regression model. The CV energy at −25°C and 0°C (−10°F and +32°F) show a poor correlation, most likely due to the large scatter in the data.

Application of these correlations to indicate the minimum plate properties to provide the required pipe properties at a 95 percent confidence level is illustrated in Figs. 13 and 14. Figure 13 is a computer plot of the pipe BDWTT 85 percent shear temperature versus the plate BDWTT 85 percent shear temperature. The solid line is the regression fit, and the dotted lines represent the $\pm 1\sigma$ and $\pm 2\sigma$ standard error of the estimate of 5.7°C (12.1°F) from Table 7. The N of 53 indicates the number of data sets, and a good correlation coefficient of 0.835 was obtained. The number shown on the computer plots indicates the number of data points at that position. Since these data include normal and low slab reheating temperatures, we could use this plot to determine the minimum plate 85 percent BDWTT shear temperature to meet design requirements of −5°C or −25°C (+23°F or −10°F). As shown in Fig. 13, a value of −25°C (−10°F) or lower in the plate will provide a −5°C (+23°F) value in the pipe with a 95 percent confidence level. The plate value to assure the lower of these requirements with a 95 percent level is −43°C (−45°F). As shown by the original plate data, there were several plates with an 85 percent shear temperature greater than −25°C (−10°F) that according to the previous analysis could have resulted in pipe with an 85 percent BDWTT shear temperature greater than −5°C (+23°F). However, as the actual pipe results indicated, these plates produced acceptable pipe because the plate-to-pipe shift in these cases was less than the 2σ limit. Of equal significance is the result that all the other plates with 85 percent BDWTT shear temperatures less than −25°C (−10°F) produced pipe within the −5°C (+23°F) requirement.

Figure 14 is a computer plot of the pipe strap yield strength (0.5 percent extension under load) versus the plate yield strength (0.2 percent offset). The solid line is the linear regression line, and the dotted lines represent the $\pm 1\sigma$ and $\pm 2\sigma$ limits for the standard error of the estimate of 13.9 MPa

TABLE 7—*Plate-to-pipe shift, linear regression model. (Numbers in parentheses indicate number of tests.)*

	All Data (48)		19-mm (0.750-in.) Data (23)		16-mm (0.630-in.) Data (25)	
	Correlation Coefficient	1σ	Correlation Coefficient	1σ	Correlation Coefficient	1σ
Ring yield strength	0.609	3.34 ksi	0.699	2.53 ksi	0.312	3.15 ksi
Strap yield strength	0.718	2.02 ksi	0.566	1.83 ksi	0.626	2.00 ksi
Tensile strength	0.639	1.89 ksi	0.729	1.54 ksi	0.616	1.51 ksi
CV_{15}	0.800	16.9°F	0.610	17.9°F	0.620	14.5°F
50% FATT	0.818	14.8°F	0.701	14.8°F	0.714	11.0°F
100% shear	0.732	21.4°F	0.501	21.8°F	0.572	15.3°F
Energy at 25°C (−10°F)	0.417	13.7 ft · lb	0.010	8.6 ft · lb	0.035	9.01 ft · lb
Energy at 0°C (+32°F)	0.502	14.4 ft · lb	0.202	11.1 ft · lb	0.263	9.05 ft · lb
BDWTT 85% shear	0.835	12.1°F	0.706	9.5°F	0.763	11.1°F

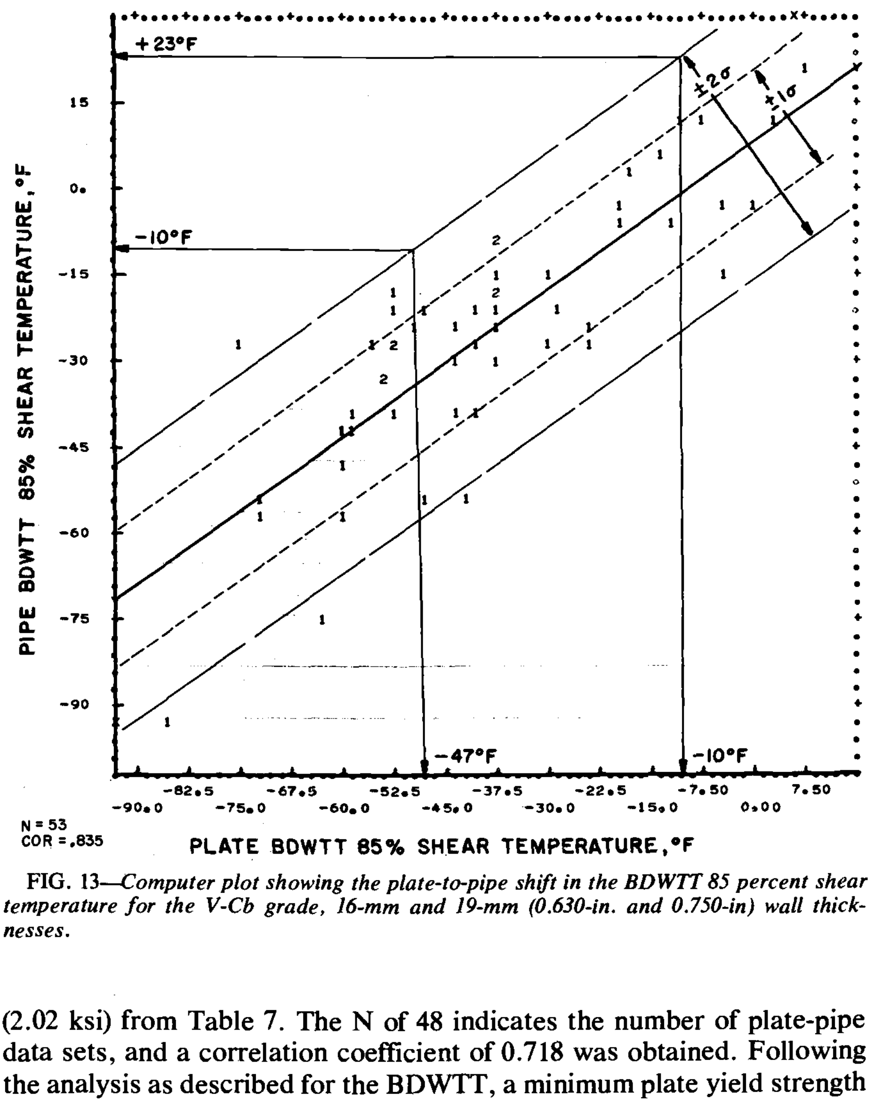

FIG. 13—*Computer plot showing the plate-to-pipe shift in the BDWTT 85 percent shear temperature for the V-Cb grade, 16-mm and 19-mm (0.630-in. and 0.750-in) wall thicknesses.*

(2.02 ksi) from Table 7. The N of 48 indicates the number of plate-pipe data sets, and a correlation coefficient of 0.718 was obtained. Following the analysis as described for the BDWTT, a minimum plate yield strength of 545 MPa (79 ksi) is required to provide an X-65 pipe requirement for a 95 percent confidence level. The statistical analysis shows that for an X-70 pipe requirement at a 95 percent confidence level a minimum plate yield of 614 MPa (89 ksi) is necessary.

With respect to an X-70 strap yield strength requirement, a minimum 614 MPa (89 ksi) plate yield strength is probably beyond the capability of a control-rolled V-Cb grade. Thus, even though a majority of the pipe would meet an X-70 specification, based on this analysis there will be a significant number of pipe that will not, and the resulting poor product yield places this requirement beyond the capability of most producers.

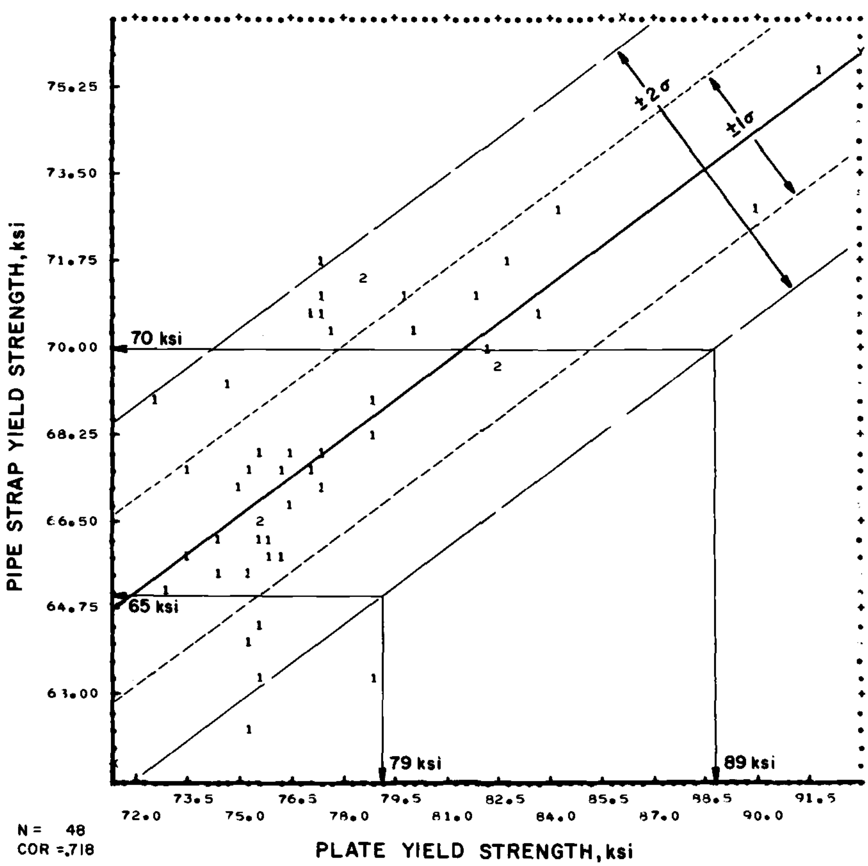

FIG. 14—*Computer plot showing the plate-to-pipe shift in the yield strength for the V-Cb grade, 16-mm and 19-mm (0.630-in. and 0.750-in.) wall thicknesses.*

However, it should be emphasized that the pipe has an actual strength in excess of X-70 as measured by the ring yield strength, which is more representative of the actual stress conditions of the pipe in service. That is, the failure to consistently meet the X-70 strap requirement is inherent in the strap test and the associated test specimen preparation and is not a proper indication of the true yield strength of the pipe.

To further document this thesis, tension test specimens were machined from the pipe [8-mm (0.357-in.) from the 16-mm (0.630-in.) wall, 13-mm (0.505-in.) from the 19-mm (0.750-in. wall)] without flattening it. This procedure largely eliminates the negative contribution of the Bauschinger effect. The yield and tensile results of these tests compared with the standard strap test results prepared by flattening using the inch method are presented in Table 8. This method of flattening involves an initial

TABLE 8—*Comparison of tests of normally flattened pipe straps and round tension specimens.*

	Normally Flattened (Inch Method)		8-mm (0.357-in.) Round Specimen	
Pipe Code	Yield Strength, ksi	Tensile Strength, ksi	Yield Strength, ksi	Tensile Strength, ksi
			×70 Requirement	
260–1F	72.1	89.9	79.2	93.0
259–2B	73.4	91.1	80.1	91.9
274–1B	71.8	89.0	75.7	92.5
277–1B	68.1	87.4	73.3	89.5
313–2F	70.6	93.7	79.4	93.5
314–1B	69.7	93.7	78.7	96.4
			13-mm (0.505-in.) Round Specimen, ×65 Requirement	
317–2F	66.6	87.1	71.0	89.1
319–1F	62.6	84.8	68.2	86.5
001–2B	67.0	90.0	67.2	90.6
009–1B	65.5	86.6	70.4	86.7

press to remove most of the pipe curvature and then individual presses in increments of about an inch along the specimen length until it is fully flat. The machined round tension specimens provided results consistently higher than the strap yield strengths—on the order of 34 to 69 MPa (5 to 10 ksi).

Although a detailed explanation of the large change in yield strength from plate to pipe is not the intent of this paper, the following discussion provides some insight into the complexity of the phenomenon. During the pipe fabrication process, the plate undergoes various cycles of compression and tension, and the complicated pattern of strain hardening and the subsequent strap specimen preparation and Bauschinger effect all combine to influence the measured strap yield strength. An attempt to correlate this change in strength with the processing variables has been unsuccessful. The only correlation that consistently explains the data is the dependence of the change on the plate yield strength. A similar result was reported by Tanaka et al [7]. Figure 15 shows this correlation, where delta strength (0.5 percent extension under load pipe yield strength minus 0.2 percent offset plate yield strength) is plotted versus the plate yield strength of the X-70, 16-mm (0.630-in.) wall data. What this plot indicates is that for a V-Cb grade the greater the strengthening introduced into the plate by thermomechanical processing, the greater is the subsequent loss upon fabrication into pipe. For example, as shown in Fig. 15, a 620 MPa (90 ksi) plate will produce a 510 MPa (74 ksi) pipe, and a 552 MPa (80 ksi) plate will produce a 480 MPa (70 ksi) pipe. The standard error for both sets of data was 14 MPa (2 ksi). Thus, a very severe controlled rolling with a very low finishing temperature can increase the plate yield strength 69 MPa (10 ksi), but the net pipe strap yield strength increase will be only about 28 MPa (4 ksi).

Conclusions

The property requirements for Arctic line pipe can be satisfied by balancing the chemistry and processing for a given specification. X-70 strength levels with severe Charpy and BDWTT requirements at design temperatures of −10 to 0°C (15 to 30°F) could be achieved by: (*a*) low-carbon low-sulfur Si-Al killing, and vanadium and columbium microalloying additions, and (*b*) processing at normal slab reheating temperatures, 150 percent TCR <900°C (1650°F), and finishing temperatures 730 to 760°C (1350 to 1400°F). To achieve X-65 strength levels with very stringent Charpy and BDWTT requirements at lower design temperatures of −25 to −18°C (−15 to 0°F), similar chemistry control is required and the processing must include low slab reheating temperatures and a finishing temperature of 705°C (1300°F).

The improved strength and toughness properties are associated with a fine ferrite grain size and a high percent fine-grain ferrite patches (% fgfp).

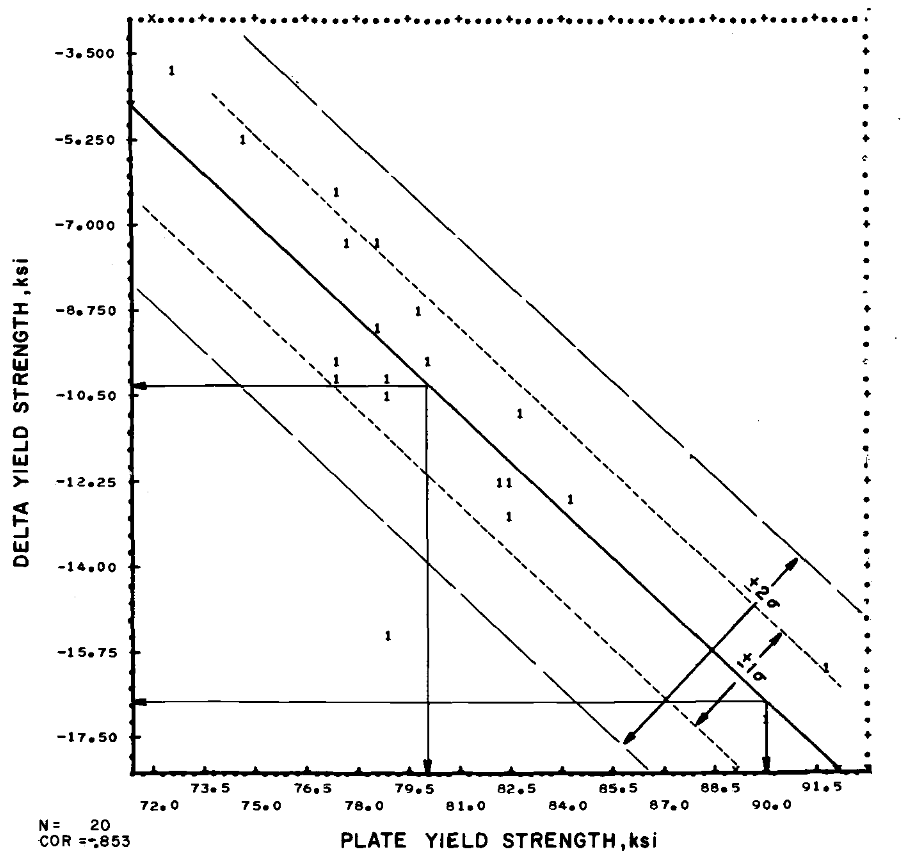

FIG. 15—*Computer plot showing the dependence of the delta yield strength (0.5 percent extension under load pipe strap yield strength minus 0.2 percent offset plate yield strength) on the plate yield strength for the V-Cb grade, 16-mm (0.630-in.) wall thickness.*

Specifically, to assure an 85 percent shear fracture appearance below −23°C (−10°F) in the pipe, the control-rolled plate must have a grain size number greater than ASTM 11 and a % fgfp value greater than 75 percent.

The application of regression analysis provided a useful correlation of mechanical properties and chemistry and processing variables. This approach provides a tool for designing alloys and processing to meet desired property requirements. In addition, the regression equations developed were useful in predicting the mechanical properties for control-rolled plates.

Based on the regression analysis at a 95 percent confidence level, a minimum plate yield strength of 614 MPa (89 ksi) is necessary to achieve an X-70 strap yield strength in the line pipe. Because of the Bauschinger effect, the higher the plate yield strength, the greater the strength loss going from plate to pipe. Thus, from a productivity yield standpoint, an X-70 strap yield strength is beyond the capability of a V-Cb alloy chemistry. However, machined tension specimens or ring yield-strength specimens both indicate that an X-70 pipe can be achieved with a V-Cb grade and practical mill processing conditions.

Acknowledgments

We would like to acknowledge the cooperation and helpful suggestions of the Sparrows Point, Burns Harbor, and Steelton personnel during the mill trials. In addition, we wish to thank the following Homer Research personnel for their many helpful discussions and contributions during this study: J. D. Dennison, P. R. Slimmon, and M. J. Roberts.

References

[*1*] Gladman, T., Dulieu, D., and McIvor, I. D., "Structure Property Relationships in High-Strength Microalloyed Steels," Microalloying 75, Session 1, 1975, pp. 25–48.

[*2*] Yamaguchi, T., Osuka, T., Taira, T., and Iwasaki, N., "Effect of Processing Conditions on the Mechanical Properties of Controlled-Rolled Plate for Large Diameter Line Pipe," Microalloying 75, Session 2B, 1975, pp. 49–57.

[*3*] Civallero, M. and Parrini, C., *Proceedings*, International Conference on the Science and Technology of Iron and Steel, Supplementary Transactions, Iron and Steel Institute of Japan, Vol. II, 1971, pp. 758–764.

[*4*] McCutcheon, D. B., Trumper, T. W., and Embury, J. D., *Revue de Metallurgie*, Feb. 1976, pp. 143–174.

[*5*] Goetz, G. J., *Journal of Metals*, Aug. 1977, pp. 12–18.

[*6*] Abrams, H., *Metallography*, Vol. 4, 1971, pp. 59–78.

[*7*] Tanaka, T., Funakoshi, T., Veda, M., Tsaboi, J., Yasuda, T., and Utahashi, C., "Development of High-Strength Steel with Good Toughness at Arctic Temperatures for Large-Diameter Line Pipe," Microalloying 75, Session 2B, 1975, pp. 38–48.

Chiaki Ouchi,[1] *Junichi Tanaka,*[1] *Isao Kozasu,*[1] *and Koshiro Tsukada*[2]

Control of Microstructure by the Processing Parameters and Chemistry in the Arctic Line Pipe Steels

REFERENCE: Ouchi, Chiaki, Tanaka, Junichi, Kozasu, Isao, and Tsukada, Koshiro, "**Control of Microstructure by the Processing Parameters and Chemistry in the Arctic Line Pipe Steels,**" *MiCon 78: Optimization of Processing, Properties, and Service Performance Through Microstructural Control, ASTM STP 672,* Halle Abrams, G. N. Maniar, D. A. Nail, and H. D. Solomon, Eds., American Society for Testing and Materials, 1979, pp. 105–125.

ABSTRACT: With the increasing demand for the higher strength and superior low-temperature toughness in arctic line pipe steels, new processings as well as the new kinds of steels have been developed. Controlled rolling, accelerated cooling after controlled rolling, and heat treatment after pipe forming are included in these processes. The characteristic features of the various microstructures obtained by each processing and their relationships with the mechanical properties are described. The recent development of controlled rolling practice tends to control the wider range of rolling temperature and to utilize the various strengthening mechanisms, accompanied with improvement of toughness. The accelerated cooling after controlled rolling, developed as a new process in plate mill, gives rise to the duplex structure composed of very fine ferrite and bainite. This process enables one to decrease carbon content or alloying elements and to improve weldability of line pipe steels. The microstructural features of heat treatment after piping and welding are described, emphasizing those of weldments.

KEY WORDS: steels, microstructure, line pipe steel, controlled rolling, accelerated cooling, heat treatment, mechanical properties, weldability, stress corrosion, high-strength steel

The remarkable technological progress in the production of the line pipe steels during the past decade should be considered from the two aspects. First, the processing of the arctic line pipe steels is one of the most

---

[1] Research metallurgist, senior researcher, and manager, respectively, Technical Research Center, Nippon Kokan K. K., Kawasaki, Japan.

[2] Research metallurgist, Fukuyama Research Laboratory, Nippon Kokan K. K., Fukuyama, Japan.

successful practical applications of the thermomechanical treatment (TMT) in the ferritic steels [*1,2*].[3] Secondly, the required properties for the arctic line pipe steels have been obtained by development of the steels having suitable compositions or alloy systems in the low-carbon low-alloy steels range. The superior low-temperature toughness and the high strength needed as the primary properties of the arctic line pipe steels have been attained by progress in the controlled-rolling practice with a beneficial utilization of microalloying elements such as columbium or vanadium [*2,3*]. The TMT effects of controlled rolling results in the general refinement of microstructure and improvement of the mechanical properties through the ingenious control of austenitic grain growth and recrystallization behavior during hot rolling.

While the demands for higher strength and more superior toughness or ductility are still increasing, the recent trend of the arctic line pipe steels is characterized in the dimensional expansion of the pipes, such as larger diameter and thicker walls. Both of these trends encourage the progress for more ingenious controlled-rolling practices within the limitations of mill facilities in the existing plate mill.

Another trend in the arctic line pipe steels is the demand for various secondary properties such as improvement of weldability, including higher toughness in weldments and resistance to cold cracking [*4*], and resistance to stress corrosion cracking in sour gas atmospheres [*5*]. These tendencies not only enhance the utilization of the fundamental metallurgical knowledge more widely, but also encourage the development of new processing to satisfy these requirements.

The processes of accelerated cooling after controlled rolling in the plate mill and heat treatment after pipe forming have been studied and developed for dealing with these demands. Both processes enable not only the production of higher grades of the arctic line pipe above strength level X-70, but also the improvement of various secondary properties through a reduction of carbon content or carbon equivalent in the high-strength low-alloy steels. Consequently, this paper describes these processes in addition to controlled-rolling practice. The particular emphasis is put on the description of the relationship of processing parameters and the mechanical properties, and the characteristic features of microstructure obtained in each processing are discussed in relation to the mechanism of strengthening or improvement of low-temperature toughness.

Materials

The studies of the controlled rolling and accelerated cooling were carried out in the experimental rolling mill. The chemical compositions of

---

[3] The italic numbers in brackets refer to the list of references appended to this paper.

TABLE 1—*Chemical compositions of steels used (weight percent).*

Steel	C	Si	Mn	P	S	Ni	Mo	Cu	Cb	V
A	0.07	0.33	1.50	0.013	0.003	0.23	0.12	...	0.040	0.072
B	0.06	0.27	1.99	0.019	0.003	0.26	0.40	...	0.052	...
C	0.12	0.33	1.38	0.021	0.007	...	...	...	...	...
D	0.13	0.26	1.25	0.014	0.004	...	...	...	0.031	...
E	0.14	0.27	1.33	0.009	0.006	...	...	...	0.024	0.033
F	0.12	0.30	1.30	0.015	0.004	...	...	...	0.032	0.038
G	0.10	0.31	1.50	0.008	0.005	0.23	...	0.17	0.036	0.092
H	0.13	0.30	1.27	0.019	0.005	0.14	...	0.25	...	...

the steels used are shown in Table 1. Steels A and B used for the investigation of the processing parameters of controlled rolling have the microstructure of polygonal ferrite-pearlite and acicular ferrite, respectively. Steels C through G were used for a study of accelerated cooling, and all of these steels have the structure of ferrite-pearlite in as-rolled condition covering the strength levels from X-52 to X-70. The study of heat treatment after pipe forming was carried out with Steel H. The plate thickness was 0.02 m in all investigations unless otherwise stated. The mechanical properties were investigated by taking specimens from the center of the plate and transverse to the direction of rolling.

Controlled Rolling

Processing Parameters and Mechanical Properties

Although refinement of microstructure was considered to be attained primarily by the low finishing temperature of rolling in the original controlled rolling [*6*], a recent advance in controlled rolling practice has been to control the wider range of rolling temperature from slab reheating temperature to dual-phase rolling of $\gamma + \alpha$ region [*3,7–9*]. The strict control of these processing parameters is particularly important for improvement of toughness in the thicker plates, where the major parameters involved are slab reheating temperature, the cumulative rolling reduction below recrystallization temperature of austenite, and the finishing rolling temperature whether it is with γ range or $\gamma + \alpha$ range.

The effects of these variables on the mechanical properties were investigated using two kinds of steel with different microstructures. Figure 1 shows the effect of slab reheating temperature under the given finishing temperature of 1053 K with 78 percent cumulative rolling reduction below 1173 K. Fracture appearance transition temperature (FATT) in Charpy impact testing is noticeably improved by a reduction of reheating temperature from 1473 to 1373 K, or 1323 K in both steels.

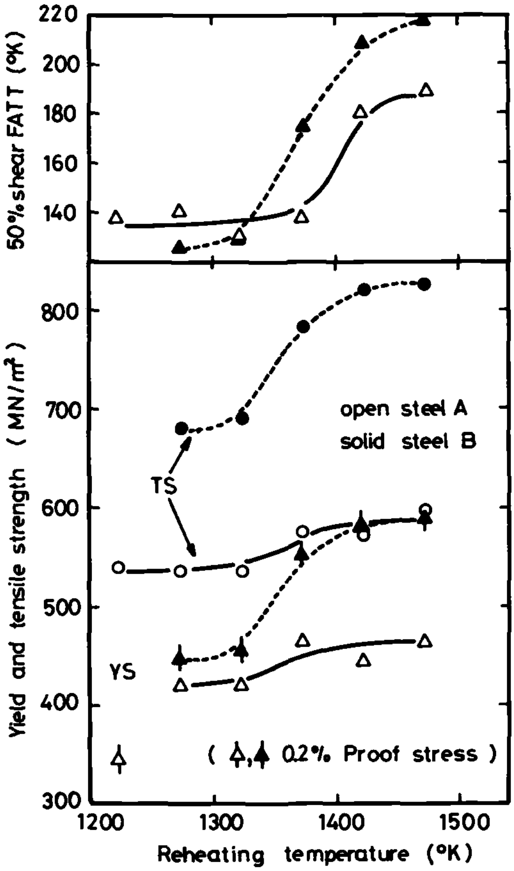

FIG. 1—*The effect of slab reheating temperature on the mechanical properties.*

However, no further improvement of toughness is observed below this reheating temperature. The strength decreases with a reduction of reheating temperature reflecting the decrease of columbium content dissolved in austenite at the reheating temperature. On the other hand, the effect of rolling in the range of nonrecrystallized austenite was confirmed as follows. The amount of the cumulative rolling reduction primarily affects the mechanical properties. Rolling pass reduction or finishing temperature, if it is within γ range, has little influence on the properties. Figure 2 shows the effect of the finishing temperature under the condition of the given cumulative rolling reduction below 1173 K, where the finishing temperatures were controlled by changing the number of rolling passes. The effect of dual-phase rolling is demonstrated in Steel A of Fig. 2, of which Ar_3 transformation temperature after controlled rolling is around 1013 K. The rapid increase of strength without sacrifice of toughness is

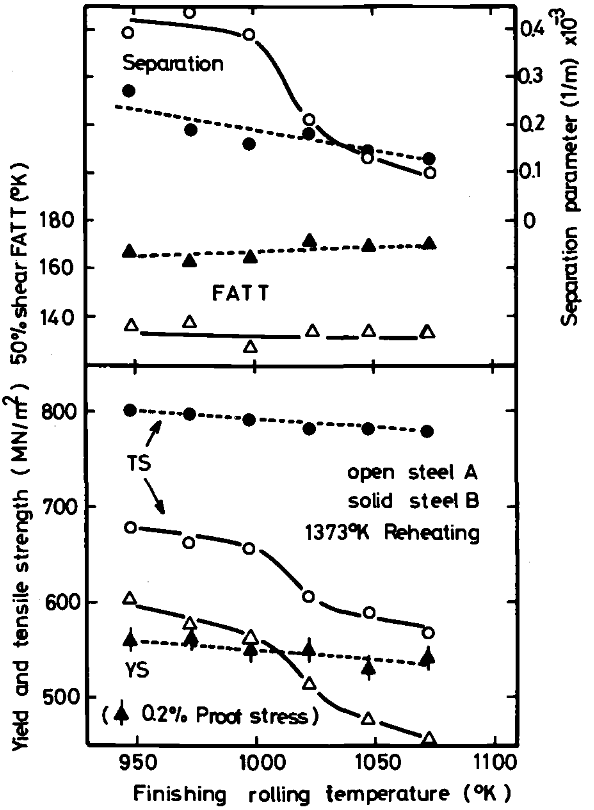

FIG. 2—*The effect of finishing temperature on the mechanical properties.*

observed below this finishing temperature. The Ar_3 transformation temperature of Steel B that exhibits 100 percent acicular ferrite structure is below 923 K. The ferrite deformed during dual-phase rolling becomes more or less dynamic with static recovery, and this is favorable for both of strength and toughness. However, the main cause for no deterioration of toughness in spite of the increase of strength is due to the remarkable increase of splitting. (The splitting parameters shown in Fig. 2 were measured as the value of the total length of splitting with the length larger than 10^{-3} m divided by fracture area of Charpy impact specimen.) Although several origins of occurrence of splitting have been pointed up such as a development of texture, elongated inclusion of magnesium sulfide (MnS), or inhomogenity of microstructure [*10,11*], very little splitting occurs in the ferrite-pearlite steel when the finishing temperature is above Ar_3 temperature, even if enough cumulative rolling reduction below recrystallization temperature is given.

Microstructure and the Effect of Alloying Elements

The properties and transformed microstructure obtained by controlled rolling are directly related to an austenitic microstructure before transformation. The authors have been investigating the changes of austenitic structure accompanied by controlled rolling. The austenitic structure that was quantitatively grasped is expressed as follows [2,*12*]

$$S_v = S_{vgb} + S_{vdb} = K_1\epsilon \; / \; d + K_2\epsilon \qquad (1)$$

where S_{vgb} and S_{vdb} are interfacial area of austenitic grain boundary (gb) and deformation band (db) per unit volume, respectively, ϵ is the cumulative rolling reduction below recrystallization temperature, and d is the recrystallized grain size attained by the final stage of rolling in the recrystallized austenitic region. As the values of K_1 and K_2 are constant when ϵ is higher than 0.3, the transformed structure depends on ϵ and d. The effects of processing variables of controlled rolling are able to be rationalized by these terms. Adoption of lower reheating temperature results in the smaller value of d and refinement of microstructure. The higher reheating temperature also gives rise to the duplex structure with coarse and fine ferrite grain as shown in Fig. 3 and then causes toughness deterioration.

The importance in attaining the smaller value of d increases in the thicker plates. An example of the effect of chemistry on refinement of the transformed structure through obtaining the smaller recrystallized austenitic grain size is demonstrated in the case of a small amount of

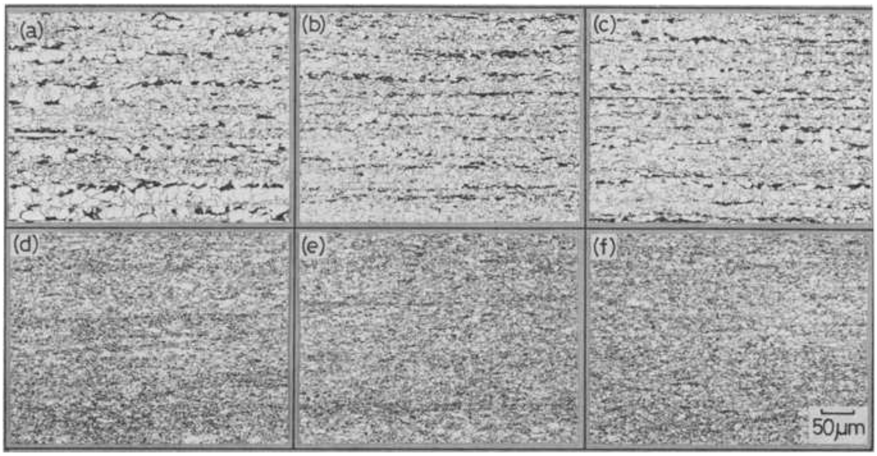

FIG. 3—*The microstructural changes with slab reheating temperature;* (a, b, c) *Steel A,* (d, e, f) *Steel B,* (a, d) *1423 K,* (b, e) *1323 K, and* (c, f) *1273 K.*

titanium added to columbium-bearing steel as shown in Fig. 4. The finely dispersed precipitations of TiN are stable in the high-temperature austenitic region, and they prevent austenitic grain growth not only at the higher reheating temperature, but also during rolling at the recrystallized austenitic region [12]. As shown in Fig. 4, the very refined and uniform microstructure is obtained by 0.02Ti addition even at the higher reheating temperature of 1473 K.

The changes of microstructures with finishing temperature of rolling were demonstrated in Fig. 5. It is evident that the dislocation density increased, and substructure was developed in the deformed ferrite at the finishing temperature below 998 K. With regard to dual-phase rolling, it is important to know the Ar_3 transformation temperature after controlled rolling, because it varies widely depending on the chemistry of the steels. From the systematic investigation of the relation of Ar_3 temperature and chemistry of the steels, the following equation was obtained based on multiple regression analysis.

$$Ar_3(K) = 1183 - 310C - 80Mn - 20Cu - 15Cr - 55Ni - 80Mo \quad (2)$$

Examples of the effect of chemistry on Ar_3 temperature are given in Fig. 6.

Equation 2 is appropriate for transformation to polygonal ferrite, but not to acicular ferrite such as Steel B in Fig. 2. Columbium or vanadium content does not affect Ar_3 temperature if ϵ is higher than 0.3. It is evident from a comparison of Steels A and B in Fig. 2 that the effect of the finishing temperature on the mechanical properties is much different depending on whether it is within γ or $\gamma + \alpha$ range. The finishing

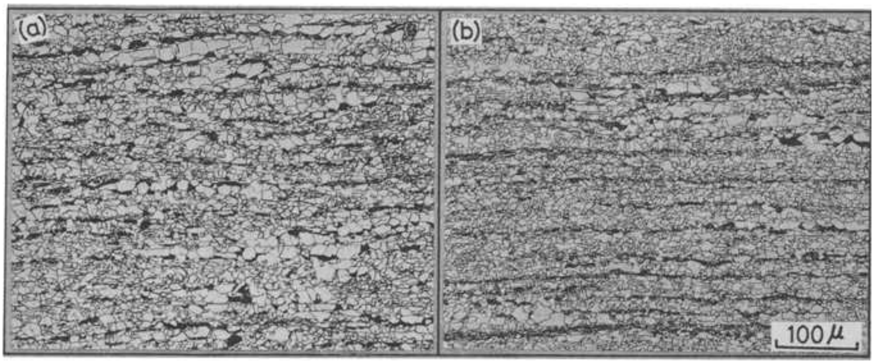

FIG. 4—*The effect of 0.02Ti addition on the microstructure of controlled-rolled plates with plate thickness of 0.032 m; base composition, 0.08C-1.37Mn-1.00Ni-0.04Cb,* (a) *no titanium,* (b) *0.02Ti addition.*

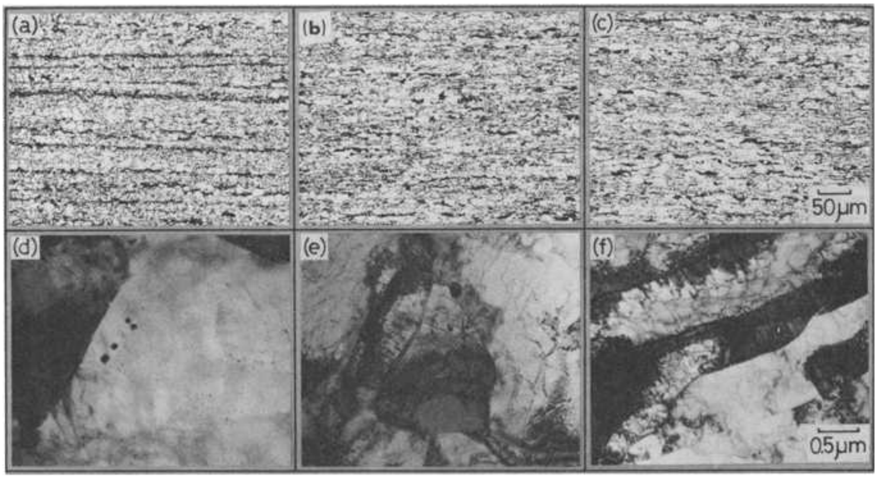

FIG. 5—*The microstructural changes with finishing temperature of rolling in Steel A;* (a, d) *1023K,* (b, e) *998 K, and* (c, f) *948 K.*

temperature should be controlled by recognizing the exact Ar_3 temperature of the steels.

Accelerated Cooling After Controlled Rolling

Processing Parameters and Mechanical Properties

While controlled rolling primarily improves low-temperature toughness, accelerated cooling after controlled rolling has the effect of strengthening the steel through a depression of transformation tempera-

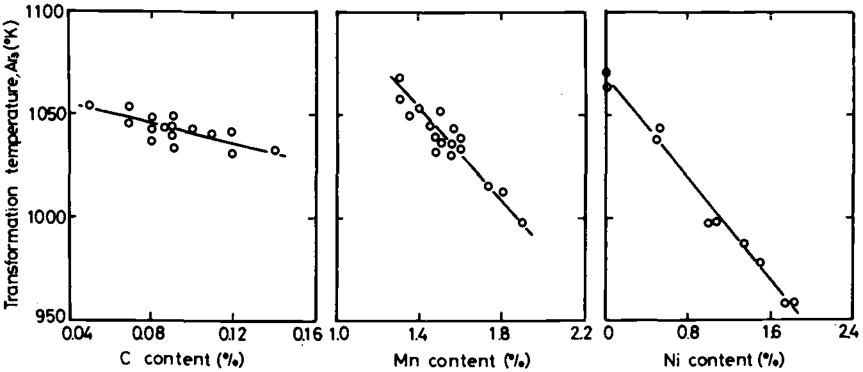

FIG. 6—*The effects of carbon, manganese, and nickel content on Ar_3 temperature after controlled rolling.*

ture or modification of the transformed microstructure. The cooling system is located behind the plate mill, and accelerated cooling is performed in the cooling zone within a particular temperature range, then followed by air cooling. Although several studies about the effects of cooling on a runout table in a hot strip mill have been undertaken [*13,14*], very few investigations have been carried out with respect to the interrupted cooling in a plate mill [*15,16*]. The primary processing parameters involved in this process are the cooling rate, the starting temperature, and the finishing temperature of accelerated cooling. Figure 7 shows the effects of the cooling rate with the given starting and finishing temperatures of 1023 and 873 K, respectively. The columbium-bearing steels exhibit relatively rapid increase of strength with the increase of cooling rate, contrasting with the slack increase in a columbium-free steel. The columbium-vanadium bearing steel with a strength of X-70 grade in as-rolled condition can be graded up to X-80 with the cooling rate around 10 K/s. Toughness is slightly improved rather than deteriorated in spite of a remarkable increase of strength. The absolute level of toughness can be controlled by a suitable selection of controlled-rolling variables such as the slab reheating temperature or cumulative rolling reduction below recrystallization temperature.

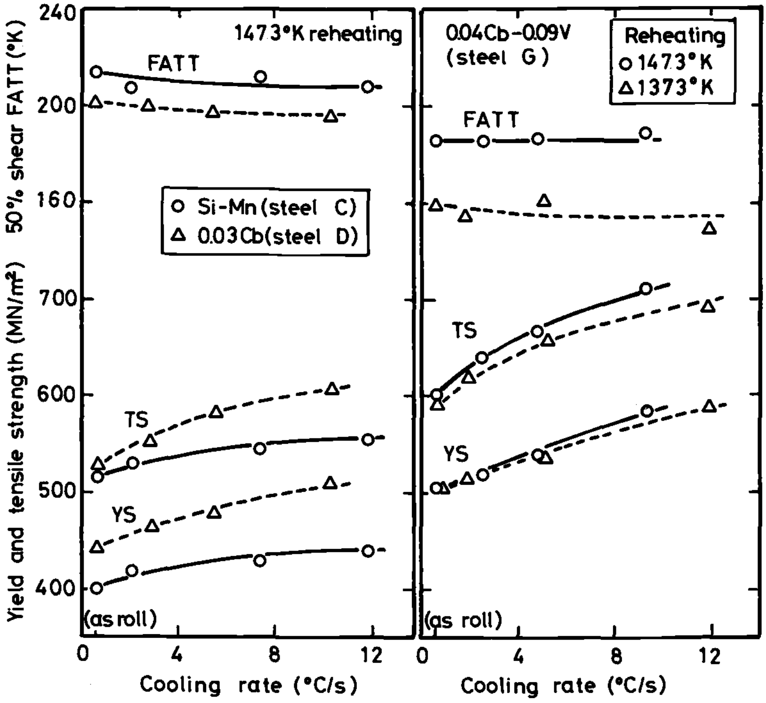

FIG. 7—*The effect of cooling rate on the mechanical properties in three steels.*

When the starting temperature of accelerated cooling is kept above Ar_3 temperature, the maximum increment of strength can be attained in a given cooling rate, otherwise, it continuously decreases with a reduction of the starting temperature below Ar_3. On the other hand, the finishing temperature of accelerated cooling gives rise to a rather complex variation, as shown in Fig. 8, where it was varied between 973 and 823 K in a given cooling rate of 10 K/s. The maximum increment of strength by accelerated cooling is obtained with the finishing temperature around 923 or 873 K. However, this result is considered to be characteristic of columbium-bearing steels, because precipitation of CbC(N) during air cooling may be prevented if the finishing temperature of accelerated cooling is as low as 823 K or below. The higher finishing temperature is also favorable for low-temperature toughness. As shown later, a cooling rate such as 10 K/s causes microstructural change from ferrite-pearlite to ferrite-bainite. Therefore, the self-tempering effect during air cooling after accelerated cooling is indispensable to keep the toughness level attained by controlled rolling and also to obtain the uniform properties within a plate.

The increment of strength by accelerated cooling investigated with

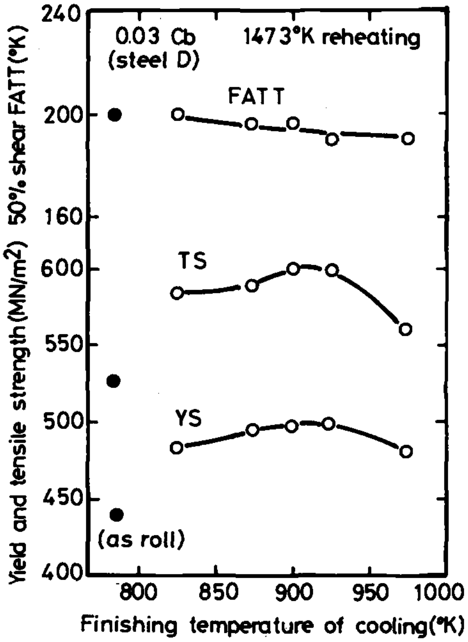

FIG. 8—*The effect of finishing temperature of accelerated cooling on the mechanical properties.*

several steels was summarized based on carbon equivalent (Ceq) as shown in Fig. 9. The slightly wider scatter of strength in the accelerated cooled plate is due to variation of cooling rate around 7 to 12 K/s. The increase of strength due to accelerated cooling in each steel is equal to the increment of strength that is attained by increasing Ceq of 0.04 to 0.06 percent in as-rolled plate. Therefore, the beneficial effect of accelerated cooling after controlled rolling not only increases the strength to grade up to X-75 or 80, but also improves weldability or other secondary properties of the arctic line pipe steels through the reduction of carbon content or carbon equivalent in a particular grade of steel.

Mechanism of Strengthening by Accelerated Cooling

The increase of strength by accelerated cooling after controlled rolling is primarily due to the microstructural change as shown in Figs. 10 and 11, where the polygonal ferrite-pearlite structure in as-rolled condition is varied to a very fine duplex structure consisting of ferrite-bainite in accelerated cooling. At a cooling rate above 4 K/s, a pearlite band that is observed in as-rolled plate completely disappears and very fine bainite is formed in place of pearlite. The ferrite grain size is further refined and also becomes more uniform, preventing a duplex structure with the coarse and

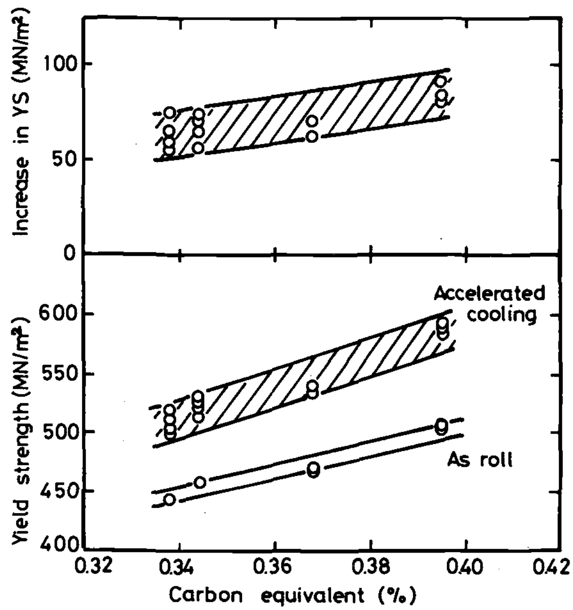

FIG. 9—*The relation of carbon equivalent and yield strength; Ceq=C+Mn/6+(Cr+Mo+V)/5+(Cu+Ni)/15.*

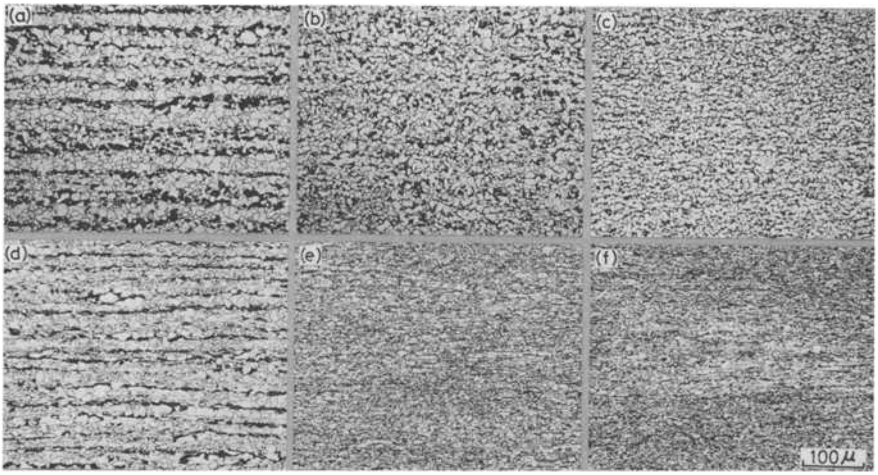

FIG. 10—*The microstructural changes with cooling rate;* (a, b, c) *Steel C,* (d, e, f) *Steel G,* (a, d) *as roll,* (b, e) *4 K/s, and* (c, f) *10 K/s.*

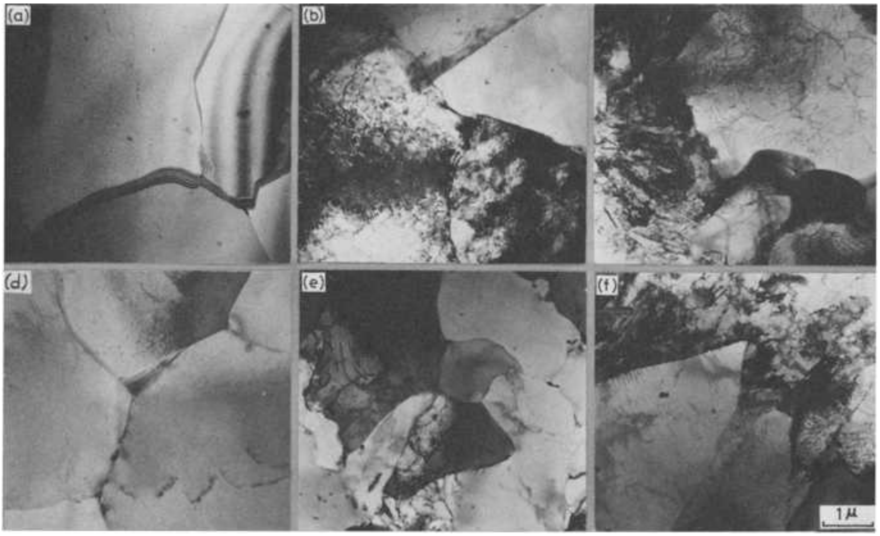

FIG. 11—*Thin foil observations of microstructures of accelerated cooled plates, Steel G;* (a, b, c) *reheating temperature of 1473 K,* (d, e, f) *1373 K,* (a, d) *as roll,* (b, e) *4 K/s, and* (c, f) *10 K/s.*

fine grain size in the as-rolled plate. These microstructural changes with cooling rate were quantitatively measured as shown in Fig. 12. The overall increment of strength by accelerated cooling therefore consists of the change of the various strengthening factors as shown in the following equation.

$$\Delta \text{ YS or } \Delta\text{TS} = K\Delta\,(d^{-1/2}) + (K_B f_B - K_P f_P) + \Delta\sigma_{ppt} \tag{3}$$

where $\Delta(d^{-1/2})$ reflects further grain refinement, f_B and f_P are volume fraction of bainite and pearlite, respectively, with the constant value of K_B and K_P. $\Delta\sigma_{ppt}$ means the increase of precipitation hardening of CbC(N) through a depression of transformation temperature by accelerated cooling. The present analysis based on measurements of each factor clarified that about 50 percent of increment of yield strength by accelerated cooling is due to grain refinement and 60 to 70 percent of increment of ultimate tensile strength is due to finely formed bainite. A novel role of columbium

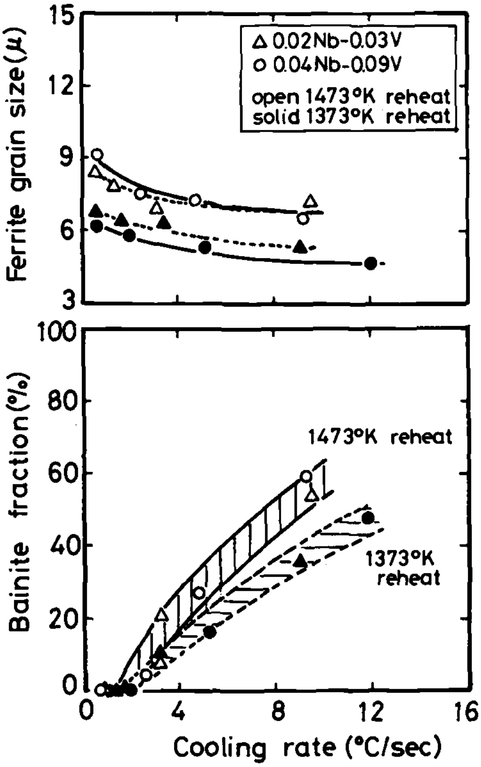

FIG. 12—*The variations of ferrite grain size and bainite fraction with cooling rate.*

in accelerated cooling is observed in the increase of hardenability. The columbium-bearing steels give rise to the higher volume fraction of bainite compared with the columbium-free steel at a given cooling rate. This is the reason why the columbium-free steel showed a slight increase of strength with cooling rate.

The reason for no deterioration of toughness in spite of a quite large increase in strength is also due to these microstructural changes. Particularly, the fineness of bainite is important for keeping superior toughness as well as grain refinement of ferrite, and this is attained by optimization of controlled-rolling practice. Another beneficial effect of the duplex structure of ferrite-bainite is observed in the improvement of ductility such as reduction of area (RA) in tension testing or shelf energy (vEs) in the Charpy impact testing. Figure 13 shows these results, where the relation of strength and RA or vEs is exhibited. In comparison with the same strength level, higher ductility is obtained in the accelerated cooled plates. Although the harmful effect of pearlite on ductility is well known [*17*], this result indicates that ductility of the very finely and uniformly formed bainite is much superior to that of pearlite. In other words, the effect of accelerated cooling after controlled rolling is con-

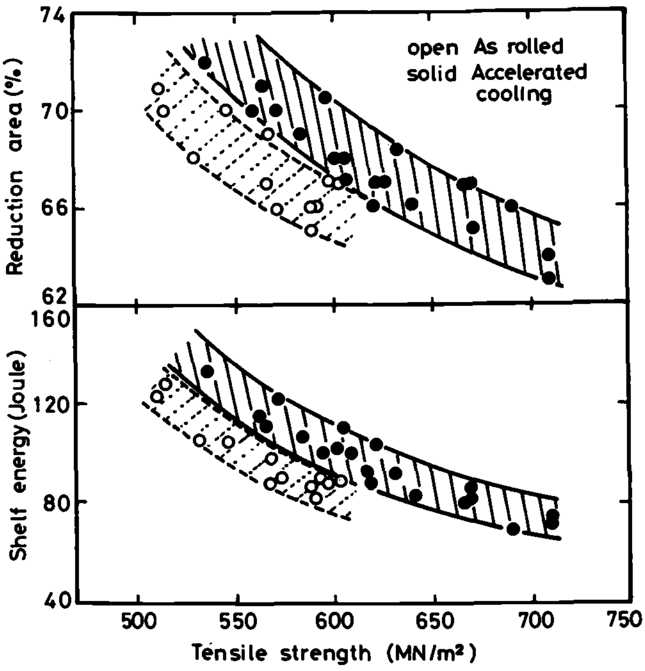

FIG. 13—*The relation of strength and shelf energy or reduction area.*

sidered to produce essentially pearlite-free steel in low-carbon low-alloy steels.

Heat Treatment After Pipe Forming

Characteristics of Quenched and Tempered Pipe

It is well recognized that the excellent combination of strength and toughness is easily obtained by means of quenching and tempering of steels [*18–21*]. The increase of yield strength around 100 to 300 MN/m^2 can be easily obtained for a given chemical composition by quenching and tempering without impairing toughness. This fact means that the higher grade pipes with the lower carbon equivalent steels can be manufactured without any difficulties by the quenching and tempering process when compared with conventional processing routes. The beneficial effect is particularly important when manufacturing heavy-walled high-strength line pipes without sacrificing weldability.

The relationship between the mechanical properties and processing variable or metallurgical factors can be treated about the same as the ones in the quenched and tempered plates [*22–25*], except that thermal cycling of quenching and tempering for pipes is extremely rapid, in many cases, because of its induction heating system. The main feature of rapid heat treatment is characterized as a typical *diffusion suppressing process* [*25*]. It makes it easy, therefore, to obtain the remarkably fine microstructure, while higher heating temperatures than those of the conventional furnace heating process for the plates are required to obtain homogeneously hardened microstructures and sufficient tempering. The factors that are expected to facilitate the diffusion of alloying elements during heating, such as plastic deformation prior to heat treatment and more uniform distribution of carbides in the prior microstructures, possibly improve the quenching microstructures and subsequently the toughness of rapidly heat-treated steels.

The most important advantage of the quenching and tempering process after cold forming and welding of pipes is the drastic improvement of mechanical properties of seam weldments by the heat treatment. As demonstrated in Fig. 14 and Table 2, hardness distribution profile and Charpy V impact properties of weldments are sufficiently improved up to the levels of base metals. It should be emphasized that the low levels of toughness in weld metals and heat-affected zones that are commonly experienced in the weldments are eliminated by the heat treatment, when appropriate weld materials and welding procedures are applied.

Another important feature of the properties of quenched and tempered pipes is the improved performance against sulfide stress corrosion cracking, particularly in the heat-affected zone. The critical stress, Sc, in the

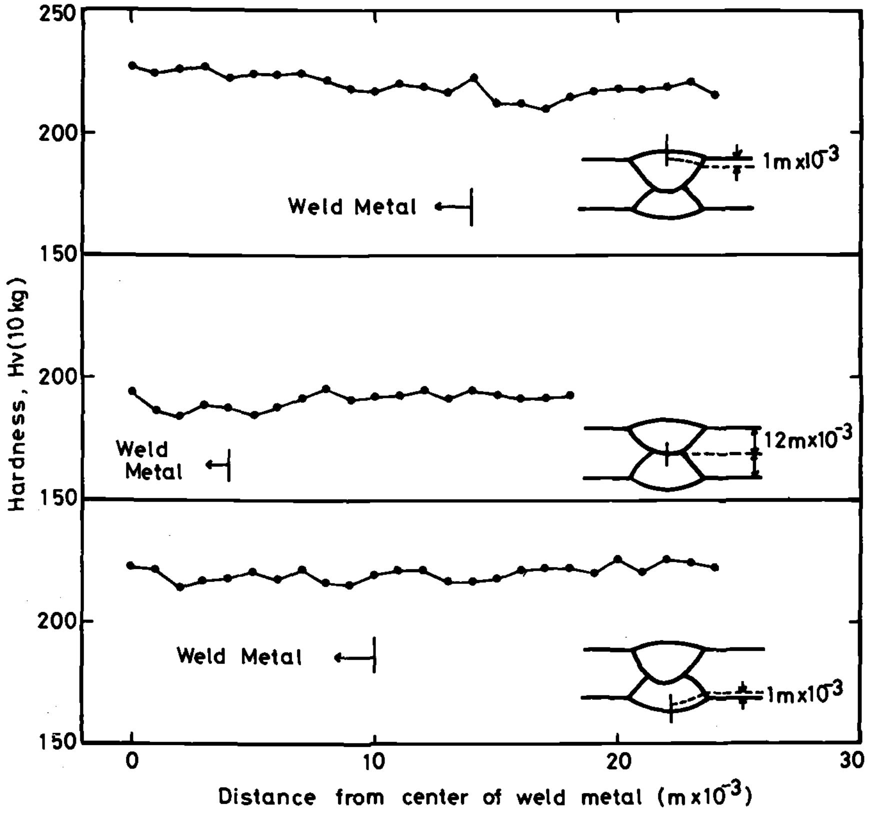

FIG. 14—*The hardness distribution profile in seam weldments before and after heat treatment; Steel H.*

TABLE 2—*Charpy impact properties in seam weldments before and after heat treatment*[a]

	Base Metal				Heat-Affected Zone		Weld Metal	
	Yield Strength, MN/m^2	Ultimate Tensile Strength, MN/m^2	FATT[b] K	vE233 K[c] (−40°C) J	FATT K	vE233 K J	FATT K	vE233 K J
Before	385.1	508.6	270	22	250	31	280	16
After	490.0	653.7	209	125	213	132	224	100

[a] Pipe size; 28 in. outside diameter by 1 in. wall thickness; Steel H.

[b] Fracture appearance transition temperature.

[c] V-notch Charpy energy at 233 K.

Shell type sulfide corrosion cracking test for quenched and tempered pipes is shown in Fig. 15 in comparison with conventional pipes. Appreciably high Sc values are obtained for both of pipe body and weldments [25]. This improvement in Sc value is explained with the extremely flat hardness distribution profile in weldments, refinement of microstructure, and elimination of residual stress by heat treatment. Hydrogen-induced cracking was also examined by British Petroleum (BP) type tests, and excellent results of quenched and tempered pipes were confirmed again.

Microstructural Features of Quenched and Tempered Pipes

The excellent performance of quenched and tempered pipes are basically explained by the microstructural features of heat-treated materials. It is well known that the mechanical properties of quenched and tempered low-carbon low-alloy steels are optimized by refinement of prior austen-

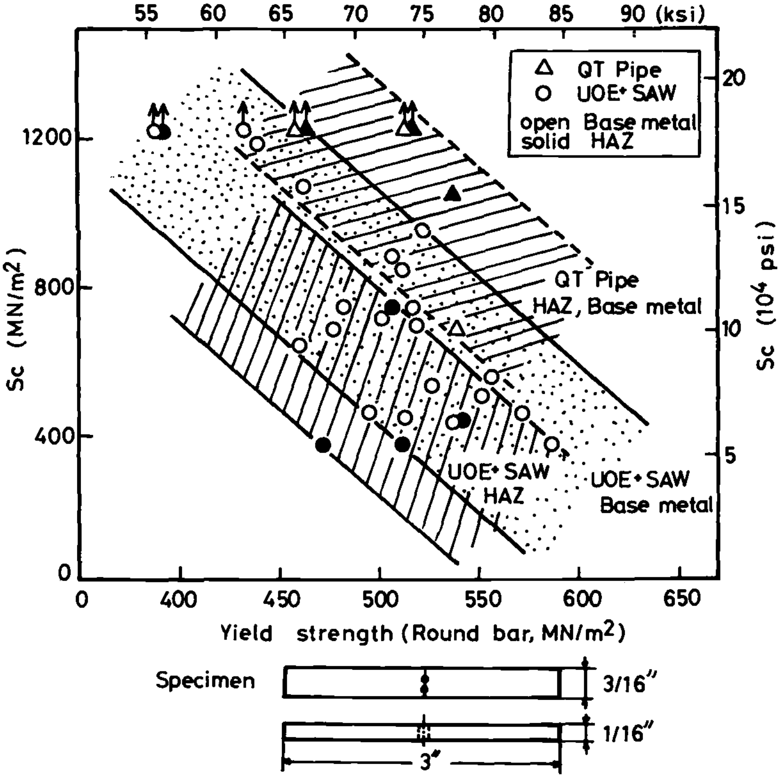

FIG. 15—*The critical stress values obtained from Shell-type sulfide corrosion cracking test.*

itic grain size, and by lowering the transformation temperature to get lower bainite, martensite, or mixed structure of both, providing fine and uniform substructures with high dislocation density as well as fine and uniform distribution of carbide precipitates [*21–24*]. The microstructures of quenched pipes are controlled with heating and cooling rates, hardenability of steels, which is a function of alloying element and prior austenitic grain size, and microstructures before heating. An example of microstructure obtained by this process is shown in Fig. 16, where it is evident that the microstructure of the heat-affected zone (HAZ) after heat treatment is similar to that of base metal. It should be noticed that the unfavorable coarse-grained microstructure in as-welded heat-affected zone is completely eliminated. The microstructure of weld metal is strongly affected by its chemical composition that is usually different from base metal, and with its as-welded microstructure that is quite different from heat-affected zone and base metal because of its as-solidified microstructure. It is important, therefore, to control the chemical composition of weld metal to obtain a similar microstructure to the base metal after heat treatment, which, in turn, means weld materials can be selected without any restrictions based on the considerations to be as-welded properties.

Conclusions

Past and present line pipe steels mainly have microstructures of polygonal ferrite-pearlite or acicular ferrite. In the newly developed processes described here, it was intended to improve various properties of the arctic line pipe steels through the effective utilization of the various microstructures, such as very refined duplex structure of ferrite-bainite or tempered martensite. The microstructures and the maximum strength levels obtained by each process are summarized in Table 3. The processes of accelerated cooling or heat treatment after pipe forming give wider and more flexible means for selection of microstructures. Taking into consideration the recent trends of the arctic line pipe steels, improvement of properties due to these processes or microstructures is indispensable. Properties such as weldability or stress corrosion resistance are surely improved by the decrease of carbon content or carbon equivalent, and the higher strength level in such steels should be attained effectively by these new processes.

Acknowledgments

We wish to thank Dr. G. Suzuki, director of Technical Research Center, for permission to publish this paper. We also acknowledge the cooperation of T. Taira, T. Sampei, T. Okita, M. Suga, and K. Matsumoto.

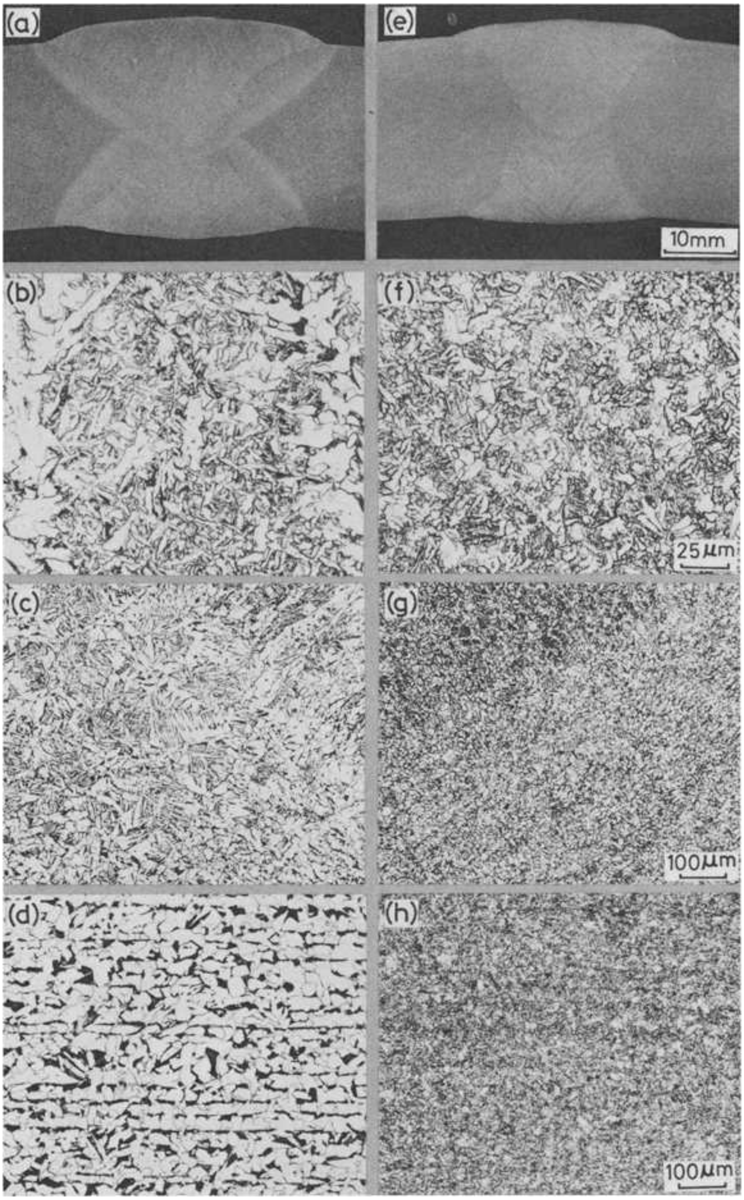

FIG. 16—*The microstructural changes before and after heat treatment, Steel H;* (a–d) *as welded,* (e–h) *after heat treated,* (a, e) *macrostructure,* (b, f) *weld metal,* (c, g) *HAZ, and* (d, h) *base metal.*

TABLE 3—*Microstructure and maximum strength level obtained by each process.*

	Microstructure	Strength Level
Controlled rolling	ferrite-pearlite, acicular ferrite	X-70/75
Accelerated cooling	ferrite-bainite, acicular ferrite	X-80/85
Heat treatment of pipe	ferrite-bainite, bainite, martensite	X-100

References

[*1*] Zackay, V. F., *Materials Science Engineering,* Vol. 25, 1976, pp. 247–261.

[*2*] Kozasu, I., Ouchi, C., Sampei, T., and Okita, T., *Proceedings,* International Conference on Microalloying 75, Washington D.C., Union Carbide, 1976, pp. 100–114.

[*3*] Kozasu, I. and Osuka, T., *Proceedings,* Processing and Properties of Low Carbon Steel. The Metallurgical Society, American Institute of Mining, Metallurgical, and Petroleum Engineers, New York, 1973, pp. 47–65.

[*4*] Stout, R. D., Vasudevan, R., and Pense, A. W., *Welding Journal,* April 1976, pp. 89S–94S.

[*5*] Moore, E. M. and Warga, J. J., *Materials Performance,* June 1976, pp. 17–23.

[*6*] Vanderbeck, R. W., *Welding Journal,* Vol. 37, 1958, pp. 114S–116S.

[*7*] Hannukainen, T. and Heikkinen, V. K., *Scandinavian Journal of Metallurgy,* Vol. 3, 1974, pp. 158–162.

[*8*] Melloy, G. and Dennison, J. D., *Proceedings,* International Conference on Strength of Metals and Alloys, Third Conference, Vol. 1, Institute of Metals, Cambridge, Aug. 1973, pp. 60–64.

[*9*] Tanaka, T., Tabata, N., Hatomura, T., and Chiga, C., *Proceedings,* International Conference on Microalloying 75, Washington D.C., Union Carbide, 1976, pp. 88–99.

[*10*] Dabkowski, D. S., Konkol, P. J., and Baldy, M. F., paper presented before Canadian Metallurgical Society Symposium on Arctic Line Pipe, Toronto, Canada, Aug. 1974.

[*11*] Speich, G. R. and Dabkouski, D. S., *Proceedings,* Hot Deformation of Austenite, The Metallurgical Society, American Institute of Mining, Metallurgical, and Petroleum Engineers, 1976, pp. 557–598.

[*12*] Ouchi, C., Sampei, T., Okita, T., and Kozasu, I. *Proceedings,* Hot Deformation of Austenite, The Metallurgical Society, American Institute of Mining, Metallurgical, and Petroleum Engineers, 1976, pp. 316–340.

[*13*] Fukuda, M., Hashimoto, T., and Kunishige, K., *Proceedings,* International Conference on Microalloying 75, Washington D.C., Union Carbide, 1976, pp. 115–129.

[*14*] Grozier, J. D., *Proceeding,* International Conference on Microalloying 75, Session 2A, Washington D.C., Union Carbide, 1976, pp. 15–22.

[*15*] Fegredo, D. M., *Metals Technology,* Sept. 1977, pp. 417–424.

[*16*] Repas, P. E., paper presented before 105th AIME Annual Meeting, American Institute of Mining, Metallurgical and Petroleum Engineers, Las Vegas, Feb. 1976.

[*17*] Pickering, F. B., *Proceedings*, Toward Improved Ductility and Toughness, Kyoto, Climax Molybdenum, 1971, pp. 9–31.

[*18*] Irvine, K. J., *Proceedings,* International Symposium on Die Verstingung Von Stahl, Zürich, Climax Molybdenum, 1969, pp. 55–65.

[*19*] Kunitake, T., *Proceedings,* International Symposium on Low Alloy High Strength Steels, Nuremberg, The Metallurg Companies, 1970, pp. 41–50.

[*20*] Taira, T. et al, *Proceedings,* The 18th Mechanical Working and Steel Processing Conference, The Iron and Steel Society, American Institute of Mining, Metallurgical and Petroleum Engineers, 1976, pp. 52–86.

[*21*] Kubota, H., Tanaka, J., Ouchi, C., and Osuka, T., *Proceedings,* International Conference on the Science and Technology of Iron and Steel, Supplemental Transactions, The Iron and Steel Institute of Japan, Vol. 11, 1971, pp. 1106–1110.

[*22*] Matsuda, S., Inoue, T., Mimura, H., and Okamura, Y., *Proceedings,* International Symposium on Toward Improved Ductility and Toughness, Kyoto, Climax Molybdenum, 1971, pp. 45–66.

[23] Kunitake, T., Terasaki, F., Ohmori, Y., and Otani, H., *Proceedings*, International Symposium on Toward Improved Ductility and Toughness, Kyoto, Climax Molybdenum, 1971, pp. 83–100.
[24] Tanaka, J., Tani, S. and Ouchi, C., *Transactions*, The Iron and Steel Institute of Japan, Vol. 15, 1975, pp. 19–26.
[25] Tanaka, J., Nose, J., Kunioka, K., Kozasu, I., and Matsubara, H., *Proceedings*, The 19th Mechanical Working and Steel Processing Conference, The Iron and Steel Society, American Institute of Mining, Metallurgical and Petroleum Engineers, 1977, pp. 21–54.

A. P. Coldren,[1] *G. T. Eldis,*[1] *and G. Tither*[1]

Structure-Property Relationships for Pearlite-Reduced Mo-Nb Steels Finish-Rolled Moderately Below Ar_3

REFERENCE: Coldren, A. P., Eldis, G. T., and Tither, G., "**Structure-Property Relationships for Pearlite-Reduced Mo-Nb Steels Finish-Rolled Moderately Below Ar_3,**" *MiCon 78: Optimization of Processing, Properties, and Service Performance Through Microstructural Control, ASTM STP 672,* Halle Abrams, G. N. Maniar, D. A. Nail, and H. D. Solomon, Eds., American Society for Testing and Materials, 1979, pp. 126–144.

ABSTRACT: A study of five laboratory steels was conducted to determine the relative effects of ferrite grain refinement, dislocation substructure, and niobium (carbon, nitrogen) [Nb(C,N)] precipitation strengthening on the as-rolled strength and toughness properties of 19-mm (0.75-in.) plates finish rolled in the two-phase region, moderately below the Ar_3 temperature. The steels were molybdenum-niobium (Mo-Nb) pearlite-reduced steels having a nominal composition range of 0.08C, 1.4Mn, 0.1Si, 0.2/0.4Mo and 0/0.6Nb. The amount of ferrite formed prior to the last pass and the percent reduction imparted on the last pass were varied while the finishing temperature was held constant at 745°C (1375°F).

It was found that the introduction of deformed ferrite into the structure brought two strengthening effects: dislocation substructure and, in the niobium-containing steels, strain-enhanced precipitation. The combined effect of these mechanisms reached a maximum in plates containing approximately 30 to 40 percent deformed ferrite that had experienced a 20 percent reduction on the final pass. The impact toughness was not impaired by this method of upgrading strength.

Regarding grain refinement, the 0.2Mo-0.035Nb steel experienced increases in yield strength of up to 85 MPa (12.4 ksi) due to the additional grain refinement produced by rolling below the Ar_3 temperature instead of finishing just above the Ar_3. This type of strengthening was smaller in the 0.2Mo-0.06Nb steel and absent in the 0.4Mo-0.06Nb steel, because the initial grain sizes of these steels were finer, and lowering the finish-rolling temperature produced little or no further refinement.

KEY WORDS: steels, microstructure, pearlite-reduced steels, ferrite grain refinement, substructure, precipitation, controlled rolling, impact toughness

The use of controlled rolling in the plate mill production of high-quality, as-hot-rolled line pipe steel is a well-established practice. Although all

---

[1] Staff metallurgist, research supervisor, and manager of High Strength Steel Development, respectively, Climax Molybdenum Company of Michigan, A Subsidiary of AMAX, Inc., Ann Arbor, Mich. 48105.

schedules for controlled rolling involve finish-rolling temperatures that are much lower than those conventionally employed in the production of hot-finished plates, the use of finish-rolling temperatures below the Ar_3 is relatively uncommon. This paper describes a laboratory investigation of the structure-property relationships in a pearlite-reduced molybdenum-niobium (Mo-Nb) steel finish-rolled moderately below the Ar_3.

When a practice of rolling below the Ar_3 is employed, an important choice must be made as to how far below that temperature the steel is to be finish-rolled. That will determine how much deformed ferrite will be in the final structure, how much accumulated deformation that ferrite will have experienced and, consequently, the degree to which deformed ferrite will influence properties. The two principal ways by which deformed ferrite could affect properties are: (1) to raise strength by the dislocation (substructure) or the strain-enhanced precipitation strengthening mechanisms; and (2) to raise or lower the impact transition temperature, depending on how low the finishing temperature is and how severe the low-temperature deformation is. Dislocation strengthening would be expected to raise the impact transition temperature, as would strain-enhanced precipitation strengthening. On the other hand, factors that would tend to counterbalance those effects and lower the transition temperature include: (1) subgrain formation (by polygonization of the dislocation structure during cooling from rolling), and (2) the phenomenon of splitting (as in the case of very severely deformed and textured structures) that reduces the effective specimen size and thereby lowers the transition temperature by reducing the triaxial stresses that occur during testing of standard size Charpy V-notch specimens.

The main purpose of the present study was to determine the optimum amount of worked ferrite and the optimum amount of deformation that must be applied to that ferrite to obtain the best properties in 19-mm (3/4-in.) gage as-rolled plate. It was also hoped to establish the relative degrees to which dislocation substructures and strain-enhanced precipitation of niobium (carbon, nitrogen) (Nb(C,N)) in the worked ferrite contribute to the as-rolled strength of Mo-Nb steels finish-rolled below the Ar_3. Published results of low-temperature rolling experiments by Little et al [*1*],[2] Repas [*2*], and Speich and Dabkowski [*3*] give a conflicting picture of whether the dislocation substructure in the deformed ferrite makes a significant contribution to the strength of pearlite-reduced steels finish-rolled at 745°C (1375°F), the finishing temperature employed in the present investigation. It was hoped that the new data obtained in the present study would shed some light on this question.

---

[2] The italic numbers in brackets refer to the list of references appended to this paper.

Experimental Procedures

General Approach

The experimental approach was to select a Mo-Nb pearlite-reduced steel (0.08C, 1.4Mn, 0.2Mo, 0.06Nb) for which the Ar_3 was known, to vary the molybdenum and niobium contents, and to hot roll the steel in accordance with several schedules devised to produce two series of conditions: (*a*) varying volume fractions of deformed ferrite at constant deformation, and (*b*) varying deformation at constant volume fraction of deformed ferrite. The finishing temperature was held constant, moderately below the Ar_3. The amount of ferrite that had formed immediately preceding the final pass was determined by quantitative metallography on identically rolled companion plates that had been iced-brine quenched at the moment that they normally would have been given the last roll pass.

Melting and Forging

The steels were induction melted, aluminum killed, and cast as 34-kg (75-lb) heats in an argon atmosphere. The melting stock included electrolytic iron (A 101-B Plastiron), ferroalloys, pure carbon, and pure niobium. The compositions of the steels were determined by analyzing buttons that were cast as an integral part of each ingot. The analyses are presented in Table 1.

The ingots were forged at 1230°C (2250°F) to 65 by 121 by 400-mm (2.5 by 4.75 by 16-in.) slabs. Seven 51 by 65 by 121-mm (2 by 2.5 by 4.75-in.)

TABLE 1—*Chemical compositions.*

Steel No.	Climax Heat No.	Element, weight percent								
		C	Mn	Si	Mo	Nb	Al	N	P	S
1	P1611A	0.080	1.41	(0.10)[a]	(0.21)	. . .[b]	(0.07)	(0.005)	(0.009)	(0.007)
1A[c]	P1816A	0.080	1.40	0.09	0.20	. . .	0.05	0.007	0.012	0.006
2	P1611B	0.080	1.39	0.10	0.21	0.035	0.07	0.005	0.009	0.007
2A	P1612	0.080	1.42	0.10	0.21	0.033	0.08	0.005	(0.009)	(0.007)
3	P1613A	0.077	1.41	(0.10)	(0.22)	. . .	(0.06)	(0.005)	(0.009)	(0.007)
4	P1613B	0.080	1.40	0.10	0.22	0.066	0.06	0.005	(0.009)	(0.007)
4A	P1614	0.079	1.40	0.10	0.20	0.058	0.07	0.006	(0.009)	(0.007)
5	P1615A	0.077	1.41	(0.11)	(0.42)	. . .	(0.04)	(0.008)	(0.009)	(0.007)
5A	P1816B	0.078	1.41	(0.09)	0.38	. . .	(0.05)	(0.007)	(0.012)	(0.006)
6	P1615B	0.077	1.38	0.11	0.42	0.067	0.04	0.008	(0.009)	(0.007)
6A	P1616	0.077	1.40	0.11	0.41	0.054	0.05	0.009	(0.009)	(0.007)

[a] Values in parentheses assumed on the basis of analysis of another ingot from same heat or another ingot made in similar manner.

[b] . . . = none added and not analyzed.

[c] Letter A in Steel No. indicates duplicate heat made for additional material.

rolling blanks were prepared from each slab. Plain carbon steel extension pieces were welded to each rolling blank to provide sufficient stability to allow each blank to be rolled with the 121-mm (4.75-in.) dimension vertical.

Rolling

Seven rolling schedules were used, as shown schematically in Fig. 1. Schedules A, D, F, and G were designed to produce varying amounts of ferrite prior to the final pass at 740°C (1375°F) by varying the amount of austenite deformation immediately above this temperature. The degree of deformation in the final pass was held constant for that series. In the series designed to vary the severity of deformation in the worked ferrite, Schedules B, C, D, and E were used to obtain a constant amount of ferrite prior to the final pass. The degree of deformation in the final pass was then varied. The niobium-containing steels were subjected to each of the seven schedules. The niobium-free steels were rolled to Schedules A and D only.

Temperatures were monitored during rolling by means of a thermocouple embedded at the center of the plate. In nearly every case, a companion plate was subjected to an identical rolling schedule, except that it was immersion quenched in iced brine in lieu of the final roll pass, to *freeze in* the structure and permit a determination of the amount of ferrite present at the time of the last pass. The brine consisted of a 10 weight percent solution of NaCl in water, maintained at −7°C (20°F) by additions of chopped dry ice. The cooling rate of a 24-mm (0.94-in.) plate (typical plate thickness prior to the last pass) quenched in this solution was approximately 40°C/s (70°F/s).

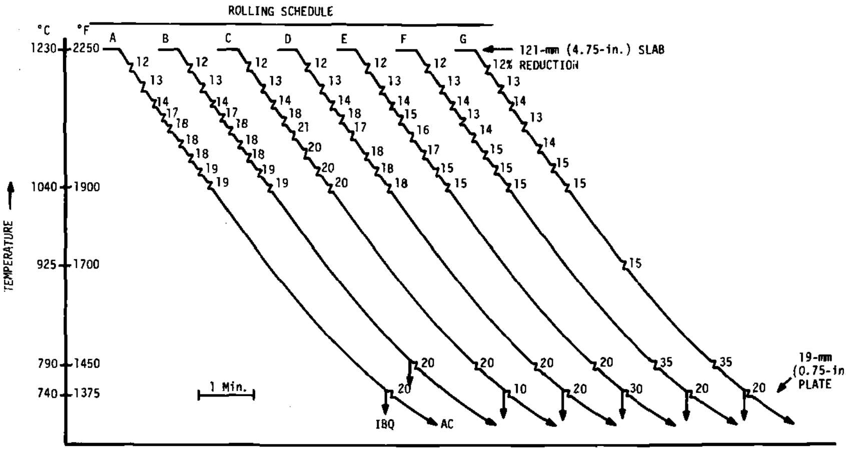

FIG. 1—*Schematic representation of rolling schedules employed.*

Tension and Impact Testing

Tension tests were performed on duplicate longitudinal specimens taken from the mid-thickness position. The specimens were of a cylindrical design, with a 6-mm (0.25-in.) diameter by 32-mm (1.25-in.) gage section, and they were tested at strain rates of 5×10^{-5}/s and 3.3×10^{-4}/s in the elastic and plastic portions of the test, respectively.

Full-size longitudinal Charpy V-notch specimens from selected plates were tested at various temperatures to obtain *approximate* values of the 50 percent shear fracture appearance transition temperature (FATT) and the shelf energy, Cv (100 percent), that is, energy absorbed at the lowest temperature at which a 100 percent shear fracture was obtained. The root of the notch was perpendicular to the plane of rolling. The small size and the erratic curvature of many of the rolled plates limited the number of impact specimens to two or three per plate. This experimental difficulty precluded exact determination of the toughness parameters. However, the authors believed the trends revealed by the approximate values would be of interest.

Quantitative Metallography

A metallographic specimen from a location near the embedded thermocouple was prepared for each plate, including the iced-brine-quenched plates. The specimens were electropolished in a 7:1 methanol/sulphuric acid electrolyte and etched in 2 percent nital. The as-rolled specimens were subjected to ferrite grain size measurements, using a linear intercept method in which a total of approximately 400 boundaries were counted per specimen. A magnification of ×1000 was employed, and the direction of traverse was 45 deg to the plate surface. The plane of examination was parallel to the rolling direction and normal to the plate surface.

The brine-quenched specimens were analyzed by point counting to determine the volume percent of polygonal ferrite present. In each determination, twenty 16-point fields were counted and averaged. The plane of examination was oriented the same as that used in the grain size measurements.

Results and Discussion

All of the data pertaining to microstructures and mechanical properties are summarized in Table 2. Selected data from Table 2 are used as needed for tables and figures in the following sections to show the effects of the variables investigated.

Microstructures

The rolling schedules employed (Fig. 1) produced a reasonably good range of volume percent deformed ferrite values. For the Mo-Nb steel

TABLE 2—*Summary of longitudinal tension and impact test results and metallographic data.*

Steel No.	Nominal weight percent[a]		Rolling Schedule[b]	Deformed Ferrite, volume percent[c]	Final Reduction at 745°C (1375°F), %	Ferrite Grain Size, ASTM No.	Offset Yield Strength, MPa (ksi)		Tensile Strength, MPa (ksi)	Yield Point Elongation, %	Total Elongation in 25 mm (1 in.), %	Reduction of Area, %	Charpy V-notch Impact	
	Mo	Nb					0.2%	1.5%					C_v(100%)[d] J (ft · lb)	50% Shear FATT[e], °C (°F)
3	0.2	0	A	5.9	20	10.4	285 (41.4)	311 (45.2)	453 (65.7)	0.82	37	76	ND[f]	ND
1A	0.2	0	D	ND	20	11.0	336 (48.7)	358 (52.0)	471 (68.3)	1.21	36	77	ND	ND
1A	0.2	0	D	ND	20	10.3	343 (49.8)	349 (50.6)	466 (67.6)	1.30	34	77	ND	ND
2	0.2	0.035	A	ND	20	11.5	426 (61.8)	441 (64.0)	554 (80.4)	0.69	35	82	ND	ND
2	0.2	0.035	B	0	0[g]	10.0	418 (60.6)	438 (63.6)	553 (80.2)	0.75	34	81	283 (209)	−50 (−60)
2	0.2	0.035	C	21.9	10	11.1	446 (64.8)	475 (69.0)	573 (83.2)	0.42	31	80	ND	−35 (−30)
2	0.2	0.035	D	30.6	20	10.9	473 (68.6)	508 (73.7)	597 (86.7)	0.20	30	81	>163 (>120)	−35 (−35)
2A	0.2	0.035	E	32.2	30	11.9	435 (63.2)	443 (64.3)	557 (80.8)	0.76	34	82	235 (173)	−50 (−55)
2A	0.2	0.035	F	45.0	20	11.2	491 (71.3)	511 (74.2)	597 (86.7)	0.60	29	80	221 (163)	−55 (−70)
2A	0.2	0.035	G	51.9	20	11.8	466 (67.7)	481 (69.8)	582 (84.5)	0.66	32	82	ND	ND
4	0.2	0.060	A	23.1	20	11.9	463 (67.2)	480 (69.6)	580 (84.2)	0.74	32	83	>231 (>170)	−25 (−10)
4	0.2	0.060	B	0	0[g]	11.0	463 (67.2)	457 (66.3)	575 (83.4)	1.56	33	82	ND	0 (+35)
4	0.2	0.060	C	ND	10	11.6	489 (70.9)	493 (71.6)	593 (86.1)	0.79	31	83	>176 (>130)	−50 (−60)
4	0.2	0.060	D	46.3	20	11.8	533 (77.3)	551 (80.0)	639 (92.8)	0.60	29	81	209 (154)	−40 (−45)
4A	0.2	0.066	E	ND	30	12.0	494 (71.7)	508 (73.7)	607 (88.1)	0.50	28	83	203 (150)	−55 (−70)
4A	0.2	0.060	F	50.0	20	12.0	526 (76.3)	545 (79.1)	630 (91.5)	0.79	28	81	ND	ND
4A	0.2	0.060	G	49.4	20	12.0	528 (76.7)	531 (77.0)	619 (89.9)	0.82	29	82	153 (113)	−60 (−80)
5	0.4	0	A	3.4	20	10.8	257 (37.3)	357 (51.8)	501 (72.7)	0	29	67	ND	ND
5A	0.4	0	D	42.5	20	10.7	351 (51.0)	424 (61.5)	524 (76.1)	0	32	75	ND	ND
6	0.4	0.060	A	10.6	20	11.6	446 (64.8)	507 (73.6)	616 (89.4)	0	32	81	ND	ND
6	0.4	0.060	B	0	0[g]	11.9	426 (61.8)	467 (67.8)	591 (85.8)	0.55	33	81	ND	ND
6	0.4	0.060	C	31.9	10	11.8	491 (71.3)	540 (78.4)	634 (92.1)	0	29	79	>136 (>100)	−35 (−35)
6	0.4	0.060	D	25.9	20	12.0	524 (76.0)	573 (83.1)	668 (96.9)	0	28	80	>136 (>100)	−45 (−50)
6A	0.4	0.060	E	33.2	30	12.0	506 (73.4)	557 (80.8)	652 (94.6)	0	28	81	>163 (>120)	−55 (−70)
6A	0.4	0.060	F	23.1	20	12.1	511 (74.1)	564 (81.8)	661 (95.9)	0	28	79	183 (135)	−50 (−55)

[a] See Table 1 for actual analyses.

[b] See Fig. 1 for details.

[c] Determined from companion plate iced-brine quenched from 745°C (1375°F).

[d] C_v(100%) = energy absorbed at lowest temperature at which 100 percent shear was obtained.

[e] FATT = fracture appearance transition temperature.

[f] ND = not determined.

[g] Finish rolled at 790°C (1450°F) with 20 percent reduction.

compositions and processing used in the present study, the temperature at which transformation to ferrite normally begins ranges from 750 to 765°C (1380 to 1410°F) for strain-free austenite. In deformed austenite, ferrite begins to form earlier as a result of strain-accelerated nucleation. Consequently, it was possible to use the percent reduction at 790°C (1450°F) as a means of controlling the amount of ferrite that would form prior to the final reduction at 745°C (1375°F). The results are presented in Table 3. It can be seen that in the series designed to hold the deformed ferrite constant at 30 percent, the average ferrite content ranged from 26.9 to 34.3 percent, with the overall average being 31.3 percent. In the series designed to vary the amount of deformed ferrite the highest average value was 50.7 percent, although from Table 2 it can be seen that individual values reached as high as 51.9 percent deformed ferrite for Schedule G.

In order to determine how well the iced-brine quench retained the structure of interest, that is, prevented additional transformation to ferrite during cooling to room temperature, the three *companion* plates for Schedule B were iced-brine quenched from 790°C (1450°F) in lieu of the last pass. These plates exhibited ferrite contents of 1.6, 3.8, and 1.9 percent for Steels 2, 4, and 6, respectively, indicating that the quench was reasonably effective. Quenching from 745°C (1375°F), after some ferrite had been nucleated, may have been somewhat less effective, and the tabulated percent deformed ferrite values may therefore be somewhat too large.

TABLE 3—*Summary of average amounts of deformed ferrite produced by the various rolling schedules.*

Rolling Schedule	Average Amount of Deformed Ferrite, volume percent[a]		Final Reduction at 745°C (1375°F), %
Percent reduction varied at constant volume percent ferrite			
B	0		0[b]
C	26.9	Average, 31.3	10
D	34.3		20
E	32.7		30
Volume percent ferrite varied at constant percent reduction			
A	16.9		20
D	34.3		20
F	39.4		20
G	50.7		20

[a] This ferrite was formed between 790 and 745°C (1450 and 1375°F). Niobium-free steels not included.

[b] Final reduction was at 790°C (1450°F).

An illustrative example of microstructures is given in Fig. 2 where optical micrographs are presented for Steel 4 in the rolled (Schedule D) and the iced-brine-quenched conditions. As can be seen in Fig. 2*a*, a clear distinction could not be made between the deformed and the undeformed ferrite, because the deformed ferrite exhibited a wide range of substructures (approaching nil) and grain-shapes (approaching equiaxed). The quenched specimen Fig. 2*b* provided the necessary sharp distinction needed for a quantitative metallographic determination of the amount of ferrite present at 745°C (1375°F).

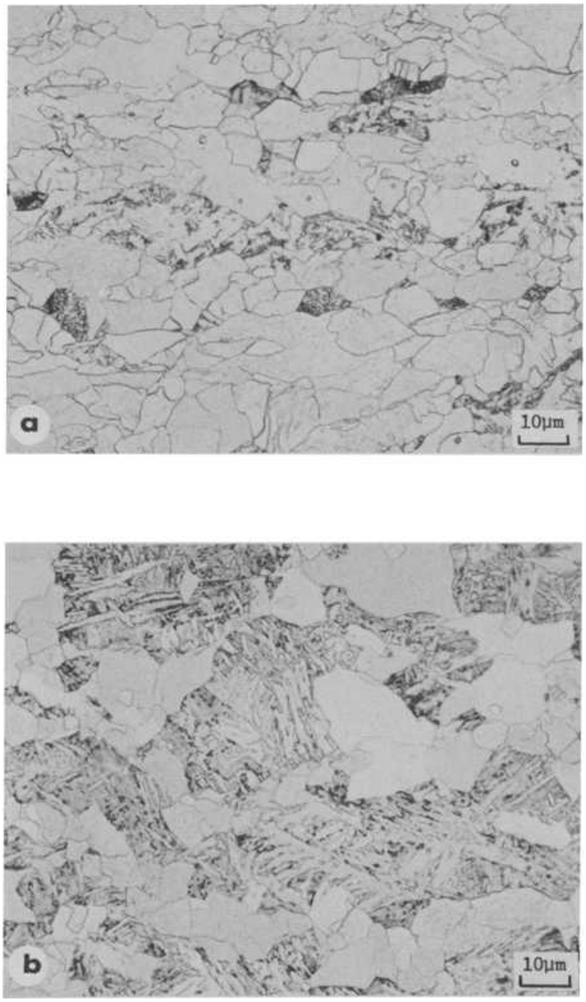

FIG. 2—*Illustrative micrographs of 0.22Mo-0.066Nb steel (No. 4) showing* (a) *as-rolled structure and* (b) *companion plate iced-brine quenched. The microstructure of the companion plate indicates 40 percent ferrite at 745°C (1375°F).*

Effect of Percent Reduction with 30 Percent Ferrite

The measured yield and tensile strength values of steels containing approximately 30 percent deformed ferrite increased with severity of deformation up to 20 percent deformation, as shown in Fig. 3. When the deformation was further increased to 30 percent, the strength values all decreased, returning in the case of the 0.2Mo-0.035Nb steel essentially to the initial strength, that is the strength of the plate receiving no deformation at 745°C (1375°F).

Because of the compositional differences among the steels and hence differences in the austenite deformation behavior, a range of ferrite grain sizes was obtained, as shown in Table 2. Grain size has a significant effect on tensile properties, and this effect is included along with other strengthening mechanisms in the data shown in Fig. 3. To more clearly reveal the relative contributions of the various strengthening mechanisms, it was necessary to correct the initial data for grain size effects. This was done by applying the basic Hall-Petch equation to the initial data

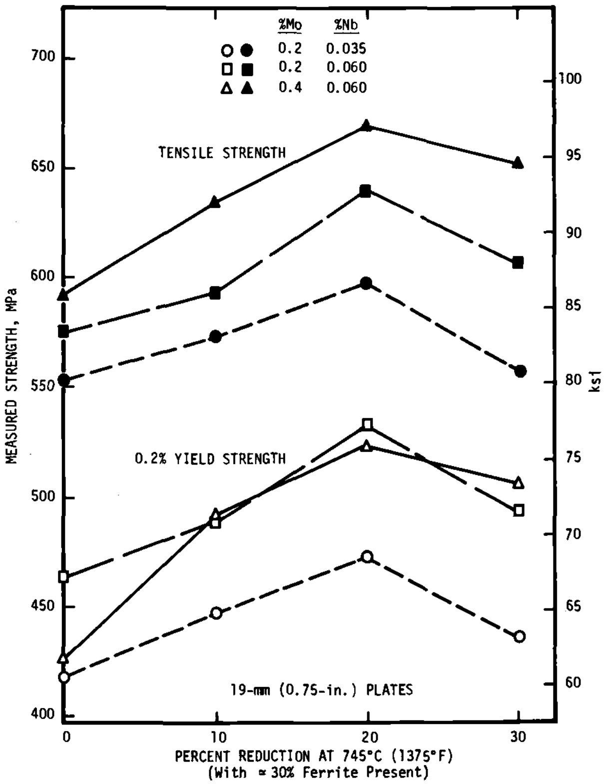

FIG. 3—*Effect of severity of deformation during the final pass on the yield and tensile strength of plates containing approximately 30 percent deformed ferrite.*

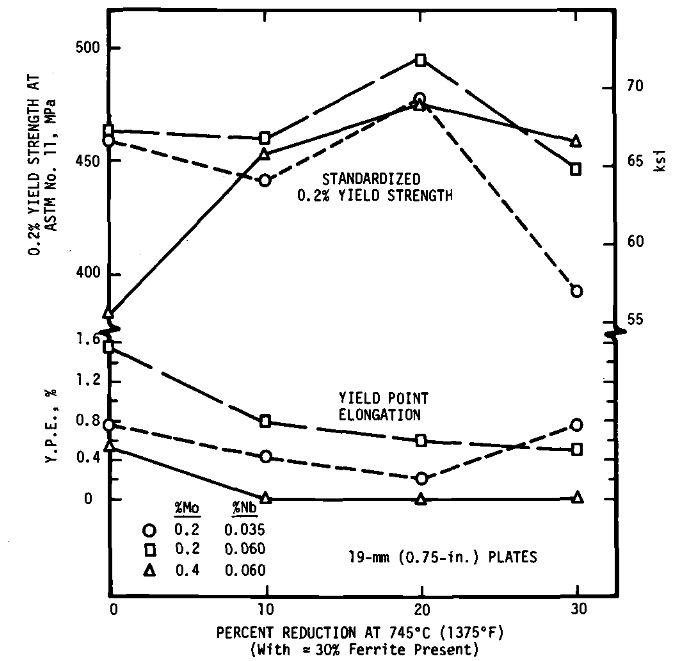

FIG. 4—*Variation of yield strength (standardized to ASTM grain size No. 11) and yield point elongation for same materials and conditions shown in Fig. 3.*

$$\sigma_y = \sigma_0 + k_y d^{-1/2}$$

where

d = grain size,
σ_y = yield stress at grain size d,
σ_0 = yield stress at infinite grain size, and
k_y = a constant.

A range of values has been measured for k_y, depending on alloy content [*4*]. A value of 20 N/mm^2/mm$^{-1/2}$ (0.58 ksi/in.$^{-1/2}$) was taken for this study as most representative of low-carbon high-manganese steels. Using this value of k_y and the Hall-Petch relationship, the yield strength data of Fig. 3 were corrected to a common grain size of ASTM No. 11. The results are plotted in Fig. 4. A consideration of the differences between Figs. 3 and 4 led to the following conclusions regarding grain size effects:

1. The lower strength of the 0.2Mo-0.035Nb steel (Fig. 3) was due to a generally coarser grain size relative to the other two steels.

2. For both of the 0.2Mo-Nb steels, the measured strength increase between 0 and 10 percent reduction was produced by grain refinement.

The yield strength increase shown by the initial data, Fig. 3, is eliminated when grain size is taken into account, Fig. 4.

3. Grain size was not a factor in the strength *variations* of the 0.4Mo-0.06Nb steel, although a fine grain size was responsible for the generally high strength level of this steel.

The variations in yield strength attributable to variables other than grain size can be seen in the upper part of Fig. 4. Mechanically, the only other variable involved would be the degree of deformation experienced by the 30 percent ferrite (and 70 percent austenite) present at 745°C (1375°F). Metallurgically, the variations in percent reduction could introduce two variables affecting strength in the deformed ferrite: dislocation substructure and strain-enhanced precipitation hardening. Deformation of the austenite on the last pass could theoretically affect the strength of the undeformed ferrite by promoting premature precipitation of Nb(C,N), reducing the potential for subsequent precipitation hardening in the ferrite. However, that possibility would appear to be remote because the transformation of the 70 percent austenite occurs very quickly after the final pass, and the precipitation might not have enough time to occur before the transformation.

The relative contributions of substructure and precipitation strengthening to the behavior shown in Fig. 4 could not be clearly separated. However, several inferences could be made. The initial low strength of the 0.4Mo-0.06Nb steel relative to the two 0.2Mo-Nb steels could be ascribed to the inhibiting effect, often seen in previous studies [5], of high molybdenum contents on Nb(C,N) precipitation strengthening in as-rolled plates. That effect is associated with the lowering of the Ar_3 by molybdenum to values below the optimum transformation temperature required for maximum precipitation strengthening in the as-rolled condition. For the natural air cooling rate of 19-mm (0.75-in.) plates, the optimum transformation-start temperature was determined to be approximately 765°C (1405°F), with higher or lower temperatures giving overaged or underaged conditions, respectively. The steady rise in strength of the 0.4Mo-0.06Nb steel with percent reduction to a maximum at 20 percent reduction (triangles in upper part of Fig. 4) could be ascribed to the combination of two effects: (1) substructure strengthening of the 30 volume percent ferrite present by the deformation in the last rolling pass; and (2) the raising of the Ar_3 of the 70 volume percent austenite present, by deformation, toward the optimum value for subsequent precipitation strengthening of the ferrite. The corresponding net increase in strength of the two 0.2Mo-Nb steels was smaller, because their initial Ar_3 values were already near the optimum for maximum precipitation strengthening.

The decreases in strength that resulted from increasing the percent reduction at 745°C (1375°F) from 20 percent to 30 percent (Fig. 4) could be ascribed to losses in both substructure and precipitation strengthening as the deformed ferrite underwent various degrees of recrystallization. The degree of recrystallization and extent of weakening ranged from very minor in the 0.4Mo-0.06Nb steel to very extensive in the 0.2Mo-0.035Nb steel. In the latter steel, the loss in yield strength was 85 MPa (12 ksi), and the recrystallization appeared to be essentially complete. The photomicrographs in Fig. 5 illustrate the variation in substructure content remaining in Steels 2A, 4A, and 6A after complete or partial recrystallization occurred in the deformed ferrite immediately after the final (30 percent) pass of Schedule E.

Decreases in yield point elongation, shown in the lower part of Fig. 4, can be associated with the introduction of dislocations in the deformed ferrite. These changes are very important for steels used in making U-O-E line pipe, because the elimination or near-elimination of yield point behavior increases the amount of work hardening experienced during the forming and final expansion of the pipe. It can also be seen that raising the molybdenum content from 0.2Mo to 0.4Mo reduced the yield point elongation from 1.6 to 0.6 percent in the plates containing no worked ferrite, and with as little as 11 percent deformed ferrite in the structure there was no yield point elongation in the 0.4Mo steel. This effect of molybdenum is well known and is caused by residual stresses associated with small islands of martensite that are introduced into the structure when the molybdenum content is raised enough to prevent nucleation of bainitic cementite [*6*].

The advantage of reducing or eliminating the yield point elongation to achieve work hardening during pipe forming and expansion can be seen by comparing the strength data plotted in Fig. 6 with the original 0.2 percent yield strength range of 420 to 460 MPa (61 to 67 ksi) for plates that were not finish-rolled below the Ar_3. These data, the 1.5 percent offset yield strength values, represent a conservative measure of the strength of a large diameter pipe in the as-expanded condition since deformation values as high as 2.5 percent are accumulated in the course of U-O-E pipe production [*2*]. As can be seen, steels in the composition range of the present study can be upgraded from the X60/X65 to the X75/X80 grade level by designing the rolling schedule to finish moderately below the Ar_3 so as to produce approximately 30 percent deformed ferrite in the structure and to subject that ferrite to a total reduction of approximately 20 percent.

Effect of Percent Deformed Ferrite with 20 Percent Reduction

The yield strength data (standardized to ASTM No. 11 grain size) presented in Fig. 7 show the influence of increasing volume percent of deformed ferrite on substructure plus precipitation strengthening when the final reduction at 745°C (1375°F) was held constant at 20 percent.

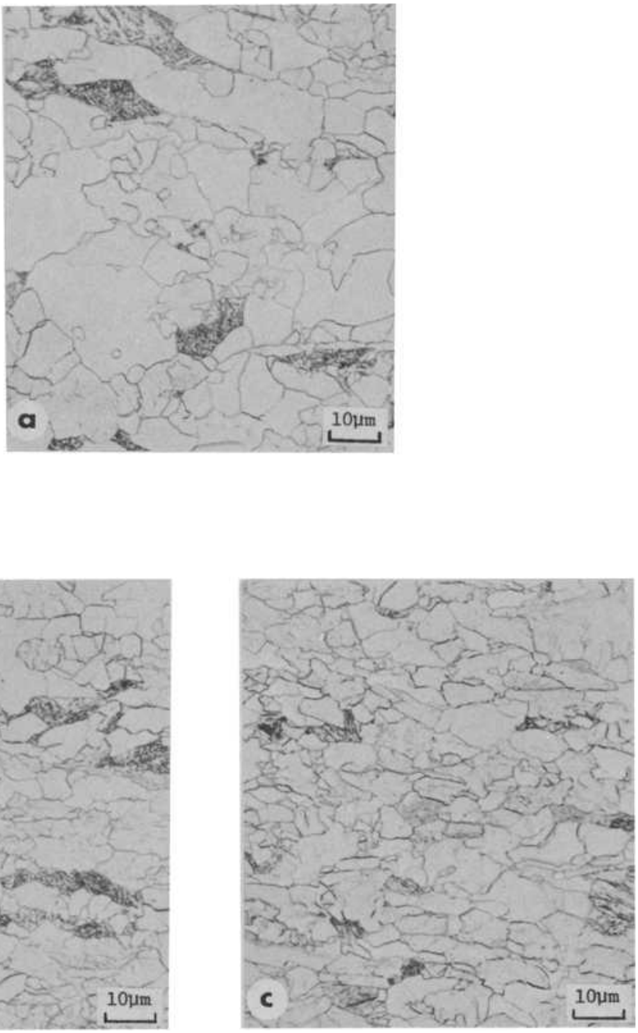

FIG. 5—*Microstructures of Steels 2A, 4A, and 6A after rolling to Schedule E, involving a 30 percent final reduction with 30 percent ferrite present. Note extensive recrystallization in* (a) *Steel 2A (0.21Mo-0.033Nb), as evidenced by near absence of substructured grains, and decreasing evidence of recrystallization (increasing substructure) in* (b) *and* (c), *Steel 4A (0.20Mo-0.058Nb) and Steel 6A (0.41Mo-0.054Nb), respectively.*

Rolling Schedules A, D, F, and G were employed for this part of the investigation.

To ascertain the contribution of dislocation substructure to the 0.2 percent yield strength, the data from the niobium-free steels (1A, 3, and 5A) were plotted in Fig. 7. These points (solid symbols) defined a sloping line representing the increasing strength contribution from the dislocation

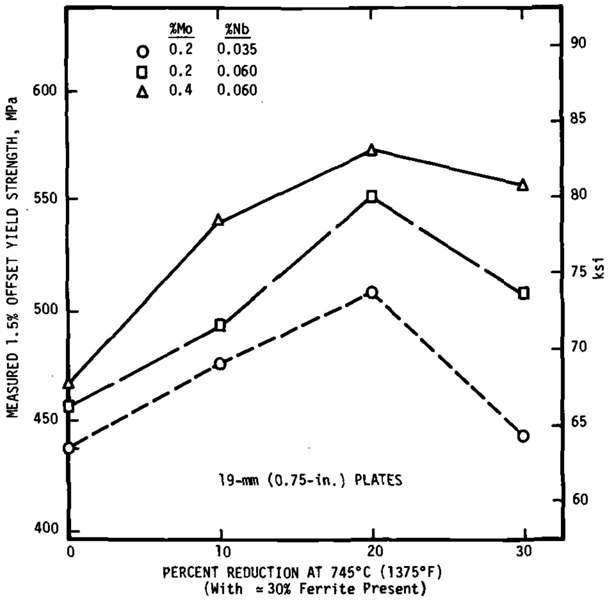

FIG. 6—*Effect of percent reduction during final pass on the 1.5 percent offset yield strength of plates containing approximately 30 percent deformed ferrite.*

substructure in the deformed ferrite. Extrapolation of that line to zero percent deformed ferrite indicated a base strength of approximately 310 MPa (45 ksi) for a steel of that composition and a ferrite grain size of ASTM No. 11. A single line can be used for the two molybdenum levels, because the difference in solid solution strengthening between a 0.2Mo steel and a 0.4Mo steel would be negligibly small (7 MPa (1 ksi)) [7].

The total precipitation strengthening contribution, that is, the precipitation in the undeformed ferrite plus the precipitation in the deformed ferrite, is the difference between the slanted line through the solid points and the curves through the open points. The 0.4Mo-0.06Nb steel exhibited a distinctly different behavior from that of the 0.2Mo-0.035Nb steel and the 0.2Mo-0.06Nb steel. The standardized yield strength increased linearly with volume percent deformed ferrite in the 0.4Mo-0.06Nb steel, while the lower-molybdenum steels exhibited a minimum at about 15 percent deformed ferrite, a maximum at about 38 percent deformed ferrite, followed by a decrease at high values of deformed ferrite content. The linear behavior of the 0.4Mo-0.06Nb steel was interpreted to be a straightforward example of strain-enhanced precipitation strengthening (added to the linear strengthening effect of the dislocation substructure) in the deformed ferrite. That is, the dislocations in the deformed ferrite promoted a greater than usual amount of precipitation of Nb(C,N), and the net increase in strength of the steel was directly proportional to

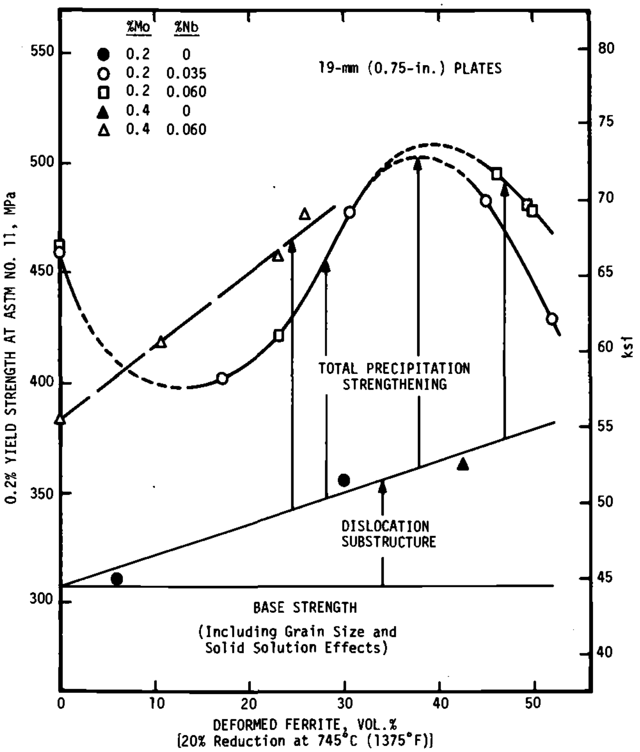

FIG. 7—*Variation of standardized yield strength for increasing amounts of deformed ferrite with 20 percent deformation at 745°C (1375°F).*

the amount of deformed ferrite present, following a simple rule of mixtures.

The overall behavior of the two 0.2Mo-Nb steels was not so easy to explain and remains a matter of considerable conjecture. The higher initial standardized strength values of these steels (with no deformed ferrite) relative to that of the 0.4Mo-0.06Nb steel could be explained if it were assumed that the $\gamma \rightarrow \alpha$ transformation temperature of the lower molybdenum steels was optimum for obtaining maximum precipitation strengthening in the as-rolled condition and that raising the molybdenum content to 0.4Mo lowered the transformation temperature and produced an underaged condition in the as-rolled plate. The reason for the early decrease in normalized yield strength in the 0.2Mo-Nb steels with the introduction of a small amount of deformed ferrite is not known. Following the minimum, the normalized yield strength values increased to the maxima at approximately 38 percent deformed ferrite. This rise could be ascribed to increasing contributions from the substructure and precipitation strengthening mechanisms.

The maxima in the standardized yield strength curves were followed by decreases of from 17 MPa (2.5 ksi) to 48 MPa (7 ksi). Since the deformed ferrite was not severely deformed (20 percent reduction), recrystallization would not be expected, and the metallographic examination confirmed that recrystallization had not occurred. Consequently, the loss in strength was here attributed entirely to a decrease in precipitation strengthening resulting from an increase in the amount of premature Nb(C,N) precipitation in austenite. The increased precipitation was caused by the use of the larger deformation (35 percent) at 790°C (1450°F) and, in the case of Schedule G, by the additional 15 percent deformation at 925°C (1700°F). The fact that a greater loss in strength was suffered by the 0.2Mo-0.035Nb steel than by the 0.2Mo-0.06Nb steel can be explained by the fact that the former steel had the smaller total niobium content. The increased precipitation of Nb(C,N) in austenite depleted the niobium supply more, proportionately, in the lower niobium steel.

Charpy V-Notch Impact Properties

The upgrading of the yield strength of the subject steels by controlled rolling moderately below the Ar_3 was achieved with reasonably good impact toughness, Table 2. The 50 percent shear FATT values associated with the highest strengths, that is, in plates rolled so as to have 30 percent ferrite that was deformed by 20 percent in the final reduction, were −35, −40, and −45°C (−35, −40 and −50°F) for Steels 2, 4, and 6, respectively. The shelf energy was above 136 J (100 ft · lb) in all plates.

A complete study of impact property variations could not be made because, as mentioned earlier, there was insufficient material for both tension and impact specimens in those instances where the plates were severely curved after rolling. However, when all of the FATT values in Table 2 were compared against grain size and identified with respect to composition and rolling schedule, it was evident that the presence of deformed ferrite in the structure did not impair the measured impact properties. The plates containing the most deformed ferrite, that is, those rolled in accordance with Schedules D, E, F, and G, tended to have the best (lowest) FATT values.

Separations or splits on the fracture surface were observed, and there appeared to be a slightly greater incidence of splitting in those specimens that contained a large amount of deformed ferrite. Because of the abbreviated scope of the impact testing in the present study, it was not possible to determine the exact effects of splitting on the FATT or shelf energy values. However, the authors believe that in those materials having the best strength properties, that is, those having 30 volume percent ferrite prior to the final roll pass and deformed 20 percent on the final pass, splitting was not a significant factor in the measured FATT values. Additional work is needed to verify this point.

General Discussion

From a practical point of view, the greatest value of the present study was that it appeared to provide a useful guideline in the art of using thermomechanical processing to upgrade the strength properties of pearlite-reduced Mo-Nb line pipe steels without sacrificing impact toughness. The guideline was that for maximizing yield strength without impairing toughness in the steel composition range investigated, there was an optimum amount of deformed ferrite (approximately 30 percent) and an optimum reduction (approximately 20 percent) to be applied below the Ar_3. This type of processing raised strength through grain refinement in the 0.2Mo-0.035Nb steel and, to a smaller degree, in the 0.2Mo-0.06Nb steel, and by dislocation substructure and strain-enhanced precipitation strengthening in all the steels. The overall superior strength of the 0.4Mo-0.06Nb steel was a result of its fine grain size that did not vary significantly throughout the study. Strength increases produced by rolling this steel below the Ar_3 were ascribed entirely to substructure and strain-enhanced precipitation.

Exceeding the optimum amount of deformed ferrite resulted in a decrease in strength. This was ascribed to the greater austenite deformation employed to raise the volume percent of deformed ferrite causing an excessive amount of premature precipitation of Nb(C,N) in the austenite. The use of reductions greater than the optimum caused partial or complete recrystallization of the deformed ferrite. To the extent that recrystallization occurred, the strengthening that had been gained from dislocation substructure and from strain-enhanced precipitation was lost.

Regarding the conflicting reports in the literature as to whether dislocation substructures make a measurable contribution to strength in steels finish rolled moderately below the Ar_3, the results of the present investigation support the observations of Repas [*2*] and of Speich and Dabkowski [*3*] that substructural strengthening is significant. The data of Little et al [*1*] showing no substructural strengthening for steels finish rolled above 725°C (1340°F) would appear to be in conflict with the present study and the studies by Repas [*2*] and by Speich and Dabkowski [*3*]. There are two possible explanations for this discrepancy. The latter two studies were known to involve thermocouple measurements of temperature at the mid-thickness of the plates, the practice used in the present study. Little et al did not mention the method of temperature measurement. If they measured surface temperatures, the surface-to-center difference would account for most of the apparent discrepancy. In addition, Little et al were working with slightly higher carbon contents than used in this study or the works of Repas and Speich and Dabkowski. The higher carbon would result in a lower Ar_3 temperature and hence require lower finish rolling temperatures before significant substructure strengthening could be observed.

Summary and Conclusions

An investigation involving five laboratory Mo-Nb pearlite-reduced pipe steels was conducted to ascertain whether finish rolling moderately below the Ar_3 is a practical means for upgrading strength and impact properties. The base composition was 0.08C, 1.4Mn, 0.1Si, 0.06Al, 0.006N, 0.010P, and 0.007S, with combinations of 0.21Mo + 0Nb, 0.21Mo + 0.034Nb, 0.21Mo + 0.062Nb, 0.40Mo + 0Nb, and 0.42Mo + 0.061Nb. These steels were controlled rolled to 19-mm (0.75-in.) plates using rolling schedules designed to produce various combinations of volume percent deformed ferrite and percent reduction on the final roll pass.

Tension and impact property data were obtained and related to the observed variations in microstructure. The study led to the following conclusions:

Controlled rolling of the subject pearlite-reduced Mo-Nb pipe steels to a temperature moderately below the Ar_3 was an effective means for improving yield strength while maintaining good toughness. Consequently, this type of controlled rolling may be considered an effective way of deriving the best properties from a given steel.

The principal mechanism for the improvement in properties in the 0.2Mo-0.035Nb steel and, to a smaller degree, in the 0.2Mo-0.06Nb steel was ferrite grain refinement resulting from the low-temperature deformation of austenite in the partially transformed structure.

In the 0.4Mo-0.06Nb steel, strength increases due to rolling below the Ar_3 were produced entirely by substructure and strain-enhanced precipitation contributions associated with the deformed ferrite. The grain size of this steel was very fine throughout the study, and that accounted for its overall superiority in strength.

For steels containing approximately 30 percent deformed ferrite, the yield and tensile strength values reached maxima for a 20 percent reduction on the last roll pass, but a 30 percent reduction produced decreases from the maximum values. The magnitudes of decreases were inversely related to the alloy content and were found to be associated with partial to essentially complete recrystallization of the deformed ferrite.

Attempts to strengthen the 0.2Mo-Nb steels by increasing the volume percent of deformed ferrite at constant final reduction were successful up to a point; further increases in percent deformed ferrite resulted in a fall-off in strength. The fall-off was caused by a decrease in the contribution from Nb(C,N) precipitation strengthening resulting from excessive precipitation in the austenite caused by the extra deformation employed to achieve the maximum amount of deformed ferrite.

References

[1] Little, J. H., Chapman, J. A., Morrison, W. B., and Mintz, B., *Proceedings*, Conference on The Microstructure and Design of Alloys, Institute of Metals, London, Vol. 1, 1973, p. 80.

[2] Repas, P. E., *Proceedings,* Conference on Microalloying '75, Union Carbide Corporation, 1977, p. 387.
[3] Speich, G. R. and Dabkowski, D. S., *Proceedings,* The Metallurgical Society, Symposium on Hot Deformation of Austenite, J. B. Ballance, Ed., American Institute of Mining, Metallurgical, and Petroleum Engineers, Nov. 1975, p. 557.
[4] Anderson, E., King, D., Law, W., and Spreadborough, J., *Transactions,* The Metallurgical Society, American Institute of Mining, Metallurgical, and Petroleum Engineers, Vol. 242, Jan. 1968, p. 115.
[5] Coldren, A. P., "Molybdenum-Columbium Pearlite-Reduced Steels for X70 Arctic Grade Line Pipe," Climax Report L-176-141, 25 Aug. 1975, unpublished research.
[6] Tither, G. and Lavite, M., *Journal of Metals,* Sept. 1975, p. 15.
[7] Lacy, C. E. and Gensamer, M., *Transactions,* American Society of Metallurgists, Vol. 32, 1944, p. 88.

G. W. Delvecchio,[1] *J. E. Hood,*[1] *and D. B. McCutcheon*[1]

Controlled Processing of Molybdenum Bearing Line Pipe Steels

REFERENCE: Delvecchio, G. W., Hood, J. E., and McCutcheon, D. B., "**Controlled Processing of Molybdenum Bearing Line Pipe Steels,**" *MiCon 78: Optimization of Processing, Properties, and Service Performance Through Microstructural Control, ASTM STP 672,* Halle Abrams, G. N. Maniar, D. A. Nail, and H. D. Solomon, Eds., American Society for Testing and Materials, 1979, pp. 145–168.

ABSTRACT: Low-carbon Mn-Mo-Cb acicular ferrite steels are being used by several steel companies for higher strength line pipe above API X60. The molybdenum addition is made to achieve a continuous stress-strain curve that gives higher strength in the final pipe than that obtainable from conventional ferrite-pearlite steels. In this paper, the effects of chemistry and controlled rolling on plate and pipe properties are described for a series of steels: low-carbon Mn-Mo-Cb, low-carbon Mn-Mo-Cb-V, and low-carbon Mn-Cb-V. Low carbon Mn-Mo-Cb steels are shown to give the best combination of pipe properties for up to X70 level with thickness as high as 12 mm.

KEY WORDS: steels, microstructure, mechanical properties, rolling, pipelines

Over the past decade, both process and alloy research for oil and gas line pipe was directed towards the development of grades with both higher strength and toughness at heavier wall thickness. In particular, this research has focused on the development of pipe grades for low-temperature (Arctic) environments [*1*].[2] New high-strength low-alloy steel chemistries, controlled-rolling practices and novel methods of improving steel cleanliness through desulfurization are now production realities [*2,3*]. Several line pipe producers are offering line pipe with excellent low-temperature notch toughness at X70 strength levels.

One of the most significant developments has been the production of steels with partially acicular ferrite microstructures as an alternative to conventional ferrite-pearlite precipitation strengthened steels [*4*]. These molybdenum bearing steels have sufficient hardenability to transform to acicular ferrite microstructures that are mixtures of polygonal ferrite,

---

[1] Research investigator, assistant research manager, and research associate, respectively, The Steel Company of Canada, Limited, Hamilton, Ontario, Canada.

[2] The italic numbers in brackets refer to the list of references appended to this paper.

pearlite, bainite, and retained austenite-martensite constituent [5]. The residual stress resulting from the formation of low-temperature transformation products causes continuous yielding. This can result in a much higher work-hardening rate during pipe forming than for ferrite-pearlite steels and accounts for the higher strength of the steel with these microstructures in pipe form [6].

Repas [7] suggested the use of lower alloy content carbon-manganese-molybdenum-columbium (C-Mn-Mo-Cb) and carbon-manganese-molybdenum-columbium-vanadium (C-Mn-Mo-Cb-V) chemistries, which were controlled rolled below the proeutectoid ferrite start temperature, as low-cost aternatives to achieve higher strength pipe. His data suggested that X70 strength levels could be achieved with a significantly reduced alloy content (1.20Mn, 0.20Mo, and 0.04Cb compared with 1.65Mn, 0.30Mo, and 0.04Cb used by other pipe producers) if the plates were rolled with at least 10 to 40 percent reduction below the proeutectoid ferrite start temperature.

In the present study, we have applied both the high-alloy and the low-alloy content approaches to X70 U and O expanded (UOE) pipe at an intermediate gage, 12 mm (0.475 in.), for conventional service, design temperature −4°C (+25°F). For these steels and processing, we relate the change in strength during the pipe forming process to the steel microstructural features and stress-strain behavior of the steel in plate form.

Procedure

Three chemistry systems were studied in this program (Table 1): (1) carbon-manganese-columbium-vanadium (C-Mn-Cb-V), (2) carbon-manganese-molybdenum-columbium (C-Mn-Mo-Cb), and (3) carbon-manganese-molybdenum-columbium-vanadium (C-Mn-Mo-Cb-V).

The steels were made as part of a series of 275 tonne open hearth heats. The aim base composition was 0.09C, 1.20 to 1.40Mn, and 0.04Cb. For the C-Mn-Mo-Cb and C-Mn-Mo-Cb-V steels, a higher manganese level (1.50 to 1.60Mn) was also studied. The vanadium contents were nominally

TABLE 1—*Steel chemistries.*

	Chemical Analysis, %					
Alloy System	C	Mn	Mo	Cb	V	Symbol Code Key
C-Mn-Cb-V	0.08/0.11	1.15/1.40	. . .	0.035/0.066	0.041	✱
C-Mn-Mo-Cb	0.08	1.25	0.22	0.035	. . .	□
	0.10	1.50	0.24	0.045	. . .	■
C-Mn-Mo-Cb-V	0.11	1.20/1.40	0.23/0.30	0.056/0.079	0.037	△
	0.12	1.60	0.20	0.062	0.040	▲

0.04 percent. All heats were made with desulfurized hot metal, and rare earth metal additions were made to the ladle and molds to achieve a final sulfur of approximately 0.010 percent with sulfide inclusion shape control.

All plates were controlled rolled from 165 mm (6.5 in.) thick slabs to 12 mm (0.475 in.) gage plate using a conventional reheat temperature of 1290°C (2354°F). The controlled-rolling practice was varied to achieve a range of finishing temperatures (Table 2). The breakdown bar thickness (intermediate slab size between the roughing and finishing stands) was held constant at 57 mm (2.25 in.). The entry temperature into the finishing stand was varied from 955 to 840°C (1751 to 1544°F) by modifying the high-pressure descale-spray-cooling practice during roughing. During the finish-rolling sequence, the drafting and temperature were controlled by specifying the temperature below which the steel was given 30 percent reduction. This controlled-rolling temperature for 30 percent reduction was varied from 860°C (1580°F) to 715°C (1319°F). The finishing temperature ranged from 770°C (1418°F) down to less than 700°C (1292°F). All temperatures were measured using Ircon pyrometers located on the entry and exit sides of the finishing stand.

The plates were formed into 914.4 mm (36 in.) outside diameter UOE pipe. All pipes were submerged-arc welded, expanded by 1.5 percent, and hydrotested to 93 percent of nominal X70 yield strength. Selected plates and pipes were tested to determine the strength, Charpy toughness, and drop weight tear test (DWTT) toughness perpendicular to both the plate rolling direction and the pipe axis. Pipe strength was measured using the flattened strap tension test.

The microstructures of the as-rolled plates were examined parallel to the plate rolling direction. The ferrite grain size was rated using a Quantimet (QTM) 720 image analyzer after etching the metallographic samples with 2 percent nital. The volume fraction of high carbon constituents in the microstructure (for example, pearlite, retained austenite-martensite constituent, and bainitic carbides) was also measured using the QTM 720 and using point counts on scanning electron micrographs.

One of the potential advantages of using a reduced alloy content is improved field weldability (resistance to heat-affected zone hydrogen-induced cracking). Bead-on-plate tests[3] were performed on several plates covering the range of carbon equivalents of each chemistry type. The beads were made with 3.17 mm (1/8 in.) E8010G electrodes using a heat input of 0.59 kJ/mm and a test temperature of 0°C (+32°F). Root run cracking tests [8,9] were also done on representative chemistries of high- and low-manganese C-Mn-Mo-Cb-V steels. This test is designed to

---

[3] Using the Standard Procedure for Conductance of the Underbead Crack Sensitivity Tests, Natural Gas Pipeline Company, 1969; and the IIW Maximum Hardness Test, IIW Document No. IX-25-53, International Institute of Welding, 1953.

TABLE 2—*Controlled rolling practices.*

Alloy System	Mn	Controlled Rolling[a] Temperatures, °C (°F)		
		Entry	30% Reduction	Finish
C-Mn-Cb-V	1.15/1.40	865/925 (1590/1697)	755/805 (1391/1481)	720/760 (1328/1400)
C-Mn-Mo-Cb	1.25	900/955 (1652/1751)	790/860 (1454/1580)	745/770 (1373/1418)
	1.50	855/930 (1571/1706)	760/850 (1400/1562)	705/745 (1301/1373)
C-Mn-Mo-Cb-V	1.20/1.40	840/910 (1544/1670)	730/780 (1346/1436)	<700/745 (<1292/1373)
	1.60	840/920 (1544/1688)	715/780 (1319/1436)	<700/740 (<1292/1364)

[a] Slabs were reheated to 1290°C (2354°F) and the rougher entry temperatures varied from 1090°C (1994°F) to 1145°C (2093°F).

simulate the field welding geometry and restraint levels. A stringer pass was deposited in the field preparation, and the weld was sectioned and examined for cracking. The weld bead was deposited using a 3.96 mm (5/32 in.) E7010G electrode and a heat input of 0.59 kJ/mm at a temperature of 4°C (40°F).

Results

Microstructure

The ferrite grain size and the volume percentage of high carbon constituents are presented in Table 3. The average ferrite grain size was dependent on the steel chemistry. The low-manganese steels (C-Mn-Cb-V, C-Mn-Mo-Cb, and C-Mn-Mo-Cb-V) had a *significantly* (statistically at the 90 percent confidence level) coarser average grain size than the high-manganese steels (~6.5 versus ~5.0 microns, respectively). The ferrite grains were elongated with the degree of elongation increasing as the controlled-rolling temperature decreased (Fig. 1). The volume percentage of high-carbon constituents was dependent upon the steel carbon and molybdenum contents, and increased from ~14 percent for the C-Mn-Cb-V steel to over 30 percent for the higher-carbon molybdenum-bearing steels.

The distribution and types of nonpolygonal ferrite transformation products were changed with the alloy content and carbon content. The C-Mn-Cb-V steels consisted entirely of proeutectoid ferrite and lamellar pearlite in heavy bands (Fig. 2). At low-managanese levels (1.20 to 1.40Mn) the C-Mn-Mo-Cb and C-Mn-Mo-Cb-V steels contained polygonal ferrite and islands of bainite (Figs. 3*a* and *b,* and 4*a* and *b*). At the higher manganese contents (1.50 to 1.60Mn), the ferrite grain size was significantly reduced and the high-carbon regions were mixtures of polygonal ferrite, upper and lower bainite, and also retained austenite-martensite constituent (Figs. 3*c* and *d,* and 4*c* and *d*).

Plate Strength

The plate (0.5 percent under load) yield strengths and ultimate tensile strengths were controlled by the alloy content and the controlled-rolling practice. Figure 5 shows the yield strength, ultimate tensile strength, and yield-to-ultimate (Y/T) ratio for each steel type as a function of the rolling practice.

The yield strength of all steels increased with reduced controlled-rolling temperatures (Fig. 5*a*). At higher controlled-rolling temperatures, all chemistries showed a similar yield strength level while at lower controlled-rolling temperatures, the higher manganese steels showed a greater increase in strength than lower manganese steels.

TABLE 3—*Quantitative metallography.*

Alloy System	Chemistry, %					Controlled Rolling Temperature for 30% Reduction, °C (°F)	Grain Size, μm		Volume Percent High Carbon Regions, %	
	C	Mn	Mo	Cb	V		$\overline{x}$[a]	s[b]	$\overline{x}$	s
C-Mn-Cb-V	0.078	1.15	. . .	0.066	0.040	755 (1391)	5.9	0.8	13.7	3.0
	0.106	1.40	. . .	0.035	0.041	805 (1481)	6.4	1.0	18.5	3.6
C-Mn-Mo-Cb	0.081	1.25	0.22	0.035	. . .	860 (1580)	6.4	0.7	19.1	2.5
	0.079	1.25	0.23	0.037	. . .	815 (1499)	6.5	1.2	15.2	2.6
	0.071	1.25	0.24	0.037	. . .	790 (1454)	6.4	1.2	16.7	2.6
	0.092	1.50	0.24	0.047	. . .	815 (1499)	4.9	0.7	21.6	3.6
	0.097	1.50	0.24	0.046	. . .	800 (1472)	4.8	0.4	24.2	2.2
	0.101	1.50	0.24	0.045	. . .	760 (1400)	4.5	0.4	26.6	3.5
	0.112	1.55	0.24	0.047	. . .	850 (1562)	6.1	1.1	28.2	3.3
	0.106	1.55	0.19	0.047	. . .	790 (1454)	4.9	0.3	29.3	2.6
	0.096	1.50	0.23	0.043	. . .	790 (1454)	6.0	0.5	27.2	2.8
C-Mn-Mo-Cb-V	0.102	1.25	0.24	0.035	0.037	770 (1418)	6.5	0.7	26.9	4.2
	0.105	1.22	0.23	0.034	0.037	730 (1346)	6.2	0.8	25.8	4.0
	0.126	1.60	0.19	0.062	0.039	780 (1436)	5.5	1.1	32.1	2.8
	0.117	1.65	0.20	0.029	0.032	760 (1400)	5.4	1.3	35.3	3.7
	0.130	1.60	0.20	0.065	0.040	715 (1319)	4.4	0.3	32.1	4.3

[a] $\overline{x}$ = mean.

[b] s = standard deviation.

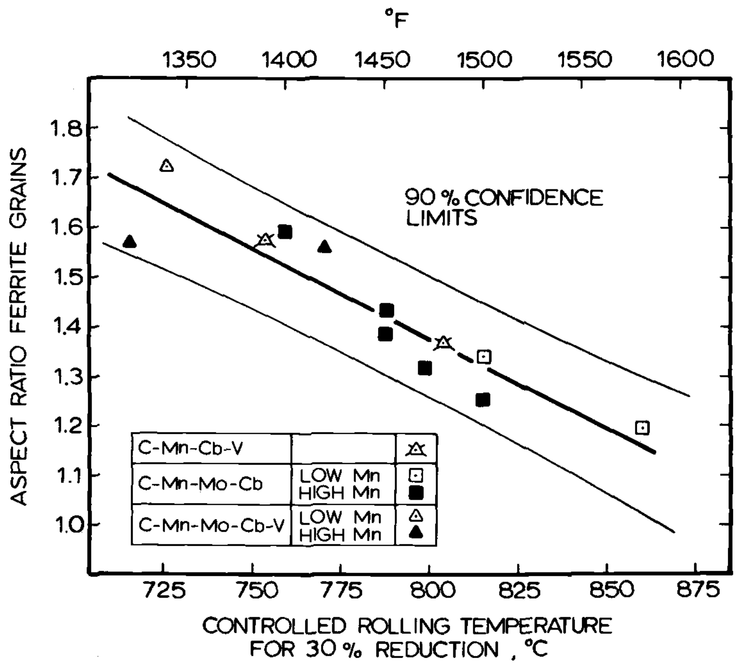

FIG. 1—*The effect of controlled rolling on the aspect ratio of the ferrite grains.*

The ultimate tensile strength of all steels also increased with reduced controlled-rolling temperatures (Fig. 5*b*). There was a significant difference in the ultimate tensile strength level for the different steel types over the entire range of rolling temperatures with the higher manganese steels exhibiting higher ultimate tensile strengths than the low-manganese steels.

The molybdenum-free chemistries showed the highest Y/T ratios for all rolling practices (Fig. 5*c*). The Y/T ratios for the low-manganese and high-manganese, molybdenum bearing steels increased with reduced controlled-rolling temperatures from 0.85 to 0.90 and 0.70 to 0.85, respectively.

Tensile Stress-Strain Behavior

For low-manganese (1.20Mn) C-Mn-Cb-V and C-Mn-Mo-Cb-V steels, the stress-strain curves exhibited a Lüders extension over almost the entire range of rolling practices. Reducing the controlled-rolling temperature increased yield strength (Figs. 6*a* and *b*) and decreased the Lüders extension (Fig. 7). All higher manganese (1.50 to 1.60Mn) C-Mn-Mo-Cb steels exhibited continuous stress-strain curves (Fig. 8). The vanadium 0.04 percent additions to the C-Mn-Mo-Cb steel did not significantly increase the plate strength (Figs. 5*a* and *b*).

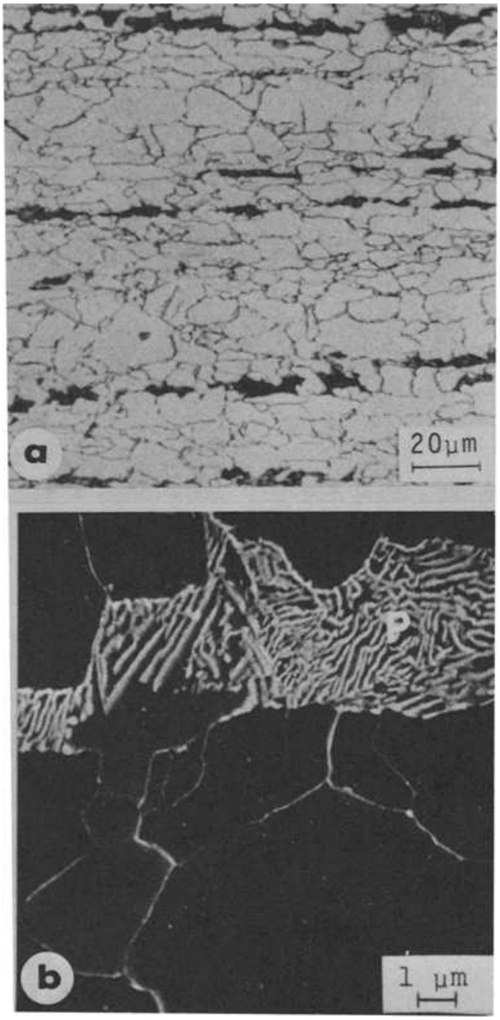

(*a*) General microstructure, 1.25Mn
(*b*) Lamellar pearlite (P), 1.15Mn

FIG. 2—*C-Mn-Cb-V steel—30 percent reduction below 755°C (1391°F).*

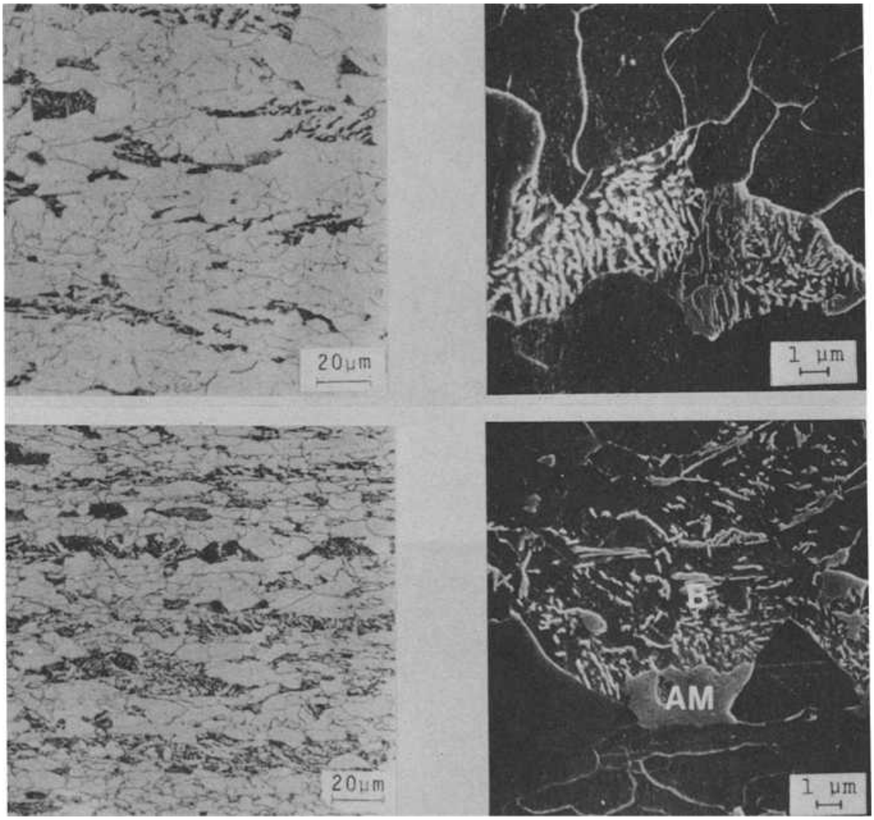

(*a*) General microstructure, 1.25Mn
(*b*) Bainitic carbides (B), 1.25Mn
(*c*) General microstructure, 1.50Mn
(*d*) Bainitic carbides (B) and retained austenite-martensite constituent (AM), 1.50Mn

FIG. 3—*C-Mn-Mo-Cb steel—30 percent reduction below 790°C (1454°F).*

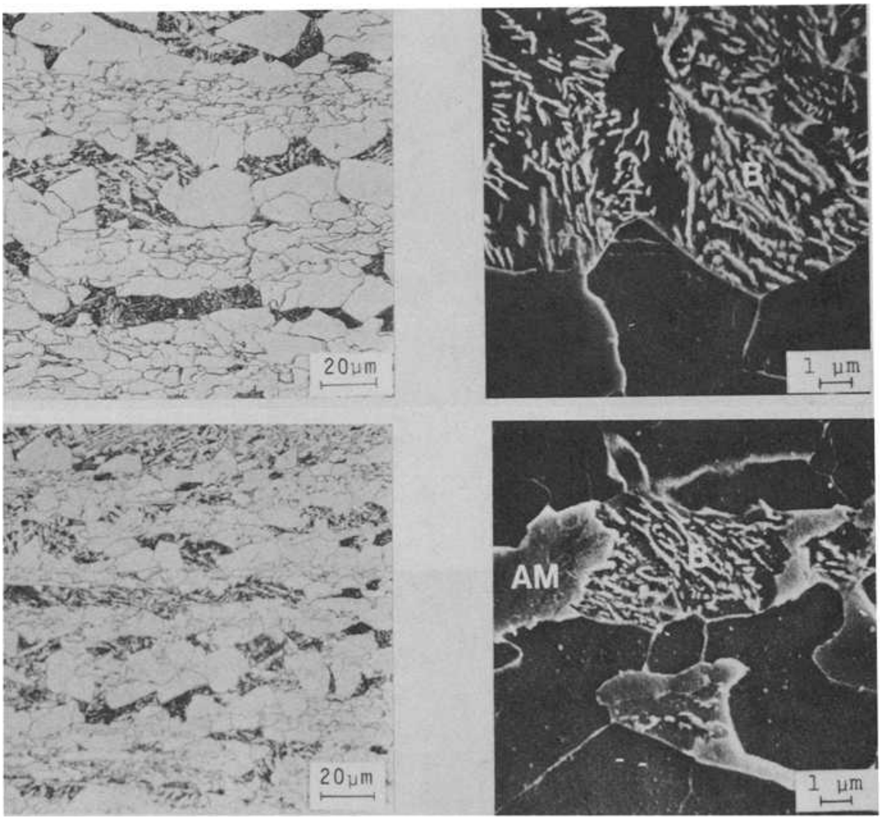

(*a*) General microstructure, 1.25Mn
(*b*) Bainitic carbides (B), 1.25Mn
(*c*) General microstructure, 1.60Mn
(*d*) Bainitic carbides (B) and retained austenite-martensite constituent (AM), 1.60Mn

FIG. 4—*C-Mn-Mo-Cb-V steel—30 percent reduction below 725°C (1337°F).*

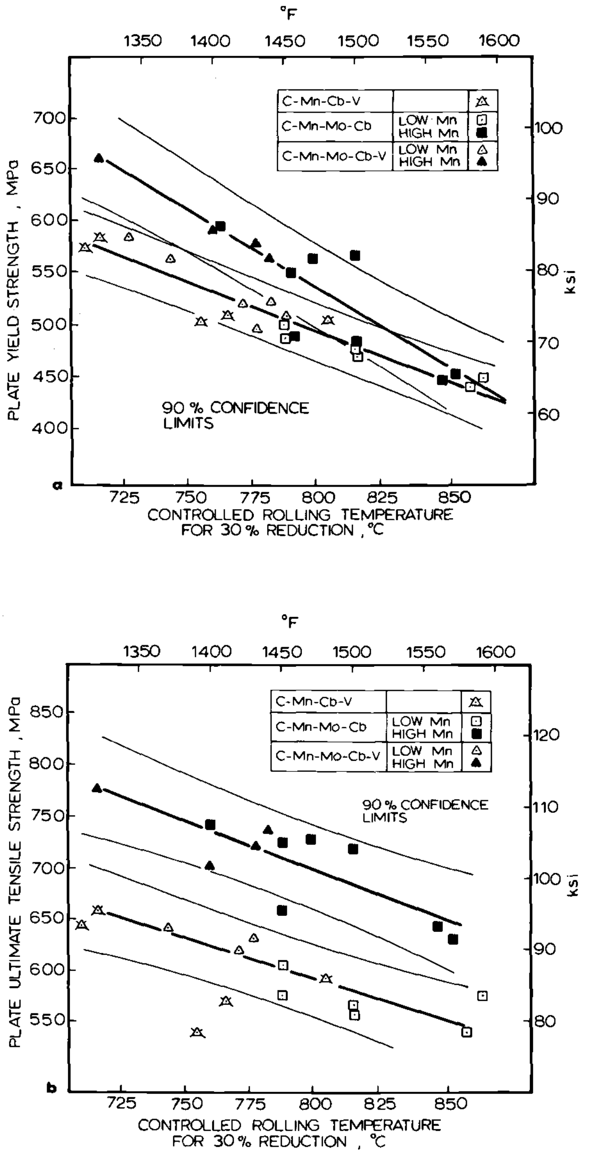

(*a*) Yield strength
(*b*) Ultimate tensile strength

FIG. 5—*The effect of controlled rolling on plate tensile properties.*

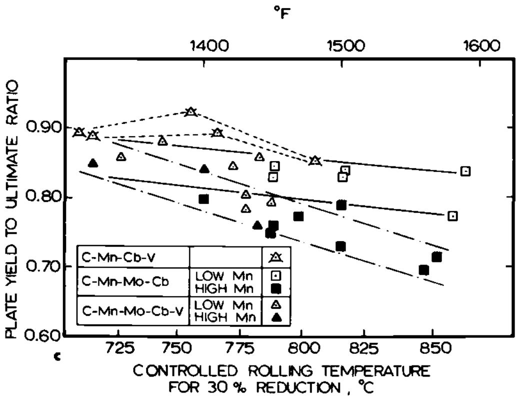

(*c*) Yield-to-ultimate ratio

FIG. 5—*continued.*

During pipe forming, subsequent expansion, and tension testing, the steel undergoes a series of strain reversals. The final strength measured in the flattened strap tension test reflects a complex combination of work hardening and the Bauschinger effect. To predict the final pipe yield strength requires knowledge of the cumulative effect of the strain cycles at different points through the wall thickness and positions around the pipe circumference. Such an analysis is beyond the scope of this paper. Qualitatively, however, we can demonstrate that the difference in the stress-strain behavior for the steels under study results in a significant difference in final pipe strength.

To give an indication of the strain hardening potential of each steel during pipe forming, we measured the difference in yield stress between 2.0 percent tensile strain and 0.5 percent ($\Delta\sigma$). The high-manganese C-Mn-Mo-Cb and C-Mn-Mo-Cb-V steels showed a constant $\Delta\sigma$ of more than 75 MPa over the entire range of rolling practices (Table 4). Both the

TABLE 4—*Yield stress increase for as-rolled plate.*

		$\Delta\sigma^a$ MPa (ksi)		
Alloy System	Mn, %	n^b	$\bar{x}^c$	s^d
C-Mn-Mo-Cb and C-Mn-Mo-Cb-V	1.20/1.40	11	25.5 (3.7)	14.5 (2.1)
C-Mn-Mo-Cb and C-Mn-Mo-Cb-V	1.50/1.60	11	77.2 (11.2)	12.4 (1.8)

[a] $\Delta\sigma = \sigma_{2.0\%\ \text{strain}} - \sigma_{0.5\%\ \text{strain}}$
[b] n = number of observations.
[c] $\bar{x}$ = mean.
[d] s = standard deviation.

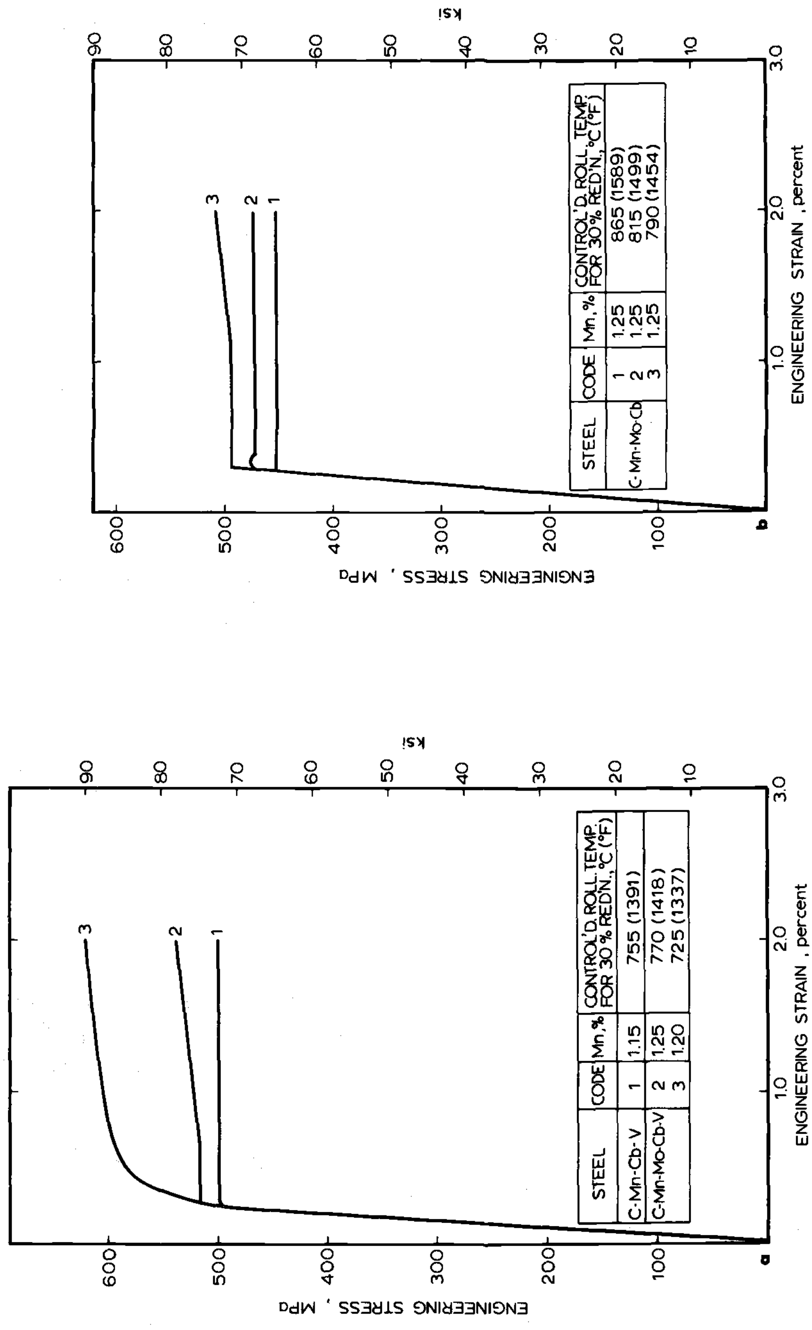

(*a*) C-Mn-Cb-V and C-Mn-Mo-Cb-V steels

(*b*) C-Mn-Mo-Cb steels

FIG. 6—*Stress-strain curves, 1.20Mn steels.*

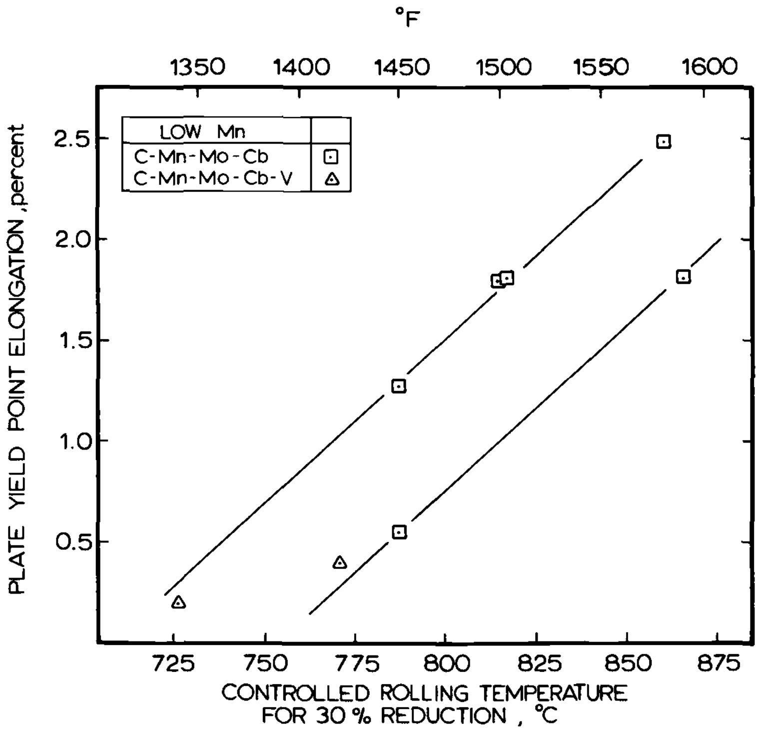

FIG. 7—*Effect of controlled rolling on yield point elongation.*

low-manganese C-Mn-Mo-Cb-V and C-Mn-Mo-Cb steels exhibited a $\Delta\sigma$ that increased from 0 to 40 MPa as the controlled-rolling temperature decreased from 870°C (1598°F) to 730°C (1346°F).

Pipe Strength

Not all plates from the C-Mn-Cb-V, C-Mn-Mo-Cb, and C-Mn-Mo-Cb-V steels were successfully formed into pipe. At the higher strength levels for these steels, we experienced significant *peaking*[4] of the pipe in the region of the seam weld. This peaking was cause for rejection of the pipe prior to hydraulic expansion. This problem can be overcome by increasing the amount of preforming at the plate edges.

The flattened strap yield strength is controlled by the stress-strain characteristics and hence the microstructure of the steels. The ferrite-pearlite C-Mn-Cb-V steels showed a loss of yield strength between plate and pipe (Fig. 9). The low-manganese C-Mn-Mo-Cb and C-Mn-Mo-Cb-V

---

[4] After forming and longitudinal seam welding, the unexpanded pipe has a *pear-shaped* cross section. Peaking describes the acuteness of the angle subtended by tangents to the pipe wall on either side of the longitudinal seam. This peaking is removed during the hydraulic expansion cycle, if it is not excessive.

steels showed, on average, no change in yield strength between plate and pipe, while the high-manganese C-Mn-Mo-Cb and C-Mn-Mo-Cb-V steels showed a consistent increase in yield strength. There was no apparent effect of vanadium on the yield strength change.

The pipe yield strength correlated with the ultimate tensile strength for all steels (Fig. 10). A similar correlation was shown by Taira [*10*]. At a 90 percent confidence level, an ultimate tensile strength (from plate or flattened strap) of at least 640 MPa (92 ksi) is needed to meet a minimum pipe yield strength requirement of 483 MPa (70 ksi). This strength level

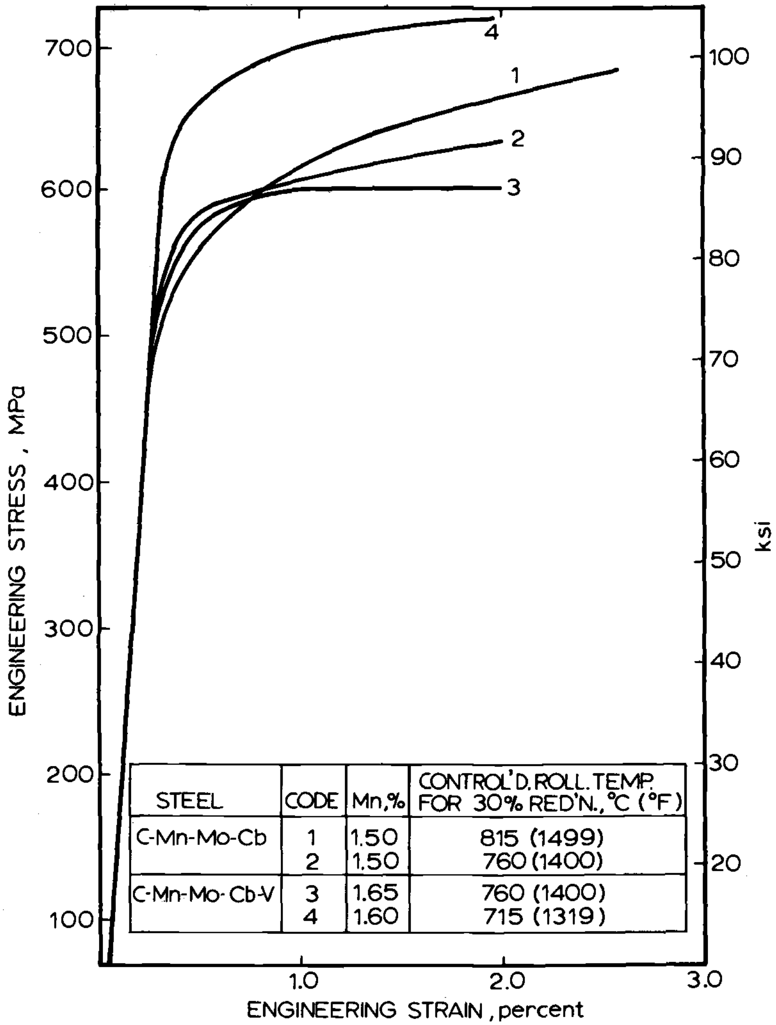

STEEL	CODE	Mn,%	CONTROL'D. ROLL. TEMP. FOR 30% RED'N., °C (°F)
C-Mn-Mo-Cb	1 2	1.50 1.50	815 (1499) 760 (1400)
C-Mn-Mo-Cb-V	3 4	1.65 1.60	760 (1400) 715 (1319)

FIG. 8—*Stress-strain curves, 1.50 to 1.60Mn.*

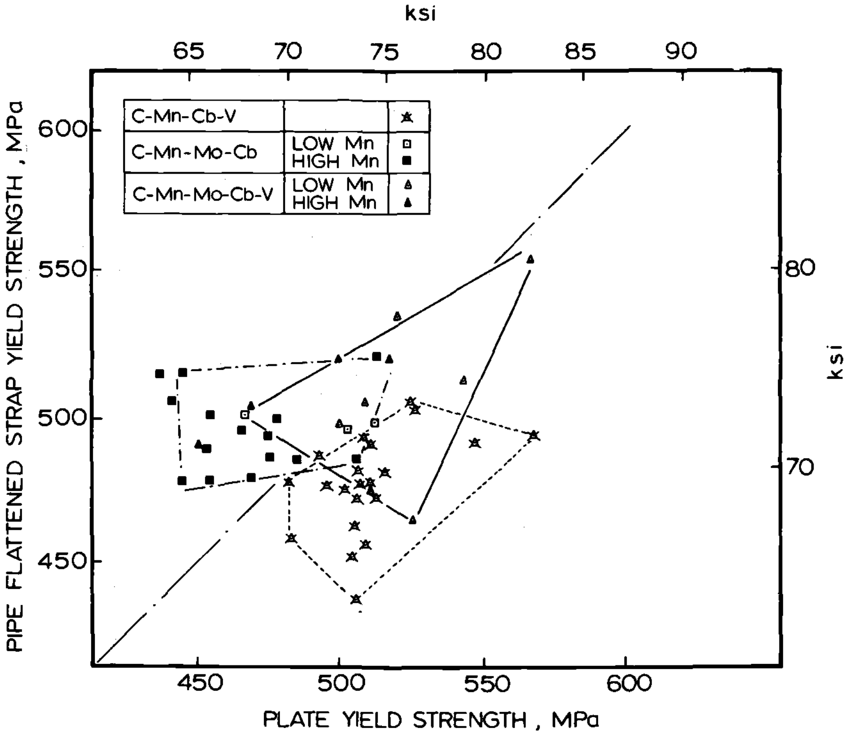

FIG. 9—*Flattened strap yield strength versus plate yield strength.*

was achieved in all the chemistries studied; however, the high-manganese C-Mn-Mo-Cb and C-Mn-Mo-Cb-V steels required much less low-temperature controlled rolling (Fig. 5).

Charpy Toughness

Both the Charpy 50 percent shear fracture appearance transition temperature (FATT) and the CVI energy (minimum Charpy energy at 100 percent shear) were influenced by the controlled-rolling practice and alloy content. The morphology and volume fraction of sulfide and oxide inclusions were not greatly different between chemistries, so that the effect of inclusions on Charpy toughness was considered to be a constant.

Over the range of rolling practices studied, decreasing the controlled-rolling temperature for 30 percent reduction below about 825°C (1525°F) raised the FATT for all steels (Fig. 11). This controlled-rolling temperature corresponds to a finishing temperature of approximately 760°C (1400°F). Other studies [*7,11*] have also shown that there is a minimum in the FATT versus finishing temperature relationship. We expect that increasing the finishing temperature above approximately 760°C (1400°F) would increase the FATT. The higher manganese content C-Mn-Mo-Cb and C-Mn-Mo-Cb-V steels had *significantly* (statistically at the 90 percent confidence level) lower FATT's than the low-manganese C-Mn-Cb-V, C-Mn-Mo-Cb, and C-Mn-Mo-Cb-V steels at a particular ultimate strength level (Fig. 12), presumably due to the finer grain size.

For heavily controlled-rolled line pipe steels, the CVI toughness is considered to give a better correlation with ductile crack arrest potential than the absorbed energy at the design temperature [*12*]. The CVI energy decreased as the controlled-rolling temperature decreased (Fig. 13) for all steels. The CVI energy also decreased as the plate ultimate tensile strength increased (Fig. 14). The high-manganese steels tended to give a higher CVI energy at any particular ultimate tensile strength level, but this effect was not statistically significant with the limited sample size.

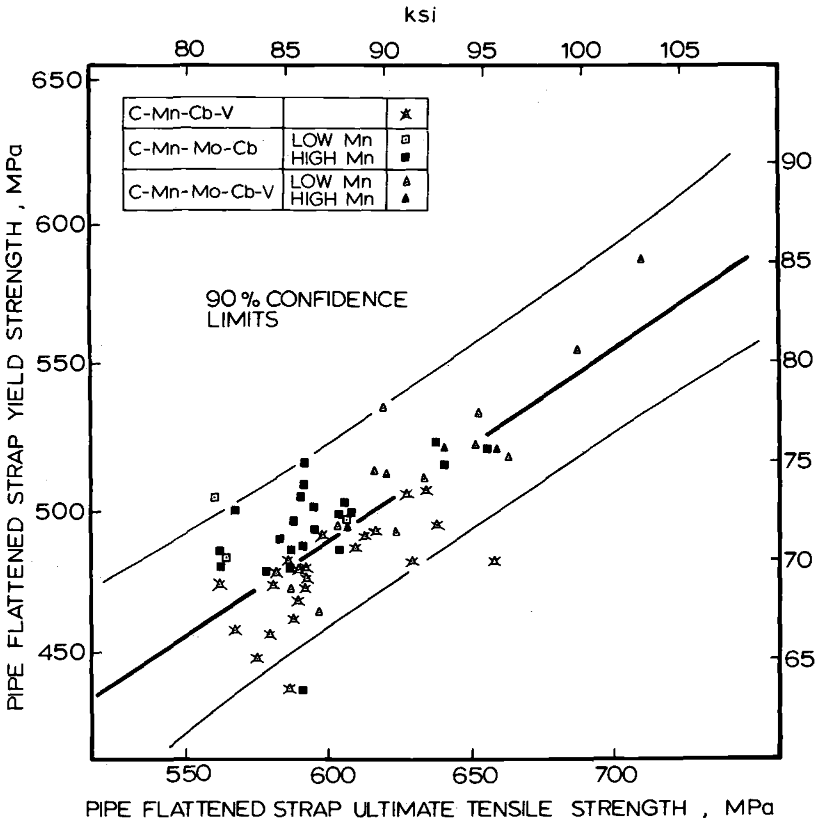

FIG. 10—*Flattened strap yield strength versus flattened strap ultimate tensile strength.*

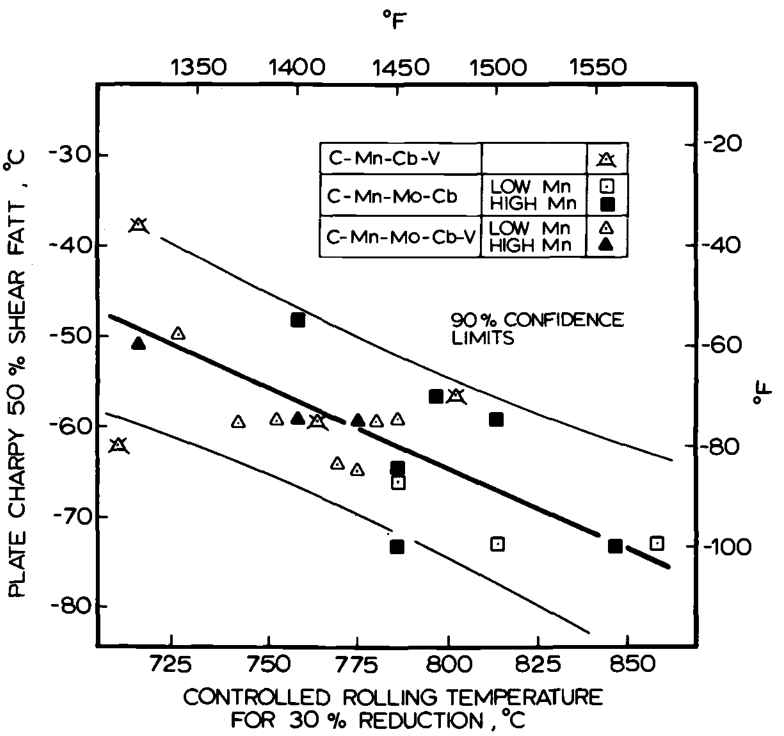

FIG. 11—*The effect of controlled rolling on Charpy 50 percent shear FATT.*

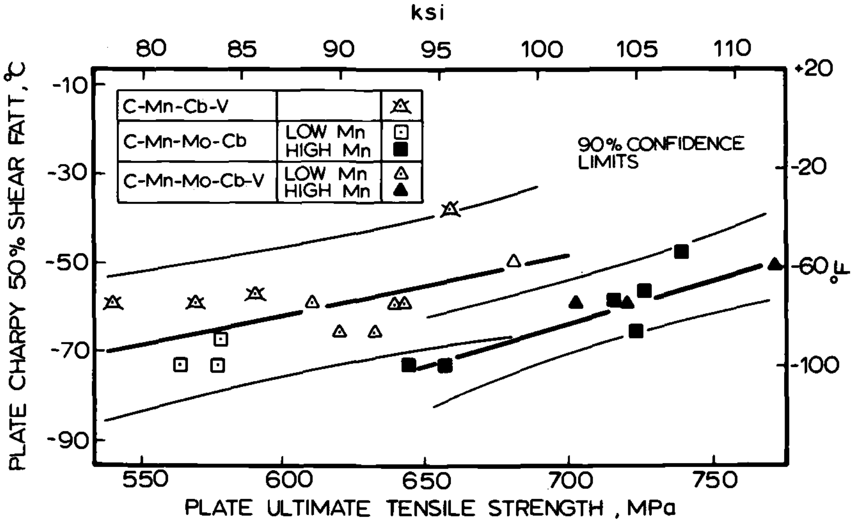

FIG. 12—*Charpy 50 percent shear FATT versus plate ultimate tensile strength.*

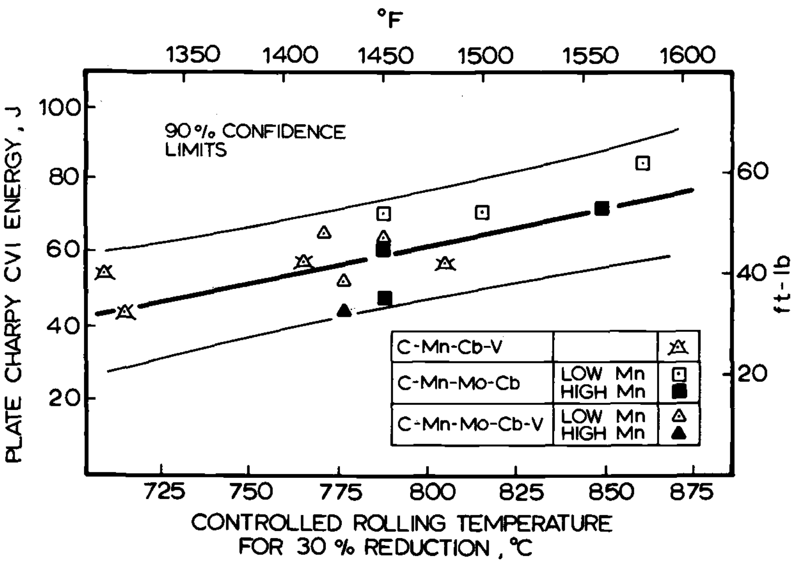

FIG. 13—*The effect of controlled rolling on plate Charpy CVI energy.*

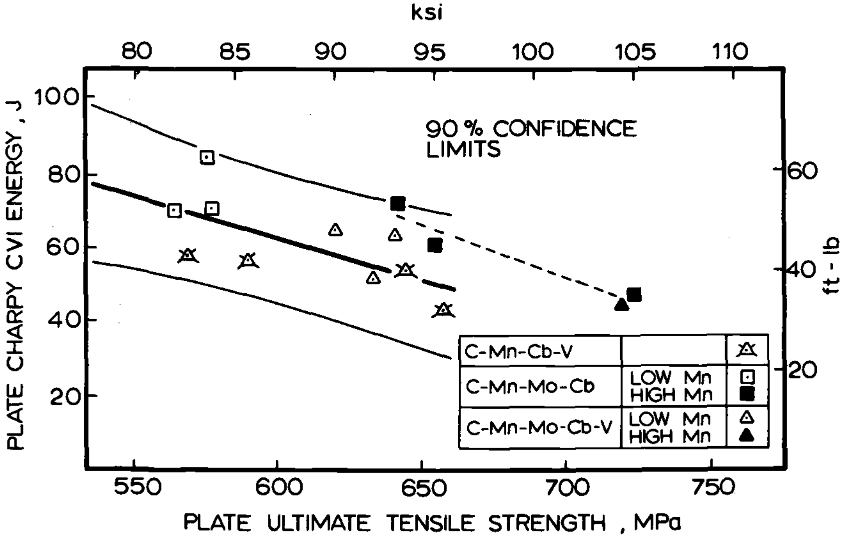

FIG. 14—*Charpy CVI energy versus plate ultimate tensile strength.*

TABLE 5—*Drop weight tear test results.*

		Drop Weight Tear Test, % shear					
		Plate, −18°C (0°F)			UOE Pipe, −4°C (+25°F)		
Alloy System	Mn	n[a]	$\bar{x}$[b]	s[c]	n	$\bar{x}$	s
C-Mn-Cb-V,	1.20/1.40	12	98.7	1.7	6	99.2	2.0
C-Mn-Mo-Cb, and							
C-Mn-Mo-Cb-V	1.50/1.60	5	91.2	5.5	2	100.0	. . .

[a] n = number of observations.
[b] $\bar{x}$ = mean.
[c] s = standard deviation.

Drop Weight Tear Test (DWTT) Toughness

The DWTT toughness was measured in both plate and pipe on samples representative of the different chemistries rolled over the range of rolling practices. All steels showed greater than 85 percent shear in both plate and pipe at the test temperatures (Table 5).

Field Weldability

Only the highest carbon and alloy content steel (0.12C, 1.50Mn, 0.20Mo, 0.03Cb) showed underbead cracking in the bead-on-plate test at 0°C (32°F). In the root run cracking test, no cracking was observed in either the low- or high-manganese C-Mn-Mo-Cb-V steel.

Research has established that the sensitivity of a steel to hydrogen-induced cracking is related to the hardness of the weld heat affected zone (HAZ). This hardness is, in turn, related to the base plate chemistry that can be characterized by carbon equivalent formulae. The two formulae that are in common use for pipeline steels are the IIW[5] carbon equivalent (CE) and the Ito-Bessyo [*13*] cracking parameter (P_{CM}).

$$CE(\%) = C + \frac{Mn}{6} + \frac{Cr + Mo + V}{5} + \frac{Ni + Cu}{15} \tag{1}$$

$$P_{CM} = C + \frac{Si}{30} + \frac{Mn + Cu + Cr}{20} + \frac{Ni}{60} + \frac{Mo}{15} + \frac{V}{10} + 5B \tag{2}$$

For all the steels studied, the maximum underbead hardness correlated best with P_{CM} (Fig. 15).

---

[5] IIW Document No. IX-537-67, International Institute of Welding, 1967.

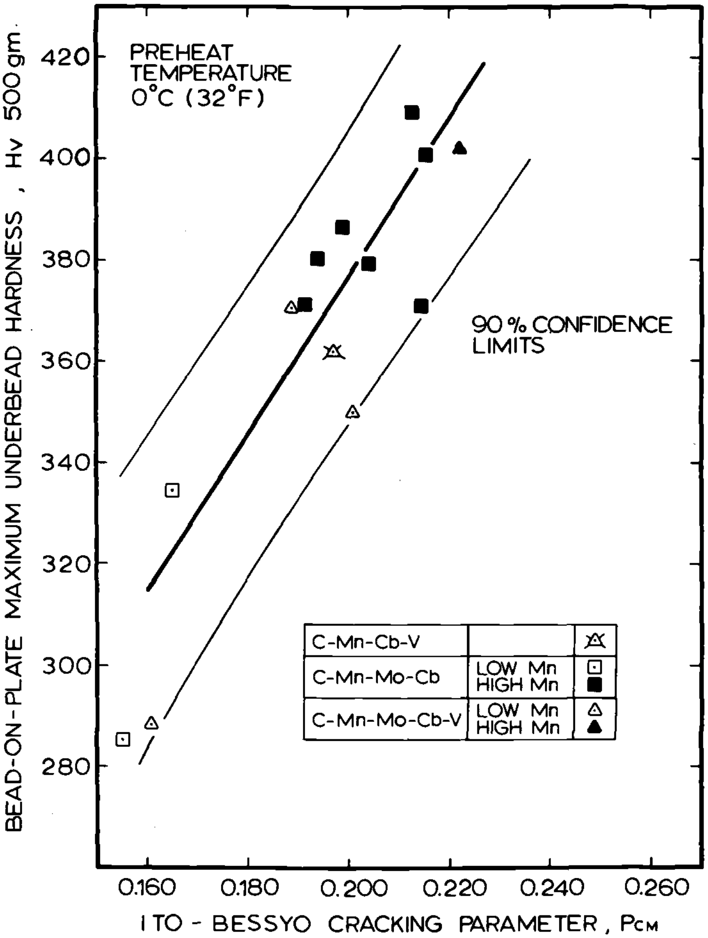

FIG. 15—*Bead-on-plate underbead hardness versus* P_{CM}.

Discussion

The yield and ultimate strengths of as-rolled plate can be markedly increased by controlled rolling below the proeuctoid ferrite start temperature. The increase in yield strength (above that due to grain size, solid solution, and Peierls stress) is attributed to dislocation, textural, and precipitation strengthening [*11,14,15*]. This plate strength increase does *not* assure a proportionate increase in pipe yield strength. Although there is a general tendency to increased flattened strap yield strength with increased plate strength, one must also consider the shape of the stress-strain curve and particularly the potential for work hardening during forming. Those steels that contained sufficient alloy hardenability to develop retained austenite-martensite constitutent in the microstructure, exhibited a significant work hardening potential, with no Lüders elongation, for all rolling practices. The lower alloy content steels all exhibited Lüders elongations and little work-hardening potential unless they were controlled rolled sufficiently to exhaust the Lüders extension. This reduction of the Lüders extension is believed to be associated with the production of mobile dislocations, work hardening [*16*], and back stresses that result from the rolling of the ferrite below the Ar_3. Even then, the steels had only a slight work-hardening potential. The ferrite-pearlite chemistry showed an extended Lüders region in which there was no work-hardening potential.

The chemistry required to form a continuous stress-strain curve was proposed by Rothwell [*17*] as

$$32.5\,(\%\,\mathrm{Mo}) + 10\,(\%\,\mathrm{Mn} + \%\,\mathrm{Cr}) + 2.5\,(\%\,\mathrm{Ni}) \geqslant 23$$

This condition holds true for the steels studied here. However, low-temperature rolling can be used to minimize Lüders extension to obtain a continuous stress-strain curve without higher alloy.

A flattened strap yield strength of 483 MPa (70 ksi) can be achieved in both the low-manganese and high-manganese C-Mn-Mo-Cb and C-Mn-Mo-Cb-V chemistries. The empirical correlation between strap yield and ultimate tensile strengths indicates that a minimum ultimate tensile strength of 640 MPa (92 ksi) is required for *all alloys* to give a minimum pipe yield strength of 483 MPa (70 ksi). Whereas this ultimate tensile strength was achieved for *all* rolling practices studied for the higher-manganese C-Mn-Mo-Cb and C-Mn-Mo-Cb-V steels, it could only be achieved in the low-manganese steels by applying a reduction below 732°C (1350°F) of at least 30 percent. Such a heavy controlled rolling practice *may* result in significant loss of productivity in the plate mill due to holding to reduce temperature prior to finishing and could cause a significant deterioration in plate shape. Furthermore, there is a significant increase in the degree of splitting [*18*] with heavy controlled rolling. Our data supports the fact that the heavy controlled rolling lowers the CVI energy.

There is a significant increase in Charpy 50 percent shear FATT with heavy controlled rolling. We anticipate a similar increase in DWTT transition temperature. Although the DWTT results for all pipe met the −4°C (25°F) design temperature requirement, higher alloy steels provide a greater potential for meeting lower design temperature specifications than the low-alloy steels.

All of the chemistries studied are considered weldable in the field. As expected, increasing the alloy and carbon contents in the steels raised the underbead hardnesses, which could increase the susceptibility to hydrogen-induced HAZ cracking. This indicates that both the carbon and manganese contents should be controlled in this grade to ensure meeting the mechanical property specifications while maintaining field weldability.

Conclusion

Both the low- and high-manganese content steels studied in this program have the potential to meet ×70 strength and toughness specifications. At the 0.20Mo level, the high-manganese content steels are better suited for this grade, because they can achieve consistently higher UOE pipe yield strength levels than the low-manganese steels. In addition, the high-manganese steels require considerably less low-temperature rolling, which permits more flexibility and higher production rates during the controlled-rolling sequence.

References

[1] Mihelich, J. L., "Controlled Rolled Steels for Offshore Pipelines," paper presented at the Eighth Annual Offshore Technology Conference, Houston, Tex., 3–6 May 1976.

[2] Yamaguchi, T., Osuka, T., Taira, T., and Iwasaki, N., *Proceedings*, Microalloying '75 Conference, 1–3 Oct. 1975, Washington, D.C., pp. 415–424.

[3] Taeffner, K. D., Gorges, G., Haneke, M. A., and Recknagel, W. T., *Proceedings*, Microalloying '75 Conference, 1–3 Oct. 1975, Washington, D.C., pp. 425–434.

[4] Smith, Y. E., Coldren, A. P., and Cryderman, R. L., *Proceedings*, Towards Improved Ductility and Toughness Conference, Kyoto International Conference Hall, Japan, 25–26 Oct. 1971, pp. 119–142.

[5] Coldren, A. P., Cryderman, R. L., and Semchyshen, M., *Proceedings*, Steel Strengthening Mechanisms Symposium, Zürich, Switzerland, 5–6 May 1969, pp. 17–44.

[6] Tither, G. and Lavite, M., *Journal of Metals*, Sept. 1975, pp. 15–23.

[7] Repas, P. E., *Proceedings*, Microalloying '75 Conference, 1–3 Oct. 1975, Washington, D.C., pp. 387–396.

[8] Cotton, H. C. and Thomas, D., "Super-Diameter Pipes for Alaska," *Tube and Pipe Production*, Iron and Steel Institute, Publication 25, Nov. 1970.

[9] Archer, J., Hart, P. H. M., and Stalker, H. W., "An Assessment of Pipeline Girth Welds," American Welding Society Meeting, May 1976.

[10] Taira, T., Osuka, T., and Ishida, Y., "Development of Heavy Wall X65 Line Pipes Manufactured from Quench and Tempered Plates for Low Temperature Service," paper presented at the 15th Mechanical Working and Steel Processing Conference, 21–22 Jan. 1976, Chicago, Ill.

[11] Melloy, G. F. and Dennison, J. D., *Proceedings*, Third International Conference of the Strength of Metals and Alloys, Cambridge, England, Vol. 1, Aug. 1973, pp. 60–64.

[12] Maxey, W. A., Podlasek, R. J., Eiber, R. J., and Duffy, A. R., "Observations on Shear Fracture Propagation Behavior," *Proceedings*, Crack Propagation in Pipelines Conference, Newcastle Upon Tyne, England, March 1974.

[13] Ito, Y. and Bessyo, K., "Weldability Formula of High Strength Steels Related to Heat-Affected Zone Cracking," Sumitomo IIW Document No IX-576-68, International Institute of Welding, 1968.

[14] Baker, T. N., Haynes, E. J., and McPherson, N. A., *Proceedings*, Third International Conference of the Strength of Metals and Alloys, Cambridge, England, Vol. 1, Aug. 1973, pp. 65–69.

[15] Little, J. H., Chapman, J. A., Morrison, W. B., and Mintz, B., *Proceedings*, Third International Conference of the Strength of Metals and Alloys, Cambridge, England, Vol. 1, Aug. 1973, pp. 80–84.

[*16*] Philips, R. and Chapman, J. A., *Journal,* Iron and Steel Institute, June 1966, pp. 615–622.

[*17*] Civallero, M. A., Parrini, C., and Pizzimenti, N., *Proceedings*, Microalloying '75 Conference, 1–3 Oct. 1975, Washington, D.C., pp. 451–468.

[*18*] Dabkowski, D. S., Konkol, P. J., and Baldy, M. F., *Metallurgical Engineering Quarterly,* Feb. 1976, pp. 22–32.

R. Viswanathan[1]

Influence of Microstructure on the Temper Embrittlement of Some Low-Alloy Steels

REFERENCE: Viswanathan, R., "**Influence of Microstructure on the Temper Embrittlement of Some Low-Alloy Steels,**" *MiCon 78: Optimization of Processing, Properties, and Service Performance Through Microstructural Control, ASTM STP 672,* Halle Abrams, G. N. Maniar, D. A. Nail, and H. D. Solomon, Eds., American Society for Testing and Materials, *1979, pp. 169–185.*

ABSTRACT: The effect of microstructural variations produced by varying the transformation product and the tensile strength level on the temper embrittlement susceptibility of steels has been the subject of some recent studies. A review of the results pertaining to chromium molybdenum (Cr-Mo), chromium-molybdenum-vanadium (Cr-Mo-V), and nickel-chromium-molybdenum-vanadium (Ni-Cr-Mo-V) steels has been completed. Based on the review, it appears that in 2.25Cr-1Mo steels embrittled by step-cooling the transformation product does not appreciably affect the temper embrittlement susceptibility. In Cr-Mo-V and Ni-Cr-Mo steels, susceptibility to embrittlement increases in the order ferrite-pearlite, bainite, and martensite. Results on the effect of strength levels are inconclusive. In general, those structures that cause the steel to have low toughness initially also result in reduced susceptibility for further embrittlement. The limited amount of Auger data available suggest that the effect of microstructure is explainable, at least in part, by differences in grain boundary segregation of impurity elements caused by differences in microstructure.

KEY WORDS: steels, microstructure, alloys, temper embrittlement

The problem of intergranular embrittlement in steels promoted by segregation of specific impurity elements to the grain boundaries has been the subject of numerous studies. Embrittlement of the steels occurs if the steels are held in or slowly cooled through the temperature range of 350 to 540°C and thus imposes severe constraints on the operational as well as heat treatment schedules. The brittle behavior resulting from exposure in the critical temperature range manifests itself as an increase in the notch

---

[1] Fellow engineer, Westinghouse Research and Development Center, Pittsburgh, Pa. 15235.

bar ductile-to-brittle fracture appearance transition temperature (FATT), and a decrease in the critical stress intensity for fracture (K_{Ic}).

The degree to which degradation of toughness occurs due to temper embrittlement can be a function of the microstructure of the steel. In heavy section components such as turbine rotors and pressure vessels, inhomogeneities in chemical composition as well as thermal gradients during heat treatment often result in nonuniformity in the microstructure. Hence, the risk of embrittlement is variable with location in the component. In thin sections, where the temper embrittlement problem restricts the operational temperatures to a range outside the critical range, microstructural control offers promise as a means of widening the operational temperature range.

Recent work has shown that the brittle fracture tendencies of steels in aggressive environments can also be exacerbated by prior temper embrittlement and that the synergistic effects due to environment and impurities varies with the strength level of the steel [*1,2*].[2] An example of this behavior is shown in Fig. 1 for a low-alloy turbine steel. The results presented in Fig. 1 show that the threshold stress intensity for cracking in hydrogen sulfide (H_2S) (K_{Iscc}) is reduced by the presence of impurities. At low-yield strength levels, the K_{Iscc} is reduced markedly by impurities [*1*]. At high-yield strength levels, however, the data for the pure and impure steels converge to a single low value. The figure also shows that temper embrittlement resulting inadvertently from heat treatment alone is sufficient to reduce the fracture properties of the steel appreciably. The commercial significance of the impurity-related brittle fracture problems cannot therefore be overemphasized.

The objective of this paper is to collect and review all the information available in the literature pertaining to the relationships between transformation product, strength level (or hardness), and temper embrittlement susceptibility of two widely used turbine steels, chromium-molybdenum-vanadium and nickel-chromium-molybdenum-vanadium (Cr-Mo-V and Ni-Cr-Mo-V, respectively) and a pressure vessel steel (2.25Cr-1Mo). This is by no means an easy task due to several reasons. Firstly, available data on each alloy system is extremely limited. Even within the available data, it is difficult to compare results from different studies since the impurity levels, embrittlement schedules, and even Charpy test procedures are different from one study to another. In order to produce measurable embrittlement in reasonable lengths of time, most studies have utilized accelerated stepwise cooling procedures through the embrittlement regime. These procedures are both arbitrary and nonstandard. The various studies generally describe the heat treatment procedure without identifying the microstructure resulting from such heat treatment.

---

[2] The italic numbers in brackets refer to the list of references appended to this paper.

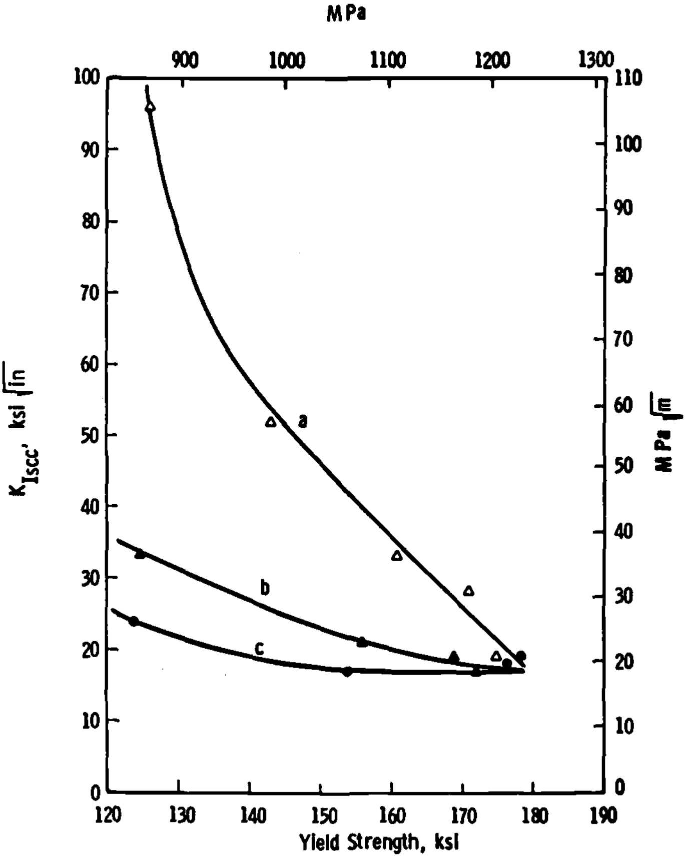

FIG. 1—*Variation of the threshold stress intensity for cracking in* H_2S *(*K_{Iscc}*) with yield strength and prior temper embrittlement for a low-alloy turbine steel* [1]. (a) *High-purity steel;* (b) *low-purity steel, as heat treated;* and (c) *low-purity steel, step-cooled.*

Despite these difficulties, an attempt is made in the following sections to synthesize various bits and pieces of data into a single broad framework, so that some understanding of the role of microstructure can be developed.

2.25Cr-1Mo Steels

Although numerous studies have been conducted relating to the temper embrittlement behavior of the 2.25Cr-1Mo steel, only four of these have even cursorily touched upon the microstructural aspects.

Results from the study of Swift and Gulya on 2.25Cr-1Mo steels exposed to various heat treatment schedules are summarized in Table

TABLE 1—*The effect of heat treatment parameters on the temper embrittlement susceptibility of 2.25Cr-1Mo steels embrittled by step cooling.*

Identification	Section Size, cm	Heat Treatment[a]	Tensile Strength, MN/m²	Yield Strength, MN/m²	Fracture Appearance Transition Temperature, °C			Reference	Transformation Product[b]
					Nonembrittled	Embrittled	Shift		
B6730	2.5	FC&T	470	294	24	32	8	3	ferrite + bainite
B6730	2.5	Q&T	582	439	−73	−62	11	3	bainite
			1076	969	−32	2	34		
A2766		Q&T	600	472	−37	−7	44	3	bainite
			917	807	110	116	6		
WA (ES weld)	15	Q&T	649	518	−37	−12	25	4	bainite + ferrite
			769	642	−1	21	20		
			922	797	99	121	22		
WB (SMAW)	15	SR	614	486	−18	24	42	4	bainite + ferrite
			711	597	26	21	47		
			852	759	29	29	0		
BB	15	Q&T	714	607	−57	−46	11	4	bainite + ferrite
			719	614	−62	−40	22		
			909	806	32	57	25		

[a] FC&T, Q&T, and SR denote furnace cooled and tempered, quenched and tempered, and stress relieved conditions, respectively.

[b] Not reported in the reference, but estimated based on the transformation curves.

1 [3]. The quenched and tempered material, containing a predominantly bainitic structure, has a much higher strength and toughness compared to the normalized and tempered material. The shifts in FATT (ΔFATT) due to subsequent embrittlement are very small and of the same magnitude for the quenched and tempered and the normalized and tempered materials. The effect of tensile strengths on temper embrittlement are conflicting. The ΔFATT is found to increase or decrease with tensile strengths for different heats.

The effect of varying the grain size was also evaluated by Swift and Gulya by varying the austenitizing temperature. The grain size was varied widely over a range of ASTM −0.4 to +7.5. The ΔFATT values ranged from 5 to 42°C, the maximum value being obtained at an intermediate grain size. The range of grain sizes encountered in commercial practice is expected to be much more narrow than that covered by the previous study. For all practical purposes, therefore, the effect of grain size variations on temper embrittlement susceptibility of these steels can be concluded to be negligible.

Results of Emmanuel, Leyda, and Rozic on two weld metals (WA and WB) and on a base plate (BB) of 2.25Cr-1Mo steel shows no systematic and appreciable effect of tensile strength on temper embrittlement susceptibility, as may be seen from Table 1 [4].

Temper embrittlement studies by Kerr showed that when 2.25Cr-1Mo steel plates were either quenched or tempered to above 840 MN/m^2 or normalized and tempered to below 600 MN/m^2 tensile strength, susceptibility to temper embrittlement was negligible [5]. The maximum susceptibility was encountered in plates quenched and tempered to tensile strengths in the intermediate range of 600 to 700 MN/m^2.

Emmer, Clauser, and Low have reported that for both quenched and tempered and normalized and tempered section plates, the susceptibility to temper embrittlement is greater compared to annealed plates [6]. For the susceptible steels, the FATT in the nonembrittled condition increased with increasing strength but the ΔFATT decreased with increasing strength in the tensile strength range of 485 to 835 MN/m^2.

Clearcut comparisons between different transformation products tempered to the same strength level are unavailable. The range of microstructures investigated is also limited and consists mostly of bainite-ferrite aggregates, see Table 1. The limited amount of published data indicate a trend of slightly increasing temper embrittlement susceptibility, with products of faster cooling rates from austenite. Variations of ΔFATT with variations in tensile strength are unsystematic and do not suggest any broad correlation between the two parameters. In general, the ΔFATT values reported are small either due to the inadequacy of the embrittling procedures used or due to the inherently lower susceptibility of the steel to embrittle. In either case, the spread in ΔFATT due to structural variations is also small, making it difficult to distinguish between real structural effects and apparent effects due to scatter in the test data.

Cr-Mo-V Steels

The class of steels containing 1 to 3Cr, 0.25 to 1.5Mo, and 0.15 to 0.5V is often used as rotors and disks in turbines and in other applications where high strengths are required for elevated temperature use and welding is not called for. In general, temper embrittlement has not been of major concern in this class of steels. In recent studies by Spink, two Cr-Mo-V disk steels tested were not found to be responsive to temper embrittling treatments. [*7*].

The hardenability of the Cr-Mo-V steels is such that a spectrum of transformation products all the way from martensite to the one end to pearlite at the other end can be produced within a practical range of cooling rates. Such is not the case for 2.25Cr-1Mo steels, where the structures contain only bainite-ferrite aggregates of varying ferrite content, or for Ni-Cr-Mo-V steels, where its extremely high hardenability makes it difficult to produce ferrite-pearlite structures. For this reason, the Cr-Mo-V steels have considerable nonuniformity in structure and properties in heavy section components.

The effect of transformation product and strength level on the temper embrittlement susceptibility of a Cr-Mo-V steel doped with phosphorous and tin has been systematically studied by Viswanathan and Joshi [*8*]. Martensite, bainite, and ferrite-pearlite structures were produced by varying the cooling rate and were then tempered to predetermined tensile strength levels followed by a step-cooling embrittling treatment.

Variations of FATT in the nonembrittled and embrittled conditions as a function of hardness is shown in Fig. 2. Several interesting features are apparent from the figure. Firstly, for the bainitic steels, FATT_{NE} actually decreases with increasing hardness up to about 23 HRC, reaches a minimum value, then increases sharply with further increase in hardness. It appears that at very low hardness FATT_{NE} of the bainitic steels may approach that of the ferrite-pearlite steel. The martensitic steels exhibit a similar behavior, with a minimum in the curve being reached at about 23 HRC. Values of FATT_{NE} and ΔFATT for the ferrite-pearlite steel fall on the same general curves as for the bainitic steels (extrapolated), indicating that bainite and ferrite-pearlite structures have the same degree of susceptibility to temper embrittlement, when compared at similar hardness levels. Even in the embrittled condition, the martensitic steels have FATT values that are lower than even the nonembrittled FATT values of the bainitic steels.

Variation of the temper embrittlement susceptibility of the various steels, as measured by ΔFATT , with hardness is illustrated in Fig. 3. At low values of hardness, the ΔFATT for bainitic steels approaches that of

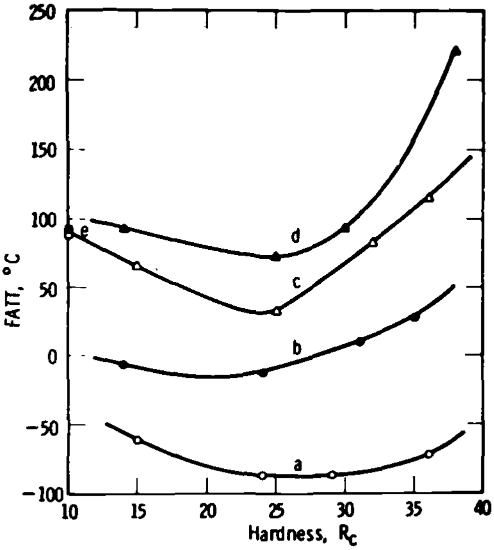

FIG. 2—*Variation of FATT with hardness for Cr-Mo-V steels* [8]. *(a) Martensite, nonembrittled; (b) Martensite, embrittled; (c) bainite, nonembrittled; (d) bainite, embrittled; and (e) ferrite-pearlite, nonembrittled and embrittled.*

the ferrite-pearlite steel, indicating comparable susceptibility for both types of steels, if compared at similar hardness. For all hardness values up to about 40 HRC, martensitic steels have a higher susceptibility for embrittlement. At greater than 40 HRC, however, the ΔFATT for the bainitic and martensitic steels begin to approach each other. In general, the ΔFATT is low for the steels that have a large FATT in the nonembrittled condition.

Intergranular fracture surfaces of the various samples were examined for

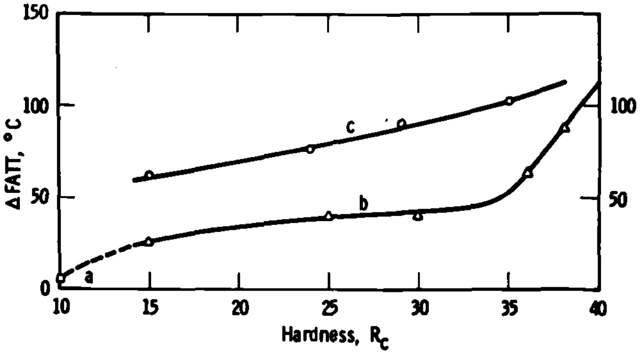

FIG. 3—*Correlation between ΔFATT and hardness for Cr-Mo-V steels* [8]. *(a) Ferrite-pearlite, (b) bainite, and (c) martensite.*

chemical composition using scanning Auger microscopy (SAM). The analysis produced clear evidence for the segregation of phosphorus, tin, and molybdenum to prior austenite grain boundaries. More interestingly, the degree of impurity segregation was found to be a function of the microstructure.

Variation of the grain boundary concentration of phosphorus, tin, and molybdenum as a function of the strength level of the steel is illustrated in Fig. 4. For martensitic steels, the amount of segregate increases with hardness. For bainitic steels, the amount of segregate appears to decrease slightly up to a hardness of about 25 HRC, then increases with further increase in hardness. At a given hardness, the amount of segregate in martensitic steels is much larger compared to bainitic steels, except at very low hardness (15 HRC), where the segregation behavior for the two types of steels become comparable.

For both martensite and bainite, the ΔFATT increases with increasing segregation of the various elements to grain boundaries. In view of microstructural and strength differences between samples and in view of the small amount of data obtained, precise quantitative correlation between the two parameters cannot be expected; nevertheless, the

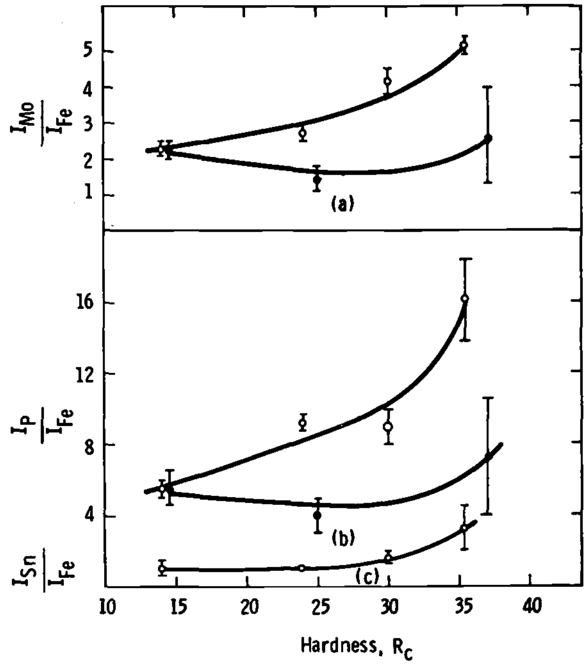

FIG. 4—*Variation of grain boundary concentrations of* (a) *molybdenum,* (b) *phosphorus, and* (c) *tin as a function of hardness for Cr-Mo-V steels* [8]. *The open points correspond to martensite and the dark points correspond to bainite.*

observed difference in segregation between steels are consistent with differences in their susceptibility to temper embrittlement.

Ni-Cr-Mo-V Steels

Steels containing nominally 3.5Ni, 1.75Cr, 0.5Mo, 0.12V, and 0.25C are in widespread use as rotors and disks in large section sizes, where high hardenability and toughness are desired in addition to high-temperature strength.

There is only one reported study wherein the effect of transformation product on temper embrittlement susceptibility of Ni-Cr-Mo-V steels has been investigated. Wada and Doane compared tempered martensite and tempered bainite at different strength levels [*9*]. A summary of their results is shown in Table 2. In all the steels tested, the martensitic structures had lower FATT values in the nonembrittled condition, but on subsequent embrittlement, the ΔFATT was larger compared to bainite. This result is very similar to that reported for Cr-Mo-V steels by Viswanathan and Joshi [*8*].

Results on the effect of tensile strength level on embrittlement are conflicting. In the study by Wada and Doane for tempered martensite, the ΔFATT increased with increasing strength in two out of three heats. In the third heat the trend was reversed. In tempered bainite, ΔFATT decreased with increasing strength in two out of three heats, with the third heat showing an opposite trend. Wessel and Hovan reported increased susceptibility for embrittlement with decreased strength [*10*], while Spink observed that the strength had no effect in his Ni-Cr-Mo-V steels (Table 2). In the statistical study of Newhouse, increase in tensile strength was reported to adversely affect the temper embrittlement behavior [*11*].

In the study of Viswanathan and Sherlock, four commercial Ni-Cr-Mo-V steels of similar composition but tempered to different tensile strength levels were isothermally embrittled for times up to 35 000 h at 315, 400, and 454°C [*12*]. The FATT values for the various conditions are listed in Table 2, and the correlation between ΔFATT and tensile strength is depicted in Fig. 5. The figure shows that the ΔFATT is independent of tensile strength at 315 and 400°C but increases markedly with tensile strength under the exposure condition that produced the most severe embrittlement (that is, 454°C for 35 000 h). Auger electron analysis of the intergranular fracture surfaces showed that in the 400°C and 35 000 h specimens, the degree of impurity segregation to grain boundaries is relatively independent of tensile strength. In the 454°C and 35 000 h specimens, however, the higher strength Steel D had markedly higher segregation of phosphorus, tin, and nickel, as may be seen from Table 3. The Auger results and the ΔFATT results are thus self-consistent, as shown in Fig. 6.

TABLE 2—*The effect of heat treatment parameters on the temper embrittlement susceptibility of Ni-Cr-Mo-V steels.*

Identification	Transformation Product	Ultimate Tensile Strength, MN/m^2	Yield Strength, MN/m^2	Fracture Appearance Transition Temperature, °C			Embrittling Procedure	Reference
				Nonembrittled	Embrittled	Shift		
P679	martensite	1138	. . .	90	290	200	step cool	9
	bainite	1084	. . .	95	210	115		
P682	martensite	1110	. . .	−100	20	120	step cool	9
	bainite	1110	. . .	30	80	50		
	martensite	876	. . .	−110	−5	105		
	bainite	856	. . .	−35	40	75		
P684	martensite	1110	. . .	−105	−40	65	step cool	9
	bainite	1110	. . .	10	60	50		
P680	martensite	985	. . .	−60	155	215	step cool	9
	bainite	985	. . .	30	200	170		
	martensite	1145	. . .	0	>260	>260		
	bainite	1082	. . .	60	190	130		
P683	martensite	985	. . .	−130	−60	70	step cool	9
	bainite	985	. . .	−30	−5	25		
	martensite	1131	. . .	−110	−55	55		
	bainite	1117	. . .	25	60	35		

D	bainite + martensite	1145	1027	−2	29	31	315°C/35 000 h	12
C	bainite + martensite	931	805	−72	−71	1		
B	bainite + martensite	793	680	−86	−78	8		
A	bainite + martensite	787	660	−59	−51	8		
D	bainite + martensite	1145	1027	−2	107	109	400°C/35 000 h	12
C	bainite + martensite	931	805	−72	38	110		
B	bainite + martensite	793	680	−86	52	138		
A	bainite + martensite	787	660	−59	52	111		
D	bainite + martensite	1145	1027	−2	512	514	454°C/35 000 h	12
C	bainite + martensite	931	805	−72	220	292		
B	bainite + martensite	793	680	−86	130	218		
A	bainite + martensite	787	660	−59	171	230		
	bainite + martensite	1161	1036	−25	20	45	slow furnace cool	7
	bainite + martensite	1004	879	−70	−25	45		
	bainite + martensite	882	661	−5	30	35		
	bainite + martensite	1161	1036	−25	25	50		
	bainite + martensite	955	818	−50	−5	45		
	bainite + martensite	825	683	−15	35	50		
9353 × 3	bainite + martensite	1159	471	−21	110	131	427°C/8760 h	10
9353 × 3A	bainite + martensite	1082	902	−85	71	156		
9353 × 3	bainite + martensite	1159	971	−21	−18	3		
9353 × 3A	bainite + martensite	1082	902	−85	−7	92		

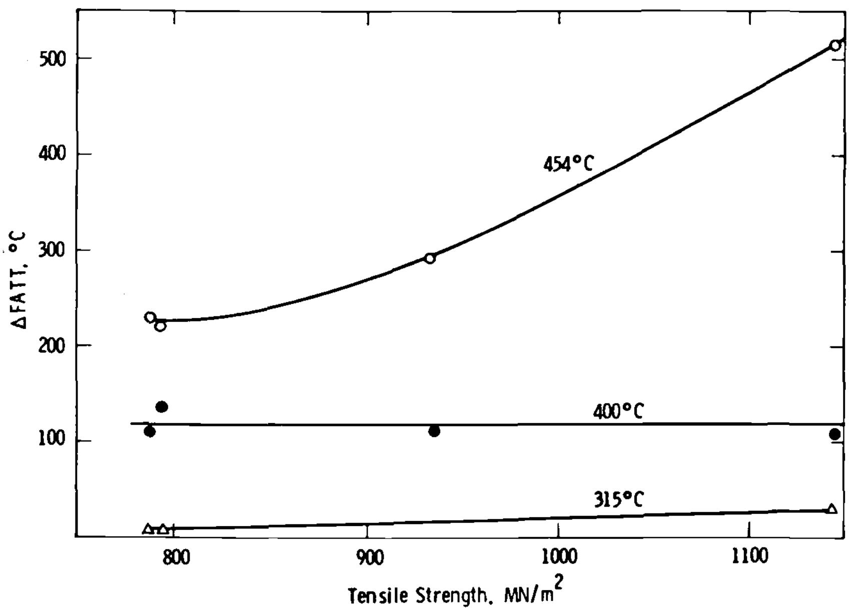

FIG. 5—*Effect of tensile strength on the ΔFATT of Ni-Cr-Mo-V steels following isothermal exposures at 315, 400, and 454°C for 35 000 h* [12].

Discussion

A review of available temper embrittlement data on several commercial grade steels shows that while the effect of transformation product on embrittlement behavior is well defined, the effect of tensile strength and the associated microstructural variation on embrittlement is not clearcut. Decreases as well as increases in ΔFATT have been reported as a function of increasing strength level. The conflicting results reported concerning the effect of strength level on temper embrittlement are in sharp contrast

TABLE 3—*Concentration of segregated elements at the intergranular fracture surfaces of Ni-Cr-Mo-V steel specimens tempered to different yield strength levels and embrittled isothermally at 400 and 454°C for 35 000 h* [12].

Specimen Identification	Yield Strength, MN/m^2	Embrittlement Temperature, °C	$\frac{\text{dN/dE Peak Height for Element Differential}}{\text{dN/dE Peak Height for Iron}}$, %		
			P	Sn	Ni
D	1027	454	14.7	5.0	16.0
A	660	454	9.1	3.3	13.0
D	1027	400	6.0	1.8	9.0
A	660	400	5.1	1.2	6.8

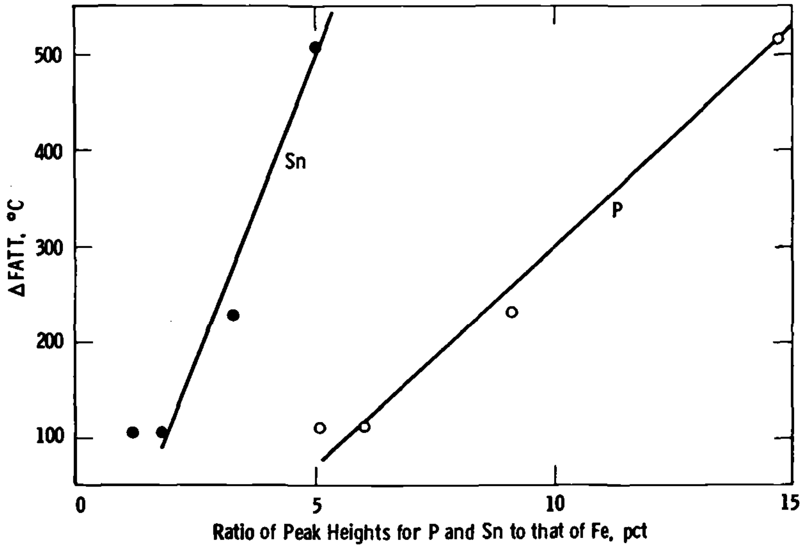

FIG. 6—*Correlation between ΔFATT and grain boundary concentration of phosphorus and tin in Ni-Cr-Mo-V steels* [12].

to the results obtained in several recent studies by McMahon and coworkers showing a systematic increase of ΔFATT with hardness in Ni-Cr steels containing phosphorus, antimony, or tin as the impurity [*13,14*]. A principal shortcoming of most of the studies on commercial steels is that they have used short-time step-cooling procedures to accelerate embrittlement. The resulting values of ΔFATT are often small and the spread in ΔFATT due to microstructural variations is also small, making it difficult to distinguish between real structural effects and apparent effects due to scatter in the data. Secondly, and more importantly, the step-cooling procedure does not give a true indication of the equilibrium long time embrittlement behavior of an alloy. This is because of the fallacy of the assumption implicit in the step-cooling procedure that the segregation phenomena responsible for embrittlement of the alloy can be described by a single set of thermodynamic and kinetic parameters. In actuality, the equilibrium amount of segregation and the rate of approach to equilibrium at a given temperature are different for different impurity species and are also subject to modification by interaction with alloying elements [*13,15*]. Hence, even for a given alloy, the position of the time-temperature embrittlement curves may be altered by microstructure, since the microstructural changes are accompanied by compositional changes in the ferrite matrix [*8,12*]. This means, for example, that for the same standard step-cool, one may be looking at embrittlement by phosphorus at one strength level, and embrittlement by tin at a different strength level. This line of reasoning is supported by the observation that isothermal embrittlement of Ni-Cr-Mo-V steels for 35 000 h at 400 and 454°C caused both tin and phosphorus to segregate to grain boundaries, whereas step cooling procedures on very similar steels failed to produce any detectable segregation of tin, even though the latter steels contained much higher levels of tin in the bulk. Phosphorus, however, was found to be segregated in large amounts following the step-cooling treatment [*1,2,12*].

Since the kinetics of impurity segregation can be modified by microstructure, the kinetics of embrittlement can vary, as demonstrated in Fig. 7. The results depicted in the figure illustrate the point that different conclusions can be reached regarding the effect of strength level, depending on the duration of isothermal exposure at which the steels are compared. A short embrittling treatment would lead to misleading conclusions regarding the effect of strength level on the long time performance of the alloy.

In studies on steels with a high susceptibility to embrittle and in those cases where specimens are heat treated as large pieces, the effect of tensile strength could be masked by inadvertent embrittlement occurring during the tempering treatment (prior to embrittling treatment). The higher strength steels are often tempered at the lower end of the spectrum of tempering temperatures where the probability of embrittlement is higher. Such steels may exhibit large FATT in the as-tempered condition and a concomitantly low value of ΔFATT due to subsequent embrittlement.

It is also conceivable that the apparently haphazard effects of tensile strengths are in fact real and result from opposing effects of tensile strength *per se* and the associated impurity segregation. In McMahon's

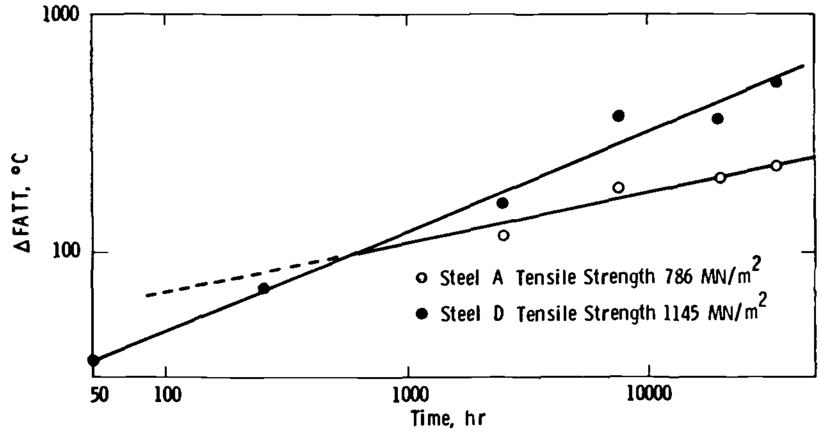

FIG. 7—*The progress of temper embrittlement with time of isothermal exposure at 454°C for Ni-Cr-Mo-V steels* [12]. (a) *Steel D, tensile strength 1145 MN/m²; and* (b) *Steel A, tensile strength 787 MN/m².*

studies, the strength effect was investigated by comparing the ΔFATT's of specimens of varying hardness but of the same grain boundary composition [*13,14*]. While relating hardness to ΔFATT for a given bulk chemistry, the grain boundary composition is also variable and can lead to unexpected results. The overall amount of embrittlement represents the balance between direct effects of strength level and many other indirect and complex segregation effects associated with changes in the strength level.

As stated earlier, microstructure can influence the segregation behavior of impurity elements by modifying either the driving force or kinetics of segregation. The various factors that are deemed important in this connection are the chemistry of the ferrite matrix, grain boundary structure, the nature of other interfaces to which partitioning of the impurities can occur, and the dislocation density.

It is well known that the amount, type, and composition of the carbides in steels vary with heat treatment. This means that the composition of the ferrite matrix would also vary correspondingly, for a given constant bulk composition of the steel. The solubilities as well as the diffusivity of impurity elements in the matrix are dependent on the composition of the matrix and can thus be modified by changes in microstructure [*15,16*].

Recent experiments by Joshi have shown that the segregation of impurities and alloying elements can occur preferentially to some boundaries and not to others, presumably due to differences in boundary structure [*17*]. Ohtani and McMahon have recently reported that the fracture path in temper embrittled bainitic steels follow ferrite-ferrite and ferrite-bainite boundaries, while in martensitic steels, the fracture path follows the prior austenite boundaries [*18*]. The results of Joshi and Ohtani and McMahon indicate that the structure and energetics of the grain boundaries could change with heat treatment, thereby modifying the driving force for segregation of impurities.

For a given tempering treatment and strength level, marked differences still exist in the carbide morphology between bainitic and martensitic steels. For instance, the bainitic structure in the Cr-Mo-V steel contained lenticular carbides in contrast to rounded carbides in the martensitic structure, as illustrated in Fig. 8 [*8*]. With the assumption that the diameter of the lenticular carbides is one half that of the rounded carbides, calculations show that for a given total volume of carbides the carbide-ferrite interface area can be as much as 50 percent higher for the lenticular carbides. This means that a significantly higher proportion of impurities may segregate to the carbide-ferrite interfaces in bainite than in martensite, with a concomitantly reduced segregation to prior austenite grain boundaries.

Keh and Porr reported that cold working a 5140 steel reduced the temper embrittlement presumably by locking the impurities at disloca-

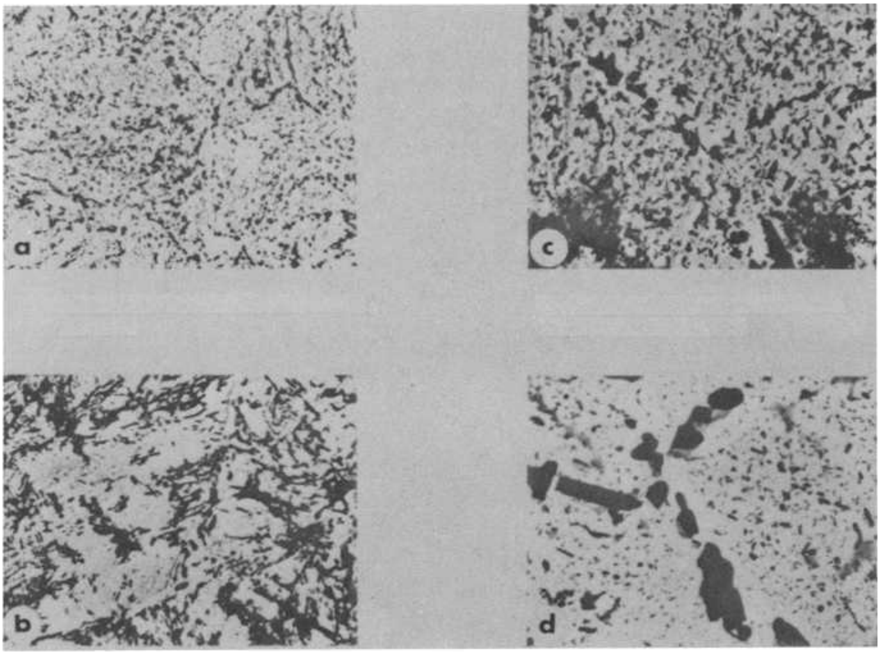

FIG. 8—*A comparative view of martensite and bainite tempered to the same hardness of about 30 HRC, in a Cr-Mo-V steel* [8]. (a) *Martensite tempered at 704°C for 1 h, 29 HRC;* (b) *bainite tempered at 704°C for 1 h, 32 HRC;* (c) *martensite tempered at 704°C for 70 h, 15 HRC; and* (d) *bainite tempered at 704°C for 70 h, 15 HRC.*

tions in the matrix [*19*]. Differences in dislocation densities associated with differences in microstructures may produce similar effects.

In-depth studies of the structure and energetics of the various interfaces in steels, the density and configuration of dislocation structures, and the effect of alloying elements on the solubility and diffusivity of impurities and on the evolution of carbides are needed before the role of microstructure in impurity segregation phenomena can be clarified.

Conclusions

In 2.25Cr-1Mo steels, microstructural variations in the range encountered in commercial practice do not appear to appreciably affect their temper embrittlement susceptibility.

In Cr-Mo-V and Ni-Cr-Mo-V type steels, susceptibility to embrittlement increases in the order: ferrite-pearlite, bainite, and martensite.

Results on the effect of tensile strength on embrittlement appear to be haphazard. Long time, isothermal embrittlement data are needed in order to verify whether the observed effects can be ascribed to microstructure or merely to the inadequacy of the step-cooling embrittlement procedures.

Limited amounts of Auger data available show that the transformation product and tensile strength can affect embrittlement, at least in part, by modifying the grain boundary segregation of impurities.

In general, those microstructures that lead to an initially large FATT, result in small shifts in FATT, upon subsequent embrittlement.

References

[1] Viswanathan, R. and Hudak, S. J., *Metallurgical Transactions A*, Vol. 8A, 1977, pp. 1633–1637.

[2] Viswanathan, R. and Hudak, S. J., *Effect of Hydrogen on Behavior of Materials*, A. W. Thompson, and I. M. Bernstein, Eds., The Metallurgical Society, American Institute of Mining, Metallurgical, and Petroleum Engineers, 1975, pp. 262–272.

[3] Swift, R. W. and Gulya, J. A., *Welding Research*, Supplement, Feb. 1973, pp. 575–675.

[4] Emmanuel, G. N., Leyda, W. E., and Rozic, E. J., *2 ¼Chrome 1 Molybdenum Steels in Pressure Vessels and Piping*, A O. Schaefer, Ed., American Society of Mechanical Engineers, 1971, pp. 78-122.

[5] Kerr, J., "Temper Embrittlement of Low Alloy Reactor Steels," Technical Report W. O. 8025.43, Standard Oil of California, 1969.

[6] Emmer, L. G., Clauser, C. D., and Low, J. R., Jr., "Critical Review of Embrittlement in 2¼ Cr-1 Mo Steel," Welding Research Council Bulletin 183, New York, May 1973.

[7] Spink, G. M., *Metallurgical Transactions A*, Vol. 8A, 1977, pp. 135–143.

[8] Viswanathan, R. and Joshi, A., *Metallurgical Transactions A*, Vol. 6A, 1975, pp. 2289–2297.

[9] Wada, T. and Doane, D. V., *Metallurgical Transactions A*, Vol. 5, 1974, pp. 231–239.

[10] Wessel, E. T. and Hovan, R. R., "Effect of Long-Time Exposures at 400 to 1000°F on the Strength and Toughness of a Ni-Cr-Mo-V High Strength, Weldable Steel," Westinghouse Scientific Paper 66-1B4-BTLFR-P1, Pittsburgh, 1966.

[11] Newhouse, D. L. and Holtz, H. G., *Temper Embrittlement in Steel, ASTM STP 407*, American Society for Testing and Materials, Phila., 1968, pp. 106–126.

[12] Viswanathan, R. and Sherlock, T. P., *Metallurgical Transactions*, Vol. 3, 1972, pp. 459–468.

[13] Mulford, R. A., McMahon, C. J., Pope, D. P., and Feng, H. C., *Metallurgical Transactions A*, Vol. 7A, 1976, pp. 1183–1194.

[14] Mulford, R. A., McMahon, Jr., C. J., Pope, D. P., and Feng, H. C., *Metallurgical Transactions A*, Vol. 7A, 1976, pp. 1269–1274.

[15] Gruzin, P. L. and Mural, V. V., *Fiz. Metal. Metalloved*, Vol. 17, No. 3, 1964, pp. 384–389.

[16] Nageswara Rao, M., McMahon, C. J., and Herman, H., *Metallurgical Transactions*, Vol. 5, 1974, pp. 1061–1068.

[17] Joshi, A., *Scripta Metallurgica*, Vol. 9, No. 3, 1975, p. 251.

[18] Ohtani, H. and McMahon, C. J., Jr., *Acta Metallurgica*, Vol. 23, 1974, p. 377.

[19] Keh, A. S. and Porr, W. C., *Transactions*, American Society of Metallurgists, Vol. 52, 1960, p. 81.

R. P. Smith[1] *and R. A. Swift*[1]

Effects of Composition and Gage on the Microstructure of A533-B Steels

---

REFERENCE: Smith, R. P. and Swift, R. A., "**Effects of Composition and Gage on the Microstructure of A533-B Steels,**" *MiCon 78: Optimization of Processing, Properties, and Service Performance Through Microstructural Control, ASTM STP 672,* Halle Abrams, G. N. Maniar, D. A. Nail, and H. D. Solomon, Eds., American Society for Testing and Materials, 1979, pp. 186–206.

ABSTRACT: The effects of composition and gage on the microstructure of quenched and tempered A533-B steel were studied. The tests were performed on experimental heats of varying carbon contents. To fully assess the effects of minor variations in composition, the carbon equivalent was calculated and used in the data analysis. Controlled cooling was used to approximate gage effects, and the makeup of microstructure was studied by lineal analysis. Equations were generated from the experimental data to predict the microstructure as a function of carbon equivalent and cooling rate. These predictions are verified by comparing them with the microstructures of commercial heats.

KEY WORDS: steels, microstructure, carbon equivalent, cooling rate, lineal analysis, alloys, gage

One of the major problems facing the producers of heavy-gage low-alloy steel plates is the ability to effectively control heat treatment conditions so as to obtain the desired mechanical properties in a variety of thicknesses and compositions. This problem is usually not met head-on but is circumvented by developing standard practices to cover the *normal* situation. The ideal situation would be to tailor the heat treating conditions to the composition and gage so as to obtain the desired set of properties.

The mechanical properties of a low-alloy steel are determined by the microstructure and tempering parameters. The microstructure is controlled by two factors: hardenability and post austenitizing cooling rate. Generally, the producer has more control over hardenability than cooling rate. Cooling rate is primarily a function of gage although the producer can exercise some control by furnace cooling, air cooling, or quenching. Hardenability is a function of composition. The producer can, therefore,

[1] Quality control engineer and supervisor of Metallurgical Department, respectively, Lukens Steel Company, Coatesville, Pa. 19320.

tailor the composition, within specification limits, to meet the property requirements for a variety of gages of plates.

The hardenability-cooling rate relationship has never been quantified for A533-B steel. There are many intuitive relationships based upon experience but no quantitative data. This problem is partially addressed in the work reported herein. A test program was developed to determine the effects of composition and cooling rate on the microstructure of A533-B steel. These results were then compared to the microstructures of commercially-produced heavy-gage plates.

Materials and Processing

The specimens used throughout this study were obtained from five experimental heats and four commercial heats of A533-B steel. The composition of the experimental heats varied primarily in carbon content, which ranged from a 0.11 to 0.24. The commercial heats were of comparable compositions. Table 1 shows the complete chemical composition of each heat. In addition, the carbon equivalent (CE) is given. This is helpful in incorporating the hardenability effects of all elements.

Table 1 shows that carbon in the experimental heats was the only element that was varied. The CE for the experimental heats ranges from 0.54 to 0.68. The commercial heats have apparent comparable compositions and could be considered similar. The CE, however, shows moderate differences between the heats that affect the hardenability.

To test for the effects of gage on the structure of A533-B steel, a series of specimens (3.1 mm by 51 mm) were control cooled from 890°C to room temperature at rates ranging from 2.9°C/min to 706°C/min. Standard cooling rates for various gage plates have been determined and were used for comparison [*1*].[2] The effects of cooling rate were studied by examining the as-cooled specimens. This allowed for determinations of the relative amounts of bainite and martensite. Tempering tends to obliterate the differences between lower bainite and martensite.

The microstructures of the heavy-gage plates produced from commercial heats were analyzed for relative amounts of ferrite. The nonferrite is called bainite but could be tempered martensite or tempered bainite. These structures were then compared to the experimental data.

Microscopy

An extensive metallographic investigation was conducted by both optical and transmission electron microscopy (TEM) to determine the effects of cooling rate on microstructure. Microscopy of experimental heats was performed on as-cooled (nontempered) specimens to maximize

---

[2] The italic numbers in brackets refer to the list of references appended to this paper.

TABLE 1—*Chemical analysis.*

Heat	C	Mn	P	S	Si	Cu	Ni	Cr	Mo	Al	CE[a]	
Experimental												
B477	0.11	1.35	0.017	0.012	0.28	0.07	0.69	0.13	0.66	0.012	0.54	
B478	0.15	1.35	0.010	0.011	0.28	0.07	0.66	0.13	0.61	0.011	0.57	
B482	0.20	1.40	0.011	0.007	0.26	0.07	0.64	0.12	0.64	0.016	0.63	
B483	0.22	1.41	0.010	0.009	0.25	0.07	0.67	0.12	0.62	0.013	0.65	
B480	0.24	1.44	0.012	0.008	0.28	0.07	0.63	0.12	0.64	0.012	0.68	
Commercial												Gage, mm
A6246	0.19	1.31	0.013	0.004	0.20	0.14	0.64	0.19	0.54	0.028	0.61	152
B1502	0.18	1.30	0.010	0.005	0.22	0.13	0.66	0.15	0.57	0.030	0.59	203
B1717	0.20	1.33	0.011	0.002	0.25	0.15	0.68	0.15	0.59	0.030	0.63	127
C7597	0.19	1.30	0.011	0.003	0.24	0.15	0.67	0.15	0.54	0.034	0.60	216
A533-B	0.25	1.10	0.035	0.040	0.13	. . .	0.37	. . .	0.41	. . .	. . .	. . .
	max	1.55	max	max	0.32	. . .	0.73	. . .	0.64	. . .	. . .	. . .

[a] CE = carbon equivalent $= C + \frac{Mn}{6} + \frac{Cr + Mo}{5} + \frac{Ni + Cu}{15}$.

the differences between the phases. Comparisons are made of both the effects of cooling rate and of composition on the microstructure.

Effects of Cooling Rate on Structure

The effects of cooling rate (and gage) on the microstructure of A533-B steel are shown in Figs. 1 and 2. Heat B482 was selected, since its CE is comparable to that of the commercial heats used in this study. The micrographs show the structures that result from a rapid quench (611°C/min), approximate quench rate at the quarterline of a 25-mm plate (114°C/min), and quench rate at the quarterline of a 305-mm plate (3°C/min).

To differentiate between bainite and martensite in the as-quenched structures, microhardness readings were used. Martensite was found to be grayish, whereas the bainite was blackish. Scatter in microhardness readings was large and could not be used to assess cooling rate effects. It was effective only in phase identification within each sample.

Figure 1 shows the gross changes in microstructure as a function of cooling rates. When rapidly quenched, the structure is primarily lower bainite and martensite. There is very little proeutectoid ferrite (Fig. 1*a*). Decreasing the cooling rate to 114°C/min results in a more familiar microstructure (Fig. 1*b*). These phases are present and can be readily identified.

Further reduction in the cooling rate to 3°C/min (Fig. 1*c*) results in a structure that is predominately proeutectoid ferrite and bainite although some martensite is present.

The TEM micrographs (Fig. 2) show a clear delineation between martensite and bainite. Martensite has a mossy or mottled structure. This type of structure has been associated with the formation of precipitate nuclei that are not yet large enough to be extracted during replication [*2,3*]. The bainite has an acicular structure similar to martensite, except the carbides are visible and there is no crossing of the individual needles. Tempering obliterates these differences.

The optical micrographs in Fig. 1 show the gross effects of cooling rate and gage on the structure. The TEM micrographs in Fig. 2 show the effects of cooling rate and on the gage structure of bainite and martensite. The bainite coarsens with decreasing cooling rate because there is more time for precipitation of carbides. When the steel cools rapidly through the bainite transformation temperature range, there is incomplete transformation to bainite. Consequently, martensitic transformation occurs. The transformation from austenite to martensite is very rapid since it is a shear mechanism. This gives high internal elastic strains. If the cooling rate is rapid, there is little or no autotempering. Upon etching, the chemical attack is vigorous with the result being an apparently coarse

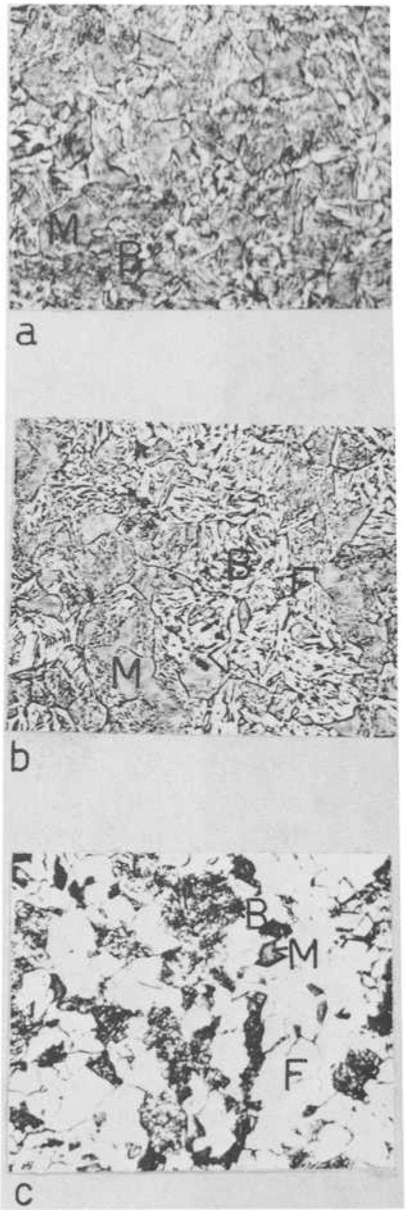

FIG. 1—*Optical micrographs of Heat 482 (CE=0.63), nital-picral etch (original magnification ×500). F is ferrite, B is bainite, and M is martensite. Cooling rates are:* (a) *611°C/min,* (b) *114°C/min, and* (c) *3°C/min.*

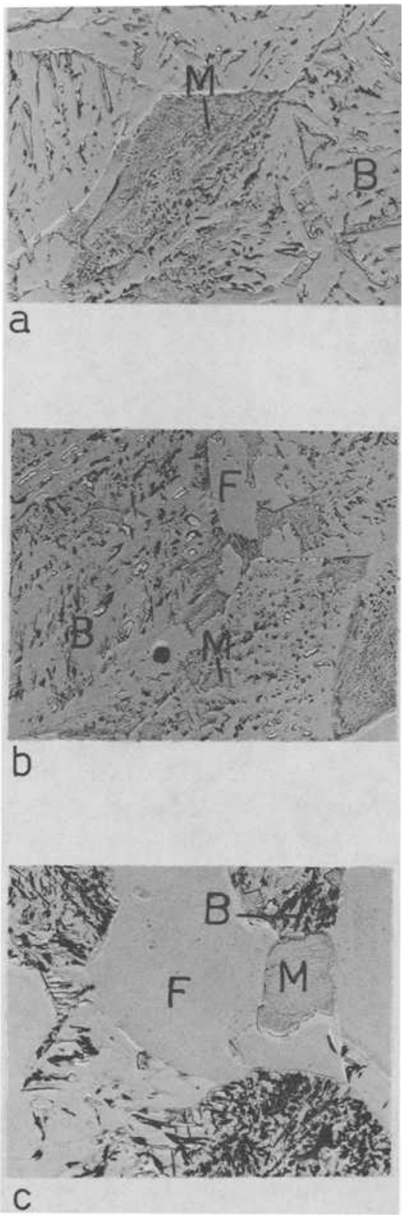

FIG. 2—*Transmission electron micrographs of Heat 482 (CE=0.63), nital-picral etch, two-stage plastic replica, gold-palladium shadowed, (original magnification ×3400). F is ferrite, B is bainite, and M is martensite. Cooling rates are:* (a) *611°C/min,* (b) *114°C/min, and* (c) *3°C/min.*

martensite. This appearance is only an artifact and does not reflect the actual structure. A slower cooling rate will allow for some strain relaxation during cooling. The observed microstructure of material cooled in this fashion is more representative of the true microstructure. Comparing Figs. 2*a* and *c* shows these effects.

Effects of Composition on Microstructure

As stated earlier, composition is a critical factor in determining structure. Figure 3 shows microstructures from samples cooled to simulate the quarterline of a water-quenched 25-mm plate. These demonstrate the effect that CE has on hardenability: the fraction of proeutectoid ferrite decreases and the fraction of martensite increases with increasing CE.

The TEM micrographs in Fig. 4 show the effect of CE on the fine structure of both martensite and bainite. The martensite appears to be a finer structure at low CE than at high CE, whereas the bainite appears to be coarser at low CE than at high CE. Figure 4*a* contains no bainite, but the coarsening of bainite carbides with decreasing CE is evident in Figs. 4*b* through *e*.

Structures in Commercial Heats

Micrographs of the structures at the quarterline of quenched and tempered commercial heats are shown in Figs. 5 and 6. The effect of gage can be seen in the optical micrographs in Fig. 5. These structures are different from those in Figs. 1 through 4 because the steels were tempered at 670°C. Tempering causes carbide precipitation that obliterates distinctions between lower bainite and martensite. Because of this, only the relative amounts of proeutectoid ferrite and transformation product can be determined. The trends with these plates are the same, however, as those noted previously, that is, the amount of proeutectoid ferrite increases with increasing gage (and decreasing cooling rate.)

The effects of gage on the fine structure of the transformation product are shown in the TEM micrographs in Fig. 6. This product is presumably bainite. As stated previously, slow cooling rates coarsen the bainite. Carbides that formed upon transformation agglomerate and a fine acicular molybdenum carbide (Mo_2C) precipitates from the saturated ferrite matrix when the steel is tempered. Also, heavier gage plates are tempered for longer times since all tempering cycles are gage dependent, that is, time at temperature increases with increasing gage. In Fig. 6*a*, there are many fine precipitates in the matrix. This plate was tempered for 2-1/2 h. The combination of a slower cooling rate and longer tempering time (4-1/4 h.) results in the microstructure shown in Fig. 6*d*. This plate has proeutectoid ferrite that is relatively free of precipitates and bainite with a few precipitates that are fairly coarse.

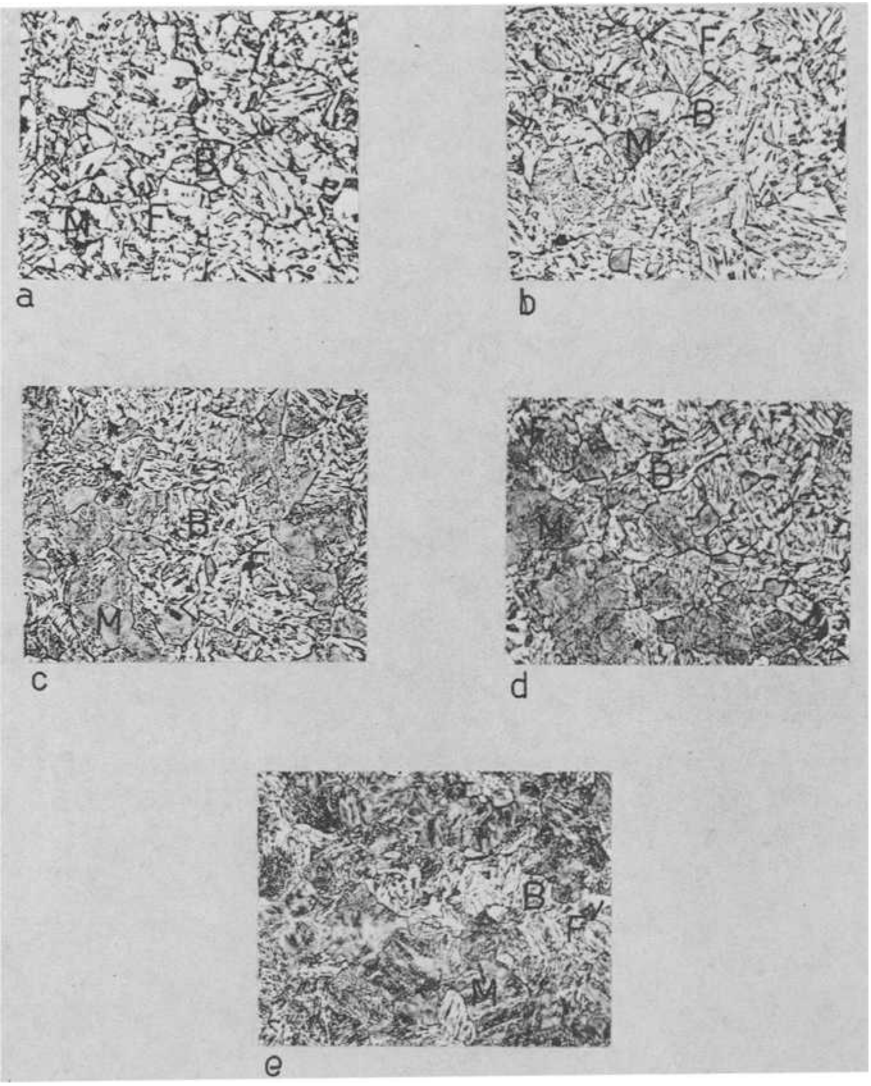

FIG. 3—*Optical micrographs of experimental heats cooled at a nominal rate of 110°C/min, nital-picral etch, (original magnification ×500). F is ferrite, B is bainite, M is martensite. Cooling rates and carbon equivalents are:* (a) *113°C/min, CE=0.54;* (b) *111°C/min, CE=0.57;* (c) *114°C/min, CE=0.63;* (d) *107°C/min, CE=0.65;* (e) *117°C/min, CE=0.68.*

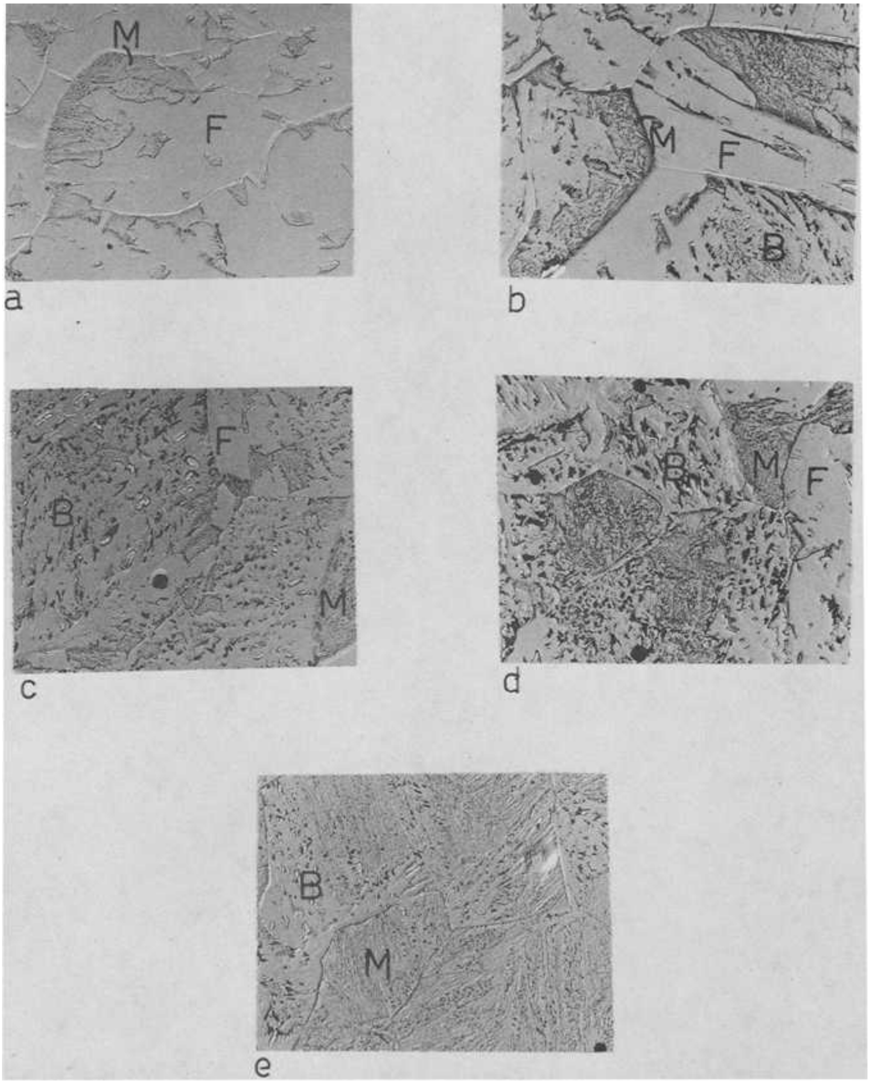

FIG. 4—*Transmission electron micrographs of experimental heats cooled at a nominal rate of 110°C/min, nital-picral etch, two-stage plastic replica, gold-palladium shadowed (original magnification ×3400). F is ferrite, B is bainite, and M is martensite. Cooling rates and carbon equivalents are:* (a) *113°C/min, CE=0.54;* (b) *111°C/min, CE=0.57;* (c) *114°C/min, CE=0.63;* (d) *107°C/min, CE=0.65;* (e) *117°C/min, CE=0.68.*

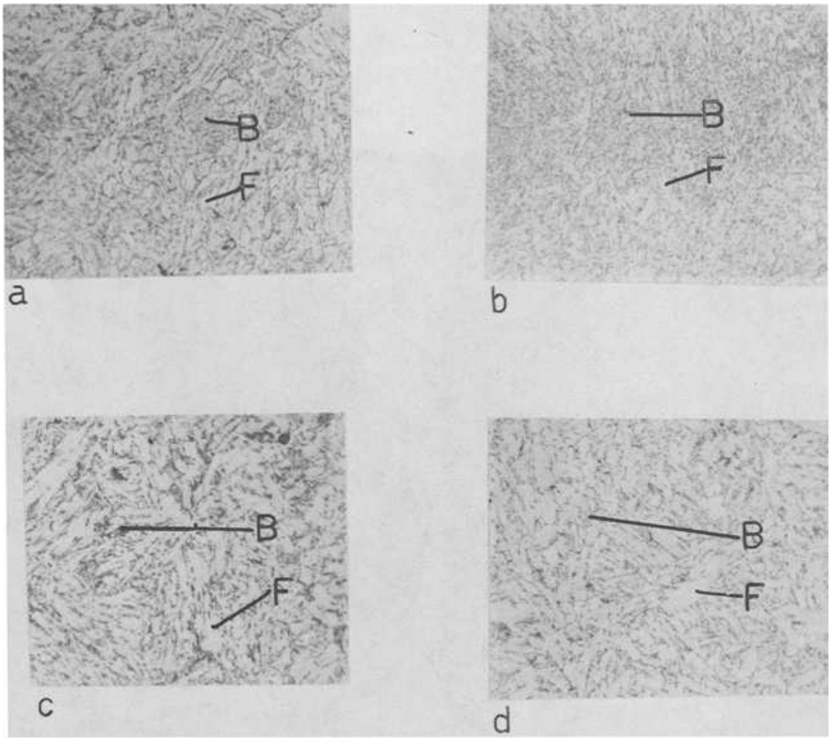

FIG. 5—*Optical micrographs of commercial heats, nital-picral etch (original magnification ×500). F is ferrite and B is tempered transformation product (bainite and martensite).* (a) *127 mm, CE=0.63, cooled at 29°C/min, 21 percent ferrite;* (b) *152 mm, CE=0.61, cooled at 18.9°C/min, 39 percent ferrite;* (c) *203 mm, CE=0.59, cooled at 11.8°C/min, 37 percent ferrite;* (d) *216 mm, CE=0.60, cooled at 7.9°C/min, 40 percent ferrite.*

At higher magnifications, this interaction of cooling rate and tempering time is more evident. Figure 7 compares the fine structure of the transformation products in the 127-mm and 216-mm plates. Mo_2C in the 216-mm plate (Fig. 7*b*) is more rod shaped and coarser than the acicular Mo_2C in the 127-mm plate (Fig. 7*a*). The longer tempering time has caused these precipitates to grow in the radial direction without much longitudinal growth. As a result, they become more rod shaped and less acicular. With continued tempering, they will agglomerate and become more circular in cross section.

Quantitative Metallography

A true determination of the effects of gage on structure can be made only by quantitatively identifying the phases present. In this study, lineal analysis was used. The procedure is straight forward: determine the linear

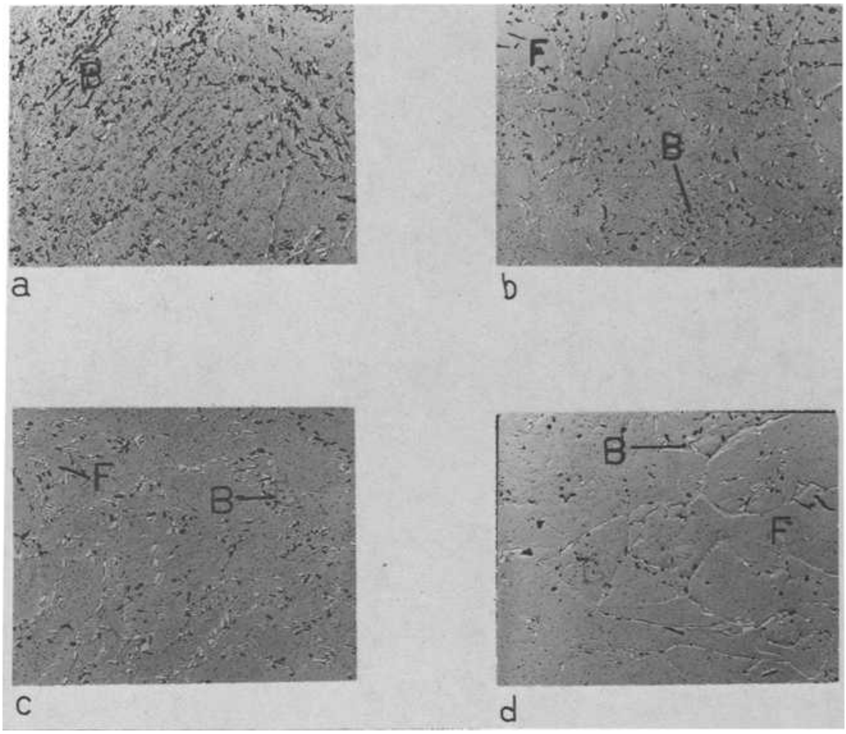

FIG. 6—*Transmission electron micrographs of commercial heats, nital-picral etch (original magnification ×3400), two-stage plastic replica, gold-palladium shadowed. F is ferrite and B is tempered transformation product (bainite and martensite).* (a) *127 mm, CE=0.63, cooled at 29°C/min, 21 percent ferrite;* (b) *152 mm, CE=0.61, cooled at 18.9°C/min, 39 percent ferrite;* (c) *203 mm, CE=0.59, cooled at 11.8°C/min, 37 percent ferrite;* (d) *216 mm, CE=0.60, cooled at 7.9°C/min, 40 percent ferrite.*

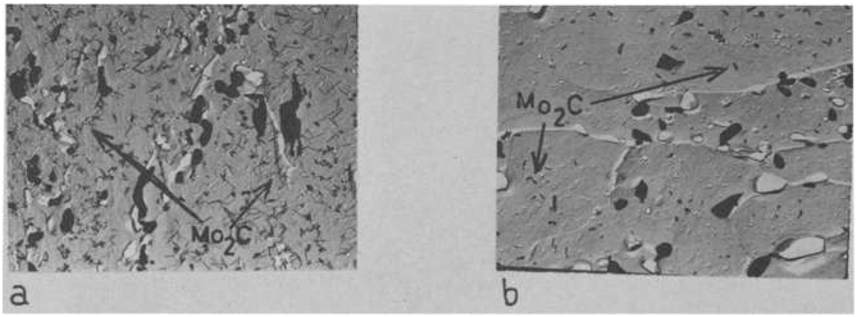

FIG. 7—*Transmission electron micrographs of commercial heats, nital-picral etch (original magnification ×10,500), two-stage plastic replica, gold-palladium shadowed.* (a) *127 mm, CE=0.63, cooled at 29°C/min, 21 percent ferrite;* (b) *152 mm, CE=0.61, cooled at 18.9°C/min, 39 percent ferrite.*

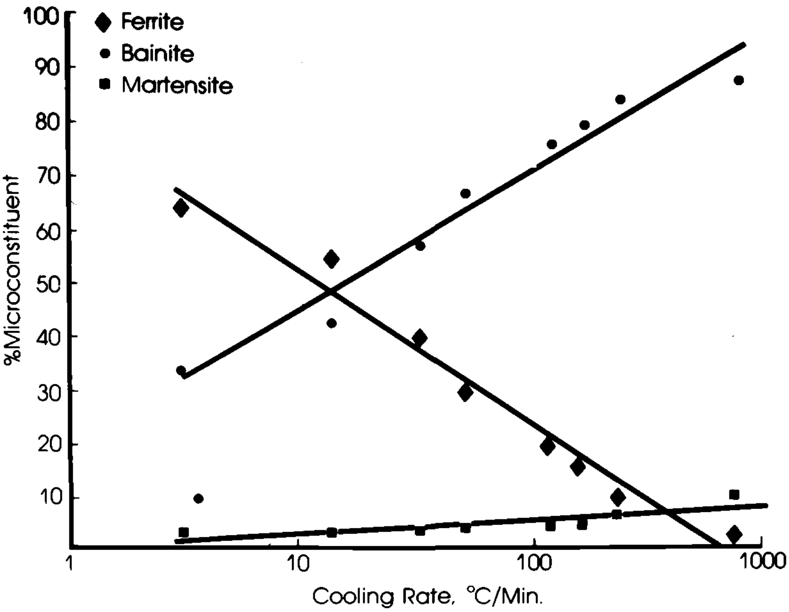

FIG. 8—*Graph of percentage of microconstituents as a function of the cooling rate for Heat B477 (CE=0.54).*

fraction of random lines that lie within each phase. This procedure gives a good measure of the relative proportions of each phase. The data for the experimental heats are listed in Tables 2 through 6 and plotted in Figs. 8 through 12. Included in Tables 2 through 6 are the equations of the curves in Figs. 8 through 12.

Figure 8 shows that the fraction of microconstituents in Heat B477 (CE 0.54) is linear with the log of the cooling rate except at very high

TABLE 2—*Quantitative metallography data for Heat B477 (CE = 0.54).*

Cooling Rate, °C/min	Martensite,[a] %	Bainite,[b] %	Ferrite,[c] %
706	10.1	87.5	2.4
222	6.5	84.0	9.4
156	4.8	79.2	16.0
113	4.7	75.8	19.5
49	4.0	66.6	29.4
31	3.6	57.1	39.3
13	3.4	42.4	54.3
3	3.3	33.1	63.7

[a] %M = 0.539 + 2.55 (log cooling rate).
[b] %B = 19.5 + 26.0 (log cooling rate).
[c] %F = 79.9 − 28.5 (log cooling rate).

TABLE 3—*Quantitative metallography data for Heat B478 (CE = 0.57).*

Cooling Rate, °C/min	Martensite,[a] %	Bainite,[b] %	Ferrite,[c] %
639	12.1	85.9	2.0
228	10.7	81.9	7.5
176	8.2	77.7	14.1
111	6.7	75.2	18.1
54	10.2	78.5	11.3
38	6.3	72.5	21.2
11	3.9	62.3	33.8
3	2.8	42.6	54.6

[a] $\frac{1}{\%\text{M}} = 0.0455 + \frac{0.160}{(\text{log cooling rate})}$.

[b] $\frac{1}{\%\text{B}} = 0.00953 + \frac{0.00666}{(\text{log cooling rate})}$.

[c] $\%\text{F} = 33.7 - 28.7 \ln (\text{log cooling rate})$.

cooling rates. Increasing CE to 0.57 (Fig. 9) results in deviations from log linearity for all constituents. Although martensite appears to remain linear, the equation for the percent of martensite is of the same form as that for the percent of bainite.

The curves for the three heats with the highest CE (Figs. 10 through 12) are similar. The most notable characteristic is the maximum in bainite. This results because of the rapid increase in the fraction of martensite at higher cooling rates that occur at the expense of the bainite transformations. As

TABLE 4—*Quantitative metallography for Heat B482 (CE = 0.63).*

Cooling Rate, °C/min	Martensite,[a] %	Bainite,[b] %	Ferrite,[c] %
611	23.7	74.8	1.5
222	18.2	80.2	1.6
169	15.2	80.9	3.9
114	13.6	80.8	5.7
59	11.1	81.6	7.3
43	4.2	86.5	9.3
15	3.3	78.5	18.2
3	1.0	48.5	50.5

[a] $\frac{1}{\%\text{M}} = -0.178 + \frac{0.563}{(\text{log cooling rate})}$.

[b] $\%\text{B} = 24.3 + 62.1 (\text{log cooling rate}) - 16.1 (\text{log cooling rate})^2$.

[c] $\%\text{F} = -8.02 + \frac{25.3}{(\text{log cooling rate})}$.

TABLE 5—*Quantitative metallographic data for Heat B483 (CE = 0.65).*

Cooling Rate, °C/min	Martensite,[a] %	Bainite,[b] %	Ferrite,[c] %
593	32.1	66.7	1.2
207	13.5	85.0	1.5
168	11.6	86.0	2.5
107	11.8	84.6	3.6
56	11.3	83.2	5.5
39	7.0	82.7	10.3
16	3.8	76.5	19.7
3	2.8	27.7	69.5

[a] $\%M = 1.44 \exp (1.03(\log \text{cooling rate})$.

[b] $\%B = -16.1 + 107(\log \text{cooling rate}) - 27.7 (\log \text{cooling rate})^2$.

[c] $$\%F = -15.3 + \frac{35.8}{(\log \text{cooling rate})}.$$

the CE increases, the cooling rate at which the maximum occurs, decreases.

The fraction of ferrite that forms decreases rapidly with increasing cooling rate in all three heats. At cooling rates faster than approximately 30°C/min, the fraction of ferrite is independent of CE for a CE of 0.63 or higher.

The fraction of martensite in heats with CE of 0.63 or higher is linear to 20°C/min. At higher cooling rates, the fraction of martensite increases rapidly with increasing cooling rate. The rate at which it increases appears to increase with increasing CE.

To show the effect of CE on microstructure, curves of percent of microconstituent as a function of CE were calculated from the data in

TABLE 6—*Quantitative metallography data for Heat B480 (CE = 0.68).*

Cooling Rate, °C/min	Martensite,[a] %	Bainite,[b] %	Ferrite,[c] %
273	34.6	64.4	1.0
217	28.8	69.9	1.3
163	23.3	74.8	1.9
117	20.3	77.5	2.3
59	12.7	80.9	6.4
38	8.1	79.5	12.4
15	5.7	75.9	18.4
3	4.5	63.9	31.6

[a] $\%M = 12.7 - 22.1 (\log \text{cooling rate}) + 12.5 (\log \text{cooling rate})^2$.

[b] $\%B = 45.1 + 45.3 (\log \text{cooling rate}) - 15.0 (\log \text{cooling rate})^2$.

[c] $\%F = 43.9 - 26.4 (\log \text{cooling rate}) + 3.44 (\log \text{cooling rate})^2$.

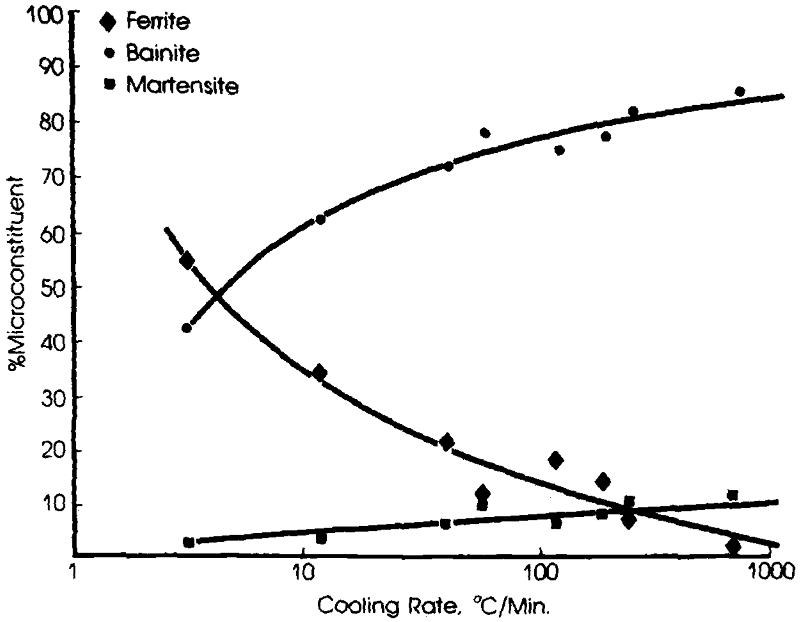

FIG. 9—*Graph of percentage of microconstituents as a function of the cooling rate for Heat B478 (CE=0.57).*

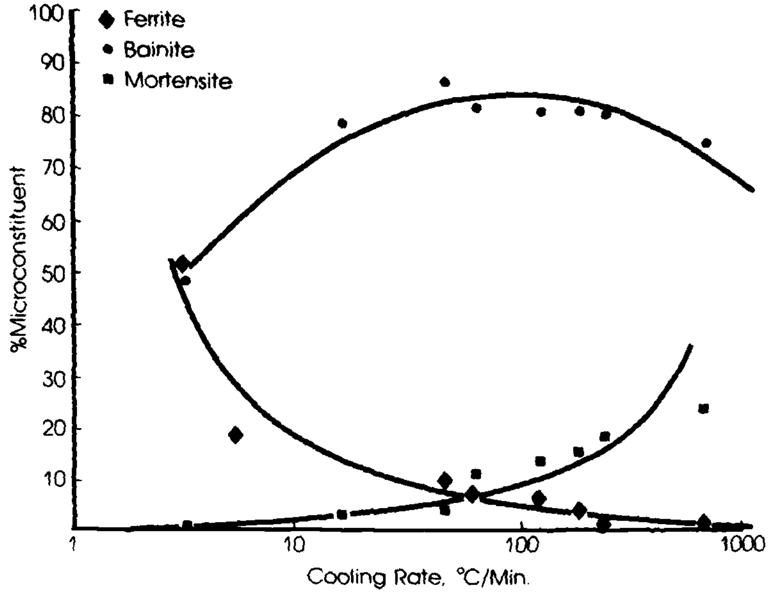

FIG. 10—*Graph of percentage of microconstituents as a function of the cooling rate for Heat B482 (CE=0.63).*

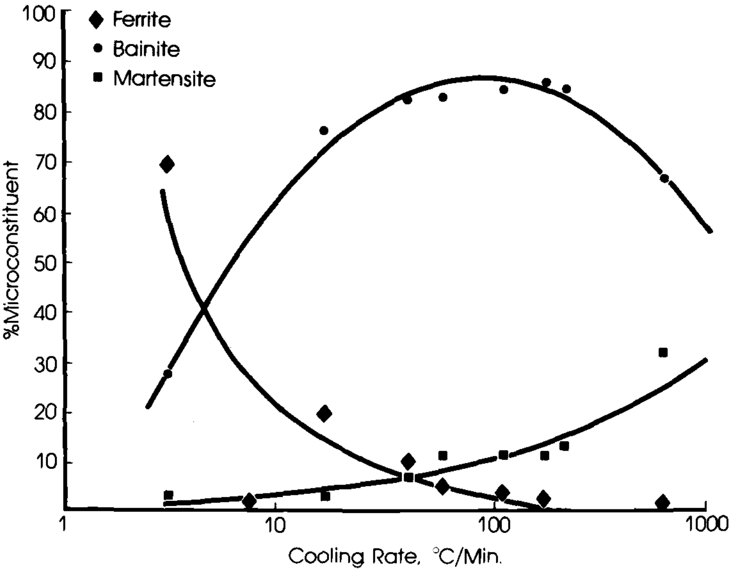

FIG. 11—*Graph of percentage of microconstituents as a function of the cooling rate for Heat B483 (CE=0.65).*

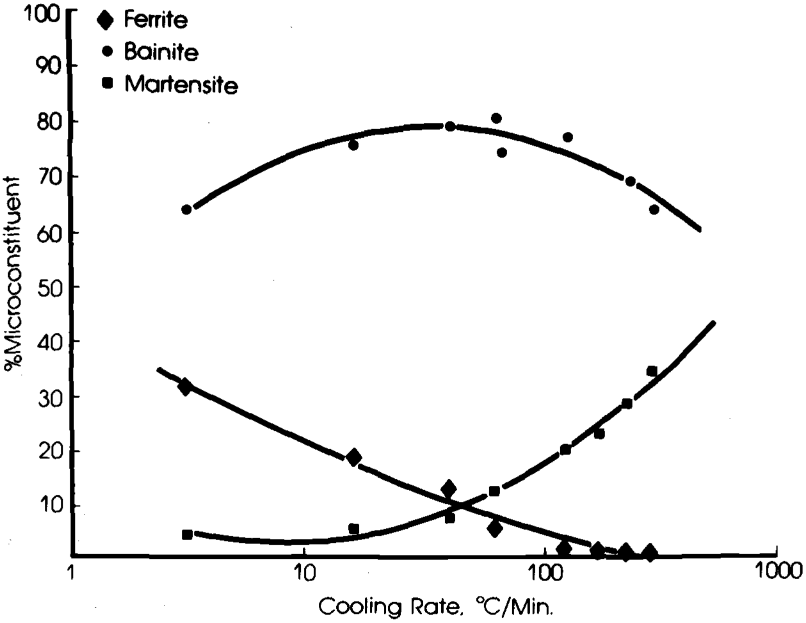

FIG. 12—*Graph of percentage of microconstituents as a function of the cooling rate for Heat B480 (CE=0.68).*

TABLE 7—*Equations for percent microconstituents as a function of carbon equivalent.*

Martensite

$$\frac{1}{\%\text{Martensite}} = \text{A} + \frac{\text{B}}{\text{CE}^{a}}$$

Cooling Rate °C/min	A	B
556	−0.3902	0.2763
278	−0.3933	0.2858
55.6	−0.3155	0.2714
27.8	−0.2815	0.2751

Bainite

$$\%\text{Bainite} = \text{A} + \text{B (CE)} + \text{C (CE)}^2$$

Cooling Rate °C/min	A	B	C
556	37.17	347.6	−459.3
278	50.29	138.4	−143.4
55.6	−477.1	1682	−1255
27.8	−813.2	2772	−2149
5.6	−2005	6998	−5781

Ferrite

$$\%\text{Ferrite} = \text{A} + \text{B(CE)} + \text{C(CE)}^2$$

Cooling Rate °C/min	A	B	C
278	283.6	−859.6	654.6
55.6	727.5	−2178	1642
27.8	1086	−3361	2631
5.6	2217	−7219	5970

[a] $\text{CE} = \text{C} + \frac{\text{Mn}}{6} + \frac{\text{Cr} + \text{Mo}}{5} + \frac{\text{Ni} + \text{Cu}}{15}$.

Tables 2 through 6. The coefficients for these calculated curves are in Table 7. The curves are shown in Figs. 13 through 15.

To develop the coefficients in Table 7, it was first necessary to calculate the fraction of each phase for each heat at prescribed cooling rates using the equations in Tables 2 through 6. The calculated values were then used to generate the coefficients in Table 7. The curves in Figs. 13 through 15 were then drawn using these coefficients.

The martensite (Fig. 13) and ferrite (Fig. 15) fractions follow a regular pattern. There is an increase in the fraction of martensite with increasing CE and with increasing cooling rate. As the cooling rate increases, the rate of change of fraction of ferrite decreases with both increasing cooling rate and CE. As the cooling rate decreases, the rate of change of fraction ferrite with CE also decreases.

Bainite responds in a different manner (Fig. 14). There appears to be a

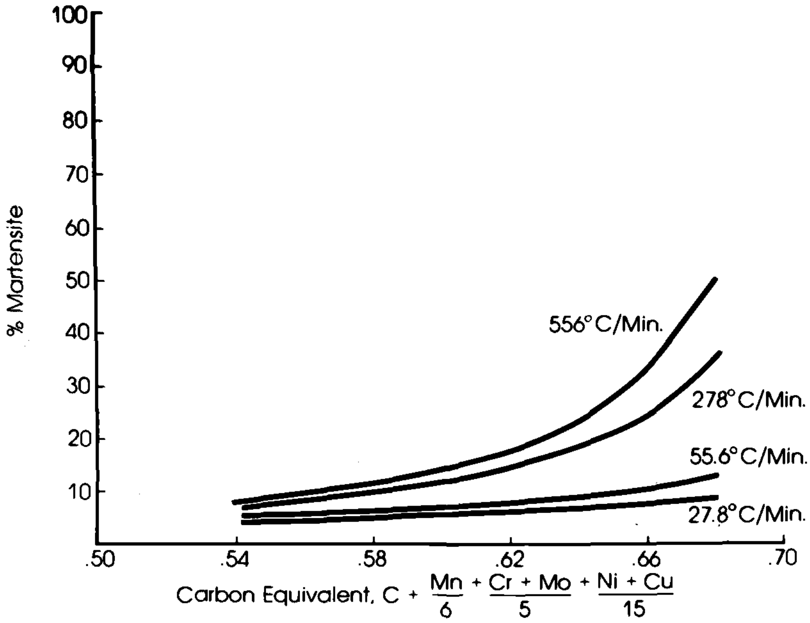

FIG. 13—*Plot of percent martensite as a function of carbon equivalent for various cooling rates.*

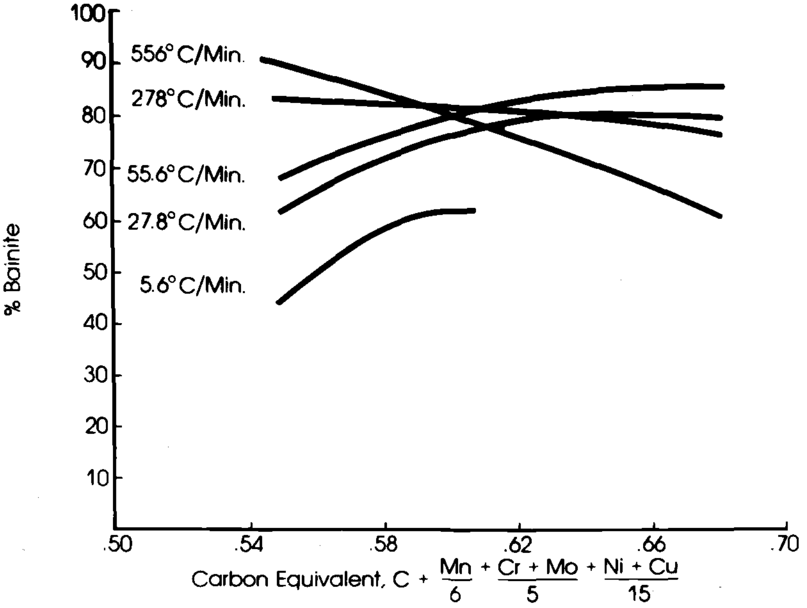

FIG. 14—*Plot of percent bainite as a function of carbon equivalent for various cooling rates.*

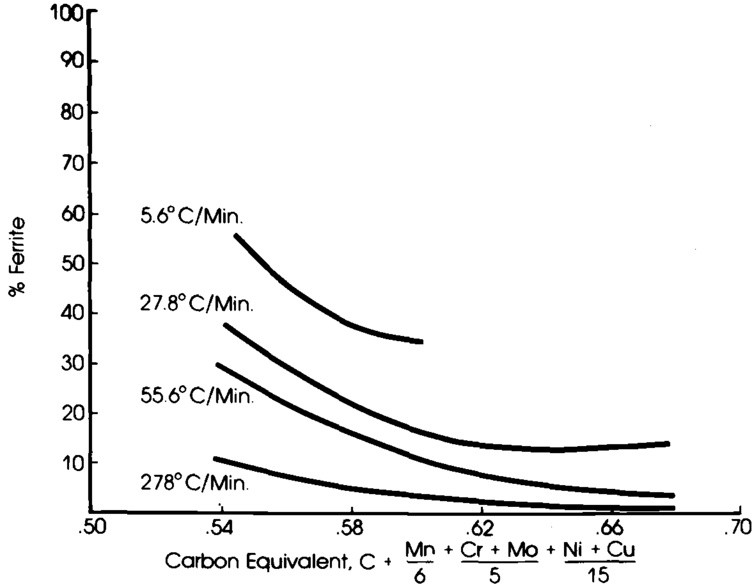

FIG. 15—*Plot of percent ferrite as a function of carbon equivalent for various cooling rates.*

rotation in the curves. At low CE, the bainite fraction increases with increasing cooling rate. At high CE, the fraction of bainite goes through a maximum at a cooling rate of 55.8°C/min. This is explained by the formation of martensite that suppresses the bainite transformation at high cooling rates.

The fraction of bainite and ferrite data for the slowest cooling rate is such that there is excellent fit up to a CE of 0.60. At higher CE, the best fit curves show rapid decreases in both constituents with increasing CE. Since this is not physically possible, and is not substantiated by the data in Tables 2 through 6, the curves in Figs. 14 and 15 are not extended past CE = 0.60.

Correlation with Commercial Heats

The quantitative metallographic data for the four commercial heats are listed in Table 8. These data show the fraction of ferrite and transformation product. The fraction of ferrite does not appear to increase with decreasing cooling rate as would be expected from the previous discussion. This apparent discrepancy is easily examined in terms of the CE, which is a critical factor in determining the microstructure. It is possible to get a high proportion of ferrite after a fairly rapid quench if the CE is

TABLE 8—*Quantitative metallographic data for commercial heats.*

Gage, mm	Heat	CE	Average Cooling Rate, °C/min	Ferrite, %	Calculated	Bainite, %[a]	Calculated
127	B1717	0.63	29	21	13	79	80
152	A6246	0.61	18.9	39	15	61	78
203	B1502	0.59	11.8	37	36	63	61
216	C7597	0.60	7.9	40	35	60	63

[a] Actual structure is a mixture of tempered martensite and lower bainite.

sufficiently low. If a material has a poor hardenability (low CE) martensite or bainite will not readily form upon cooling of the austenite.

To verify the observed microstructures in the commercial heats, the fraction of ferrite and transformation products were calculated from the equations in Table 7 for cooling rates of 27.8°C and 5.6°C/min. The more rapid rate was used for the two light gage plates, and the slower rate was used for the heavier plates.

The data in Table 8 show good correlation between calculated and measured fractions of transformation product. The calculated value represents only bainite where as the measured value is tempered bainite and tempered martensite. The error associated with this is reflected in the fraction of ferrite. At high cooling rates, the discrepancy between calculated and measured values is high. This difference decreases at the lower cooling rates (heavier gage plates.)

The agreement between experimental and commercial heats is relatively good when one considers the many variables associated with such a program as this one. The experimental quench rates are accurately controlled on small samples. The commercial quench rates are statistical averages based upon many plates. There is a lag time between removal from the furnace and immersion in the quench water, and the temperature of the quench water varies depending upon plate size, quenching load on the facility, and the efficiency of cooling the quench water. While all of these factors are tightly controlled and exceed commercial standards, correlating the precise experimental data with data from commercial practices and their inherent variables can be only approximate.

Conclusions

This study has shown that the structure of a low-alloy steel plate can be determined by knowing the composition and gage. The composition is used to calculate the carbon equivalent (CE), which is a measure of the hardenability. The gage is used to determine the cooling rate during quenching. Using both CE and cooling rate, the relative amounts of each constituent phase can be calculated.

It was shown that these data can approximate the structure of commercially-produced plates. The inherent variability of commercial practices, however, precludes the accurate prediction of microstructure.

References

[1] "Heavy Plate Section Cooling Curves" Lukens Steel Company, Coatsville, Pa., 1967.
[2] Swift, R. A., *Welding Research*, supplement, Vol. 50, No. 5, 1971, pp. 195S-200S.
[3] Baker, R. G. and Nutting, J., *Journal*, Iron and Steel Institute, London, Vol. 192, pp. 257–268, 195–199.

D. E. Diesburg[1]

High-Hardenability Carburizing Steels for Rock Bits

REFERENCE: Diesburg, D. E., **High-Hardenability Carburizing Steels for Rock Bits,"** *Micon 78: Optimization of Processing, Properties, and Service Performance Through Microstructural Control, ASTM STP 672,* Halle Abrams, G. N. Maniar, D. A. Nail, and H. D. Solomon, Eds., American Society for Testing and Materials, 1979, pp. 207–229.

ABSTRACT: High stresses experienced in rolling cutter rock bits during the drilling of large-diameter, deep oil wells require steels having extra high levels of hardenability. Nickel-molybdenum steels provide the needed hardenability and are being used successfully in the drilling industry. New EX-grades of steel were evaluated in the carburized condition by means of several laboratory tests and compared to the high-nickel SAE 4800 or SAE 9300 grades. The tests included impact fatigue, high-cycle fatigue, impact fracture stress, and plane-strain fracture toughness. In each test, the excellent performance of EX55 (0.87Mn-0.58Cr-1.85Ni-0.75Mo) was demonstrated.

Several compositional variables of EX55 were evaluated to determine their importance on mechanical properties. The variables included core carbon content as well as alloy modifications of chromium, nickel, and molybdenum. Steels having a core carbon content of 0.14 to 0.17 percent were observed to have more potential for exhibiting high impact fatigue resistance than 0.20 percent carbon steels.

KEY WORDS: steels, carburized steels, high hardenability, mechanical tests, high-cycle fatigue, impact fracture stress, impact fatigue, fracture toughness, microstructure

The rising cost of energy has made it economical to recover hard-to-get oil and gas. Many of todays known reserves require deep drilling using large diameter rock bits. Such drilling is particularly expensive because of the time required to pull long lengths of drill pipe and collars to replace worn or broken rock bits. The longer the life of the rock bits, the less will be the number of required replacements.

The rolling cutter rock bit is a sophisticated piece of equipment and has

---

[1] Staff metallurgist, Ann Arbor Research Laboratory of Climax Molybdenum Company of Michigan, a subsidiary of American Metal Climax, Inc., Ann Arbor, Mich. 48105.

been successful in increasing the efficiency of drilling. There are many critical areas of the rock bit that require different properties, many of which must be provided by the same steel. In most instances, the best combination of properties is obtained by carburizing, quenching, and tempering. The final product must be resistant to both overload fractures as well as high- and low-cycle fatigue fractures. Increasing the diameter of the bits requires properties of the steel that exceed the capability of the commonly used steels for the cutters of smaller diameter rock bits.

Experience has shown that the best resistance to fracture occurs when the steel can be quenched to a high hardness, even at the center of large sections. Steels exhibiting at least HRC 34 at J 20[2] are desired. Until the development of the new experimental EX-steel grades, the most widely used steels in rock-bit applications were high-nickel grades such as SAE 4800 or SAE 9300. However, high-nickel SAE 4800 steels exhibit a decrease in hardness at the J 10 to J 12 location as shown in Fig. 1. SAE 4817 exhibits a maximum hardness of HRC 25 at J 20, and SAE 9310 exhibits a maximum value of HRC 35. Clearly, the SAE 4817 steel will not meet the hardness requirement of the large rock bits, and the SAE 9310 will exhibit the required hardness only with a high-side composition.

A new steel having extra-high hardenability was developed and is being used successfully to meet the stringent hardness requirements for large-diameter rolling-cutter rock bits. The alloy content was adjusted to obtain the most hardenability in the most economical manner. [*1*].[3] The purpose of this investigation was to demonstrate the relative resistance to fracture of high-hardenability rock-bit steels in the carburized condition. The steels were compared in several laboratory tests involving both high-stress and low-stress fatigue loading.

Steels

The primary steels being evaluated were the high-hardenability steels SAE 4817, SAE 4820, SAE 9310, EX55 and EX32. The compositions are given in Table 1. A few low-hardenability steels were included for some comparisons, particularly when evaluating the influence of various alloy additions on fracture properties. All the high-hardenability steels except SAE 9310 were prepared as 57 kg air-induction melted laboratory heats. The laboratory heats were poured as 90 or 135 mm (3½ or 5¼ in.) ingots and forged to 32 mm (1¼ in.) diameter bar. SAE 9310 and a second heat of EX55 were evaluated as commercial heats. The prior austenite grain sizes for all the laboratory heats after quenching into water from 925°C (1700°F) ranged from ASTM No. 9.0 to 9.5 while the grain sizes of the commercial heats were 6.5 and 8.0. The grain sizes were determined by lineal analysis.

---

[2] J 20 refers to the location 20/16 in. from the quenched end of a Jominy bar.

[3] The italic numbers in brackets refer to the list of references appended to this paper.

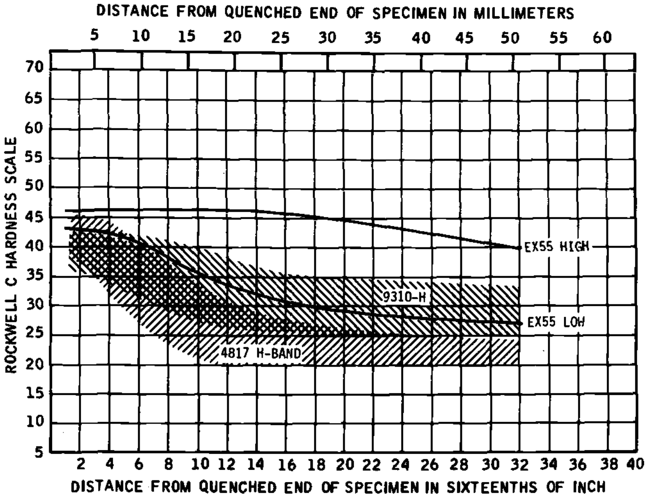

FIG. 1—*Core hardenability of laboratory heats (high- and low-side chemistries) of EX55 compared with the hardenability bands for commercial SAE 4817 and SAE 9310.*

The EX55 steel is a relatively new composition designed to exhibit the extra high hardenability required in large-diameter rock bits. Figure 1 shows that EX55 has much more hardenability than either SAE 4817 or SAE 9310. The balanced alloy content of EX55 was chosen in a manner that attained the most hardenability in the most economical manner, without jeopardizing quality or fracture resistance. Combining at least 1 percent nickel with molybdenum takes advantage of a known synergistic effect on hardenability [2]. Chromium content was kept at 0.5 percent, because above 0.75 percent is believed to cause low fracture resistance in carburized cases of low and medium nickel steels. The originally pro-

TABLE 1—*Composition of high-hardenability steels.*

	Element, weight percent									ASTM Grain Size
Steel[a]	C	Mn	Si	Cr	Ni	Mo	P	S	Al	
EX55(C)	0.17	0.88	0.33	0.50	1.81	0.73	0.010	0.011	ND	6.5
EX55	0.17	0.87	0.28	0.49	1.84	0.74	0.015[b]	0.02[b]	0.08[b]	9.5
SAE 9310(C)	0.13	0.68	0.26	1.23	3.14	0.14	0.012	0.021	ND[c]	8.0
SAE 4817	0.17	0.54	0.33	NA[d]	3.54	0.27	0.015[b]	0.02[b]	0.08[b]	9.5
SAE 4820	0.19	0.60	0.28	NA	3.48	0.27	0.016	0.020	0.075	9.5
EX32	0.19	0.82	0.27	0.53	0.80	0.52	0.017	0.020	0.082	9.0

[a] (C) = commercial heat.
[b] Amount added.
[c] ND = not determined.
[d] NA = none added.

posed composition suggested using 0.75 percent chromium, but the presence of grain boundary carbides after austenitizing at several temperatures of interest forced the chromium level to a maximum of 0.65 percent. The rest of the desired hardenability was obtained by adding manganese and molybdenum. Since manganese is less expensive than molybdenum, the manganese content was raised to a maximum value of about 0.9 percent. At higher amounts, the manganese level is difficult to control and can cause a wide hardenability band. With these levels of manganese, chromium, and nickel, it was necessary to add 0.75 percent molybdenum to achieve the desired hardenability.

For applications where the hardenability of SAE 4820 is adequate, a steel having a lower alloy content than EX55 has been developed. EX32 has a similar hardenability to SAE 4820 (Fig. 2), and is being used successfully in rock bits requiring this hardenability level. EX32 is included in several of the comparisons of fracture properties.

The steels being evaluated were all tested in the carburized condition. The steels were gas carburized in a Leeds and Northrup Homocarb furnace at 925°C (1700°F) to obtain the desired case depth, cooled to 840°C (1550°F) (except where noted), quenched directly into agitated warm oil, and tempered at 170°C (340°F) for 1 h. The surface carbon contents of the case were maintained between 0.7 and 1.0 percent, depending on the alloy content of the steel and the amount of retained austenite desired.

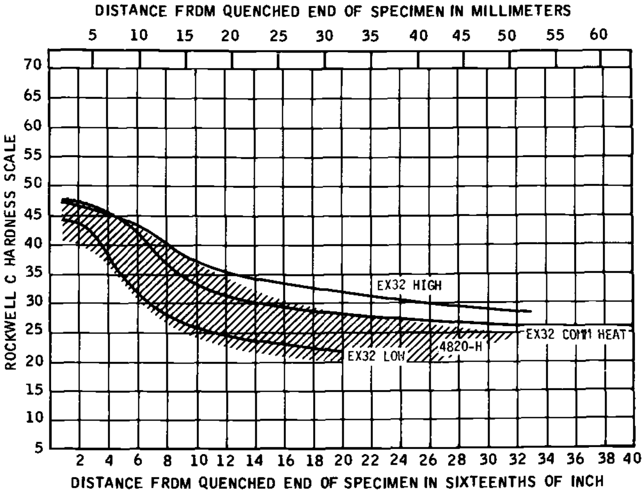

FIG. 2—*Core hardenability of commercial heat compared with 4820H hardenability band and high and low chemistry heats of EX32.*

Laboratory Fracture Studies

A common test for evaluating relative fracture resistance is the Charpy V-notch (CVN) impact test. This test was used to evaluate quenched-and-tempered properties. Unfortunately, the test does not lend itself to evaluating the steels in the carburized condition. There are also several unanswered questions about extending the behavior observed in small uncarburized CVN specimens to the behavior expected in larger section sizes, especially sections surrounded by a hard carburized case. Although all the EX-grades of steel to be discussed exhibit similar or superior CVN values as SAE 4800 or 9300 steels in the quenched-and-tempered condition, as shown in Table 2, more information about fracture behavior was required for the steels in the carburized condition.

A single test cannot evaluate all the properties of interest; therefore, several tests were used to evaluate various aspects of the fracture properties of carburized specimens. One test evaluated high-cycle fatigue properties, another evaluated impact fatigue and impact fracture stress properties, and a third evaluated fracture toughness. The test specimens used in these three basic tests were kept as uniform in cross-sectional area as possible. The high-cycle and impact tests were performed on specimens having the same critical dimensions given in Fig. 3, whereas the fracture toughness specimens were precracked slow-bend specimens having the dimensions of an unnotched standard-sized Charpy impact specimen.

When evaluating fracture properties of carburized specimens, it is important that the steels being evaluated are compared on a common basis. There are three situations that can cause unfair comparisons: (1) unequal case carbon contents, (2) unequal case depths, and (3) unequal core strengths. The first and second situations become particularly important when comparing high-nickel steels with low-nickel steels.

TABLE 2—*Properties of quenched-and-tempered*[a] *high-hardenability steels.*

Steels[b]	Hardness, HRC	0.2% Offset Yield Strength, MPa (ksi)	Tensile Strength, MPa (ksi)	Room Temperature CVN Energy Absorbed, J (ft-lb)
EX55(C)	42	1140 (165)	1370 (199)	68 (50)
EX55	43	1100 (159)	1430 (207)	68 (50)
SAE 9310(C)	38	1110 (161)	1300 (188)	57 (42)
SAE 4817	40	1130 (178)	1430 (207)	41 (30)
SAE 4820	42	1100 (160)	1380 (200)	27 (20)
EX32	43	1170 (169)	1500 (217)	34 (25)

[a] Austenitized at 925°C (1700°F), cooled to 840°C (1550°F), quenched in 65°C (150°F) oil, and tempered at 170°C (340°F) for 1 h.

[b] (C) = commercial heat.

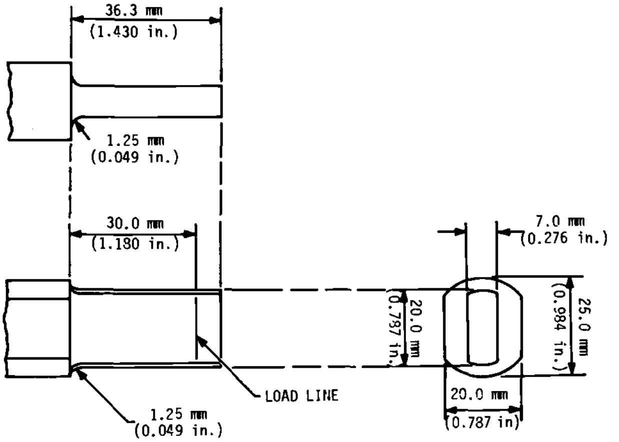

FIG. 3—*Dimensions of the critical tooth portion of high-cycle fatigue, impact fatigue, and impact fracture stress specimens.*

High-nickel steels accept carbon at a very slow rate compared to high-manganese, high-molybdenum, and high-chromium steels. The third area of concern deals with the strength level of the core. As long as the core region behaves elastically during the test, differences in core strength should not lead to unfair comparisons. Carburized specimens that exceed the yield point in the core prior to fracture can lead to unfair comparisons. In bend specimens of the type used in the present study, the required yield strength of the core is highly dependent on case depth. The deeper the case, the less strength is required in the core to prevent yielding. There are few guidelines as to what strength level is required, but it is generally accepted that premature yielding of the core can cause low fracture resistance in the case. One publication [*3*] recommended that for a 7-mm (0.28-in.) thick specimen, the core should exhibit at least a 980 MPa (140 ksi) (tensile) strength level if the case depth (at 610 VH1) is 0.76 mm (0.030 in.) The quenched-and-tempered tensile properties of the steels being compared are given in Table 2. The gage sections of the tension specimens were quenched as 10-mm (0.4-in) diameter cylinders that was considered to approximate the cooling rate of the specimens used to evaluate fracture properties. In all instances, the strength levels exceeded the value recommended for the case depth used. Therefore, the core was expected to behave elastically in all steels up to the stress level required to cause fracture in the case.

The fracture properties evaluated in the present study are primarily case fracture properties, independent of the strength properties of the core. The energy required for fracture was not considered as a fracture criterion in this study because of the large dependency of this measurement on the hardness and carbon content of the core. All fracture properties will be expressed as a fracture stress, that is, the stress required to cause fracture of the carburized case.

High-Cycle Fatigue

The fatigue resistance of the various high-hardenability steels shown in Table 1 were evaluated in the carburized condition. Typical curves of stress versus cycles-to-failure, as shown in Fig. 4, were obtained with specimens having the *tooth* dimension shown in Fig. 3. The specimens were tested in three-point bending and cycled in tension-tension tests with the ratio of minimum-to-maximum load being <0.1. The bend specimens consisted of a *tooth* at each end and a larger section in the center where the load was applied. All tests were performed in a load-control mode, meaning the maximum and minimum load levels were controlled until the specimen fractured completely.

Figure 4 compares the fatigue behavior of EX55 to that of SAE 4817 [*4*]. Both steels contain 0.17 percent carbon in the core and were carburized together to produce a case depth (0.5 percent carbon) between 1.0 and 1.3 mm (0.04 and 0.05 in.). EX55 exhibited a carbon content of 1.0 percent near the surface while the SAE 4817 exhibited 0.9 percent. Both steels exhibited similar amounts of retained austenite, determined by X-ray diffraction to be about 40 percent in SAE 4817 and 45 percent in EX55. The similarity in retained austenite exists despite different nickel contents in the two steels, because the higher nickel SAE 4817 steel had a lower surface carbon than the lower nickel EX55 steel. Both nickel and carbon stabilize retained austenite. Figure 4 shows that the fatigue properties of

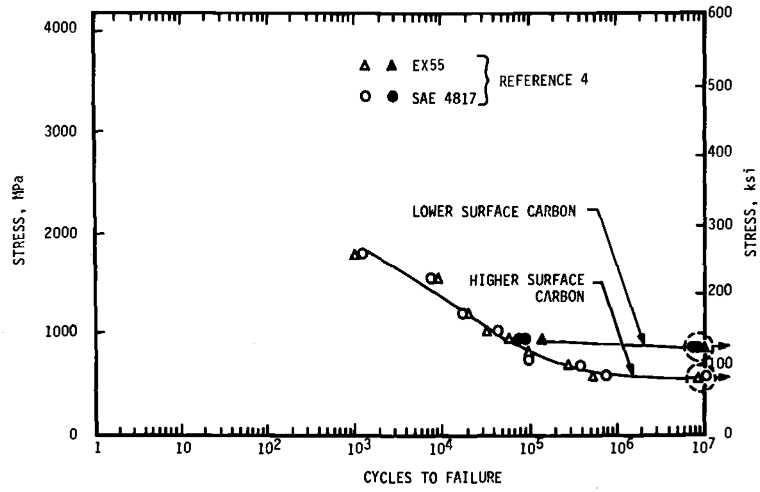

FIG. 4—*Fatigue curves of carburized EX55 (0.79 and 1.0 percent surface carbon) and SAE 4817 (0.74 and 0.9 percent surface carbon).*

EX55 and SAE 4817 in this condition (lower surface carbon) are similar. Reducing the amount of retained austenite in EX55 by carburizing in a reduced carburizing potential during the last 2 h of the carburizing cycle resulted in an improved endurance limit. The amount of retained austenite in the case of both steels was similar, estimated to be about 20 percent. In both steels, only the surface carbon content was varied; the same case depths were tested. Although the fatigue limits can be adjusted by altering the surface carbons, and probably by altering case depth [5], it is reasonable to expect that similar levels of fatigue resistance can be obtained with the two steels by choosing the proper carburizing variables.

A second comparison of fatigue properties involving EX55 is shown in Fig. 5. Again, the specimens of EX55 and the high-nickel steel, SAE 9310, were carburized together. Both steels in the comparison were produced commercially. Specimens were intentionally machined oversize so that 0.25 mm (0.010 in.) could be ground from the surface after carburizing. The surface carbon levels, after finish grinding, were 0.7 and 0.8 percent for the SAE 9310 and EX55, respectively. Again, metallography showed similar amounts of retained austenite (estimated to be about 20 percent) in the case of each steel. The high-cycle fatigue properties from the finish-ground specimens, shown in Fig. 5, indicate similar endurance limits for both steels. The case depth (610 VHl) was 0.71 mm (0.028 in.) for SAE 9310 and 0.84 mm (0.033 in.) for EX55. These steels were

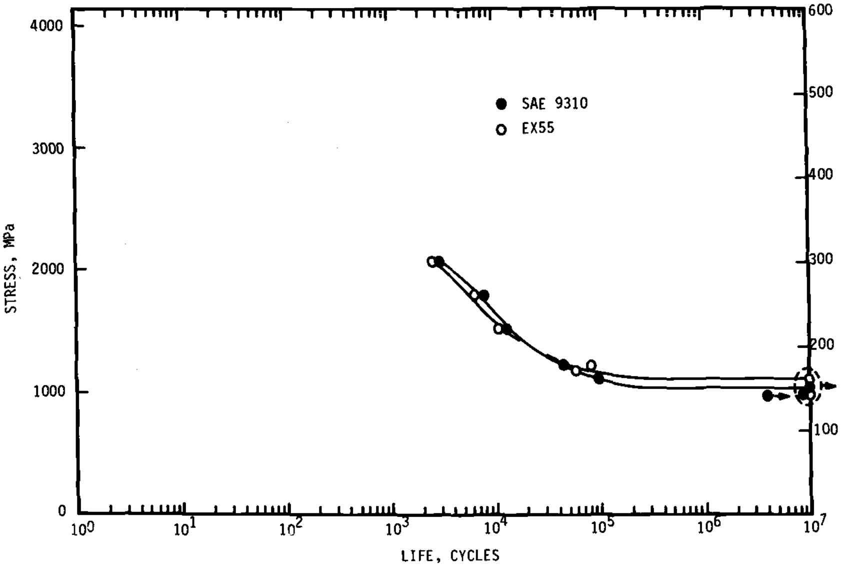

FIG. 5—*Fatigue curves of carburized and finish ground EX55 and SAE 9310.*

intentionally carburized to have similar case hardness gradients rather than similar carbon gradients.

In the comparison of fatigue properties of EX32 and SAE 4820 shown in Fig. 6, the surface carbon content was similar for both steels: 0.80 percent for EX32 and 0.84 percent for SAE 4820 [*4*]. The EX32 was also fatigue tested with a surface carbon level of about 1.0 percent. The fatigue limits of all steels were similar, although the value for EX32 at both surface carbon levels was slightly higher than that for SAE 4820. Both steels contained about 40 percent retained austenite in the high-carbon condition. The endurance limit of EX32 was about the same as that for EX55 with the low 0.8 percent surface carbon.

Fatigue Crack Growth Rate

The number of cycles required for complete fracture of high-cycle fatigue studies depends on the cycles required for initiation and the cycles required for propagation. A separate study was performed to determine whether retained austenite content influenced fatigue crack propagation rates in high-carbon steels. Two base compositions were selected, one having a nickel content of 1.0 percent and the other a content of 1.8 percent. Three carbon levels (0.6, 0.8, and 1.0 percent) of each steel were evaluated. In this way the amount of retained austenite was controlled by the two variables: carbon and nickel.

The high-carbon steels were cast as 90-mm (3.5 in.) diameter ingots and forged into 16-mm (0.625-in.) plates. Fracture toughness specimens, 13

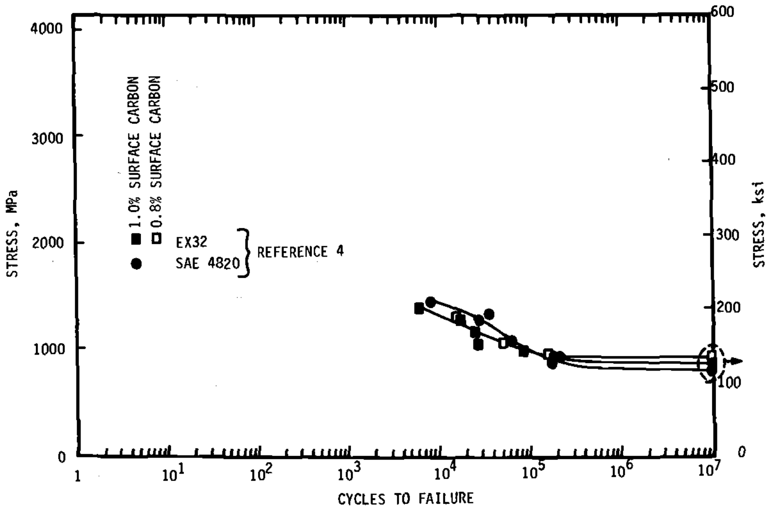

FIG. 6—*Fatigue curves of carburized EX32 (0.8 and 1.0 percent surface carbon) and SAE 4820 (0.8 percent surface carbon).*

mm (0.5 in.) thick, were machined to have the notch oriented in the longitudinal direction. Finish-machined specimens were heated to 925°C (1700°F) in a carbon atmosphere matching the carbon content of the steel, held for 1/2 h, cooled to 840°C (1550°F), and quenched into 65°C (150°F) oil. All specimens were tempered at 170°C (340°F) for 1 h. The preceding time and temperature were not sufficient to dissolve all the carbides formed during the forging operation. The specimens had to be reheated to 980°C (1800°F) and held for 1½ h prior to cooling, quenching, and tempering.

The plane-strain fracture mechanics approach to fatigue crack growth rate measurements was used employing compact tension specimens [*6*]. It was also possible to obtain plane-strain fracture toughness values from these studies. The mode of fracture in each steel was the same, dependent on the carbon content but independent of nickel content. The 0.6 percent carbon steels fractured transgranularly, and the 0.8 and 1.0 percent carbon steels fractured intergranularly. Differences in the amount of retained austenite, due to the different nickel contents, had no influence on fracture behavior. Similarly, the plane-strain fracture toughness values, as shown in Table 3, were dependent only on the carbon content and not on the amount of retained austenite. The fatigue crack growth rates were difficult to measure, because the rate of propagation was irregular. This was because the threshold stress required for crack propagation was close to the critical stress required for complete fracture. It was concluded that any differences in fatigue crack growth rates resulting from differences in the amount of retained austenite in high-carbon steels is of minor importance.

Since similar fatigue-crack growth rates are exhibited by steels having vastly different retained austenite levels, the differences in endurance limits in Fig. 4 (due to the lower surface carbon) appear to be caused by differences in the number of cycles required for crack initiation and not by differences in the rate of crack propagation. Microstructures containing excessively high levels of retained austenite, >40 volume percent, appear

TABLE 3—*Retained austenite content, hardness, and fracture toughness of steels.*

Steel	Carbon Level, %	Retained Austenite, %	Hardness, HRC	Plane-Strain Fracture Toughness, MPa $\sqrt{m}$	(ksi $\sqrt{in.}$)
1.0Ni	0.61	14.0	62.2	24	(22)
	0.82	31.1	61.1	21	(19)
	1.04	49.5	59.3	20	(18)
1.9Ni	0.60	16.4	61.3	25	(23)
	0.78	33.2	59.8	21	(19)
	1.06	63.5	52.3	21	(19)

less resistant to crack initiation than microstructures having larger amounts of martensite. This could result from a lower proportional limit in the steel having high amounts of retained austenite [5].

Impact Fatigue and Impact Fracture Stress

Impact fatigue properties of carburized steels were obtained with specimens having the same tooth dimensions as the high-cycle fatigue specimens. However, the specimens were not loaded in three-point bending, but rather were cantilevered. The specimens were held rigidly in the anvil of a Riehle impact machine in a manner similar to that used in testing Izod impact specimens and were impacted with an instrumented Izod striker attached to a 27-kg (60-lb) pendulum hammer. The drop height was reduced to less than an inch to prevent complete fracture on the first impact. The total range of energy input was between 4 and 6 J (35 and 54 in·lb). In most instances, the instrumented striker allowed the number of cycles for crack initiation to be separated from the cycles required for complete fracture. A sudden drop in the load observed on the oscilloscope of an otherwise elastic response was interpreted as a crack initiation event.

The impact fracture stress of each steel was determined using the same setup as that used for the impact fatigue tests. The drop height was raised to cause fracture with one impact. The instrumented striker measured the fracture load that was then used to calculate a stress using bending equations and a stress concentration factor of 1.56. It has been shown that impact fatigue properties are related to the impact fracture stress [7]. Figure 7 shows that for a broad range of steels, the higher the impact fracture stress, the more resistant the steels are to fracture in impact fatigue. EX55 and SAE 4817 are the most resistant to fracture of any of the steels evaluated.

Fracture Toughness

Fracture-toughness measurements were obtained from carburized Charpy-size specimens with fatigue precracks grown to various depths into the case. The length of the precrack was controlled by notching the specimen with electrodischarge machining (EDM) techniques. A fatigue crack was extended beyond the EDM notch about 0.13 mm (0.005 in.). Fatigue cracks that were allowed to grow much beyond 0.13 mm (0.005 in.) generally did not maintain a uniform crack length across the width of the specimen. Control over the growth of fatigue crack was best maintained by fatigue cycling specimens having water at the base of the EDM notch. Once precracked, the water was removed by heating to 120°C (250°F) and the specimens were broken in slow-bend tests. The fracture load and crack length were used to calculate fracture toughness as

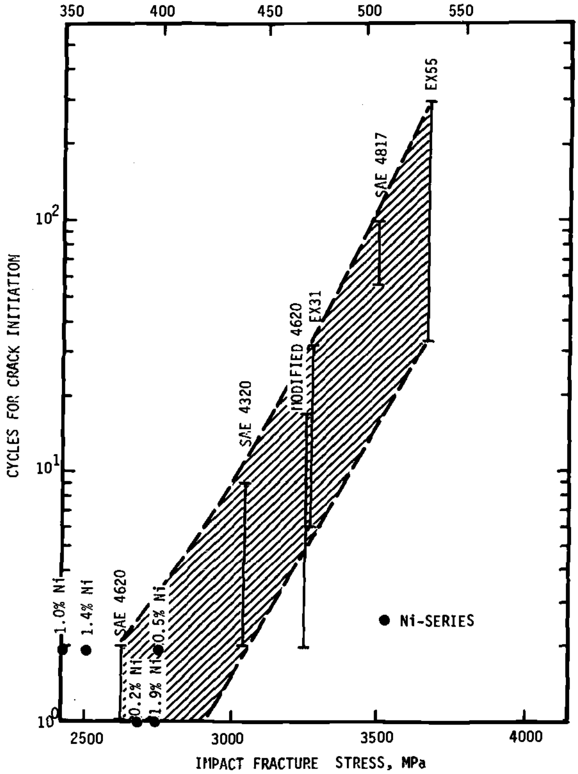

FIG. 7—*Correlation between impact fracture stress and the number of impacts required for crack initiation under repeated impacts at an energy level of 4.0 J (from Ref 7).*

described in ASTM Test for Plane-Strain Fracture Toughness of Metallic Materials (E 399-74). Each data point in Fig. 8 represents one test specimen with the tip of the precrack at the indicated depth.

The fracture toughness values for EX55, EX32, SAE 9310, and SAE 4820 are shown in Fig. 8 to be very similar, much higher than the values observed for the low-hardenability SAE 8620 steel. The EX55, SAE 9310, and SAE 8620 steels were commercially produced, whereas the EX32 and SAE 4820 steels were laboratory heats. The section thickness of the test specimens was sufficiently small in the fracture area that all steels were through-hardened, even the lower hardenability SAE 8620 steel. The excellent fracture toughness properties of EX32 and SAE 4820 were obtained by quenching directly from 925°C (1700°F) into an oil at 170°C (340°F). All the steels represented in Fig. 8 were carburized to produce case depths (0.5 percent carbon) between 0.76 and 1.02 mm (0.030 and 0.040 in.).

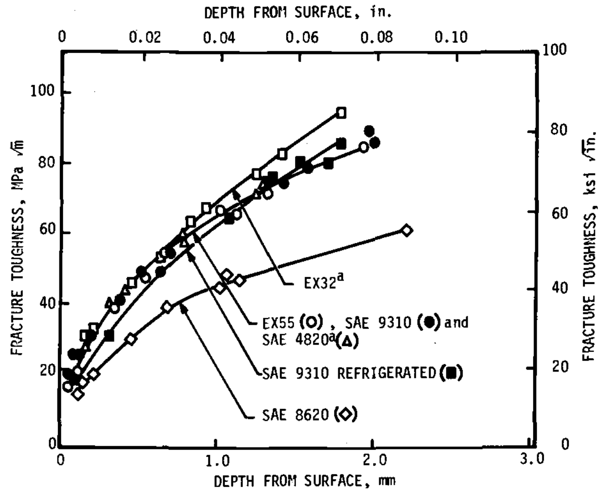

[a] EX32 and SAE 4820 were quenched directly from 925 C (1700 F) into 170 C (340 F) oil. Other steels were cooled to 840 C (1550 F) and quenched into 65 C (150 F) oil.

FIG. 8—*Fracture toughness gradients in carburized cases of commercial heats of EX55, SAE 9310, and SAE 8620. EX32 and SAE 4820 were laboratory heats.*

Influence of Alloy Content

Several series of steels were produced to evaluate the influence of alloy content on the impact fatigue and impact fracture stress. The compositions of the steels are given in Table 4. Each series of steels represents the base composition of a low-hardenability steel, either an SAE 8800 or SAE 4600 grade. The SAE 8800 grade (Series A) had a core carbon content of 0.20 percent, whereas the carbon content of the SAE 4600 grade (Series B and C) was varied from 0.14 to 0.16 percent. The steels of Series A were air-induction melted and forged the same as the alloys represented in Fig. 2 and had a prior austenite grain size of ASTM No. 10. In an attempt to produce steels with a grain size more representative of commercial heats, the steels of Series B and C were vacuum melted, argon backfilled, and carbon deoxidized. The grain size of the steels of Series B and C was about ASTM No. 6. All grain sizes were determined as described earlier. This portion of the investigation was initiated to determine which combination of alloy content, similar to that in EX55, is required for high fracture resistance. All steels were evaluated in the carburized condition and had a 0.5 percent carbon case depth between 0.76 and 1.02 mm (0.030 and 0.040 in.). The impact fracture stress values are given in Table 5.

The series of steels having the base composition of SAE 8800 evaluated the influence of nickel content [7]. The impact fracture stress values shown in Fig. 9 indicate that no significant influence on fracture stress

TABLE 4—*Series of steels with base composition of SAE 8800 and 4600.*

Steel Series	Element, weight percent								
	C	Mn	Si	Cr	Ni	Mo	P	S	Al
A	0.20	0.81	0.28	0.50	0.19	0.34	0.018	0.020	0.08
	0.20	0.87	ND[a]	0.50	0.47	0.33	ND	ND	ND
	0.20	0.80	ND	0.50	0.91	0.34	ND	ND	ND
	0.21	0.78	ND	0.50	1.43	0.34	ND	ND	ND
	0.22	0.73	ND	0.50	1.88	0.33	ND	ND	ND
B	0.16	0.58	0.24	NA[b]	1.81	0.47	0.024	0.013	0.005
	ND	0.57	ND	NA	1.80	0.69	ND	ND	ND
	ND	0.57	ND	0.52	1.80	0.68	ND	ND	ND
C	0.14	0.58	0.24	NA	1.80	0.47	0.024	0.013	0.005
	ND	0.58	ND	0.51	1.81	0.47	ND	ND	ND
	ND	0.57	ND	0.51	1.80	0.71	ND	ND	ND

[a] ND = not determined but assumed to be similar to the first ingot of each series of steels.
[b] NA = none added.

was observed as the nickel content was increased from 0.2 to 1.9 percent. The impact fatigue properties were also evaluated and are shown in Fig. 7 to be at the low end of the range. High nickel content alone is not sufficient to improve fracture resistance. SAE 4620 contains 1.8 percent nickel, and it also exhibited a low impact fracture stress and impact fatigue behavior (Fig. 7).

TABLE 5—*Impact fracture stress of carburized cases.*

Steel	Element Variable, %	Impact Fracture Stress, MPa (ksi)
Series A	0.19Ni	2620 (380)
(SAE 8820)	0.47Ni	2650 (385)
	0.91Ni	2410 (350)
	1.43Ni	2450 (355)
	1.88Ni	2620 (380)
Series B	0.47Mo–0Cr	3650 (530)
(4616)	0.69Mo–0Cr	3925 (570)
	0.68Mo–0.52Cr	4065 (590)
Series C	0.47Mo–0Cr	3650 (530)
(4614)	0.47Mo–0.51Cr	3650 (530)
	0.71Mo–0.51Cr	3925 (570)
SAE 4620	0.25Mo	2620 (380)
	0.49Mo	3240 (470)

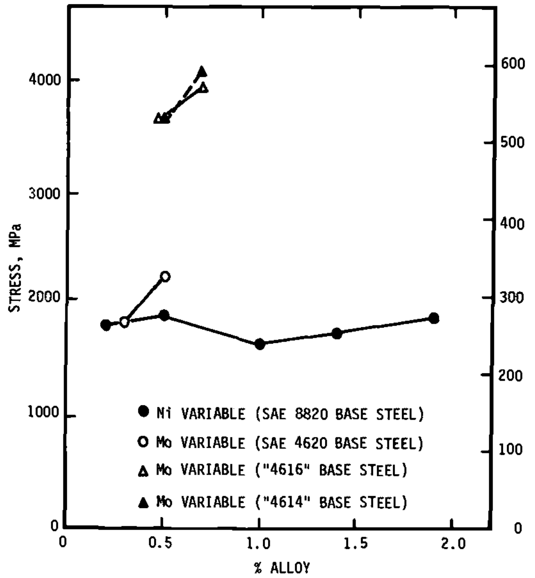

FIG. 9—*Impact fracture stress of carburized steels with either a nickel or a molybdenum variable.*

Increasing the molybdenum content of the SAE 4620 steel with 1.8 percent nickel (Modified 4620) improved the impact fracture stress, as can be seen in Figs. 7 and 9. A similar increase in impact fracture stress was observed in both the 4616 (Series B) and the 4614 (Series C) steels (Fig. 9) when the molybdenum content was increased. The highest impact fracture stress observed was in 4616 modified to contain 0.68 percent molybdenum and 0.52 percent chromium. This composition is close to that of EX55 (EX55 has a slightly higher molybdenum and manganese content).

The excellent fracture resistance of EX55 has been attributed to a balanced addition of 0.7 percent molybdenum in a 1.8 percent nickel steel and the chromium content not exceeding 0.5 percent. The base carbon content is important also. All the steels at the low end of the range in Fig. 7 contain 0.20 percent carbon. The steels exhibiting the best impact fracture stress in this study contained 0.14 to 0.17 percent carbon. Increasing the core carbon content of EX55 to only 0.20 percent is expected to lower the impact properties of the carburized case. The adverse effect of at least 0.20 percent carbon on impact fracture stress is probably related to the influence of core carbon content on the residual stress distribution in the case.

Residual Stress

Some interesting influences of composition on fracture properties of carburized specimens have been shown, but the exact reason is not evident. The amount of retained austenite in the case has ranged from 10 to 50 percent and there appears to be no good correlation with fracture properties. The maximum case hardness values ranged from 665 to 780 VH1, and again no correlation was observed. The core carbon content appears to be critical between 0.17 and 0.20 percent, and yet the strength levels of all the cores have been sufficient to guarantee elastic behavior at stress levels required to cause fracture.

A separate investigation was aimed at producing a variety of residual stress levels in the carburized cases of EX32 and SAE 4820. The level of compressive residual stress in the case has a strong influence on fracture properties. X-ray diffraction was used to measure residual stress values in the carburized cases of selected test specimens. Measurements were obtained on the surface and at 0.08 to 0.10 mm (0.003 to 0.004-in.) increments through the case, to a total depth of 0.86 mm (0.34 in.). In some instances the measurements extended to a depth of 1.32 mm (0.052 in.). The incremental layers of the case were removed by electrochemical polishing techniques. The data are shown in Table 6. Surface carbon, case depth, and quenching temperature were varied to alter the amount of retained austenite and the resulting level of compressive residual stress. The impact fracture stress was determined and plotted against the maximum compressive residual stress value in the outer 0.76 mm (0.030 in.) of the carburized case [*7*]. As shown in Fig. 10, the higher the compressive residual stress, the higher the impact fracture stress. The correlation was good for carburized cases containing less than 50 percent retained austenite. Cases exhibiting greater than 50 percent retained austenite behaved in a random fashion, sometimes exhibiting more fracture stress and sometimes less than expected from the correlation in Fig. 10. The reason for this behavior is probably related to the residual stress level in the austenite. The standard procedure for measuring residual stress values[4] only determines the stress in the martensite. Austenite has been shown to exhibit various levels of tensile residual stress [*8*]. Since most carburized cases contain less than 50 percent retained austenite because of (minimum) hardness requirements, the cases having higher levels of retained austenite need not be considered. The good correlation in Fig. 10 indicates that the residual stress of the austenite need not be of concern in carburized cases containing less than 50 percent retained austenite.

Composition controls residual stress distribution by controlling the relative time of transformation to martensite from one location in the case

---

[4] Residual Stress Measurement by X-ray Diffraction, SAE J 784a, Society of Automotive Engineers, 1971.

TABLE 6—*Residual stress and retained austenite date for EX32 and SAE 4820.*

EX32							SAE 4820						
Distance from Surface, mm	(in.)	Carbon, %	Microhardness, VHI	Retained Austenite, %	Residual Stress, MPa	(ksi)	Distance from Surface, mm	(in.)	Carbon, %	Microhardness, VHI	Retained Austenite, %	Residual Stress, MPa	(ksi)
Condition A^a—0.18% core carbon													
0	(0)	ND^b	ND	28	−83	(−12)	0	(0)	ND	ND	18	−131	(−19)
0.08	(0.003)	0.80	ND	33	−331	(−48)	0.08	(0.003)	0.72	ND	14	−462	(−67)
0.15	(0.006)	0.78	715	20	−331	(−48)	0.15	(0.006)	0.70	695	13	−372	(−54)
0.25	(0.010)	0.74	730	23	−372	(−54)	0.25	(0.010)	0.68	680	13	−448	(−65)
0.36	(0.014)	0.72	735	21	−317	(−46)	0.36	(0.014)	0.64	690	14	−316	(−46)
0.46	(0.018)	0.69	730	14	−331	(−48)	0.46	(0.018)	0.62	695	8	−407	(−59)
0.56	(0.022)	0.64	715	13	−316	(−46)	0.56	(0.022)	0.59	690	14	−193	(−28)
0.66	(0.026)	0.59	695	13	−221	(−32)	0.66	(0.026)	0.55	675	10	−290	(−42)
0.76	(0.030)	0.56	680	14	−262	(−38)	0.76	(0.030)	0.50	655	13	−200	(−29)
0.86	(0.034)	0.51	660	10	−234	(−34)	0.86	(0.034)	0.46	620	6	−172	(−25)
Condition E^a—0.18% core carbon													
0	(0)	ND	ND	4	−76	(−11)	0	(0)	ND	ND	11	−276	(−40)
0.08	(0.003)	ND	ND	34	−448	(−65)	0.08	(0.003)	ND	ND	22	−510	(−74)
0.15	(0.006)	ND	730	25	−496	(−72)	0.15	(0.006)	ND	645	21	−558	(−81)
0.25	(0.010)	ND	725	27	−448	(−65)	0.25	(0.010)	ND	665	14	−524	(−76)
0.38	(0.015)	ND	710	24	−510	(−74)	0.36	(0.014)	ND	645	16	−496	(−72)
0.46	(0.018)	ND	665	14	−517	(−75)	0.46	(0.018)	ND	640	24	−283	(−41)
0.56	(0.022)	ND	630	9	−483	(−70)	0.56	(0.022)	ND	630	21	−358	(−52)
0.66	(0.026)	ND	625	6	−593	(−86)	0.66	(0.026)	ND	615	5	−510	(−74)
0.76	(0.030)	ND	620	4	−324	(−47)	0.76	(0.030)	ND	625	8	−324	(−47)
0.86	(0.034)	ND	570	ND	−290	(−42)	0.86	(0.034)	ND	595	ND	−352	(−51)
0.97	(0.038)	ND	550	ND	−276	(−40)	. . .		. . .	. . .	. . .	. . .	
1.07	(0.042)	ND	ND	ND	−269	(−39)	. . .		. . .	. . .	. . .	. . .	

TABLE 6—*Continued.*

EX32							SAE 4820						
Distance from Surface, mm	(in.)	Carbon, %	Microhardness, VH1	Retained Austenite, %	Residual Stress, MPa	(ksi)	Distance from Surface, mm	(in.)	Carbon, %	Microhardness, VH1	Retained Austenite, %	Residual Stress, MPa	(ksi)
Condition E—0.21% core carbon													
0	(0)	ND	ND	3	−41	(−6)	0	(0)	ND	ND	17	−193	(−28)
0.08	(0.003)	0.90	ND	41	−483	(−70)	0.08	(0.003)	0.72	ND	31	−476	(−69)
0.15	(0.006)	0.81	660	26	−489	(−71)	0.15	(0.006)	0.70	680	17	−496	(−72)
0.25	(0.010)	0.76	680	21	−483	(−70)	0.25	(0.010)	0.68	690	20	−365	(−53)
0.36	(0.014)	0.72	665	18	−476	(−69)	0.36	(0.014)	0.64	675	ND	−455	(−66)
0.46	(0.018)	0.69	650	16	−414	(−60)	0.46	(0.018)	0.61	665	17	−483	(−70)
0.56	(0.022)	0.66	645	12	−531	(−77)	0.56	(0.022)	0.59	650	18	−414	(−60)
0.66	(0.026)	0.60	630	10	−476	(−69)	0.66	(0.026)	0.57	630	9	−524	(−76)
0.76	(0.030)	0.56	560	10	−510	(−74)	0.76	(0.030)	0.50	620	7	−386	(−56)
0.86	(0.034)	0.52	545	ND	−420	(−61)	0.86	(0.034)	0.46	595	ND	−407	(−59)
0.97	(0.038)	0.46	535	ND	−455	(−66)	0.97	(0.038)	0.42	565	ND	−310	(−45)
1.07	(0.042)	0.42	530	ND	−414	(−60)	. . .		. . .	. . .	. . .	. . .	
1.19	(0.047)	0.38	ND	ND	−441	(−64)	. . .		. . .	. . .	. . .	. . .	
1.32	(0.052)	0.33	ND	ND	−393	(−57)	. . .		. . .	. . .	. . .	. . .	

Condition E—0.24% core carbon

0.	(0)	ND	ND	4	−145	(−21)	. . .		ND	ND	ND	ND	
0.08	(0.003)	ND	ND	33	−510	(−74)	. . .		ND	ND	ND	ND	
0.15	(0.006)	ND	755	27	−476	(−69)	0.13	(0.005)	ND	610	ND	ND	
0.25	(0.010)	ND	760	24	−455	(−66)	0.25	(0.010)	ND	580	ND	ND	
0.36	(0.014)	ND	745	20	−434	(−63)	0.38	(0.015)	ND	575	ND	ND	
0.46	(0.018)	ND	740	16	−462	(−67)	0.51	(0.020)	ND	560	ND	ND	
0.56	(0.022)	ND	725	15	−483	(−70)	0.64	(0.025)	ND	545	ND	ND	
0.66	(0.026)	ND	690	11	−462	(−67)	0.76	(0.030)	ND	515	ND	ND	
0.76	(0.030)	ND	660	10	−476	(−69)	0.89	(0. 035)	ND	505	ND	ND	
0.86	(0.034)	ND	630	ND	−469	(−68)	1.02	(0.040)	ND	495	ND	ND	
0.97	(0.038)	ND	600	ND	−476	(−69)	. . .		ND	. . .	ND	ND	

Condition F^a—0.21% core carbon

0	(0)	ND	ND	7	76	(+11)	0	(0)	ND	ND	22	−234	(−34)
0.08	(0.003)	1.06	ND	56	−221	(−32)	0.08	(0.003)	0.93	ND	53	−310	(−45)
0.15	(0.006)	0.85	710	33	−345	(−50)	0.15	(0.006)	0.75	615	38	−352	(−51)
0.25	(0.010)	0.75	740	38	−414	(−60)	0.25	(0.010)	0.68	650	12	−386	(−56)
0.38	(0.015)	0.69	730	17	−434	(−63)	0.36	(0.014)	0.63	640	21	−303	(−44)
0.46	(0.018)	0.66	720	18	−414	(−60)	0.46	(0.018)	0.59	645	20	−393	(−57)
0.58	(0.023)	0.61	690	14	−448	(−65)	0.56	(0.022)	0.55	640	16	−421	(−61)
0.69	(0.027)	0.57	650	11	−469	(−68)	0.66	(0.026)	0.51	630	9	−421	(−61)
0.79	(0.031)	0.53	615	10	−483	(−70)	0.76	(0.030)	0.47	620	5	−290	(−42)
0.86	(0.034)	0.49	600	ND	−441	(−64)	0.86	(0.034)	0.42	605	ND	−338	(−49)
0.97	(0.038)	0.45	585	ND	−503	(−73)	. . .		. . .	. . .	. . .	. . .	
1.07	(0.042)	0.41	560	ND	−414	(−60)	. . .		. . .	. . .	. . .	. . .	
1.19	(0.047)	0.37	530	ND	−400	(−58)	. . .		. . .	. . .	. . .	. . .	
1.32	(0.052)	0.33	500	ND	−331	(−48)	. . .		. . .	. . .	. . .	. . .	

TABLE 6—*Continued.*

EX32							SAE 4820						
Distance from Surface, mm	(in.)	Carbon, %	Microhardness, VH1	Retained Austenite, %	Residual Stress, MPa	(ksi)	Distance from Surface, mm	(in.)	Carbon, %	Microhardness, VH1	Retained Austenite, %	Residual Stress, MPa	(ksi)
Condition G^a—0.21% core carbon													
. . .		ND	ND	ND	ND		0	(0)	ND	ND	23	−103	(−15)
. . .		ND	ND	ND	ND		0.08	(0.003)	0.78	ND	56	−393	(−57)
0.13	(0.005)	ND	700	ND	ND		0.15	(0.006)	0.73	625	28	−441	(−64)
0.25	(0.010)	ND	770	ND	ND		0.25	(0.010)	0.69	680	26	−427	(−62)
0.38	(0.015)	ND	790	ND	ND		0.36	(0.014)	0.66	695	20	−379	(−55)
0.51	(0.020)	ND	765	ND	ND		0.48	(0.019)	0.62	725	12	−455	(−66)
0.64	(0.025)	ND	750	ND	ND		0.56	(0.022)	0.59	705	8	−372	(−54)
0.76	(0.030)	ND	755	ND	ND		0.66	(0.026)	0.56	690	7	−372	(−54)
1.02	(0.040)	ND	715	ND	ND		0.76	(0.030)	0.54	690	12	−358	(−52)
1.27	(0.050)	ND	620	ND	ND		0.86	(0.034)	0.54	660	13	−269	(−39)
Condition H^a—0.21% core carbon													
. . .		ND	ND	ND	ND		0	(0)	ND	ND	9	−90	(−13)
. . .		ND	ND	ND	ND		0.08	(0.003)	0.73	ND	21	−358	(−52)
0.13	(0.005)	ND	680	ND	ND		0.15	(0.006)	0.72	620	30	−434	(−63)
0.25	(0.010)	ND	700	ND	ND		0.25	(0.010)	0.69	625	18	−407	(−59)
0.38	(0.015)	ND	720	ND	ND		0.36	(0.014)	0.65	635	12	−455	(−66)
0.51	(0.020)	ND	710	ND	ND		0.46	(0.018)	0.63	635	15	ND	
0.64	(0.025)	ND	675	ND	ND		0.56	(0.022)	0.60	615	17	−483	(−70)
0.76	(0.030)	ND	660	ND	ND		0.66	(0.026)	0.56	585	14	−386	(−56)
1.02	(0.040)	ND	600	ND	ND		0.76	(0.030)	0.54	590	10	−303	(−44)
1.27	(0.050)	ND	615	ND	ND		0.86	(0.034)	0.50	575	ND	−455	(−66)

Condition M[a]—0.18% core carbon

0	(0)	ND	ND	12	−41	(−6)	0	(0)	ND	ND	ND	ND
0.08	(0.003)	1.08	ND	56	−110	(−16)	0.08	(0.003)	0.95	ND	ND	ND
0.15	(0.006)	0.97	650	44	−152	(−22)	0.13	(0.005)	0.86	585	ND	ND
0.25	(0.010)	0.86	720	32	−221	(−32)	0.25	(0.010)	0.74	670	ND	ND
0.36	(0.014)	0.79	735	27	−365	(−53)	0.38	(0.015)	0.68	660	ND	ND
0.46	(0.018)	0.72	740	17	−441	(−64)	0.51	(0.020)	0.61	650	ND	ND
0.56	(0.022)	0.66	725	13	−510	(−74)	0.64	(0.025)	0.54	660	ND	ND
0.66	(0.026)	0.58	700	10	−476	(−69)	0.76	(0.030)	0.48	600	ND	ND
0.76	(0.030)	0.53	680	6	−489	(−71)	1.02	(0.040)	0.38	605	ND	ND
0.86	(0.034)	0.45	640	ND	−517	(−75)	1.27	(0.050)	0.30	460	ND	ND
0.97	(0.038)	0.39	600	ND	−434	(−63)	1.52	(0.060)	0.24	420	ND	ND
1.07	(0.042)	0.34	555	ND	−358	(−52)	1.78	(0.070)	0.21	425	ND	ND

[a]

Condition	Carbon Potential Setting, %	Carburizing Time, h	Temperature of Quench Oil, °C	(°F)
A	0.9	7	65	(150)
E	0.90	7	170	(340)
F	0.90	9	170	(340)
G	0.90	12	170	(340)
H	0.90	16	170	(340)
M	1.05	7	170	(340)

[b] ND = not determined.

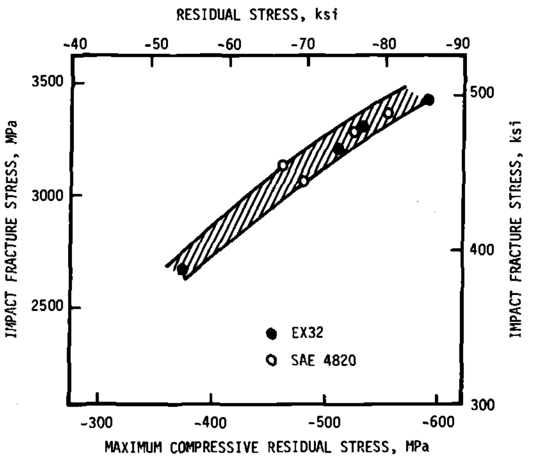

FIG. 10—*Relationship between impact fracture stress and compressive residual stress in the outer 0.76 mm (0.030 in.) of the carburized case (all cases contained <50 percent retained austenite).*

to another. Cooling rate, and therefore, section size is also important. The impact fracture stress data presented in this paper were obtained from 7-mm (0.28-in.) thick specimens. Future research will be conducted, not only to further define alloy influences, but also to evaluate the influence of section-size on the previous observations.

Discussion and Summary

The performance of several high-hardenability steels, including the recently developed EX55 steel, have been evaluated in the carburized condition in several laboratory tests. The EX55 steel, having extra-high hardenability, was developed to meet the stringent hardness requirements of large-diameter rolling-cutter rock bits. Compared to SAE 4817 and SAE 9310, only the EX55 steel consistently exhibited an HRC 34 hardness at the J 20 position of an end-quenched Jominy specimen.

In general, the fracture properties of EX55 in laboratory tests were similar or superior to the properties exhibited by SAE 4817 or SAE 9310. High-cycle fatigue properties were similarly controlled by surface carbon in both EX55 and SAE 4817. Decreasing the surface carbon raised the endurance limits. Large differences in the amount of retained austenite in high-carbon steels due to differences in nickel content did not alter the fatigue crack propagation behavior of high-carbon steels. The fracture mode was controlled by the carbon content in the carburized case. Plane-strain fracture toughness tests, impact fatigue, and impact fracture stress tests demonstrated similarly good fracture resistance for EX55. Several series of alloys were evaluated to determine which alloy combinations were required for the excellent fracture properties of EX55. The core carbon content between 0.14 and 0.17 percent appears to cause higher fracture stress values than 0.20 percent carbon steels. Increasing the nickel content from 0.2 to 1.9 percent did not alter the fracture stress values of a 0.20 percent carbon steel. Increasing the chromium content to about 0.7 percent did not detract from the properties of a 1.8 percent nickel steel, but it was previously observed [7] that chromium contents of 1.0 and 1.2 percent decreased the impact fracture stress values of a 0.5 percent nickel steel. The good properties of EX55 were partly attributed to the chromium content not exceeding 0.7 percent in a 1.8 percent nickel steel. Increasing the molybdenum content resulted in improved impact fracture stress values. An influence of molybdenum in a 1.8 percent nickel steel was observed previously [7], when an increase to 0.5 percent molybdenum improved the fracture properties of an SAE 4620 steel. In general, the excellent fracture resistance of EX55 resulted from the balanced additions of manganese, chromium, molybdenum, and nickel in a base steel containing a maximum of 0.17 percent carbon.

The laboratory tests performed in this investigation required specimens having relatively small cross-sectional areas. All steels exhibited core hardness in excess of HRC 38. In the section size experienced in large-diameter rock bits, the relative behavior of the steels is expected to remain the same as long as the core hardness values for each steel are similar. As the core hardness in a large section of one steel, such as EX55, remains greater than HRC 34 while that of SAE 4817 drops to HRC 24, then the similarity in behavior observed in the laboratory tests is not expected to exist. A reduction of core strength is known to lower the performance life of rolling-cutter rock bits. Therefore, EX55 is expected to perform better as large-diameter rock bits than SAE 4817.

References

[1] Smith, Y. E. and Eldis, G. T., *Metals Engineering Quarterly*, Vol. 2, May 1976, pp. 13–20.

[2] deRetana, A. F. and Doane, D. V., *Metal Progress*, Vol. 100, 1971, p. 65.

[3] Brugger, H., *Schweizer Archiv fur Angewandte Wissenschaft und Technik*, Vol. 36, No. 7, 1970, p. 219.

[4] Diesburg, D. E. and Eldis, G. T., "Fracture Resistance of Various Carburized Steels," presented at the Fall AIME Meeting, Cincinnati, American Institute of Mining, Metallurgical, and Petroleum Engineers, Sept. 1975, to be published.

[5] Langraf, R. W. and Richman, R. H., *Fatigue of Composite Material, ASTM STP 569*, American Society for Testing and Materials, 1973, pp. 130–142.

[6] Hudak, S. J., Jr., Bucci, R. J., and Malcom, R. C., "Development of Standard Methods of Testing and Analyzing Fatigue Crack Growth Rate Date," AFML Contract F33615-75-C-5064, report from Westinghouse Research Laboratories, 10 March, 1977.

[7] Diesburg, D. E. and Bulla, W., "Resistance of Carburized Steels to Crack Initiation in Impact Fatigue," presented at the Annual Heat Treaters Convention, Wiesbaden, Germany, Oct. 1977.

[8] Hartman, V. R., "Möglichkeiten und Grenzen der röntgendifraktometrischen Spannungsanalyse (RSA) in der Martensit und Austenitphase einsatzgehärteter Stähle," thesis, Universität Karlsruhe, 1973.

Discussion—Steels Session

Design of High Hardness, Tough Steels for Energy-Related Applications by V. F. Zackay

Question: Dr. Halle Abrams[1]—As to the aluminum-silicon interaction you referred to—would you explain why you were getting the fracture behavior you observed? Where is the aluminum or silicon going so that it produces the observed behavior?

Answer: Dr. Zackay—The effect of the combined aluminum plus silicon on fracture is a complicated one. About 20 years ago, people at both MIT and various specialty steel companies studied the role of silicon in steel. They observed that it delays the onset of softening. How does it do it?

There are certain chemical and crystal-chemical reasons that have been postulated to explain this effect. One is that aluminum, silicon, cobalt, and other similar noncarbide-forming elements increase the activity of carbon. By increasing the activity, they favor the formation of epsilon carbide over iron carbide. Another reason that has been suggested is based on the fact that silicon does not fit in the lattice of iron carbide. For iron carbide to form, the silicon must diffuse out into the surrounding matrix. Silicon diffusion at ordinary tempering temperatures is very slow and thereby delays the onset of softening. The aluminum-iron phase diagram is very similar to that of the iron-silicon system. In general, everything that can be said for the silicon-iron system is applicable to that of the aluminum-iron system. With respect to fracture in these systems, I think it was Prof. McMahon who noted, in his studies of temper embrittlement, that silicon goes preferentially to grain boundaries. He noted a large concentration of silicon, at certain tempering temperatures, at the grain boundaries. From reference to the Fe-Si system, it is well known that above about 3Si short-range order is observed and long-range order at about 5Si. So, if the silicon segregates preferentially to, or near, the grain boundaries either short-range or long-range order occurs and embrittlement is likely to be observed.

Aluminum has a different size than silicon. As far as is known, it does not segregate to the grain boundaries. Therefore, a combination of silicon and aluminum on the one hand, enhances the solid strength, while on the

---

[1] Bethlehem Steel Corp., Bethlehem, Pa.

other the silicon (if less than 1.5 percent) does not segregate and the onset of softening is delayed to a maximum degree. Prof. Ritchie at MIT has shown that, in addition, there is apparently some enhanced stress corrosion behavior in these silicon plus aluminum alloys.

Question: L. Thompson[2]—Have you looked at the effects of thermal aging in service on the mechanical properties in the secondary hardening steels?

Answer: Dr. Zackay—Not as yet—this is, however, a subject of considerable interest to us. We are just beginning long tempering time experiments at relatively low temperatures. Results to date indicate that significant increases in toughness can result with little deterioration in hardness. Eventually these alloys will have to undergo long-time aging experiments to test their structural stability after such exposure.

Microstructural Control in Microalloyed Steels by Morris Cohen and S. S. Hansen

Question: I. F. Hughes[3]—You mentioned in your talk the necessity for control of niobium content, and we feel from our experience in making the 80 ksi hot rolled steel that at about 0.1Nb, the carbon level is extremely critical and that holding carbon to a range of 0.03 percent is an acceptable limitation for the BOF shop.

My first question is do you have data showing the influence of a change in carbon content from 0.03 to 0.06 percent on Cb (CN) precipitation kinetics at a columbium level of 0.1 percent? The second part of my question is that we seem to find some influence of silicon on improving toughness in these Mn-Cb grades, and I wondered whether you had seen a similar effect.

Answer: Dr. Hansen—We have no data showing the influence of carbon variations at the 0.1Cb level on the Cb (CN) precipitation kinetics in the austenite. Certainly, changes in the carbon content would affect the amount of columbium that could be dissolved in the austenite at the soaking temperature. How this might affect the response of the austenite to hot-working is debatable, however, there might be a significant effect on the subsequent ferrite strength due to changes in the amount of dissolved columbium available for subsequent precipitation hardening.

I am familiar with recent work that shows a similar influence of silicon on toughness in a titanium high-strength low-alloy steels. However, to the best of my knowledge the nature of this effect is still unclear.

---

[2] General Atomic Co., San Diego, Calif.

[3] Inland Steel Research Labs., East Chicago, Ind.

Question: Dr. R. Cornwell[4]—Can present-day rolling mills handle the schedule you are suggesting where you do not get any recrystallization of the austenite? Because it seems to me you are just cold rolling the austenite.

Answer: Dr. Hansen—I think they can, provided the rolling schedules are designed to avoid large reductions per pass. While mill loads certainly will limit what can be achieved, especially when rolling unrecrystallized austenite, this paper was not aimed at designing an optimum processing schedule. Rather, it was meant to provide a framework for considering how to maximize the degree of austenitic grain refinement obtaining during rolling.

Comment: Dr. Abrams—I'd like to add a little bit to that. I like to think of the process as warm rolling. And you have to tailor your rolling schedule to your mill capability. The Japanese and Italians have much higher mill capacity than we have domestically, or certainly what Bethlehem has. But you can design a rolling practice consistent with your mill capability and still achieve the Stage III Processing that Dr. Hansen showed. In fact, this Stage III Processing ties in with another question: I'm not quite sure why there is a limiting austenitic grain size of 20 to 25 μm. Can you comment why that is? Why can't one get further grain refinement?

Answer: Dr. Hansen—I'm not completely sure either, but one way of perhaps rationalizing it might be to remember that as you refine the austenitic grain size by repeated recrystallization, you also increase the surface-to-volume ratio, and decrease the average growth dimension for recrystallized grain. Eventually, a *limiting grain size* might be approached when you have essentially one nucleation event per grain, and rapid growth of that nucleus, consuming the deformed grain prior to the next nucleation event. While speculative, this may be a reasonable way of explaining the observation. Actually, we're really not trying to explain this observation, but rather point out that there does, in practice, appear to be a *limiting recrystallized grain size.*

Comment: Dr. Abrams—What you're saying makes some sense, because I could see that if it's a thermodynamic limitation and there are surface-to-volume energies associated with it, then at some point you are just going to violate a law of thermodynamics and so that's it—that's all there is left in your system at the temperature involved. It's not a precipitate-pinning restriction or anything like that.

Still another question I had is on one of your initial slides where you showed these very very fine precipitates along the prior austenite grain

---

[4] Texas A&M University, College Station, Texas.

boundary. You indicated that these coarsen and that they coarsen very rapidly. It's not an Ostwald ripening mechanism. Do you have any thoughts as to how they're coarsening?

Answer: Dr. Hansen—It is likely that this rapid grain boundary coarsening is due to enhanced diffusion along such boundaries. As far as the precipitate sizes are concerned, they are about 50 Å on initial observation, but grow to >150 Å within 100 s at 950°F. This is a substantially faster growth rate than is observed for the Cb (CN) precipitates on austenitic subboundaries.

Comment: Dr. Abrams—Of course, when one is speaking of diffusion, 100 s may not really be that fast.

Question: Dr. Malcolm Gray[5]—Did I understand you correctly when you said you did not think precipitates were involved in that equilibrium between the temperature and limiting grain size? There are people probably better qualified than I am here to address that subject, but in my experience, I would have thought that precipitates were one of the most important facts. I do not know whether Dr. Pickering would agree.

Answer: Dr. Hansen—Let me comment first, if I might. Although the presence of precipitates may influence the grain size/temperature equilibrium, via a Zener-Gladman type of precipitate/boundary interaction, it might be fruitful to point out that recent data developed by Dr. Lee Cuddy of U.S. Steel seems to indicate a limiting grain size in plain carbon and vanadium steels as well.

Question: Dr. Gray—Is it the same size?

Answer: Dr. Hansen—In Dr. Cuddy's work, vanadium and plain carbon steels approached a limiting grain size of about 40 μm, while the limiting grain size for columbium steels was about 20 μm. A similar effect has also been observed by Sekine and Maruyama (see Ref *14* of Cohen and Hansen's paper).

Comment: Dr. F. B. Pickering[6]—The question of a limiting refinement of the austenite grain size and the resulting transformed ferrite grain size produced by thermomechanical processing is an important one. In the case of the recrystallized austenite grains, one must consider not only the nucleation at deformed grain boundaries, sub-boundaries, deformation bands, and other lattice defects, but also at dispersed particles. The size of such particles that can act as recrystallization nuclei is also of crucial importance. In addition, particles may also limit the grain growth of the recrystallized austenite by a grain boundary pinning effect. There is

---

[5] Microalloying International, New York City, N.Y.

[6] Sheffield City Polytechnic, Sheffield, England.

clearly going to be some critical particle size at which particles can change their behavior from inhibiting recrystallization to accelerating recrystallization. Thus, one needs to study what affects the size distribution of not only the undissolved particles but also those precipitated during thermomechanical processing. Such factors as the degree of supersaturation and the defect induced nucleation may be anticipated to be important. The matter is presumably one of the energy balance, and if one continually refines the prior austenite grain size, the total grain boundary energy of the system will increase to some limit at which the energy available in the deformed and recovered structure is insufficient to balance it. Do we know what this limiting grain size is?

Also, the equally important question of the ferrite grain size produced by transformation of the thermomechanically processed austenite requires to be examined, as this is the critical parameter of relevance to the mechanical properties. Again there will presumably be a limiting small grain size. The factors affecting the nucleation and growth of the ferrite formed during transformation, particularly those influencing nucleation, need to be quantified. However, because there is energy arising from the transformation, the limiting ferrite grain size is much smaller than the limiting austenite grain size. Again one would wish to know the quantitative effects of such features as austenite grain and subgrain boundaries, second phase particles, deformation bands, and lattice defects, as well as of residual solute, on the rate of nucleation. The factors governing the rate of growth of the ferrite during transformation are equally as important, and those governing the grain growth of the fully transformed ferrite structure must also be considered. The experimental difficulties in obtaining such quantitative data are, however, formidable.

Evaluation of Steels for Arctic Line Pipe by Halle Abrams and G. J. Roe

Question: F. Sczenzenie[7]—Could you perhaps comment on the microstructural rationale for the small positive effect of carbon on the 85 percent shear test results?

Answer: Dr. Roe—There are a couple of things to point out, and I only use the following as an example. First, we're working within a very tight chemical compositional range—the carbon varied only from 0.08 to 0.13. Secondly, carbon was the least important in the regression analysis work. It was the fifth or sixth term to kick out. So it's pretty far down the line.

Comment: Dr. Abrams—When doing regression analysis, one often has to take into consideration very strong interactions between the independent variables. If you looked at the independent variables we used, you

---

[7] Special Metals Corp., New Hartford, N. Y.

noted that there were several that strongly interacted. For example, percent total cumulative reduction is very strongly interactive with average mill load. You could get an inverse effect, where the total cumulative reduction is going in the expected direction and also takes into account the effect of average mill load; but then the coefficient of average mill load would be altered and might even become negative because of this interaction effect. And this interaction and the resulting inconsistencies are something you can't avoid, because the time-deformation-temperature interactions during processing are indeed extremely complex. And which is the lesser of two evils? Trying to represent 90 percent of what's really happening in the steel, or just representing maybe 50 percent of what's happening because one fails to take into account additional parameters that interact.

Now, in the case of carbon, as Dr. Roe pointed out, it would probably influence the drop weight, let's say, plus or minus two degrees over the temperature range we're talking about. So it could be an inverse effect, or it might be just a total ambiguity.

In view of the frequently complex higher order interactions and the consequently complex regression analysis, we deliberately did not give the regression coefficients, because we didn't want such coefficients to become, as it were, *the final word.* You know, the kind of deceptive simplication where you multiply carbon by, say, 0.437, and you think you've got it. So, rather than give coefficients that could be falsely restrictive, we chose to show the trends or directions in qualitative terms.

Question: F. Sczenzenie—Perhaps I understand you to mean there is no microstructural rationale for that particular result?

Answer: Dr. Abrams—Yes, that is the case, although in the course of our study we did take into account microstructure. You see, one of the problems is that a statistical empirical analysis can sometimes be at variance with the conclusions one might get from a strictly physical metallurgical approach. It's simply very tough to make these two approaches come together, and sometimes you get results you can't explain. I believe Dr. Roe has one more slide he didn't use in his presentation that would be helpful in demonstrating the contributions of a statistical empirical approach. (See Tables 4 and 5 on p. 94.)

Comment: Dr. Roe—We didn't make all these heats at one time. Over a period of time we made four heats and used this information to predict what we expected to get for the subsequent heats (especially for the vanadium-columbium heats). Some of our guys didn't have much faith in Dr. Abrams' predicted values, especially for yield strength; yet, as these subsequent heats showed, the predicted values were quite accurate.

Comment: Dr. Abrams—As Dr. Roe pointed out, in this study we were able to effectively use regression analysis to predict the mechanical properties so that once the chemistry was known, the processing could be adjusted to achieve the desired properties. Specifically, this is what we did: we processed four heats, and, based on these four heats and the properties obtained, we predicted what the properties would be for the next three heats. For example, for 0.630-in. plate, we predicted an 80 ksi yield strength for vanadium-columbium plate.

And some of the fellows up at our research labs just didn't believe you could get that high a yield strength with a vanadium-columbium grade. In fact, when I gave them my prediction, I granted that the yield strength value was probably high. The average measured value was 80.5 ksi. And then with CV_{15} transition temperature, and drop weight, others from our labs were at first quite skeptical on this one, because they're usually within 50 or 60 degrees when trying to do similar kinds of things—and here we were predicting the drop weight shear within 10 degrees. These numbers are extremely impressive to me.

I don't say that we're all the way there yet. After all, as Dr. Roe pointed out, we were working with only a very narrow range of alloying and a narrow range of processing. Nevertheless, the fact that we got as close an agreement between predicted and measured as we did is pretty good, considering that a property such as the drop weight shear can vary all the way from −80 to +60, depending on chemistry and processing. And so I think that this type of application is where regression analysis can be really useful.

Question: Dr. H. Solomon[8]—These pipeline steels are all welded together, but I haven't heard anybody mention anything this morning about the properties of the heat-affected zones of the welds. How do they change and how does the structure change in the heat-affected zone of the weld?

Answer: Dr. Abrams—We didn't dodge this issue. Dr. Roe was talking at about 88 rpm to get in at least the highlights of a project that represented about three and a half years of work. The internal report on that work was a pretty thick one. In that report are all the welding studies, and that's really the topic of a separate paper.

I would like to make this comment. People have had problems with the hardness tracing across the heat-affected zone. The hardness was a problem for us, too, but that's because some of these specifications were changed as rapidly as the weather. In the case of several specifications, they asked for a pre-mill qualification requirement as well as what we would do under normal production conditions.

---

[8] General Electric Co., Schenectady, N. Y.

I think one of the problems was that we had to use a 1-kg load for the pre-trial, but then for the actual production pipe, we were able to go to either a 30- or 10-kg load, I've forgotten which. The scatter band with the 1-kg load was much greater than with the higher load. So we found that several of the steels we tested didn't meet this particular hardness requirement. But I don't think that's a serious problem.

Now, the work done by our welding group goes into a lot more of the details of this—the effect of alloying and diffusion, and things of that nature.

Question: Dr. Solomon—Specifically, do you get any grain growth right next to the weld in that portion of the heat-affected zone right at the fusion line?

Answer: Dr. Abrams—Of course. If you look at the microstructure, going from the weld through the fusion line into the base plate, there's no question but that you have transformation products—you have a bainite/acicular ferrite and some martensite, and then you get a much coarser ferrite than you have in the base plate. That's why it's a heat-affected zone.

Question: Dr. Solomon—I'm surprised that you say there's very little difference in properties?

Answer: Dr. Abrams—I didn't say that there was *no* difference in properties. In this sort of thing one gets into the whole problem of just how one tests for heat-affected zone properties. For example, with respect to notch toughness, after you etch the weld area and reveal the curved fusion zone, where do you put the notch to effectively measure the HAZ notch toughness? Is it at 1 mm, 3 mm, or 5 mm from the fusion line? The effect of test procedures and the interpretation of results would require a separate paper. Naturally, when you get the kinds of microstructural changes previously mentioned, there will be some deterioration of properties in the heat-affected zone. But the point is that if the base plate has the right properties to begin with and the proper welding practice is followed, the HAZ properties will still meet the specifications for Arctic requirements, which is what we as the producer are trying to do.

Question: Dr. Solomon—One other question. These materials look like they would have very anisotropic properties, especially impact properties with this long, elongated structure. Do you find that there is a significant amount of anisotropy, and if so, what is the direction of crack growth in your impact measurements that you reported?

Answer: Dr. Abrams—All of the data is transverse data that we're reporting, which is the worst direction of testing. The longitudinal direction would, of course, be much superior.

Question: Dr. M. Korchynsky[9]—You have shown that the difference between the strength properties of plate and pipe necessary to meet X70 specifications can be traced to the strap tensile testing. You also have shown pretty good correlation between the true yield strength of the engineering product line pipe, as measured by the ring expansion test, and by the machined round tensile test. I have two questions.

First, what are the chances to introduce the machined round tensile test into the line pipe specification and eliminate the misleading test performed on flattened straps?

Second, do you have any information whether the difference between the minimum plate strength properties needed to meet specified pipe properties could not be decreased by reducing the Luders band expansion by means of accelerated cooling from the finishing temperature to, say, 1200 or 1150°F?

Answer: Dr. Roe—I don't really think accelerated cooling would probably help these steels because we're talking heavy-gage plate. Let me point out in response to the first question that right now I think the only acceptable test is the strap test. And this bothers me a little bit. The producer is going to manufacture the pipe in accordance with the specs for the pipeline. But something the users have to consider is that even for the columbium-molybdenum steels that work harden, when measured by the ring test, they have a yield strength of 80 000 psi just like the vanadium-columbium. If you're going to measure the pipe by a ring test, I wonder if anybody has considered that they're measuring only 70 000 psi on the strap test but really they have an 80 000 or 90 000 psi yield strength piece of pipe. How does this affect their fracture toughness requirements?

What I'm saying is, if I was going to do it, I'd pick a more representative test, which I believe to be the ring test, or, a machined tensile would be another possibility.

Comment: Dr. Abrams—I'd like to add something. What we hoped to show here was that the user is deceiving himself. He's getting this extra strength that he's requiring in the strap test at a sacrifice in toughness. And all of his models for ductile running fractures, which are based on strength, will then be screwed up.

To answer your question specifically, E. Jonas from our central metallurgical group has a proposal before API for the use of a machined round tensile in evaluating the pipe yield strength. I think that if we can present enough data to support this proposal, it could become a reality.

As to the second question about the Luders extension, I agree with Dr. Roe only from the point of view that it's kind of impractical to do accelerated cooling on the plate mill. That is the main limitation. But you could probably get some benefit from it via continuous yielding.

---

[9] Union Carbide Corp., Pittsburgh, Pa.

But one of the things that I have found that is very strange—and I have data to support this—is that, if you test enough specimens, you find that some of the acicular ferrite grades that are supposed to have continuous yielding behavior actually don't all have continuous yielding behavior. Likewise, some of the vanadium-columbium grades that have discontinuous yielding behavior and Luders extensions sometimes have continuous yielding behavior.

Comment: Dr. Korshynsky—I would like to point out that the practicality of accelerated cooling of plates at least up to ¾ in., has been demonstrated, as reported in a paper by J. D. Grozier, published in *Proceedings Microalloying '75* pp. 241–250. The effect of accelerated controlled cooling on improvement of properties of plates has been reported also by researchers, K. Tsukada et al of Nippon Kokan.

Answer: Dr. Abrams—I'm not saying it's not feasible; it's very feasible. It's just a question of paying for the facilities and so forth.

Question: G. Delvecchio[10]—Is it practical to use a plate yield strength of 89 ksi if the required flattened strap yield strength is 70 ksi?

Answer: Dr. Abrams—Definitely not! Again, there's the question of the economics. You could develop a rolling practice, consistent with your mills, to achieve the specified properties. Because you want to have sufficient product yields, you just don't want to be rejecting plates like crazy after you put this much money into it, and you know it's not going to go into pipe.

The other thing that you have to be very careful of, and I don't think this point came across, is that these two sigma 95 percent confidence intervals can be very misleading. Because it doesn't mean, if you have a plate say, 77 ksi, that it won't be a 70 ksi pipe. In other words, we're saying that at a 95 percent confidence level you want minimum 89 ksi plate and then you will be assured of making X70 pipe. And in the paper, I think we have some examples. With regard to the Battelle drop weight requirement of +23°F in the pipe, it has to be −10°F in the plate to assure this requirement at a 95 percent confidence level. And there were four plates, one might have been +7, one might have been −5, and they were not −10 but they still made pipe that were within +23. And all that meant was that the plate-to-pipe shift for these particular pipes plus the two sigma variation that you're trying to predict from the data was less than expected; so you were able to still meet the pipe requirement.

Question: G. Delvecchio—The present specification for the Alaska Highway Pipeline requires a CV_{100} energy of 80 ft·lb. Have you done work examining the CV_{100} energy?

---

[10] The Steel Company of Canada, Ltd., Hamilton, Ontario, Canada.

Answer: Dr. Abrams—Yes, we have. When we get into the data, we can also see what the CV_{100} is, because we rate the fracture appearance of each Charpy test specimen and plot full Charpy fracture appearance and energy curves. The way you would do this is to go to very low carbon and to very low sulfur. With these conditions, we have seen CV_{100}'s in excess of 100 ft·lb. But I would hate to have to agree to that kind of a number. It should realistically depend on the design temperature.

Once again, I think this is where the specification writers or the users of this pipe are not necessarily being practical, because if you combine your chemistry and processing, you can reach 100 percent shear at, say, −60 or −100. And your CV_{100} at that point might be 40 ft·lb. But at the design temperature, let's say −10, since your curve is constantly rising, it might be 80 or 90 ft · lb. And again they're asking for a requirement that has no relation to what the pipe has to do in service at the design temperature. And I hope there are some pipe users out there. This is where some education has to come in. Because you just don't get CV_{100}'s of 80 ft · lb for free; and if it turns out to be at −60 or −80°F, they don't need it.

Question: G. Delvecchio—Can you comment on splitting in these steels?

Answer: Dr. Abrams—Actually, that's another paper, but here are some brief comments.

Obviously, if you go into the two-phase region or if you do very severe controlled rolling, you do get splitting. And when you get splitting, you get lower shelf energies. Surprisingly enough, the conditions at which we rolled these pipe had only very minimal splitting. But this whole presentation—and what we're showing—has gone through a learning experience.

If a few years ago somebody had said, "I want 85 percent shear at −50 or −60°F in the plate for ¾-in. plate," you would have laughed at him and wanted to add 3 percent nickel or something like that. But users want to get specified properties without going to expensive alloying. Through this learning curve, we did try novel and relatively extreme processing conditions, and you might be familiar with some of the continuum rolling work that was reported out of Bethlehem. In this work, we did see extensive splitting. And I think Dr. Bruce Bramfitt just published one of the papers on splitting observed in our laboratory.

But now we're trying to avoid splitting, because it's a fracture result we do not want. And so you could compromise and raise your finishing temperature sufficiently to try to avoid splitting.

Question: L. Luyckx[11]—You mentioned sulfurs between 0.002 and 0.010 as one of the chemical variables, and you mentioned also that all

---

[11] Reactive Metals and Alloys Corp., West Pittsburgh, Pa.

your plate was tested in the transverse direction. Other studies have shown some major property differences between these two values, suggesting that you could have variations between 0.002 and 0.010 sulfur and you never mentioned that in your results. Could you elaborate, please?

Answer: Dr. Roe—The earliest heat was the 0.013 sulfur, the last heats we made were 0.002 to 0.003, the highest was 0.006. They were desulfurized hot metal plus a misch metal plunge in the ladle to get the sulfur way down and get the shelf energies up.

Control of Microstructure by the Processing Parameters and Chemistry in Arctic Line Pipe Steels by C. Ouchi, J. Tanaka, I. Kozasu, and K. Tsukada

Question: Dr. M. Korchynsky—First, what was the maximum gage of plate to which accelerated cooling was applied?

Answer: K. Tsukada—The accelerated cooling is basically applicable to any thickness plate.

Question: Dr. Korchynsky—What was the gage in your experiments?

Answer: K. Tsukada—The plate thickness investigated here was 20 mm.

Question: Dr. Korchynsky—Was the shape of the stress-strain curve of plate subject to accelerated cooling different from that of hot rolled and air cooled plate? Particularly, was the yield point or elongation any different?

Answer: K. Tsukada—Most of the steels showed the yield point if the suitable controlled rolling is taken before the accelerated cooling. In a higher cooling rate above 20°C/s or in the relatively higher carbon equivalent steels, the yield point tends to disappear. However, ductility such as elongation is not changed by the accelerated cooling.

Question: G. Delvecchio—You presented some data showing the effect of titanium for improving toughness of the plate. Is this effect applicable to the hot strip rolling of skelp?

Answer: K. Tsukada—Yes, titanium addition is useful in a strip mill rolling. Titanium nitride prevents the growth of austenite grain size in addition to the refinement of the austenite grain size attained at the slab reheating temperature. We confirmed the beneficial effect of the small amount of titanium on toughness in hot strip mill process.

Question: G. Delvecchio—What are the limitations of using a titanium nitride mechanism?

Answer: K. Tsukada—The amount of titanium addition is very important, because it depends on that of nitrogen. The cooling rate of solidification process is also important to obtain finely dispersed TiN.

Question: Dr. M. Gray—Do you find that the amount of titanium or nitrogen or the titanium to nitrogen ratio that you use for control of grain coarsening is affected by the vanadium and niobium levels? That is, do you have to adjust the amounts or the ratio when you have other microalloying elements present?

Answer: K. Tsukada—Titanium addition is 3.5 times nitrogen content. The formation of TiN might be affected by vanadium or columbium, but the effect is not clear.

Question: Dr. Gray—You don't change it—you always use the same 3.5 to 1 ratio?

Answer: K. Tsukada—All the same.

Question: L. Luyckx—The effect of quench and temper on the properties was tremendous, but you showed the first improvement after accelerated rolling.

My question is, do you still need accelerated rolling when you're going to ultimately use the quench and temper practice in the pipe? In other words, does it make any difference in the quench and temper properties whether you've applied it to as-rolled steel or after accelerated cooling practice?

Answer: K. Tsukada—Accelerated cooling and quench and temper treatment after pipe forming is a completely independent process. Accelerated cooling in plate is not necessary for heat treatment after pipe forming. Although both processes give rise to different effects to the properties, production costs in each process are also different.

Question: L. Luyckx—Regarding your quench and temper results, were they after accelerated cooling or as rolled?

Answer: K. Tsukada—As rolled.

Influence of Microstructure on the Temper Embrittlement of Some Low-Alloy Steels by R. Viswanathan

Question: L. Luyckx—In one of your very first slides, you showed *very pure steel* with that curve going down from the top; what do you mean by *very pure steel?*

Answer: Dr. Viswanathan—The *pure* steel contained phosphorus, sulfur, antimony, and tin below about 15 ppm. Details regarding the composition of the steel are provided in Ref. *1* of my paper.

Question: Dr. S. Banerji[12]—Molybdenum is fairly well known to be an inhibitor of temper embrittlement; why would you expect any kind of temper embrittlement in a chemistry loaded with molybdenum?

Answer: Dr. Viswanathan—The effect of molybdenum on temper embrittlement is rather complex. It may be beneficial or detrimental depending on the level of molybdenum. Interaction effects between chromium and molybdenum are also important in this connection. Furthermore, for a given nominal bulk composition of molybdenum, the molybdenum content of the ferrite matrix decreases with prolonged tempering. This could lead to attendent changes in segregation of impurity elements to grain boundaries.

Question: Dr. Banerji—In the tempering kinetics, when you said the alloy carbide begins precipitating, you lose molybdenum from the ferrite, so, you are losing the effect. As long as you are in a range where you can hold molybdenum in solution, would you not expect a suppression of temper embrittlement?

Answer: Dr. Viswanathan—It is not clear to me whether the low temper embrittlement susceptibilities reported for Cr-Mo steels reflect the true embrittlement behavior of these steels or whether it is due to the fact that the steels have not been exposed under the conditions producing maximum embrittlement. Presently available data are inadequate to resolve this question.

Question: Dr. Banerji—What I really think I am asking is, is temper embrittlement as critical in Cr-Mo-base steel as it is in Ni-Cr-base steel, for example?

Answer: Dr. Viswanathan—In general, available data suggest that the Cr-Mo-type steels are less susceptible to embrittlement than steels that contain nickel and chromium in combinations.

Comment: Dr. R. Swift[13]—I do not want to defend the data, I just want to explain something. When we started to look at commercial Cr-Mo steels, we were trying to determine the susceptibility of a plate once it got out into the user's shop. In looking back, we could have done things a lot differently. Had we been smarter in the beginning, we would have taken smaller sections and water quenched them after tempering. Any embrittlement would then be a measure of the true susceptibility of the material. That would have helped to eliminate a lot of the confusion that has resulted from trying to interpret early data. You are looking at relative effects of different heat treatments on susceptibility to embrittlement. I

---

[12] Foote Mineral Co., Exton, Pa.

[13] Lukens Steel Co., Coatsville, Pa.

think that the work you and Prof. McMahon of the University of Pennsylvania have done shows that Cr-Mo steels have a low susceptibility to embrittlement. I agree with you, the data is often very confusing.

Question: R. Gaitonde[14]—About the level of impurity elements in commercial heats—what do you think is the minimum amount of antimony or phosphorous you could have before you can eliminate temper embrittlement from rotor forgings? Can you really attain that?

Answer: Dr. Viswanathan—I really don't have a simple answer to the question. All we know is that in terms of embrittlement potential, antimony is the worst, then tin and phosphorous in that order. Tolerable levels for each element would, of course, depend on the alloy chemistry, strength level, grain size, and numerous variables. Because of this, it is difficult to write specifications for impurity elements without regard to the other parameters.

Question: R. Gaitonde—My actual question is that Westinghouse is a turbine manufacturer, and I represent a utility who buys turbines from Westinghouse. Could Westinghouse supply us a rotor now with a more controlled chemistry or do you buy one with a more controlled chemistry that is less susceptible to temper embrittlement than the early '50s or do you still buy to the same specification you had then?

Answer: Dr. Viswanathan—By and large, turbine steels today are of much better quality than those produced 30 years ago and impurity levels have steadily gone down; but we are not at a point where we can lay down stringent requirements in terms of impurity contents, since we don't have quantitative data relating steel purity and the component performance. We had a simple solution to the temper embrittlement problem 15 years ago; we had found that if you eliminate carbon from steels, you will have embrittlement-free steels. The steel manufacturers won't agree to this proposal for some strange reason!

Question: L. Luyckx—The rare earths are known to be making intermetallic compounds with all those tramp elements you were mentioning. I'm sure you've been looking at that before; cerium, lanthanum, and praseodymium produce very high melting point intermetallics where they meet at the grain boundaries with lead, tin, antimony, etc. All those elements are insoluble and they tend to eliminate some of that temper embrittlement. Is that right or wrong?

Answer: Dr. Viswanathan—I am not aware of much published work concerning the addition of rare earth elements to eliminate temper embrittlement. One should be careful to ensure that low melting rare earth

---

[14] Commonwealth Edison, Maywood, Ill.

intermetallic compounds (for example lanthanum-nickel compounds) are not formed at grain boundaries, since this would impair the forgeability of the product.

Comment: L. Luyckx—That's right. The rare earths are insoluble as well as some of the other elements such as lead, bismuth, etc., so the only useful way to use them is as getters. In other words, the rare earth metals go after oxygen, sulfur, and those tramps to form intermetallics at grain boundaries. If that's exactly the quantity that is used, then you eliminate embrittlement. If you go beyond that, then of course you create a problem with the lanthanum-nickel lanthanum-chromium intermetallics or eutectics at the grain boundary.

Answer: Dr. Viswanathan—A range of concentrations of the rare earth element may have to be explored to identify the optimum level of the additions.

Comment: R. Anderson[15]—We did some work on a high-temperature alloy indicating rare earths may be used to control *tramp elements*. We added lanthanum to an experimental heat of 901 to remove sulfur. By monitoring the sulfur level of the bath and making a controlled addition of lanthanum, we were able to remove sulfur to a very low level (<5 ppm) and also prevent the occurrence of any lanthanum-nickel intermetallics. We concluded one can control the intermetallic if one is very careful with the addition.

Comment: Dr. M. K. Koul[16]—All your data showed that all these impurities, phosphorus particularly, go to the grain boundaries. And in my boron steel work, I know that the hardenability effect you get is from boron going to the grain boundary. So, I ran an experiment with steel at various levels of phosphorus—0.01, 0.02, 0.04, and at a fixed boron level. And what I found there was that after 0.02P, the boron hardenability effect was not present. The boron hardenability effect, which is due to the free boron at the grain boundaries, was absent due to phosphorus-boron interaction, and so I thought that this would be a very good way of working against the phosphorus segregation, that is, the effect of phosphorus on temper embrittlement, with the boron addition.

And since then, we have run some experiments. Not extensive, but some experiments, where we have added controlled quantities of boron with titanium, zirconium, and vanadium to varying degrees, that is adding vanadium as you have—0.1, 0.2, or so—and together with that vanadium, have some boron, titanium, and zirconium, and we do see some improvement in temper embrittlement.

---

[15] Universal Cyclops Specialty Steel, Bridgeville, Pa.

[16] Foote Mineral Co., Exton, Pa.

Comment: Dr. Viswanathan—I find the results regarding the beneficial effects of boron on temper embrittlement to be quite interesting.

Structure-Property Relationships for Pearlite-Reduced Mo-Nb Steels Finish-Rolled Moderately Below Ar_3 by A. P. Coldren, G. T. Eldis, and G. Tither

Question: Dr. Abrams—I'm just curious as to how you could put a certain slope to your strength results and attribute so much of your strengthening due to substructure if you didn't actually measure the substructure; for example, how well it developed, what the subcell size was, or something along those lines.

Answer: Dr. Coldren—Just by reasoning. In a zero niobium steel, there would be no precipitation strengthening, so after correcting for grain size differences any remaining effects can be ascribed to substructure.

Question: Dr. Abrams—All right, but how did you come up with the slope of the substructure line? Did you just use a standard Hall-Petch slope and attribute it to that?

Answer: Dr. Coldren—I'm not sure which diagram you're referring to.

Question: Dr. Abrams—You've normalized everything to ASTM grain size 11, you start out with some base strength, and you have a contribution due to substructure and everything left over is due to total precipitation. How do you know what was due to your substructure if you didn't measure how much substructure you had in your final microstructure?

Answer: Dr. Coldren—This is on the assumption that only substructure plus precipitation could cause strengthening after you take out the grain size effect. I can't think of anything else that might have caused the increase. In a zero niobium steel, there can be precipitation.

Question: Dr. Abrams—That gives you your intercept, but how do you know what the slope of your substructure component is going to be, based on the amount of deformation you introduce?

Answer: Dr. Coldren—We just drew a line through the three points. The line is purely empirical.

Question: Dr. Abrams—But you still don't know what the substructure associated with those points is?

Answer: Dr. Coldren—No, I don't. We didn't quantify it. All I know is that's what you get when you have 30 percent ferrite deformed 20 percent. And what else can it be besides substructure if there can be no precipitation effect?

Question: Dr. Abrams—There's something bothering me about how you normalize all these interactions out. Maybe somebody has some comments?

Author's written comment—The only normalization was to correct the yield strength values to a common grain size, ASTM No. 11, using the Hall-Petch relationship with a K_y value of 20 N/mm^2/mm$^{-1/2}$ (0.58 ksi/in.$^{-1/2}$).

Question: J. M. Leitnaker[17]—On your last rolling, last pass, what was the reheating cycle?

Answer: Dr. Coldren—There was no reheating on rolling; it was carried out on a falling temperature.

Question: J. M. Leitnaker—You don't go back up in temperature?

Answer: Dr. Coldren—Once we started rolling, the temperature was falling continuously.

Question: G. Delvecchio—How did you measure your temperature? With a pyrometer or with a thermocouple?

Answer: Dr. Coldren—Embedded thermocouple at the midthickness, midwidth position.

Question: Dr. Koul—If you could find out the amount of columbium in solution, could you find out how much columbium has precipitated and how much has not?

Answer: Dr. Coldren—By extracting and analyzing? Yes, I suppose.

Question: Dr. Koul—The other question I had was, how does this differ from the U.S. Steel work?

Answer: Dr. Coldren—It's quite similar, I believe. Their patented process plus composition—in the processing, as I recall, they recommend rolling to obtain 10 to 40 percent ferrite—deformed ferrite—and their composition is quite similar to our 0.2Mo-0.06Nb steel, except that they had 1.2Mn instead of 1.4Mn. I understand that more recently they have changed their composition, but originally that's what they were using.

Question: Dr. Koul—And I think the amount of deformation that you use below the transformation temperature is to control the amount of splitting rather than anything else; and that the amount of splitting increases as the amount of deformation increases.

Answer: Dr. Coldren—Our results seem to confirm that idea.

---

[17] Oak Ridge National Labs., Oak Ridge, Tenn.

Question: Dr. Abrams—I'd like to go back to the substructure question. Is it possible that the amount of recovery with the alloyed material is such that at 10 or 15 percent deformation you don't have this dislocation substructure?

Answer: Dr. Coldren—This is not 15 percent deformation. This is volume percent of deformed ferrite. It's all at 20 percent deformation.

Comment: Dr. Abrams—This still doesn't explain what's happening.

Question: Dr. F. B. Pickering—When we introduce a given deformation into a steel comprising a duplex structure, do we know the distribution of strain in the two phases? Presumably, because the material is being plastically deformed, this will depend on the respective flow stress values and work hardening rates of the two phases, and, of course, on their volume fractions. Don't you think that this strain distribution would have a marked effect on the subsequent behavior of the steel?

Answer: Dr. Coldren—At this temperature, you may have a point there.

Comment: Dr. Pickering—The analysis of the effect of microstructural variables on the properties of acicular ferrite structures is complex, particularly when there are recovery substructures, such as subgrains, present. The total strengthening over and above grain size and solid solution strengthening is by no means solely the result of precipitation. In fact, it comprises at least three terms, namely, precipitation strengthening, subgrain boundary strengthening, and *forest* dislocation strengthening. Whiteman[18] has analyzed such strengthening in these terms, but it is also possible that there are further complications due to solute-defect interactions. Moreover, when we have such elements as niobium and molybdenum present, they can markedly retard recovery and thus lead to it being necessary to apply this rather difficult type of analysis. However, the results of Whiteman do indicate that the analysis has much to recommend it.

Comment: Dr. Abrams—That's the thing that bothered me. In our continuum rolling studies, we observed very complete substructure by means of electron microscopy and saw very well-defined subcells, and, with this microstructure, we were getting strength increases like 40 or 50 ksi. Whereas if you just had dislocation tangles and things of that nature, then I think you'd see the types of strength increases you're seeing in your study.

---

[18] Whiteman, J. A., "Low Carbon Steels for the Eighties," Institution of Metallurgists Spring Residential Conference, Manadon, April 1977: published by the Institution of Metallurgists, London, England.

Controlled Processing of Molybdenum Bearing Line Pipe Steels by G. W. Delvecchio, J. E. Hood, and D. B. McCutcheon

Comment: Dr. Abrams—You could go back to our paper where Dr. Roe presented a plot of pipe yield strength at 0.5 percent offset versus plate yield strength at 0.2 percent offset. This plot showed that at the highest strengths you lose more strength, and Tanaka showed the same thing at the Microalloying '75 Conference.

We tried to correlate the delta strength with chemistry and microstructural variables; and the only thing it correlated with was the initial yield strength. So the point I want to make is that although you get significant work hardening with a high manganese, columbium-molybdenum grade, which we used in our mill trial, you might be at a 90 ksi yield strength level in the plate. But when you make your strap test from the pipe, you might lose as much as 18 or 20 thousand and still come back to a pipe yield strength of 70 ksi.

The other point is that you had said it is beyond the scope of your paper to look at circumferential properties.

Comment: G. Delvecchio—The Japanese have done that to some extent.

Comment: Dr. Abrams—Well, we at Bethlehem also looked at these properties. What we did is this: with reference to the 89 pipe we produced, we chose a continuous yielding material—a high manganese, molybdenum-columbium grade and then a vanadium-columbium grade, which is discontinuously yielding, and we selected several pipe. We took round, machined tensiles at various positions from 12 o'clock, 1 o'clock, 2 o'clock, 3 o'clock, all around the circumference; and then the other thing we did, which is really interesting, was we actually made sheet tensile specimens to represent the outer fibre, which would be in tension, a center section, and then inside diameter, which is in compression. And we got some interesting results.

Although these were preliminary results and, of course, require verification, they do explain a lot about what is happening with these two grades. That is, when you talk about the pipe, the U and O processing, the strain rates, and the amount of strain across the width of the plate, what you see at 6 o'clock, you don't see at 4 o'clock, or at 1 o'clock. And so a grade that appreciably work-hardens is going to be very susceptible to the amount of strain and strain rate that you're putting in, whereas let's say a grade that doesn't, might not. And you can see some unusual results. For example, when your neutral residual-stress axis through the thickness is not at the midpoint.

It's interesting that a lot of people are aware of a lot of the same things and are working on them, but since these things cost a lot of money to do, it would be good if we could join together and say, "you do this, I'll do that, and share the workload." I just wanted to make these comments.

Comment: G. Delvecchio—Can I refer you to a presentation that was made by F. Christensen at the CIM conference, where we presented some of our results. We've done the same thing. We used round specimens. And the differences that we found—probably the same results—you get a very high yield strength on the outer fiber, and you go down to a very low level on the other side, and it's amazing how much strength difference there is.

Question: F. Logan[19]—Dr. Gray in the Italsider paper indicated that the martensitic-austenitic islands in the manganese-molybdenum steel resulted in inferior sulfide stress cracking resistance. Have you looked at this in your high manganese steels at all?

Answer: G. Delvecchio—We are looking at it right now. I don't think I can divulge any data or tell you what the results are, but it's being done. This may be presented at a later date.

Written answer: G. Delvecchio, J. E. Hood, and D. B. McCutcheon—We have conducted studies examining the hydrogen induced cracking behavior of several line pipe grades using both the Shell[20] and BP tests.

With the Shell test, we examined the sulfide stress cracking behavior of the following types of steel: (*a*) conventional ferrite-pearlite steels, (*b*) partially acicular C-Mn-Mo-Cb steels, (*c*) fully acicular C-Mn-Mo-Cb steels, (*d*) SAW weld metal from the preceding steels (welds were made with Linde 585X flux in combination with both Linde 44 wire and experimental Stelco wire), and (*e*) HAZ from the previous steels.

The Shell test results were compared to those of API grades obtained from literature. These included: (*a*) N80—normalized, normalized and tempered, and quenched and tempered conditions; (*b*) J55—normalized condition; (*c*) P105—normalized condition; and (*d*) P110—quenched and tempered condition.

The results indicated that the resistance to sulfide stress cracking of the steels and SAW weld metals was equivalent to or better than that of the API grades at a given strength level. The sulfide stress corrosion cracking resistance of the heat affected zones was comparable to that of normalized J55 or N80 at approximately the same strength level. As yet, we have not examined the microstructural aspects of the sulfide stress cracking failures in these steels.

For the BP tests conducted on partially acicular C-Mn-Mo-Cb steels,

---

[19] Cameron Iron Works, Houston, Tex.

[20] Fraser, J. P., Eldredge, G. G., and Treseder, R. S., *Corrosion*, Vol. 14, Nov. 1958, p. 517t.

we have found that the cracking was associated with inclusions (particularly Type II manganese sulfides). We have not observed cracking related to islands of austenite-martensite constituent. In addition, Climax Molybdenum Company has conducted an excellent metallographic study[21] on samples of C-Mn-Cb-V and C-Mn-Mo-Cb steels cracked using the BP test. They also found that the hydrogen-induced cracks were associated with nonmetallic inclusions and that the main crack paths were not influenced by pearlite or by the presence or absence of martensite islands or bainite.

Question: L. Lucykx—In view of the growing steelmaking challenges with high manganese, low carbon, and low silicon content, I have a question to ask you. What is your *gut* feeling right now on the optimum silicon content and on how silicon affects the properties of your steels. In other words, do you have a silicon specification and what is it?

Comment: G. Delvecchio—For what steel?

Question: L. Lucykx—For these Arctic line pipe steels.

Answer: G. Delvecchio—Our philosophy with respect to silicon is that it is beneficial for developing the partially acicular ferrite structure that we intend to use for Arctic grade pipe. We have produced steels with silicon contents ranging from 0.08 to 0.35 percent, and have shown through regression analysis that silicon significantly raises the strength of the final product without adversely affecting toughness. Thus, we intend to produce steels with a nominal silicon content of 0.25 percent.

Question: L. Luyckx—Have you explained various carbon levels and their effect on properties? Do you feel that extra-low-carbon steels will be required for these large Arctic line pipe orders?

Answer: G. Delvecchio—We have analyzed data from both experimental and production heats of C-Mn-Mo-Cb steel, and have developed regression equations for the effects of carbon and the other alloying elements on the plate strength. For the high manganese heats (1.80 to 2.10 percent), the carbon range was 0.035 to 0.090 percent. Carbon has a very pronounced effect on microstructure, particularly the volume fraction of retained austenite-martensite constituent, which in turn, controls the plate strength (and, consequently, the pipe strength). Although carbon is economical and has a significant effect on strength, it can have an adverse effect on both toughness and weldability. Accordingly, we control the carbon content in balance with the total alloy content. For most of the anticipated Arctic Grade 70 pipe that will be produced, the carbon content will be typically 0.06 percent.

---

[21] Coldren, A. P. and Tither, G., *Journal of Metals*, May 1976, pp. 5–10.

Comment: Dr. M. Gray—I am interested in the work concerning the strain distribution around the perimeter of mechanically expanded U and O pipe and all the unpublished results that exist. I am familiar with other results that are also in the *banned and burned* category. If one examines the same position on the outer perimeter of the pipe, it is found that for some methods of pipe forming, the local strain (measured by X-ray) varies all the way from about 0.5 to about 4.5 percent for a nominal expansion of 1.5 percent. This could give rise to substantial variation in properties, especially for the acicular ferrite type steels that have rapid work hardening rates.

These observations are rather worrying for those people involved in specifying pipe properties and pipe buyers. I guess you're just as concerned as a supplier with a liability for the final product. I think it would be nice if all the people having results that haven't been published, could get together and see if there is any kind of unanimity and what they really mean.

Comment: Dr. Abrams—Since this is really the last paper on HSLA steels dealing with pipe and the other two don't, I might summarize some of the comments that were made about these steels.

Basically, what we're saying is that there are a variety of alloying systems and processing options that can meet the proposed specifications for Arctic applications. And, depending on your melting facilities or whether you want to restrict yourself to a very low-carbon high-manganese grade with the attendant problems in the BOF shop, I think the whole thing is going to boil down to cost effectiveness. None of us have mentioned the costs here, but that factor is certainly present in all of our internal reports. Of course, cost effectiveness, as a function of properties and microstructure, is bound to play a very important role.

Another point: I don't know if we're all going to participate in whatever lines are going in, but we wouldn't in any event all be using precisely the same grade and processing. As producers, we all have to meet the property requirements, regardless of what particular method we each select.

Question: G. Delvecchio—What is the power of your plate mill? And what is the maximum size pipe you can make?

Answer: Dr. Abrams—Well, we have two 160-in. plate mills. Right now our capacity in our pipe mill is 42 in. diameter, and we probably could make a 48-in.-diameter pipe on our pipe mill if we changed our dies; but then on a 160-in. plate mill the width of the plate does not allow much room between the plate and the side guards. Additionally, there will be shape problems—crown and so on. Consequently, I do not think we would be prepared to participate in pipe requirements beyond the 42-in. diameter. As far as our mill capacities are concerned, the Burns Harbor

Mill is rated at 12 million pounds and the Sparrows Point Mill at 9 million pounds. Although we have at times exceeded these capacities in some of our rolling trials, I do not think we'd want to do this sort of thing on a routine basis. What it amounts to is that one has different restrictions, depending on the mill. We as well as other domestic producers do not have anywhere near the capacities that Italsider or the Japanese have.

However, in designing our processing, we put a great deal of study into mill loads and the time-temperature-deformation on our experimental mill at the Homer Research Labs. We then related our findings to what we could get in our big mills, with the result that we could predict the mill loads so the superintendent could go to sleep at night knowing that we're not destroying his mill. Most of the time we were very successful and got to the point where they wouldn't even be around when we did our rolling—the mill people were quite confident that we wouldn't exceed the mill capacity. With maximum productivity as the goal, we tailored our processing to our mill, just as everybody else does. After all, maximum productivity is a key factor in achieving an economic cost.

Author's written comments: G. W. Delvecchio, J. E. Hood, and D. B. McCutcheon—We have conducted a study to develop an understanding of the stress-strain behavior of both low and high manganese C-Mn-Mo-Cb steels during UOE pipe making. In this study, we machined small tensile specimens (mini-tensiles) from 914 mm (36 in.) outside diameter by 12 mm (0.475 in.) wall pipe at five locations through the pipe wall thickness (Fig. 1). The specimens were only taken at a position 180 deg to the longitudinal seam weld and were orientated transverse to the pipe axis. Mini-tensile specimens were taken both before and after the expansion/hydrotest cycle.

In the as-formed pipe condition, both the low and high manganese UOE pipes showed similar trends, with the inside diameter of the pipe having lower yield strengths than the outside diameter of the pipe. On the pipe inside diameter (compression side of neutral axis), there is a loss in yield strength relative to that of the as-rolled plate due to the Bauschinger effect, while on the pipe outside diameter (tension side of the neutral axis), there is an increase in yield strength due to work hardening. For UOE pipe, the 1.5 percent expansion (followed by a 93 percent SMYS of Grade 70 hydrotest) increased the pipe yield strength and tended to reduce the strength variation through the pipe wall for both the low and high manganese steels (Fig. 2).

The stress-strain curves of the individual mini-tensile specimens were combined mathematically to develop a *composite* stress-strain curve that represents the true stress-strain behavior of the pipe. For the limited data, the composite stress-strain curve yield strength correlated with both the ring expansion (true pipe strength) and the flattened strap yield strengths.

(a) TEST SPECIMENS

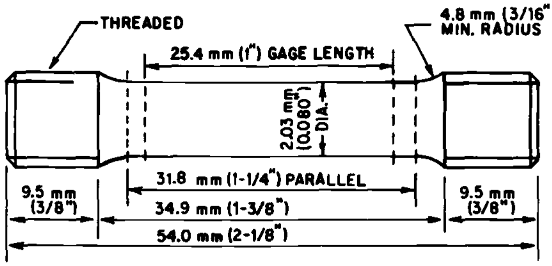

(b) TEST LOCATIONS

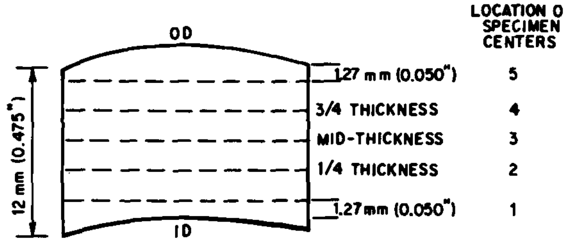

FIG. 1—*Mini-tensile test specimen.*

Previous studies at STELCO have shown no statistically significant difference between the pipe ring expansion and the composite mini-tensile yield strengths. The limited expanded pipe data from this investigation suggest that the ring expansion and mini-tensile yield strengths are equivalent (Fig. 3). The flattened strap yield strength of as-formed pipe agreed with the mini-tensile yield strength (Fig. 4). For expanded pipe, the flattened strap yield strength was significantly (statistically at the 90 percent confidence level) lower than the minitensile yield strength, indicating that the flattened strap test is a conservative measure of the true expanded pipe strength.

Effects of Composition and Gage on the Microstructure of A533-B Steels by R. P. Smith and R. A. Swift

Question: Dr. Korchynsky—In the range of plate thicknesses investigated, is the austenitic grain size a factor that might influence the hardenability? Could this not explain that in thinner thickness, for example, 120 mm, you have more ferrite than predicted by calculation?

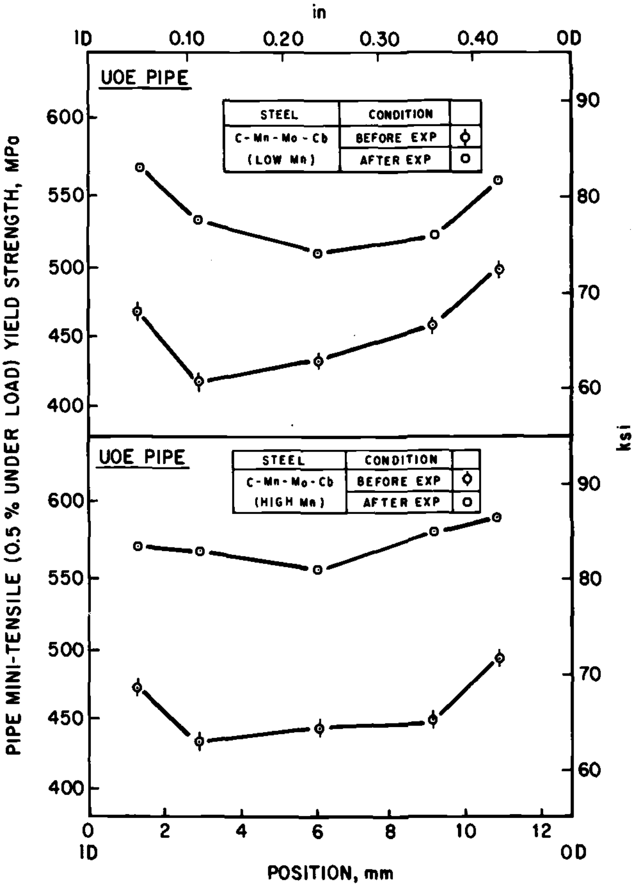

FIG. 2—*Variation in yield strength through the pipe wall thickness.*

Answer: Dr. Swift—Generally, when you take a particular grade of steel, that is not a factor.

At Lukens, we find that grain size of a particular specification is relatively constant. For example, with the Cr-Mo steels, since it is an extremely high toughness material, we use a coarse grain practice to get the higher strengths required of the material while still having acceptable toughness. The opposite is true of Mn-Mo-Ni steels. These steels are produced by a fine grain practice so as to capitalize on toughness since strength is not as critical a factor. I guess that what I am saying is that producers use melting practices that restrict grain sizes over a fairly narrow range so that it is not a critical factor in heat-to-heat hardenability.

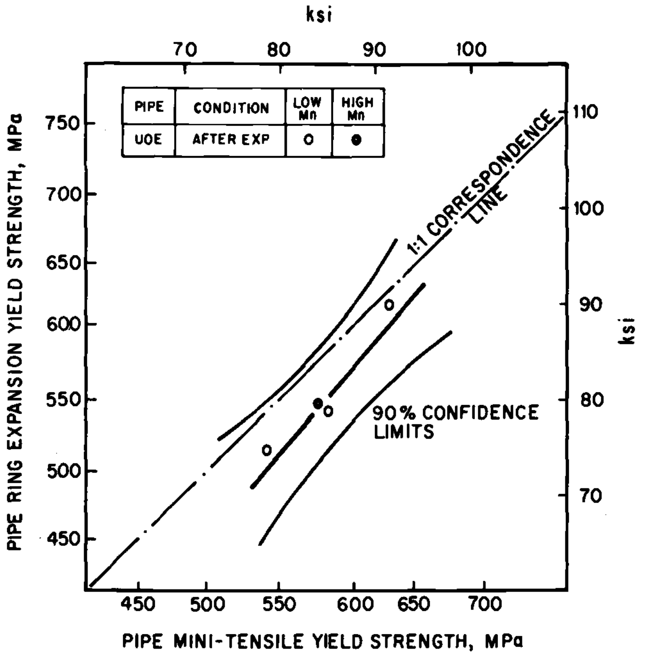

FIG. 3—*The relationship between pipe ring expansion and mini-tensile yield strengths.*

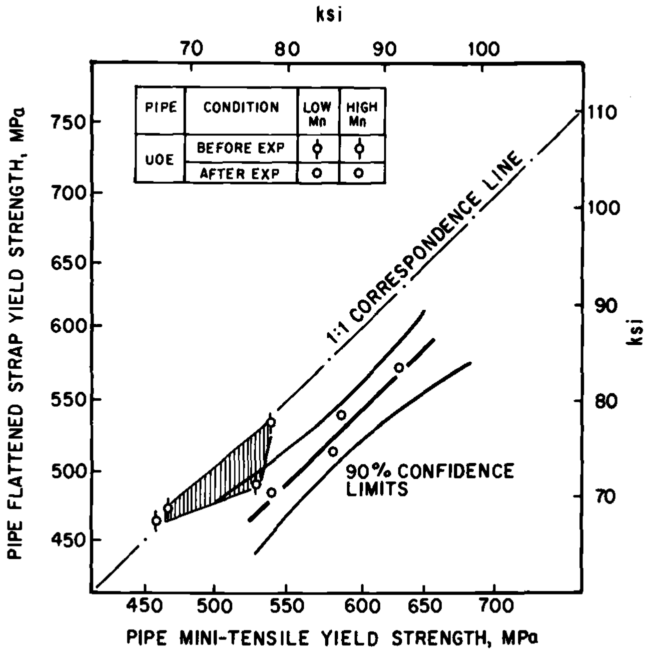

FIG. 4—*The relationship between pipe flattened strap and mini-tensile yield strengths.*

High-Hardenability Carburizing Steels for Rock Bits by D. E. Diesburg

Question: W. Mankins[22]—The slide showing your second specimen was for the fatigue impact test. Superimposed on the test specimen was the outline of what appeared to me to be an involute gear tooth. What is the significance of that shape in your study?

Answer: Dr. Diesburg—Originally, the test specimen was designed to simulate a carburized gear tooth and the fillet radius was put into the specimen to represent a radius that might be expected at the root of a tooth.

Question: W. Mankins—The second question I have concerns the performing of the test. I didn't quite understand from your apparatus whether you had the arm strike the test specimen, manually caught it on the rebound, and returned the hammer to its rest position, or if another method was used?

Answer: Dr. Diesburg—The drop height was adjusted to a few inches. The technician had to catch the hammer as it bounced off the specimen after each impact.

Question: W. Dwyer[23]—How did you measure your residual stresses inside the case? I noticed your depths are on the order of millimeters.

Answer: Dr. Diesburg—The residual stresses were measured by X-ray diffraction on surfaces exposed by electrochemically polishing away successive layers of the case.

Question: Dr. Banerji—Would you explain a little bit more, I don't know how you got the fracture toughness, K_{Id} values from the precracked Charpy specimens. Do you have a carburized case there?

Answer: Dr. Diesburg—Several unnotched Charpy-size specimens of each steel were carburized to have the desired case depth. The specimens were notched by electrodischarge machining, each to a different depth. Fatigue cracks were grown at the base of the EDM notches. This procedure produced a set of specimens for each steel having crack tips at various locations in the case. Fracture toughness is a measure of the resistance to crack extension of the material surrounding the crack tip. Therefore, by measuring the loads required to break each set of specimens, it was possible to calculate the fracture toughness gradient through the case. The K_{Ic} values were calculated using slowly applied fracture loads, whereas K_{Id} values were calculated from loads applied dynamically and measured with an instrumented striker.

---

[22] Huntington Alloys, Inc., Huntington, W. Va.

[23] AC Spark Plug Div., GMC, Flint, Mich.

Stainless Steels

Summary—Stainless Steels Session

The papers of the Stainless Steels Session were grouped in terms of the various types of stainless steels. Emphasis was given to alloy manufacturing as well as use problems. There was a discussion of recrystallization during hot working of austenitic stainless steels and duplex stainless steel tube production. Welding was considered from the viewpoint of narrow gap welding and weld sensitization. The embrittlement of ferritic stainless steels and the ferrite in a duplex stainless steel as the result of thermal exposure was considered and similarities were shown to exist. The corrosion of ferritic steels was also considered as was the corrosion in the ferrite and ferrite-austenite interfaces of duplex stainless steels. The precipitation hardened steels were looked at from the stand point of the kinetics of the precipitation.

As can be seen, these papers covered stainless steels from the ingot to the final product. The microstructure was considered at all stages from initial alloy production to the microstructural effects on service applications, particularly where corrosion is encountered or where embrittlement might result from high-temperature exposures.

The session on stainless steels began with Prof. Pickering's excellent review of the structure-property relationships for the major types of stainless steels. Ferritic, martensitic, austenitic, and duplex stainless steels were discussed. Particular emphasis was given to the relationship of structure to the formability of these steels and to the stability of the microstructure. The subsequent talks were grouped into those dealing with austenitic, ferritic, precipitation hardened, and duplex stainless steels.

Ahlblom and Roberts of the Swedish Institute for Metals Research followed Prof. Pickering in the program. Their paper was concerned with the development of fine-grain microstructures during hot working. Their paper was followed by one by Simpson and Kossonsky of the Westinghouse Electric Research and Development Center. Unfortunately this paper, which dealt with the structure developed in narrow gap welds, is not included in these written proceedings. Nakagawa et al of IHI Ltd. of Tokyo, Japan, discussed the sensitized structures that are developed in welds in Type 304 stainless steel. They compared the sensitization with the prior thermomechanical history of the pipe with the structure that resulted from such treatments. Another paper of the group that dealt with the sensitization of austenitic stainless steel was that of Rao of the General Electric Corporate Research and Development Center. His paper dealt with structures developed during sensitization and with measurements of the chromium depletion that accompanies carbide precipitation. The final paper dealing with austenitic stainless steel was that of Anderson et al of the Sandvik Steel Research Center of Sweden and the Swedish Institute for Metal Research. This paper dealt with the mechanical properties and precipitation in a 19Cr-25Ni stainless steel. They presented data on the corrosion resistance and embrittlement of this alloy.

There were two papers on the program dealing with precipitation hardened stainless steels. Kosa and DeBold of Carpenter Technology Corp. reported on the effect of heat treatment and the microstructure on the mechanical and corrosion properties of Custom 450. Murali et al of the Virginia Polytechnic Institute and State University studied the influence of hydrogen on age hardening in 15-5 pH stainless steel.

The session ended with two papers dealing with ferritic-austenitic duplex stainless steels. Bodine and Sump of Combustion Engineering discussed the effects of composition and heat treatment on the production of tubing and the resulting mechanical and corrosion properties. The final paper of the session was by Solomon and Devine of the General Electric Corporate Research and Development Center. This paper dealt with the various precipitates that form in the duplex stainless steel Uranus 50 and their influence on the mechanical and corrosion properties of this alloy.

H. D. Solomon
Research and Development Center, General Electric Co., Schenectady, N. Y., session chairman.

F. B. Pickering [1]

Relationship Between Microstructure and Properties in Stainless Steels

---

REFERENCE: Pickering, F. B., "**Relationship Between Microstructure and Properties in Stainless Steels,**" *MiCon 78: Optimization of Processing, Properties, and Service Performance Through Microstructural Control, ASTM STP 672*, Halle Abrams, G. N. Maniar, D. A. Nail, and H. D. Solomon, Eds., American Society for Testing and Materials, 1979, pp. 263–295.

ABSTRACT: A review has been presented of the structure-property relationships in the major types of stainless steels, including the 12Cr transformable steels, the 17–25Cr ferritic steels, and the austenitic stainless steels. Quantitative relationships have been presented between microstructural parameters and the various mechanical properties that they control. Recent work on structure-property relationships in 12Cr steels have been summarized. Particular attention has been paid to the factors that describe the strength, toughness, and formability of the ferritic stainless steels, and attention has also been focused on the relationships that can be used to optimize the formability of the austenitic stainless steels, with particular reference to the stability of the austenite during straining.

KEY WORDS: steels, microstructure, stainless steels, austenitic stainless steels, ferritic stainless steels, transformable stainless steels, structure-property relationships, strength, toughness, formability

A recent discussion of the physical metallurgy of stainless steel [*1*][2] has categorized stainless steels into martensitic, ferritic, and austenitic, and indeed this is convenient for reviewing the physical metallurgical basis of the structure-property relationships in these steels. In general, the controlled transformation steels are best classified with the martensitic steels, while the duplex austenite-ferrite steels that are currently of considerable interest [*2*] can be grouped as far as structure-property relationships are concerned, with the austenitic steels that in many cases contain varying amounts of delta ferrite.

The most important property of the stainless steel is their corrosion resistance, without which they would find little industrial application. In fact, their general mechanical properties can be more than matched by

---

[1] Reader in Metallurgy, Sheffield City Polytechnic, Sheffield, England.
[2] The italic numbers in brackets refer to the list of references appended to this paper.

much less costly materials. While there have been innumerable studies of the corrosion properties, it is significant that there is a considerable lack of systematic and especially quantitative data between parameters describing the corrosion resistance and composition or microstructure. However, considerable progress has been made in relating the mechanical properties, including the formability, of stainless steels to structure-composition parameters. The present brief review will concentrate on these relationships, and particularly the room-temperature properties, although many stainless steels are also used for high-temperature and creep-resisting applications. Such properties however are beyond the scope of this paper.

Martensitic Stainless Steels

Composition and Constitution

These alloys contain 12–17Cr, 0–4Ni, and 0.10–1.0C with additions of varying elements such as molybdenum, vanadium, niobium, aluminum, titanium, and copper. By virtue of their high hardenability, the austenite forms martensite even at fairly slow cooling rates, but, due to their composition, they may contain varying amounts of delta ferrite at a typical solution treatment temperature of 1050°C. Many of the steels are used in applications where some measure of toughness is required, and in many cases other than the tool and cutlery steels, the carbon content is restricted to about 0.1 percent. Such 0.1C, 12Cr steels are borderline with regard to delta ferrite formation [*3*], and delta ferrite decreases the maximum available strength even when, as frequently is the case, the steels are heavily tempered. Consequently, it is essential that excessive delta ferrite should not be formed, that the M_s temperature of the austenite should not be so low that considerable amounts of retained austenite are produced, and that the Ac_1 temperature should not be depressed too far with a consequent limitation on the maximum tempering temperature that can be used.

The constitution of the steels, in terms of the amount of delta ferrite as a function of alloying element additions, has been determined [*4,5*] and it has been shown that the effects may be summarized [*6*] by the use of nickel and chromium equivalents in conjunction with a modified Schaeffler-type diagram [*7*]. Similarly, the M_s temperature of the steels has been determined as a function of temperature by many workers, and equations are available by which it can be calculated [*4,5,8–10*]. The Ac_1 temperature may also be calculated as a function of composition [*5*]. It is therefore possible to predict, albeit on an empirical basis, the constitution and transformation behavior of the untempered 12–17Cr steels as a basis for structure-property investigations.

Strength

The strength of untempered martensite has not been fully quantified in terms of the composition and microstructure, although the mechanisms contributing to the strength are generally appreciated [*11*]. In the low-carbon 12Cr martensite, strengthening is due to carbon and nitrogen in solution, solid solution hardening by the chromium and other substitutional solutes, the fine martensite lath size, and the dislocations present in the lath martensite. Due to the low M_s temperature, there is less likely to be carbide precipitation strengthening in the untempered martensite but, in the tempered condition, strengthening by carbides does occur albeit at the expense of solid solution strengthening. Many of these features interact, or are mutually influenced by, for example, carbon, and the various mechanisms may not be simply additive [*12*].

Solid solution hardening by carbon is often reported to be linearly related to the square root of the concentration [*13*], although other workers use a cube root function of concentration [*14–16*]. The hardness values of alloy martensites are usually higher than those of plain carbon martensites [*17*], not so much due to solid solution strengthening by the alloying elements but rather due to the fact that the M_s is depressed and less autotempering occurs. It has been suggested that carbon as carbide precipitated in martensite may be twice as effective as that in solid solution [*18,19*].

The martensite lath size is difficult to define and measure, but it has been estimated that the fine grain size, less than ~2 μm, causes an increase in the yield stress of 450 to 600 MN/m^2. Other workers [*20*] have shown that the strength of martensite depends on the prior austenite grain size, but it is probable that this only controls the size of the martensite crystals.

With regard to the effect of dislocation density in low-carbon martensite, it has been estimated that the contribution to the strength is of the order of 150 to 300 MN/m^2 [*11*]. There would seem to be no reason why this should not apply to 12Cr steels. The dislocations however, play an important role by interacting with interstitial carbon, as indicated by internal friction effects [*21*], and this could be related to observations that aging occurring during quenching is greater than if a steel is aged after the quench. The suggested explanation [*18*] is that the dislocations are moving during quenching and thus continually nucleate precipitates, but it could also be the case that they are able to sweep up interstitial atoms and form more effective interactions or atmospheres.

Despite the complexity of the interactions of the strengthening mechanisms outlined, attempts have been made to relate quantitatively the yield strength of martensite to the carbon content, which of course does not differentiate between the carbon dependent effects of the individual strengthening mechanisms. Typical equations are for up to 0.4C [*14*]

$$\sigma_y (\mathrm{MN/m^2}) = 290 + 1800\,(\%\mathrm{C})^{1/3} \qquad (1)$$

and for up to 0.25C [22]

$$\sigma_y (\mathrm{MN/m^2}) = 815 + 3850(\%\mathrm{C}) \qquad (2)$$

These equations, which give similar strength values up to 0.2 percent, probably apply equally well to 12–17Cr steels, but with a different constant incorporating the effects of solid solution strengthening by chromium and other substitutional solutes.

A recent analysis of the yield stress of low-carbon lath martensite [23] has employed the well-known basic equation for ferrite, but modified to take account of the dislocation density, the martensite lath packet size, and a lath boundary term. The resulting equation is

$$\sigma_{sy} (\mathrm{MN/m^2}) = 88 + 37(\%\mathrm{Mn}) + 38(\%\mathrm{Si}) + \alpha\mu b \rho^{\frac{1}{2}} + 28d^{-\frac{1}{2}} + \sigma_b \qquad (3)$$

where

μ = shear modulus,
b = Burgers vector of slip dislocations,
ρ = dislocation density in lines/mm^2, and
d = mean linear intercept of packet size.

The term, σ_b, is a balancing term to take into account the strengthening contribution from martensite lath boundaries themselves. There seems to be no reason why this term should not entirely replace the *packet* size strengthening term, especially as applying the analysis to experimental data showed that in some cases the martensite *packet* boundaries did not contribute to the strength. Another feature of the analysis was that the dislocation contribution to the strength, $\alpha\mu b \rho^{\frac{1}{2}}$, varied considerably from case to case. Various workers have shown that the dislocation density of lath martensite is a function of carbon content [24,25], but the absolute magnitudes of ρ, and thus of $\alpha\mu b \rho^{\frac{1}{2}}$, vary appreciably. There is clearly a need to determine more closely the dislocation density of low-carbon martensites. An interesting feature of Eq 3 is the absence of a precipitation strengthening term due to the low-carbon content, and so the equation might well be applicable to the low-carbon 12–17Cr untempered martensites. The constant, however, may have to be adjusted to account for the extra substitutional solid solution strengthening.

Attempts have been made to describe quantitatively the strength of tempered martensite [16,26,27], and this is very relevant to the 12Cr steels that are often used in the heavily tempered condition. There are great differences between the equations that have been proposed, but all involve the square root of the dislocation density and a reciprocal function of the carbide interparticle spacing. Not all involve the martensite or tempered martensite grain size, which sometimes must be incorporated in the dispersion strengthening term when the interparticle spacing is less than the mean linear intercept of the grain size. The problems are acute in 12–17Cr steels in which the carbide type may be changing with increasing tempering temperature, and multi-modal carbide distributions may occur. Recent work on very heavily tempered plain carbon martensites [28] has provided information, however, that may be apposite to heavily tempered 12Cr steels. It was possible to differentiate between structures in which the carbides were exclusively at the ferrite grain boundaries, and those that also contained carbides within the ferrite grains. In the former, the carbides contributed no strengthening effect, and grain size was the major factor

$$\sigma_y\,(\mathrm{MN/m^2}) = 108 + 18.2\,d^{-\frac{1}{2}} \tag{4}$$

where d is the recrystallized ferrite grain size in the tempered martensite. On the other hand, the structures containing carbides within the grains showed an additional strengthening effect that could be described by the Ashby-Orowan [29] contribution of the carbides to dispersion strengthening, and the equation derived was

$$\sigma_y\,(\mathrm{MN/m^2}) = 71 + \frac{0.015}{\lambda} \cdot \ln \frac{D}{2b} + 23.9\,d^{-\frac{1}{2}} \tag{5}$$

where

D = carbide particle diameter,
b = Burgers Vector of slip dislocations,
λ = carbide particle spacing, and
d = mean linear intercept of grain size.

A similar analysis has also been used to describe the flow stress of the different structures at any given strain. It would seem appropriate to attempt to apply these equations to 12Cr martensites in the heavily tempered condition.

In the tempered 650°C condition, the effect of both carbon and nitrogen on the proof stress has been quantified [1,6], Fig. 1. It has been shown that the proof stress can be described by the empirical equation

$$0.2\%\ \text{proof stress}\ (\mathrm{MN/m^2}) = 710 + 770\,(\mathrm{C} + 2\mathrm{N}) \tag{6}$$

where carbon and nitrogen are in mass percent.

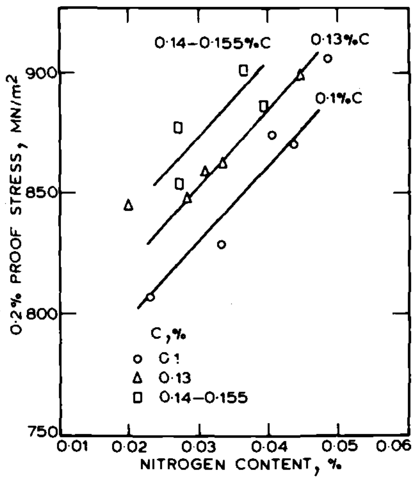

FIG. 1—*Effect of carbon and nitrogen on 0.2 percent proof stress of 12Cr-Mo-V steels.*

This relationship probably simply reflects the increased volume fraction of carbides/nitrides as the carbon and nitrogen content increases, and relates to the particle diameter and particle spacing parameters incorporated in Eq 5.

Toughness

The quantitative analysis of the effect of microstructure on the impact transition temperature (ITT) and the Charpy shelf energy (CSE) values for structures so complex as tempered martensite presents great difficulties, and it is not surprising that data is very sparse. Also, the difficulties are compounded by various embrittling phenomena often encountered in tempered martensitic structures. Of these embrittling effects, only upper nose embrittlement seems capable of quantitative evaluation, and indeed may be described by the coefficient describing the effect of grain size on the ITT [*30*], which, because the tempered ferrite has a polygonal structure after the high temperatures involved, is the same coefficient as obtained in ferrite-pearlite structures [*31*]. An increase in grain size of the ferrite during tempering of $d^{-\frac{1}{2}} = 1$ causes an increase in the ITT of 11.5°C, or a decrease in σ_y of 1 MN/m² causes an increase in the ITT of ~0.7°C.

An analysis of the effect of microstructure on the ITT of low-carbon martensite, which may well be very applicable to low-carbon 12Cr martensite, has used the equation

$$\text{ITT}\ (^\circ\text{C}) = -19 + 44\,(\%\text{Si}) + 700\,(\sqrt{\%\text{N}_f}) + 0.26\,(\sigma_p + \sigma_d) - 11.5\,d^{-\frac{1}{2}} \qquad (7)$$

where

σ_p = precipitation strengthening as described by the Ashby-Orowan relationship,
σ_d = strengthening caused by random dislocations and dislocations in low-angle ferrite lath boundaries, and
d = the mean spacing between high-angle boundaries, that is, *packet* or prior austenite grain boundaries.

The value of σ_d can thus be considered to comprise a term for forest dislocation strengthening, σ_{fd}, and a term for low-angle boundary strengthening, σ_b

$$\sigma_d = \sigma_{fd} + \sigma_b \tag{8}$$

σ_{fd} can be described by

$$\sigma_{fd} = \alpha \mu b \rho^{\frac{1}{2}} \tag{9}$$

where μ = the shear modulus, b = Burgers vector of the dislocations, and ρ = dislocation density; α being a constant. The value of σ_b is more difficult to assess, but is only given by part of the normal coefficient for the martensite lath size, which has been shown to be the same [*23*] as the coefficient for the low-carbon bainite lath size [*32*]. Now, high-angle boundaries increase strength and lower the ITT by acting as barriers to crack propagation, the vector being −0.7°C/MN/m² increase in yield stress. On the other hand, low-angle boundaries increase the strength, and by so doing, raise the ITT because they do not act as barriers to crack propagation. The value of σ_b can be obtained from the difference in yield strength between structures with a high-angle grain size of d and those with a martensitic lath size of d_L

$$\sigma_b = 15.1\,(d_L^{-\frac{1}{2}} - d^{-\frac{1}{2}}) \tag{10}$$

Good agreement has been achieved, using this approach, between the calculated and observed ITT values of low-carbon martensite if the austenite grain size is employed as a measure for d in Eq 7. It has long been appreciated that the prior austenite grain size controls the ITT of martensite and its tempered derivatives, but there is a common observation that it is the *facet* size, which is usually identified with the martensite *packet* dimensions, that controls the ITT [*24,33,34*], Fig. 2. However, there seems to be a clear relationship between the prior austenite grain size and the *packet* or fracture facet size, as shown by data on both martensite and bainite, and the ITT can often be directly related to the

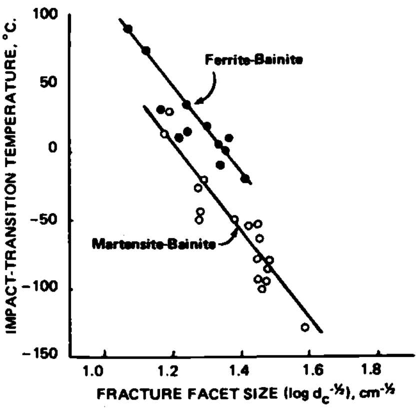

FIG. 2—*Effect of fracture facet size on the impact transition temperature of steels containing martensite and bainite.*

prior austenite grain size [*33*]. This has been confirmed on low-carbon 12Cr steels tempered at quite high temperatures, in which it has been shown that an increase in the prior austenite grain size of $d^{-1/2} = 1$ mm$^{-1/2}$ results in an increase in ITT of 23°C [*35*]. This is much greater than the value of 11.5°C/mm$^{-1/2}$ obtained in polygonal ferrite structures, but is identical with the value obtained by other workers on martensitic type structures [*33*].

There is little systematic data to derive quantitative relationships, but there is evidence to indicate that the ITT of martensite and its temper products increases with increasing carbon content, as is observed for many other ferrous structures. In fact, it might be inferred that in tempered martensite the ITT increases more or less linearly with the strength by a factor of 0.2/0.3°C per MN/m^2. For 12Cr steels [*35*], the increase in ITT per MN/m^2 increase in proof stress was observed to be 0.2/0.5°C, which is the same order as the effect for precipitation and dislocation strengthening on the ITT of ferrite-pearlite steels [*11*].

There is very little quantitative data available on the effect of composition and microstructure on the CSE value of martensite and its tempered products. Some evidence indicates that the prior austenite grain size has no effect on the CSE. By inference, because there is a direct relationship between the CSE value and the total ductility at fracture, ϵ_T, [*36*], it may be concluded that the CSE decreases as the carbon content increases for tempered martensite, but this may be an exponential rather than a linear decrease. In fact, it has been observed that the CSE value decreases exponentially with increasing proof stress in tempered 12Cr steels [*35*].

It seems that, despite the rather fragmentary data available, relationships based on Eq 7 but with account taken of the dislocation density, carbide dispersion strengthening and the fracture *facet* or martensite *packet* size will be appropriate starting points for the analysis of the ITT of martensites and their tempered products, and the evidence available on various alloyed 12Cr stainless steels seems to support this [*35*].

Ferritic Stainless Steels

Composition and Constitution

The chromium contents range generally from 17 to 26 percent, and the steels are essentially free from nickel. Iron-chromium alloys of this composition would be entirely ferritic up to their melting points [*6*] but in the presence of 0.1C, the 17Cr steels consist of ferrite with a little austenite at temperatures of about 1000°C [*37,38*]. The amount of austenite depends critically on the carbon and nitrogen contents [*37*], and also on the relative amounts of austenite and ferrite forming elements [*39*]. With increasing temperature, the amount of austenite first increases and then decreases at the highest temperatures. Thus the higher chromium steels, and the 17/18Cr steels containing about 2Mo, are fully ferritic at all temperatures. Above 1150°C, the 17Cr steels usually become completely ferritic and grain growth is pronounced. On cooling, austenite often precipitates at the ferrite grain boundaries, and as a Widmanstatten structure. Under rather special conditions, this austenite may be retained, but usually the austenite transforms to martensite on cooling to room temperature. The martensite can then be tempered at temperatures up to ~780°C, at which austenite reforms, the tempering producing ferrite and carbide. At the higher chromium contents and higher temperatures, $Cr_{23}C_6$ is the stable carbide, but Cr_7C_3 tends to form at lower chromium contents [*38*]. The nitrogen present mainly forms Cr_2N [*39*] and both the carbide and nitride begin to dissolve on heating above 850°C. Solution is largely complete above 1100°C.

Sigma phase may precipitate, albeit slowly, at temperatures less than 600°C, but may be accelerated by cold deformation and by the presence of sigma stabilizing elements such as silicon and molybdenum [*1,40*]. In some cases, chi phase may form and is stable over a wider temperature range than sigma phase [*1*]. The occurrence of a precipitate based on the chromium-rich α', which results from a fairly wide miscibility gap in the iron-chromium system below 600°C [*1*], can lead to the marked embrittlement that can occur in chromium ferritic stainless steels. The 17–25Cr steels suffer from 475°C embrittlement when heated to temperatures in the range 400 to 550°C, due to the precipitation of coherent chromium-rich particles in the miscibility gap in the iron-chromium system, α' phase [*41–50*]. The phase forms by spinodal decomposition and occurs as fine spherical zones that at higher temperatures develop into disks on $\{100\}$ ferrite. The precipitation effect and accompanying embrittlement, becomes more pronounced with increasing chromium content, and with very low interstitial contents the development of 475°C embrittlement is retarded but not eliminated [*48,51*]. Recent evidence also indicates that alloying elements such as molybdenum, niobium, and titanium may intensify α' precipitation [*51*].

Structure-Property Relationships

The yield stress of ferritic stainless steel is greater than that of austenitic stainless steel, being 280 to 460 MN/m^2 compared with ~230 MN/m^2 for austenitic steels. Ferritic steels, however, work harden much less rapidly than do the austenitic steels, Fig. 3, but the tensile ductility and especially the impact resistance are lower than for austenitic steels. High chromium ferrite is notoriously brittle, and exhibits a ductile-brittle cleavage transition. The structure-property relationships [*52*] are complex, but the following factors have been shown to be important.

In many ferritic stainless steels, grain growth is rapid. Due to the greater atomic mobility in ferritic structures, they show more rapid grain growth and lower grain coarsening temperatures than do the austenitic stainless steels [*38*], often starting to coarsen from about 600°C, compared with about 900°C for austenitic steels. The presence of austenite, Ti(CN) or Nb(CN) second phase particles, retards grain growth and increases the grain coarsening temperature.

Strength—Refinement of the ferrite grain size increases the yield and tensile strengths according to the Hall-Petch relationship. However, the macro-ferrite grains contain many subgrains, which themselves influence the strength. Consequently, the yield and tensile strengths depend on the subgrain size. A recently established relationship for the yield strength,

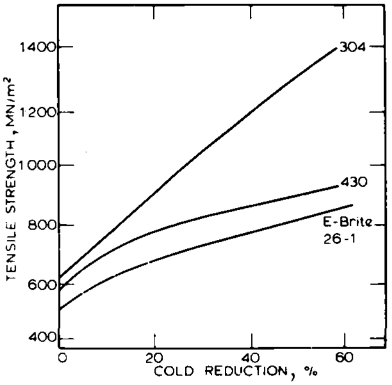

FIG. 3—*Work hardening of ferritic stainless steels compared with austenitic stainless steels.*

σ_y, of fully recrystallized ferrite containing 17–25Cr, without subgrains, is [53]

$$\sigma_y(\mathrm{MN/m^2}) = 36 + 8.5\ (\%\mathrm{Cr}) + 58\ (\%\mathrm{Mo}) - 107\ (\%\mathrm{Ti}) + 15.9\, d^{-\frac{1}{2}} \qquad (11)$$

The coefficient of $d^{-\frac{1}{2}}$ is very similar to that obtained for low-carbon ferrite-pearlite steels [*11*], but the friction stress is considerably lower. However, there is clearly some effect of interstitial solutes, carbon and nitrogen, as can be seen by the negative coefficient for titanium due to it removing carbon, and particularly nitrogen from solution in the chromium-rich ferrite. Solid solution hardening effects have been reported to be similar to those in low-carbon steels [*52*], but the effects are probably more complex than at first realized. For example, the solid solution hardening coefficients for chromium and molybdenum given in Eq 11 are significantly greater than those in low-carbon steels [*11*], and possibly indicate increased efficiency of strengthening due to interaction with interstitial elements to form complex clusters. In the presence of some austenite (martensite), the effects depend on the nature of the alloying element. Austenite forming elements increase the strength rapidly by increasing the amount of austenite, which subsequently transforms to martensite. Ferrite forming elements, however, first decrease the strength by decreasing the amount of austenite, and only when the structure is wholly ferrite does normal solid solution hardening become apparent, Fig. 4. The interstitial solutes, carbon and nitrogen, increase the yield strength [*38,52*], Fig. 5, and their effects seem to be more or less a linear function of concentration [*54*]. Nitrogen seems more

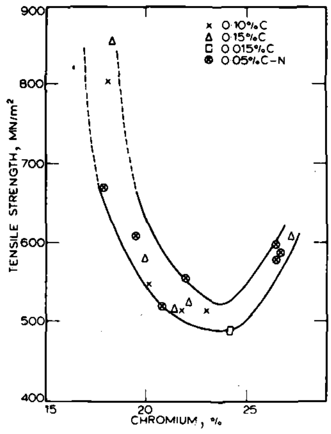

FIG. 4—*Effect of chromium content on the tensile strength of 17Cr ferritic stainless steels.*

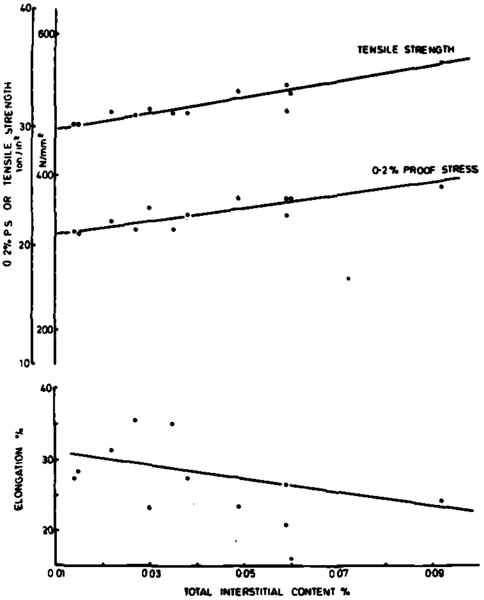

FIG. 5—*Effect of interstitial carbon and nitrogen on the proof stress and tensile strength of 18Cr-2Mo ferritic stainless steel.*

effective than carbon due to its greater solubility. However, the coefficient of solid solution hardening by carbon and nitrogen is only ~800 MN/m^2 per percent, which is much less than in low-carbon steels [*11*], and again probably indicates considerable interaction with chromium.

Increasing amounts of austenite that have transformed to martensite cause a linear increase in strength [*52*], Fig. 6, which seems to indicate a simple law of mixtures. However, this may not be the case as with increasing martensite volume fraction, the carbon content, and, therefore, the strength of the martensite will decrease. Increasing amounts of martensite, however, first lower the yield stress, but more than 15/20 percent martensite then causes the proof or yield stress to increase, Fig. 7. However, increasing amounts of austenite at the solution treatment or annealing temperature also cause a refinement of the ferrite grain size, Fig. 8. This grain refinement complicates the strengthening effects, and also tends to offset the detrimental effects of martensite on the impact properties, as will be discussed later.

Toughness—Because the subgrain boundaries do not apparently greatly impede the propagation of cleavage cracks, the impact properties depend on the coarse, more readily observed macrograin size. Ferritic stainless steels show a ductile-cleavage transition, the impact transition temperature being considerably higher than that for mild steel due to the embrittling effect of chromium dissolved in ferrite [*54*]. As the grain size

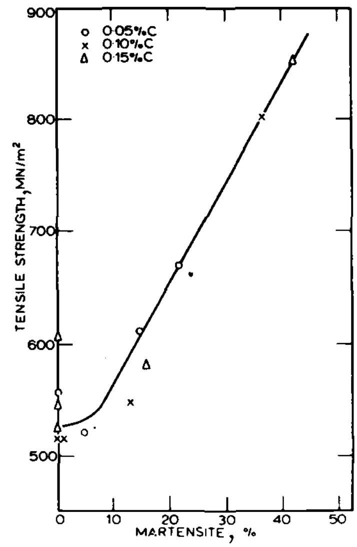

FIG. 6—*Effect of martensite content on the tensile strength of 17Cr ferritic stainless steels.*

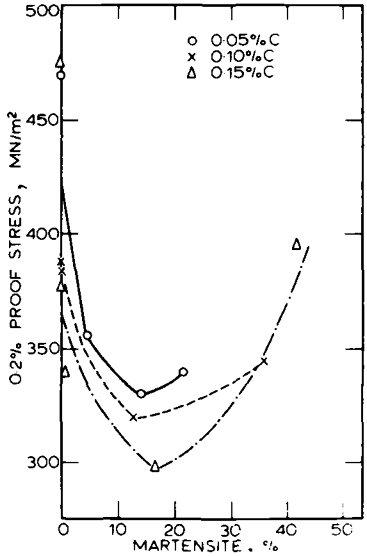

FIG. 7—*Effect of martensite content on the proof stress of 17Cr ferritic stainless steels.*

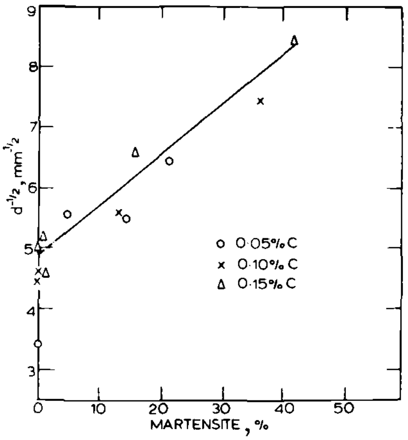

FIG. 8—*Effect of martensite content, resulting from austenite present at the solution treatment temperature, on the ferrite grain size of ferritic stainless steels.*

decreases, so the impact transition temperature decreases, Fig. 9, and the coarse grain size in these steels, due to their nontransformable nature, is a major problem. It has recently been reported that in high chromium ferritic steels, the impact transition temperature is not greatly influenced by grain size, particularly if they contain low interstitial contents [55]. The full explanation of this effect, which is contrary to expectations, awaits further elucidation.

Many substitutional solutes increase the impact transition temperature [54], Fig. 10, but titanium or niobium may initially have a beneficial effect by lowering the dissolved interstitial solutes, followed by a detrimental effect at higher titanium and niobium contents [40,55]. However, nickel is reported to improve the toughness [40,56]. Interstitial solutes are particularly detrimental in raising the impact transition

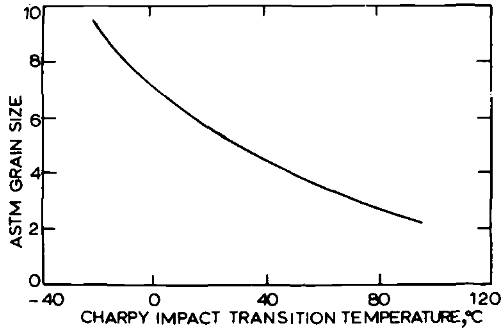

FIG. 9—*Effect of ferrite grain size on the impact transition temperature of 17Cr ferritic stainless steels.*

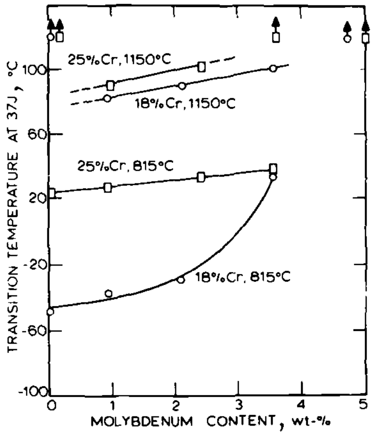

FIG. 10—*Effect of molybdenum on the impact transition temperature of ferritic stainless steels.*

temperature [*38,52,54,57–59*], Fig. 11. When in combination with elements that form stable nitrides or carbides, carbon and nitrogen can be beneficial in providing particles that restrain grain growth and thus improve the impact toughness. Recent evidence [*55,57*] suggests that there is little difference between carbon and nitrogen on the impact transition temperature, which is increased by 80/110°C/0.01% (C+N). This is of the same order as the effect observed for nitrogen in low-carbon low-alloy steels [*11*]. The effect of second phase particles is interesting in that martensite may be expected to increase the impact transition temperature, but because the austenite from which it forms causes the ferrite grain size to be refined, Fig. 8, the opposite effect has been reported [*55*]. On the other hand, large chromium nitrides precipitated at

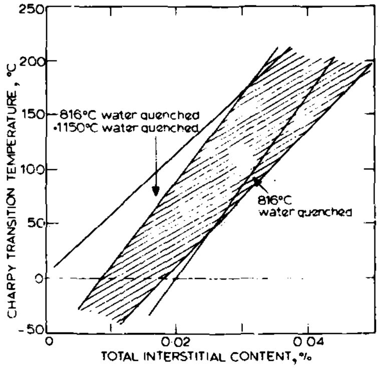

FIG. 11—*Effect of interstitial content on the impact transition temperature of 18Cr-2Mo ferritic stainless steels.*

ferrite grain boundaries have been shown to be most detrimental to toughness [*1,55*], the effect apparently being analogous to that caused by large iron carbides at the ferrite grain boundaries of low-alloy steels [*11*].

It can be seen that the complexity of the interactions between the microstructural parameters and toughness have so far rendered quantitative correlations impossible. However, from the limited quantitative evidence, certain clear similarities with low-carbon low-alloy steels can be discerned.

Formability—Quantitative data on the effects of microstructure on ductility are not available, and a recent attempt to quantify the tensile ductility was not able to explain a significant proportion of the results [*53*]. Perhaps this is not surprising in view of the complex interactions that occur, illustrated by there apparently being a minimum in the tensile ductility when the structure contains ~40 percent martensite.

Ferritic stainless steels have very different forming characteristics compared with the austenitic steels [*40,60*]. They have generally lower work hardening rates, which renders them similar to low carbon mild steel in that they can be easily cold spun or deep drawn, that is, using forming processes that emphasize metal flow. They are however, very much less successful in stretching operations, due to their low work hardening rate and low maximum uniform strain. Being ferritic, they also show stretcher strains during drawing or stretching [*38,57*].

A recent analysis of the work hardening rate of fully recrystallized ferritic steels containing molybdenum [*53*], has developed the following relationship

$$\frac{d\sigma}{d\epsilon_{\epsilon=0.1}} \text{ (MN/m}^2\text{)} = 862 + 113(\%\text{Mo}) + 29.5d^{-\frac{1}{2}} \qquad (12)$$

The high coefficient of $d^{-\frac{1}{2}}$ is similar to that obtained for the work hardening of low-carbon low-alloy steels [*11*].

The crystallographic texture is important in determining the average strain ratio, $\bar{r}$, which controls the deep drawability [*61–64*]. As high $\bar{r}$-values as possible are essential, and this is best achieved by a cube on corner $\{111\}$ texture. For the conventional ferritic stainless steels, the $\bar{r}$-value is close to 1, but with very low interstitial contents and heavy reductions prior to annealing [*40*], $\bar{r}$-values of 1.6 can be achieved [*61*]. In fact, r-values up to 2.0 have been reported for laboratory processed materials [*60*]. Several relationships have been recently obtained for the correlation of limiting drawing ratio with texture and $\bar{r}$-value [*53*]

$$\text{limiting drawing ratio} = 0.98 + 0.26\bar{r} \qquad (13)$$

$$\text{limiting drawing ratio} = 2.17 + 0.13 \log{}^{I_{(111)}}/_{I_{(100)}} \qquad (14)$$

$$\bar{r} = 0.77 + 0.36 \log{}^{I_{(111)}}/_{I_{(100)}} \qquad (15)$$

It is reported that limiting drawing ratios of up to 2.5 can be obtained [*53,61*].

A problem in the forming of the ferritic stainless steels is roping, which produces markings not unlike stretcher strains. However, rope markings are not due to a yield phenomenon, but are due to a crystallographic textural effect, the marks being parallel to the rolling direction and thus differentiated from stretcher strains. The unfavorable texture producing roping is developed during hot working, and is the result of bands of an orientation that has a low plastic anisotropy.

Austenitic Stainless Steels

The Constitution of Austenitic Steels

Nickel added to 18Cr steels enlarges the gamma loop and increases the amount of austenite present at any solution treatment temperature [*65–68*]. At low nickel contents this austenite may transform wholly or partially to martensite. Nickel also decreases the M_s temperature [*8,9,69*], so that with about 8Ni, the M_s temperature is just below room temperature, and stable austenite is retained after cooling from the solution treatment temperature. An 18Cr, 8Ni, carbon-free steel is borderline with respect to a fully austenitic structure, but may contain a little delta ferrite. Because carbon is a powerful austenite forming element, an 18Cr–8Ni–0.1C alloy is fully austenite above about 900°C, although the M_s temperature is only just below room temperature, so that the austenite would transform partially to martensite either during a refrigeration treatment or during cold working. The interaction between chromium and nickel in promoting the formation of stable austenite in 0.1 percent steels, after cooling from 1050 to 110°C is therefore of the utmost importance. Some of the main effects are

(*a*) At low chromium contents, chromium acts as an austenite stabilizer.
(*b*) At 18Cr, a minimum nickel content is required to promote a fully austenitic structure that is stable at room temperature.
(*c*) With more than 18Cr, the ferrite forming tendency of chromium requires additional nickel to eliminate delta ferrite, but the formation of martensite is further suppressed.

The effect of other alloying elements is also important in that, depending upon whether they are austenite or ferrite forming elements, they will decrease or increase the tendency for delta ferrite formation. Many workers have considered the effect of alloying elements on the constitution of austenitic stainless steels, using chromium and nickel equivalent compositions, calculated from the composition [*67,70*], and used in conjunction with the well-known Schaeffler type of diagram [*6,7*]. However, care is required in steels containing undissolved carbo-nitrides of titanium or niobium, as correction factors have to be used [*70*].

The carbides present can be most important, particularly in relation to the corrosion properties. The usual carbide that is formed is $Cr_{23}C_6$, and for the carbon contents typical of conventional commercial steels, occurs below about 800°C.

The Transformation of Unstable Austenite to Martensite

Austenite in the less highly alloyed steels may transform to martensite when the M_s temperature is above room temperature, or martensite may occur during refrigeration in more stable alloys in which the M_s temperature is below room temperature. In these latter alloys, the M_d temperature may still be above room temperature, and thus martensite may be formed by deformation. Apart from cobalt, almost all alloying elements depress the M_s [*8,9,69*] and recent data have shown that the M_s is related to composition by the following equation, which has been specifically determined for austenitic stainless steels [*71*]

$$\begin{aligned} M_s(°C) = {} & 502 - 810(\%C) - 1230(\%N) - 13(\%Mn) \\ & - 30(\%Ni) - 12(\%Cr) - 54(\%Cu) - 46(\%Mo) \qquad (16) \end{aligned}$$

This type of relationship is important, particularly if used to establish the M_d temperature, in assessing the cold formability of austenitic stainless steels [72]. A typical equation for the $M_{d_{30}}$ temperature at which 50 percent martensite is produced under the action of a true strain of 0.30 is [*71*]

$$\begin{aligned} M_s(°C) = {} & 497 - 462(\%C + \%N) - 9.2(\%Si) \\ & - 8.1(\%Mn) - 13.7(\%Cr) - 20(\%Ni) - 18.5(\%Mo) \qquad (17) \end{aligned}$$

This equation is very similar to other published equations [*69*].

Structure-Property Relationships

Strength—Relationships have been obtained between compositional and microstructural parameters, and the tensile strength and proof stress values of austenitic stainless steels [*36,52,73*], as shown by the following equations

$$\begin{aligned} 0.2\% \text{ proof stress } (MN/m^2) = {} & 68 + 354(\%C) + 20(\%Si) + 3.7(\%Cr) \\ & + 14.5(\%Mo) + 18.5(\%V) + 4.5(\%W) \\ & + 40(\%Nb) + 26(\%Ti) + 12.6(\%Al) \\ & + 493(\%N) + 2.5(\%\delta\text{-ferrite}) \\ & + 7.1\, d^{-\frac{1}{2}} \qquad (18) \end{aligned}$$

$$\begin{aligned}\text{Tensile strength} = (\text{MN/m}^2) = {} & 447 + 540(\%\text{C}) + 847(\%\text{N}) \\ & + 37(\%\text{Si}) + 1.7(\%\text{Ni}) + 18.5(\%\text{Mo}) \\ & + 77(\%\text{Nb}) + 46(\%\text{Ti}) + 18.5(\%\text{Al}) \\ & + 2.2\ (\%\delta\text{-ferrite}) + 12.6\,t^{-\frac{1}{2}} \qquad (19)\end{aligned}$$

where

d = mean linear intercept of grain size (mm), and
t = twin spacing (mm).

It can be seen that the twin spacing does not affect the proof stress, because the stacking fault energy, which controls the work-hardening rate, has little or no effect at the low strains at which the proof stress is measured. A small twin spacing or high twinning frequency, is a natural consequence of a low stacking fault energy [*74*] that in turn leads to a high work-hardening rate. The twin spacing is much more important than the grain size in controlling the tensile strength, because the effect of stacking fault energy on the work-hardening rate is significant. However, in high stacking fault energy austenites, in which there are relatively few twins, the tensile strength will depend on the grain size, and increasing the grain size decreases the proof stress. Delta ferrite increases the proof stress and tensile strength values by a dispersion strengthening effect. Recent analyses of the effect of grain size on the yield or proof stress of austenitic stainless steels [*75,76*], have shown coefficients of $d^{-\frac{1}{2}}$ similar to that given in Eq 18. Moreover, it has been shown that the grain size coefficient of the yield or proof stress increases by a factor of about 2.5 as the nitrogen increases to 0.27 percent [*75*]. For a steel containing 0.05N at room temperature the proof stress obeys the equation [*76*]

$$\begin{aligned}0.2\%\ \text{proof stress}\ (\text{MN/m}^2) = 134 + 10.12d^{-\frac{1}{2}} \qquad (20) \\ (\pm\ 15\text{MN/m}^2)\end{aligned}$$

The interstitial solutes carbon and nitrogen have the greatest solid solution strengthening effects, followed by the ferrite forming substitutional solutes, while the austenite forming substitutional solutes have very little solid solution strengthening effect, Fig. 12. The effect of nitrogen has recently received further attention, and while at room temperature, the solid solution hardening coefficient seems to be similar to that given in Eq 18 [*75*], that is, ~500 MN/m^2 per 1N, there seems to be a marked interaction between grain size and the solid solution hardening effect of nitrogen. Moreover, some results relate the strengthening linearly to the nitrogen content, whereas others indicate that it is proportional to the square root of the nitrogen content. It has been suggested that the total solid solution hardening effect is composed of two different contributions [*76*]: one

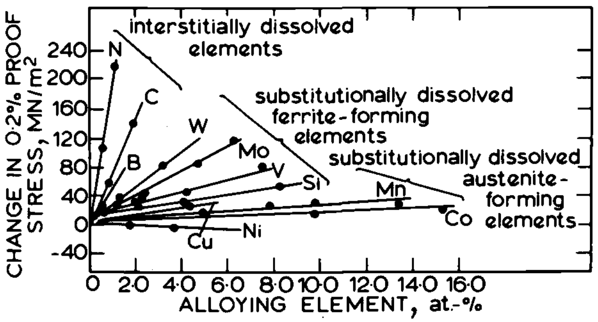

FIG. 12—*Solid solution strengthening effects of alloying elements in austenitic stainless steels.*

dependent on grain size and the other independent of grain size. The latter grain size independent component is strongly dependent on temperature and may be considered to be genuine solid solution strengthening. The grain size dependent component is that which increases the value of the grain size coefficient of the proof stress as the nitrogen increases. Thus, the strengthening effect of nitrogen increases greatly as the grain size decreases. This might be due to nitrogen either promoting planar arrays of dislocations that might be expected to enhance the effect of grain size on the proof stress, or it may be due to an increased number of twin boundaries, which effectively decreases the mean linear intercept of slip barriers. Both these possible causes would directly result from nitrogen decreasing the stacking fault energy [77]. The effect of nitrogen, grain size, and temperature has recently been shown to obey the following equation [76]

$$\begin{aligned} 0.2\%\,\text{proof stress (MN/m}^2) &= 15 + \frac{33000}{T} + 65\left(\frac{1690-T}{T}\right)\cdot(\%\text{N})^{\frac{1}{2}} \\ (\pm\ 15\ \text{MN/m}^2) &\qquad + \left[7 + 78(\%\text{N})\right]\cdot d^{-\frac{1}{2}} \qquad (21) \end{aligned}$$

where d is in millimetres, and T in kelvin.

The solid solution strengthening effects also reflect the atomic diameter of the solute, which influences the lattice parameter of the austenite, and thus the strain introduced into the lattice by the alloying element [78]. The lattice parameters of austenitic stainless steels can be related to the solute concentration by multiple regression analysis [78].

Martensite formation from metastable austenite is important, largely due to its effect on ductility, but it also influences the strength [73]. Martensite can occur either prior to straining, or can be produced during straining in the tensile test. Up to 35 percent martensite present prior to straining does not affect the 0.2 percent proof stress, and up to 20 percent martensite prior to straining may actually lower the 0.2 percent proof stress due to internal stresses produced. Because of the low strains involved at the proof stress, very little martensite forms at this strain level, and thus it has little effect. More than 35 percent martensite prior to straining means that the martensite becomes the load bearing phase, and the 0.2 percent proof stress then increases with increasing martensite content.

The effect of martensite on the tensile strength is complex [73]. In steels that contain martensite prior to testing, there may or may not be more martensite formed during straining, depending on the stability of the austenite. The tensile strength of such steels increases linearly with increasing amounts of martensite prior to straining, according to

$$\text{Tensile stress (MN/m}^2\text{)} = 15.4\,T_c + 185 + 12.6\,(\%\text{M}) \qquad (22)$$

Where T_c is the tensile strength calculated from Eq 18, and %M is the percentage of martensite prior to tensile testing. This equation can be rewritten

$$\delta T\ (\text{MN/m}^2) = 185 + 9.84\,(\%\text{M}) \qquad (23)$$

where δT is the difference between the observed and calculated tensile strengths, Fig. 13. The intercept of 185 MN/m² at 0 percent prior martensite probably represents the strengthening produced by martensite that is formed during straining up to the maximum uniform strain, that is, the strain at which the tensile strength is measured.

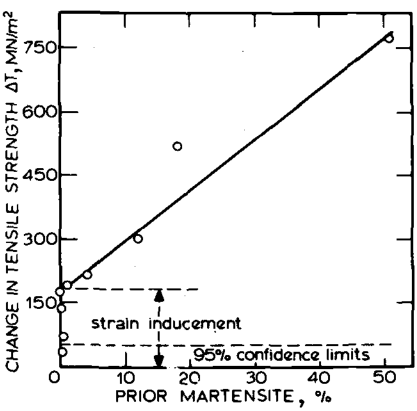

FIG. 13—*Effect of martensite present prior to testing on the tensile strength of austenitic stainless steels.*

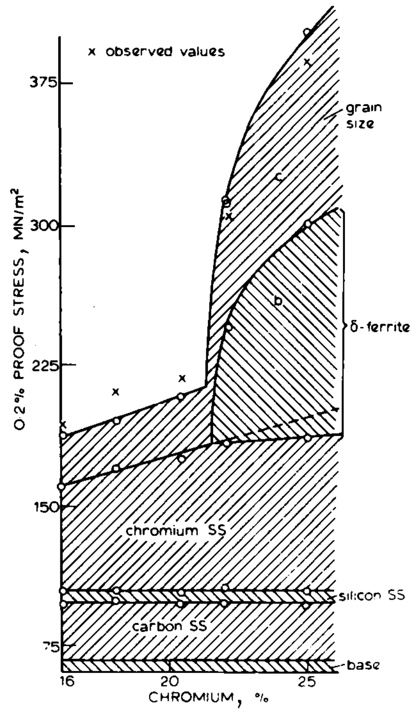

FIG. 14—*Effect of chromium on the 0.2 percent proof stress of austenitic stainless steels in terms of various strengthening mechanisms.*

Using the relationships shown in Eqs 18 and 19, it is possible to indicate the effects of a particular alloying element, such as chromium, in terms of the various operative strengthening mechanisms, Fig. 14

Cold Working and Formability—Many applications of austenitic stainless steels involve cold working by either deep drawing or stretch forming. For improved deep drawing, softness, the correct crystallographic textures and high $\bar{r}$ values are important, while for improved stretch forming, a high maximum uniform strain is required.

Deep drawing—To minimize the forming loads, the steels should have a low proof stress value and as low a work-hardening rate as possible. These features can be obtained by a well-annealed structure, an absence of delta ferrite, and a minimum of alloying additions that lower the stacking fault energy. The formation of martensite during cold forming should also be avoided, so that the steel should be stable with a low M_s temperature. In addition, however, the crystallographic texture is important, as this controls the $\bar{r}$ value. Preferred textures are produced during cold deformation and recrystallization annealing. In addition to the effect of strain on the development of a deformation texture, account must also be taken of the effect of the stacking fault energy of the austenite and of the tendency for the austenite to transform to strain-induced martensite.

During cold rolling, textures typical of ferrite, that is, martensite, are produced together with a texture common to most face centered cubic (fcc) alloys with a low stacking fault energy [*79,80*]. With increase in rolling temperature, the ferritic texture is eliminated as the M_d temperature is exceeded and martensite does not form. With a further increase in rolling temperature the austenite textures become typical of high stacking fault energy fcc metals [*81*]. The intensity of the ferritic or martensitic texture, depends on the austenite stability and on how early in the deformation process the martensite forms. If martensite is formed late in the deformation process, it will not have time to develop its own characteristic texture, and thus will show a texture related to that of the austenite through the normal orientation relationship.

Annealing a cold deformed austenitic steel may cause any strain induced martensite to revert to austenite, and recrystallization textures therefore depend on the initial texture of the deformed austenite, and on the texture of any original martensite that reverts to austenite on annealing. Considerable variations in texture have been reported [*82,83*], which have also been shown to be dependent upon the annealing temperature, the occurrence of secondary recrystallization, and the presence of second phase particles such as carbides and nitrides.

The pattern of deformation during deep drawing indicates that drawability would be favored by a texture having a high through thickness strength, and that this should be achieved in fcc metals by textural components with $\{111\}$ or $\{110\}$ planes parallel to the sheet surface [*84*]. It has proved difficult in commercial practice to achieve consistently the required recrystallization texture. In general, considerable variation in the effects of texture on deep drawability have been reported [*83,85*]. It is reported that $\bar{r}$ values greater than unity are difficult to achieve, even using large cold-rolling reductions [*69*]. There are many reported cases of the deterioration of the deep drawability of Type 304 austenitic steels with decreasing nickel content, due to the formation of strain induced martensite. This is in contrast to the effect of strain induced martensite on stretch forming.

Stretch forming—Increasing the work-hardening rate relative to the flow stress will increase the maximum uniform elongation and improve the stretch formability. In considering the stretch formability of austenitic steels, two types of steel must be considered, namely, stable and unstable steels that, respectively, do not or do transform to martensite during straining.

(*a*) *Stable Steels*—In stable austenitic steels that do not form martensite during straining, the M_s temperature has not been raised sufficiently for the M_d temperature to be at or above the temperature of straining. The work-hardening rate decreases continually as the strain increases, and the steels usually contain relatively high concentrations of nickel, manganese, carbon, nitrogen, chromium, and molybdenum, which depress the M_s temperature. For the best stretch formability in a stable austenitic steel, there should be a low proof stress and a low work-hardening rate, so that the steel does not work harden appreciably and the forming loads are low. The work-hardening rate depends on the stacking fault energy, a high work-hardening rate being a consequence of a low stacking fault energy that is decreased by chromium, molybdenum, cobalt, silicon, carbon, and nitrogen [*77,86–88*] but increased by nickel [*86,89*] and copper [*86*]. As high stacking fault energy as possible is therefore required in order to keep the forming loads low. It is also necessary to consider how a high stacking fault energy and a low work-hardening rate would affect ductility. In general, a decrease in the work-hardening rate will lower the maximum uniform ductility and be detrimental to the stretch forming characteristics unless there is a corresponding decrease in the level of the flow stress. This latter effect can be achieved by decreasing the initial proof stress by a coarse grain size and by using alloying elements that increase the stacking fault energy but have as small a solid solution strengthening as possible. High nickel contents are not economic, and it is perhaps not surprising that stable steels developed for good formability contain high manganese and copper contents replacing some of the nickel. In austenitic steels of the 300 series, replacement of nickel by manganese does not greatly alter the stacking fault energy, and, in fact, slightly lowers the work-hardening rate [*90*]. In the manganese replacement 200 series stainless steels, however, a high nitrogen is used to assist the manganese in replacing larger amounts of nickel, and this nitrogen markedly increases the flow stress and work-hardening rate, so giving less general formability than in the 300 series austenitic stainless steels.

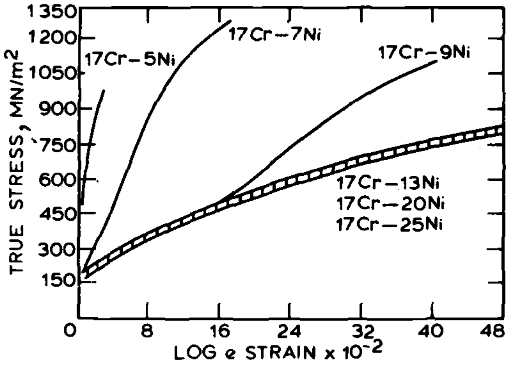

FIG. 15—*Effect of nickel on the true-stress true-strain curves of stable and unstable austenitic stainless steels.*

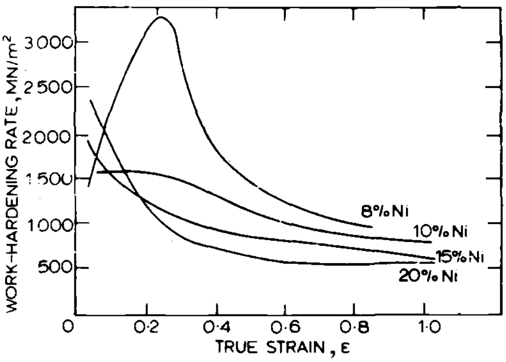

FIG. 16—*Effect of nickel on the work-hardening rate of 0.1C-18Cr stable and unstable austenitic stainless steels.*

(*b*) *Unstable Steels*—When the M_d temperature is high enough for martensite to form during straining, a transformation strain is produced that augments the applied strain. The result is a low initial work-hardening rate compared with a stable steel. As more martensite is formed during continued straining, the flow stress rapidly increases as the martensite itself starts to participate in the deformation. This produces an increase in the work-hardening rate to a level much above that for a stable steel at the same strain, because the martensite deformation more than counterbalances the transformation induced strain. The effects are shown in Figs. 15 and 16. In a steel that forms martensite as soon as strain is applied, the work-hardening rate rapidly increases to a maximum as more martensite is formed (Fig. 16) and then decreases as the formation of strain-induced martensite ceases. The maximum uniform strain for an unstable steel will therefore be considerably greater than that for a stable steel because of the higher work-hardening rate at intermediate strain values. This greatly improves the stretch forming characteristics.

Any given alloying element will not have a unique effect, as its effect will depend on the stability of the base steel into which it is introduced. For example, in a steel with the M_s temperature above room temperature, the presence of martensite prior to straining will give high flow stress values and low uniform elongations. Adding alloying elements will depress the M_s temperature so that martensite only forms during straining, in which case, the uniform ductility will be increased. More alloying addition will cause the steel to be completely stable, with a low work-hardening rate, and the uniform ductility will then decrease [*91*]. Thus with increasing alloying addition, there will be a maximum uniform strain value at some critical alloy content (Fig. 17), the critical alloy content, and the value of the maximum in the uniform strain depending on the base composition of the steel. The strain inducement of an optimum amount of

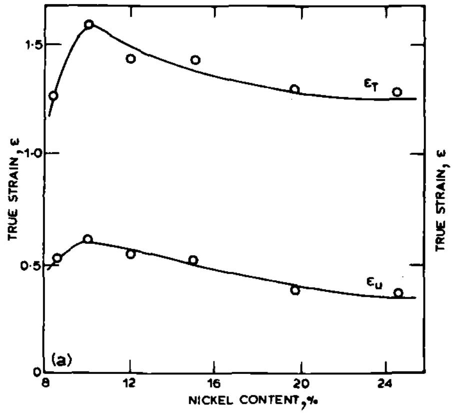

FIG. 17—*Effect of nickel on the maximum uniform strain* (ϵ_u) *and strain at fracture* (ϵ_T) *of austenitic stainless steels.*

martensite, ~2 to 6 percent, must occur at an appropriate stage in the deformation cycle, that is, at $\epsilon = 0.2$, in order to obtain the highest value of the uniform strain and thus optimum stretch formability. This means that there will be an optimum M_d temperature, that is, an optimum combination of alloying contents for maximum stretch formability [*36,72*]. It is possible to optimize these variables so that the composition of a steel with optimum stretch-formability, can be predicted [*92*]. The higher the (C + N) and chromium equivalent contents, the less nickel is required for the optimum composition. This confirms the well-known observation that it is the leaner nickel steels that generally have the better stretch formability.

Once the amount of alloying addition has been reached that effectively inhibits the formation of martensite during straining, further alloying additions will have no effect through the mechanism of transformation-induced plasticity, although they may have effects through the stacking fault energy and work-hardening rate.

General ductility—In view of the factors outlined in the previous discussions, it is perhaps not surprising that not much success has been achieved in attempts to relate tensile ductility parameters to composition and microstructure.

The general ductility, as measured by the percentage reduction of area in a tension test, decreases with increasing amounts of martensite in the structure prior to straining. However, it is reported that grain size within the normal range encountered, has no significant effect on tensile ductility [*93*]. The failure of an austenitic stainless steel during any forming operation is invariably by ductile fracture. The role of nonmetallic inclusions is therefore important, the total strain at fracture decreasing exponentially with increasing volume fraction of inclusions [*36*]. In general, austenitic steels have rather lower total ductilities than do low-carbon ferrite-pearlite steels, possibly due to the angular nature of the nonmetallic inclusions giving more strain concentration and more rapid void growth. Ti(CN) and Nb(CN) particles behave in a similar way, and the massive undissolved carbo-nitrides can be considered as second-phase particles from the point of view of general ductility. Delta ferrite does not seem to have a great effect on the total ductility. There is some evidence [*36*] that there is an optimum alloy content for the maximum total strain at fracture, ϵ_T, which indicates some effect due to instability of the austenite. Possible reasons for this are that strain-induced martensite does not contribute to void growth during ductile fracture, or that the strain-induced martensite, being most intense around void surfaces, prevents the voids from growing.

Effect of Processing on the Development of Improved Combinations of Properties

Cold Working

Particularly in the unstable steels that transform to martensite during cold working, very high strengths of more than 1500 MN/m^2 proof stress can be achieved by cold working [*90,94,95*]. Even in stable steels, proof stress values in excess of 1250 MN/m^2 can be achieved, and a low-temperature tempering or aging treatment at ~400°C can, by a strain-aging effect, increase the proof stress by ~150 MN/m^2. The achievement of high strengths by cold working, which requires some 60 to 80 percent reduction during deformation, is limited to thin flat-rolled products or to wire, and one of the main disadvantages is that the strength is rapidly lost at temperatures above 600°C, and also in the heat affected zones of a weld.

Controlled Rolling (Warm Working)

Controlled rolling may be carried out at temperatures below 950°C, and to as low as 700°C, that is, below the recrystallization temperature [*94*]. At the lower rolling finishing temperatures, only dynamic recovery takes place, and the increase in strength is associated with the fine subgrain size produced. At somewhat higher rolling finishing temperatures, recrystallization may occur, but the grain size is fine, and this also produces strengthening. The effect of composition is also of interest, in that solid solution hardening by nitrogen is retained at all rolling finishing temperatures, and additions of niobium or titanium inhibit recrystallization and maintain fine grain or subgrain sizes with a still further increase in strength. Also there is probably a small amount of dispersion strengthening by strain induced NbC or TiC precipitation, Fig. 18. The strengthening

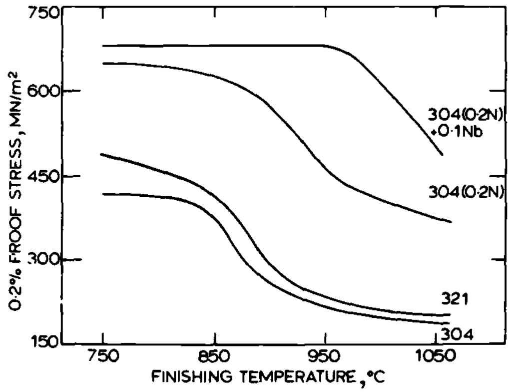

FIG. 18—*Effect of finishing rolling temperature on the properties of austenitic stainless steels.*

mechanisms contributing to the proof stress values of Type 304 and Type 347 steels after finishing rolling at high and low temperatures are shown in Fig. 19 [*73*]. A certain lack of uniformity of properties in thin material may be overcome by reheating to temperatures below the recrystallization temperature, without loss of strength, Fig. 20. Additions of niobium and titanium, which retard recrystallization, allow the use of higher reheating temperatures [*94*].

Duplex-Austenite Delta-Ferrite Steels

It has already been shown that an increase in the delta ferrite content increases the tensile strength and proof stress. A further advantage of the presence of delta ferrite is that it causes grain refinement of the austenite, which produces additional strengthening. These two effects can be combined and accentuated by a further refinement of both the austenite and ferrite grain sizes by thermomechanical treatments at or below 900 to 950°C. A type of steel currently of considerable interest is one in which the composition is so adjusted that it contains about 50 percent ferrite [*2,96–100*] and the austenite can be precipitated from the ferrite either during thermomechanical processing, or by reheating cold-worked ferrite.

The fine dispersion of ferrite in a fine-grained austenite results in increased strength, proof stress values of 500 to 600 MN/m^2 being obtained. However, the general ductility is rather lower than in the fully austenitic steels, due to the higher strength, and the impact toughness is somewhat decreased. It is reported that the steels are rather less cold formable than conventional austenitic steels, although possessing good corrosion and stress corrosion resistance. There is, however, a danger of losing the micro-duplex structure on welding.

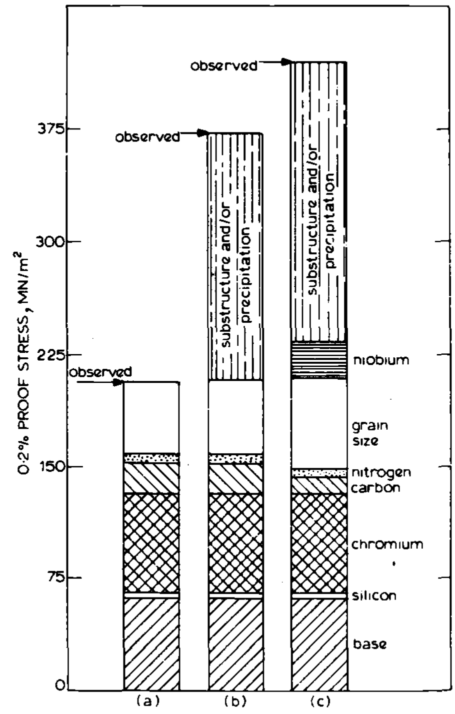

(*a*) Type 304 finished rolling at high temperatures.
(*b*) Type 304 finished rolling at low temperatures.
(*c*) Type 347 finished rolling at low temperatures.

FIG. 19—*Effect of various strengthening mechanisms on controlled-rolled austenitic stainless steels.*

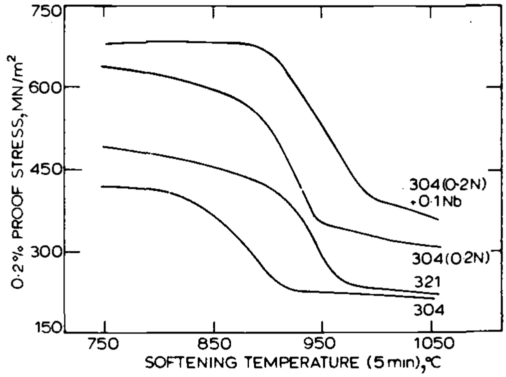

FIG. 20—*Effect of reheating temperature on properties of controlled-rolled austenitic stainless steels.*

Recent attempts have been made to improve the formability, while retaining the improved strength [*101*]. It has been found possible to destabilize the austenite so that it transforms to martensite during tension testing and cold forming, with the result that the maximum uniform elongation is increased. This should improve the stretch forming characteristics. It may well be possible to improve the deep drawing characteristics by devising thermomechanical treatments that induce preferred textures into both the ferrite and austenite phases, and thus increase the $\bar{r}$ value. Such an improvement may not, however, be very great as the austenite and ferrite are related in orientation by the Kurdjumov-Sachs orientation relationship, which seems to militate against the development of the optimum texture in both phases simultaneously.

The mention of the transformation induced plasticity in stainless steels leads to the consideration of the stainless TRIP steels [*1,102*], but this subject is rather too extensive for inclusion in this review, as also is the subject of precipitation hardening in the various types of stainless steels [*1,103–105*], that is, the transformable 12 to 17Cr stainless steels, the ferritic and the austenitic stainless steels.

Closing Remarks

While this review only presents a generalized account of structure property relationships in various types of stainless steels, it is in large measure confined to the more standard types of stainless steel and to room-temperature properties. Particular attention has been paid to the factors that describe strength, toughness and ductility or formability, and, where possible, quantitative relationships have been described.

Despite fragmentary data, many of the properties of the transformed 12 to 17 percent chromium steels can be reasonably described by the modification of relationships initially derived for low alloy steels and their transformation products. There is however, a need for more information on toughness, particularly fracture toughness parameters, and it is also important that work should be done to characterize more quantitatively the microstructural parameters for the structures.

The many interactions observed in the fully ferritic stainless steels makes the quantitative predictions of their properties difficult, and particularly more knowledge is required of the solubility of the different carbides and nitrides, and the substitutional-interstitial interactions. While the structure-property relationships in the austenitic steels are reasonably well documented, continued refinement of the models describing formability parameters and ductility is necessary. Finally, while a start has been made in predicting the various corrosion parameters for austenitic stainless steels in terms of composition and structure [*1*], a similar approach for all types of stainless steels might well yield interesting and useful results.

References

[1] Pickering, F. B., *International Metallurgical Reviews,* Review No. 211, Dec. 1976, p. 227.

[2] "Stainless Steel '77," Climax Molybdenum Company Symposium, London, Sept. 1977.

[3] Bungardt, K., Kunze, E., and Horn, E., *Archive Eissenhuttenwesen,* Vol. 29, 1958, p. 193.

[4] Irvine, K. J., Crowe, D. J., and Pickering, F. B., *Journal,* Iron and Steel Institute, Vol. 195, 1960, p. 386.

[5] Irvine, K. J., Pickering, F. B., and Llewellyn, D. T., *Journal,* Iron and Steel Institute, Vol. 192, 1959, p. 218.

[6] Briggs, J. Z. and Parker, T. D., "The Super 12%Cr Steels," Climax Molybdenum Company.

[7] Schneider, H., *Foundry Trade Journal,* Vol. 108, 1960, p. 562.

[8] Monkman, F. C., Cuff, F. B., and Grant, N. J., *Metals Progress,* Vol. 71, 1957, p. 94.

[9] Eichelman, G. H., and Hull, F. C., *Transactions,* American Society of Metals, Vol. 45, 1953, p. 77.

[10] Payson, P. and Savage, C. H., *Transactions,* American Society of Metals, Vol. 33, 1944, p. 261.

[11] Pickering, F. B., "The Optimisation of Microstructures in Steel and Their Relationship to Mechanical Properties" in *Proceedings* ASM/ASTM Symposium on Hardenability, Chicago, Oct. 1977.

[12] Leslie, W. C., *Strengthening Mechanisms,* Syracuse University Press, 1966, p. 43.

[13] Chilton, J. M., and Kelly, P. M., *Acta Metallurgica,* Vol. 16, 1968, p. 637.

[14] Cohen, M., *Transactions,* American Institute of Mining, Metallurgical, and Petroleum Engineers, Vol. 224, 1962, p. 638.

[15] McEvily, A. J., et al. *Transactions,* American Institute of Mining, Metallurgical, and Petroleum Engineers, Vol. 236, 1966, p. 108.

[16] Cox, A. R., *Journal,* Iron and Steel Institute, Vol. 205, 1967, p. 51.

[17] Irvine, K. J., et al. *Journal,* Iron and Steel Institute, Vol. 196, 1960, p. 66.

[18] Kelly, P. M. and Nutting, J., Iron and Steel Institute Special Report 93, 1965, p. 166.

[19] Kelly, P. M., Iron and Steel Institute, Special Report 93, 1965, p. 180.

[20] Grange, R. A., *Transactions,* American Society of Metals, Vol. 59, 1966, p. 26.

[21] Gladman, T. and Pickering, F. B., *Journal,* Iron and Steel Institute, Vol. 204, 1966, p. 112.

[22] McFarland, W. H., *Transactions,* American Institute of Mining, Metallurgical, and Petroleum Engineers, Vol. 233, 1965, p. 2028.

[23] Whiteman, J. A., "Low Carbon Structural Steels for the Eighties" The Institution of Metallurgists, Spring Residential Course, 1977, Series 3, No. 6, p. I–1.

[24] Norstrom, L. A., *Scandinavian Journal of Metals,* Vol. 5, 1976, p. 159.

[25] Kehoe, M. and Kelly, P. M., *Scripta Metallurgica,* Vol. 4, 1970, p. 473.

[26] Malik, L. and Lund, J. A., *Metallurgical Transactions,* Vol. 3, No. 6, 1972, p. 1403.

[27] Leslie, W. C. and Sobers, R. J., *Transactions,* American Society of Metals, Vol. 60, 1967, p. 459.

[28] Onel, K., Ph.D. thesis, Leeds University, 1977.

[29] Ashby, M. F., "Oxide Dispersion Strengthening," AIME Conference, American Institute of Mining, Metallurgical, and Petroleum Engineers, New York, 1966, p. 143.

[30] Pickering, F. B., "Transformation and Hardenability in Steel," Climax Molybdenum Company Symposium, Ann Arbor, 1967, p. 109.

[31] Pickering, F. B., "Micro-Alloying 75," Union Carbide Corp. 1977, p. 9.

[32] Gladman, T., Dulieu, D., and McIvor, I. D., "Micro-Alloying 75," Union Carbide Corp. 1977, p. 32.

[33] Ohtani, H., Terasaki, F., and Kunitake, T., *Transactions,* Iron and Steel Institute of Japan, Vol. 12, 1972, p. 118.

[34] Naylor, J. P. and Krahe, P. R., *Metallurgical Transactions,* Vol. 5, 1974, p. 1699.

[35] Little, E. A., Harries, D. R., Pickering, F. B., and Keown, S. R., *Metals Technology,* April 1977, p. 205.

[36] Pickering, F. B., "Towards Improved Ductility and Toughness," Climax Molybdenum Company Symposium, Kyoto, 1971, p. 9.

[37] Kaltenhauser, R. H., *Metallurgical Engineering Quarterly*, Vol. 2, 1972, p. 41.

[38] Schmidt, W. and Jarleborg, O., "Ferritic Stainless Steels with 17%Cr," Climax Molybdenum Company, 1974.

[39] Castro, R. and Tricot, R., *Metal Treatments*, Vol. 33, 1964, pp. 401, 436, and 469; Vol. 33, 1966, p. 401.

[40] Steigerwald, R. F., Dundas, H. J., Redmond, J. D., and Davison, R. M., "Stainless Steel 77," Paper No. 4, Climax Molybdenum Company Symposium, London, Sept. 1977.

[41] Lena, A. J. and Hawkes, M. F., *Transactions*, American Institute of Mining, Metallurgical, and Petroleum Engineers, Vol. 194, 1954, p. 607.

[42] Fisher, R. M., Dulis, E. J., and Carrol, K. G., *Transactions*, American Institute of Mining, Metallurgical, and Petroleum Engineers, Vol. 197, 1957, p. 690.

[43] Marcinkowski, M. J., Fisher, R. M., and Szirmae, A., *Transactions*, American Institute of Mining, Metallurgical, and Petroleum Engineers, Vol. 230, 1964, p. 676.

[44] Blackburn, M. J. and Nutting, J., *Journal*, Iron and Steel Institute, Vol. 202, 1964, p. 610.

[45] Moller, G. E., *Materials Protection*, May 1966, p. 62.

[46] Lagneborg, R., *Transactions*, American Society of Metals, Vol. 60, 1967, p. 67.

[47] Chandra, D. and Schwartz, L. H., *Metallurgical Transactions*, Vol. 2, 1971, p. 511.

[48] Grobner, P. J., *Metallurgical Transactions*, Vol. 4, 1973, p. 251.

[49] Williams, R. O., *Metallurgical Transactions*, Vol. 5, 1974, p. 967.

[50] Koutaniemi, P., Heikkinen, V., and Saarinen, A., *Metal Science Journal*, Vol. 8, 1974, p. 94.

[51] Courtnall, M. and Pickering, F. B., *Metals Science*, Aug. 1976, p. 273.

[52] Pickering, F. B., *Heat Treatment Aspects of Metal-Joining Processes*, The Iron and Steel Institute, London, 1972, p. 84.

[53] Lewis, D. B., Ph.D. thesis, Sheffield City Polytechnic, England, 1979.

[54] Semchysen, M., Bond, A. P., and Dundas, H. J., "Towards Improved Ductility and Toughness," Climax Molybdenum Company Symposium, Kyoto, 1971, p. 239.

[55] Abo, H., Nakazawa, T., Takemura, S., Onoyama, M., Ogawa, H., and Okada, H., "Stainless Steel '77," Paper No. 2, Climax Molybdenum Company Symposium, London, Sept. 1977.

[56] Aslund, C., "Stainless Steel '77," Paper No. 12, Climax Molybdenum Company Symposium, London, Sept. 1977.

[57] Llewellyn, D. T., Hooper, R. A. E., and McNeeley, V. J., *Sheet Metal Industries*, Jan. 1972, p. 26.

[58] Wright, R. N., *Welding Journal*, Oct. 1971.

[59] Binder, W. R. and Spendelow, H. O., *Transactions*, American Society of Metals, Vol. 43, 1951, p. 759.

[60] Blom, K. J., "Stainless Steel '77," Paper No. 16, Climax Molybdenum Company Symposium, London, Sept. 1977.

[61] Jarleborg, O., *A New Stainless Steel That Has Come to Stay; 18Cr-2Mo*, Climax Molybdenum Company, 1977.

[62] Brickner, K. G., *Selection of Stainless Steels*, American Society of Metals, 1968, p. 1.

[63] Gokyu, I., Hamasaki, N., and Okamura, S., *Nippon Kinzoku Gahkai-Si*, Vol. 34, 1970, p. 452.

[64] Wright, J. C., *Sheet Metal Industries*, May 1974, p. 263; June 1974, p. 324.

[65] Zappfe, C., *Stainless Steels*, American Society of Metals, 1949.

[66] Cook, A. J. and Brown, B. R., *Journal*, Iron and Steel Institute, Vol. 171, 1952, p. 345.

[67] Pryce, L. and Andrews, K. W., *Journal*, Iron and Steel Institute, Vol. 195, 1960, p. 415.

[68] Hattersley, B. and Hume-Rothery, W., *Journal*, Iron and Steel Institute, Vol. 207, 1966, p. 683.

[69] Angel, T., *Journal*, Iron and Steel Institute, Vol. 173, 1954, p. 165.

[70] Andrews, K. W., private communication.

[71] Gladman, T., Holmes, B., and Pickering, F. B., unpublished work.

[72] Gladman, T., Hammond, J., and Marsh, F. W., *Sheet Metal Industries*, Vol. 51, No. 5, 1974, p. 219.

[73] Irvine, K. J., Gladman, T., and Pickering, F. B., *Journal*, Iron and Steel Institute, Vol. 207, 1969, p. 1017.

[74] Nutting, J., *Journal*, Iron and Steel Institute, Vol. 207, 1969, p. 872.

[75] Sandstrom, R. and Bergqvist, H., *Scandinavian Journal of Metals*, Vol. 6, No. 4, 1977, p. 156.

[76] Norstrom, L. A., *Metal Science*, Vol. 11, No. 6, 1977, p. 208.

[77] Schramm, R. E. and Reed, R. P., *Metallurgical Transactions*, Vol. 6A, 1975, p. 1345.

[78] Holmes, B. and Dyson, D. J., *Journal*, Iron and Steel Institute, Vol. 208, 1970, p. 469.

[79] Goodman, S. R. and Hu, H., *Transactions*, American Institute of Mining, Metallurgical, and Petroleum Engineers, Vol. 230, 1964, p. 1413.

[80] Dickson, M. J. and Green, D., *Materials Science Engineering*, Vol. 4, 1969, p. 304.

[81] Hu, H., Cline, R. S., and Goodman, S. R., *Recrystallisation, Grain Growth and Textures*, American Society of Metals, 1965, p. 295.

[82] Goodman, S. R. and Hu, H., *Transactions*, American Institute of Mining, Metallurgical, and Petroleum Engineers, Vol. 233, 1965, p. 103.

[83] Goodchild, D., Roberts, W. T., and Wilson, D. V., *Journal*, Iron and Steel Institute, Vol. 209, 1971, p. 283.

[84] Dillamore, I. L., Roberts, W. T., and Wilson, D. V., *Stainless Steels*, Iron and Steel Institute, 1968, p. 37.

[85] Dickson, M. J. and Green, D., *Sheet Metal Industries*, Vol. 46, p. 1969, p. 994.

[86] Nutting, J. and Dulieu, D., Iron and Steel Institute, Special Report 86, 1964, p. 140.

[87] Swann, P. R., *Corrosion*, Vol. 19, 1963, p. 102.

[88] Barnartt, S., Stickler, R., and Van Rooyen, D., *Corrosion Science*, Vol. 3, 1963, p. 9.

[89] Gallagher, P. C. J., *Metallurgical Transactions*, Vol. 1, 1970, p. 2429.

[90] Llewellyn, D. T. and Murray, J. D., Iron and Steel Institute, Special Report No. 86, 1964, p. 197.

[91] Ludwigson, D. C. and Berger, J. A., *Journal*, Iron and Steel Institute, Vol. 207, 1969, p. 63.

[92] Gladman, T., British Corporation, private communication.

[93] Norstrom, L. A., *Scandinavian Journal of Metals*, Vol. 6, No. 4, 1977, p. 145.

[94] Llewellyn, D. T. and McNeeley, V. J., *Sheet Metal Industries*, Vol. 49, No. 1, 1972, p. 17.

[95] Parkin, G., Iron and Steel Institute, Special Report No. 76, 1962, p. 87.

[96] Hayden, H. W. and Floreen, S., *Transactions*, American Society of Metals, Vol. 61, 1968, pp. 474 and 489.

[97] Ward, D. M., *Iron and Steel*, American Society of Metals, Feb. 1970, p. 11.

[98] Gibson, R. C., Hayden, H. W., and Brophy, S. H., *Transactions*, American Society of Metals, Vol. 61, 1968, p. 85.

[99] Gibson, R. C. and Brophy, J. H., Technical Paper 650-T-OP, International Nickel Co., Sept. 1969.

[100] Wessling, W. and Bock, H. E., "Stainless Steel '77," Paper No. 17, Climax Molybdenum Company Symposium, London, Sept. 1977, to be published.

[101] Hull, J. B. and Pickering, F. B., unpublished work.

[102] Zackay, V. F., *Journal*, Iron and Steel Institute, Vol. 207, 1969, p. 894.

[103] Irvine, K. J., Llewellyn, D. T., and Pickering, F. B., *Journal*, Iron and Steel Institute, Vol. 199, 1961, p. 153.

[104] Dulis, E. J., *Journal*, Iron and Steel Institute, Special Report No. 86, 1964, p. 162.

[105] Pickering, F. B., *Heat Treatment '73*, The Metals Society, London, 1975, p. 1.

Bertil Ahlblom[1] *and William Roberts*[1]

Possibilities for Microstructural Control During Hot Working of Austenitic Stainless Steels

REFERENCE: Ahlblom, Bertil and Roberts, William, **Possibilities for Microstructural Control During Hot Working of Austenitic Stainless Steels,"** *MiCon 78: Optimization of Processing, Properties, and Service Performance Through Microstructural Control, ASTM STP 672,* Halle Abrams, G. N. Maniar, D. A. Nail, and H. D. Solomon, Eds., American Society for Testing and Materials, 1979, pp. 296–305.

ABSTRACT: The development of fine-grained microstructures by hot working to strains sufficient to effect at least partial dynamic recrystallization has been investigated by hot compression experiments on two austenitic stainless steels. After deformation, specimens were either held at the working temperature or cooled at a constant rate. As expected, fine structures are produced after working at low temperatures but, unfortunately, these tend to be mixed, the smaller grains originating from dynamic recrystallization and the coarser from static *(metadynamic)* recrystallization during holding/cooling. This heterogeneity is less pronounced after working at higher temperatures and, for given deformation conditions, tends to be eliminated as the cooling rate is reduced.

KEY WORDS: steels, microstructure, hot working, austenitic stainless steels, recrystallization, continuous cooling, grain size, heterogeneous grain structure

Several investigations have demonstrated clearly that austenitic stainless steels, in common with other face centered cubic (fcc) alloys with low stacking-fault energy, can undergo restoration by dynamic recrystallization during hot working [*1–4*].[2] This transformation is initiated once the material is deformed to a strain that exceeds a relatively large critical value, ϵ_c, and proceeds during the actual deformation concurrently with work hardening and dynamic recovery.

Dynamic recrystallization requires a high driving force, and nucleation of new grains is accordingly prolific; hence, the grain size affected by this reaction is much finer than that generated by the recrystallization that takes place after straining has been terminated or during pauses between separate deformation steps (static recrystallization). This is demonstrated

---

[1] Group leaders, Swedish Institute for Metals Research, Stockholm, Sweden.

[2] The italic numbers in brackets refer to the list of references appended to this paper.

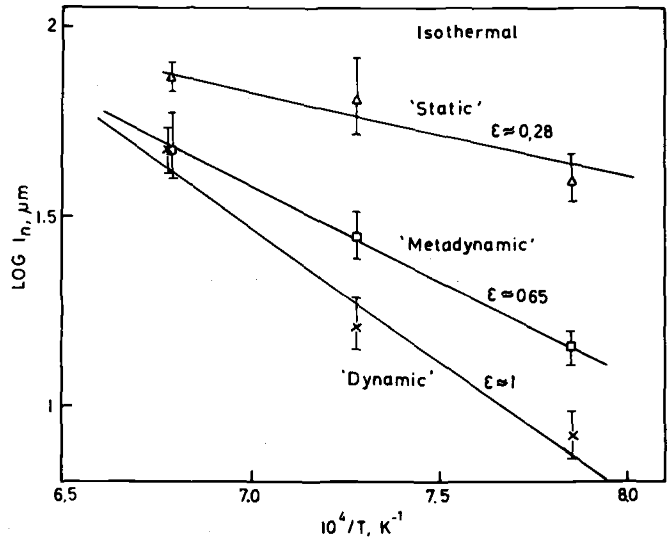

FIG. 1—*Linear intercept grain size in Type 304 steel due to dynamic recrystallization* (*ϵ = 1 ±0.05) compared with that produced by recrystallization after straining to ϵ = 0.28 ±0.02 (static) and ϵ = 0.65 ± 0.03 (metadynamic)* [1].

in Fig. 1 [*1*], where the linear intercept grain size (twin boundaries excluded) produced by dynamic recrystallization of AISI 304 steel deformed at a strain rate of 1 s^{-1} is presented as a function of temperature. The dynamically recrystallized microstructure has been preserved as far as possible by rapid quenching after cessation of deformation. The grain sizes affected by complete isothermal recrystallization of the same material after deforming under equivalent conditions to a strain of 0.28 ±0.02 are presented for comparison. Also included in Fig. 1 are data for the mean grain sizes produced by partial dynamic recrystallization (ϵ = 0.65 ± 0.03) followed by holding at the working temperature until the remaining material has recrystallized statically. Under such conditions, it is thought that the recrystallization that takes place during holding proceeds extremely quickly because of the pre-existence of nuclei created by the prior dynamic recrystallization, that is, no incubation period is required. The term *metadynamic recrystallization* has been coined in the literature to describe this type of transformation. At the highest temperature (1200°C) in Fig. 1, a strain of 0.65 corresponds to almost complete dynamic recrystallization and, hence, the metadynamic grain size is virtually the same as the dynamic one. As the deformation/holding temperature is reduced, then the proportion of the microstructure that recrystallizes metadynamically increases, and, in consequence, the dynamic and metadynamic lines diverge. The size of both statically and metadynamically recrystallized grains decreases with strain as might be

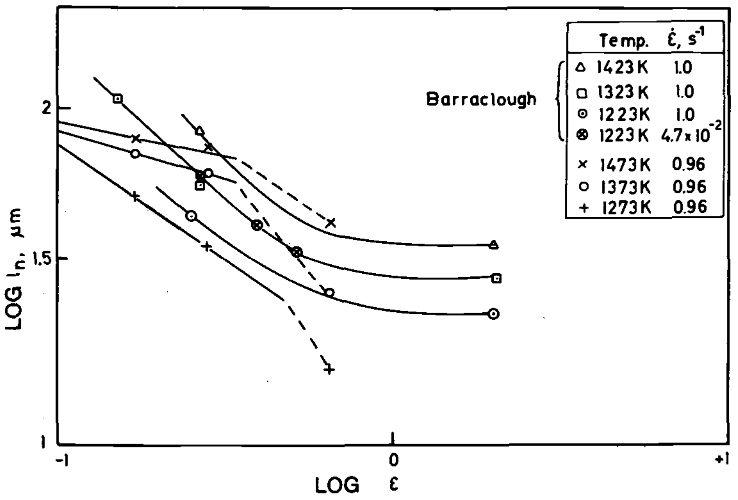

FIG. 2—*Linear intercept static or metadynamic recrystallized grain size as a function of strain in Type 304 steel. (After Ahlblom* [5] *including results from Barraclough* [2]*).*

expected (higher driving force); this is illustrated by Fig. 2 [*5*]. The dynamically recrystallized grain size, on the other hand, is generally regarded as strain independent [*6*]; nor does it change much if the pre-existing grain size is altered within wide limits [*1,7*]. Since the preferential nucleation sites for all types of recrystallization are pre-existing grain boundaries, then the recrystallization rate is always enhanced by a fine initial grain size [*1,3,7*].

From the preceding discussion, it is clear that for hot-working processes that engender sufficiently large strains in individual steps (for example, extrusion and piercing), then a fine grain size can, in principle, be produced in austenitic stainless steels by two essentially different routes: *(a)* by working at a high temperature so affecting a relatively large amount of dynamic and little metadynamic recrystallization; and *(b)* by working at a lower temperature that gives less dynamic recrystallization but ensures that the metadynamically recrystallized grains are relatively small.

This investigation represents an attempt to discover if either of these procedures can engender effective grain refinement and, if so, to establish which one is the most efficient. Furthermore, since the results presented in Figs. 1 and 2 are from isothermal experiments involving *quenching-in* of the various recrystallized microstructures, then it is important to establish how normal air cooling from the deformation temperature coarsens the grain-refined steel. Particular attention has been given to: *(a)* the degree of stability of the dynamically recrystallized grains against further static recrystallization (these will contain a small but significant dislocation density, since they are formed during the actual deformation.); and *(b)* the extent of general microstructural coarsening as a result of normal grain growth on completion of recrystallization. Clearly, both these effects will be more pronounced at slower cooling rates.

We are not aware of any other investigation that has been aimed specifically at elucidating the stability during continuous cooling of fine-grained microstructures generated by hot working to large strains.

Experimental Procedure

Axisymmetric compression testing of cylindrical specimens has been carried out with a materials testing system (MTS) machine fitted with a *clamshell*-type infrared furnace. The specimen and the nimonic compression tools (the actual compression surfaces are aluminum oxide inserts) are maintained at the same temperature during testing; the temperature is controlled by a closed-loop control circuit via a thermocouple (platinum/platinum-10 percent rhodium) welded to the specimen. The testing machine is programmed to perform the compression with a decreasing tool velocity, such that a constant true strain rate is maintained.

After deforming to a strain of 1 ± 0.05 (strain rate 1 s^{-1}), the specimens were either held at the working temperature until the recrystallization was complete or cooled directly after deformation at a constant rate of decrease of temperature. In the continuous-cooling tests, the desired cooling behavior was affected via a standard Data-track program controller. For a more detailed description of the hot compression equipment the reader is referred to earlier reports [*1*,*5*].

The experiments reported here have been carried out on two different austenitic steels (AISI Type 304 and Wnr 1.4439), the analyses of which are given in Table 1. The Type 304 steel was annealed at 1250°C, 2 h prior to testing, thus producing rather coarse grains, linear intercept = 400 μm. The corresponding treatment of Steel 4439 was at 1150°C, 15 min (90 μm). For the continuous cooling experiments, two cooling speeds were chosen, namely, 50°C/min and 10°C/min. The former rate is meant to correspond roughly to air cooling of a product with fairly small dimensions (~10 mm plate) and the latter to considerably heavier gage material, for example, ~50 mm slab.

The deformed specimens were sectioned axially and prepared for

TABLE 1—*Composition of Type 304 and 4439 Steels.*

Steel	C	Si	Mn	P	S	Cr	Ni	Mo	N
304	0.042	0.53	1.29	0.008	0.011	18.3	9.34	0.01	0.024
4439	0.027	0.53	1.59	0.017	0.015	15.8	14.0	4.3	0.14

metallographic examination by standard methods; the grain size was measured as the mean linear intercept from 20 separate fields.

Results and Discussion

AISI Type 304

It should be made clear from the outset that for the deformation conditions adopted in this work, the imposed strain ($\epsilon = 1.0 \pm 0.05$) was sufficient to engender partial dynamic recrystallization in both steels. The regions that had not transformed during working were then recrystallized metadynamically either by holding at the deformation temperature or under continuous cooling at a fixed rate.

The results from Type 304 steel are summarized in Fig. 3. After predeforming at both 1000 and 1100°C, the finest grains are obtained after isothermal metadynamic recrystallization; the holding times at the working temperatures were 120 s and 40 s, respectively. These holding times have been selected with a view to engendering complete metadynamic recrystallization in those regions that have not recrystallized dynamically during deformation, coupled as far as possible with the avoidance of grain growth. The grain sizes so obtained constitute a metadynamic line for $\epsilon = 1.0 \pm 0.05$ (compare with Fig. 1 where the metadynamic data refer to $\epsilon = 0.65 \pm 0.03$). It should be pointed up that for the particular degree of

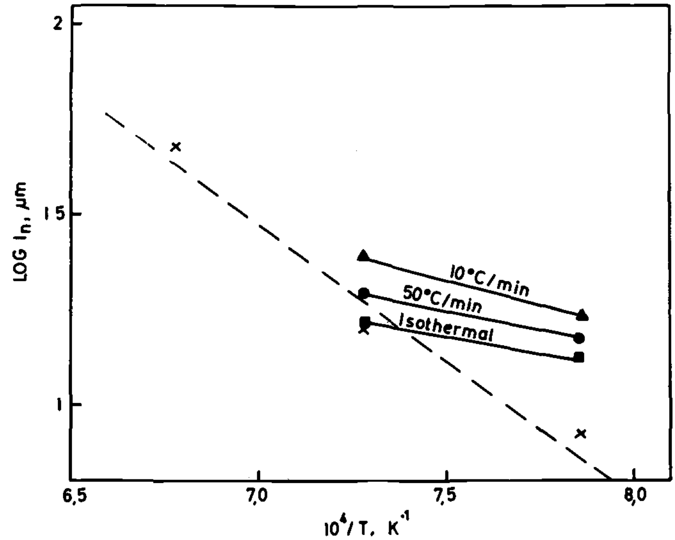

FIG. 3—*Linear intercept grain size obtained after various thermomechanical treatments adopted in this work. Specimens were deformed to $\epsilon = 1$ at a strain rate of 1 s^{-1}. The broken line is identical to the line for dynamic recrystallization in Fig. 1.*

predeformation adopted ($\epsilon = 1.0 \pm 0.05$), the volume fraction occupied by dynamically recrystallized grains was 0.7 after working at 1100°C; the corresponding figure for deformation at 1000°C is 0.3. Hence, at 1100°C, the *mean* grain size after metadynamic recrystallization is not much greater than the value characteristic for the dynamic transformation, because the volume fraction of the microstructure occupied by the coarser metadynamic grains is relatively small. For predeformation at 1000°C, the mean grain size is increased considerably over the dynamic value; in this case, the amount of prior dynamic recrystallization is low and the metadynamic grains formed subsequent to deformation dominate the microstructure. The mean grain size obtained at 1000°C in these experiments ($\epsilon \simeq 1$) is smaller than that shown on the metadynamic line in Fig. 1 ($\epsilon \simeq 0.65$). This is to be expected in view of the difference in predeformation strain.

As regards the continuous cooling results, it is clear that the mean grain sizes for both predeformation temperatures are marginally increased, at least for the cooling rates studied here. This observation is perhaps not surprising for the slower cooling rate; for cooling at 50°C/min, on the other hand, one might intuitively guess that the recrystallized grains formed in those regions that have not recrystallized dynamically during deformation should be progressively refined if the temperature falls rapidly, that is, the mean grain size should be less than the isothermal value. That this is not the case can perhaps be understood in terms of the following argument. The recrystallized grain size produced by static (or metadynamic) recrystallization at some particular temperature is determined solely by the rates of nucleation and growth, which may be functions of time, and on the way in which the nucleation sites are distributed within each pre-existing grain. The nucleation and growth kinetics both depend in their turn on the available driving force and the temperature. Now, since the nucleation and growth rates exert opposite influences on the recrystallized grain size (an increased nucleation rate promoting finer and an increased growth rate coarser grains), then it is not at all directly obvious how the latter is affected by alterations in driving force and temperature. Our understanding of recrystallization is quite inadequate for any concrete predictions from first principles. For example, if we appeal to experiment, it is well established that in isothermal tests involving static or metadynamic reactions, the recrystallized grain size engendered by a given degree of prestrain decreases with decreasing deformation (and holding) temperature (see Fig. 1, for example). However, it is not possible to say whether or not this behavior is a result of fast nucleation at the lower temperature or slower grain boundary migration, or some combination of both. In the present instance, the driving force in the isothermal and continuous cooling experiments is, to a first approximation, the same (this statement needs to be qualified if static recovery is rapid). Hence, if the nucleation rate exhibits a stronger temperature dependence than the mean grain boundary velocity, then one could arrive at a situation where even rapid cooling generates coarser grains than produced in an isothermal experiment, due to the dearth of nuclei. Another consideration, which is possibly important at 1000°C, is that in a situation where the temperature decrease is rapid, coarse unrecrystallized regions might remain in the microstructure; of course, the presence of these will tend to increase the mean grain size. The larger average grain size in samples cooled at 10°C/min as opposed to 50°C/min (for both predeformation temperatures) probably arises as a result of a greater degree of post recrystallization grain growth in the former case.

It is clear from Fig. 3 that a microstructure comprising a fairly large volume fraction of dynamically recrystallized grains (1100°C) is only marginally coarsened during continuous cooling (even at very slow rates) after deformation; in fact, the difference between the dynamically recrystallized grain size at 1100°C and the mean grain size produced after straining to $\epsilon \simeq 1$ and cooling at 10°C/min is only slightly greater than the combined standard deviation in the measurements. Hence, an important point from this investigation is that the fine microstructures engendered by dynamic recrystallization are surprisingly stable during continuous cooling. Dynamic recrystallization is therefore a real possibility as regards grain refinement in appropriate industrial operations. However, we should qualify this line of argument by emphasizing that in all three cases investigated, that is, isothermal holding and continuous cooling at two rates, the 1000°C treatment promotes a finer grain size than does the 1100°C one in spite of the lower fraction of dynamic recrystallization at 1000°C for the strain chosen. Hence, if a fine average grain size is to be imparted by hot working, it seems more important to maintain a low working temperature rather than to engender a considerable degree of dynamic recrystallization. In commercial processing, however, other considerations such as hot ductility or plant capacity might well limit the minimum feasible working temperature.

It will be appreciated from the earlier discussion that the measurements of mean linear intercept do not contribute any information regarding the spread of grain size, that is, the tendency to mixed structure formation. The significant size difference between grains produced by recrystallization during and subsequent to working results quite naturally in a mixed microstructure for all the thermomechanical schedules investigated, see Fig. 4(*a* and *b*).

Since the relative sizes of various types of recrystallized grains as well as the proportion of the microstructure taken up by them vary strongly with the deformation conditions (temperature, strain rate, and strain), then it is difficult to quantitatively describe the structure heterogeneity in a satisfactory way. Judging visually, the microstructure is certainly more

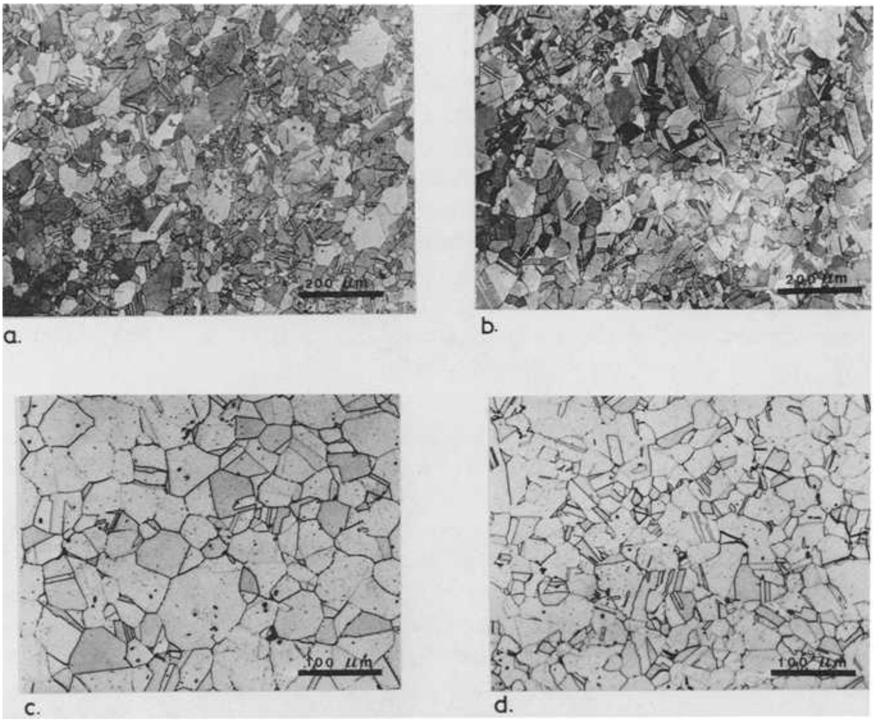

(*a*) Held 120 s at 1000°C and water quenched.
(*b*) Cooled at 10°C/min.
(*c*) Cooled at 10°C/min.
(*d*) Cooled at 50°C/min.

FIG. 4—*Micrographs illustrating the degree of microstructural heterogeneity after hot compression ($\epsilon \approx 1$) at 1000°C (Type 304 steel:* a *and* b*) and 1150°C (Steel 4439:* c *and* d*).*

homogeneous after continuous cooling as opposed to isothermal holding, especially if the cooling rate is low; this is clear from Fig. 4. Also, working at 1100°C seems to promote a microstructure that is less obviously mixed than that produced by 1000°C deformation.

Wnr 1.4439

The results from Steel 4439 are slightly different. Rapid cooling from the working temperature, 1150°C, at 50°C/min generates a grain structure having a mean linear intercept of 27 µm that can be compared with 25 µm from dynamic recrystallization under equivalent deformation conditions [7]. However, cooling at 10°C/min gives rise to much larger grains (47 µm); isothermal holding for 30 s also results in appreciable coarsening (39 µm).

It is noteworthy that in this material the microstructures produced by all these thermomechanical treatments are remarkably homogeneous, at least, as far as can be estimated visually; see Fig. 4*c* and *d*. This is surprising since, all other things being equal, the various recrystallization reactions for Steel 4439 at 1150°C proceed at roughly the same rate as they do in Type 304 steel at 1050°C. Hence, on the basis of what was just said, one would anticipate considerable grain size heterogeneity.

We think that the reason for the anomaly lies in the much smaller initial grain size of the more highly-alloyed steel (the pre-existing grain size in this material was selected so as to affect the same degree of dynamic recrystallization for the adopted strain (1.0 ± 0.05) at 1150°C as was obtained with Type 304 steel at 1100°C.

In material with smaller initial grain size, the average distance between the regions of dynamic recrystallization (which always delineate the pre-existing grain boundaries) will be low. Hence, the heterogeneity of microstructure engendered by the combination of metadynamic and dynamic recrystallization will be on a finer scale than when the initial grains are coarse. The fact that the blocks of material with different grain sizes are smaller, in turn, facilitates the rapid elimination of the microstructural heterogeneity irrespective of whether this occurs by (1) retransformation of the dynamically recrystallized areas (these contain a significant dislocation density driving force) or (2) through general structural coarsening via grain growth. The observation that the microstructure produced by isothermal holding at 1150°C and cooling at only 10°C/min is considerably coarser than that obtained after the 50°C/min cooling indicates that, for Steel 4439, the beneficial grain refinement affected by the combination dynamic/metadynamic recrystallization starts to be seriously counteracted by rapid grain growth at temperatures in the region of 1150°C. This temperature is probably somewhat lower for Type 304 quality.

Conclusions

The necessary conditions for effective grain refinement of austenitic stainless steels by hot deformation to relatively large strains are:

(a) Hot working at a low temperature gives a finer average grain size compared with deformation at higher temperatures even though a much greater degree of dynamic recrystallization is affected in the latter case.

(b) As long as the working temperature is not too high, the fine-grained structures produced by the combination dynamic/metadynamic recrystallization do not coarsen appreciably during even fairly slow cooling.

(c) When the material has been completely recrystallized during holding or air cooling after partial dynamic recrystallization, then a mixed grain structure is produced. This heterogeneity tends to be eliminated if the

working temperature is raised (higher fraction of dynamic recrystallization), if the cooling rate is reduced, or if the initial grain size is kept fine.

Acknowledgments

Sandvik AB and Uddeholms AB have provided material for this investigation, and this is gratefully acknowledged.

References

[1] Ahlblom, B., "A Metallographic Study of Dynamic Recrystallization in an 18/8 Austenitic Stainless Steel," Swedish Institute of Metals Research, IM-1208, 1977.

[2] Barraclough, D. R., "Hot Working and Recrystallization of a Stainless and a Low Alloy Steel," Ph.D. thesis, University of Sheffield, 1974.

[3] Hengerer, D., "Statische und dynamische Rekristallisation bei der Warmverformung," Radex-Rundshau, Heft 1, 1977, pp. 72–82.

[4] Pethen, R. W. and Honeycombe, R. W. K., "Dynamic Recrystallization in Austenitic Steels," ISI/IOM Meeting on Recrystallization in the Control of Microstructure, 1973.

[5] Ahlblom, B., "A Metallographic Study of Recrystallization After Hot Working in an 18/8 Austenitic Stainless Steel," Swedish Institute of Metals Research, IM-1210, 1977.

[6] McQueen, H. J. and Jonas, J. J. in *Treatise on Materials Science and Technology,* R. J. Arsenault, Ed., Academic Press, New York, Vol. 6, 1977, pp. 393–493.

[7] Roberts, W., Boden, H., and Ahlblom, B., "Dynamic Recrystallization Kinetics," Report No. 1276, Swedish Institute for Metals Research; presented at Metals Society Conference on Recrystallization in the Development of Microstructure, Leeds, England, April 1978.

Y. G. Nakagawa,[1] *T. Kawamoto,*[1] *M. Fukagawa,*[1] *and*
Y. Saiga[1]

Correlation of Sensitization with Thermomechanical History of Type 304 Stainless Steel Pipe Joint

---

REFERENCE: Nakagawa, Y. G., Kawamoto, T., Fukagawa, M., and Saiga, Y., "**Correlation of Sensitization with Thermomechanical History of Type 304 Stainless Steel Pipe Joint,**" *MiCon 78: Optimization of Processing, Properties, and Service Performance Through Microstructural Control, ASTM STP 672,* Halle Abrams, G. N. Maniar, D. A. Nail, and H. D. Solomon, Eds., American Society for Testing and Materials, 1979, pp. 306–320.

ABSTRACT: A correlation of sensitization with thermomechanical work accumulated in a weld heat affected zone of Type 304 pipe was investigated in conjunction of heat-to-heat difference, and of a welding simulation. Highly susceptible pipe heats for stress corrosion crackings were introduced primarily through inappropriate mill practices that left pre-existing grain boundary carbides or strained subsurface layers in pipes. These undesirable heats that may have a sufficient corrosion resistance in the as-received state, most rapidly lose the resistance after being exposed to weld heat cycles. A weld simulation study was made to evaluate the thermomechanical effect on sensitization development, and distinct differences from isothermal sensitizations were confirmed by microstructure observations and some corrosion tests. The thermomechanical work and the successive continuous cooling enhance sensitization significantly.

KEY WORDS: steels, microstructure, stress corrosion cracking, thermomechanical strain, weld simulation, heat affected zone, corrosion tests, pipe, sensitization

The sensitized microstructure is one of the essential ingredients for intergranular stress corrosion cracking (IGSCC) incidents in weld heat affected zones (HAZ) of Type 304 stainless steels of boiling water reactor (BWR) piping systems. In the course of the failure analyses [*1–5*][2] and recent extensive studies on working models of IGSCC in the particular environment [*5–7*], it became clear that there was a great deal of variability [*8*] in the pipe material quality with respect to mechanical

---

[1] Staff, section manager, deputy manager, and supervisory assessor, respectively, Metallurgy Department, Research Institute, Ishikawajima-Harima Heavy Industries Co., Ltd. Toyosu, Koto-ku, Tokyo, Japan.

[2] The italic numbers in brackets refer to the list of references appended to this paper.

properties, residual elements, IGSCC susceptibility [*9*], and sensitization response to electrochemical measurements [*10*]. A recent metallurgical study demonstrated the importance of the heat variation in terms of microstructural changes due to a joint fabrication by welding Dresden II heat with another typical 10.16 cm (4 in.) diameter pipe [*11*]. The other major element to contribute the sensitization variability exists in details of a welding procedure. The superposition of multiple heat pulses and simultaneous deformations due to the deposit metal shrinkage changes the pipe microstructure into the sensitized states of various degrees. The distinct difference from isothermal sensitization has been confirmed in an experiment on sensitization enhancement by continuous cooling [*12*], however, the effect of the thermomechanical strain and the relationship with the microstructural change is yet to be fully understood.

In the present program, the correlation of sensitization with overall thermomechanical work accumulated in the pipe HAZ's was investigated in conjunction with the heat-to-heat difference of a total of ten nuclear grade Type 304 pipes, mostly produced in Japan, and of a weld simulation composed with a thermomechanical straining and a successive continuous cooling. The objectives in the heat-to-heat difference study were: (1) to obtain the variability data of the domestic pipe heats, and (2) to identify major causes for the heat-to-heat difference. The weld simulation study was performed to establish the significance of thermomechanical straining and continuous cooling in development of IGSCC susceptibility through welding, and the approach to the sensitization enhancement by the weld simulation was extended to evaluate the reliability of some alternate pipe materials, Types 304L and 316L.

Experimental

Heat-to-Heat Difference Study

Procedure—Small sections of Type 304 pipes (7.62 to 25.4 cm) (3 to 8 in.) originated from ten different heats, including ones applied in nuclear power plants with or without stress corrosion cracking (SCC) failure were prepared, and were processed through the format illustrated in Fig. 1. In the present work, the ten heats are designated by E through O in alphabetical order. Heats E, F, and G were forged pipes used as flanges or nozzles, and other samples were all seamless pipes made through the conventional extrusion process. The procedure was composed of three major steps: (1) characterization of as-received pipes by metallography, microhardness measurement, and chemical analyses; (2) observation of IGSCC susceptibility development by furnace sensitizations; and (3) examination of solution heat treatment effect in response to furnace sensitizations. The test details are described in the following.

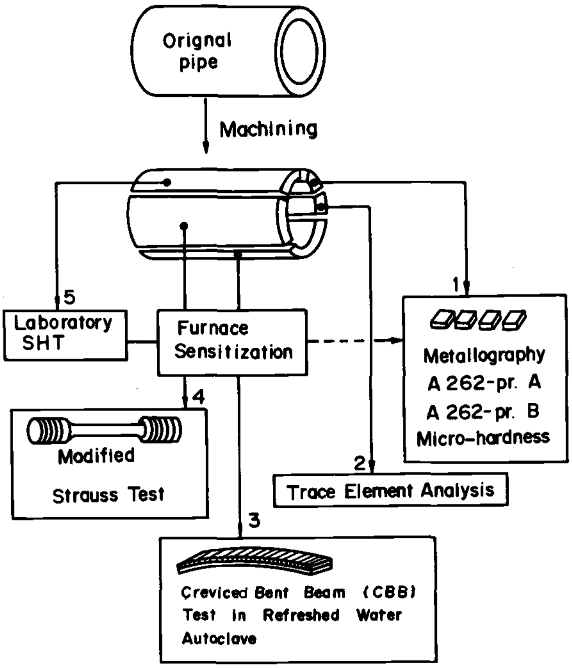

FIG. 1—*Experimental format in heat-to-heat difference study.*

Heat Treatment—Sensitization heat treatments (SHT) were given pipe sections at 500°C for 24 h and at 680°C for 5, 30, 60, and 180 min. The heat treatments at 500°C for 24 h and at 680°C for 5 min are referred to as mild sensitization conditions in this paper. For the solution heat treatment effect study, pipe sections were solutionized at 1075°C for 30 min in order to strike out the thermomechanical effect induced during the pipe fabrication process.

Metallography—Micrographs were taken of longitudinal pipe sections etched electrochemically in 10 percent oxalic acid.

Microhardness Measurement—Microhardness measurements were made on a transverse cross section of the pipes from the inner to the outer surface with test loading of 200 g.

Corrosion Test—ASTM Recommended Practices for Detecting Susceptibility to Intergranular Attack in Stainless Steels (A 262-75) Practice A was performed to longitudinal pipe sections in the as-received state to examine the grain boundary structure. ASTM A 262-75 Practice B was given sensitized plates (20 by 50 by 2 mm) extracted for as-received and solution heat treated pipe sections. The modified Strauss test [*12*] was applied to a round bar tension test specimens with a gage section of 2.5 mm diameter by 25 mm long. Degree of sensitization in the modified

Strauss test was quantified by means of ASTM A 262-75 Practice E with 100 h duration and of a subsequent tension test. Index, Ist, expresses

$$\text{Ist} = 1 - (\text{UTS after Strauss test/UTS})$$

where UTS is tensile strength.

IGSCC Test in High Temperature Water—IGSCC susceptibility of the as-received and solution heat treated pipe heats was studied by creviced bent beam (CBB) tests that allowed examination of SCC occurrence in a large number of samples in a relatively short period. Rectangular shaped samples (5 by 10 by 2 mm) were placed in the unique CBB fixture as shown in Fig. 2, and the artificial crevice made of graphite fiber wool was introduced onto the tensile side of the samples. The fixtures of the sandwich composite structure were immersed for 100 h in a water autoclave operated at 290°C with 20 ppm oxygen and pH 5.5. After the CBB test, the samples were further bent mechanically to examine SCC occurrences.

Weld Simulation (WS)

Procedure—Thermomechanical straining by torsional deformation either at 700°C (Type 304) or at 800°C (Types 304L and 316L) for 5 min, and successive continuous cooling, passing through relatively low temperatures (600 to 300°C) at a constant rate, were performed for a number of samples of a cylindrical tension test specimen extracted from 10.16 cm (4 in.) seamless pipes. The background in this WS procedure is to assume that the welding, in essence, is a process of repeating high-temperature deformation followed by the continuous cooling as schematically shown in Fig. 3. The WS process was conducted in a vacuum bell jar by the use of an experimental setup that could impose preprogrammed heat cycles

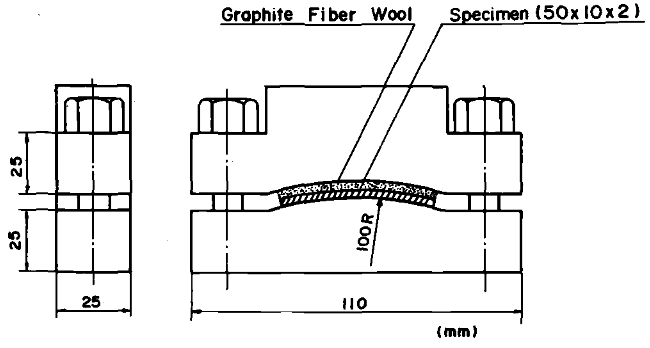

FIG. 2—*Creviced bent beam (CBB) fixture used for IGSCC susceptibility test in high temperature water.*

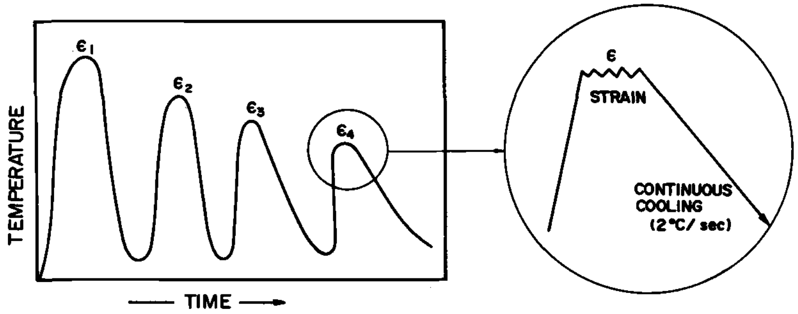

FIG. 3—*Welding process represented by summation of unit thermomechanical straining followed by continuous cooling.*

by direct-current feeding, and simultaneously could give the torsional straining by rotating the sample grips. For evaluation of the weld simulation induced IGSCC susceptibility, the conventional metallography, the modified Strauss test as just described, and two other methods were employed as explained later.

Uniaxial Constant Load (UCL) Test—The tension samples after the weld simulation were loaded at a constant stress, 20 kg/mm^2 in the water environment conditioned at 250°C, and the cumulative time consumption to failure was monitored.

Electrochemical Potentiokinetic Reactivation (EPR) Method [10]—Transverse cross sections of the weld simulation samples were positively polarized at a sweep rate of 100 mV/min from a corrosion potential of −400 mV versus saturated calomel electrode (SCE) in a deaerated electrolyte (0.5M H_2SO_4 + 0.01M KSCN, at 30°C) and inversely swept after passivation while holding it at +200 mV for 2 min. The reactivation charge, Pa, representing the area under the back scan curve expressed the degree of sensitization. The EPR test surface was observed by a scanning electron microscope (SEM).

Result

Heat-to-Heat Difference Study

Microstructural characteristics observed by 10 percent oxalic acid etching, and the results of ASTM A 262-75 Practice A conducted to the as-received pipe heats are summarized in Table 1. All forged pipes were found to be of a mixed structure, revealing grain boundary carbide precipitates yet to be dissolved by mill annealing. As for the seamless pipes, a large number of grain boundary carbides was also observed in Heat O, while the tendency was less pronounced in the microstructure of Heat H and J, having locally different etching characteristics, and occa-

TABLE 1—*Results of ASTM A 262-75 Practice A and microstructure characteristics.*

Heat	Material	Grain Size	Characteristics
E	forged	2.5	mixed structure, insufficient SHT
F	forged	2.0	mixed, insufficient SHT
G	forged	2.0	mixed, insufficient SHT
H	seamless	6.0	step, partly undesirable SHT
J	seamless	6.0	step, partly undesirable SHT, 1.5% Ferrite
K	seamless	4.5	step, excessive inclusions
L	seamless	5.0	step
M	seamless	5.0	step
N	seamless	6.0	step
O	seamless	4.5	mixed, insufficient SHT

sionally carbide precipitates were observed. The other seamless pipes, namely Heats L, M, and N showed complete step-wise boundaries, and the microstructures were generally sound. The results of the modified Strauss test for the as-received pipes are summarized in Fig. 4. All pipes in the as-received state showed no corrosion attack by the Strauss solution though the existence of grain boundary carbide was observed in

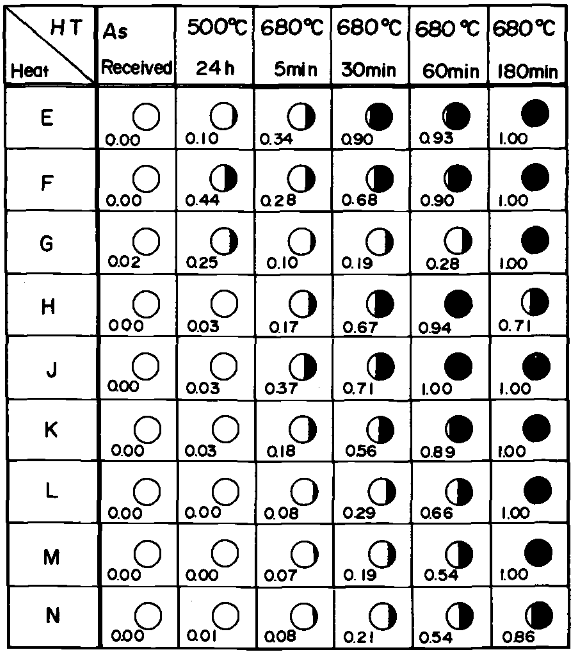

HT / Heat	As Received	500°C 24h	680°C 5min	680°C 30min	680°C 60min	680°C 180min
E	0.00	0.10	0.34	0.90	0.93	1.00
F	0.00	0.44	0.28	0.68	0.90	1.00
G	0.02	0.25	0.10	0.19	0.28	1.00
H	0.00	0.03	0.17	0.67	0.94	0.71
J	0.00	0.03	0.37	0.71	1.00	1.00
K	0.00	0.03	0.18	0.56	0.89	1.00
L	0.00	0.00	0.08	0.29	0.66	1.00
M	0.00	0.00	0.07	0.19	0.54	1.00
N	0.00	0.01	0.08	0.21	0.54	0.86

HT : Heat Treatment

FIG. 4—*Result of the modified Strauss test conducted for as-received heats. Ist indices are expressed schematically in the closed area of circles.*

some of the heats. However, those with the pre-existing carbides rapidly degraded the corrosion resistance after being exposed to the mild sensitization heat input such as 500°C for 24 h or 680°C for 5 min. It was noted that Heats L, M, and N with the sound microstructure showed the least degradation upon the mild sensitization treatments.

In Fig. 5, results of the creviced bent beam test in the high-temperature water are summarized together with results for the solution heat treated heats. The tests for Heat O was carried out with ceramic fibre wool as the crevice former, and the results of this particular heat illustrate the different behavior due to the partial dissolution of the wool. All as-received heats shown in as-received column in Fig. 5 cracked with the mild sensitizations except Heat K. Heats F and G (forged pipe with pre-existing carbides) cracked without any sort of heat treatments, and thus the creviced bent beam test may be regarded as the more sensitive representation of the sensitization than the Strauss test.

To demonstrate the solution heat treatment effect, results of ASTM, A 262-75 Practice B, and the creviced bent beam tests are shown in Fig. 6, and in SHT column of Fig. 5, respectively. By the modified Strauss test, the effect of solution heat treatment was also studied for the mild sensitization conditions, and the significant reduction of the corrosion rate was evident. The reduction of the corrosion rate was seen for ASTM A 262-75 Practice B, as well as in Fig. 6. In both cases, the heat-to-heat difference was completely eliminated by SHT. More remarkable improvement by SHT was obtained for SCC resistance in the high temperature water, as none of the heats showed cracking by the mild sensitizations.

● CRACKED ○ NOT CRACKED, AR : As Received, SHT : SHTed pipe
HT : Heat Traeatment, — : Not Tested

HEAT	E		F		G		H		J		K		L		M		N		O	
H.T	AR	SHT	AR	SHT	AR	SHT	AR	SHT	AR	SHT	AR	SHT	AR	SHT	AR	SHT	AR	SHT	AR	SHT
NIL	○	○	●	○	●	○	○	○	○	○	○	○	○	○	○	○	○	○	○	○
500°C 24h	●	○	●	○	●	○	●	○	●	○	○	○	●	○	●	○	○	○	○	○
680°C 5MIN	○	○	●	○	●	○	○	○	○	○	○	○	●	○	●	○	●	○	○	○
680°C 30MIN	●	●	●	●	●	○	●	●	●	●	●	○	●	—	●	●	●	●	○	○
680°C 60MIN	●	●	●	●	●	○	●	—	●	—	●	●	●	—	●	—	●	●	●	○
680°C 180MIN	●	—	●	—	●	—	●	—	●	—	●	—	●	—	●	—	●	—	●	●

HT : Heat Treatment

Ceramic Fiber Wool

FIG. 5—*IGSCC-go/no go test result for the creviced bent beam (CBB) test in high temperature water.*

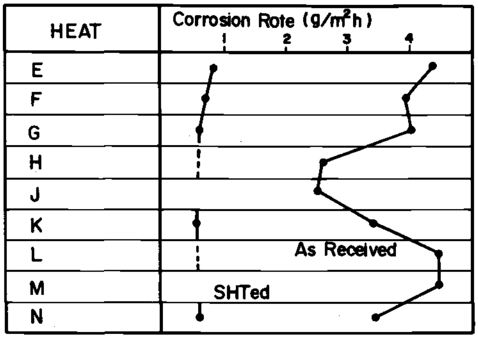

FIG. 6—*Effect of solution heat treatment (SHT) on furnace sensitization response measured by ASTM A 262-75 Practice B. As-received and SHT pipes were sensitized at 680°C for 5 min.*

Though the microstructures of Heats L, M, and N were observed to be relatively as sound as Heat K, they cracked severely in the creviced bent beam test. When the microhardness was measured in the pipe thickness direction, two heats (L and N) were proved to have abnormally high hardness layers at the inner subsurface region as much as 2 mm deep, while no such layer was detected in other pipes. The two representative examples are illustrated in Fig. 7. This high hardness layer indicates the existing strain in the pipe surface induced during the mill process.

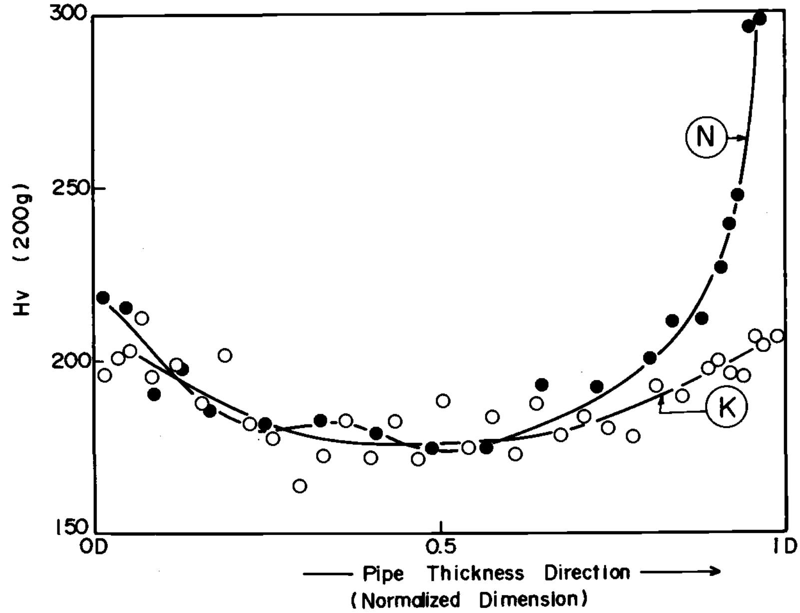

FIG. 7—*Microhardness distribution for Heats K and N in transverse cross sections.*

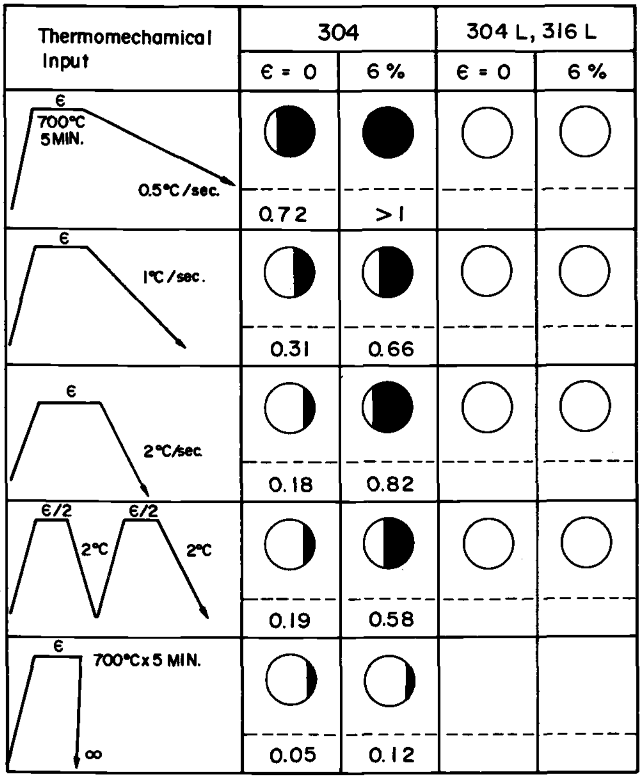

FIG. 8—*Results of the modified Strauss test for weld simulated Types 304, 304L, and 316L. Ist indices are expressed schematically in the closed area of circles.*

Weld Simulation Study

The results of the modified Strauss test are illustrated in Fig. 8. The UCL results are summarized in Table 2. The continuous cooling following the thermomechanical straining markedly enhanced sensitization for Type 304. However, no susceptibility development was detected for Types 304L and 316L treated in the similar way. In the UCL test, all the Type 304 specimens (thermomechanical straining plus cooling) failed by SCC within several hundred hours, but the sample (No. 432) without the continuous cooling did not show SCC. The micrographs in Fig. 9 illustrate the weld simulated microstructures of (*a*) Type 304 after isothermal annealing at 700°C for 5 min, (*b*) Type 304 after annealing at 700°C for 5 min followed by continuous cooling at a rate of 1°C/s, (*c*) Type 304 after 6 percent straining at 700°C for 5 min followed by continuous cooling at 1°C/s, (*d*) Type 304L after 6 percent straining at 800°C for 5 min followed by continuous cooling at 1°C/s, and (*e*) Type 316 after 6 percent straining

TABLE 2—*Summary of UCL tests conducted for weld simulated Types 304, 304L, and 316L.*

Test Piece No.	Material	Thermomechanical Straining		Continuous Cooling Rate, (°C/s)	Post Heat Treatment	Surface Finish	SCC Occurrence	Rupture Time, h
		Temperature/Time	Strain, %					
430	Type 304	700°C/5 min	0	0.5	. . .	paper	yes	481
422	Type 304	700°C/5 min	6	0.5	. . .	paper	yes	355
420	Type 304	700°C/5 min	0	1.0	. . .	paper	yes	182
435	Type 304	700°C/5 min	6	1.0	. . .	paper	yes	544
421	Type 304	700°C/5 min	0	2.0	. . .	paper	yes	377
414	Type 304	700°C/5 min	6	2.0	. . .	paper	yes	388
411	Type 304	700°C/5 min	6	2.0	. . .	grinding	yes	79
432	Type 304	700°C/5 min	6	∞	. . .	paper	no	. . .
L-1	Type 304L	800°C/5 min	6	0.5	. . .	paper	no	. . .
L-2	Type 304L	800°C/5 min	6	1.0	. . .	paper	no	. . .
L-3	Type 304L	800°C/5 min	6	1.0	500°C/24 h	shot peening	yes	282
75	Type 316L	800°C/5 min	0	1.0	500°C/24 h	paper	no	. . .
76	Type 316L	800°C/5 min	0	1.0	500°C/24 h	shot peening	no	. . .
77	Type 316L	800°C/5 min	6	1.0	500°C/24 h	shot peening	no	. . .

at 800°C for 5 min followed by continuous cooling at 1°C/s. The conventional microscopy failed to distinguish the effect of the straining and the continuous cooling. The degree of sensitization of the samples with the identical weld simulation as the previous, Fig. 9*a* through *e*, were measured by the EPR method. The results are expressed in terms of the charge density as shown in Fig. 9. The EPR gave considerable differences in the charge density among those three samples made of Type 304, Fig. 9*a*, *b*, and *c*. The EPR also represented the WS sensitization for Types 304L and 316L, while the modified Strauss test failed to detect it. The EPR test surfaces were observed by SEM, and the microstructures clearly showed the distinct difference as seen in Fig. 10.

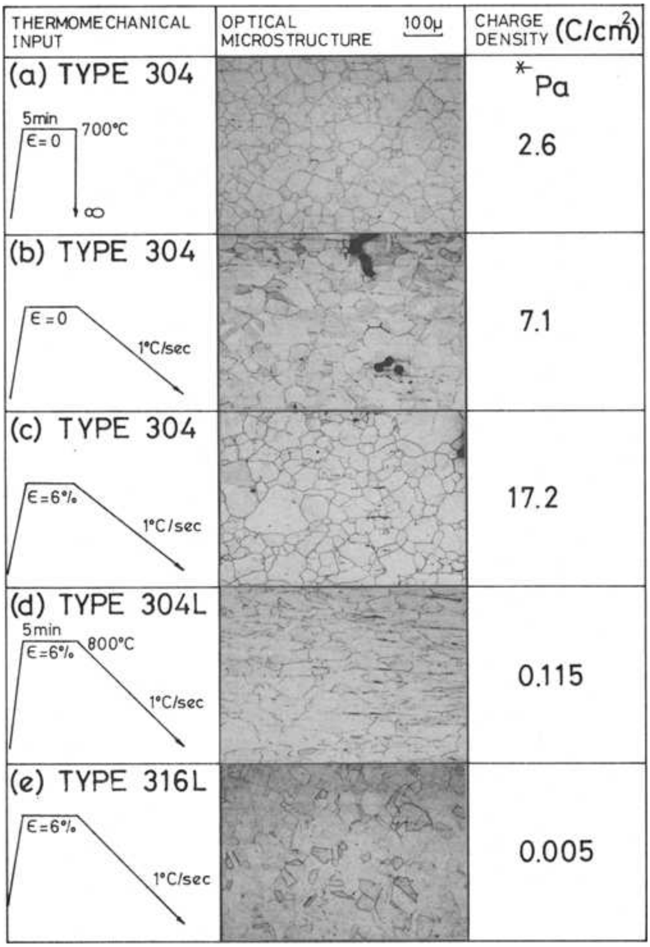

FIG. 9—*Optical microstructures and charge density of EPR measurement for various WS samples.*

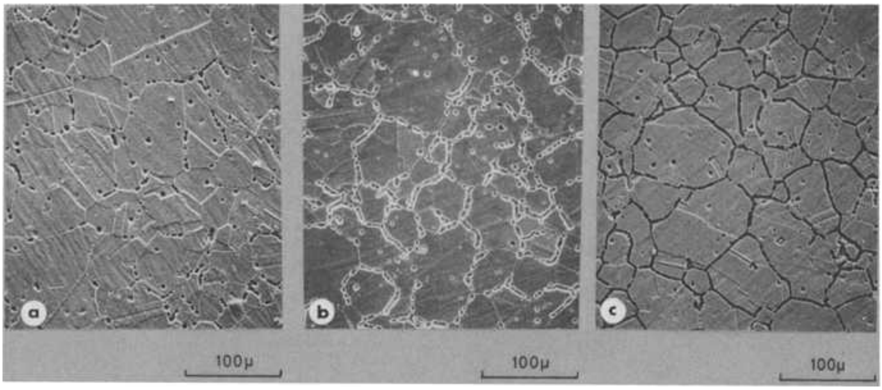

(*a*) 700°C/5 min.
(*b*) 700°C/5 min + 1°C/s.
(*c*) 700°C/5 min with 6 percent strain plus 1°C/s.

FIG. 10—*SEM micrographs of Type 304 after EPR test.*

Discussion

Through a series of tests conducted in the present investigation, the origin of good heat versus bad heat difference seems to become rather clear as the bad heats contain the pre-existing grain boundary carbides or the pre-existing surface strain or both due to improper mill practices. With the pre-existing grain boundary carbides, the nucleation stage (the important rate control process particularly at low temperatures) is already completed, and thus the sensitization with a short incubation time takes place even at 500°C at which it would not be possible without the prenucleation stage [*13*]. While there have been a number of the theories proposed for the sensitization [*14–16*], the chromium depletion theory is widely accepted and reasonably explains the present observation. The carbides in the as-received pipe were supposedly formed or left out at a relatively high temperature at which the minimum chromium level at the carbide-matrix interface was maintained to be more than 12 percent with a sufficient chromium replenishment, but the successive heat input quickly reduced the interface chromium concentration equilibrating with the test temperatures.

As for the pre-existing strain, again the sensitization enhancement is obvious due to the excessive number of vacancies promoting faster chromium diffusion during welding process, or due to microstructural changes in the material as the formation of martensites. A crude estimate of chromium diffusion activation energy for the as-received and the well-solutionized heats [*17*] suggests that the depletion zone width in the prestrained heats can increase at a rate approximately 100 times faster than the solutionized heats. Or, in terms of the required sensitization time, the critical depletion zone, if any, can be developed in a matter of a few seconds for the prestrained heat while several hours are required for the annealed heats.

The weld simulation experiment clearly demonstrated the significance of the thermomechanical input associated with a welding process. A considerable amount of data regarding the welding thermal pulses has been generated [*5*] as a function of the heat input, the distance from the fusion line, the number of passes, and the pipe size. In a representative measurement for a 10.16 cm (4 in.) pipe weld joint, rather slow cooling rates of the order of 2 to 3°C/s was noted during the final few passes at locations where the pipe IGSCC was identified. Thus, the cooling rates employed in the present investigation are comparable to welding practices. As for the deformation associated with a typical 10.16 cm (4 in.) pipe HAZ, a finite element analysis conducted in an in-house project estimated the strain in the order of few percent, and, therefore, the torsional straining in the weld simulation is not considered to be of an unreasonable magnitude. Multiheat pulse weld simulation works are currently conducted, but may not be suitable to understand the basic elements in the sensitization enhancement since a successive pulse tends to eliminate a thermomechanical history due to previous pulses by a solutionizing effect [*12*] when the temperature exceeds 900°C, and, in fact, outcomes in resultant degree of sensitization are occasionally confusing.

The modified Strauss test results and the UCL test results in Fig. 8 and in Table 2, respectively, suggest the importance of the continuous cooling during which quick establishment of a critical chromium level at the interfaces is promoted at relatively lower temperatures. The thermomechanical work serves the carbide *doner* prior to continuous cooling. If the weld simulation sensitization observed by EPR is allowed to be compared to the isothermal sensitization, the charge density and the SEM microstructure of the weld simulated Type 304 roughly correspond to those of Type 304 after a furnace sensitization at 650°C for 120 min.

For evaluating some of the candidates for the alternate pipe material, Types 304L and 316L were UCL tested. The samples were so conditioned that all ingredients to give significant influence on SCC in high temperature water were included, such as the weld simulation (straining at 800°C and continuous cooling, 1°C/s), in-service sensitization accelerated by annealing at 500°C for 24 h and shot peening surface finishes for the effect of cold works. It must be noted here that Type 304L (thus conditioned) failed by UCL at 282 h as shown in Table 2.

Conclusion

A large variability in the sensitization response and IGSCC susceptibility was observed for Type 304 pipe heats produced in Japan. The laboratory solution heat treatment markedly improved the corrosion resistance and minimized the heat-to-heat difference, thus the thermomechanical history of the pipe was considered to be primarily responsible for the variability. High corrosion susceptibility observed in some heats was apparently caused by pre-existing grain boundary carbides or pre-existing strain or both at subsurface layers. These conditions enhance the sensitization process at an unexpectedly rapid rate. The thermomechanical deformation associated with pipe welding markedly accelerates sensitization. A simple weld simulation by thermomechanical straining followed by continuous cooling at the rate of 2°C/s gave enough sensitization in Type 304 to produce IGSCC in the high temperature water.

Acknowledgment

The authors wish to thank Dr. Umemura for his help in the EPR measurement.

References

[1] Board, J. A., *Journal,* Institute of Metals, Vol. 101, 1973, p. 241.
[2] Cheng, C. F., *Journal of Nuclear Materials,* Vol. 56, 1975, p. 11.
[3] Kondo, T., Nakajima, H., and Nagasaki, R., *Nuclear Engineering and Design,* Vol. 16, 1971, p. 205.
[4] Ando, Y., "Present Status of Boiling Water Reactor Pipe Cracking and Its Research and Development in Japan," Report IAEA Technical Committee Meeting on Stress Corrosion Cracking Problems in Primary Pressure System, Palo Alto, Calif., March 1976.
[5] Klepfer, H. H., "Investigation of Cause of Cracking in Austenic Stainless Steel Piping," Technical Report, General Electric Co., NEDO-21000, July 1975.
[6] Staehle, R. W., "Mechanisms of Stress Corrosion Cracking," Report of the IAEA Technical Committee Meeting on Stress Corrosion Cracking Problems in Primary Pressure System, Palo Alto, Calif., March 1976.
[7] Hanneman, R. E. and Rao, P. "Intergranular Stress Corrosion Cracking in 304SS BWR Pipe Weldments," Technical Report TMS-AIME Fall Meeting, Chicago, American Institute of Mining, Metallurgical, and Petroleum Engineers, Oct. 1977.
[8] Smith, R. E., *Metal Progress,* Vol. 112, No. 2, July 1977, p. 42.
[9] Walker, W. I., "Relationships Between Mechanical Properties, Degree of Sensitization and Intergranular Stress Corrosion Cracking of Type 304 Stainless Steel," Technical Report No. 52, The Protection and Performance of Materials, Chicago, March 1974.
[10] Clarke, W. L., "Detection of Sensitization in Stainless Steel Using Electrochemical Techniques," Technical Report, The 4th Water Reactor Safety Research Information Meeting, Gaithersburg, Md., Sept. 1976.
[11] Rao, P., "Microstructural Studies of Weld Heat Affected Zones in 304 Stainless Steel Pipes," Technical Report No. 117, NACE Annual Symposium, San Francisco, March 1977.
[12] Solomon, H. D., "Weld Sensitization Simulation," Technical Report TMS-AIME Fall Meeting, Chicago, American Institute of Mining, Metallurgical, and Petroleum Engineers, Oct. 1977.
[13] Cowan II, R. L. and Tedmon, Jr., C. S. in *Advances in Corrosion Science and Technology,* Vol. 3, M. G. Fontana, and R. W. Staehle, Eds., Plenum Press, New York-London, 1973, pp. 293–395.

[*14*] Bain, E. C., Aborn, R. H., and Rutherford, J. B., *Transactions,* American Society of Steel Treating, Vol. 21, 1933, p. 481.

[*15*] Stickler, R. and Vinckier, A., *Corrosion Science,* Vol. 3, 1963, p. 1.

[*16*] Aust, K. T., Armijo, J. S., and Westbrook, J. H., *Transaction Quarterly,* American Society of Metals, Vol. 59, 1966, p. 544.

[*17*] Nakagawa, Y. G., to be published.

Prakash Rao[1]

Microstructural and Microchemical Studies in Weld Sensitized Austenitic Stainless Steels

---

REFERENCE: Rao, Prakash, "**Microstructural and Microchemical Studies in Weld Sensitized Austenitic Stainless Steels,**" *MiCon 78: Optimization of Processing, Properties, and Service Performance Through Microstructural Control, ASTM STP 672,* Halle Abrams, G. N. Maniar, D. A. Nail, and H. D. Solomon, Eds., American Society for Testing and Materials, 1979, pp. 321–333.

ABSTRACT: Considerable attention has been focused recently on understanding the detailed mechanism of intergranular stress corrosion cracking (IGSCC) in weld-sensitized austenitic stainless steels used as structural material components in light water nuclear reactors. It is well recognized that three major factors (namely, a sensitized microstructure, a stress and consequent strain-time behavior, and a corrosive environment) need to coexist in order that IGSCC may occur. This paper is only concerned with the characterization of the sensitized microstructure. In order to fully understand weld-sensitized microstructure, it is necessary to carry out detailed microstructural studies on the nature of grain boundary chromium-rich $M_{23}C_6$ carbides in the sensitized region adjacent to the weld bead. In addition, techniques have now been developed for performing detailed quantitative microstructural measurements that allow the determination of carbide size, number density per unit area of grain boundary, grain boundary areal fraction coverage, and micrograms of chromium depleted from the neighboring grains. Qualitative and quantitative microstructural observations from several pipe heats, pipe diameters, and grain sizes are presented. Since the shape and depth of the chromium depletion profile in the vicinity of carbide particles is expected to govern the extent of susceptibility of the weld heat affected zone to the corrosive environment, a more realistic picture would be obtained if it were possible to map such depletion profiles. Only recently has it become possible with major developments in microanalytical instrumentation to use a combination of scanning-transmission electron microscopy (STEM) and high spatial resolution thin foil X-ray microanalysis for this purpose. Chromium depletion profiles are presented as a function of distance from austenite-austenite and austenite-carbide interfaces to demonstrate the feasibility of performing systematic sensitization studies on austenitic stainless steels used in reactor piping.

KEY WORDS: steels, microstructure, microstructural studies, microchemical studies, weld sensitization, austenitic stainless steels, transmission electron microscopy, quantitative microstructure, scanning transmission electron microscopy, thin foil X-ray microanalysis

---

[1] Acting manager, Chemical and Structural Analysis Branch, General Electric Company, Corporate Research and Development, Schenectady, N. Y. 12301.

Considerable attention has been focused recently on understanding the detailed mechanism of intergranular stress corrosion cracking (IGSCC) in weld-sensitized austenitic stainless steels used as structural material components in light water nuclear reactors. Although the general elements of IGSCC of isothermally or furnace sensitized stainless steels of the 18Cr chromium, 8Ni type have been known for many years, this prior knowledge has proven to be inadequate to describe quantitatively the cracking phenomenon in weld heat affected zones (HAZ). It is now well recognized that three major factors (namely, a sensitized microstructure, a stress and consequent strain-time behavior, and a corrosive environment) need to coexist in order that IGSCC may occur. This paper is only concerned with the characterization of the sensitized microstructure.

In order to fully understand weld-sensitized microstructure, it is necessary to carry out detailed studies on the nature of grain boundary chromium-rich $M_{23}C_6$ carbides in the sensitized region adjacent to the weld metal. Rigorous transmission electron microscopy (TEM) evidence is now available for the existence of such carbides at sensitized grain boundaries in the HAZ. Presence of grain boundary carbides is a necessary but not sufficient condition for the existence of a sensitized microstructure.

In addition, techniques have now been developed for performing quantitative microstructural measurements that allow the determination of carbide size, number density per unit grain boundary area, grain boundary areal fraction carbide coverage and micrograms of chromium depleted from neighboring grains.

Both qualitative and quantitative microstructural observations from several pipe heats, pipe diameters, and grain sizes are presented in this paper.

Short-term temperature excursions of the weld HAZ, which characterize the welding process, preclude the long-range diffusion of both chromium and carbon. As a result, depletion of these two elements occurs to only a few thousand angstroms from the sensitized grain boundary, concurrent with the formation of chromium-rich $M_{23}C_6$ carbides. Since the shape and depth of the chromium depletion profile can be expected to govern the extent of susceptibility of the weld HAZ to the IGSCC environment, a more realistic picture of the latter would be obtained if it were possible to map the chromium depletion profiles. It is important to recall that chromium concentrations below about 12 percent can be expected to make austenitic stainless steels susceptible to IGSCC [*1*].[2] Only recently has it become possible with major developments in microanalytical instrumentation to use a combination of scanning-transmission electron microscopy (STEM) and high spatial resolution thin foil X-ray microanalysis for this purpose [*2*]. Chromium depletion profiles

---

[2] The italic numbers in brackets refer to the list of references appended to this paper.

have been determined as a function of distance from austenite-austenite and austenite-carbide interfaces, demonstrating the feasibility of performing systematic sensitization studies on several austenitic stainless steels including those used in reactor piping.

The qualitative and quantitative microstructural and microchemical characteristics of weld sensitized austenitic stainless steels are covered in this paper.

Microstructural Studies

To illustrate the magnitude and importance of the subject under investigation, a typical in-service IGSCC crack in a 10.2 cm (4 in.) diameter Type 304 stainless steel pipe in reactor service is shown in Fig. 1. The light optical micrograph in Fig. 1*a* shows a typical IGSCC crack in a longitudinal pipe section at a distance of 0.63 cm (0.25 in.) from the weld center line (WCL). Figure 1*b* is a scanning-electron micrograph (secondary electron image) of the surface of a partially electropolished 3 mm diameter specimen punched out of a thin (0.01 cm) longitudinal pipe section containing the crack tip shown in Fig. 1*a*. This specimen was subsequently electropolished carefully to create a perforation at the very tip of the crack. TEM micrographs of this area are shown in Fig. 2. The crack itself, filled with iron oxide, appears at the lower left hand corner

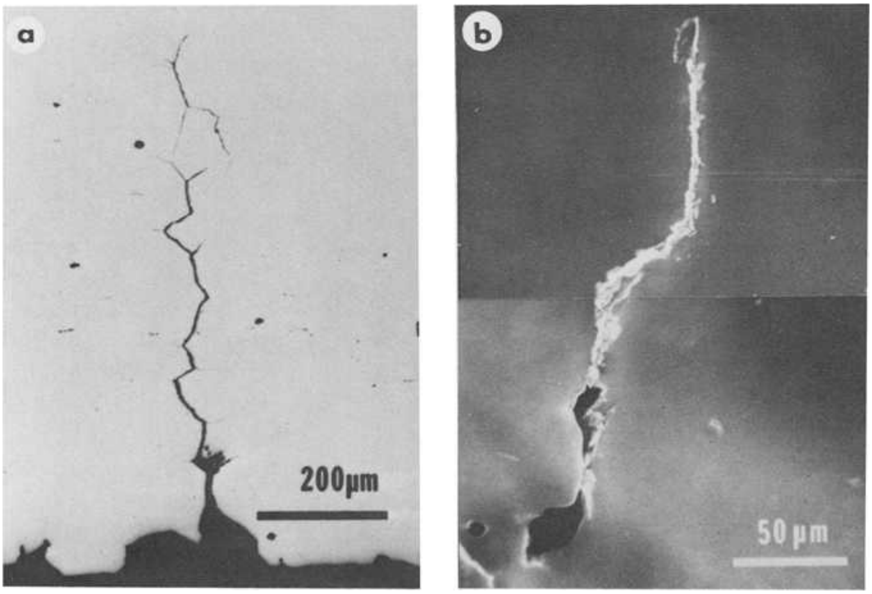

FIG. 1—*Light optical* (a) *and scanning electron* (b) *micrographs of an in-service intergranular stress corrosion crack progressing from the inside pipe surface of a Schedule 80, 10.2 cm diameter Type 304 austenitic stainless steel pipe.*

and progresses towards the electropolished perforation in the center of the figure. The *only* grain boundary exiting the perforation winds its way to the upper right of the composite micrograph, and subsequently splits into two boundaries. Bright field and dark field images of the region at which the grain boundary exits the perforation are also shown in Fig. 2. These images confirm the presence of a high density of grain boundary carbides. The dark field image was obtained using a $M_{23}C_6$ carbide diffraction spot. In terms of grain boundary areal fraction covered with carbides, the coverage is very high. It is significant to note that the crack, if allowed to progress, would have followed this highly sensitized grain boundary. This observation on piping in reactor usage adds credence to the significance of the weld-sensitized microstructure in promoting IGSCC.

Experimental Procedure

In order to study the microstructural characteristics of weld sensitization further, specimens were obtained from laboratory weldments of Schedule 80 Type 304 austenitic stainless steel pipes. Details concerning the pipe heats and welding procedures are available elsewhere [*3*]. Similarly, details of TEM specimen preparation are available in another publication [*4*]. It is sufficient to state here that the electrolytic polishing conditions, using an electrolyte of 62 ml perchloric acid, 137 ml water, 700 ml ethanol, and 100 ml butylcellusolve at 30 V dc and −30°C, have to be carefully controlled to obtain electron transparent foils with large areas of uniform thickness. This latter requirement is particularly critical for STEM/thin-foil X-ray microanalysis to be discussed later in this paper.

Experimental Results

A number of weld HAZ's in the proximity of the inside pipe surface were examined. In each case, the specimen was obtained from a thin longitudinal pipe section across the weldment and adjacent HAZ. For example, a light micrograph of such a longitudinal pipe and weld section is shown at the top of Fig. 3. The pipe heat on the left (Heat 2P1486) (ASTM grain size 4.5) was more susceptible to IGSCC than the pipe heat on the right (Heat 454659) (ASTM grain size 6.8). Specimens for TEM were taken from the longitudinal section at locations indicated by arrows in Fig. 3. Three millimetre diameter disks for electropolishing were punched out from the proximity of the inside pipe surface (that is, lower edge of light micrograph in Fig. 3). In effect, all the microstructural and microchemical data came from a depth of about 1 mm below the inside pipe surface. Typical TEM micrographs from a systematic experiment conducted as a function of distance on the left side of the WCL (that is, A through E) are shown in Fig. 3. A summary of the microstructural features observed

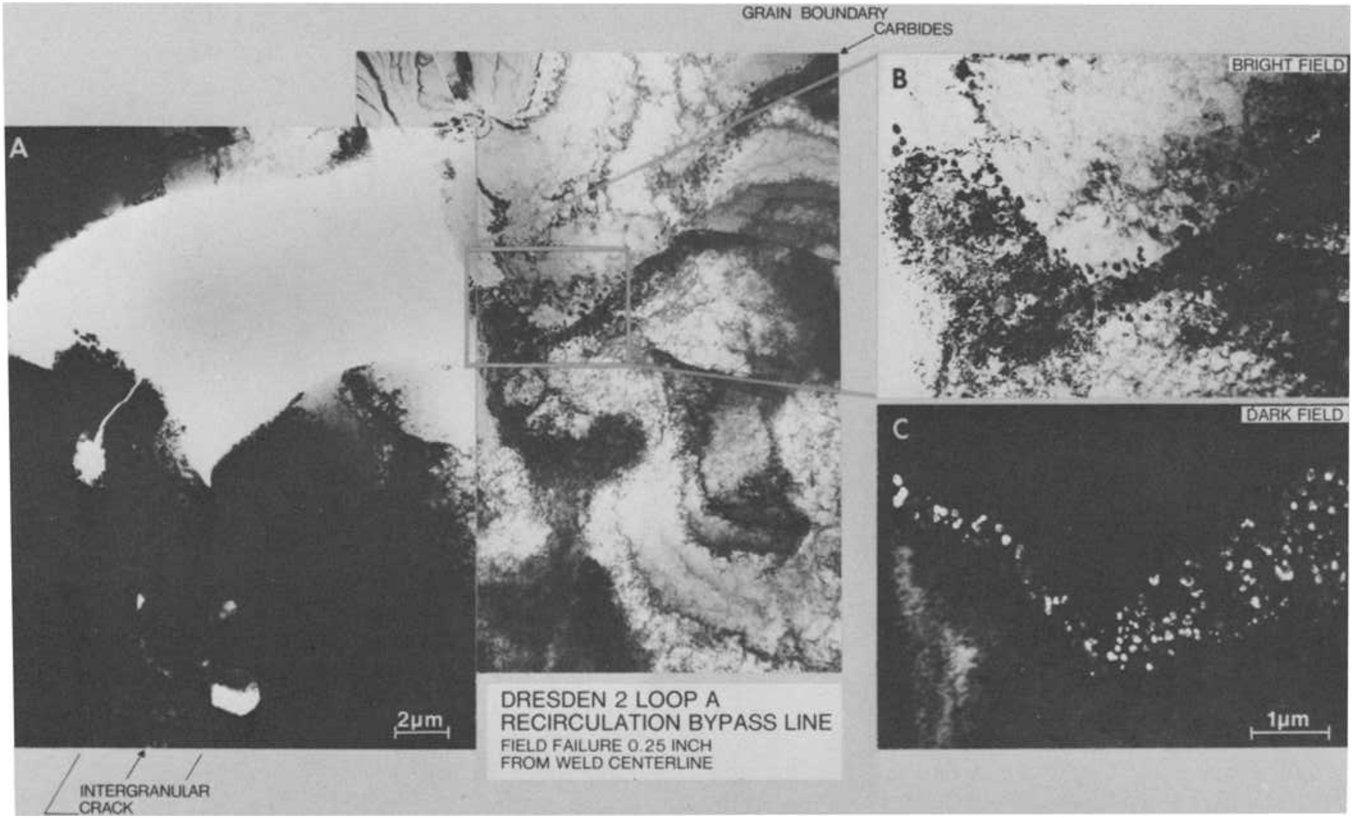

FIG. 2—*Bright field and dark field images of grain boundary chromium-rich* $M_{23}C_6$ *carbides at the tip of the in-service crack illustrated in Fig. 1.*

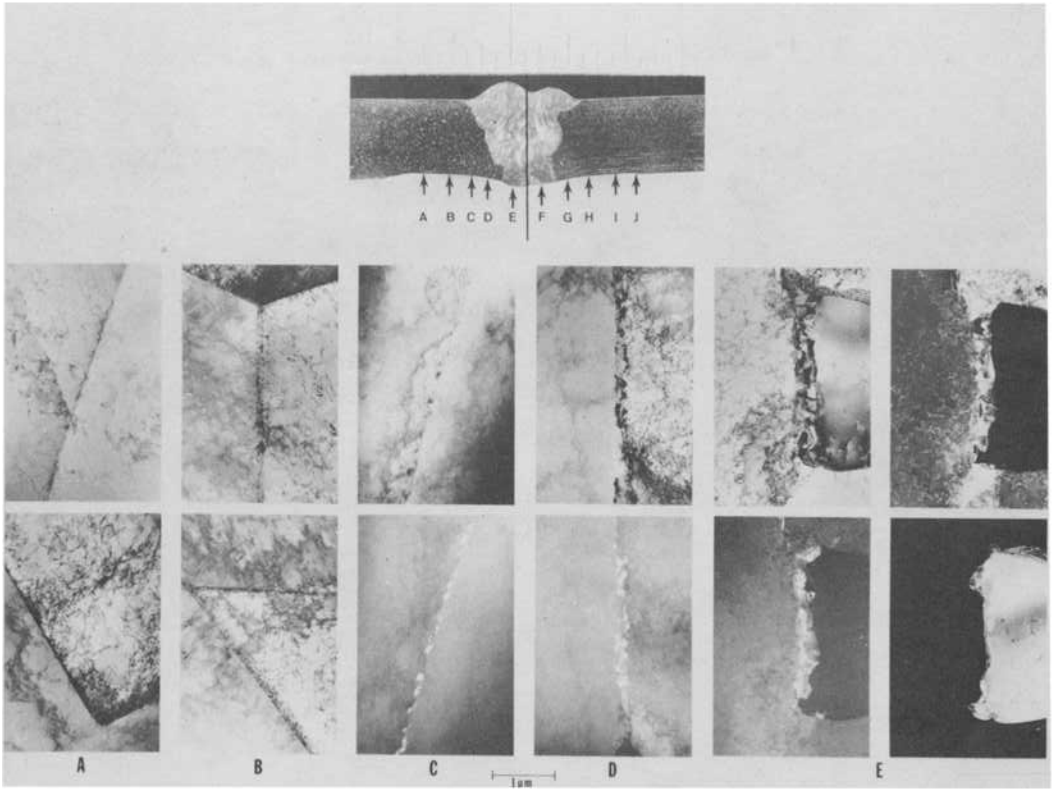

FIG. 3—*Light and TEM micrographs of a systematic study of microstructure as a function of distance from the weld center line in a Schedule 80 10.2 cm (4 in.) diameter Type 304 austenitic stainless steel pipe susceptible to intergranular stress corrosion cracking.*

in these TEM images is given in Table 1. Although, as will be seen later, there is quite a significant variation in size and density of carbides, the summary of observations in Table 1 is valid for all pipes irrespective of variations in heat number or diameter.

Quantitative microstructural measurements were made from a large number of TEM micrographs after careful specimen foil thickness determination. A novel STEM foil thickness technique applicable here is discussed in another publication [5]. The carbide sizes, carbide number densities, and dislocation density measurements on the two heats are shown in Fig. 4. Quite dramatic differences are observed in the various quantitative microstructural features between the more susceptible (2P1486) and the less susceptible (454659) heats. For example, while the grain boundary carbide size is smaller in the more susceptible pipe heat, the number of carbides per square centimetre grain boundary area is much larger, when compared with the less susceptible heat. Although carbide sizes peak at 0.57 cm (0.225 in.) from the WCL, the number densities peak at 0.76 cm (0.3 in.) from the WCL. That is, the maximum carbide size and number density do not occur at the same distance from the WCL. This observation points to the fact that the real effect of carbide size and distribution must be their influence on the extent of chromium depletion in the austenite matrix adjacent to the carbide, which appears to be key factor in determining the extent of sensitization.

A striking correlation has been observed between grain size and the number of carbides per square centimetre grain boundary area. These observations are summarized for four grain sizes in Table 2. The larger the grain diameter, the greater the number of carbides per unit grain boundary area. This is not surprising since in a given volume of material, a larger average grain diameter implies lesser grain boundary area and thus a large number of carbide nuclei to achieve the same degree of sensitization.

Dislocation density (Fig. 4) is observed to peak at about 0.57 cm (0.225 in.) from the WCL, with a slightly higher value in the more susceptible

TABLE 1—*Summary of TEM microstructural observations.*

Distance from Weld Center Line	TEM Microstructural Features
0 to 2.5 cm (0 to 0.1 in.)	Weld region, duplex structure, 5% ferrite-chromium carbides decorate ferrite-austenite boundaries only
0.25 to 0.50 cm (0.1 to 0.2 in.)	Few widely separated large ellipsoid grain boundary carbides-longer carbide dimension along boundaries
0.50 to 0.75 cm (0.2 to 0.3 in.)	Numerous small spherical carbides closely spaced together
0.75 to 1.00 cm (0.3 to 0.4 in.)	Grain boundary carbides disappear rapidly to yield *clean* boundaries

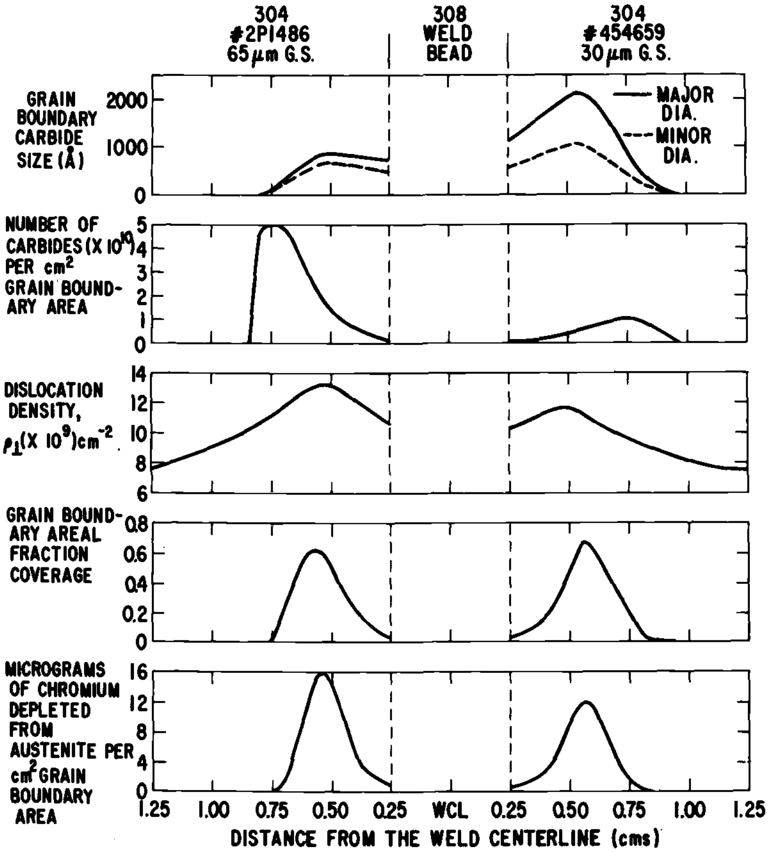

FIG. 4—*Quantitative microstructural measurements illustrating the variation of carbide size, carbide number density, dislocation density, grain boundary areal fraction coverage, and micrograms of chromium depleted from the austenite matrix, as a function of distance from the weld center line.*

heat. A dislocation density peak in the HAZ can be attributed to plastic strain created in the pipe material by the welding process.

An estimation of the degree of sensitization can be obtained by rearranging the carbide size and number density data to provide information on grain boundary areal fraction covered with carbides (Fig. 4) and micrograms of chromium depleted from the adjacent austenite per square centimetre grain boundary area. Peak grain boundary areal fraction coverage and micrograms of chromium depleted at 0.64 cm (0.25 in.) from the WCL can be taken as a good measure of the maximum degree of sensitization.

The peak grain boundary areal fraction coverage does not appear to vary significantly between the more and less susceptible heats, but the peak micrograms of chromium depleted is distinctly greater in the more

TABLE 2—*Grain size dependence of number of carbides per unit grain boundary area.*

ASTM Grain Size	Average Grain Diameter, μm	Carbides per cm²Grain Boundary Area	Pipe Diameter, cm
3.6	88.88	8.5×10^{10}	66.0
4.5	65.31	4.1×10^{10}	10.2
5.5	46.68	2.3×10^{10}	25.4
6.8	29.77	0.6×10^{10}	10.2

susceptible heat. A key factor, then, in determining the susceptibility of a heat to weld sensitization and subsequent IGSCC must be the *shape* and *depth* of the chromium depletion profile associated with grain boundary carbide formation, and how it varies with time on exposure at operating temperature. This is the subject of discussion in the next section.

Microchemical Studies

Since the shape and depth of the chromium depletion profile in the vicinity of carbide particles is expected to govern the extent of susceptibility of the weld HAZ to IGSCC, a more realistic picture would be obtained if it were feasible to map such depletion profiles. Only recently has it become an experimental reality, with major developments in microanalytical instrumentation, to use a combination of STEM and high spatial resolution X-ray microanalysis for this purpose.

Experimental Procedure

A modified JSEM-200 scanning-transmission electron microscope (STEM) operated at 200 kV and equipped with a Nuclear Semiconductor Autotrace retractable solid state X-ray detector and a Tracor Northern NS 880 minicomputer-based multichannel analyzer was used. Further details concerning our STEM/X-ray microanalytical system and a rigorous consideration of the assumptions made in converting X-ray integrated intensities after background subtraction into elemental concentrations are available elsewhere [*2*]. It is sufficient to state here that the Cliff and Lorimer internal standard method [*6*] has been used in the present X-ray data analysis. Our experimental and instrumental developments allow us to acquire quantitative chemical information from regions of the order of 400 Å. In comparison, conventional microprobe analysis samples areas of the order of 2 μm.

Experimental Results

Systematic X-ray microanalysis studies on TEM type specimens from longitudinal pipe sections in the vicinity of the inside pipe diameter and at

0.64 cm (0.25 in.) from the WCL show that depletion of chromium extends into the austenite matrix up to 4000 Å from the grain boundary. Figure 5*a* and *b* show chromium, iron, and nickel composition profiles across a grain boundary, (*a*) without and (*b*) with a carbide particle, respectively. The specimens examined microchemically are from the 10.2 cm (4 in.) diameter Schedule 80 Type 304 stainless steel pipe of the more susceptible Heat 2P1486.

The interface chromium, iron, and nickel compositions are determined by correcting for any error in interface tilt from the vertical, and by fitting the segregation profiles to an error function expected from normal interface-diffusion model concepts [*2*]. The interface chromium composition determined in this manner is 10.8 percent at both the austenite-austenite (without carbide) and the austenite-carbide interfaces. In addition, the technique also allows us to estimate the $M_{23}C_6$ carbide composition, which in this case is $(Cr_{0.77}Fe_{0.20}Ni_{0.03})_{23}C_6$.

In an independent investigation, Povich and Rao [*7,8*] have shown that carbides nucleated during the weld sensitization process can be expected to continue to grow during prolonged exposure at temperatures lower than those normally associated with sensitization. In this phenomenon, termed low temperature sensitization (LTS), no new carbides are nucleated, but carbides previously nucleated during weld sensitization continue to grow [*7,8*]. This low temperature carbide growth can be expected to result in further chromium depletion below the critical 12 percent value, thereby increasing susceptibility to IGSCC.

The as-welded specimen examined in Fig. 5 was subjected to a typical

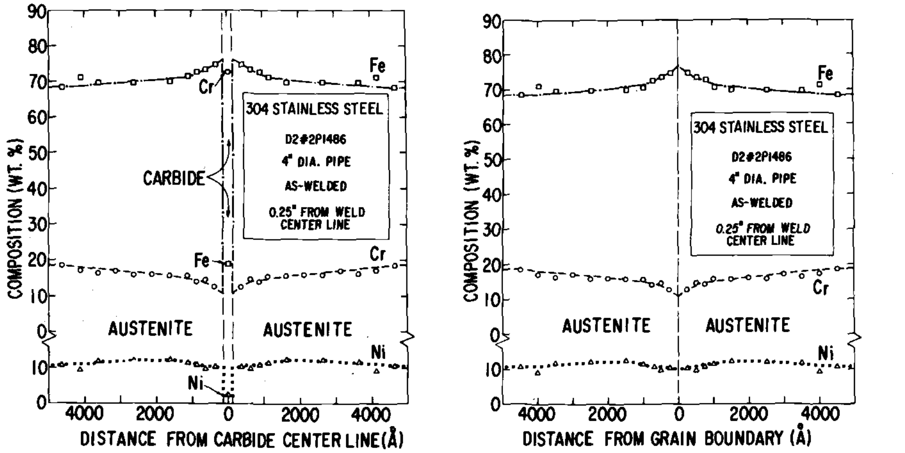

FIG. 5—*Chromium, iron, and nickel composition profiles as a function of distance from a weld sensitized grain boundary* (a) *in the absence of and* (b) *in the presence of a chromium rich carbide, in the susceptible Type 304 stainless steel pipe Heat 2P1486.*

LTS treatment of exposure to 500°C for 24 h and then re-examined using the STEM/X-ray microanalysis technique. Table 3 summarizes the various matrix and interface chemical compositions determined in the as-welded condition and after the heat treatment. Special note should be taken of the decrease in the austenite-carbide interface chromium composition from 10.8 to 8.2 percent, while the austenite-austenite interface chromium composition drops from 10.8 to 9.4 percent after the LTS treatment. Examination of Table 3 shows that most of the enhanced chromium depletion at the carbide-austenite interface is replaced by nickel, which rises from 9.8 to 12.3 percent. The carbide composition itself remains essentially unchanged.

Discussion

The results of this study indicate that the weld-sensitized microstructure is characterized by chromium-rich $M_{23}C_6$ carbides covering up to 60 percent of the total grain boundary area. The carbides are present only up to 0.8 cm from the WCL. A significant observation is that even in the region of peak sensitization, at about 0.64 cm from the WCL, the grain boundaries are not completely covered with carbides. In fact, the carbides are invariably present as individual particles (for example, Figs. 2 and 3). In the past, it had been assumed that a continuous carbide coverage was a prerequisite for propagation of a stress corrosion crack. Instead, the present investigation indicates that only a continuously sensitized path, characterized by a chromium content of less than 12 percent, is required. This implies that the austenite-austenite and austenite-carbide interfaces need to be depleted to below 12 percent chromium in the region of maximum sensitization. The STEM/X-ray microanalysis results summarized in Table 3 indicate that this is true in the weld HAZ of Heat 2P1486.

The results presented in Figs. 1 and 2 from an in-service IGSCC crack, and those in Fig. 3, the left side of Fig. 4, and Fig. 5 from a laboratory weld HAZ, come from the same heat of Type 304 stainless steel pipe, namely, 2P1486. The type of grain boundary areal fraction coverage in Fig. 2 and that measured and shown in Fig. 4 are comparable (that is, ~60 percent). Since the former is an in-service crack while the latter is a laboratory experiment, considerable credibility can be given to laboratory simulations of field conditions, especially in terms of the weld HAZ microstructure.

Although quantitative microstructural measurements such as carbide size and number density provide a unique insight into weld-sensitized microstructure, the microchemical studies demonstrate the importance of detailed and systematic measurements of interfacial chromium compositions to determine the extent of sensitization. For example, the data in Fig. 5 shows that indeed a continuous sensitized path exists in the region

TABLE 3—*Matrix and interface chemical compositions in weld-sensitized Type 304 stainless steel determined by STEM/X-ray microanalysis.*

	Austenite Matrix			Austenite-Austenite Interface			Austenite Carbide Interface			Carbide Matrix		
	Cr	Fe	Ni	Cr	Fe	Ni	Cr	Fe	Ni	Cr	Fe	Ni
As-welded (0.64 cm from weld center line)	18.6	68.4	10.6	$\boxed{10.8}$	76.6	9.8	$\boxed{10.8}$	76.6	9.8	72.8	18.9	2.4
As-welded plus low temperature sensitization (500°C/24 h/WQ)	18.6	68.4	10.6	$\boxed{9.4}$	80.4	8.0	$\boxed{8.2}$	77.5	12.3	72.8	19.0	2.4

of peak sensitization, wherein the chromium concentration is well below the critical 12 percent value.

Qualitative microstructural observations also play an important role in understanding and detecting weld sensitization. For example, Fig. 2 demonstrates graphically the progression of an in-service IGSCC crack along a heavily sensitized grain boundary characterized by extensive coverage with $M_{23}C_6$ carbides.

The long-term, relatively low temperature aging phenomenon, known as low temperature sensitization (LTS) [*7,8*] appears to have a drastic effect on interfacial chromium compositions. The potential relevance of LTS to industrial processes is that, after many years at process operating temperatures, the degree of sensitization in welded Type 304 stainless steel may progress via LTS to enhance the possibility that IGSCC would occur. The experimental results reported elsewhere [*7,8*] suggest that this LTS enhancement can occur to a significant level with ten years at 300°C in certain heats of Type 304 stainless steel.

The long-term nature of LTS suggests that an increase in corrosion problems might develop after years of relatively trouble-free operation, particularly in equipment constructed from heats of stainless steel susceptible to LTS. Such occurrences are familiar to many industries and are not limited to stainless steel.

Acknowledgments

The author acknowledges the considerable contributions of Drs. E. Lifshin and R. E. Hanneman in helping understand X-ray microanalysis and intergranular stress corrosion cracking, respectively. Dr. M. J. Povich provided the specimens used in the low temperature sensitization study. Without the unique expertise of E. F. Koch in electropolished thin foil preparation, this investigation would not have been possible.

References

[*1*] Bain, E. C., Aborn, R. H., and Rutherford, J. J. B., *Transactions*, American Society for Steel Treating, Vol. 21, 1933, pp. 481–509.

[*2*] Rao, P. and Lifshin, E., *Proceedings*, Eighth International Conference on X-ray Optics and Microanalysis, Boston, Vol. 1, 1977, pp. 118A–118F.

[*3*] Klepfer, H. H., "Investigation of Cause of Cracking in Austenitic Stainless Steel Piping," General Electric Company Report NEDO-2100-1, July 1975.

[*4*] Rao, P., "Topical Report on Microstructural Studies of BWR Pipe," General Electric Company Report NEDC-21229, April 1976.

[*5*] Rao, P., *Proceedings*, 34th Annual Meeting, Electron Microscopy Society of America, 1976, pp. 546–547.

[*6*] Cliff, G. and Lorimer, G. W., *Journal of Microscopy*, Vol. 103, 1975, pp. 203.

[*7*] Povich, M. J. and Rao, P., "Low Temperature Sensitization of Welded 304 Stainless Steel," General Electric Company Report 77CRD251, Dec. 1977.

[*8*] Povich, M. J. and Rao, P., "Low Temperature Sensitization of Welded 304 Stainless Steel," Paper 191, Corrosion 78, National Association of Corrosion Engineers, Houston, March 1978.

G. Aggen,[1] *H. E. Deverell,*[1] *and T. J. Nichol*[1]

Microstructures Versus Properties of 29-4 Ferritic Stainless Steel

REFERENCE: Aggen, G., Deverell, H. E., and Nichol, T. J., "**Microstructures Versus Properties of 29-4 Ferritic Stainless Steel,**" *MiCon 78: Optimization of Processing, Properties, and Service Performance Through Microstructural Control, ASTM STP 672,* Halle Abrams, G. N. Maniar, D. A. Nail, and H. D. Solomon, Eds., American Society for Testing and Materials, 1979, pp. 334–366.

ABSTRACT: The subject of this investigation is a low interstitial 29Cr-4Mo ferritic stainless steel developed and patented by E.I. duPont de Nemours and Co., Inc. The alloy, commonly known as 29-4, is characterized by exceptionally high resistance to chloride pitting and stress corrosion cracking and by comparatively good room temperature toughness and ductility.

Sheet specimens from a commercial heat were exposed for times up to 100 h at temperatures from 371 to 982°C (700 to 1800°F). Metallographic changes that were observed were correlated to changes in impact and tensile properties, crevice corrosion in ferric chloride, and intergranular corrosion resistance in ferric sulfate-sulfuric acid. Excess phase identifications and studies of failure modes were conducted on selected samples.

Two embrittlement regions were found centered at about 482°C (900°F) and 760°C (1400°F). The lower temperature embrittlement region is quite narrow and was ascribed to 475°C (885°F) embrittlement. No deterioration in corrosion resistance was detected in this embrittlement region. Embrittlement occurred much more rapidly in the higher temperature region and existed over a wide temperature range. Crevice corrosion resistance and corrosion resistance to ferric sulfate-sulfuric acid deteriorated rapidly in this embrittlement region. Changes in mechanical properties and corrosion resistance upon heat treating in the region were ascribed primarily to the precipitation of sigma and chi phases.

KEY WORDS: steels, microstructure, ferritic stainless steels, corrosion resistance, temperature testing, heat treatment, embrittlement

Higher chromium-molybdenum (Cr-Mo) ferritic stainless steels possessing excellent resistance to pitting corrosion have recently been developed. Streicher [*1*][2] demonstrated that Fe-28Cr-4Mo and Fe-28Cr-4Mo-2Ni alloys were resistant in laboratory tests to severe pitting and crevice corrosion conditions. In addition, by limiting the maximum

---

[1] Manager, research specialist, and market development specialist, respectively, Research Center, Allegheny Ludlum Steel Corporation, Brackenridge, Pa. 15014

[2] The italic numbers in brackets refer to the list of references appended to this paper.

carbon and nitrogen content (100 ppm carbon (C) and 200 ppm nitrogen (N) with total C + N less than 250 ppm), the alloys demonstrated good ductility and were not susceptible to intergranular corrosion after welding. The two alloys are currently manufactured by Allegheny Ludlum Steel Corporation (ALSC) and are designated AL 29-4 and AL 29-4-2. This paper will describe the effects of various isothermal heat treatments on the mechanical properties and corrosion properties of the AL 29-4 alloy. This alloy is designated UNSS44700 in the ASTM designations.

Although the alloy was developed primarily for corrosion resistance, it also possesses excellent ductility as determined by bend tests. As a primary result of the low interstitial content, this steel has excellent room temperature toughness as measured by impact tests. In addition to carbon and nitrogen content, the room temperature toughness of ferritic stainless steels is influenced by the cooling rate from elevated temperatures. Recent studies [*2,3*] showed that there are two temperature zones through which slow cooling can result in embrittlement of high chromium and molybdenum stainless steels—a higher temperature zone, 593 to 927°C (1100 to 1700°F) where phases such as sigma and chi precipitate and a lower temperature zone 427 to 510°C (800 to 950°F) commonly referred to as 475°C (885°F) embrittlement where a chromium-rich phase precipitates. Exposure to these temperature ranges manifests itself in the degradation of the room temperature ductility and toughness of ferritic stainless steels upon subsequent cooling from the embrittlement temperature to room temperature. Both forms of embrittlement can be removed by heat treatment to redissolve the precipitates followed by rapid cooling to room temperature.

The higher chromium and molybdenum contents of AL 29-4 and AL 29-4-2 render the alloys susceptible to both forms of embrittlement. Streicher [*4*] demonstrated that 1-h exposures to either embrittlement zone did not adversely affect the bend properties, however, 100-h exposures resulted in a loss of ductility. Brandis et al [*2*] studied the effects of heat treatments upon mechanical properties and microstructures of high-purity 20 to 28Cr, 0 to 5Mo ferritic stainless steels. Their data from a 28Cr, 3.5Mo alloy is most relevant to our study. The alloy was annealed 30 min at 1000°C (1832°F), water quenched, and held for times to 10 000 h in the temperature range of 350 to 900°C (662 to 1652°F). They showed the presence of a rapid embrittlement range centered at about 750°C (1382°F) and a slower embrittlement range centered at about 525°C (977°F). The rapid embrittlement was attributed to sigma and chi precipitation, while the slower embrittlement was attributed to 475°C (885°F) embrittlement. Nichol [*3*] observed that the room temperature impact resistance of AL 29-4-2 was degraded faster after the high-temperature type of embrittlement and failure was characterized by an intergranular fracture mode. Embrittlement after exposure to 482°C (900°F) resulted in a slower degradation in toughness and failure by transgranular cleavage mode.

The high-temperature embrittlement zone results from the precipitation of sigma and chi phases. Precipitation of sigma phase is normally associated with decreased corrosion resistance. For example, Type 316L shows high intergranular corrosion rates in boiling 65 percent nitric acid. This has been attributed to the formation of submicroscopic sigma phase, because it occurs in sigma-prone alloys and the corrosion behavior in other media negates the possibility of carbides being responsible. Deverell and Maurer [5] have observed a decrease in the crevice corrosion resistance of a 20Cr-24Ni-6Mo austenitic alloy containing sigma phase. In a more detailed study of this phenomenon, Aggen [6] observed that the crevice corrosion resistance in a room temperature 10 percent ferric chloride solution was decreased rapidly when the precipitate was finely distributed at grain boundaries. He concluded that crevice attack was affected more by morphology than amount of sigma precipitation. These studies contrast with work on 28Cr-4Mo ferritic alloys. Streicher [4] evaluated both crevice corrosion resistance and intergranular corrosion resistance in 28Cr-4Mo alloys. He did not detect any change in corrosion resistance between precipitate-free microstructures and precipitate-containing microstructures. He evaluated structures that contained either a fine precipitate (sigma phase) in the grain boundary as well as structures containing very coarse precipitates at boundaries and within the matrix. In the same study, Streicher noted that in a 28Cr-4Mo-2Ni alloy containing 50 percent chi phase and a small amount of sigma phase, the ferrite phase was selectively attacked in both boiling 50 percent H_2SO_4-$Fe_2(SO_4)_3$ and 10 percent $FeCl_3$ at 50°C (122°F).

The 475°C (885°F) embrittlement phenomenon has been recognized in ferritic stainless steels for many decades and was known to be enhanced by increasing chromium contents. The cause of embrittlement remained a puzzle for many years, since it occurred in the absence of microstructural changes that could be detected by optical microscopy or by X-ray analysis. In 1953 Fisher et al [7], using the electron microscope, showed that the embrittlement of a 27Cr ferritic steel incurred after 10 000 h at 482°C (900°F) was accompanied by the precipitation of a very fine chromium-rich body centered cubic (bcc) phase with a lattice parameter close to that of the matrix. The phase, termed α', was about 200 Å in diameter and contained up to 80Cr. To explain the presence of the phase, which was not predicted from existing iron-chromium (Fe-Cr) binary phase diagrams, Williams and Paxton [8] proposed a modified diagram having a solid-state solubility gap below about 516°C (960°F). This diagram was further modified by Williams [9] and appears to be generally accepted as a correct description of the Fe-Cr binary phase diagram.

The precipitation of α' in high purity Fe-Cr alloys can occur by either spinodal decomposition or by nucleation and growth, depending upon composition and aging temperature, according to the work of DeNys and Gielen [*10*] among others. Spinodal decomposition is favored by high chromium contents and low aging temperatures. Embrittlement in high-purity alloys has been frequently shown to occur only after an incubation period of varying length. The presence of an incubation period and its extent is confused by the various property measurements used to show embrittlement. Usually these have been room-temperature hardness, tensile, or impact strengths. Perhaps the most sensitive measure of embrittlement is the impact energy transition temperature [*11*]. These investigators showed the presence of a 3- to 10-h incubation period in three 18 to 29Cr ferritic alloys, one of which is very similar to AL 29-4 except for the addition of 2Ni. In a companion study, Datta et al [*12*] showed by electron microscopy that 475°C (885°F) embrittlement in the alloy with 2Ni was accompanied by evidence of homogeneous precipitation of α' probably via spinodal decomposition.

The rate of 475°C (885°F) embrittlement increases with increasing chromium content and appears to decrease with increasing purity. The apparent purity effect, however, may be related to carbide and nitride precipitation acting as competing or supplementary reactions to that of α' precipitation [*13*]. Molybdenum is reported to have no effect or to increase the rate of 475°C (885°F) embrittlement [*2,14,15*]. The effect may be negligible at 14Cr [*14*] but becomes pronounced at 28Cr [*2*]. The latter study [*2*], however, was based upon exposure time needed to decrease room temperature impact energy to 50 J. Apparent embrittlement times would be affected by the properties of the initial solid solution. Also the annealing temperature of 1000°C (1832°F) may not have been sufficiently high to dissolve all remnants of sigma or chi phase or both in the higher Cr-Mo alloys although the reported microstructures appeared clear of second phases. Even small amounts of these phases, as shown on this study, appear to increase impact energy transition temperatures markedly.

Aging near 475°C (885°F) has been shown to promote deformation by twinning in high-chromium ferritic alloys [*3,12,16,17*]. This occurs well before α' particles can be observed by electron microscopy and during early stages of spinodal decomposition [*12*]. Concurrently, the dislocation structure changes from a cellular to a planar array upon deformation [*12*]. The effect of 475°C (885°F) precipitation upon the corrosion resistance has not been extensively studied. Lizlovs and Bond [*18*], in a study on 18Cr-2Mo-Ti steels, found that embrittlement reduced corrosion resistance in a manner consistent with chromium depletion of the matrix. When embrittlement occurs during spinodal decomposition, particularly during early stages, the effects on corrosion resistance are not clear. Effects on corrosion resistance, however, appear to occur more slowly and have less significance than the effects upon mechanical properties.

The intent of this study is to determine the effects of isothermal treatments on the structure and properties of a commercially available high Cr-Mo ferritic stainless steel. Corrosion tests were used that the alloy is required to pass under existing specifications in the annealed condition. Mechanical property tests were selected that appear to provide some important information as to the alloy's behavior during manufacture, fabrication, and use.

Material and Experimental Procedure

The AL 29-4 alloy is vacuum induction melted to obtain the specified low levels of carbon (100 ppm maximum) and nitrogen (200 ppm maximum). The material used in this study was obtained from a 5.4 Mg (12 000 lb) commercial vacuum induction Heat 8-4638. The ladle chemistry and specified ASTM ranges (UNS-S44700) are given in Table 1. The material was hot rolled to 3.5 mm (0.14 in.), annealed, cold rolled to 1.65 mm (0.065 in.), and line annealed at 1010°C (1850°F) on production equipment.

Panels 305 mm (12 in.) square were taken from the mill-produced material for this study. These were reannealed at the laboratory at 1010°C (1850°F) for 2 min at temperature and water quenched to assure that all second phases were in solution. Longitudinal tensile blanks, transverse Charpy V-notch blanks, and 25 mm by 50 mm (1 in. by 2 in.) corrosion coupons were sheared from these panels. A group of samples was retained as annealed. The tensile blanks were isothermally heat treated at 482, 760, and 816°C (900, 1400 and 1500°F) for times of 20, 60, 300, 1200,

TABLE 1—*Chemical composition of AL 29-4, percent by weight.*

Element	ASTM UNS-S44700	H8-4638
Chromium	28–30	29.4
Molybdenum	3.5–4.2	3.95
Nickel	0.15 max	0.11
Copper	0.15 max	< 0.10
Manganese	0.30 max	0.02
Phosphorus	0.025 max	0.010
Sulfur	0.025 max	0.013
Silicon	0.20 max	0.04
Carbon	0.0100 max	0.0050
Nitrogen	0.0200 max	0.0140
C + N	0.0250 max	0.0190
Iron	balance	balance

and 6000 min at temperature and water quenched. The Charpy blanks and corrosion coupons were isothermally heat treated at temperatures from 371 to 982°C (700 to 1800°F) in 55°C (100°F) increments for times of 0.3, 1, 3, 10, 30, and 100 h at temperature and water quenched. The surfaces of all the corrosion coupons were ground smooth after the final heat treatment. Including the annealed specimens, these time-temperature combinations resulted in 73 different conditions that were evaluated.

Tension and Charpy V-notch tests were conducted in accordance to ASTM Methods and Definitions for Mechanical Testing for Steel Products (A 370–76) and ASTM Standard Method for Tension Testing of Metallic Materials (E 8-77a), respectively. Attempts were made to encompass impact transition temperatures for all conditions with the 12 specimens per condition that were prepared. In several cases, this was not possible since brittle behavior was observed to test temperatures in excess of 371°C (700°F). Transition temperatures were estimated from impact energy levels and from visual examination of the fracture surfaces.

Samples examined by optical microscopy were generally etched electrolytically in concentrated nitric acid. In some cases a *mixed acids* etchant was used when the concentrated nitric failed to clearly delineate all microstructural constituents. This etchant consists of 5 cm^3 of glycerin in a solution of 20 cm^3 concentrated nitric, 20 cm^3 concentrated acetic, and 30 cm^3 concentrated hydrochloric acids. The etchant must be used freshly mixed and is applied by swabbing at room temperature. Impact fracture surfaces were examined in a Cambridge Mark 2A Stereoscan scanning electron microscope.

Intergranular corrosion tests were conducted in a boiling sulfuric acid-ferric sulfate solution in accordance to ASTM Recommended Practices for Detecting Susceptibility to Intergranular Attack in Stainless Steels (A 262–75), Practice B. Crevice corrosion tests were conducted in 10 percent ferric chloride according to ASTM Test for Pitting and Crevice Corrosion Resistance of Stainless Steels and Related Alloys by the Use of Ferric Chloride Solution (G 48–76). Specimens heat treated for times to 30 h were tested at 50°C (122°F). Specimens heat treated for 100 h were tested at 21°C (70°F).

Results

Mechanical Properties

The grain size measured on an annealed specimen was about ASTM No. 5–6. Several additional samples were also examined with about the same results that indicated that grain sizes were fairly uniform and did not change significantly during any of the isothermal heat treatments.

Table 2 lists the longitudinal room-temperature tensile properties of

TABLE 2—*Room temperature tensile properties of annealed and annealed plus exposed samples.*[a]

Annealing Conditions[b]	Exposure Temperature, °C	Exposure Time, min[c]	0.2% Yield Strength, MPa	Ultimate Tensile Strength, MPa	Elongation in 51 mm,%	Hardness
1010C-2 min-AC	. . .	. . .	504	618	25.5	R_B94
1010C-2 min-WQ	. . .	. . .	437	588	27.6	R_B91
1010C-2 min-WQ	482	20	533	663	23.0	R_B95
1010C-2 min-WQ	482	60	576	691	22.8	R_B97
1010C-2 min-WQ	482	300	617	715	20.8	R_B99
1010C-2 min-WQ	482	1200	687[d]	808	16.5	R_c25
1010C-2 min-WQ	482	6000	843[d]	978	3.0	R_c30
1010C-2 min-WQ	760	10	432	573	26.3	R_B88
1010C-2 min-WQ	760	20	431	566	27.3	R_B89
1010C-2 min-WQ	760	60	426	568	27.5	R_B87
1010C-2 min-WQ	760	300	391	595	24.8	R_B89
1010C-2 min-WQ	760	1200	373	652	15.5	R_B91
1010C-2 min-WQ	816	10	437	569	27.5	R_B90
1010C-2 min-WQ	816	20	436	578	26.8	R_B89
1010C-2 min-WQ	816	60	395	583	25.5	R_B87
1010C-2 min-WQ	816	300	384	619	13.0	R_B91

[a] Results are averages of duplicate tests.

[b] AC = air cooled and WQ = water quenched.

[c] Samples were water quenched after the exposures.

[d] Pronounced serrations in tensile curves.

annealed specimens and those subsequently heat treated for various times at 482, 760, and 816°C (900, 1400, and 1500°F). These isothermal treatments were performed only on specimens that had been water quenched from the anneal, and all isothermal treatments were followed by water quenching. Tensile coupons had also been heat treated 1200 min at 816°C (1500°F), but these were very brittle and broke when attempting to machine them.

Air cooling from the annealing temperature produces higher yield and ultimate strengths and lower elongations than does water quenching. The effect is most noticeable upon the yield strength. Serrations in the tensile curves, frequently accompanied by crackling noises, were noted only in annealed and water quenched specimens and those heat treated at 482°C (900°F). The serrations and accompanying noises were very pronounced in specimens tested after 1200 and 6000 min at 482°C (900°F).

The yield strengths and elongations of specimens heat treated at 482 and 760°C (900 and 1400°F) are shown in Fig. 1 as functions of heat treating time. The 482°C (900°F) treatments are characterized by rapid, apparently discontinuous, changes in yield strength and elongation fol-

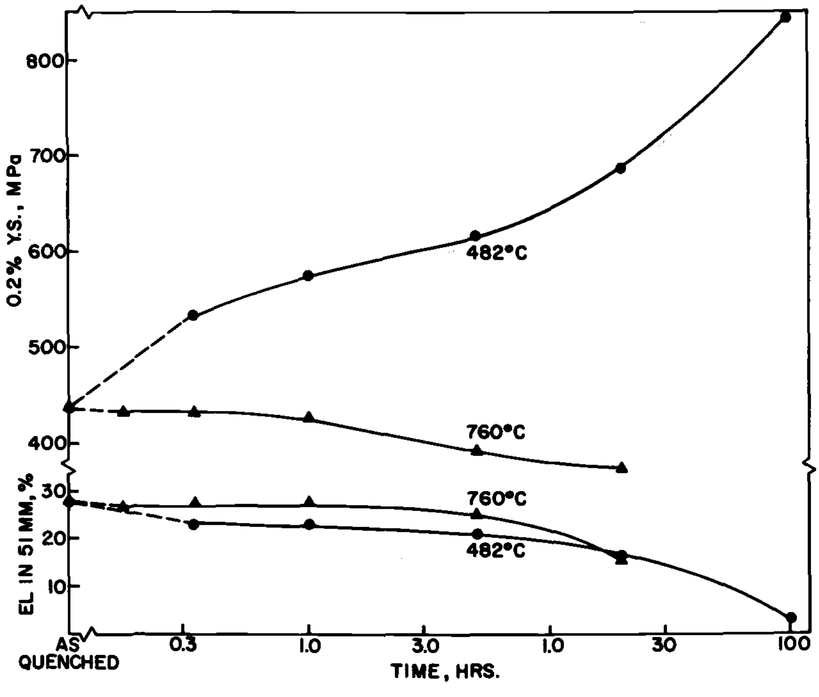

FIG. 1—*Yield strengths and elongations of specimens heat treated at 482 and 760°C (900 and 1400°F) as functions of heat treating time.*

lowed by further, regular changes in these properties with longer heat treating times. Upon heat treating at 760°C (1400°F), however, yield strengths and elongations decrease regularly with times. Ultimate strengths and hardnesses decrease with short heat treating times and then rise with longer times such that they exceed the annealed values after 5 h or longer. Treatments at 816°C (1500°F) resulted in similar behavior.

Table 3 is a summary of subsize Charpy V-notch tests conducted on transverse specimens. Two values for the apparent ductile-to-brittle transition temperatures (DBTT) are shown in the table. Those without parentheses are based upon the fracture appearance, being those temperatures where approximately 50 percent ductile shear and 50 percent brittle fractures were observed in the broken specimens. These were determined visually, supplemented in some cases by binocular examinations at 10 to 30 magnifications and examinations under a scanning electron microscope at 20 and higher magnifications. In general, the examinations at the higher magnifications agreed well with the visual estimates. Small amounts (to about 20 percent) of brittle facets distributed within a predominantly shear failure (and vice versa) were not always observed visually. The values within parentheses are those temperatures at which the impact energy levels were approximately midway between lower and upper shelves.

The DBTT of annealed specimens (1010°C (1850°F)—2 min at temperature and water quenched) was about −50°C (−60°F) based upon fracture appearance and about −73°C (−100°F) based upon energy level. Annealed and air-cooled specimens were not tested. The annealed specimens, those heat-treated to 100 h at 371 to 482°C (700 to 800°F) and those heat treated to 3 h at 538°C (1000°F) exhibit curves with sharp transition temperatures normally characteristic of ferritic stainless steels. The other treatments, although less pronounced at 927 and 982°C (1700 and 1800°F), resulted in broad DBTT regions. In such cases, it was not uncommon to observe varying mixtures of ductile and brittle failures over a 150 to 200°C (270 to 360°F) temperature range.

Embrittlement occurs most rapidly in the 760 to 871°C (1400 to 1600°F) temperature range. In this range, the lower and upper (where measurable) shelf energies were measurably lowered. Long exposures (100 h) in the 649 to 927°C (1200 to 1700°F) range caused brittle failures at all test temperatures up to and exceeding 371°C (700°F). Figure 2 shows typical examples of the different behaviors observed.

Figure 3 is a somewhat idealized representation of the impact behavior at room temperature, in some cases extrapolated from tests at higher temperatures. Embrittlement occurs very rapidly in the temperature range of 760 to 871°C (1400 to 1600°F), which is characterized by reductions in upper and lower shelf energy. A second, slower embrittlement region is seen at about 482°C (900°F) where no such reductions in shelf energies are seen. The embrittlement behavior is also illustrated in

TABLE 3—*Charpy V-notch transition temperatures as functions of heat treatments.* [a]

Heat Treating Temperature, °C	Ductile to Brittle Transition Temperatures[b] versus Time at Indicated Temperatures, °C					
	0.3 h	1.0 h	3.0 h	10 h	30 h	100 h
371	−80(−79)	−81(−87)	−52(−87)	−63(−73)	−49(−48)	−33(−46)
427	−50(−87)	−46(−57)	−39(−51)	−10(−46)	0(7)	140(124)
482	−27(−46)	6(−15)	22(7)	43(24)	213(204)	256(249)
538	−12(−21)	0(10)	13(7)	15(13)	58(43)	93(60)
593	0(−37)	38(4)	82(43)	38(43)	52(53)	107(96)
649	41(24)	52(38)	57(60)	275(129)	235(202)	>371
704	52(29)	45(38)	45(43)	115(93)	255(260)	>371
760	44(52)	95(96)	153(143)	>371	>371	>371
816	69(85)	142(142)	>371	>371	>371	>371
871	59(57)	180(149)	>371	>371	>371	>371
927	−3(−7)	21(10)	63(52)	135(107)	>371	>371
982	−36(−46)	−18(−46)	31(29)	72(71)	30(26)	100(66)

[a] Annealed and water quenched specimens exhibited transition temperatures of about −50(−73)°C.

[b] Values in parentheses are based on mid-height energy level, others are based on fracture appearance.

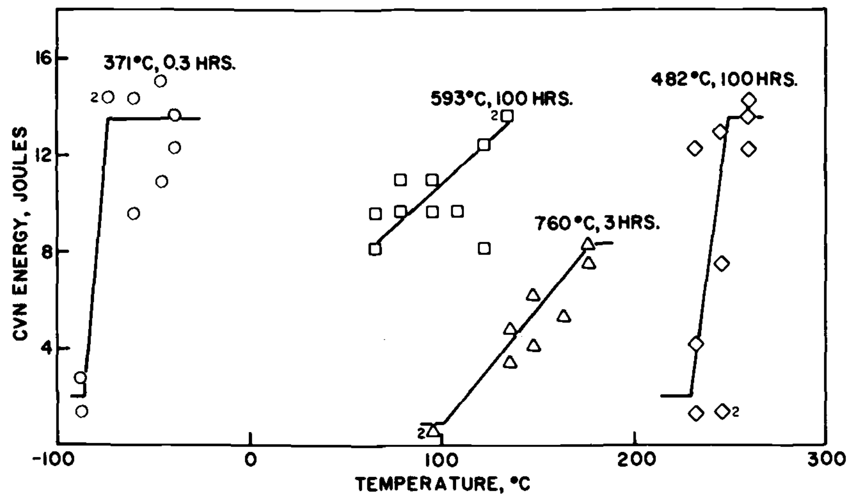

FIG. 2—*Typical examples of different impact behaviors.*

Fig. 4 where constant DBTT profiles of 25 and 100°C (77 and 212°F) are plotted as functions of heat-treating temperatures and times. The presence of a wide, rapid embrittlement region centered at about 775°C (1427°F) and a narrower, slower embrittlement centered at about 482°C (900°F) is clearly observed.

Figures 5 to 8 are SEM photographs at two magnifications of fractures

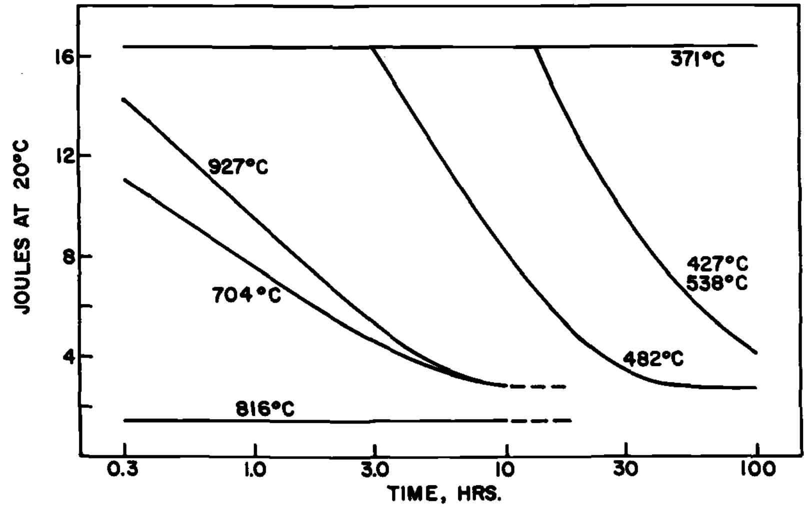

FIG. 3—*Impact behavior at room temperature.*

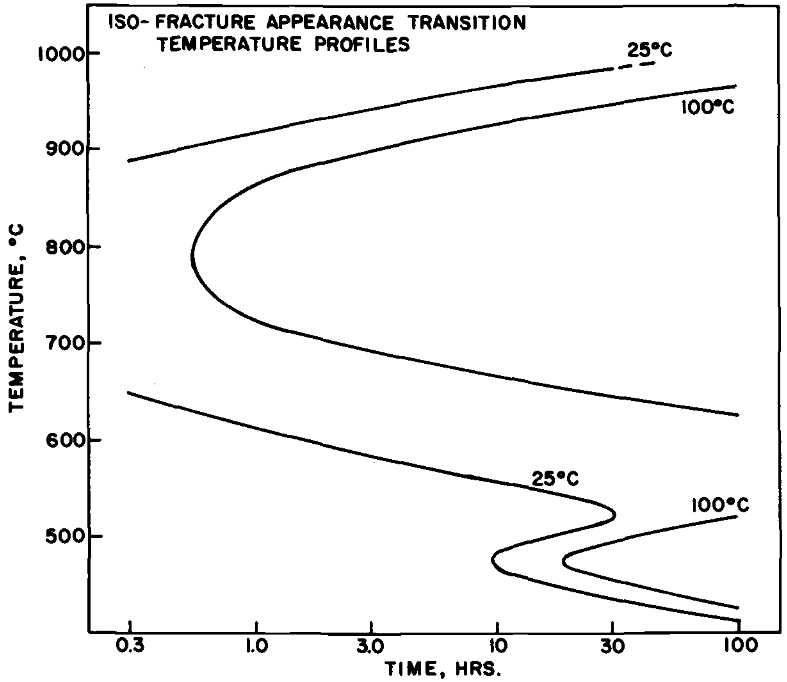

FIG. 4—*Impact embrittlement behavior.*

below and above apparent DBTT of the typical examples described in Fig. 2. In all cases the photographs were taken near the centers of the fractures. The fractures of the specimens treated 0.3 h at 371°C (700°F) and 100 h at 482°C (900°F), are illustrated in Figs. 5 and 6, respectively. The fractures appear nearly identical both below and above the DBTT for either treatment, although mechanical properties and test temperatures differ substantially. Both fractures below the transition temperatures appear to be completely quasi-cleavage. Fractures above the transition temperatures show quasi-cleavage facets within predominantly dimpled structures. These facets appear somewhat larger and fewer in the 482°C (900°F) heat-treated specimen. The impact fractures of the annealed, water-quenched specimens were similar to these examples.

The samples treated 100 h at 593°C (1100°F) and 3 h at 760°C (1400°F), shown in Figs. 7 and 8, respectively, exhibit similar quasi-cleavage facets and dimpled rupture. The dimple sizes appear somewhat smaller than in those heat treated at 371 and 482°C (700 and 900°F). The 760°C (1400°F) treated sample, broken below the apparent DBTT of 93°C (200°F) with only 0.7 J absorbed, exhibits 10 to 20 percent dimpled rupture (Fig. 8). Those treated at 371 and 482°C (700 and 900°F) that broke in an apparently

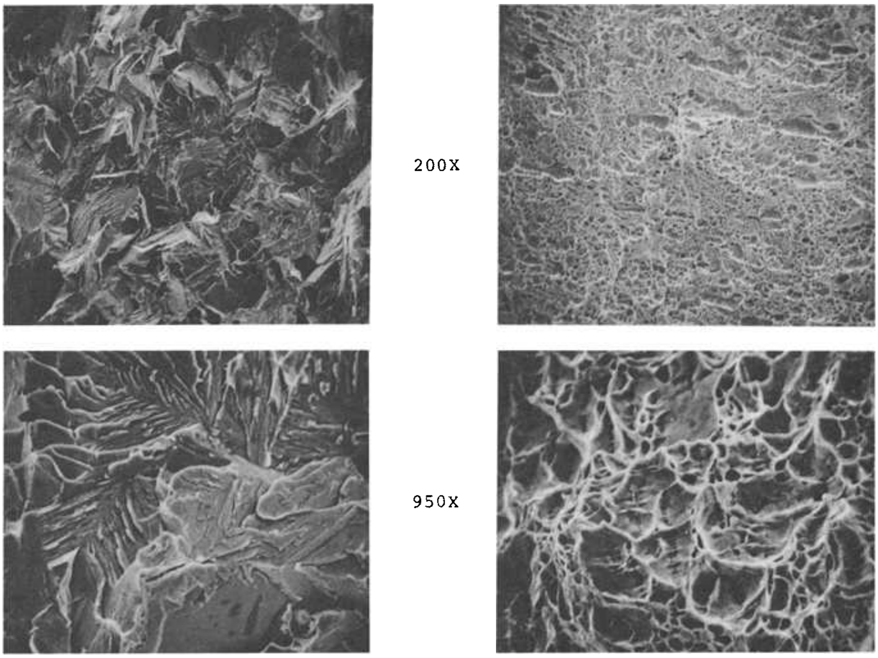

FIG. 5—*Fractures of specimens treated 0.3 h at 371°C* (left) *2.7 J at −87°C and* (right) *13.6 J at −32°C.*

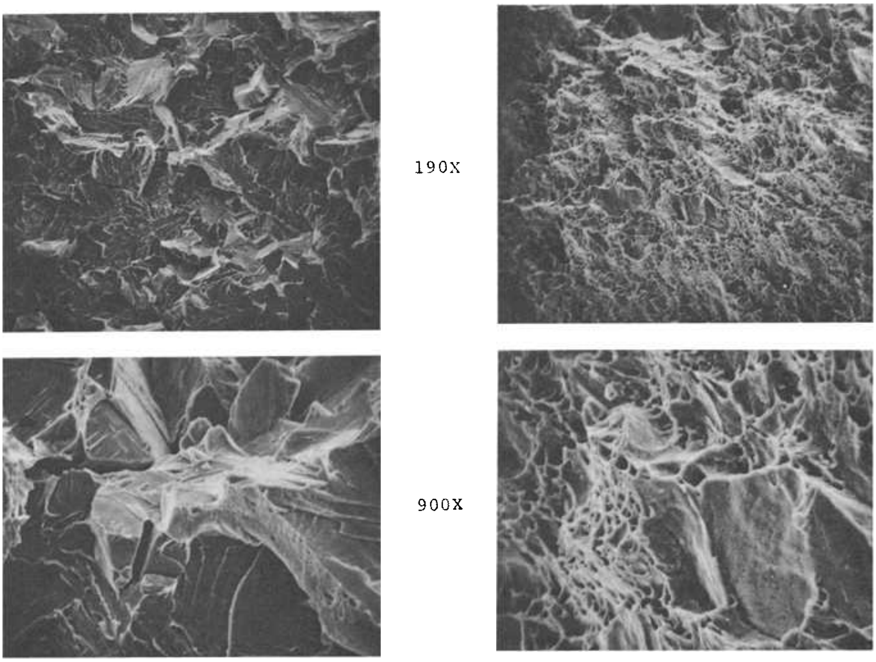

FIG. 6—*Fractures of specimens treated 100 h at 482°C;* (left) *1.4 J at 232°C and* (right) *14.2 J at 260°C.*

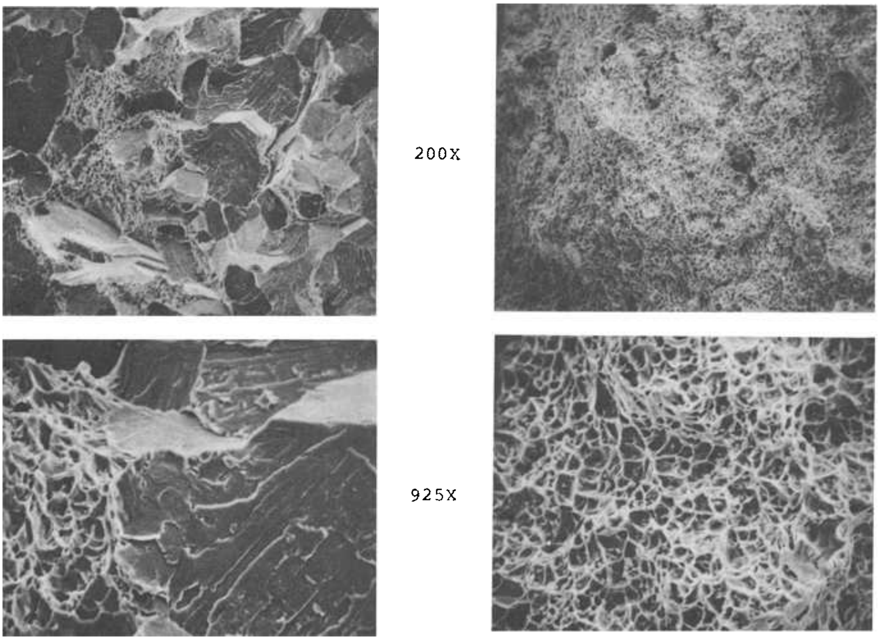

FIG. 7—*Samples treated 100 h at 593°C;* (left) *8.1 J at 66°C and* (right) *13.6 J at 135°C.*

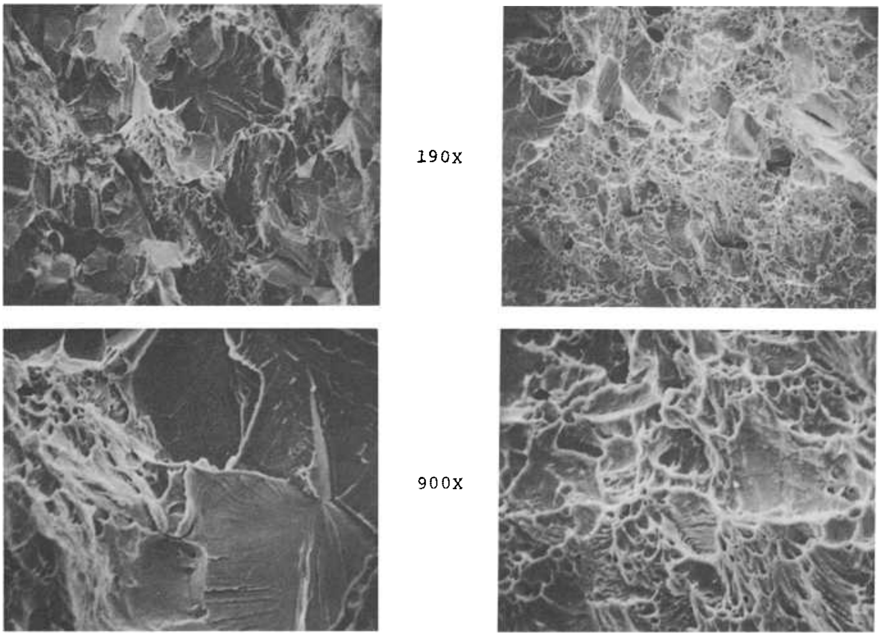

FIG. 8—*Samples treated 3 h at 760°C;* (left) *0.7 J at 93°C and* (right) *8.1 J at 177°C.*

completely quasi-cleavage mode absorbed more energy during fracture. The *brittle* sample of Fig. 7 and the *ductile* sample of Fig. 8 both absorbed the same amount of energy during fracture, but the former exhibits only 10 to 20 percent and the latter 80 to 90 percent dimpled rupture. The brittle facets in the latter are quite smooth and curved suggesting an intergranular fracture mode with little energy absorption.

Figures 9 to 22 are photomicrographs, generally at 500 magnifications, in selected heat-treated conditions. Figure 9 shows the annealed and water-quenched structure. The microstructure is clear except for scattered, fine oxide inclusions. Rather long etching times are required to delineate grain boundaries in this condition. Heat treatments at 371 and 427°C (700 and 800°F) to 100 h produced no discernible changes in microstructure from the annealed condition. As shown in Table 3, however, long times at 371 and 427°C (700 and 800°F) produce elevations in DBTT.

Figure 10 shows the microstructure after the treatment at 482°C (900°F) for 100 h at 2000 magnifications. A fine, grain boundary precipitate is clearly visible at the higher magnification. The grain-boundary precipitate was not observed in the shorter times (to 30 h) at 482°C (900°F). Figure 11 is a photomicrograph of the structure after 100 h at 538°C (1000°F). The microstructure is similar to the 482°C (900°F) 100-h sample, but the grain boundary precipitate is somewhat more profuse and coarser.

Figure 12 shows the structure after 100 h at 593°C (1100°F). Many grain boundaries exhibit relatively deep grooves indicating they are less resistant to attack by the etchant. Fine but resolvable particles are seen at grain boundaries and within the matrix. Heat treatment at 649°C (1200°F) for 100 h produces the first marked change in microstructure (Fig. 13). The grain boundaries are nearly completely enveloped by one or more massive phases. A relatively coarse intragranular precipitate is also present.

Figure 14 shows the microstructure after 100 h at 704°C (1300°F). The grain boundary phase or phases are more continuous and much larger. The intragranular precipitate appears only slightly larger. At temperatures to 704°C (1300°F) the intergranular phase is intermittently etched or stained gray and clear white suggesting that it varies in composition. No clear boundaries between the gray and white regions were detected as would be expected if two distinct phases were present. The intragranular phase, with few exceptions, is uniformly clear white in color.

Figures 15 to 18 are photomicrographs of the structures after 100-h exposures at 760 to 927°C (1400 to 1700°F). The precipitate is uniform in color indicating that it is a single, homogeneous phase. Small particles are observed within the intergranular networks of Figs. 15 and 16 that could be an additional phase or particles of the matrix. The precipitate forms a completely intergranular network and comprises nearly 50 percent of the

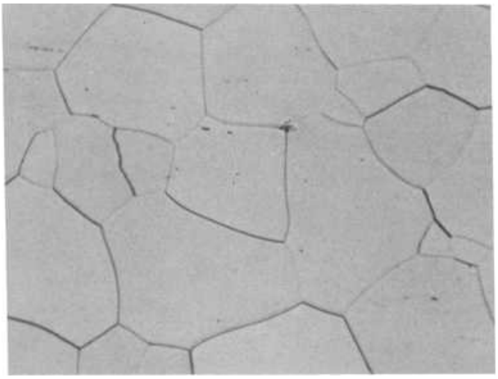

FIG. 9—*Annealed and water-quenched structure (×500 original magnification).*

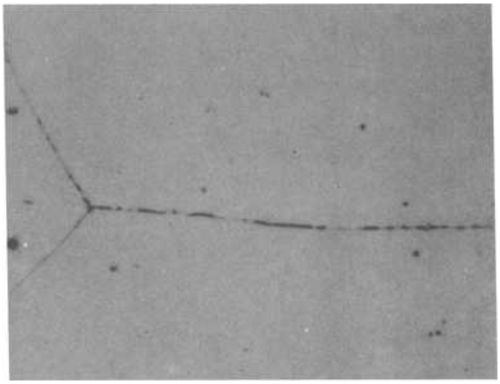

FIG. 10—*Microstructure after the treatment at 482°C (900°F) for 100 h (×2000 original magnification).*

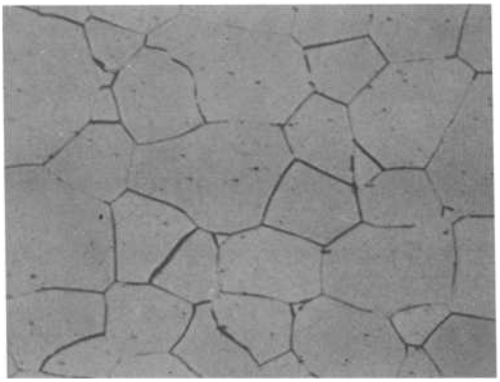

FIG. 11—*Microstructure after 100 h at 538°C (1000°F) (×500 original magnification).*

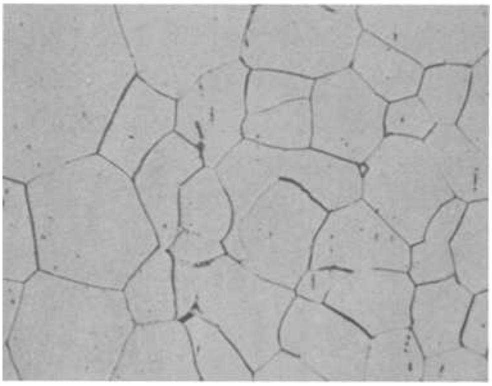

FIG. 12—*Microstructure after 100 h at 593°C (1100°F) (×500 original magnification).*

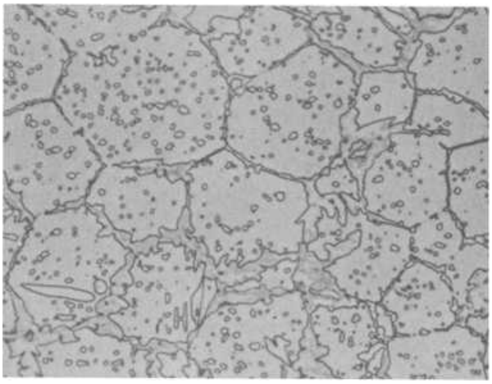

FIG. 13—*Microstructure after 100 h at 649°C (1200°F) (×500 original magnification).*

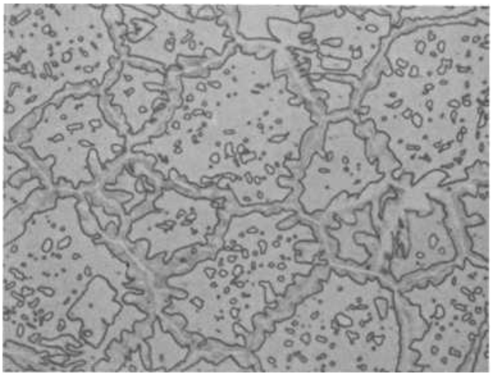

FIG. 14—*Microstructure after 100 h at 704°C (1300°F) (×500 original magnification).*

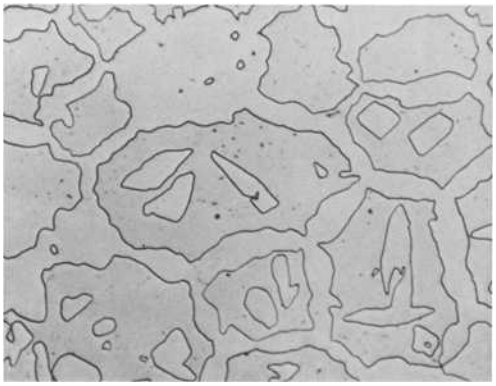

FIG. 15—*Microstructure after 100 h at 760°C (1400°F) (×500 original magnification).*

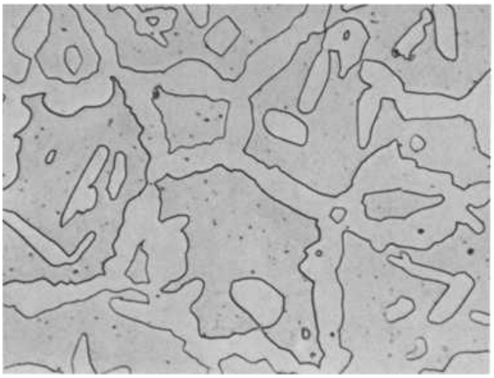

FIG. 16—*Microstructure after 100 h at 816°C (1500°F) (×500 original magnification).*

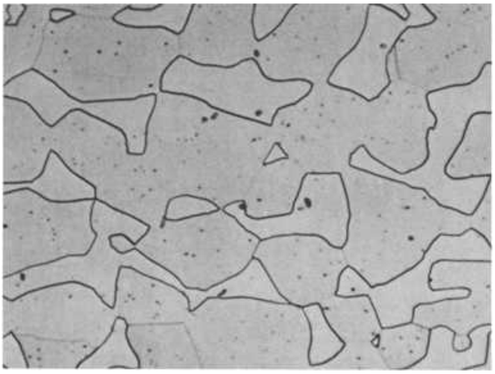

FIG. 17—*Microstructure after 100 h at 871°C (1600°F) (×500 original magnification).*

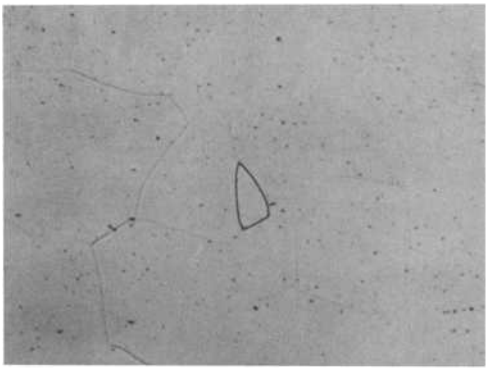

FIG. 18—*Microstructure after 100 h at 927°C (1700°F) (×500 original magnification).*

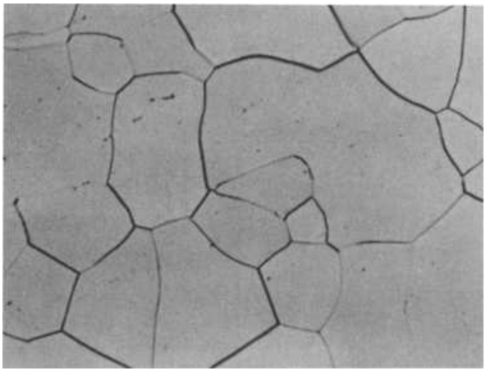

FIG. 19—*Microstructure after 100 h at 982°C (1800°F) (×500 original magnification).*

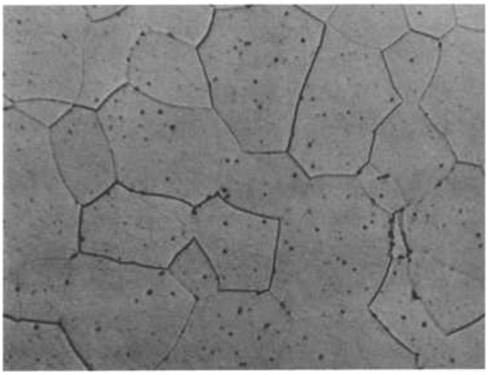

FIG. 20—*Microstructure after 0.3 h at 816°C (1500°F) (×500 original magnification).*

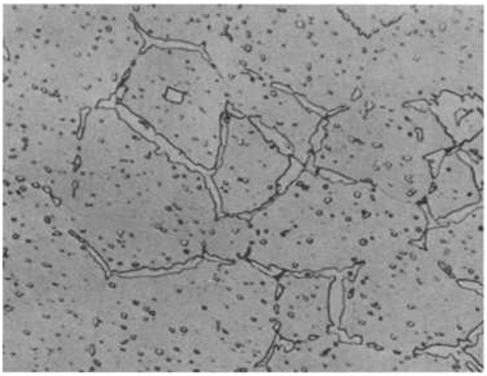

FIG. 21—*Microstructure after 3 h at 816°C (1500°F) (×500 original magnification).*

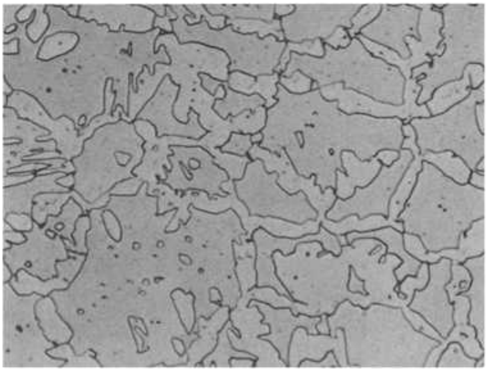

FIG. 22—*Microstructure after 10 h at 816°C (1500°F) (×500 original magnification).*

structure in Figs. 15 and 16 (100 h at 760 and 816°C (1400 and 1500°F), respectively). After 100 h at 871°C (1600°F) large amounts of the precipitated phase are also present, but they no longer form intergranular networks (Fig. 17). Only isolated particles of the second phase are precipitated after 100 h at 927°C (1700°F) as shown in Fig. 18. Greater amounts of the phase were observed near the surfaces of the sample. A fine, dimly-etched precipitate appears to be uniformly dispersed throughout the structure also. None of the second phase was observed in the sample heat treated at 982°C (1800°F) for 100 h (Fig. 19). Its microstructure is indistinguishable from that of the annealed specimen illustrated in Fig. 9.

At the lower temperature end of the broad 775°C (1427°F) embrittlement region described in Fig. 4, large elevations in DBTT can be correlated to the formation of the intergranular phase of phases. The 100-h exposure at 593°C (1100°F) produces small particles of a second phase as the major structural change (Fig. 12) and causes an increase in DBTT to about 100°C (212°F) as described in Table 3. A nearly continuous intergranular network is formed after 100 h at 649°C (1200°F) as shown in Fig. 13 and is associated with a DBTT in excess of 371°C (700°F). Thirty hours at 704°C (1300°F) produces scattered, fairly large intergranular and intragranular precipitates whereas a nearly continuous network is produced after 100 h (Fig. 14). The corresponding transition temperatures from Table 3 are about 260 and >371°C (500 and >700°F), respectively.

The microstructures of specimens heat treated 0.3, 3, and 10 h at 816°C (1500°F) are shown in Figs. 20, 21, and 22, respectively. A fine general precipitate is observed after 0.3 h, a semicontinuous intergranular network is formed after 3 h and a continuous network of a massive phase is formed in 10 h. The DBTT associated with the first structure is about 58°C (136°F) and over 371°C (700°F) for the latter two structures (Table 3). The 20-h treatment at this temperature produced a structure too brittle to be machined into a tensile coupon (Table 2). Impact fractures below and above the apparent DBTT of the 0.3-h treated specimen and fractures at low and high temperatures of the latter two conditions were also examined under the scanning electron microscope. The fractures of the 0.3-h and 10-h treated specimens are shown in Figs. 23 and 24, respectively. The brittle fracture of Fig. 23 is predominantly conventional quasi-cleavage with some interspersed dimpled rupture. The brittle fractures of Fig. 24 have a smeared debris-laden appearance with many curved facets, the latter being suggestive of intergranular fracture. Semiquantitative energy dispersive spectroscopy (EDS) analyses for iron, chromium, and molybdenum were conducted on the 0.3-h specimen fractured at 65°C (150°F) and the 10-h specimen fractured at 149°C (300°F). An attempt was made to center the beam on large, flat facets. The iron and chromium contents were about the same on each, but the molybdenum content was three times as high on the sample exposed 10 h at 816°C (1500°F).

The nature of the severe embrittlement occurring at 927°C (1700°F) is not clearly related to the optical microstructure. The relatively minor amount of second phase seen after 100 h at 927°C (1700°F) appears inadequate to explain the increase in DBTT to over 371°C (700°F) after 30 h or more at temperature (Table 3).

Corrosion Resistance

Corrosion rates in boiling ferric sulfate, 50 percent sulfuric acid (ASTM A 262–75 Practice B) were measured by weight loss and converted into millimetres per year (mm/yr) (inches per month in./mo) penetration. Duplicate samples were placed in the same flask and tested simulta-

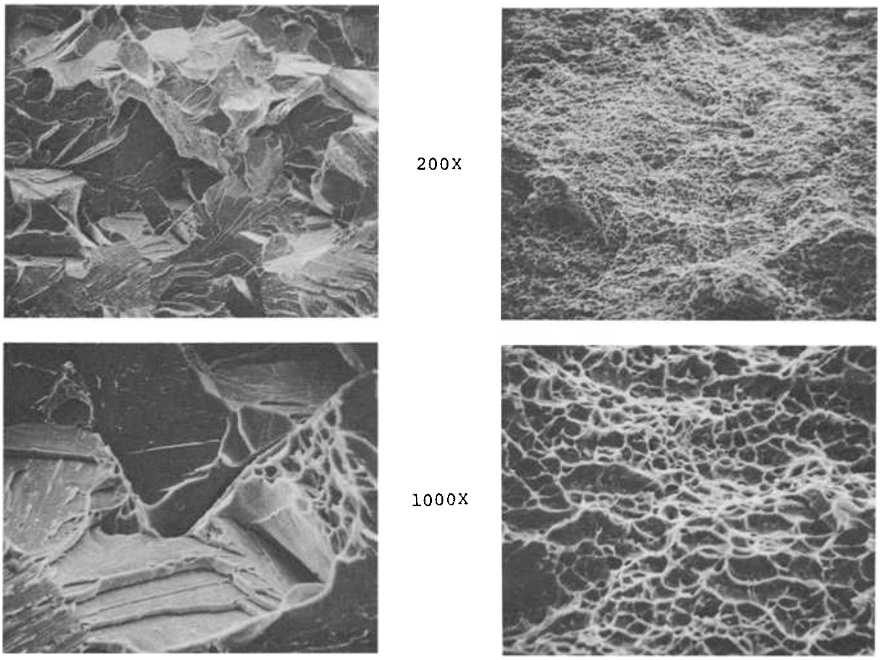

FIG. 23—*Fractures of specimen after 0.3 h at 816°C (1500°F);* (left) *2.7 J at 65°C and* (right) *12.2 J at 121°C.*

neously. In several cases, they became activated upon insertion into the test solution and were destroyed before additional inhibitor could be added. Since only two specimens were prepared in each condition of heat treatment, the tests were not repeated.

Annealed specimens exhibited corrosion rates of about 0.12 mm/yr (4×10^{-4} in./mo). Reproducibility between duplicate test coupons was erratic. The region of high corrosion rates can be described by a single C-curve centered at about 760°C (1400°F). High rates were seen within 10-h exposures in the 649 to 871°C (1200 to 1600°F) temperature range, while 100-h exposures caused high rates from 538 to 927°C (1000 to 1700°F).

Figures 25 to 28 are photomicrographs at 250 magnifications illustrating the attack that was observed metallographically. The 100-h treatment at 538°C (1000°F) produced a microstructure with discontinuous intergranular precipitation (Fig. 11). Figure 25 is the same condition after the sulfuric acid-ferric sulfate test showing intergranular attack one to three grains deep with little evidence of grain removal at the surfaces. This particular specimen exhibited a corrosion rate of 0.153 mm/year (5.1×10^{-4} in./mo), whereas its duplicate, which appeared the same metallographically,

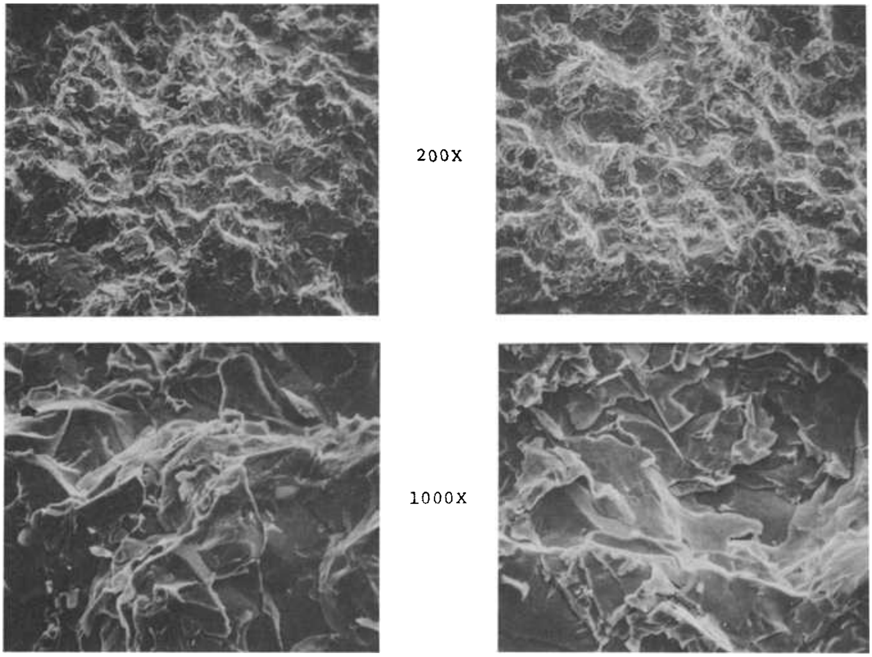

FIG. 24—*Fractures of specimen after 10 h at 816°C (1500°F);* (left) *0.7 J at 149°C and* (right) *0.7 J at 371°C.*

exhibited a corrosion rate four times as high. Figures 26 to 28 are photomicrographs of corrosion test coupons that had been heat-treated at 816°C (1500°F) for 1, 10, and 100 h, respectively. Low corrosion rates, and no intergranular attack, were exhibited after 1 h (Fig. 26). After 3 h at 816°C (1500°F), the intergranular phase becomes more continuous (Fig.

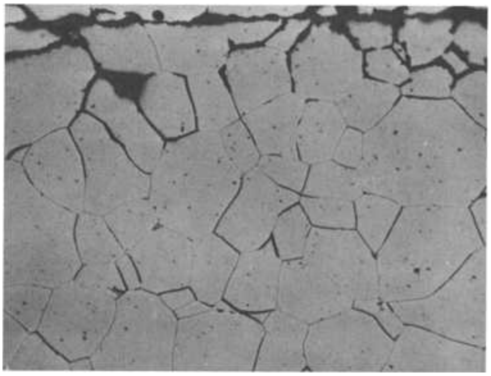

FIG. 25—*The 100-h treatment at 538°C (1000°F) (×250 original magnification).*

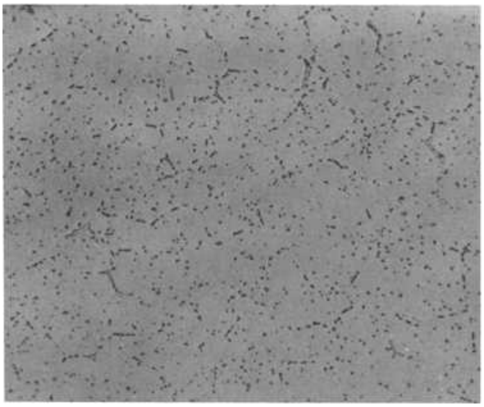

FIG. 26—*The 1-h treatment at 816°C (1500°F) (×250 original magnification).*

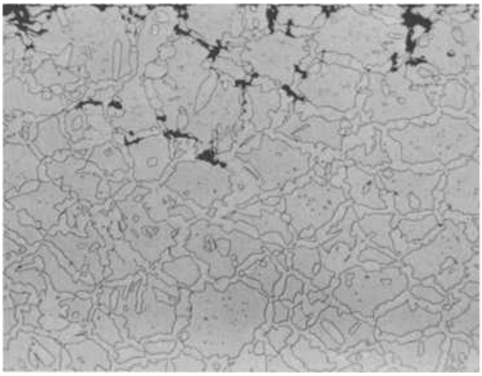

FIG. 27—*The 10-h treatment at 816°C (1500°F) (×250 original magnification).*

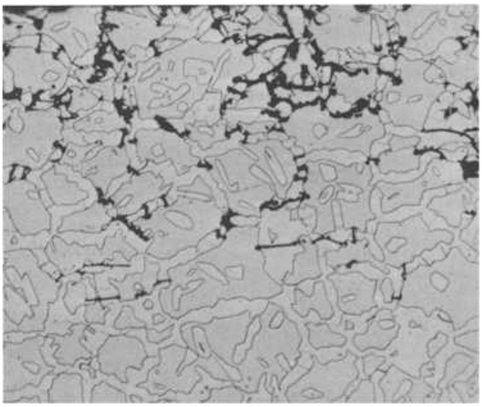

FIG. 28—*The 100-h treatment at 816°C (1500°F) (×250 original magnification).*

21), the corrosion rates increase to about 0.2 mm/year (6.7 × 10^{-4} in./mo) and grain removal to the depth of about one grain is sporadically seen on both surfaces. Preferential intergranular attack, however, is not noticeable. As the intergranular phase becomes interconnected and grows with longer holding times at 816°C (1500°F), intergranular attack to a considerable depth below the surface is observed (Figs. 27 and 28). The corrosion rate after 10 h at 816°C (1500°F) was 1.17 mm/yr (3.9 × 10^{-3} in./mo) and after 100 h was 2.04 mm/year (6.8 × 10^{-3}in./mo). The intergranular attack appears to concentrate at interconnecting boundaries of the intergranular phase (or phases) and at boundaries between the phase and matrix.

In other instances, high corrosion rates were obtained without metallographic evidence of preferential grain boundary attack. An example is a specimen held 3 h at 704°C (1300°F) that exhibited a high corrosion rate of over 3 mm/year (1 × 10^{-2} in./mo). The microstructure contains second phase particles in a relatively random distribution. Obvious attack is observed at both surfaces, but it appears to be of a general nature. In such cases, it is not clear if the sulfuric acid-ferric sulfate is a measure of intergranular susceptibility or is causing general attack of the matrix.

The region of crevice attack, like the sulfuric acid-ferric sulfate tests, can be described as a C-curve centered at about 760°C (1400°F) on a time-temperature plot. The nose appears somewhat broader and crevice attack is observed at earlier times than in sulfuric acid-ferric sulfate testing. Crevice attack was observed at 50°C (122°F) within 1 h of exposure in the wide temperature range of 593 to 871°C (1100 to 1600°F) and after 10-h exposures at 538°C (1000°F). The 100-h exposures were tested according to the same procedure but at a lower test temperature of 20°F (68°F) instead of 50°C (122°F). Crevice attack was again seen on samples heat-treated within the 538 to 927°C (1000 to 1700°F) temperature range, but the attack was relatively light on the 538 and 927°C (1000 and 1700°F) specimens.

Figure 29 is a photomicrograph describing an example of the crevice attack that was observed. Figure 29 is at the surface adjacent to a heavily attacked region in the sample heat-treated 10 h at 816°C (1500°F) and tested at 50°C (122°F). The attack in ferric chloride appears to concentrate in the matrix adjacent to the intergranular phase that, in this case, is interconnected.

Discussion

Mechanical Properties

AL-29-4 alloy is subject to at least two separate embrittlement phenomena that can be represented by a composite of two C-curves (Fig. 4). The lower C-curve is centered at about 482°C (900°F) and is attributa-

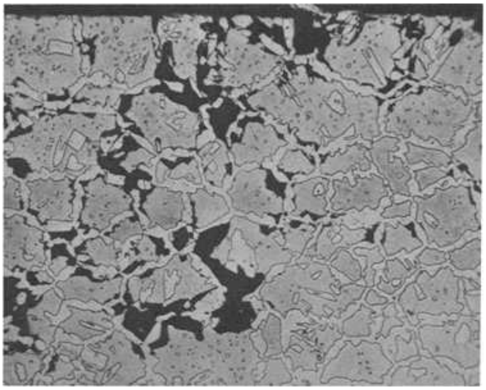

FIG. 29—*Example of crevice attack observed.*

ble primarily to 475°C (885°F) embrittlement. The upper C-curve is centered near 760°C and is primarily caused by the precipitation of two or more intermetallic compounds that include the sigma and chi phases.

The 475°C (885°F) embrittlement is characterized by apparent discontinuous increases followed by continuous increases in hardness and strength and decreases in ductility and toughness (Tables 2 and 3). These property changes are similar to those reported many times in the literature as being representative of 475°C (885°F) embrittlement. Room temperature tensile data reported for a similar alloy containing 2 Ni [*3*] are nearly identical except that the 2Ni appears to slow the rate of embrittlement slightly. No obvious incubation period prior to tensile or impact embrittlement is apparent from the data reported in Tables 2 and 3. However, slowing the cooling rate from the anneal by air cooling in place of water quenching causes changes in tensile properties approaching that obtained by heat treating 20 min at 482°C (900°F) as illustrated in Table 2. Nichol [*3*] shows that the tensile properties of a similar alloy are affected in the same fashion by slowing the cooling rate from the anneal. He also showed that the impact transition temperature of the similar alloy at 1.65 mm (0.065 in.) thickness is increased about 20°C (36°F) by air cooling in place of water quenching from the anneal. This is about the same increase in fracture appearance transition temperature (FATT) observed for the AL 29-4 alloy from the annealed water-quenched condition to the 0.3-h treatment at 482°C (900°F) shown in Table 3. It should be recognized that the impact DBTT values in this study were obtained from subsize specimens, approximately one-sixth the thickness of the standard Charpy V-notch specimen. Nichol [*3*], from work on a similar alloy, shows that impact testing at this thickness causes a depression in apparent DBTT of about 100°C (180°F) from that of a full-size specimen.

Early discontinuous changes in tensile and impact properties followed by apparent incubation periods have been observed in three other commercial ferritic stainless steels containing 18 to 29Cr by Nichol et al [*11*]. The presence of such apparent incubation periods indicates that the very early changes in properties that were observed may be due to another mechanism such as precipitation of carbides or nitrides. The fine intergranular precipitate observed after 100 h at 482°C (885°F) tends to support this supposition (Fig. 10). The absence of discontinuous changes in tensile properties upon aging at 760 and 816°C (1400 and 1500°F) show that these early property changes produced by air cooling occur at lower temperatures. Work done at our laboratory on a titanium-stabilized 26Cr-1Mo alloy further show that these changes start to occur at about 538°C (1000°F) during cooling.

Tensile embrittlement at 482°C (900°F) is accompanied by increased twinning that was detected audibly and by serrations in the tensile curves. The same observations were noted in a similar alloy containing 2Ni [*3*] and are accompanied by changes in deformation mode from cross-slip to planar slip [*12*]. The change in deformation mode occurs very early during aging when only faint evidence of spinodal decomposition can be observed by transmission electron microscopy [*12*].

Impact embrittlement at 482°C (900°F) is accompanied by large increases in FATT (Table 3 and Fig. 4), but the upper and lower shelf energies do not change significantly and transition temperatures remain sharp and well defined (Fig. 2). The fractures of embrittled impact specimens were indistinguishable from annealed specimens at temperatures above and below their respective transition temperatures (Figs. 5 and 6). No evidence of twinning was observed on the fractures of embrittled specimens in contrast to the observations of Nichol [*3*] on a similar alloy with 2Ni.

Other than a fine intergranular precipitate seen after 100 h at 482°C (900°F), no optically observable changes in microstructure accompany 475°C (885°F) embrittlement in agreement with numerous other studies. This intergranular precipitate, shown in Fig. 10, is believed to be carbides, or possibly nitrides, even though the interstitial content of the heat is quite low.

The upper C-curve is characterized by gradual decreases in yield strength, ductility, and toughness. Tensile strength and hardness decrease with short exposure times at 760 and 816°C (1400 and 1500°F) and then rise slightly at times of 5 h or more (Table 2). The high temperature embrittlement, as measured by impact tests, occurs much more rapidly and extends over a wider temperature range than 475°C (885°F) embrittlement (Table 3 and Fig. 4). Impact embrittlement in this range caused reductions in upper and lower shelf energies and led to diffuse transition regions.

Heat treating high Cr-Mo ferritic alloys in the temperature range of about 550 to 900°C (1022 to 1652°F) has been reported to result in the precipitation of both sigma and chi phases [*2,3,4,12*]. Streicher [*4*] evaluated the ductility of a high-purity 29Cr-4.3Mo alloy by room-termperature bend tests after 1- and 100-h treatments at 593 to 927°C (1100 to 1700°F). The 1-h treatments resulted in ductile bends, although grain-boundary precipitates were optically observed in the 704 to 927°C (1300 to 1700°F) range. Those present after the 760 to 871°C (1400 to 1600°F) treatments were identified as sigma phase. A 100-h treatment at 593°C (1100°F) resulted in a ductile bend and a clear microstructure. Specimens heat treated 100 h at 704 to 927°C (1300 to 1700°F) cracked during bending and contained precipitates of sigma and chi phases.

Brandis et al [*2*] evaluated the structure and mechanical properties of a high-purity 28Cr-3.5Mo alloy annealed 30 min at 1000°C (1832°F) and held for times to 10 000 h at 350 to 900°C (662 to 1652°F). Sigma and chi phases were identified metallographically and checked with a microprobe while α' was inferred from impact energy changes. They showed chi phase to form within 0.2 h at 750°C (1382°F) and sigma phase to form within 5 h at 750 to 850°C (1382 to 1562°F). $Cr_{23}C_6$ was also identified in 0.2 to 100 h at 750 to 875°C (1382 to 1607°F). They constructed Deutscher Verband für die Materialprüfung der Technik (DVM) isoimpact energy contours (50 J) in a manner similar to that of Fig. 4. They obtained a similar double C-curve with a lower nose at about 525°C (977°F) and 20 h and an upper nose at 750°C (1382°F) and 0.2 h. Sigma and chi phases were observed metallographically from 600 to 850°C (1112 to 1562°F) but were assumed to extend from 550 to 900°C (1022 to 1652°F) from the impact behavior. The 475°C (885°F) embrittlement range was assumed to extend from 400 to 550°C from the impact property changes.

Nichol [*3*] identified chi phase in a 29Cr-4Mo-2Ni alloy held at 760°C (1400°F) for 3 h by X-ray diffraction on a solid sample. Datta et al [*12*] on the same 2Ni alloy found sigma phase and at least one other unidentified phase by X-ray diffraction on solid samples and extracts in a specimen held 1000 h at 593°C (1100°F). Electron diffraction indicated that R phase may have been one of the unidentified constituents.

The tensile properties upon heat treating at 760 and 816°C (1400 and 1500°F) change in a different manner than that accompanying 475°C (885°F) embrittlement. Yield strengths decrease continually whereas tensile strengths and hardnesses first decrease then rise. Tensile elongation is slightly decreased after 5 h at either temperature and then plummets to very low values. The coupons held 20 h at 816°C (1400°F) were too brittle to be machined into tensile specimens. The marked fall in elongation appears to coincide with the development of a continuous grain-boundary network of massive precipitates (Figs. 21 and 22). The same changes in tensile behavior were obtained in a similar 2Ni alloy [*3*] but, in this case, specimens aged 20 h at 760°C (1400°F) were also too brittle to be machined into tensile specimens. These data and other data generated at our laboratory show that 2Ni accelerates the high-temperature embrittlement reaction. Bend test data by Streicher [*4*] on the 2Ni alloy also lead to this conclusion.

Nichol [*3*] has proposed that the tensile property changes in the similar 2Ni alloy after heat treating at these temperatures are consistent with solute depletion of the matrix. Since molybdenum is the most potent solid-solution strengthener in AL 29-4 [*2*], the precipitation of a molybdenum-rich phase, such as chi phase, in a form ineffective for dispersion hardening might be expected to cause the observed changes. As the brittle phases attain continuity at grain boundaries, slip is impeded and fracture proceeds through these brittle phases with very little signs of ductility.

The impact properties, to varying degrees, are adversely affected by heat treatments over the entire 371 to 982°C (700 to 1800°F) temperature range that was studied. Precipitation of phases assumed to be sigma and chi was observed optically in the microstructures after 100-h treatments at 593 to 927°C (1100 to 1700°F). This agrees well with the metallographic observations of Brandis et al [*2*] at the lower temperature end. They only saw these phases up to 850°C (1562°F), however, in their leaner 28Cr-3.5Mo alloy. A mild increase in DBTT is observed at 538°C (1000°F) and is accompanied by a fine intergranular precipitate at long aging times (Fig. 11). This treatment also resulted in some intergranular attack in sulfuric acid-ferric sulfate (Fig. 25). It is not clear whether embrittlement at this temperature is caused by 475°C (885°F) embrittlement, traces of sigma or chi phase or both, or by a separate species such as carbides or nitrides. The incipient intergranular attack seen in Fig. 25 appears to favor the latter two mechanisms. The mild increases in DBTT upon exposures at 982°C (1800°F) is not accompanied by precipitates that can be seen optically. Based upon studies of another AL-29-4 heat at our laboratory, however, the chi or sigma solvus or both are slightly above 982°C (1800°F).

For our purposes, the high temperature embrittlement range is defined as 593 to 927°C (1100 to 1700°F) where phases believed to be sigma or chi or both are visible optically after 100-h treatments. The impact properties in this embrittlement range are characterized by wide transition temperatures (Fig. 2). Where precipitation of sigma or chi or both becomes profuse, the upper and lower shelf energies are substantially lowered (Fig. 2) and the brittle fractures appear to show curved facets and a *smeared* appearance (Figs. 8 and 24). Semiquantitative EDS analyses of these brittle facets show the molybdenum content to be thrice that of the matrix indicating that much of the fractures are occurring at grain boundaries through a molybdenum-rich phase. The occurrence of grain-boundary fractures appears to agree with grain-boundary precipitation of phases observed optically in those samples evaluated. Even when impact fractures appeared predominantly ductile in such samples, the impact energy absorbed was comparatively low (Fig. 8). Work by Nichol [*3*] on a similar alloy with 2Ni showed clear evidence of intergranular facets in a broken impact specimen aged 30 min at 760°C (1400°F). In this case, however, definitely curved but otherwise featureless facets were observed.

The etching behavior of the alloy indicates that a change occurs in the structure or composition of the precipitated phases upon increasing the 100-h heat treatment temperature from 704 to 760°C (1300 to 1400°F). The microstructures are shown in Figs. 14 and 15, respectively. To check this premise, broken halves of impact specimens representing these conditions were metallographically polished on one surface to remove oxides and examined by X-ray diffraction in a General Electric Company XRD-5 Diffractometer using chromium radiation with a vanadium filter.

All X-ray lines in both samples could be indexed to bcc iron, a tetragonal phase with an a_0 of 8.814 Å and c_0 of 4.580 Å and a bcc phase with an a_0 of 8.89 Å. The tetragonal phase, identified as sigma, precisely matches that reported by Datta et al [*12*] on a similar alloy with 2Ni after heat treating at 593°C (1100°F) for 1000 h. The extraneous bcc phase matched well with chi phase reported by Koh [*19*]. The X-ray intensities indicate the ratio of chi to sigma phases was greater in the sample heat treated at 704°C (1300°F). The reason for the different etching behavior, which was reproducible, is not evident from the X-ray data.

Corrosion Properties

Tests in boiling 50 percent sulfuric acid-ferric sulfate (ASTM A 262–75 Practice B) will produce intergranular corrosion in the high-chromium ferritic alloys if carbides or second phases, such as sigma, are precipitated at grain boundaries and cause continuous paths of chromium-depleted regions. The ferric sulfate serves as an inhibitor to prevent general attack from the boiling sulfuric acid. Properly heat treated AL 29-4 alloy is expected to show no crevice attack in 10 percent $FeCl_3$ at 50°C (122°F) when tested as specified by ASTM Test for Pitting and Crevice Corrosion Resistance of Stainless Steels and Related Alloys by the Use of Ferric Chloride Solution (G 48–76). Material fails this test if either significant weight loss, on the order of 0.001 g from a 14 g sample, can be measured or if attack can be seen after the test. Attack is generally observed first where the rubber bands contact the edges of the test coupons.

Heat treatments to 100 h at temperatures from 371 to 482°C (700 to 900°F) produced no detectable changes in corrosion resistance under the given corrosion test conditions. The effects of 475°C (885°F) embrittlement on corrosion properties has not been extensively studied, possibly because the effects are minor compared to those upon mechanical properties. Investigations conducted on alloys with substantial interstitial contents would be confused by carbide and nitride precipitation. Work by Lizlovs et al [*18*] shows effects on titanium-stabilized 18Cr-2Mo alloy that are consistent with chromium depletion through the precipitation of α'. When 475°C (885°F) embrittlement occurs by spinodal decomposition, as would be expected in AL 29-4 [*10,12*], the effects upon corrosion are difficult to predict. Presumably, no effects would be seen until discrete α' particles are formed.

Heat treatments at 538°C (1000°F) caused attack in sulfuric acid-ferric sulfate within 100 h (Fig. 25) and in 10 percent $FeCl_3$ within 30 h. The attack is associated with an intergranular precipitate (Fig. 11). The attack is relatively mild and is believed to be caused by the precipitation of carbides or nitrides or both. It does not seem attributable to 475°C (885°F) embrittlement since no attack was observed where the mechanical property changes are largest and the temperature seems too low to be caused by incipient precipitation of sigma or chi phases or both [*2*].

Corrosion resistance in sulfuric acid-ferric sulfate and 10 percent $FeCl_3$ was significantly reduced upon relatively short exposures in the high-temperature embrittlement range. The ferric chloride crevice-corrosion test at 50°C (122°F) was the more severe test of the two generally used. Attack in sulfuric acid-ferric sulfate is seen within 10 h upon heat treating at 649 to 871°C (1200 to 1600°F) and within 100 h at 538 to 927°C (1000 to 1700°F). Crevice attack at 50°C (122°F) is seen within 1-h treatments at 593 to 871°C (1100 to 1600°F) and within 10-h treatments at 538 to 927°C (1000 to 1700°F). No attack in either test was observed upon heat treatments at 982°C (1800°F) for 100 h or less.

Attack in both media can be described by C-curves centered at about 760°C (1400°F). The curve for crevice attack extends to shorter times and appears to have a broader nose. Corrosive attack correlates well with the appearance of sigma and chi phases in the microstructure (Figs. 9 to 22). Corrosive attack observed in specimens heat treated at 927°C (1700°F) appears somewhat surprising in view of the small amount of second phase shown in the microstructure (Fig. 18). More of this phase, however, was seen at the surfaces.

High corrosion rates in sulfuric acid-ferric sulfate were sometimes associated with preferential intergranular attack (Figs. 25, 27, and 28). In the high-temperature embrittlement range of 593 to 927°C (1100 to 1700°F) preferential intergranular attack occurred when grain-boundary precipitation became interconnected. In some cases, intergranular attack appears to concentrate at the interconnecting boundaries of the grain phases and at the boundaries between those phases and the matrix. In other instances, high corrosion rates were associated with roughening of surfaces but without obvious evidence of preferential intergranular attack. Attack of this nature appeared to be associated with microstructures containing sigma and chi phases as separated particles and may be simply general corrosion caused by alloy depletion of the matrix. Crevice attack in ferric chloride, in the few samples examined metallographically, appears to concentrate at grain boundaries or, when continuous intergranular precipitates are present, at the matrix adjacent to the intergranular phases (Fig. 29). These regions are most likely to be depleted of molybdenum and chromium as the sigma and chi phases form and, hence, are most susceptible to crevice attack.

Other than limited information presented by Streicher [*4*], no data were found in the literature concerning effects of heat treatments in the high-temperature embrittlement zone upon the corrosion properties of AL 29-4 or closely related alloys. His work was performed upon a laboratory heat containing 29.0Cr, 4.3Mo, 25 ppm carbon, and 110 ppm nitrogen. Other residual contents were not reported. His exposures in the 482 to 982°C (900 to 1800°F) temperature range were either 1 or 100 h and were preceded by a 1-h solution treatment at 1093°C (2000°F) followed by a water quench. We observed noticeable crevice attack within 1-h exposures at 593 to 871°C (1100 to 1600°F), whereas he observed none. In agreement with his results, we observed low rates in sulfuric acid-ferric sulfate with the 1-h exposure times.

The only corrosion test result reported by Streicher after the 100-h exposure was a sulfuric acid-ferric sulfate test after the 816°C (1500°F) treatment. He reported no intergranular attack, whereas we detected high corrosion rates and attack to a considerable depth after this same treatment. The differences between our results and his are unresolved at present but may have been influenced by differences in residual contents, initial annealing treatments, or specimen preparation and testing.

Summary and Conclusions

The effects of heat treatments to 100 h on the mechanical properties and corrosion resistance of AL 29-4 have been evaluated. The alloy is subject to embrittlement upon exposures to two temperature ranges.

Embrittlement can be described by two overlapping C-curves centered at about 482 and 760°C (900 to 1400°F). Embrittlement occurs most rapidly in the higher temperature embrittlement range that appears to extend from about 593 to 927°C (1100 to 1700°F) and is caused by the precipitation of sigma and chi phases. Embrittlement becomes most pronounced as these phases form complete intergranular networks and result in intergranular tensile and impact failures. The corrosion properties (ASTM A 262-75 Practice B and ASTM G 48-76) are adversely affected by the precipitation of these phases also. Deterioration in mechanical properties and corrosion resistance is consistent with solute depletion of the matrix as these phases are formed.

The lower temperature embrittlement range is relatively narrow and occurs much less rapidly. It is doubtlessly associated to the 475°C (885°F) embrittlement phenomenon. As embrittlement proceeds, twinning becomes an increasingly important deformation mechanism at room temperature. No deterioration in corrosion properties were observed that could be ascribed to 475°C (885°F) embrittlement with heat treatments to 100 h.

Acknowledgments

The authors appreciate the contributions made to this manuscript by L. D. Bachman, J. F. Kisiel, P. J. Pavlik, J. W. Lord, M. Gatial, and W. E. Curry.

References

[*1*] Streicher, M. A., *Corrosion*, Vol. 30, No. 3, 1974, pp. 77–91.

[*2*] Brandis, H., Kiesheyer, H., and Lennartz, G., *Archive Eisenhuttenwes*, Vol. 46, 1975, pp. 799–804.

[*3*] Nichol, T. J., *Metallurgical Transactions A*, Vol. 8A, 1977, pp. 229–37.

[*4*] Streicher, M. A., *Corrosion*, Vol. 30, No. 4, 1974, pp. 115–24.

[*5*] Deverell, H. E. and Maurer, J. R., "Stainless Steels in Seawater," to be published in March 1978 issue of *Material Performance*.

[*6*] Aggen, G., "Processing Technology of Pit Resistant Stainless Steels," presented at AMAX, Inc. Stainless Steel '77 Symposium, London, England, 27 Sept. 1977.

[*7*] Fisher, R. M., Dulis, E. J., and Carroll, K. G., *Transactions*, American Institute of Mining, Metallurgical, and Petroleum Engineers, Vol. 197, 1953, pp. 690–695.

[*8*] Williams, R. O. and Paxton, H. W., *Journal*, Iron and Steel Institute, Vol. 185, 1957, pp. 358–74.

[*9*] Williams, R. O., *Transactions*, TMS-AIME, American Institute of Mining, Metallurgical, and Petroleum Engineers, Vol. 212, 1958, pp. 497–502.

[*10*] DeNys, T. and Gielen, P. M., *Metallurgical Transactions* Vol. 2, 1971, pp. 1423–1428.

[*11*] Nichol, T. J., Aggen, G., and Datta, A., "Embrittlement of Ferritic Stainless Steels", presented at TMS-AIME in Denver, Colo., American Institute of Mining, Metallurgical, and Petroleum Engineers, 27 Feb. 1978.

[*12*] Datta, A., Aggen, G., and Nichol, T. J., "Microstructures of Embrittled Ferritic Stainless Steels", presented at TMS-AIME in Denver, Colo., American Institute of Mining, Metallurgical, and Petroleum Engineers, 27 Feb. 1978.

[*13*] Tisinai, G. F. and Samans, C. H., *Journal of Metals, Transactions*, American Institute of Mining, Metallurgical, and Petroleum Engineers, Oct. 1957, pp. 1221–1226.

[*14*] Grobner, P. J., *Metallurgical Transactions*, Vol. 4, 1973, pp. 251–260.

[*15*] Courtnall, M. and Pickering, F. B., *Metal Science*, Aug. 1976, pp. 273–276.

[*16*] Kondys, A. I., Tkach, A. N., Astashkin, V. I., and Zamora, F. M., *Fiziko-Khimicheskaya Mekhanika Materialov*, Vol. 10, No. 5, 1974, pp. 24–28.

[*17*] Marcinkowski, M. J., Fisher, R. M., and Szirmae, A., *Transactions*, American Institute of Mining, Metallurgical, and Petroleum Engineers, Vol. 230, 1964, pp. 676–689.

[*18*] Lizlovs, E. A. and Bond, A. P., *Journal*, Electrochemical Society, Vol. 122, 1975, pp. 589–593.

[*19*] Koh, P. K., *Transactions*, American Institute of Mining, Metallurgical, and Petroleum Engineers, Vol. 197, 1953, pp. 339–343.

T. Kosa[1] *and T. A. DeBold*[1]

Effect of Heat Treatment and Microstructure on the Mechanical and Corrosion Properties of a Precipitation Hardenable Stainless Steel

---

REFERENCE: Kosa, T. and DeBold, T. A., "**Effect of Heat Treatment and Microstructure on the Mechanical and Corrosion Properties of a Precipitation Hardenable Stainless Steel,**" *MiCon 78: Optimization of Processing, Properties, and Service Performance Through Microstructural Control, ASTM STP 672,* Halle Abrams, G. N. Maniar, D. A. Nail, and H. D. Solomon, Eds., American Society for Testing and Materials, 1979, pp. 367–381.

ABSTRACT: Custom 450 is a martensitic precipitation hardenable stainless steel. The strengthening mechanism during aging is attributed to precipitation of a very fine Laves phase. The precipitate was found to be relatively stable with respect to coarsening at aging temperatures above 811 K (1000°F). The aging reaction is accompanied by austenite reversion. The decrease in hardness and strength and increase in impact strength with increasing aging temperature and time when aging above 811 K are shown to be related to the increasing reverted austenite content of the alloy. Data are presented showing the effect of heat treatment on resistance to stress corrosion cracking. The relationship of cracking to toughness and general corrosion resistance is discussed.

KEY WORDS: steels, microstructure, stainless steels, precipitation hardening steels, precipitation hardening, phase transformations, austenite, mechanical properties, tensile strength, impact strength, corrosion resistance, stress corrosion cracking, hydrogen embrittlement

Custom 450[2] is a martensitic precipitation hardenable stainless steel developed to meet requirements for an alloy with corrosion resistance similar to Type 304 stainless, but with strength comparable to Type 410 stainless. The alloy is normally supplied in the solution-treated (annealed) condition. In this condition, Custom 450 can be easily formed or ma-

---

[1] Metallurgist, Stainless Alloy Metallurgy, and supervisor, Corrosion and Welding Research, respectively, Carpenter Technology Corporation, Research and Development Center, Reading, Pa. 19603.

[2] Registered trademark of Carpenter Technology Corporation.

chined. The desired mechanical properties are then obtained with a 4-h age-hardening treatment in the range of 755 to 894 K (900 to 1150°F).

The effect of heat treatment on the mechanical and corrosion properties of Custom 450 has been well established [*1*].[3] For instance, maximum strength is obtained by aging the alloy at 755 K (900°F), while mechanical properties similar to the solution-treated condition with better resistance to stress corrosion cracking are obtained by aging at 894 K (1150°F).

Research studies published in the literature have discussed the relationship between material properties and aged microstructure in precipitation hardenable steels. Of particular interest are the effects of reverted austenite formation and precipitate coarsening and coalescence [*2–7*]. However, although it was known that substantial amounts of reverted austenite formed in Custom 450 during aging, particularly at higher aging temperatures, the relationship of heat treatment to this and other microstructural factors and, consequently, the relationship of microstructure to mechnical and corrosion properties had not been systematically investigated.

Accordingly, this study was undertaken to provide some insight into the relationship between heat treatment and microstructure, and the mechanical and corrosion properties of Custom 450.

Procedure

The Custom 450 used in the microstructural and mechanical property portion of this study was obtained from a production heat as 76.2-mm-round bar. Chemical analysis of the heat (in weight percent) is as follows:

C	Mn	Si	P	S	Cr	Ni	Mo	Cu	Cb	Fe
0.032	0.34	0.23	0.029	0.008	14.96	6.52	0.77	1.51	0.68	balance

All specimen blanks cut from the bar were solution treated at 1311 K (1900°F) for 1/2 h and water quenched. Longitudinal tension specimens (6.4-mm gage diameter, 25.4-mm gage length) and Charpy V-notch impact specimens (standard 10.0-mm square) were machined from solution-treated blanks and tested as solution treated and as aged at 755, 811, and 839 K (900, 1000, and 1050°F) for times of 4 and 8 h.

Rockwell C hardness and austenite content were determined for specimens in the solution-treated condition and as aged at 755, 811, 839, 866, and 894 K (900, 1000, 1050, 1100, and 1150°F) for times ranging from 4 to 200 h. For austenite determination, specimens were metallographically polished and lightly etched in the following special etchant: 2 g cupric chloride, 7 g ferric chloride, 5 cm^3 nitric acid, 100 cm^3 hydrochloric

---

[3] The italic numbers in brackets refer to the list of references appended to this paper.

acid, 200 cm^3 methyl alcohol, and 100 cm^3 distilled water. The volume percent austenite was measured by an X-ray diffraction technique using vanadium filtered Cr-Kα radiation. The integrated intensities from the (100), (200), and (211) martensite and the (111), (200), and (220) austenite reflections were used in order to minimize the effects of any preferred orientation in the specimens.

Selected specimens were examined by light and electron microscopy as aged at 755, 811, and 839 K (900, 1000, and 1050°F) for times in the range of 4 to 200 h. For examination by light microscopy, specimens were metallographically polished and etched in the previously-noted special etchant. For surface replica electron microscopy, chromium shadowed parlodian replicas were prepared from specimens etched in glyceregia. Extraction replicas for electron diffraction were prepared using a double plastic/carbon technique with glyceregia as the etchant. Thin foils for transmission electron microscopy were prepared by grinding 0.5-mm thick wafers to 0.1-mm thick. The foils were electrolytically thinned in a chromic/acetic acid mixture using the modified window technique.

The corrosion data presented in this report were abstracted from previous studies on Custom 450.

Results

Hardness and Mechanical Properties

The effect of aging time and temperature on the hardness of Custom 450 is shown in Fig. 1. As expected for a precipitation hardenable steel, the hardness is dependent upon both aging temperature and aging time [*2,3*]. For a particular constant length of time at aging temperature (at or beyond 4 h), the highest hardness is attained by aging at 755 K (900°F), with higher aging temperatures producing lower hardness. At 755 K (900°F) hardness increases for aging times beyond the normal 4-h treatment, indicating that the age-hardening reaction is still proceeding. However, at aging temperatures of 811 K (1000°F) and above, the highest hardness for each aging temperature is evidently reached at or before 4 h, with hardness decreasing for longer aging times, that is, *overaging* occurs.

The effect of aging temperature (for times of 4 and 8 h) on the mechanical properties of Custom 450 is shown in Fig. 2. Aging at 755 K (900°F) produces a large increase in yield strength and ultimate tensile strength and a large decrease in impact strength as compared to the solution-treated material. Higher aging temperatures, 811 and 839 K (1000 and 1050°F), decrease strength while increasing impact strength relative to aging at 755 K (900°F). Aging for 8 h has little effect on tensile and impact strength at 755 K (900°F), but produces lower tensile strength and

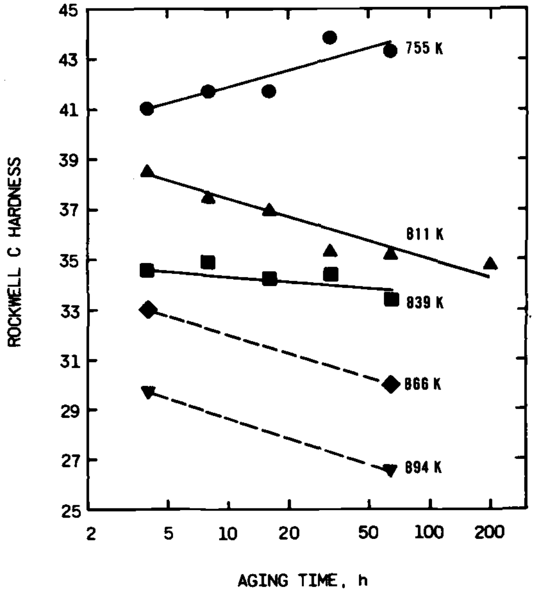

FIG. 1—*Effect of aging time and temperature on hardness (solution-treated hardness is 27 HRC).*

higher impact strength at 811 and 839 K (1000 and 1050°F) compared with the standard 4-h treatment.

Reverted Austenite Formation

In the solution-treated condition, no austenite was detected in the Custom 450. During aging, austenite evidently forms from the martensite in a reversion reaction. Figures 3 and 4 show that, in general, the amount of reverted austenite present after aging in the range of 755 to 894 K (900 to 1150°F) increases with both increasing aging temperature and time. The rate of reversion is rather slow at 755 K (900°F) but is significantly higher in the range of 811 to 866 K (1000 to 1100°F). However, at 894 K (1150°F) the amount of reverted austenite is the same for aging times of 4 and 64 h. A possible reason for the seemingly anomalous behavior upon aging at 894 K (1150°F) is shown in Fig. 4. The amount of reverted austenite appears to reach a peak in the range of 30 to 40 percent in the vicinity of 866 K (1100°F). Such a limiting *peak* amount of reverted austenite has been noted by others [2,*4*].

Metallography

Figure 5 shows light micrographs of aged Custom 450. The matrix appears to be fully martensitic—no reverted austenite can be detected.

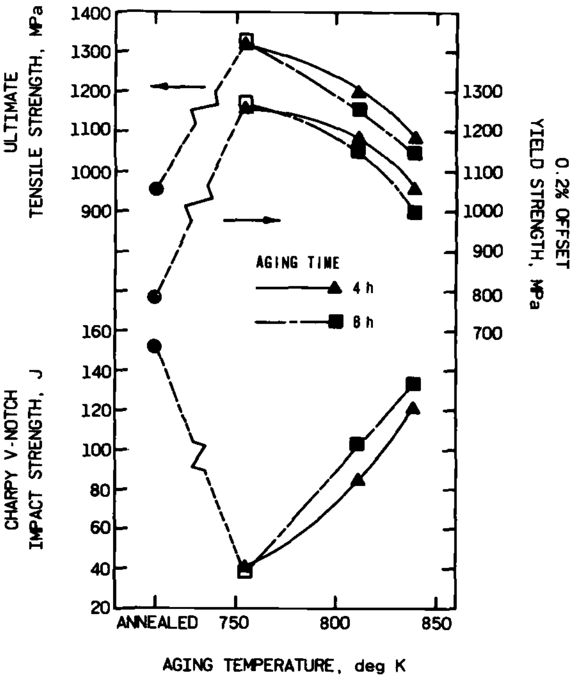

FIG. 2—*Effect of aging temperature on mechanical properties.*

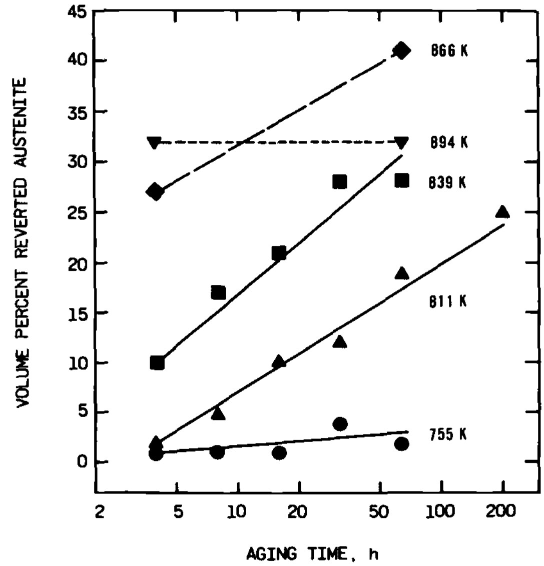

FIG. 3—*Effect of aging time and temperature on reverted austenite content.*

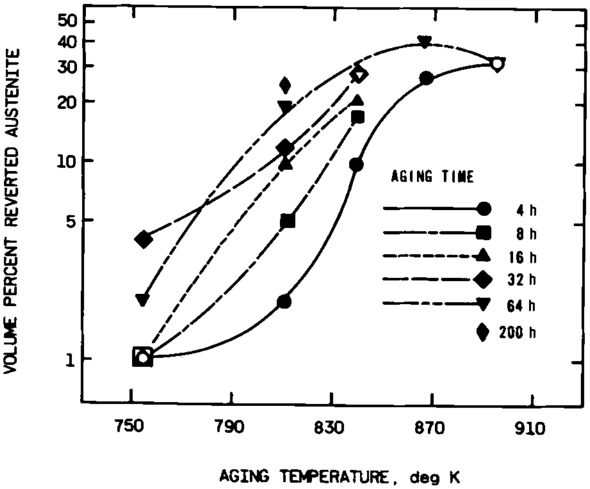

FIG. 4—*Effect of aging temperature for various aging times on reverted austenite content.*

The matrix contains randomly dispersed residual carbides that are coarser as aged at 811 and 839 K (1000 and 1050°F). These were identified as MC and M_6C by X-ray diffraction.

An attempt was made to characterize and identify the age-hardening precipitate by electron microscopy. However, no age-hardening precipitate could be delineated in structural replicas from a sample aged at 755 K (900°F) for 4 h. In addition, selected area electron diffraction patterns from the particles imbedded in an extraction replica in the same condition showed only a diffuse halo. Similar results were obtained using an extraction replica from a specimen aged at 839 K (1050°F) for 8 h. The electron diffraction results indicate that the precipitate particle size is extremely fine (estimated to be about 2 nm) and that the precipitate is relatively stable, that is, it apparently does not coarsen to a large degree for aging temperatures in the range of 755 to 839 K (900 to 1050°F) for times up to 8 h.

In order to further characterize the precipitate, additional structural replicas and extraction replicas from specimens aged at 755, 811, and 839 K (900, 1000, and 1050°F) for 64 h and 811 K (1000°F) for 200 h were examined.

Figure 6 shows the structural replica electron micrographs for the aforementioned aging series. The precipitate in the specimen aged at 755 K (900°F) is still very fine, even after 64 h at the aging temperature. The precipitate is somewhat coarser in the specimens aged at 811 K (1000°F), 64 and 200 h, and 839 K (1050°F), 64 h. However, there is little difference in precipitate size or distribution among these latter three specimens. The

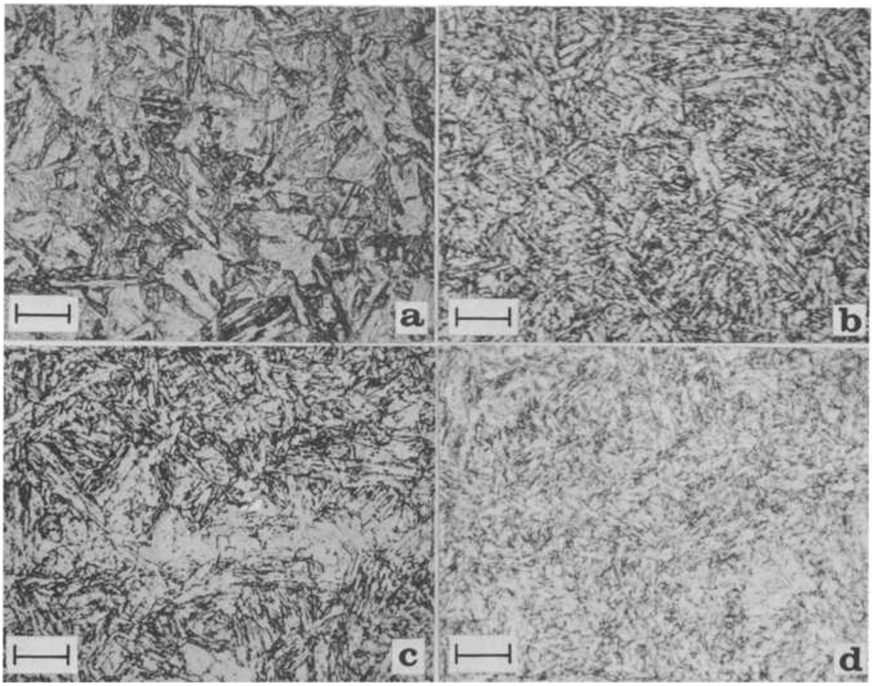

(*a*) 755 K, 4 h
(*b*) 811 K, 4 h
(*c*) 839 K, 4 h
(*d*) 839 K, 8 h

FIG. 5—*Light micrographs (scale mark indicates 20 μm).*

extraction replicas (not shown) yielded the same results with respect to precipitate size and distribution.

The structural replica electron micrographs from the specimens aged at 811 and 839 K (1000 and 1050°F) also show substantial amounts of ribbon-like reverted austenite along the martensite lath boundaries [*6*]. (Because of the large amounts of reverted austenite, the lath boundaries are not well delineated.) Little reverted austenite is seen in the replica of the specimen aged at 755 K (900°F). This correlates with the actual amounts of reverted austenite present as determined by X-ray diffraction (noted in the figure captions.)

Selected area electron diffraction patterns obtained from the particles imbedded in the extraction replicas contained distinct diffraction reflections, compared with the diffuse halos previously noted for shorter aging times. The difference in diffraction patterns indicates that the precipitate coarsens with extended aging time. The precipitate was identified as Laves

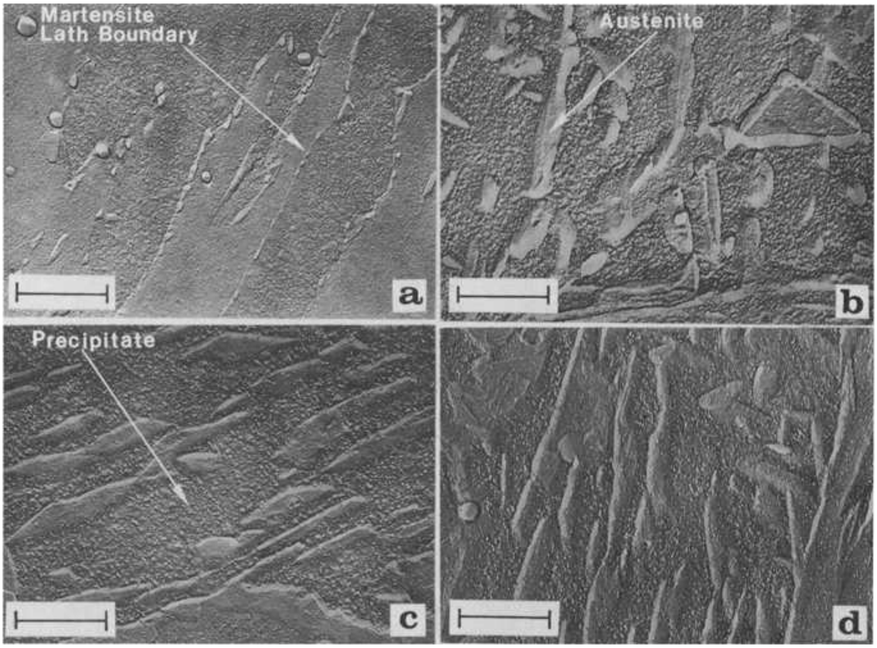

(*a*) 755 K, 64 h (2% austenite)
(*b*) 811 K, 64 h (19% austenite)
(*c*) 839 K, 64 h (28% austenite)
(*d*) 811 K, 200 h (25% austenite)

FIG. 6—*Electron micrographs of chromium shadowed parlodian replicas (scale mark indicates 1 μm).*

phase (A_2B type, in which the atomic radius of B is larger than the atomic radius of A), however, the constituents of the phase were not determined.

To further characterize the precipitate, thin foils were examined by transmission electron microscopy at high magnification. These electron micrographs are shown in Fig. 7. After 4 h at 755 K (900°F), the precipitate is very fine and not resolvable. After 64 h at 755 K (900°F), the precipitate is resolvable but is still very fine. As noted before, after aging at 811 and 839 K (1000 and 1050°F) the precipitate is somewhat coarser than after aging at 755 K (900°F).

The preceding comments concerning the age-hardening precipitate formed in Custom 450 during aging in the range of 755 to 839 K (900 to 1050°F) can be summarized as follows:

(*a*) The precipitate is extremely fine after the normal 4-h aging treatment.

(*b*) The precipitate coarsens somewhat with increasing time at aging temperature (up to 64 h), but the precipitate still remains relatively fine.

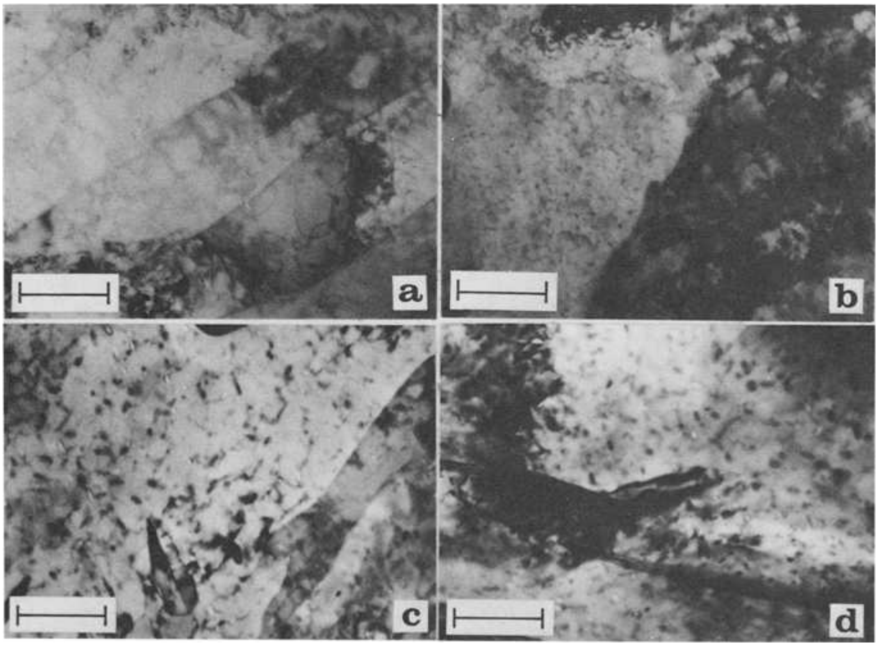

(*a*) 755 K, 4 h
(*b*) 755 K, 64 h
(*c*) 811 K, 64 h
(*d*) 839 K, 64 h

FIG. 7—*Transmission electron micrographs (scale mark indicates 0.2 μm).*

(*c*) The precipitate formed during aging at 811 and 839 K (1000 and 1050°F) is coarser than the precipitate formed during aging at 755 K (900°F).

(*d*) There is no significant difference in precipitate size and distribution between aging temperatures of 811 and 839 K (1000 and 1050°F), indicating the precipitate size and distribution are relatively constant for these aging temperatures.

Discussion

Relationship of Microstructure to Hardness and Mechanical Properties

It was shown previously that aging temperatures of 811 K (1000°F) and above result in overaging of Custom 450, that is, hardness and tensile strength decrease and impact strength increases with both increasing aging temperature and aging time. The microstructural work showed that the reverted austenite content generally increases with both increasing aging temperature and time. However, electron microscopy showed no significant difference in precipitate size or distribution between aging temperatures of 811 and 839 K (1000 and 1050°F). Thus, overaging of Custom 450 appears primarily due to reverted austenite formation [*6,7*]. (Coarsening of the precipitate with increasing time at temperature may have a small contributing effect on the trends in hardness and mechanical properties.) Figures 8 and 9 show the relationship between the reverted austenite content of the alloy and the decrease in tensile strength and hardness and increase in impact strength at aging temperatures of 811 K (1000°F) and above.

On the other hand, at 755 K (900°F) the hardness increases with increasing aging time, rather than decreases. Evidently, when aging at 755 K (900°F), the predominant factor in determining the hardness is the continuing age-hardening reaction, while the formation of small amounts of reverted austenite and slight coarsening of the precipitate have little or no effect. This is further substantiated by published data showing a further increase in tensile strength and decrease in impact strength at 755 K (900°F) between aging times of 4 and 16 h [*1*].

The one anomaly in the preceding data is the low hardness value for the specimen aged at 894 K (1150°F), 64 h (Fig. 8). The reason for this anomaly was not investigated in this study, but is probably due to one or both of the following:

(*a*) The age-hardening precipitate may begin to coarsen further at

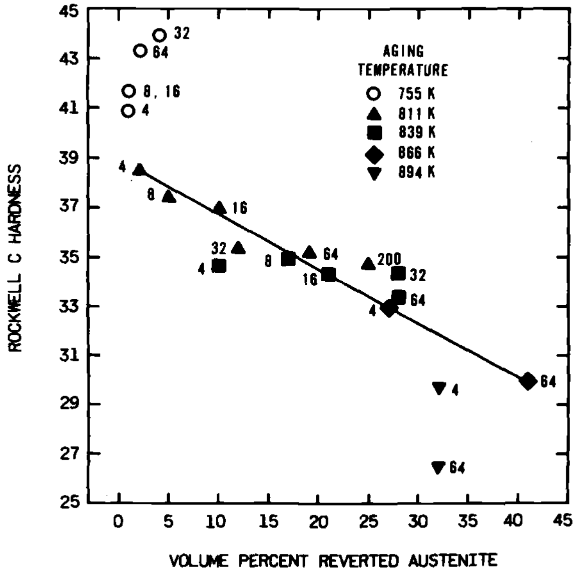

FIG. 8—*Effect of reverted austenite content on hardness (numbers by symbols indicate aging time in hours).*

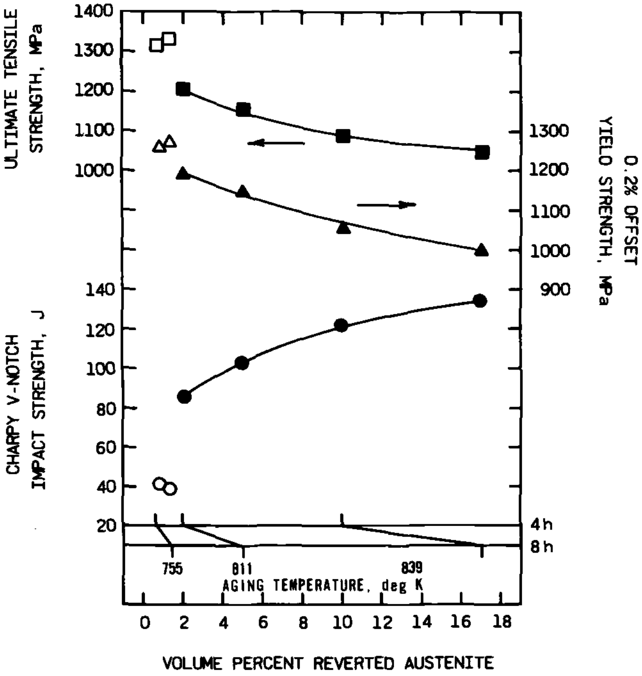

FIG. 9—*Effect of reverted austenite content on mechanical properties.*

higher aging temperatures, resulting in lower hardness than expected based on reverted austenite content alone.

(*b*) For the higher age-hardening temperatures, the amount of reverted austenite formed at the age-hardening temperature may be greater than the amount that is retained at room temperature. That is, part of the reverted austenite formed at the aging temperature may transform to an unaged martensite upon cooling to room temperature, resulting in a lower hardness than would be expected based on aged martensite and retained reverted austenite content alone.

The phenomenon of differences in the amount of reverted austenite formed at aging temperature compared with the amount retained at room temperature has been noted in the literature [*5*].

Relationship of Heat Treatment and Microstructure to Corrosion Resistance

The resistance of Custom 450 to cracking in boiling 45 percent magnesium chloride is shown in Fig. 10 [*8*]. This is a very severe environment, capable of cracking annealed austenitic stainless steels. Figure 11 shows the resistance of Custom 450 to cracking in a sulfide

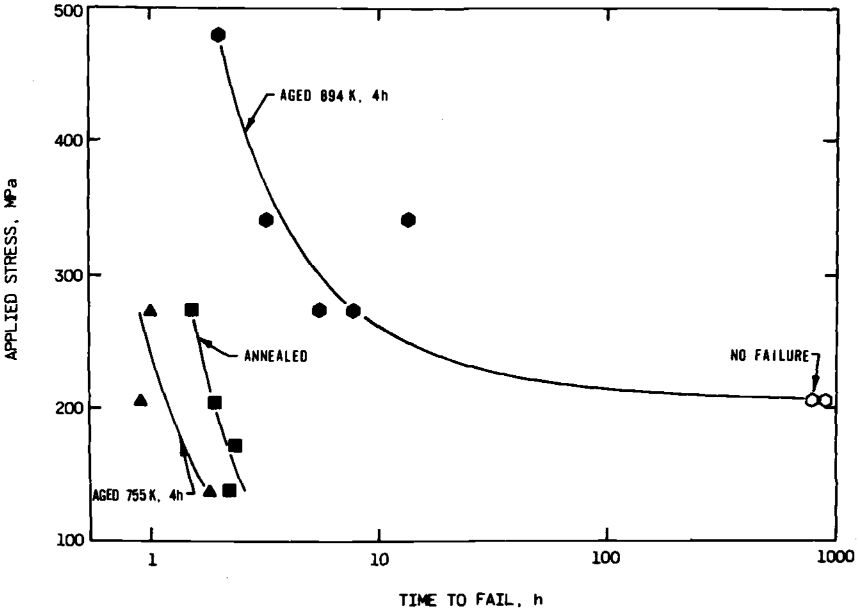

FIG. 10—*Resistance to cracking in boiling 45 percent* $MgCl_2$.

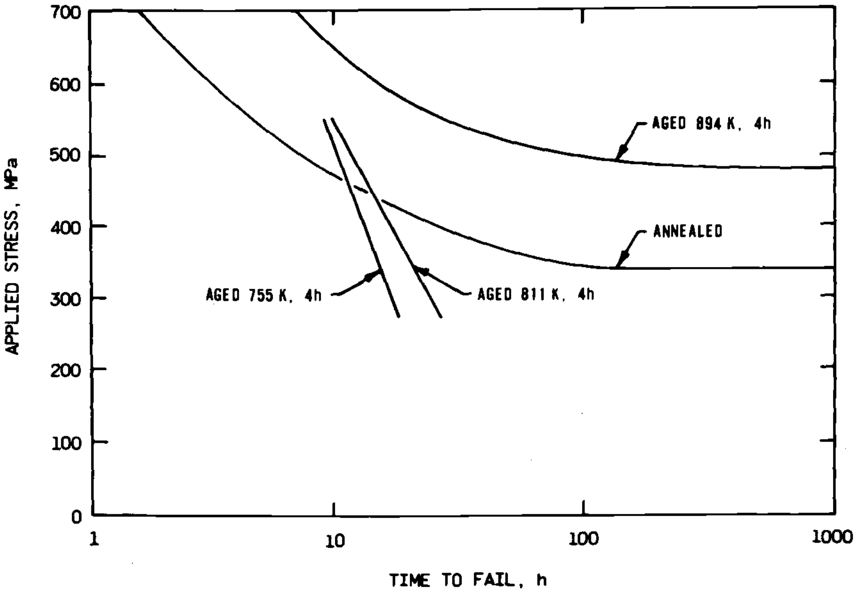

FIG. 11—*Resistance to cracking in 0.1 percent NaCl + 0.5 percent acetic acid +* H_2S.

environment (0.1 percent sodium chloride plus 0.5 percent acetic acid plus hydrogen sulfide) designed to promote cracking by a hydrogen mechanism [*8*]. For both of these environments, resistance to cracking improves with increasing aging temperature. Resistance of annealed material (1311 K or 1900°F) will be discussed later.

Resistance of Custom 450 to general corrosion in acids is shown in Table 1 [*1*]. There is no effect of higher aging temperatures except a slight increase in rates (all rates being low) for 5 percent sulfuric acid at room temperature. Table 2 shows resistance to localized corrosion (pitting and crevice attack) for simple immersion in ferric chloride and anodic polarization in sodium chloride [*8*]. Improved behavior in the latter test is represented by increased positive values for pitting potential (E_c) and smaller differences between the pitting and protection potential (E_p). Smaller values for this difference appear related to better resistance to attack in crevices [*8*]. Results of both tests show that material aged at 755 K (900°F) and 894 K (1150°F) are generally similar, although there are indications of a slight loss in resistance at the higher aging temperatures.

There is an increasing amount of data to suggest that stress corrosion cracking in this type of alloy occurs by *hydrogen embrittlement,* that is, atomic hydrogen entering the metal at the crack tip and resulting in brittle failure [*9–12*]. Therefore, to resist cracking, it is preferable that the stainless steel have good resistance to general, pitting, and crevice corrosion. This minimizes both the formation of hydrogen and the occurrence of pits. It is well known that pits are often the origin of cracking in high strength stainless steels [*9,10,12,13*]. A high level of toughness is also desirable to resist cracking in order to tolerate small amounts of hydrogen that may enter the metal. The relationship between toughness and resistance to hydrogen embrittlement in high strength martensitic stainless steels is well documented [*9,14,15*]. A relationship between fracture toughness and percent austenite has also been demonstrated [*16*].

Therefore, the two most important factors affecting the cracking of

TABLE 1—*Corrosion resistance in acids.* [a]

Aging Temperature, K	Rockwell C Hardness	Corrosion Rate, g/m^2/h 20% Nitric Acid, 366 K	 5% Sulfuric Acid, 297 K	 50% Acetic Acid, boiling
755	41	0.04	0.02	0.02
811	37	0.04	0.07	0.02
894	30	0.04	0.20	0.02

[a] Samples exposed for one 48-h test period.

TABLE 2—*Corrosion resistance in two chloride environments.*

Aging Temperature, K	5% $FeCl_3$, 3 h at 297 K (average weight loss, mg)	Anodic Polarization in 3.5% NaCl (pH 5) at 297 K	
		E_c,[a] mv	E_p,[b] mv
755	35	201	− 92
811	39	. . .	. . .
894	39	158	−142

[a] E_c = pitting potential versus saturated calomel electrode.
[b] E_p = repassivation potential versus saturated calomel electrode.

hardenable martensitic stainless steels are toughness and general pitting, and crevice corrosion resistance. For Custom 450, aging does not have a great effect on corrosion resistance. Figure 9 shows, however, that toughness (as indicated by Charpy V-notch values) increases due to increased austenite at the higher aging temperatures. It seems obvious to conclude that the increased austenite is responsible for the improved resistance to cracking of aged Custom 450. The intermediate cracking resistance of annealed material (Figs. 10 and 11) may be a compromise between the absence of austenite and good mechanical properties (tensile and impact data similar to 894 K (1150°F) age).

A similar beneficial effect of austenite appears present in other alloys. Gaugh studied 17Cr-4Ni and 13Cr-8Ni-Mo in a sulfide environment roughly similar to that of Fig. 11 [*17*]. He found that increased austenite could be correlated with increased time to failure. He suggested that the improved resistance to hydrogen embrittlement was a result of austenite forming at the aging temperature.

Acknowledgments

The authors wish to acknowledge J. E. Bridge, Jr., and H. M. James for their work on the effect of reverted austenite, which is the basis for most of this paper.

References

[*1*] "Carpenter Custom 450, Multiple-Strength Stainless Steel," Carpenter Technology Technical Data Booklet, 1971.

[*2*] Carter, C. S., *Metallurgical Transactions*, Vol. 1, June 1970, pp. 1551–1559.

[*3*] Underwood, E. E., Austin, A. E., and Manning, G. K., *Journal*, Iron and Steel Institute, Aug. 1962, pp. 644–651.

[*4*] Hall, R. C., McInnis, G. N., and Kluz, S., *Journal*, Iron and Steel Institute, Oct. 1969, pp. 1310–1313.

[*5*] Pampillo, C. A. and Paxton, H. W., *Metallurgical Transactions*, Vol. 3, Nov. 1972, pp. 2895–2903.

[6] Burnett, H. C., Duff, R. H., and Vacher, H. C., *Journal of Research*, National Bureau of Standards, Vol. 66C, No. 2, April–June 1962, pp. 113–119.
[7] Cheng, I-Lin and Thomas, G., *Transactions*, American Society for Metals, Vol. 61, 1968, pp. 14–25.
[8] Henthorne, M., DeBold, T. A., and Yinger, R. J., "Custom 450—A New High Strength Stainless Steel," Paper No. 53, Corrosion '72 Conference, National Association of Corrosion Engineers, 1972.
[9] Henthorne, M., "Stress Corrosion Cracking of Martensitic Precipitation Hardening Stainless Steels," paper reprinted from *Proceedings*, Specialists Meeting on Stress Corrosion Testing Methods, Brussels, 1971, AGARD/NATO, 92 Neuilly-sur-Seine, France.
[10] Wilde, B. E., *Corrosion*, Vol. 27, No. 8, Aug. 1971, pp. 326–333.
[11] Denhard, E. E., "Stress Corrosion Cracking of High Strength Stainless Steels," *Proceedings*, Air Force Materials Laboratory Anniversary Technical Conference on Corrosion in Military and Aerospace Equipment, AFML-TR-67-329, 1967, Wright Patterson AFB, Ohio.
[12] Brown, B. F., "ARPA Coupling Program on Stress Corrosion Cracking-Final Technical Report," Report 7168, Naval Research Laboratories, Washington, D. C., 21 Sept. 1970.
[13] Bloom, F. K., *Corrosion*, Vol. 11, No. 8, Aug. 1955, pp. 351t–361t.
[14] Carter, C. S., Farwick, D. G., Ross, A. M., and Uchida, J. M., *Corrosion*, Vol. 27, No. 5, May 1971, pp. 190–197.
[15] Raymond, L. and Kendall, E. G., "Hydrogen-Stress Cracking of 17-4 PH Stainless," Report AD 661 958, Defense Documentation Center/Defense Supply Agency, Federal Clearinghouse, U. S. Dept. of Commerce, Aug. 1967.
[16] Webster, D., *Transactions*, American Society for Metals, Vol. 61, 1968, pp. 816–828.
[17] Gaugh, R. R., "Sulfide Stress Cracking of Precipitation-Hardening Stainless Steels," Paper No. 109, Corrosion '77 Conference, National Association of Corrosion Engineers, 1977.

J. Murali,[1] *M. R. Louthan, Jr.,*[1] *and R. P. McNitt*[1]

Influence of Hydrogen on Age-Hardening Processes in 15-5 Precipitation Hardened Stainless Steel

---

REFERENCE: Murali, J., Louthan, M. R., Jr., and McNitt, R. P., "**Influence of Hydrogen on Age-Hardening Processes in 15-5 Precipitation Hardened Stainless Steel,**" *MiCon 78: Optimization of Processing, Properties, and Service Performance Through Microstructural Control, ASTM STP 672,* Halle Abrams, G. N. Maniar, D. A. Nail, and H. D. Solomon, Eds., American Society for Testing and Materials, 1979, pp. 382–392.

ABSTRACT: The aging characteristics of 15-5 precipitation hardened stainless steel were altered when age-hardening took place in a hydrogen environment. The presence of hydrogen increased the peak hardness and decreased the time to achieve peak hardness. Furthermore, the hardness of the hydrogen-aged samples increased to a maximum value with time of storage at room temperature. These observations are discussed in terms of proposed mechanisms for hydrogen embrittlement.

KEY WORDS: steels, microstructure, hydrogen, age-hardening, stainless steels, X-ray

Precipitation hardened martensitic steels are generally susceptible to hydrogen embrittlement. This susceptibility can be minimized by overaging or other treatments or both that alter the microstructure. One possible explanation of the beneficial effect of overaging is the development of incoherent precipitates, the interfaces of which act as hydrogen traps and alter the stress or strain induced localization of hydrogen. The interface phenomenon has been observed in TD-nickel and in selected austenitic steels [*1*].[2] Interaction of hydrogen with lattice defects has been shown to play a vital role in the embrittlement processes [*2*]. Such interactions occur because the system energy is minimized when hydrogen segregates

---

[1] Graduate research assistant; professor, Materials Engineering; and professor, Engineering Science and Mechanics; respectively, Virginia Polytechnic Institute and State University, Blacksburg, Va. 24061.

[2] The italic numbers in brackets refer to the list of references appended to this paper.

to regions of localized lattice distortion or internal surfaces or both. Localized lattice strains, alloy segregation, and development of interfaces (coherent or incoherent or both) that are part and parcel of any precipitation process are in part due to the interactions of defects in the material. Due to the fact that hydrogen diffusion is rapid compared to other interstitial atoms, and hydrogen is known to interact with defects and segregate to regions of localized lattice dilation, one may expect the aging kinetics and the resulting properties to be altered if the process takes place in a hydrogen environment.

The present work attempts to demonstrate the effect of hydrogen on the aging process of 15-5 precipitation hardened (PH) stainless steel. Argon was employed as a control aging environment for the sake of comparison. The aging temperatures ranged from 371 to 593°C. Hardness measurements were the principal means of following the aging process although tension tests and X-ray diffraction studies were used to obtain supplemental data. The results presented conform to three broad categories: (1) aging in argon environment and subsequent measurement of properties, (2) aging in hydrogen environment and measurements of properties immediately after treatment, and (3) aging in hydrogen environment and measurement of properties after outgassing the hydrogen at room temperature.

Experimental Procedures

The material used in this study was Armco 15-5 PH stainless steel (0.041C, 0.36Mn, 0.023P, 0.008S, 0.44Si, 15.08Cr, 4.67Ni, 3.42Cu, and 0.30Cb) supplied by Armco Steel Corporation in 3.5-cm-diameter bar form. Typical microstructure is shown in Fig. 1. The bar was cut into thin sections and polished through 600 grit emery paper for the purposes of hardness and X-ray measurements. Thin sections of material were used so that hydrogen saturation of the sample would be complete during short aging time. Therefore subsized specimens (rectangular cross-section 1.7 mm by 1.6 mm and of gage length 14 mm) were employed for tensile studies. The material was recieved in Condition A (solution treated at 1035 ± 15°C, ½ h, oil or air cool). The argon and hydrogen gases used as aging environments were purified by passing successively through glass wool to trap dirt particles, a palladium catalyst to convert oxygen to moisture and a moisture trap where the gas was cooled to liquid nitrogen temperature. Little or no oxide was formed on the surface of the specimens during the heat treatments, and all samples were bright after the anneal. Aging temperatures ranged from 371 to 593°C, and aging times at these temperatures ranged from 3 min to 48 h. Hardness measurements were taken after the specimens air cooled to room temperature (usually within 2 min). In the case of heat treatments in hydrogen environment,

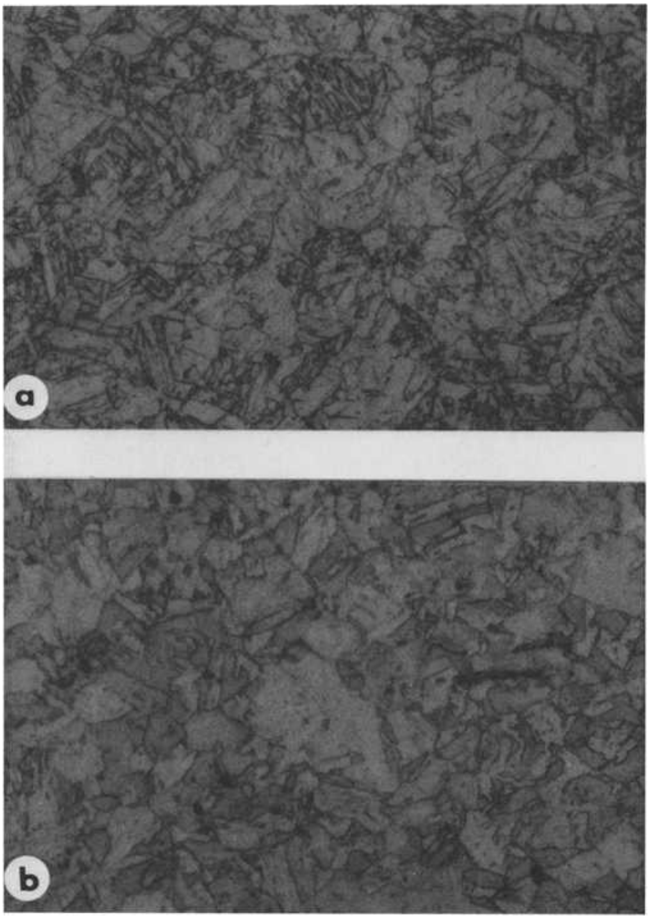

FIG. 1—*Microstructure of as-received and aged 15-5 PH stainless steels.* (a) *Micrograph of as-received 15-5 PH (original magnification* ×400*), and* (b) *micrograph of 15-5 PH aged at 427°C for 2 h (original magnification* ×400*).*

hardness measurements were taken immediately after aging and several weeks later (thus allowing sufficient time for hydrogen outgassing). There was little or no change in hardness of the specimens aged in argon even after several weeks at room temperature. The hardness of the polished and heat treated specimens was measured on a Rockwell hardness tester. Fifteen readings were made for each heat treatment, and the arithmetic average was chosen as the representative value. Results of hardness measurements are shown in Figs. 2 through 6 and the small scatter typical of the results is indicated on each figure.

X-ray diffraction studies were done using monochromated Cu-K_α

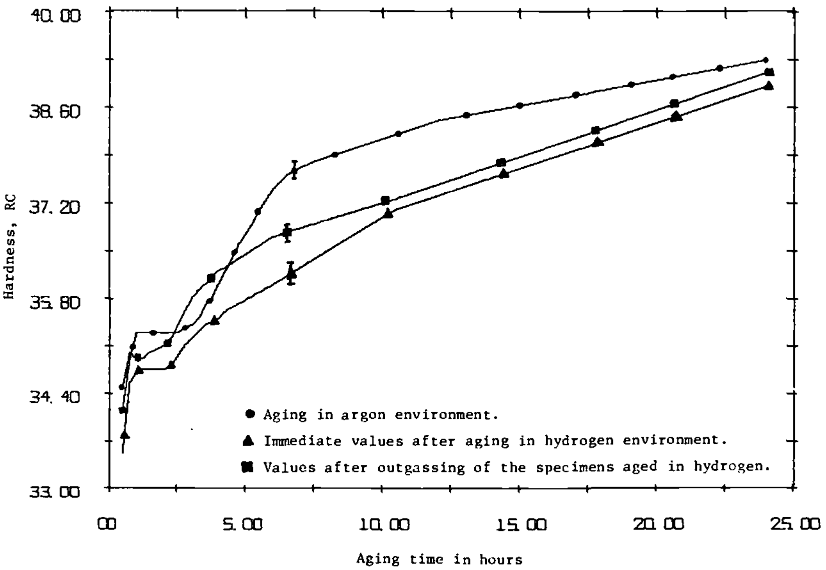

FIG. 2—*Aging curves for 15-5 PH stainless steel at 371°C.*

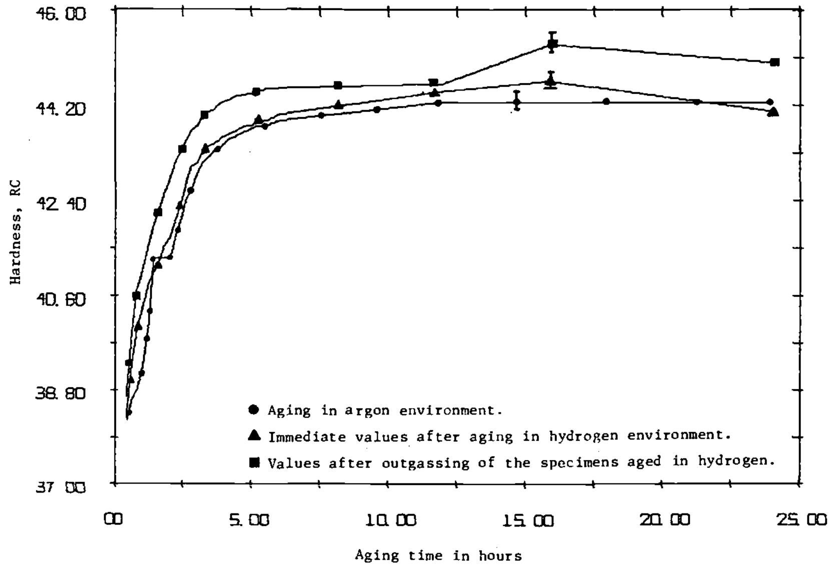

FIG. 3—*Aging curves for 15-5 PH stainless steel at 427°C.*

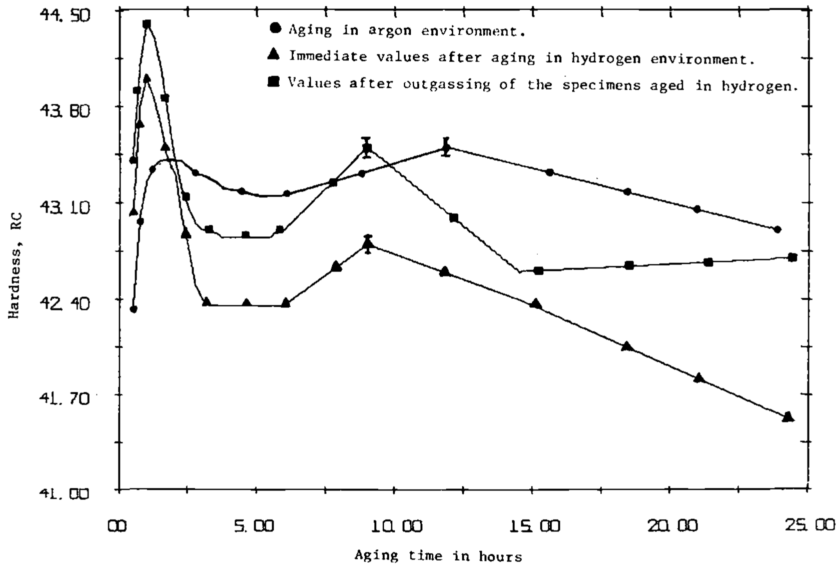

FIG. 4—*Aging curves for 15-5 PH stainless steel at 482°C.*

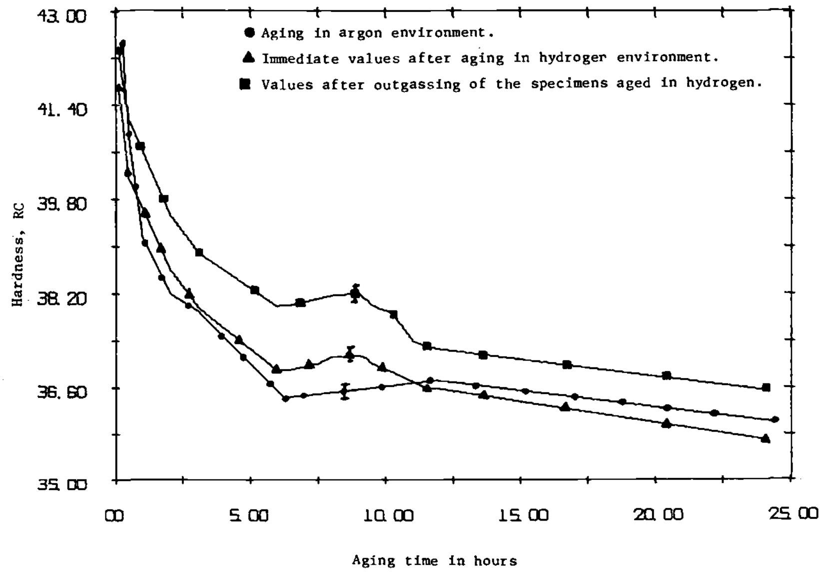

FIG. 5—*Aging curves for 15-5 PH stainless steel at 538°C.*

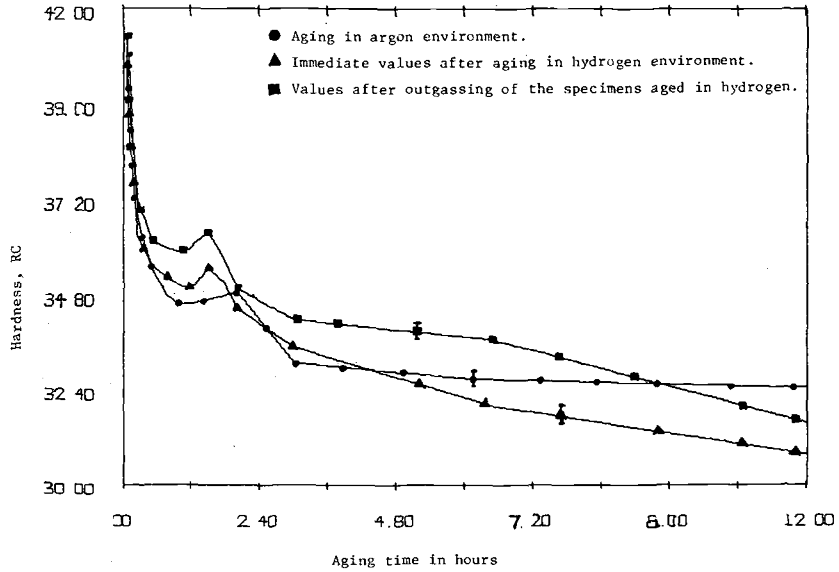

FIG. 6—*Aging curves for 15-5 PH stainless steel at 593°C.*

radiation. Scanning speed was 0.25 deg/min, and entry and receiving slits were 1 deg and 0.2 mm, respectively. The (110) and (200) peak profiles of the specimens aged to peak hardness in hydrogen and argon (482°C 1-h anneal) are shown in Fig. 7.

Tension tests were conducted on specimens aged at 482°C, because the most pronounced effects of hydrogen on hardness was observed at that temperature. For specimens aged in hydrogen, tension tests were done immediately after the heat treatment and after one week of outgassing. Yield strength, ultimate strength, and elongation to fracture varied with aging time and are shown in Figs. 8 through 10. The values were taken from engineering stress-strain curves.

Discussion

The hardness versus aging time curves shown in Figs. 2 through 6 indicate the following trends:

1. There are two phases precipitating, one of which only develops during higher temperature anneals 482°C and up.

2. Short time aging in hydrogen atmosphere results in higher hardness than corresponding aging treatment in argon environment.

3. Outgassing of the specimens aged in hydrogen increased the hardness in most cases.

4. Peak hardness is higher and is attained sooner on aging in a hydrogen

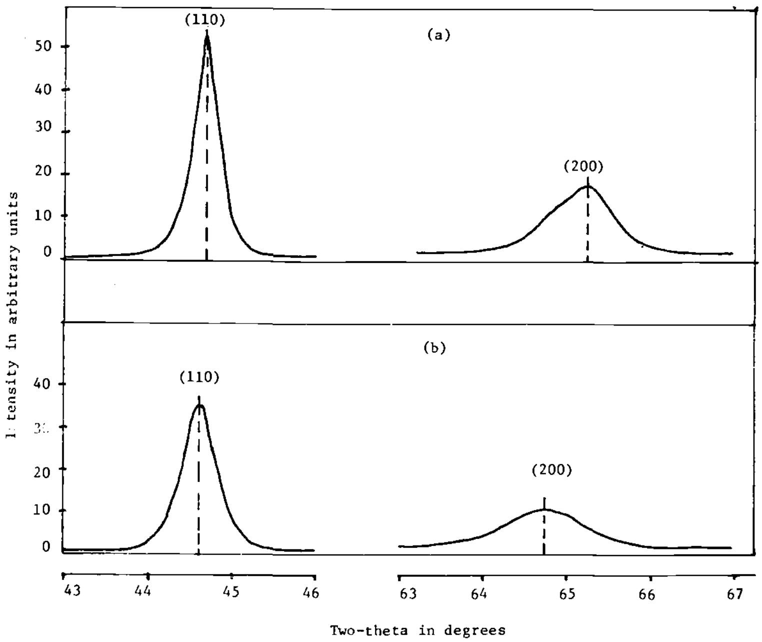

FIG. 7—*(110) and (200) peaks for 15-5 PH stainless steel aged 1 h at 482°C in* (a) *hydrogen and* (b) *argon.*

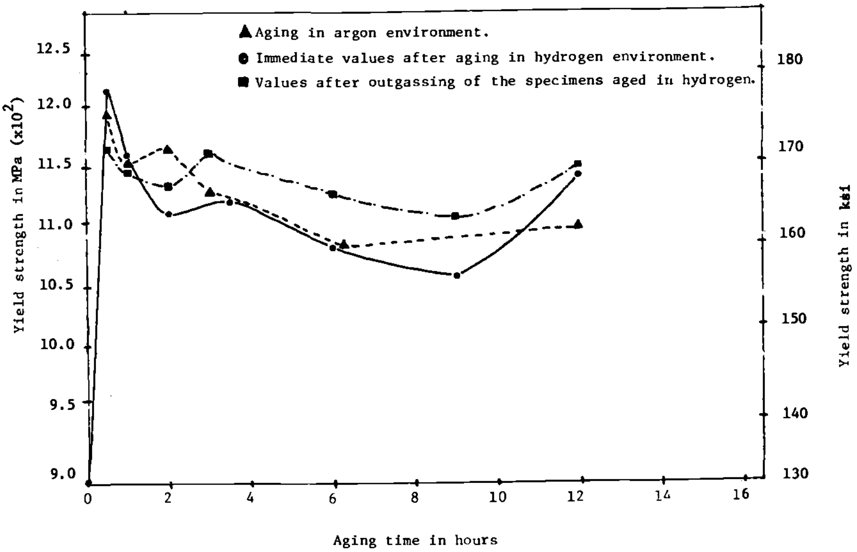

FIG. 8—*Yield strength versus aging time for 15-5 PH stainless steel at 482°C.*

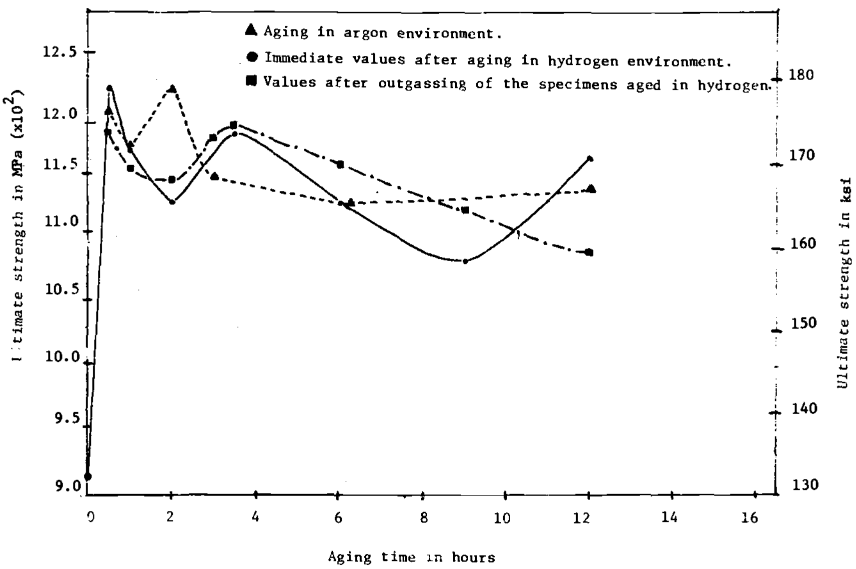

FIG. 9—*Ultimate strength versus aging time for 15-5 PH stainless steel at 482°C.*

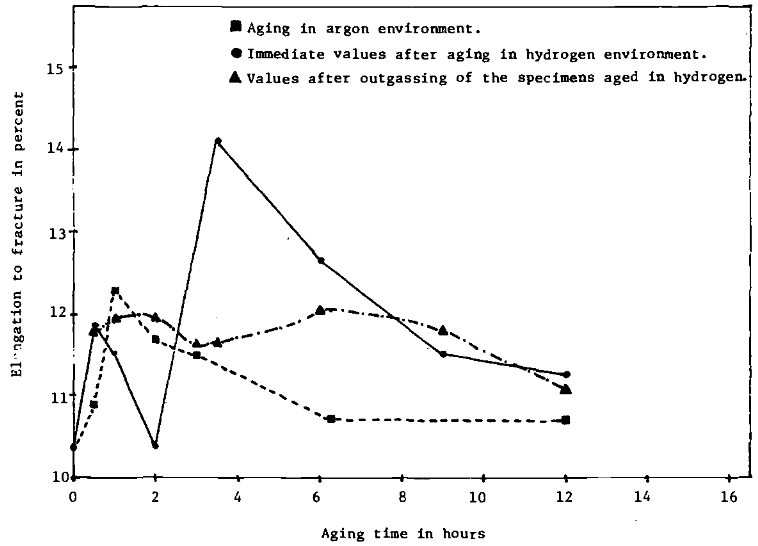

FIG. 10—*Elongation in fracture versus aging time for 15-5 PH stainless steel at 482°C.*

environment. The peak hardness further increases on outgassing the hydrogen.

5. Loss of coherency and subsequent development of incoherent precipitates occurs at a faster rate for specimens aged in hydrogen environment.

The preceding observations are general to all cases except for 371°C aging, and hold for the two types of precipitates.

Wilkins et al [*3*] have postulated solute segregation to areas of lattice defects during the aging of semiaustenitic PH stainless steels. It appears that the aging sequence for PH stainless steels follows that of the aluminum-copper (Al-Cu) system, that is, supersaturated solution → Guinier-Preston zone → intermediate precipitate → equilibrium precipitate [*3,4*]. Precipitation may occur on martensitic laths, ferrite martensitic interfaces, and on dislocations [*3–6*].

The higher hardness values in the initial stages of aging in a hydrogen environment as compared to argon environment indicate that hydrogen enhances nucleation of the second phase. This would be expected if hydrogen decreased the surface energy of the particle-matrix interface. The higher peak hardness values and shorter times to achieve peak hardness in the hydrogen environment indicate a higher mobility of solute atoms. The decohesion theory proposed to explain some effects of hydrogen in metals requires that hydrogen weaken the metallic bond [*7–9*]. If, in fact, such a weakening takes place, atomic mobility may be enhanced because the activation energy for atom movement should be reduced. This could account for the apparent rapid precipitation. Furthermore, if hydrogen weakens the metallic bond, the development of semicoherent and incoherent interfaces should be enhanced by the presence of hydrogen. This would explain the observed higher rates of loss of coherency (overaging) for the sample treated in hydrogen.

A hydrogen atmosphere could also interact with the stress fields around dislocations and coherent and semicoherent interfaces and thereby permit dislocations to approach closer in the presence of hydrogen than under similar conditions when no hydrogen was present. Because hardness measurements are based on plastic deformation (thus dislocations must approach each other or the precipitate or both), the increased hardness with hydrogen offgassing from the lattice could be due to changes in the distances of approach of dislocations.

X-ray peaks for specimens aged to peak hardness at 482°C are shown in Fig. 6. Contrary to the general expectation that a harder material will show a broader peak, we find that the peaks of specimens aged in hydrogen (harder material) are sharper than those aged in argon. This observation is consistent with the postulate that factors other than lattice strains play a vital role in the precipitation process. It has been proposed that order-disorder transformations are important in the initial stages of precipitation [*3*]. Moreover, lattice defects such as dislocations may affect X-ray line profiles. The lower the dislocation density, the sharper the peaks will be. Thus, one may consider the possibility of hydrogen affecting the order-disorder transformation or dislocation density or both as well as hydrogen effects on the strain fields around dislocations. Because precipitates may form on dislocations, more nucleation may lead to increased *consumption* of dislocations, thus lowering dislocation density and possibly sharpening X-ray peaks. This preliminary observation is in a broad sense in agreement with enhanced nucleation as detected by hardness measurement.

The results of the tension tests for samples aged at 482°C are shown in

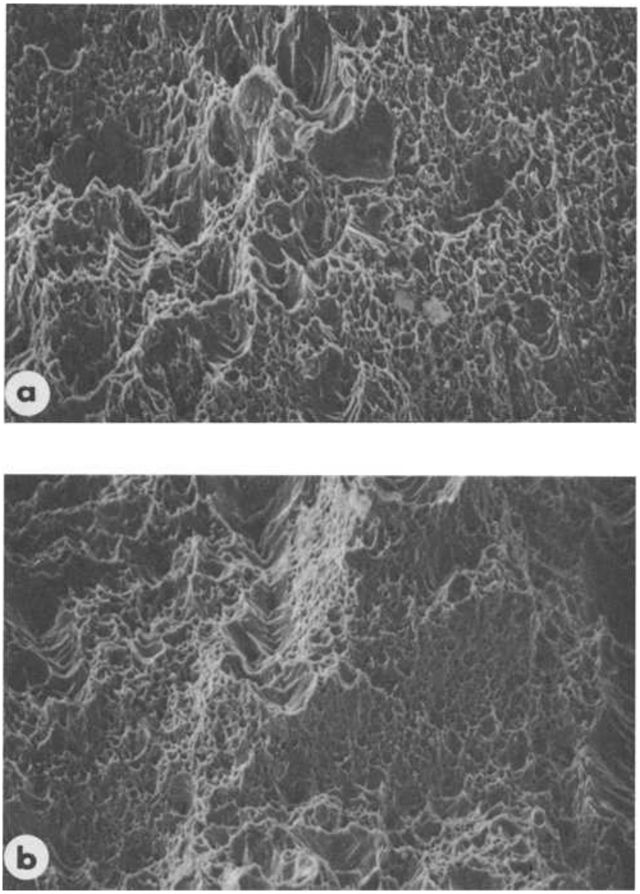

FIG. 11—*Fracture surface topography of samples aged in argon and hydrogen (original magnification ×850).* (a) *SEM fractograph of 15-5 PH stainless steel aged 1 h at 1100°F in hydrogen.* (b) *SEM fractograph of 15-5 PH stainless steel aged 1 h at 1100°F in argon.*

Figs. 8 through 10. There is a good correlation between ultimate tensile strength versus aging time and yield strength versus aging time curves. These results do not correlate on a one-to-one basis with hardness measurements. However, in general, the strength values are higher for most cases when the specimens aged in hydrogen are compared to those aged in argon, and the hydrogen values increase on outgassing. Strain to fracture is different in the presence of hydrogen and does not revert to the values for the corresponding treatment in argon on outgassing. Elongation to fracture is also generally higher for samples aged in hydrogen. Fractographs of several samples are shown in Fig. 11. The microvoid size for the hydrogen-aged sample is larger than for the argon-aged sample. This observation is consistent with the conclusion that hydrogen affects the nature of the precipitate in this steel if it is assumed that microvoids are nucleated at precipitates.

Conclusion

This study has demonstrated that a hydrogen atmosphere affects the aging process in 15-5 PH stainless steel. These initial data indicate the hydrogen aging and subsequent offgassing can alter the mechanical properties when compared to conventional aging treatments. Although further work is clearly necessary, this study should stimulate additional study of the potential improvement of product properties by careful selection of aging environments.

References

[1] Thompson, A. W., *Hydrogen in Metals,* American Society of Metals, 1973, p. 91.
[2] Louthan, M. R., Caskey, G. R., Donovan, J. A., and Rawl, D. E., *Materials Science Engineering,* Vol. 10, No. 357, 1972.
[3] Wilkins, J. C., Pence, R. E., and Perry, D. C. in *Advances in the Technology of Stainless Steels and Related Alloys, ASTM STP 369,* American Society for Testing and Materials, Phila., Pa. 1963, p. 331.
[4] Wilkins, J. C. and Pence, R. E. in *Symposium on Advances in Electron Metallography and Electron Probe Microanalysis, ASTM STP 317,* American Society for Testing and Materials, Phila., Pa. 1962, p. 140.
[5] Spiridonov, B., *Metallovedenie i Termicheskaya Obrabotka Metallov,* No. 4, April 1971, pp. 2–6.
[6] Kelly, A. and Nicholson, R. B., *Progress in Materials Science,* Vol. 10, No. 3, 1963, p. 239.
[7] Tetelman, A. S., *Fundamental Aspects of Stress Corrosion Cracking,* National Association of Corrosion Engineers, 1969, p. 446.
[8] Troiano, A. R., *Transactions,* American Society of Metals, Vol. 52, 1960, p. 54.
[9] Oriani, R. A., *Berichte der Bunsen-Gesellschaft für Physikalische Chemie,* Vol. 76, No. 848, 1973.

T. Andersson,[1] *H. Törnblom,*[1] *and A. Samuelsson*[2]

Structure and Properties of a 19Cr-25Ni-Mo-Ti Steel

REFERENCE: Andersson, T., Törnblom, H., and Samuelsson, A., "**Structure and Properties of a 19Cr-25Ni-Mo-Ti Steel,**" *MiCon 78: Optimization of Processing, Properties, and Service Performance Through Microstructural Control, ASTM STP 672,* Halle Abrams, G. N. Maniar, D. A. Nail, and H. D. Solomon, Eds., American Society for Testing and Materials, 1979, pp. 393–405.

ABSTRACT: SANDVIK 12RN72 is a 19Cr-25Ni austenitic steel with additions of molybdenum, titanium, and boron. In this paper structure, mechanical properties, and high-temperature corrosion properties of 12RN72 are presented.

The structure of 12RN72 in the solution heat treated condition consists of a fully austenitic matrix with some undissolved carbides and nitrides of type TiC and TiN. During creep, $M_{23}C_6$ precipitates in the grain boundaries, and both $M_{23}C_6$ and finely dispersed TiC-particles precipitate in the grains. The small TiC-particles, which precipitate at dislocations, are very stable and their growth rate is low.

The precipitates of TiC and $M_{23}C_6$ greatly contribute to a high creep-rupture strength. For instance, at 700°C the 100 000 h creep-rupture strength of 12RN72 is at least twice that of TP316 and TP347 and about 50 percent higher than that of Alloy 800H. Another prominent feature is the high creep ductility with a transcrystalline rupture behavior.

The high chromium and nickel contents of 12RN72 account for an improved corrosion resistance at elevated temperature in comparison with the standard austenitic steels. Up to about 1000°C, the corrosion properties are similar to those of Alloy 800H that has been verified by tests in air, steam, and impure helium.

KEY WORDS: steels, microstructure, austenitic stainless steels, precipitation hardening steels, electron microscopes, metallographic structures, dislocations, chromium carbides, titanium carbides, tensile properties, creep properties, oxidation resistance

Beside the conventional austenitic 18Cr-8Ni steels, there exists a group of austenitic alloys of type 16Cr-13Ni and 15Cr-15Ni also containing such elements as molybdenum, titanium, and niobium. These elements are added primarily to improve the long-term mechanical properties. One

---

[1] Research metallurgists, Sandvik Steel Research Centre, S-811 01 Sandviken, Sweden.

[2] Research metallurgist, Swedish Institute for Metal Research, S-114 28 Stockholm, Sweden.

steel belonging to this group is SANDVIK 12R72, which is a 15Cr-15Ni steel with additions of molybdenum, titanium, and boron. The most characteristic feature of this steel is the unique combination of high creep strength and excellent ductility over a wide range of temperatures and stresses [*1,2*].[3]

Steels of type 16Cr-13Ni and 15Cr-15Ni have a corrosion resistance similar to that of the 18Cr-8Ni. However, there is a great need for steels with better high-temperature corrosion properties. Significant improvement can be achieved by increasing the chromium and nickel contents. One example of such a steel is the 19Cr-25Ni-Mo-Ti steel grade SANDVIK 12RN72. This steel, designed by the same principles as earlier applied for SANDVIK 12R72, is characterized by a high creep strength and ductility combined with a corrosion resistance superior to that of the steel types just mentioned and similar to that of Alloy 800H up to about 1000°C.

In this paper, structure, mechanical properties, and high-temperature corrosion resistance of SANDVIK 12RN72 are presented.

Alloy Design

The development work that resulted in 12RN72 (composition see Table 1) was aimed at finding an austenitic steel combining the creep strength and ductility of 12R72 with a greatly improved corrosion resistance. The creep-rupture strength of 12R72 is 70 to 130 percent higher than that of, for example, T316H, in the temperature range 550 to 750°C [*3*]. Regarding the corrosion properties, the main effort was to produce a steel with a resistance similar to that of Alloy 800H for the service conditions foreseen, namely, temperatures in the range 600 to 900°C and environments such as superheated steam, hydrocarbons, and flue gases. A specific application considered early was superheater tubes in fossil fired and nuclear power plants.

In order to achieve the improved high-temperature corrosion resistance, the basis chosen was a 19Cr-25Ni steel. This ratio of chromium to nickel was set to get a thermodynamically stable austenitic structure. To obtain the desired strength, the following alloying elements were added.

Molybdenum

Molybdenum primarily gives a solution hardening effect but also promotes the stability of the carbide. The amount has to be restricted in order to avoid the precipitation of intermetallic phases like sigma and chi.

---

[3] The italic numbers in brackets refer to the list of references appended to this paper.

TABLE 1—*Nominal chemical composition of SANDVIK 12RN72 in percent by weight.*

C	Si	Mn	P, max	S, max	Cr	Ni	Mo	Ti	B
0.10	0.4	1.8	0.030	0.015	19	25	1.4	0.5	0.006

Titanium

Titanium combines with carbon to a very stable carbide, TiC. To ensure that a sufficiently large volume fraction of finely dispersed TiC-particles precipitate at dislocations at the service temperature, the steel should be solution heat treated and rapidly cooled before being put into service.

Carbon

Carbon is the prerequisite for the precipitation hardening by TiC. In addition, carbon combines with chromium and to some extent molybdenum to form carbides of type $M_{23}C_6$. These carbides form primarily at the grain boundaries but also to some extent within the grains. If the grain boundary carbides are suitably distributed and if there is a strong carbide-matrix interphase, they may strengthen the boundaries. Consequently, the formation of grain boundary cracks should be prevented.

Boron

Boron, which is dissolved in the $M_{23}C_6$-carbides, provides for the matching between the carbide and the matrix lattices, and thereby contributes to the strength of the grain boundaries.

Microstructure

The microstructure of 12RN72 at 700°C has been investigated by means of 1 mV transmission electron microscopy. Material solution heat treated at 1150°C for 15 min and water quenched was examined both in aged condition and after creep testing. Samples from creep tested specimens were spark cut transversely from the gage section. In order to investigate the influence of applied stress and time to rupture on the structure, specimens tested at two stress levels giving fracture after about 1000 h and 10 000 to 20 000 h, respectively, were chosen.

In the solution heat treated condition, the structure consists of a fully austenitic matrix with some undissolved micron-sized carbides and nitrides of type TiC and TiN. After aging at 700°C for 100 h, precipitates of finely distributed TiC at dislocations can be identified. The size of these particles is roughly 25 nm, see Fig. 1. Intergranular precipitation of $M_{23}C_6$

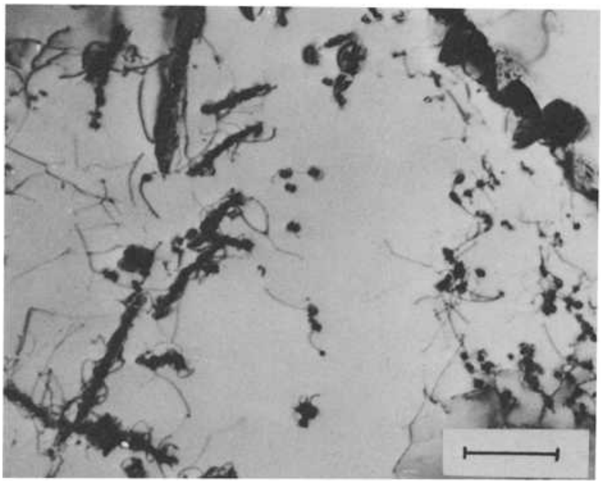

FIG. 1—*Structure after aging at 700°C for 100 h. TiC at dislocations and part of a grain boundary with $M_{23}C_6$. (Scale mark indicates 0.5 μm.)*

also occurs and to some extent, intragranular precipitation at dislocations of the same kind.

In creep tested specimens, three types of precipitates have been identified by means of electron diffraction, namely, TiC, $M_{23}C_6$ and, after longer testing times, sigma phase. Two types of TiC-particles are present, undissolved particles with a size of 1.5 to 3.0 μm and finer particles with a typical diameter of 20 nm nucleated along the dislocations. $M_{23}C_6$ carbides appear both inter- and intragranularly, the latter take the form of equiaxed particles at dislocations with a size of about 0.1 μm, although coarser carbides have occasionally been observed. Sigma appears after about 4000 h as elongated particles with a size of 1.0 to 5.0 μm in the grain boundaries, preferentially at triple points. The fraction of sigma increases slowly and is less than 5 percent by volume after about 20 000 h.

After about 1000 h of creep, small carbides of type TiC appear in the form of individual particles or continuous chains along dislocations, Fig. 2. The grain boundaries are decorated with carbides of $M_{23}C_6$, some boundaries to the extent that they are totally covered, Fig 3. However, the individual particles can normally be distinguished. As a result of the orientation relationship and coherency strains between the $M_{23}C_6$ carbide and the austenite, the particles grow faster in the direction of noncoherence resulting in unsymmetrical growth. Also, coherent and incoherent twin boundaries contain a high amount of $M_{23}C_6$ precipitates. In addition, intragranular precipitation of $M_{23}C_6$ at dislocations occurs but to a smaller extent.

Specimens creep tested for 10 000 to 20 000 h exhibit a slightly different structure as compared with those having a rupture life of about 1000 h, Fig.

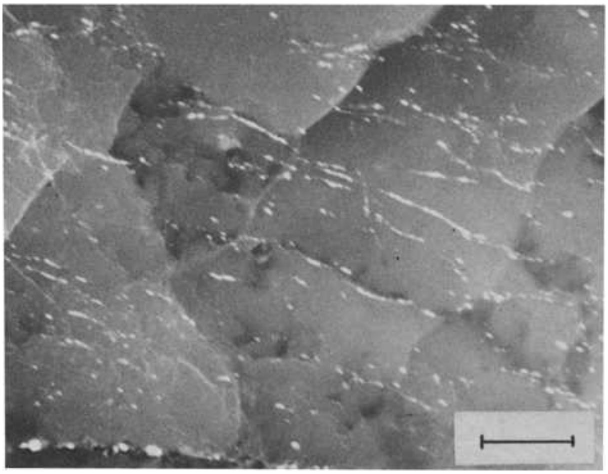

FIG. 2—*Structure after creep at 700°C (153 MN/m^2, 1323 h). Dark field micrograph. Stringers of TiC along subgrain boundaries and within subgrains. Some $M_{23}C_6$ particles in a grain boundary can also be seen. (Scale mark indicates 0.5 μm).*

4. First, there are fewer TiC particles precipitated at dislocations. At the same time, the dislocations containing TiC-particles are more heavily decorated than after 1000 h. Second, the amount of intergranular $M_{23}C_6$ carbide is reduced and the number of intragranular particles increased. The intragranular particles are often found attached to dislocations, preferably those being decorated with TiC. A striking feature is the very

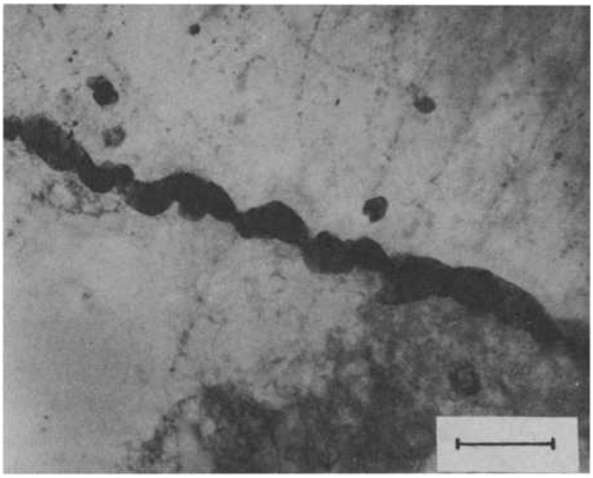

FIG. 3—*Structure after creep at 700°C (153 MN/m^2, 1137 h). $M_{23}C_6$ in a grain boundary and within the grains. Chains of TiC at dislocations. (Scale mark indicates 0.5 μm.)*

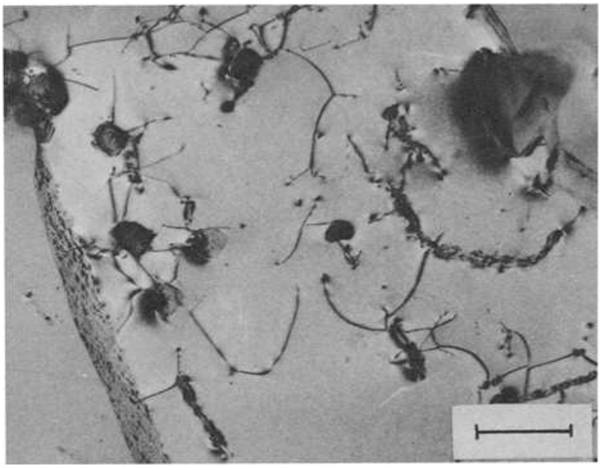

FIG. 4—*Structure after creep at 700°C (93.6 MN/m², 23 490 h). Particles of TiC and $M_{23}C_6$ at dislocations. (Scale mark indicates 0.5 μm.)*

low particle growth rate. The individual TiC and $M_{23}C_6$ particles are with few exceptions, not appreciably coarser than those in the 1000 h specimens. Occasional sigma particles are also observed. The area around the sigma phase is often depleted of TiC.

The dislocation density is lower in the 10 000 h specimens than in the 1000 h ones, and most dislocations are arranged in well-defined low-angle boundaries. The dislocations within the subgrains have often disappeared from the rows of TiC precipitates.

A comparison between the thread and the gage section of a specimen tested for 10 000 h, reveals much less intragranular $M_{23}C_6$ carbide in the thread. It is obvious that the applied load increases the amount of $M_{23}C_6$ precipitation, a conclusion that is also supported by observed differences between aged and creep-tested specimens. The thread also contains much less sigma phase. In a comparison of structures obtained after short and long testing times, respectively, it appears that the higher stress level for short times leading to higher dislocation densities favors intragranular precipitation of TiC at dislocations.

Mechanical Properties

The tensile properties at room temperature of 12RN72 in the solution heat treated condition are given in Table 2. The effect of test temperature on the minimum yield strength is shown in Fig. 5 for temperatures up to 650°C. The short-term properties of 12RN72 are similar to those of the conventional austenitic steels.

The average creep-rupture strength of solution heat treated 12RN72 at

TABLE 2—*Tensile properties of SANDVIK 12RN72 at 20°C.*

Yield Strength, MN/m²		Tensile Strength, MN/m²	Elongation, Percent A5[a] min.	Vickers Hardness Number, about
0.2% min.	1.0% min.			
205	230	490–640	40	155

[a] A5 corresponds to $5.65\sqrt{S_o}$. For the gage length 2 in., the same figure is valid.

600 to 900°C is presented in Table 3. These values for rupture in 10 000 and 100 000 h are based on in-house tests on bar and tube material from a large number of heats. The number of individual specimens and the rupture lives obtained at 600, 700, and 800°C are demonstrated in Fig. 6. A characteristic feature is the very good long-term stability over a wide temperature range. As illustrated in Fig. 5, where the 100 000 h rupture curve is drawn, the cross-over temperature for designs based on elastic and creep properties, respectively, is 600 to 625°C.

As already mentioned, one objective in developing 12RN72 was to reach a creep strength level similar to that of the 15Cr-15Ni steel 12R72. In Fig. 7, the average creep-rupture strength for 12RN72 is compared with data for 12R72, Alloy 800H, TP316, and TP347 at 700°C as a function of

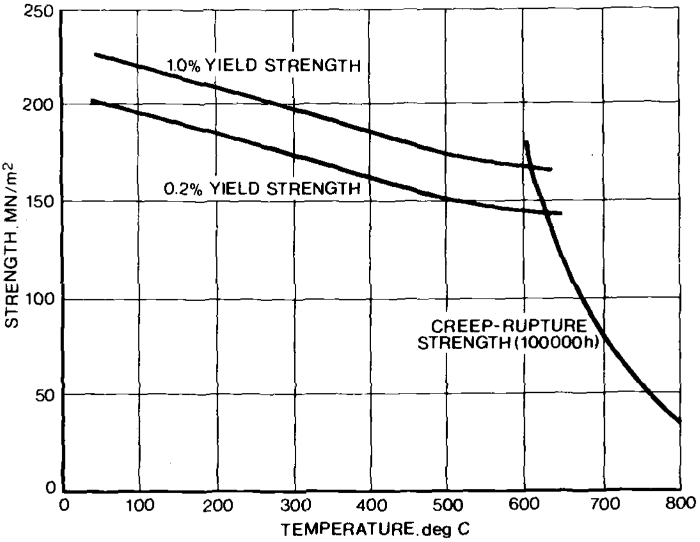

FIG. 5—*Minimum yield strength and average creep-rupture strength (100 000 h) for solution heat treated SANDVIK 12RN72.*

TABLE 3—*Average creep-rupture strength of SANDVIK 12RN72 in the solution heat treated condition.*

	Stress, MN/m², to cause rupture in	
Temperature, °C	10 000 h	100 000 h
600	235	175
650	158	120
700	105	80
750	74	56
800	50	35
850	33	20
900	17	8.5

rupture life. It is obvious that the 100 000-h creep-rupture strength of 12RN72 is, first, about the same order as for 12R72 and, second, at least twice that of the two 18Cr-8Ni grades and about 50 percent higher than that of Alloy 800H. At higher temperatures, the strength of 12RN72 is somewhat higher than that of 12R72. For instance, at 800°C the 100 000-h value for 12RN72 is 35 MN/m², which is to be compared with 30 MN/m² for 12R72.

A common feature of the conventional austenitic 18Cr-8Ni steels, particularly those strengthened by carbide dispersions, is that the ductility has a tendency to drop with time. Regarding 12R72, no loss of ductility, measured as reduction of area, was found for rupture lives up to about 100 000 h [3]. The objective to retain the excellent creep ductility of 12R72 also for 12RN72 was indeed achieved as shown in Fig. 8, where the area

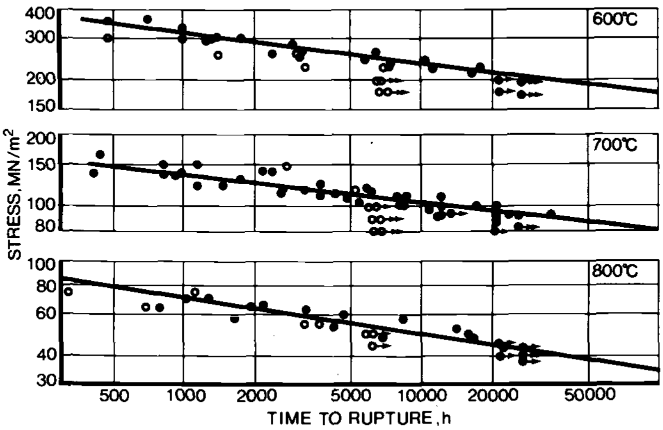

FIG. 6—*Creep-rupture strength of SANDVIK 12RN72 at 600 to 800°C.*

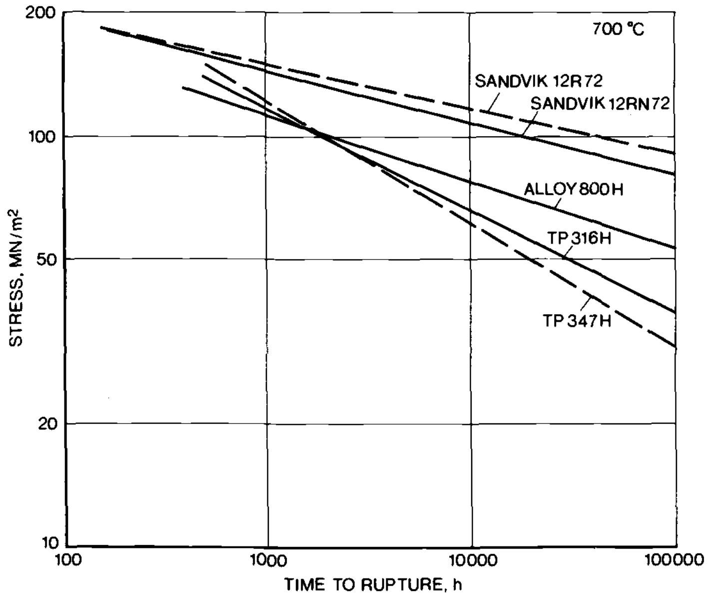

FIG. 7—*Creep-rupture strength at 700°C for SANDVIK 12RN72, 12R72, Alloy 800H, AISI TP316H, and TP347H.*

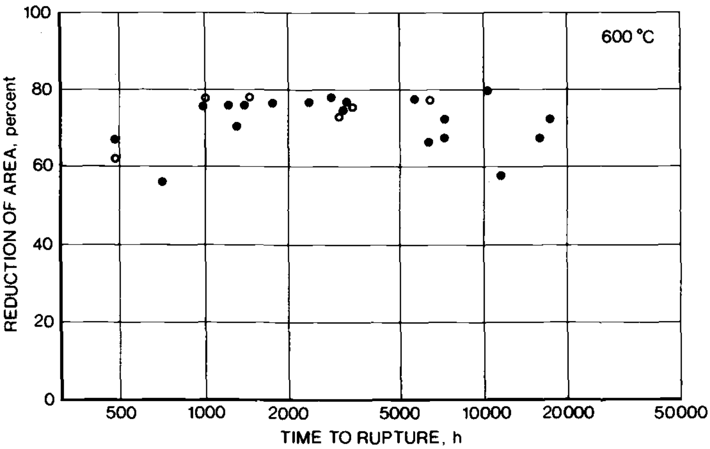

FIG. 8—*Creep-rupture ductility at 600°C of SANDVIK 12RN72.*

reduction has been plotted for specimens tested to rupture at 600°C. The high creep ductility is an effect of a transcrystalline rupture behavior.

Corrosion Properties

The high chromium and nickel contents give 12RN72 an improved oxidation and corrosion resistance at high temperatures. The oxidation resistance in air has been measured both at constant and cyclically varied temperatures. The isothermal data for 12RN72, 12R72, Alloy 800H, and some standard 18Cr-8Ni steels compiled in Table 4 show little difference between the alloys up to 800°C. At higher temperatures, 12RN72 has an oxidation rate that is similar to that of Alloy 800H and considerably lower than that of the conventional austenitic steels. In cyclic testing 120 h at temperature and intermediate cooling to ambient temperature, 12RN72 has a lower oxidation rate at temperatures above 700°C than 12R72 and the other austenitic steels, which fall in the scatter band indicated in Fig 9. When compared with Alloy 800H, the weight loss of 12RN72 is somewhat lower up to about 950°C. However, above 1000°C, 12RN72 exhibits a higher oxidation rate, for example, at 1100°C the weight loss is 3.7 $g/m^2 \cdot h$, which is to be compared with 1.3 $g/m^2 \cdot h$ for Alloy 800H. This implies that the maximum working temperature in air is about 1000°C for 12RN72.

12RN72 has been tested under conditions corresponding to superheated steam. Data published by Stenqvist and De Pourbaix [*4*] on 12RN72 and Alloy 800H show that the metal loss after 5000 h exposure to superheated steam at 750°C is somewhat lower for 12RN72 than for Alloy 800H, 0.0038 $g/m^2 \cdot h$ and 0.0048 $g/m^2 \cdot h$, respectively.

The corrosion properties of a 20Cr-25Ni steel similar to 12RN72 have been studied in helium containing small amounts of methane, carbon oxides, and water. After 3000 h exposure at 1000°C, the 20Cr-25Ni steel had suffered a carbon pick-up corresponding to a mean carbon content of 0.45 percent by weight, whereas specimens of a 20Cr-30Ni steel exhibited

TABLE 4—*Descaled weight loss after isothermal oxidation in air during 1000 h.*

	Weight loss, $g/m^2 \cdot h$			
Grade	700°C	800°C	900°C	1000°C
12RN72	0.009	0.015	0.041	0.125
12R72	0.016	0.016	0.052	2.450
Alloy 800H	. . .	0.015	0.050	0.099
TP304	0.008	0.026	0.194	. . .
TP316	0.010	0.022	0.129	1.815
TP321	0.013	0.019	0.155	1.190
TP347	0.010	0.022	0.158	1.915

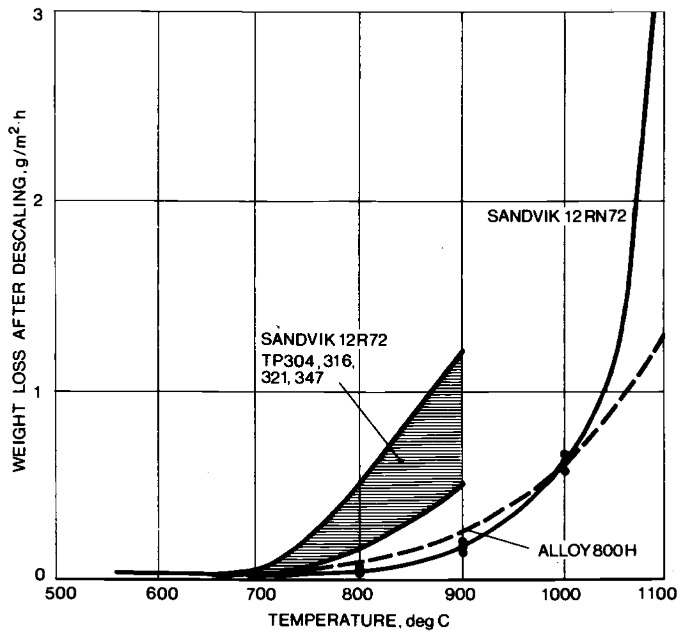

FIG. 9—*Cyclic oxidation 120 h in air with 4 drops to room temperature of SANDVIK 12RN72, 12R72, Alloy 800H, and some conventional 18Cr-8Ni grades.*

a content of 0.75 percent by weight. This test indicates that the carburization resistance of 12RN72 is of the same order as that of Alloy 800.

Discussion

The microstructural observations on SANDVIK 12RN72 show that the supersaturation of alloying elements after solution heat treatment, mainly carbon and titanium but also chromium, reduces the creep rate, that is, improves the creep strength, through the formation of numerous particles within the grains during creep. The particles are effective barriers against the movement of dislocations, which may also be expected from their size and distribution. A striking feature in a comparison with 12R72 is the higher amount of TiC particles precipitated at dislocations in 12R72 [5]. In addition, 12R72 contains virtually no intragranular $M_{23}C_6$. The solubility of TiC in austenite at the solution temperature is lower for 12RN72 than for 12R72, but not low enough to account for the different amounts observed. The higher chromium and nickel contents in 12RN72 lower the solubility of $M_{23}C_6$ in austenite [6–8], thus influencing the general pattern of precipitation. This leads to a higher amount of intragranular $M_{23}C_6$ precipitation at the expense of that of TiC. Despite the lower amount of TiC at dislocations, 12RN72 exhibits a creep strength very similar to that of 12R72. This indicates that not only small carbides of TiC but also intragranular $M_{23}C_6$ contribute to the high creep strength of the steel. However, the finer particles of TiC exert the strongest effect.

The high creep ductility of 12RN72 depends on a smaller tendency to intercrystalline cracking than in most other austenitic steels. The explanation is that the grain boundary carbides of $M_{23}C_6$ due to a strong carbide-matrix interface favorably influence the fracture behavior by strengthening the boundaries thereby reducing boundary sliding and preventing the initiation and linking of cracks. Boron, which is incorporated in the grain boundary carbides, contributes to the matching between the carbides and the matrix and, hence, to the strength of the grain boundaries.

Sigma phase precipitates in 12RN72 after about 4000 h at 700°C. The fraction of sigma increases slowly and is less than 5 percent by volume after about 20 000 h. However, the sigma phase has not been found to have any adverse effect on creep strength and ductility.

The improved high-temperature corrosion resistance of 12RN72, here exemplified by results from tests in air, steam, and impure helium, together with the excellent creep properties strongly demonstrate that the steel offers distinct advantages over standard 18Cr-8Ni steels as, for instance, superheater tubing in the power and process industry. It is evident that 12RN72 is a strong candidate material also for process furnace components up to about 900°C where high creep strength is required. For such applications, 12RN72 can replace more highly alloyed grades used today, for example, Alloy 800H.

Conclusions

A 19Cr-25Ni austenitic steel SANDVIK 12RN72 with additions of molybdenum, titanium, and boron has been developed. Precipitates of finely distributed carbides of type TiC at dislocations and of $M_{23}C_6$ inter- and intragranularly during creep contribute to a high creep-rupture strength. Another characteristic feature is a high creep ductility with a transcrystalline rupture behavior. These properties have been verified by creep testing up to around 20 000 h.

The high chromium and nickel contents account for better high-temperature corrosion properties than those of the standard 18Cr-8Ni steels. Up to about 1000°C, the corrosion properties are similar to those of Alloy 800H, which has been verified by tests in air, steam, and impure helium. This combination of creep and corrosion properties makes 12RN72 a suitable steel, for instance, for superheaters in power and process industries.

Acknowledgments

We are indebted to Sandvik and to the Swedish Institute for Metal Research for the opportunity to carry out the present work, and to the Swedish Board for Technical Development for financial support. We especially wish to thank Prof. Roland Kiessling, Director of Sandvik Steel Research and Development, for his permission to publish the paper and Prof. Rune Lagneborg, the Swedish Institute for Metal Research, for his encouragement. We also wish to thank Dr. Agneta Odén, who has carried out some of the transmission electron microscopy work and helped to stimulate progress.

References

[*1*] Egnell, L., *Metal Progress*, Vol. 98, No. 3, 1970 p. 102.
[*2*] Egnell, L., Kiessling, R., and Persson, N. G., "SANDVIK 12R72-Evaluation of Its Properties as Canning Material in Fast Reactors," presented at a conference in Paris, 10 Dec. 1971.
[*3*] Persson, N. G. and Lauri, P., "SANDVIK 12R72—A Strong and Ductile Austenitic Steel for High-Temperature Service," presented at ASM Materials Conference, American Society of Metals, Chicago, 25–27 Oct. 1977.
[*4*] Stenqvist, C. and De Pourbaix, M., AB Atomenergi Sweden, Report AE-MK-282, (in Swedish), 1971.
[*5*] Odén, A., PhD thesis, Royal Institute of Technology, Stockholm, Sweden, 1975.
[*6*] Lagneborg, R., Östberg, G., and Attermo, R., *Jernkontorets Ann.*, Vol. 155, 1971, p. 601.
[*7*] Kegg, G. R. and Silcock., J. M., *Metals Science Journal*, Vol. 6, 1972, p. 47.
[*8*] Keown, S. R., "Creep Strength in Steel and High Temperature Alloys," Conference Proceeding, The Metal Society, London, 1974.

G. C. Bodine, Jr.,[1] *and C. H. Sump*[1]

Microstructure and Related Material Characteristics of Some Duplex Austenitic-Ferritic Alloys with Less Than 40 Percent Ferrite

REFERENCE: Bodine, G. C., Jr., and Sump, C. H., "**Microstructure and Related Material Characteristics of Some Duplex Austenitic-Ferritic Alloys with Less Than 40 Percent Ferrite,**" *MiCon 78: Optimization of Processing, Properties, and Service Performance Through Microstructural Control, ASTM STP 672,* Halle Abrams, G. N. Maniar, D. A. Nail, and H. D. Solomon, Eds., American Society for Testing and Materials, 1979, pp. 406–429.

ABSTRACT: Duplex austenitic-ferritic stainless steel alloys with major composition variants were prepared as induction melted heats and were converted to tubing by centrifugal casting and cold pilger reduction. Ferrite content of the tubing ranged from 19 to 30 percent depending upon composition and heat treatment. The effects of composition and heat treatment variants on the characteristics of microstructure and related corrosion properties were determined.

KEY WORDS: steels, microstructure, corrosion resistant steels, stress corrosion resistance, centrifugal casting, metal tubing, austenite, ferrite

Centrifugally cast duplex austenitic-ferrite stainless steel alloys have been investigated at the Combustion Engineering Metallurgical and Materials Laboratory. The emphasis of the work has been directed towards developing cast compositions practical for commercial conversion by direct cold reduction to wrought seamless pipe and tube. Pilot production of wrought duplex austenitic-ferritic tubing has been accomplished while still retaining the stress corrosion cracking resistance of the cast duplex stainless steels. One alloy composition, MC 20 (0.06C,

---

[1] Manager of metals processing and senior research and product development engineer, respectively, Metallurgical and Materials Laboratory, Combustion Engineering, Inc., Chattanooga, Tenn. 34702.

[2] The italic numbers in brackets refer to the list of references appended to this paper.

22Cr, 8Ni with Schaeffler ferrite number of 20), demonstrated an improved stress corrosion cracking resistance as compared to TP-304.[3]

In this investigation, a pilot production heat of MC 20 alloy was melted, centrifugally cast to hollows, and converted to pipe and tube by cold pilger reduction. In addition to this activity, production of variant MC 20 alloys by conversion of laboratory centrifugal castings to wrought sections was completed. This was undertaken to study the effect of major alloy variants of the MC 20 base composition upon metallurgical, mechanical, and corrosion properties. Specific emphasis was directed to the character of microstructure as related to the effects of cold reduction, heat treatment, and alloy composition variants. This paper will review the results noted in the metallographic examinations and testing of the duplex austenitic-ferritic stainless alloys.

Procedure

Pilot Production of MC 20 Alloy

A 1360 kg (3000 lb)[4] induction melted heat was centrifugally cast into six tube hollows. Cast hollows were machined and heat treated at 1177°C (2150°F). Two of the machined and heat treated hollows were cold pilger reduced in one pass to 101.6 mm (4 in.) schedule 80 pipe size of 114.3 mm (4.5 in.) outside diameter by 8.6 mm (0.337 in.) wall thickness. The remaining four hollows that were machined to 133.4 mm (5 1/2 in.) outside diameter by 22.2 mm (7/8 in.) wall thickness were cold reduced to 44.5 mm (1 3/4 in.) outside diameter by 4.6 mm (0.180 in.) wall thickness through four cold pilger passes. Interstage process heat treatment was 1177°C (2150°F) after the first reduction pass to 114.3 mm (4 1/2 in.) outside diameter by 19.1 mm (3/4 in.) wall thickness and 1066°C (1950°F) after the second and third reduction passes (76.2 mm (3 1/2 in.) and 63.5 mm (2 1/2 in.) outside diameter by 10.1 mm (0.400 in.) and 7.6 mm (0.300 in.) wall, respectively). Final heat treatment temperature was at 1066°C (1950°F) for both 101.6 mm (4 in.) schedule 80 pipe and the 44.5 (1 3/4 in.) outside diameter by 4.6 mm (0.180 in.) wall tubing. All heat treatment was done in a continuous hydrogen atmosphere furnace with a refrigerated hydrogen cooling chamber. Pipe and tubing were rotary straightened after final heat treatment. Chemical analyses of heat and tubing are shown in Table 1.

A section of machined and heat treated cast hollow was flattened and cold rolled to 12.7 mm (0.500 in.) thick bar. The bar was cut into three equal lengths and each length heat treated at 927°C (1700°F), 982°C

---

[3] Bodine, G. C., Jr., and Sump, C. H., *Materials Performance*, Vol. 16, No. 6, June 1977, pp. 13–21.

[4] All measurements were taken in English units.

TABLE 1—*Chemical analysis (percent by weight) of pilot production MC 20 base composition alloy.*

	As cast		Cold reduced			
Element	7/8 in. wall XZY18K1	1/2 in. wall XZY18K6	4 in. pipe XAF18K6	3 1/2 in. OD XZF18K1	2 1/2 in. OD XZF18K1	1 3/4 in. OD XZF18K1
Carbon	0.06	0.06	0.06	0.05	0.06	0.06
Manganese	1.68	1.69	1.65	1.60	1.67	1.63
Silicon	0.89	0.91	0.92	0.90	0.89	0.88
Nickel	8.2	7.9	8.4	8.3	8.3	8.4
Chromium	21.9	22.0	23.5	23.5	23.6	23.5
Nitrogen	0.057	0.059	0.062	0.056	0.057	0.059

(1800°F), and 1038°C (1900°F), respectively. Each 12.7 mm (0.500 in.) thick bar was then cold rolled to 6.4 mm (0.250 in.) thickness and respectively heat treated at 927°C (1700°F), 982°C (1800°F), and 1038°C (1900°F) once more. A gas-fired furnace atmosphere and air cooling was used during the heat treatment of 12.7 mm (0.500 in.) and 6.4 mm (0.250 in.) thick bar. This material was used for a study of the effect of process and final heat treatment on microstructure and corrosion properties.

Processing of MC 20 Variant Compositions

Induction melted laboratory heats 45.4 kg (100 lb) were centrifugally cast into tube hollows. The castings were machined and heat treated at 1177°C (2150°F). One pair of castings represented a base MC 20 composition with the variant being the addition of molybdenum. Another pair represented a variant composition with lower nickel content. Two other pairs of castings included variant compositions stressing higher chromium and high chromium and nickel content. Six of the castings were reduced through two cold pilger passes to 60.3 mm (2 3/8 in.) outside diameter by 4.2 mm (0.166 in.) wall tubing and two castings were reduced through two passes to 60.3 mm (2 3/8 in.) outside diameter by 5.5 mm (0.218 in.) pipe size (higher chromium and nickel variants). Interstage process heat treatment after the first reduction pass was 1177°C (2150°F) and final heat treatment was 1066°C (1950°F). Heat treatment was done in a continuous hydrogen atmosphere furnace with refrigerated hydrogen cooling. Chemical analyses of the variant compositions are shown in Table 2.

Microstructural Characterization

Metallographic specimens were prepared from representative specimens of the pilot production MC 20 alloy and MC 20 variant alloy material. Specimens included sections transverse and parallel to the direction of working as well as transverse and axial sections of centrifugal castings. Specimens for metallographic specimen preparation were removed from MC 20 alloy centrifugal castings and 88.9 mm (3 1/2 in.) outside diameter by 10.2 mm (0.400 in.) wall tubing before and after heat

TABLE 2—*Chemical analysis (percent by weight) of MC 20 variant alloy analysis*

	Sample (2 3/8 in. OD by 0.166 in. wall)				Sample (2 3/8 in. OD by 0.218 in. wall)			
	Lower Nickel Variant		Higher Chromium Variant		Molybdenum Additive Variant		Higher Chromium and Nickel Variant	
Element	XS3301	XS3302	XS3300	XS3312	XS3310	XS3311	XS3303	XS3308
Carbon	0.057	0.059	0.067	0.065	0.060	0.063	0.054	0.066
Manganese	1.74	1.71	1.42	1.78	1.57	1.64	1.98	1.80
Silicon	0.50	0.52	0.59	0.64	0.54	0.56	0.49	0.61
Nickel	6.0	6.3	8.9	7.2	8.8	8.8	12.2	10.4
Chromium	19.8	22.7	25.7	24.7	23.7	25.1	26.4	26.6
Molybdenum	0.02	0.03	0.04	0.06	1.75	1.64	0.05	0.05

treatment. Specimens removed from 101.6 mm (4 in.) schedule 80 pipe, 63.5 mm (2 1/2 in.) outside diameter by 7.6 mm (0.300 in.) and 44.5 mm (1 3/4 in.) outside diameter by 4.6 mm (0.180 in.) wall tubing were all in the heat treated condition. Tubular specimens of MC 20 variant alloys were removed from finished dimension heat treated 60.3 mm (2 3/8 in.) outside diameter tubing and 50.8 mm (2 in.) pipe sizes. Metallographic specimens were also prepared from 6.4 mm (0.250 in.) thick bars cold rolled from an MC 20 alloy centrifugal casting section and representing 927°C (1700°F), 982°C (1800°F), and 1038°C (1900°F) thermal treatments.

All metallographic specimens were optically examined and microhardness surveys were made on the austenite and ferrite phases. Magne-Gage surveys for approximate ferrite content were also conducted on the metallographic specimens. After completion of the optical metallographic examination, hardness and Magne-Gage surveys, the specimens were used for austenite and ferrite analyses by electron microprobe technique.

Corrosion Testing

Corrosion testing included stress corrosion cracking resistance in boiling 42 percent magnesium chloride solution (ASTM Recommended Practice for Performing Stress-Corrosion Cracking Tests in a Boiling Magnesium Chloride Solution (G 36–73)), and susceptibility to intergranular attack in boiling acidified ferric sulfate solution (ASTM Recommended Practices for Detecting Susceptibility to Intergranular Attack in Stainless Steels (A 262–75) Practice B). A comparative corrosion test in boiling 80 percent formic acid[5] was performed on tubing material representing fully austenitic TP-304 and MC 20 alloy variant with molybdenum additive.

Stress corrosion cracking resistance test specimens were prepared as restrained U-bends. Tubing and bar specimens that possessed sufficient

---

[5] Fontana, M. G. and Greene, N. D., *Corrosion Engineering*, McGraw-Hill, 1967, pp. 263–264.

wall thickness were machined to dimensions of 6.4 mm thick by 19.1 mm wide by 152.4 mm long (1/4 in. thick by 3/4 in. wide by 6 in. long). When sufficient tube wall thickness was not available, as in the case of the 44.5 mm (1 3/4 in.) outside diameter by 4.6 mm (0.180 in.) wall MC 20 alloy and the 60.3 mm (2 3/8 in.) outside diameter by 4.2 mm (0.166 in.) wall MC 20 variant alloy, the inside and outside diameter surfaces were polished. All inside and outside bend specimen surfaces were final polished with 600 grit silicon carbide paper. Centerlines of 9.5 mm (3/8 in.) diameter bolt holes were 12.7 mm (1/2 in.) from the specimen ends. The long dimension of all specimens was parallel to the tube axial or bar rolling direction. U-bends were formed by bending the specimen around a 21.3 mm (0.840 in.) diameter mandrel until a 63.5 mm (2 1/2 in.) span was obtained between the inside surfaces at the lower extremity of the bolt holes. The bent specimen was paralleled into a U-bend by bolting and tightening to 0.1 mm (0.005 in.) past the parallel point that was done to allow for expansion during testing. Stress corrosion test specimens were removed for examination at periods of 2, 4, 6, and 8 h for the first day. Examination periods continued for each successive day in the morning and at various periods throughout the day. This routine was repeated through 712 h exposure time for tube specimens and 768 h for bar specimens.

Specimens for testing susceptibility to intergranular corrosion in boiling acidified ferric sulfate (ASTM A 262–75 Practice B) were prepared as follows:

a. Specimens 12.7 mm (1/2 in.) thick were removed from machined and heat-treated MC 20 alloy centrifugal castings and cut to 31.8 mm by 16.5 mm by 12.7 mm (1.250 in. by 0.650 in. by 0.500 in.) specimen dimensions.

b. Wrought pipe and tube specimens were cut to 25.4 mm (1 in.) square by pipe or tube wall thickness specimen dimensions.

c. 6.4 mm (1/4 in.) holes were drilled in each specimen for glass hangers.

All specimens were finished by polishing with 180-grit silicon carbide paper. Corrosion testing was done in accordance to ASTM A 262–75 Practice B. Specimen preparation and testing procedure for corrosion susceptibility in boiling 80 percent formic acid was essentially the same as used in the ASTM A 262–75 Practice B test series. However, boiling 80 percent formic acid testing was limited to a comparison between TP-304 tubing and the MC 20 alloy variant tubing with molybdenum addition. The TP-304 tubing was produced by the same centrifugal casting and cold reduction process used for the duplex alloys. The test period was arbitrarily set at 120-h immersion time.

Tension Testing

In ASTM Standard Method of Tension Testing of Metallic Materials (E 8–77a), standard 12.7 mm (0.500 in.) round tension test specimens were used for MC 20 alloy castings. Wrought pipe and tubing specimens were prepared as specified in ASTM E 8–77a for longitudinal tension test specimens for large-diameter tubular products. Tension testing was according to specified ASTM E 8–77a procedures.

Experimental Results

Microstructure Characterization

Distribution and orientation of ferrite within the austenitic matrix of MC 20 alloy and alloy variants are illustrated in Figs. 1 through 10. The

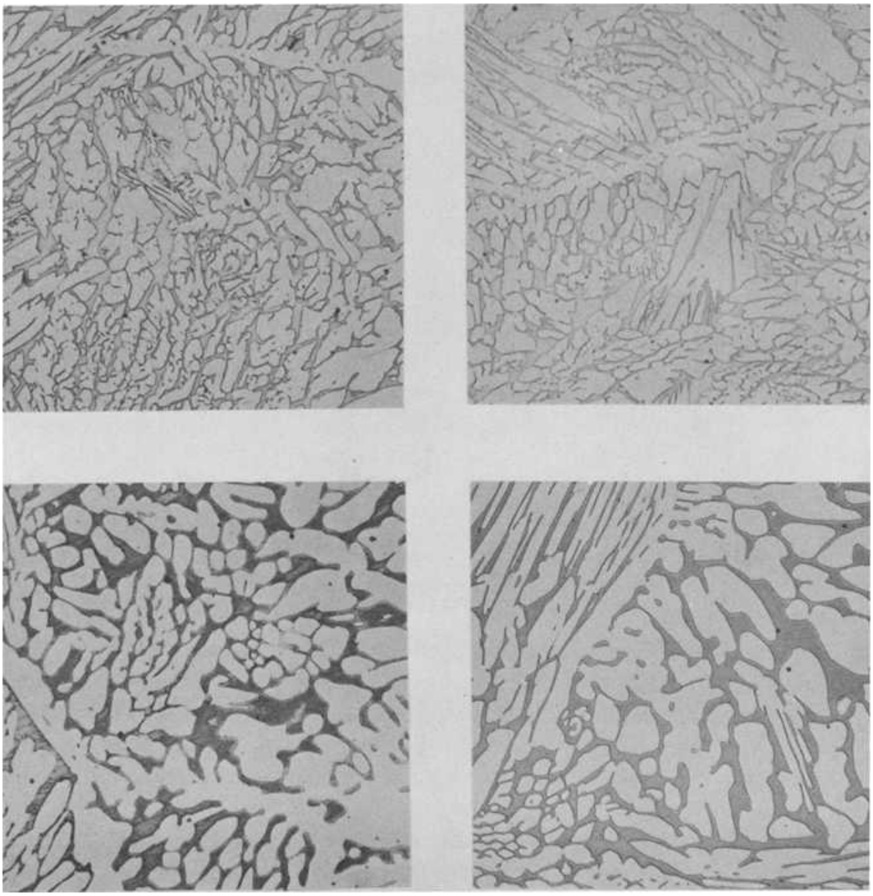

FIG. 1—*Longitudinal* (left) *and transverse* (right) *microstructure at* ~ ×*200 electrolytic 10N KOH etch. MC 20 alloy, Heat XZF18K, 12.7 mm (1/2 in.) wall centrifugal casting K-6. As-cast* (top) *and annealed* (bottom).

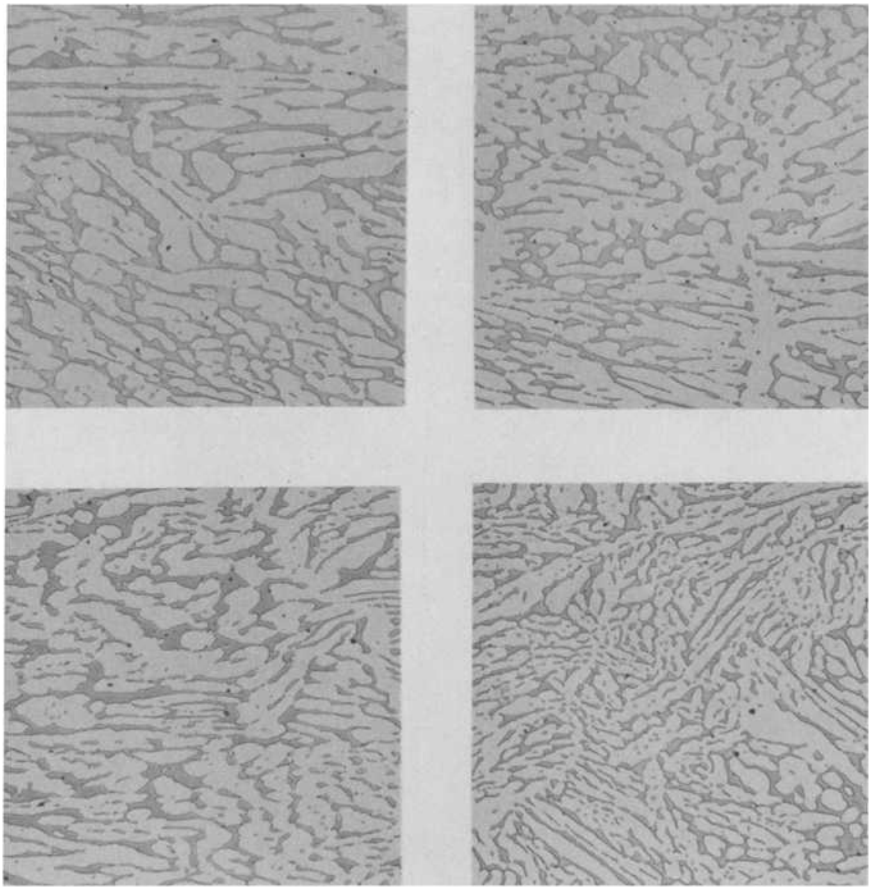

FIG. 2—*Longitudinal* (left) *and transverse* (right) *microstructure ~ ×200 electrolytic 10N KOH etch. MC 20 alloy, Heat XZF18K, annealed 101.6 mm (4 in.) schedule 80 114.3 mm (4 1/2 in.) OD by 8.6 mm (0.337 in.) pipe from centrifugal casting No. 5* (top)*; and from centrifugal casting No. 6* (bottom).

ferrite appears as the darker phase that is the result of an electrolytic 10N potassium hydroxide etching technique. Examination of the microstructures shown in Figs. 1 through 10 disclose the progressive effect of cold reduction in breaking up of the random cast ferrite orientation and developing a more banded axial orientation. Change in the distribution and orientation of ferrite as the result of process heat treatment is not apparent when comparing both the respective as-cast and as-reduced microstructures with microstructure after heat treatment. This observation may be noted when comparing the microstructures in Figs. 1, 2, 3, and 4. However, the significant difference in ferrite content of variant MC 20 alloy Heats XS3301 and XS3302 is clearly shown in the micrographs in

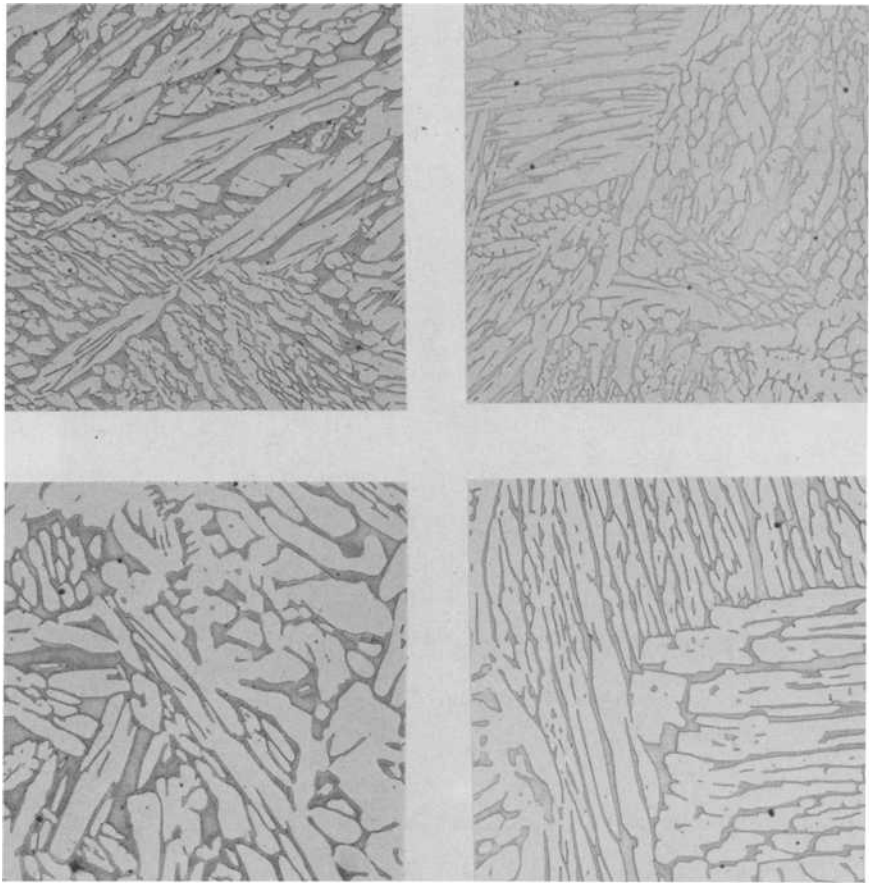

FIG. 3—*Longitudinal* (left) *and transverse* (right) *microstructure at ~ ×200 electrolytic 10N KOH etch. MC 20 alloy, Heat XZF18K, 22.2 mm (7/8 in.) wall centrifugal casting K-1. As-cast* (top) *and annealed* (bottom).

Fig. 8. Heat XS3301 had a calculated Schaeffler ferrite number of 25 and a Magne-Gage reading of 19 on a specimen of 60.3 mm (2 3/8 in.) outside diameter tubing. Schaeffler ferrite number for Heat XS3302 was 41, and the Magne-Gage number was approximated at between 30 and 40.

The effect of process and final heat treatment at 927°C (1700°F), 982°C (1800°F), and 1038°C (1900°F) is shown in Fig. 6. The microstructures are representative of 6.4 mm (0.250 in.) thick MC 20 alloy bar rolled from a centrifugally casting section with an interstage anneal at 12.7 mm (0.500 in.) bar thickness. Microstructures from top to bottom in Fig. 6 are the results of respective heat treatment temperature of 927°C (1700°F), 982°C (1800°F), and 1038°C (1900°F). There is a noticeable trend for ferrite coarsening as the heat treatment temperature is increased.

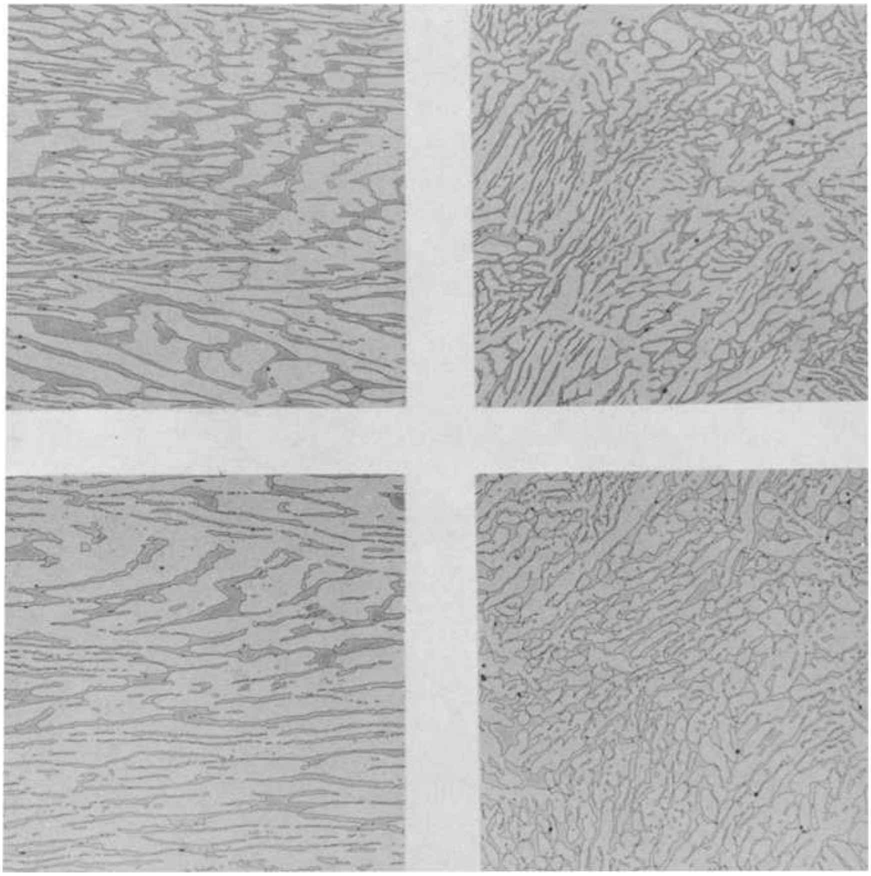

FIG. 4—*Longitudinal* (left) *and transverse* (right) *microstructure at ~ ×200 electrolytic 10N KOH etch. MC 20 alloy, Heat XZF18K, as-reduced 88.9 mm (3 1/2 in.) OD by 10.2 mm (0.400 in.) wall tubing* (top); *and same size tubing in the annealed condition* (bottom).

Electron microprobe analyses of the ferrite and austenite phases in MC 20 alloy casting and MC 20 alloy and alloy variant wrought tubular sections are shown in Fig. 11. The same metallographic specimens used for the micrographs in Figs. 1 through 10 were used for the microprobe analysis. The MC 20 alloy chromium content in ferrite is generally 5 to 6 percentage points higher than in the austenite and the ferrite nickel content is from 4 to 5 percentage points lower. A similar trend is found for higher chromium and lower nickel content in the ferrite of MC 20 alloy variants, but the differences are not as consistent. For example, the ferrite chromium content of the lower nickel alloy variants, XS3301 and XS3302, is from 3 to 4 percentage points higher than in the austenite. But, the

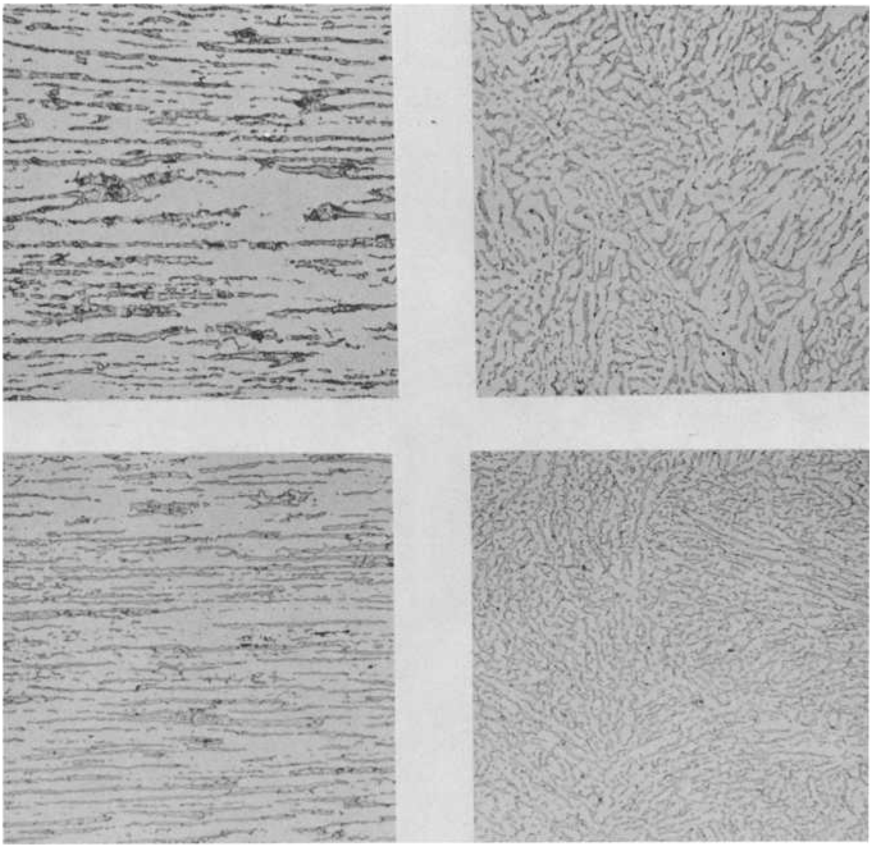

FIG. 5—*Longitudinal* (left) *and transverse* (right) *microstructure at* ~ ×*200 electrolytic 10N KOH etch. MC 20 alloy, Heat XZF18K, 65.5 mm (2 1/2 in.) OD by 7.6 mm (0.300 in.) wall tubing* (top); *and 44.5 mm (1 3/4 in.) OD by 4.6 mm (0.180 in.) wall tubing* (bottom).

ferrite chromium content in the higher chromium and nickel variants, XS3303 and XS3308, is 7 to 8 percentage points higher. The ferrite molybdenum content in the variants with molybdenum added, XS3310 and XS3311, is almost double that in the austenite.

Microhardness survey of ferrite and austenite phases in MC 20 alloy castings showed a ferrite hardness of approximately 8 percent higher than the austenite. The ferrite remained consistently harder throughout the processing, but the difference had dropped to about 4 percent at the 44.5 mm (1 3/4 in.) outside diameter by 4.6 mm (0.180 in.) wall tube dimension. Ferrite microhardness of the 6.4 mm (0.250 in.) thick bar was also approximately 8 percent harder than the austenite regardless of heat treatment at 927°C (1700°F), 982°C (1800°F), and 1038°C (1900°F).

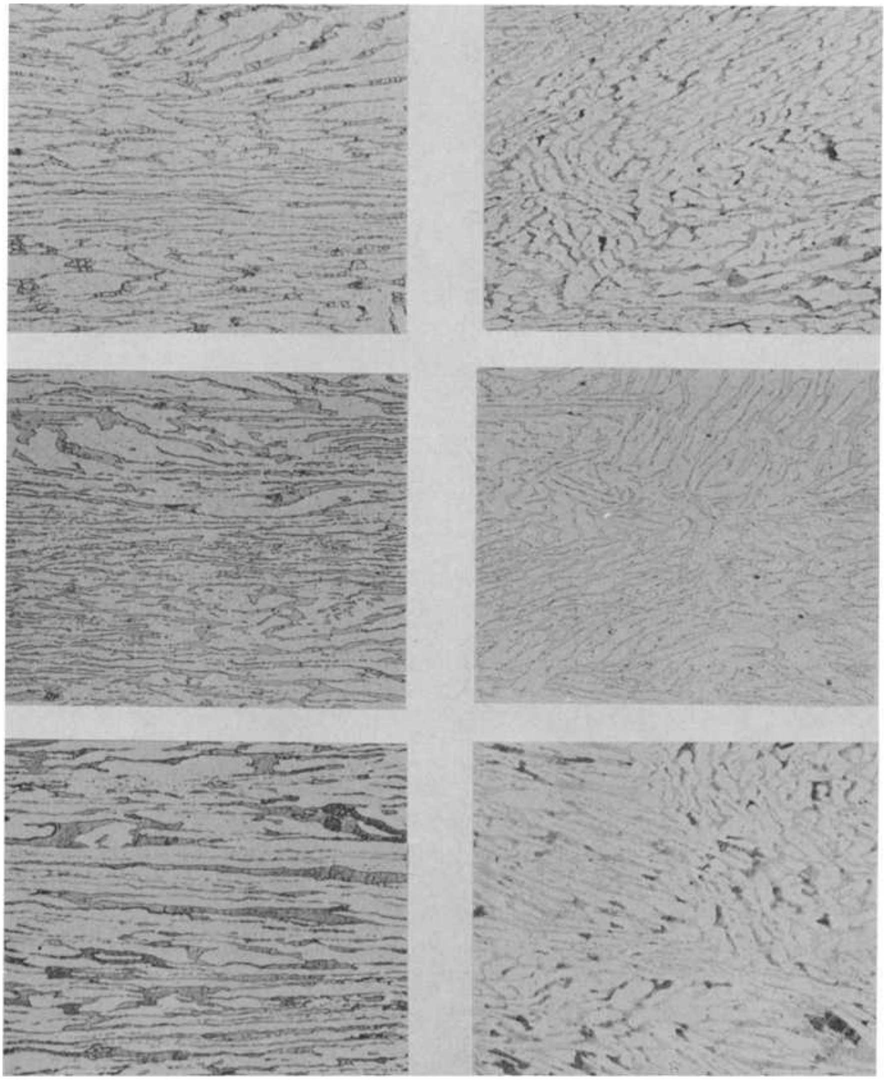

FIG. 6—*Longitudinal* (left) *and transverse* (right) *microstructure at* ~ ×*200 electrolytic 10N KOH etch. MC 20 alloy, Heat XZF18K, 6.4 mm (0.250 in.) thick bar. Process and final heat treatment at 927°C (1700°F)* (top); *at 982°C (1800°F)* (middle); *and at 1038°C (1900°F)* (bottom).

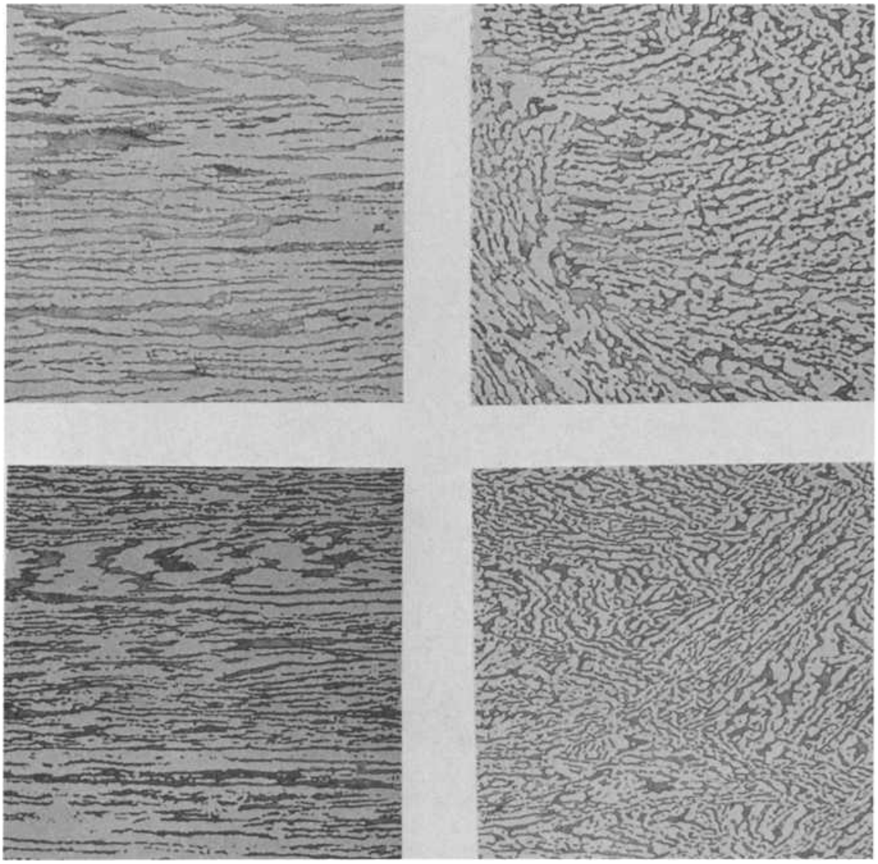

FIG. 7—*Longitudinal* (left) *and transverse* (right) *microstructure at* ~ ×*200 electrolytic 10N KOH etch. MC 20 alloy variants with molybdenum addition Heat XS3311* (top) *and Heat XS3310* (bottom) *60.3 mm (2 3/8 in.) OD by 4.2 mm (0.166 in.) wall tubing.*

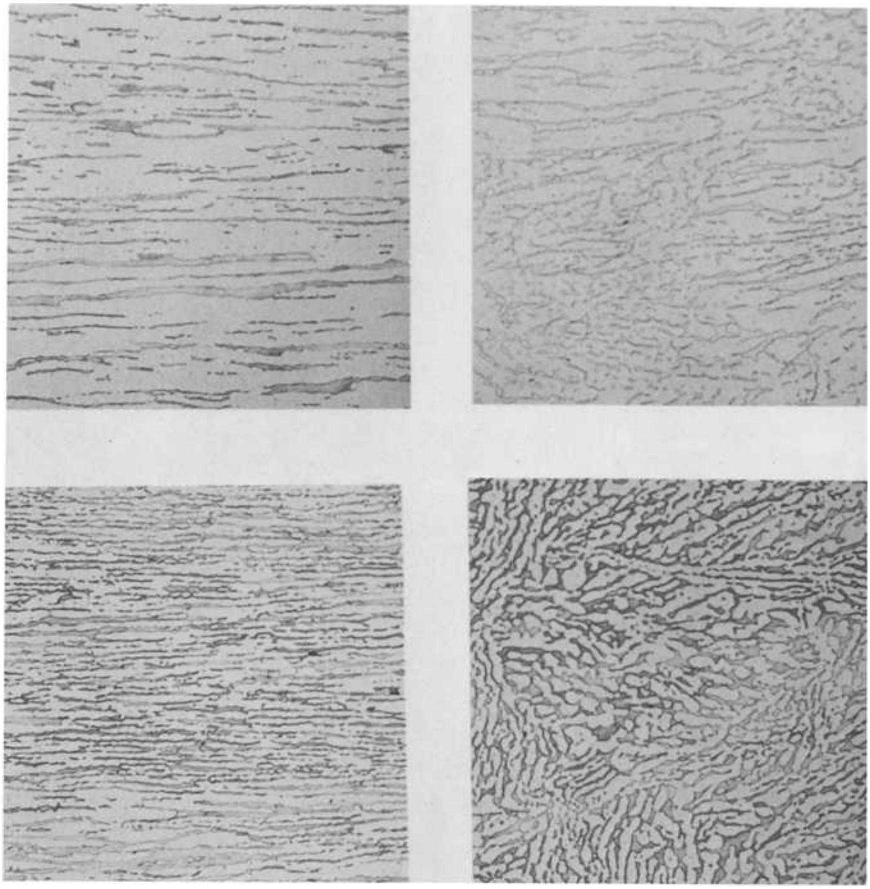

FIG. 8—*Longitudinal* (left) *and transverse* (right) *microstructure at ~ ×200 electrolytic 10N KOH etch. MC 20 alloy variants with lower nickel content Heat XS3301* (top) *and Heat XS3302* (bottom) *60.3 mm (2 3/8 in.) OD by 4.2 mm (0.166 in.) wall tubing.*

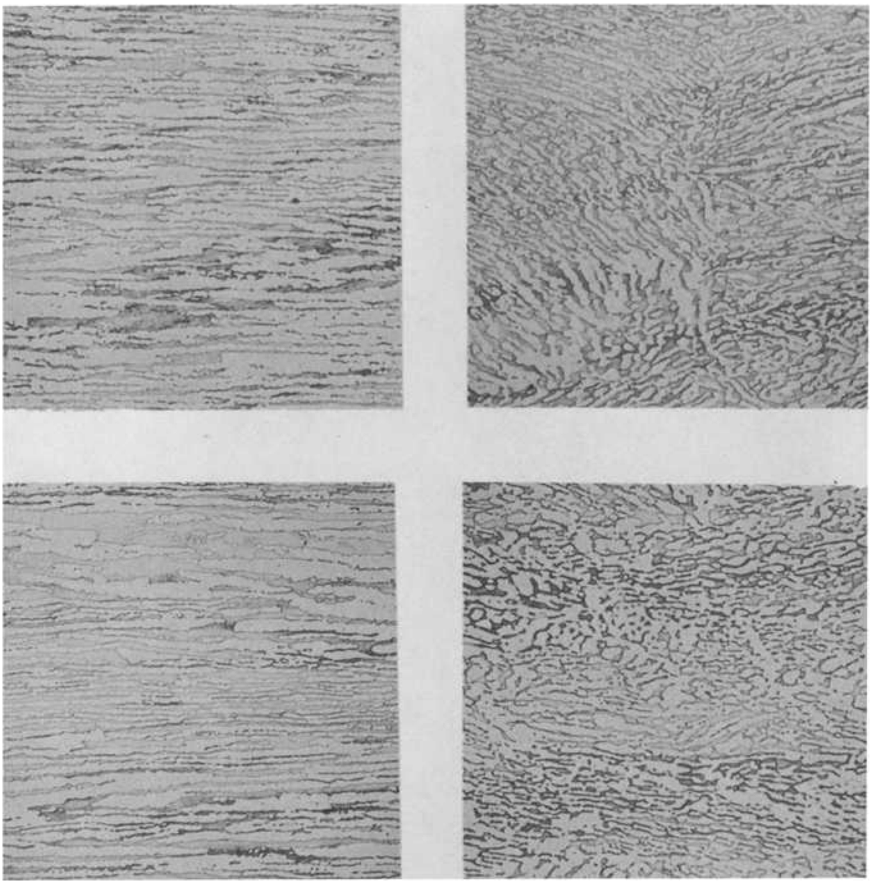

FIG. 9—*Longitudinal* (left) *and transverse* (right) *microstructure at ~ ×200 electrolytic 10N KOH etch. MC 20 alloy variants with higher chromium content, Heat XS3300* (top) *and Heat XS3312* (bottom) *60.3 mm (2 3/8 in.) OD by 4.2 mm (0.166 in.) wall tubing.*

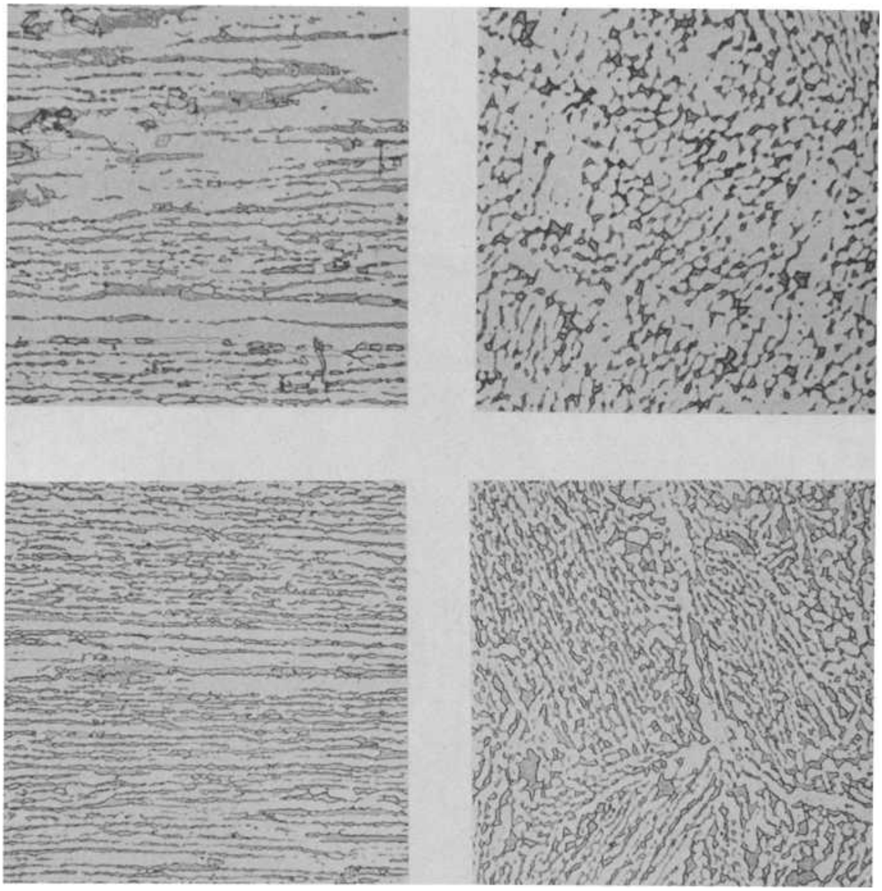

FIG. 10—*Longitudinal* (left) *and transverse* (right) *microstructure at electrolytic 10N KOH etch. MC 20 alloy variants with higher chromium and nickel content, Heat XS3303* (top) *and Heat XS3308* (bottom), *60.3 mm (2 3/8 in.) OD by 5.5 mm (0.218 in.) tubing.*

Corrosion Testing—Boiling 42 Percent Magnesium Chloride

A summary of the boiling 42 percent magnesium chloride stress corrosion cracking (SCC) resistance test results is graphically shown in Figs. 12 and 13. The results indicate a significantly improved resistance to stress corrosion cracking from centrifugal casting to wrought section as cold reduction increased. This is illustrated by the comparatively low value of 2 h to observation of cracking for the MC 20 alloy castings and 19 to 117 h for 63.5 mm (2 1/2 in.) outside diameter by 7.6 mm (0.300 in.) wall tubing produced from the same castings and alloy. Improvement continues with repetitive 70-h values for 44.5 mm (1 3/4 in.) by 4.6 mm (0.180 in.) wall tubing. MC 20 alloy 6.4 mm (0.250 in.) thick bar rolled from a

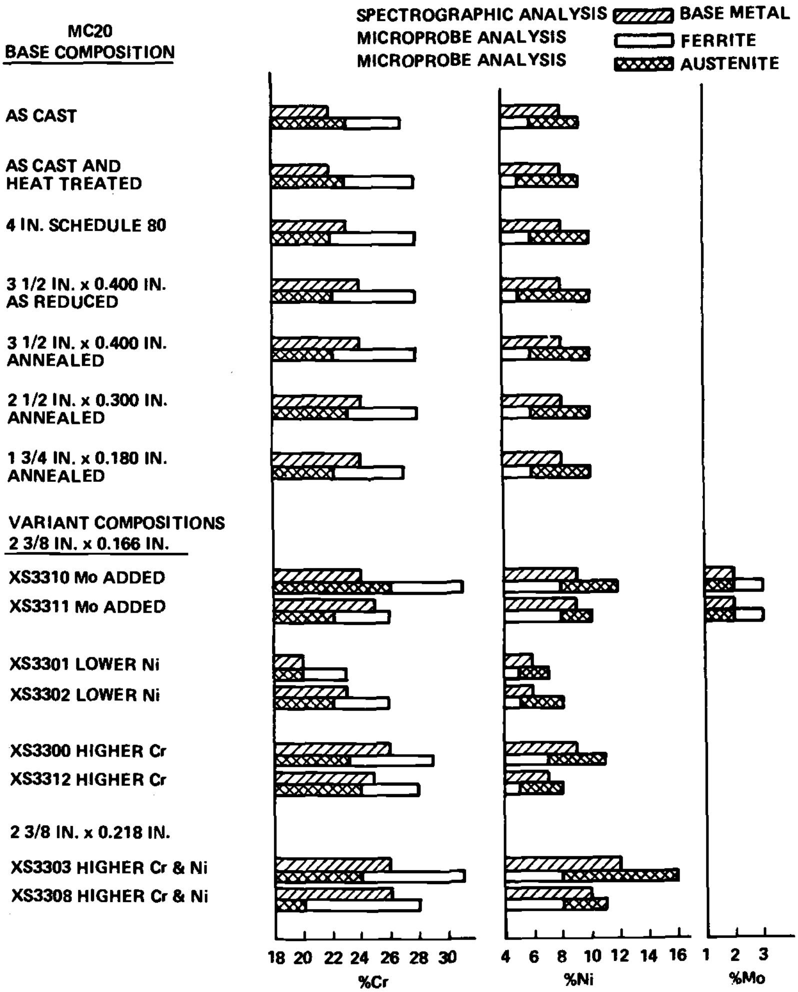

FIG. 11—*Composition of base metal, ferrite, and austenite.*

centrifugal casting section showed improved resistance to stress corrosion cracking as heat treatment temperature was increased from 927°C (1700°F) to 982°C (1800°F) and 1038°C (1900°F). One specimen prepared from a bar sample heat treated at 927°C (1700°F) failed after 124 h while another showed no failure after 768 h. Material heat treated at 982°C (1800°F) resulted in one specimen failure at 500 h and one with no failure after 768 h. Specimens representing a 1038°C (1900°F) heat treatment did not show evidence of cracking after 768 h.

The MC 20 variant alloys, XS3301 and XS3302 with 2 percent lower nickel content than the MC 20 alloy base composition, demonstrated

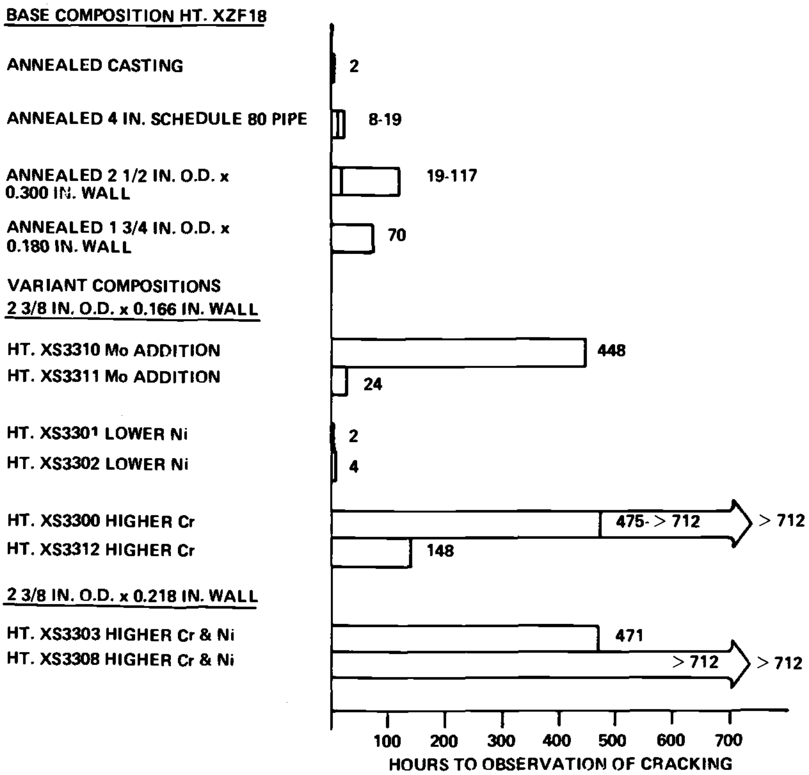

FIG. 12—*Duplex alloys. Comparative stress corrosion cracking resistance. Restrained U-bends, boiling 42 percent $MgCl_2$, MC 20 alloy variants, casting, pipe, and tube.*

much reduced resistance to SCC than variants with higher chromium and base composition nickel content (XS3300, XS3312); and those with higher chromium and nickel content than the MC 20 alloy base composition (XS3303, XS3308). Observation of cracking was noted in the XS3301 specimens within 2 h and within 4 h for XS3302 specimens. In contrast, specimens from XS3300 and XS3312 resisted cracking for at least 148 h, and one specimen of XS3312 exceeded 712 h. The increased chromium and nickel content of variant alloys XS3303 and XS3308 resulted in crack-free exposure of 471 h for XS3303 and over 712 h for XS3308. All of the variant alloy specimens were prepared from either 60.3 mm (2 3/8 in.) outside diameter by 4.2 mm (0.166 in.) wall or 60.3 mm (2 3/8 in.) outside diameter by 5.5 mm (0.218 in.) wall tubing.

Corrosion Testing—Boiling Acidified Ferric Sulfate Solution

The corrosion test results are shown as graphical representation in Figs. 14 and 15. Lowest corrosion rate trends for the MC 20 alloy base

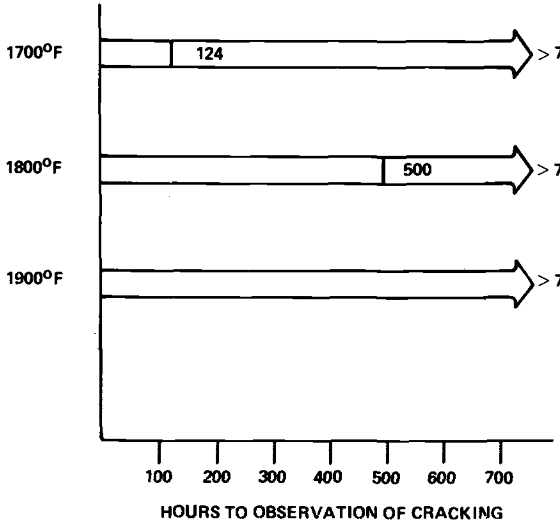

FIG. 13—*Duplex alloy Heat XZF18. Effect of heat treatment temperature on stress corrosion cracking resistance of 6.4 mm (0.250 in.) thick bar restrained U-bend, boiling 42 percent* $MgCl_2$.

composition are found in the values for annealed castings and 44.5 mm (1 3/4 in.) outside diameter by 4.6 mm (0.180 in.) wall tubing. A trend to much higher corrosion rates is demonstrated by the values obtained from 101.6 mm (4 in.) schedule 80 pipe and 63.4 mm (2 1/2 in.) outside diameter by 7.6 mm (0.300 in.) wall tubing. Values obtained from testing the same heat and alloy as 6.4 mm (0.250 in.) thick bar material are similar to those of the 44.5 mm (1 3/4 in.) outside diameter by 4.6 mm (0.180 in.) tubing. There does appear to be some improvement in corrosion resistance when the bar was heat treated at 927°C (1700°F) instead of 982°C (1800°F) or 1038°C (1900°F), but the difference is slight.

The variant MC 20 alloys with higher chromium and nickel content (XS3303 and XS3308) showed low corrosion rates as did the variant alloys with molybdenum addition (XS3310 and XS3311). The lower nickel variant alloys XS3301 and XS3302 had the highest corrosion rates among the variant compositions.

Corrosion Testing—Boiling Formic Acid

The duplex MC 20 variant with molybdenum addition, XS3311, was found to have less than one third the corrosion rate in boiling 80 percent formic acid as a fully austenitic TP-304 specimen. Since both the variant and TP-304 specimens were both prepared from tubing of approximately the same dimensions and process history, the test results should be comparatively valid. Corrosion rate for MC 20 alloy variant Heat XS3311

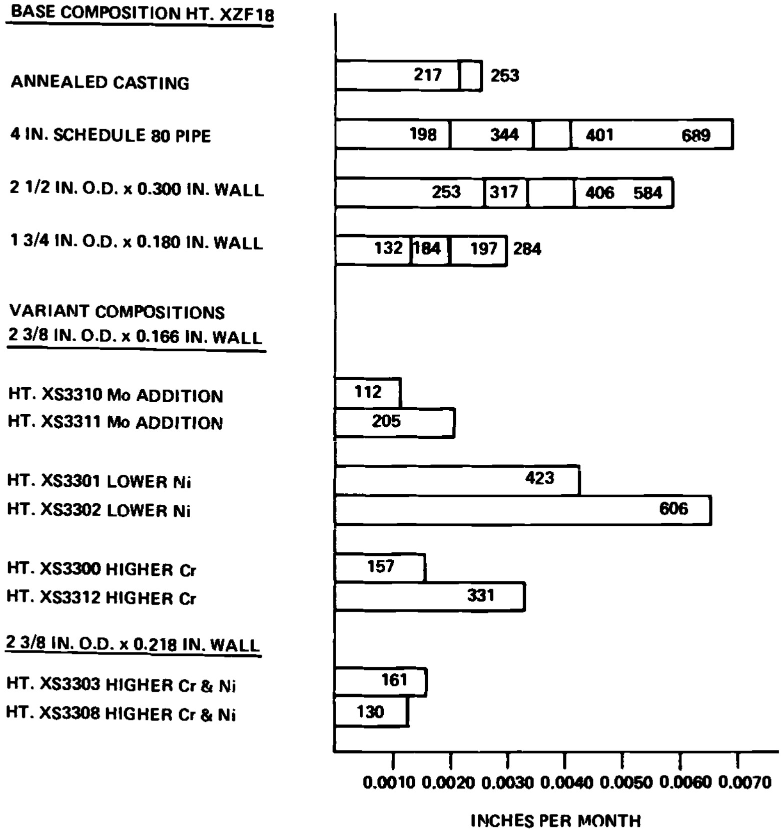

FIG. 14—*Duplex alloys. Corrosion rate in acidified ferric sulfate ASTM A 262-75 Practice B. MC 20 alloy and alloy variants, casting, pipe, and tube.*

and TP-304 Heat XS3294 were 0.61 mm (0.024 in.) and 2.3 mm (0.090 in.) per year, respectively. The comparative corrosion test results are shown in Fig. 16.

Tensile Properties

The results of tension testing are shown in Fig. 17. All results are for annealed material and are for properties parallel to the axial direction of casting, pipe, and tubing. The wrought pipe and tube of both the MC 20 base composition and variant alloy possessed yield strengths between 330.9 and 462.0 MPa (48 and 67 ksi) and ultimate tensile strength between 620.5 and 875.6 MPa (90 and 127 ksi). Elongation in 50.8 mm (2 in.) gage length ranged from 30 to 48 percent.

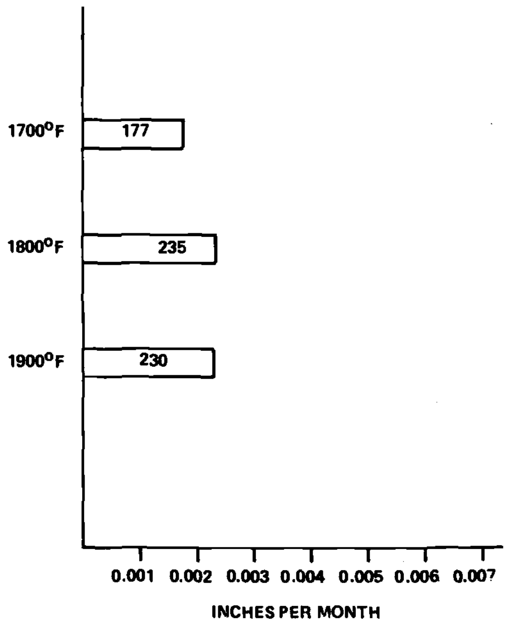

FIG. 15—*Effect of heat treatment temperature on corrosion rate in acidified ferric sulfate ASTM A 262-75 Practice B. MC 20 alloy 6.4 mm (0.250 in.) thick bar.*

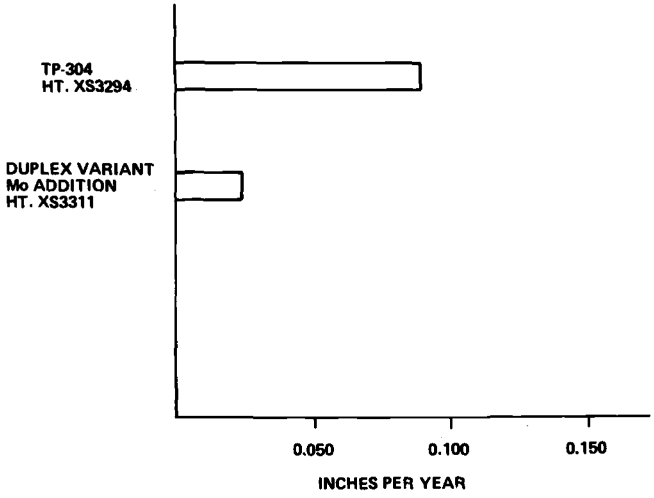

FIG. 16—*Comparative corrosion rate in boiling 80 percent formic acid, TP-304 versus duplex MC 20 alloy variant with molybdenum addition.*

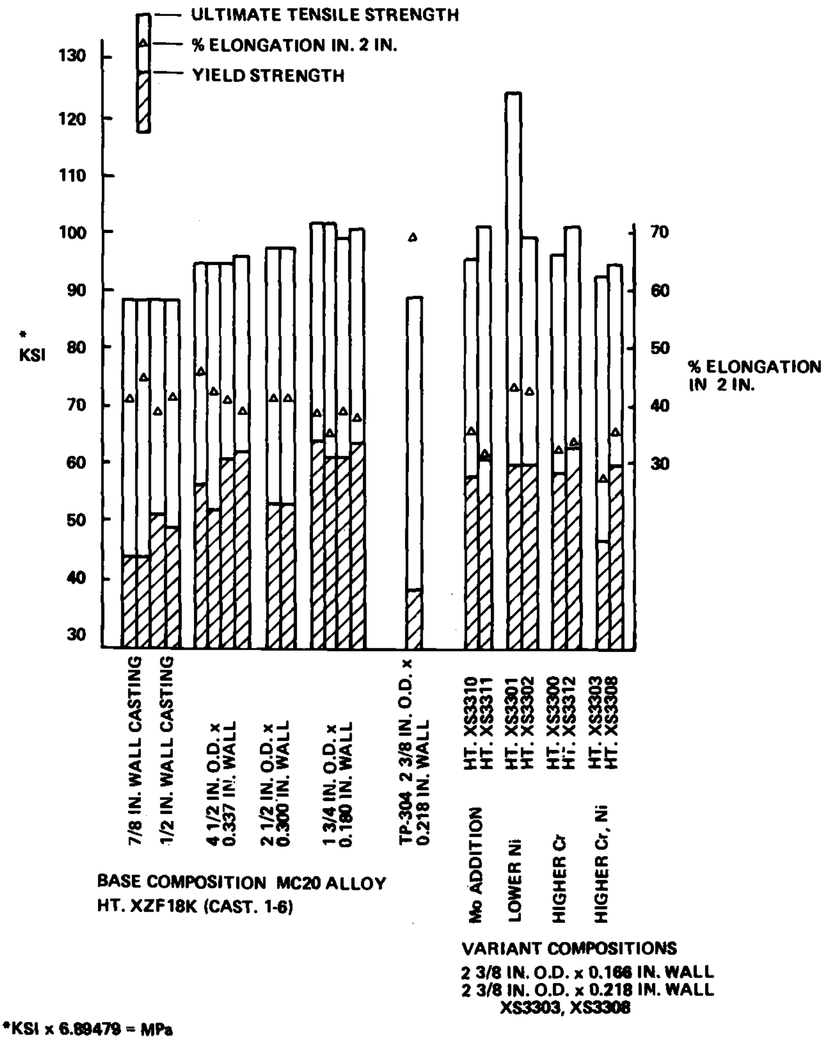

FIG. 17—*Duplex alloy tensile properties.*

Discussion

The boiling 42 percent magnesium chloride test results indicated that the stress corrosion cracking resistance of the duplex austenitic-ferritic alloys was associated with a complexity of conditions. One of the conditions could be the nature of the test procedure itself when using restrained U-bend specimens. Stress control during testing would have been better controlled with a testing technique using dead weight loaded tension specimens. However, in a previous investigation by Bodine and

Sump[3] reasonable correlation was found between restrained U-bends and dead weight loaded tension specimens. The trend towards more improved SCC resistance of the pilot production MC 20 alloy as degree of cold reduction increased was significant. The improvement might be related to the breaking up of the massive austenite networks and ferrite pools in the casting to more discontinuous distribution as cold reduction progressed. Also, the reduction of the austenite and ferrite grain size might have contributed to the improvement as well as changes in orientation of both phases. Comparison of the cast structure in Fig. 3 with the wrought structure in Fig. 5 and the corresponding improvement in SCC resistance supports the concepts regarding condition of microstructure. However, the density of ferrite distribution and composition must have an influence when considering the SCC resistance exhibited by the lower nickel content MC 20 alloy variants XS3301 and XS3302. Both variant alloys had a similar lower nickel content of approximately 6 percent as compared to the MC 20 base composition of 8 percent nickel. The 2-h and 4-h cracking times of XS3301 and XS3302 were considerably below similar tube sizes of MC 20 base composition that resisted cracking for periods of 19 to 117 h. Contribution of ferrite content might be considered when comparing the cracking time of 2 h for XS3301 with 19 percent ferrite (Magne-Gage) and 4 h for XS3302 with between 30 and 35 percent (estimated Magne-Gage). The benefit of a higher chromium content is demonstrated by the longer time to cracking for specimens representing alloy variants XS3300, XS3312, XS3303, and XS3308. Alloys XS3303 and XS3308 also included a higher nickel content as well as a higher chromium content, and this combination appeared to provide yet more improvement to the SCC resistance. The SCC resistance of MC 20 alloy 6.4 mm (0.250 in.) thick bar rolled from a casting section was consistently good, and better than the 7.6 mm (0.300 in.) wall by 63.5 mm (2 1/2 in.) outside diameter tubing of the same material. There was a trend towards improved SCC resistance as heat treatment temperature increased from 927°C (1700°F) to 1038°C (1900°F). The improved SCC resistance of the bar material introduces consideration towards the effect of processing variables.

Review of the corrosion rate testing data for pilot production base composition MC 20 alloy is somewhat puzzling. The rather extreme spread of corrosion rates for 101.6 mm (4 in.) schedule 80 pipe and 63.5 mm (2 1/2 in.) outside diameter by 7.6 mm (0.300 in.) wall tube is difficult to understand when considering the more consistent lower corrosion rates of annealed casting and 44.5 mm (1 3/4 in.) outside diameter by 4.6 mm (0.180 in.) wall tubing. The effect of heat treatment cooling rate might be considered if one excludes the casting corrosion rates. The casting was heat treated at 1177°C (2150°F) rather than the 1066°C (1950°F) used for the wrought material. Even though the cooling rate of the casting was slower, the effect of higher temperature heat treatment might have had an overriding effect. But, the corrosion rates for 6.4 mm (0.250 in.) thick MC 20 alloy bar did not show appreciable difference between heat treatment temperatures of 927°C (1700°F), 982°C (1800°F), and 1038°C (1900°F). The corrosion rates for the MC 20 alloy variant specimens prepared from 60.3 mm (2 3/8 in.) outside diameter by 4.2 mm (0.166 in.) and 5.5 mm (0.218 in.) wall tubing were essentially similar to the MC 20 alloy 44.5 mm (1 3/4 in.) outside diameter by 4.6 mm (0.180 in.) wall tubing with the exception of the lower nickel XS3301 and XS3302. The lower nickel variants had much higher corrosion rates that duplicated the poor results obtained in SCC testing.

The effect of molybdenum in the MC 20 alloy variant was particularly significant when testing in boiling 80 percent formic acid. It had been noted that MC 20 alloy base composition did not show any appreciable advantage over TP-304. But when variant alloy XS3311 with 1.6 percent molybdenum was tested againt TP-304, the results were a corrosion rate almost four times lower than that of TP-304.

Conclusions

Stress corrosion cracking resistance of medium carbon austenitic-ferritic alloy MC 20 was related to microstructure with improvement the consequence of break up of ferrite into a more discontinuous and finer structure within the austenitic matrix. Ferrite refinement increased as cold reduction and heat treatment progressed from casting to wrought section.

The resistance to stress corrosion cracking of alloy MC 20 appeared to be associated in some way with processing variables since cold rolled bar exhibited greater resistance than similar section thickness tubing that was cold reduced from the same casting. The stress corrosion cracking resistance of cold rolled bar increased as annealing temperature was raised from 927°C (1700°F) to 1038°C (1900°F).

Resistance to stress corrosion cracking was found to be reduced as the result of lowering the nickel content of MC 20 alloy and was increased by raising the chromium and nickel content.

MC 20 alloy variants with increased chromium and nickel contents or with molybdenum addition demonstrated corrosion rates lower than MC 20 when tested in acidified ferric sulfate solution as in ASTM A 262–75 Practice B.

Distribution of chromium and nickel in ferrite and austenite phases of alloy MC 20 and alloy variants was consistent in both centrifugal casting and wrought sections as determined within the limits of electron microprobe analysis. Chromium content is higher and nickel content lower in the ferrite phase in comparison to the austenite phase. Molybdenum content of ferrite in variant MC 20 alloys with molybdenum additive was almost twice that of austenite phase.

The corrosion resistance of the MC 20 alloy variant with 1.6 percent molybdenum in boiling 80 percent formic acid was consistent with the improvement of TP-316 over TP-304. This was shown by an almost four-fold improvement over TP-304.

Microhardness of the ferrite phase was generally 7 to 8 percent higher than the austenite phase. Wrought MC 20 alloy pipe and tube showed improved yield and tensile strength as compared to fully austenitic TP-304 while retaining good ductility.

H. D. Solomon[1] *and T. M. Devine*[1]

Influence of Microstructure on the Mechanical Properties and Localized Corrosion of a Duplex Stainless Steel

---

REFERENCE: Solomon, H. D. and Devine, T. M., "**Influence of Microstructure on the Mechanical Properties and Localized Corrosion of a Duplex Stainless Steel,**" *MiCon 78: Optimization of Processing, Properties, and Service Performance Through Microstructural Control, ASTM STP 672,* Halle Abrams, G. N. Maniar, D. A. Nail, and H. D. Solomon, Eds., American Society for Testing and Materials, 1979, pp. 430–461.

ABSTRACT: The alloy studied, U50, is a ferritic-austenitic duplex stainless steel. In addition to the two major phases (that is, ferrite and austenite), several additional phases form during low and intermediate temperature aging, namely, M_7C_3, $M_{23}C_6$, σ, χ, R, γ_2, and α'. This study details the precipitation of these phases and their influence on the mechanical and localized corrosion properties. The sigma phase has the most deleterious influence on the impact properties. The α' produces the largest increase in the yield and ultimate tensile strength. The precipitation of $M_{23}C_6$ and σ adversely affects the pitting resistance of U50 in 0.1NHCl because of the accompanying chromium and molybdenum depletion of the matrix. The formation of α' also severely reduces the chromium content of the ferrite phase and thereby inhibits its passivation. The large volume percent of ferrite in the alloy prevents intergranular corrosion that typically accompanies grain boundary precipitation of $M_{23}C_6$ in single-phase stainless steels.

KEY WORDS: steels, microstructure, embrittlement, duplex stainless steels, austenite, localized corrosion, pitting, ferrite, mechanical properties

A duplex stainless steel is one that contains two phases, generally austenite and ferrite, although other duplex combinations such as ferrite-martensite [*1*][2] are also possible. The alloy we have studied, Uranus 50 (U50), is an austenite-ferrite duplex stainless steel.

The existence of two phases creates a wide variety of possible microstructural combinations. In addition, neither the austenite nor the ferrite are completely stable. Their decomposition creates still more possible microstructures. The possible combinations of austenite-ferrite-

---

[1] Research and development staff metallurgists, General Electric Corporate Research and Development Center, Schenectady, N. Y. 12301.

[2] The italic numbers in brackets refer to the list of references appended to this paper.

decomposition products are too great to cover in a single paper, and, therefore, we will restrict our attention to one austenite-ferrite morphology, the morphology that is typically encountered in wrought product, and will report our findings on the influence of various additional precipitates. We shall discuss the structures and then their influence on mechanical and localized corrosion properties.

Experimental Procedures

All of the test specimens studied were made from a single heat of U50 supplied by the Creusot-Loire Steel Company in the form of a 45.7 mm (1.8 in.)[3] diameter bar. The composition of this heat is listed in Table 1. The bar was hot forged and hot rolled at 1100 to 1150°C to a 12.7 mm (0.5 in.) plate with a short (~10 min) final soak and water quench from 1150°C being used after all the hot working operations. Tensile and Charpy specimens were taken from this plate. Additionally, a 1-ft-long piece was turned into a 12.7 mm (0.5 in.) diameter bar and swaged and cold drawn into 0.8 mm (0.030 in.) diameter wire. All intermediate annealing was done at 1150°C.

Tension tests were performed on a flat friction griped specimen with a 2.5 mm by 5 mm (0.1 in. by 0.2 in.) cross section and a 12.7 mm (0.5 in.) long gage section. Standard full-size Charpy specimens were used for the impact measurements.

Transmission electron microscopy (TEM) was performed on pieces of the 12.7 mm (0.5 in.) plate that were cold rolled to 0.13 mm (0.005 in.) prior to a final 1150°C annealing treatment. The final thermal treatments on these samples and any intermediate annealing treatments were performed in evacuated quartz capsules. The TEM was performed in a 100-kV Semens microscope or a 200-kV JEOL, and preliminary polishing was in a solution of 20 percent perchloric acid in ethanol at −40°C.

In order to determine the influence of the various microstructural changes that occur with aging on the corrosion resistance of the duplex structure, anodic polarization experiments in 0.1NHCl and direct immersion corrosion experiments in acidified $CuSO_4$ were performed on 0.8 mm (0.03 in.) wires. The latter were conducted as specified by ASTM Recommended Practices for Detecting Susceptibility to Intergranular Attack in Stainless Steels (A 262–75) Practice E. Prior to testing, specimens for both tests were electrolytically polished in 60 percent H_3PO_4 plus 40 percent H_2SO_4 at 40° to 60°C for approximately 3 min at 2 A/cm^2. Samples for anodic polarization were soldered to an electrical test lead, and the area to be tested was masked off with Glyptal ®[4] paint. The anodic polarization tests were conducted in a three-electrode glass cell

---

[3] All measurements were originally made with English units.

[4] Registered trade mark of General Electric Co.

TABLE 1—*Composition of U50 heat used in this study (average of mill certification and independent analyses).*

Heat No.	Percent by Weight												Percent α
	C	Cr	Ni	Mo	Cu	Mn	Si	S	P	N	B	Ti	
83826	0.032	21.08	7.38	2.39	1.33	0.62	0.45	0.021	0.022	0.071	0.003	<0.01	33

TABLE 2—*Bulk alloy composition and composition of α and γ phases for a specimen fabricated and heat treated at 1150°C (Heat No. 83826).*

	Composition,[a] percent by weight												
	Fe	Cr	Ni	Mo	Cu	Mn	Si	C	N	S	P	B	Ti
α	65.3 ±0.3	24.0 ±0.1	5.3 ±0.1	3.1 ±0.1	1.1 ±0.1	0.66 ±0.08	0.40 ±0.02	...	...	...	...	...	...
γ	68.1 ±0.5	19.5 ±0.1	8.3 ±0.1	2.0 ±0.1	1.6 ±0.1	0.59 ±0.03	0.44 ±0.02	...	...	...	...	...	...
Bulk Alloy	balance	21.08	7.38	2.39	1.33	0.62	0.45	0.032	0.071	0.021	0.022	0.003	<0.01

[a] Bulk alloy composition (average of mill certification and laboratory analysis).

containing two platinum mesh screens that served as counter electrodes and 800 ml of electrolyte that was deaerated by bubbling ultra-high purity nitrogen through the solution at a rate of 0.2 standard cubic feet per hour (SCFH) for a minimum of 4 h prior to testing. A Luggin-Haber probe provided a low-resistance path between the anode and a saturated calomel reference electrode (SCE). Upon immersion in the test solution, samples were cathodically polarized to −1400 mV versus (SCE) for approximately 20 s. With the aid of a Princeton Applied Research potentiostat Model 173, samples were then potentiodynamically anodically polarized at a rate of 60 mV/min, starting at a potential 100 mV below the corrosion potential. This technique provided very reproducible pitting potential measurements. Samples were polarized into the transpassive region or, in cases where pitting occurred, samples were polarized until an anodic current density of 200 mA/cm^2 was attained. Following anodic polarization and ASTM A 262–75 Practice E testing, specimens were examined with an optical microscope at ×250 to ×1200 for evidence of localized corrosion. Selected samples were also viewed in a scanning electron microscope.

Results and Discussions

Microstructures

Working U50 at 1150°C produces the microstructure shown in Fig. 1. The α phase is found in bands, elongated in the working direction, in a γ matrix. Typically, working or annealing U50 at 1150°C establishes 30 to 35 percent α. Lowering the temperature below 1150°C decreases the ferrite content. The etch used in Fig. 1*a* slightly darkens the α, whereas that used in Fig. 1*b* brings out the grain boundaries.

The α phase was identified using a magnetic particle technique [2]. An external magnetic field lines up the domains in the α grains and attracts magnetic particles held in a liquid suspension. The α was further identified by electron selected area diffraction and via an X-ray microprobe analysis. The results of this analysis are listed in Table 2 where the composition of the α and γ regions are compared. A scan was made across four α and four γ regions with as many as 14 analyses being made in each region. The results of Table 2 are the averages of these readings.

The structure shown in Fig. 1 is not stable at high temperatures. Among the additional phases that have been identified are carbides, sigma, *R*, chi, α', and γ_2. The temperatures of precipitation and relative kinetics of precipitation are illustrated in Fig. 2. This figure represents a combination of the work of Hochmann et al [3] and data developed in this present study. The phases of interest are discussed in the following paragraphs.

M_7C_3—M_7C_3 precipitates at the α-γ grain boundaries at elevated

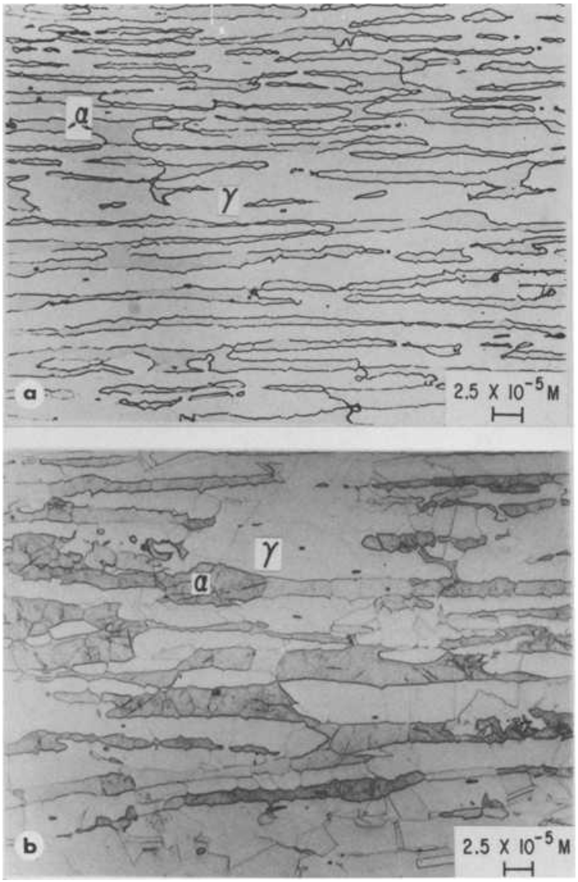

FIG. 1—*Structure of U50 established by working and annealing at 1150°C. The etch used in* (a) *darkens the α. The etch used in* (b) *delineates the α/α* and *γ/γ grain boundaries. The etch for* (a) *was electrolytic (5 VDC for 5 s) 40 percent KOH. The etch for* (b) *was 20 percent Picral in concentrated HCL.*

temperatures (950 to 1050°C). This precipitation can be avoided by cooling past this temperature region in less than about 10 min.

$M_{23}C_6$—Below 950°C, the carbide that precipitates is $M_{23}C_6$. This precipitation is very rapid, requiring less than 1 min to form at 800°C. The precipitates are found predominantly at the α-γ grain boundaries, but are also present at the ferrite/ferrite and austenite/austenite grain boundaries and to a lesser degree inside the ferrite and austenite grains.

Sigma Phase—Perhaps the most deleterious phase to form in duplex stainless steels is sigma phase. In binary iron-chromium (Fe-Cr) alloys where σ is only present below about 820°C, the rate of σ phase formation is very slow, requiring hours to form [*4*]. Therefore, it is not much of a problem in so far as transformations during cooling from higher temperatures are concerned. This is not the case in U50. The molybdenum and to a lesser extent the nickel in the α phase stabilize σ phase and allow it to form at temperatures in excess of 950°C. The σ phase that forms in U50 is probably not binary Fe-Cr but is a multicomponent phase also containing molybdenum. Figure 2 shows that one must cool past 900°C in less than 2 to 3 min to prevent its formation in the ferrite of U50. Since the σ phase greatly reduces toughness, it is important to avoid its formation. Therefore, this places the requirement that U50 must be rapidly cooled after working or annealing at 1150°C.

The formation of σ phase in U50 is illustrated in Fig. 3. Figure 3*a* shows the structure after a 3-h age at 800°C, and Fig. 3*b* after a 3-h age at 700°C. Sigma phase is not the only precipitate to form, in addition to the γ of the original structure, new γ is formed inside the α as a result of σ phase. The same thing happens when chromium is removed by carbide precipitation. Carbides are clearly seen in Fig. 3 outlining the prior α/γ grain boundaries. The chromium depletion caused by carbide formation has resulted in growth of the γ grains into the α grains.

The structure of σ phase and newly precipitated γ is more clearly shown in the transmission electron micrographs of Fig. 4. These phases were formed in the α of U50 after 100 h at 675°C. The twinned precipitate in Fig. 4*a* is γ_2, of which more will be said shortly. Austenite growing into the prior α grain as a result of σ phase precipitation can be seen in the upper right-hand corner of Fig. 4*b*. The α and γ adjacent to the σ phase particles are highly strained. This can be seen by the presence of a high

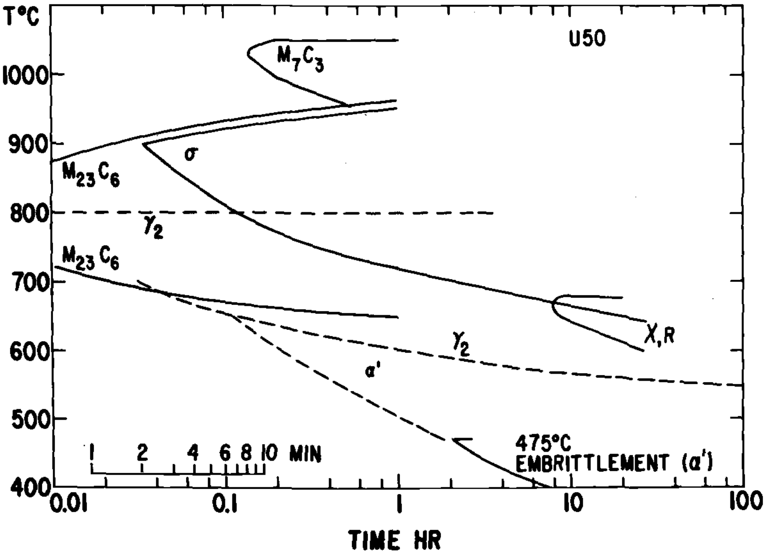

FIG. 2—*Time-temperature diagram showing the precipitation that occurs in U50.*

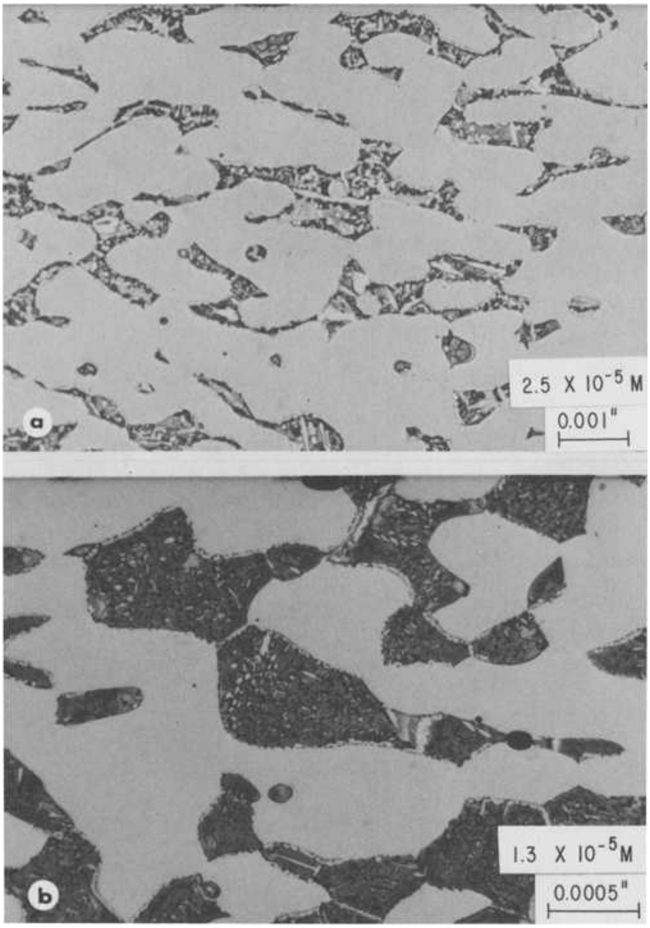

FIG. 3—*Precipitation of σ phase in U50:* (a) *after 3 h at 800°C, and* (b) *after 3 h at 700°C.*

density of dislocations (see Figs. 4*a* and 4*b*). This strain results from the large volume of the σ compared to the parent ferrite.

Chi, R *Phases*—Aging at 600 to 700°C for more than 6 to 10 h results in the formation of chi (χ) phase. Chi phase is, like σ, brittle and undesirable. It has an ordered cubic structure with a composition of $Fe_{36}Cr_{12}Mo_{10}$ [5]. Chi phase was identified via TEM and an X-ray analysis of extracted precipitates. The X-ray analysis also showed the presence of *R* phase (Fe_2Mo) that is also undesirable. The *R* phase was shown by the X-ray patterns to be present in lesser amounts than the χ phase and has not been observed in TEM. Hochmann et al [3], however, observed only *R* in their study of U50. The χ, *R* region of Fig. 2 reflects both their study and the present one by showing that both χ and *R* are present.

Gamma Precipitation in α—Two conditions that give rise to γ formation have already been discussed. Austenite is formed during the initial processing at 1150°C and also results from the subsequent precipitation of chromium- or molybdenum-rich phases. Austenite can also form inside of the α grains independently of the precipitation of other phases. This type of austenite is morphologically quite different from the first two types. To distinguish it from the standard type of γ, it will be denoted as γ_2. Hochmann et al [3] found the upper limit for γ_2 formation to be 775°C; but, in this study, it has been observed as high as 800°C (the highest aging temperature studied).

γ_2 is extremely fine and is generally not clearly resolved by light microscopy. The darkening of the ferrite grains shown in Fig. 5 is a manifestation of barely resolved γ_2. (Figure 5*a* is from a specimen aged 100 h at 600°C and Fig. 5*b* from one aged 300 h at 550°C.)

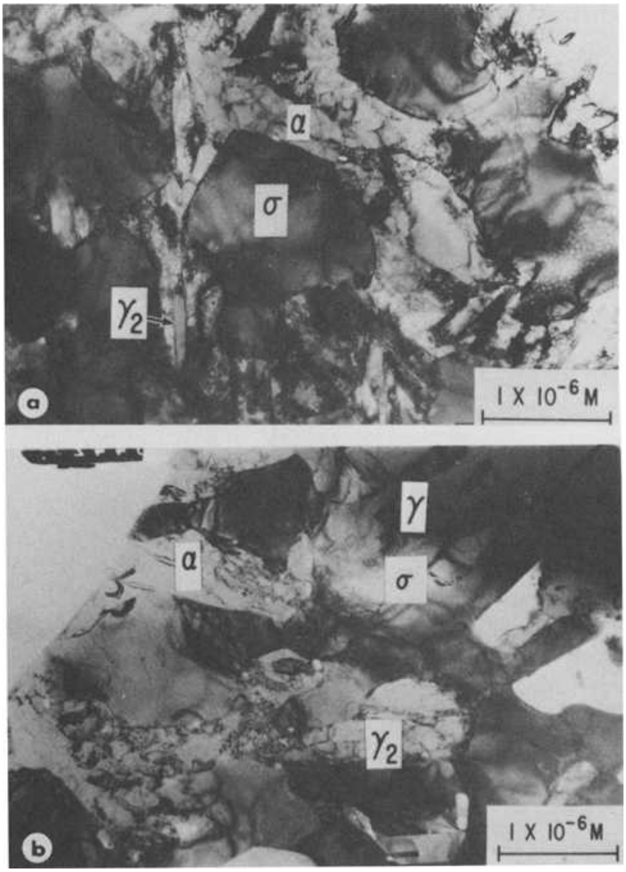

FIG. 4—*TEM of precipitation in U50 after 100 h at 675°C.*

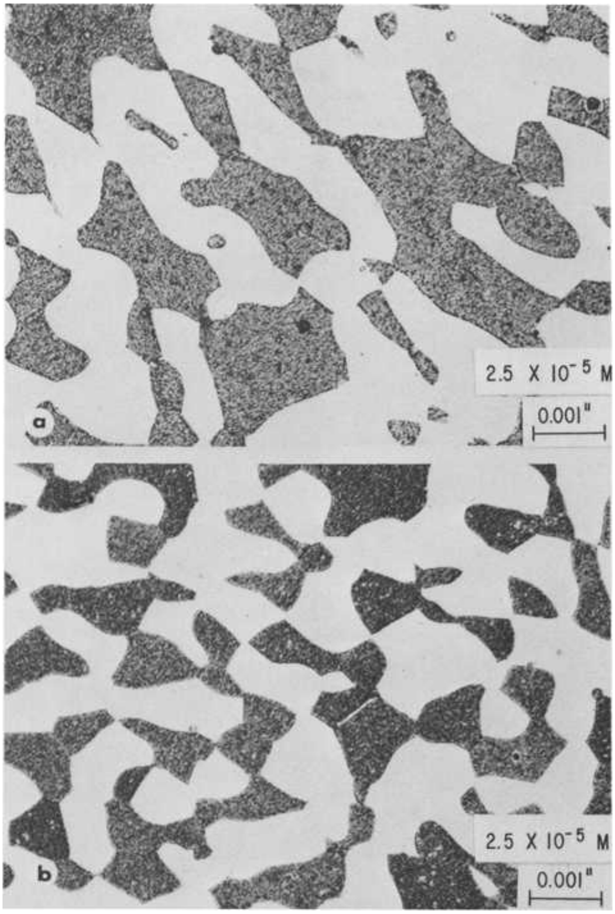

FIG. 5—*Precipitation of* γ_2 (a) *after 100 h at 600°C and* (b) *after 300 h at 550°C.*

The characteristic structure of γ_2 is shown clearly in Fig. 6. (The structures shown in Figs. 6*a* and *b* were established at 621°C after 100 h and that of Fig. 6*c* after 2 h at 800°C). γ_2 is characterized by its being lath-like in shape with a midrib separating the twinned regions. It can form in the absence of σ or $M_{23}C_6$, as in Fig. 6*c*, or where these phases are present (as in Fig. 4*a*).

There are fine precipitates that have the same relative orientation to the α matrix as the γ_2. This is clearly shown in Fig. 6*a*. These small precipitates can be very fine or incipient γ_2 or possibly copper precipitates [*6*]. Copper precipitates in α iron have the same morphology as that observed in Fig. 6*a* [*7*]. Unfortunately, they are almost impossible to distinguish from fine γ_2 since both phases have almost the same lattice parameter and precipitate in α with the same habit relationships.

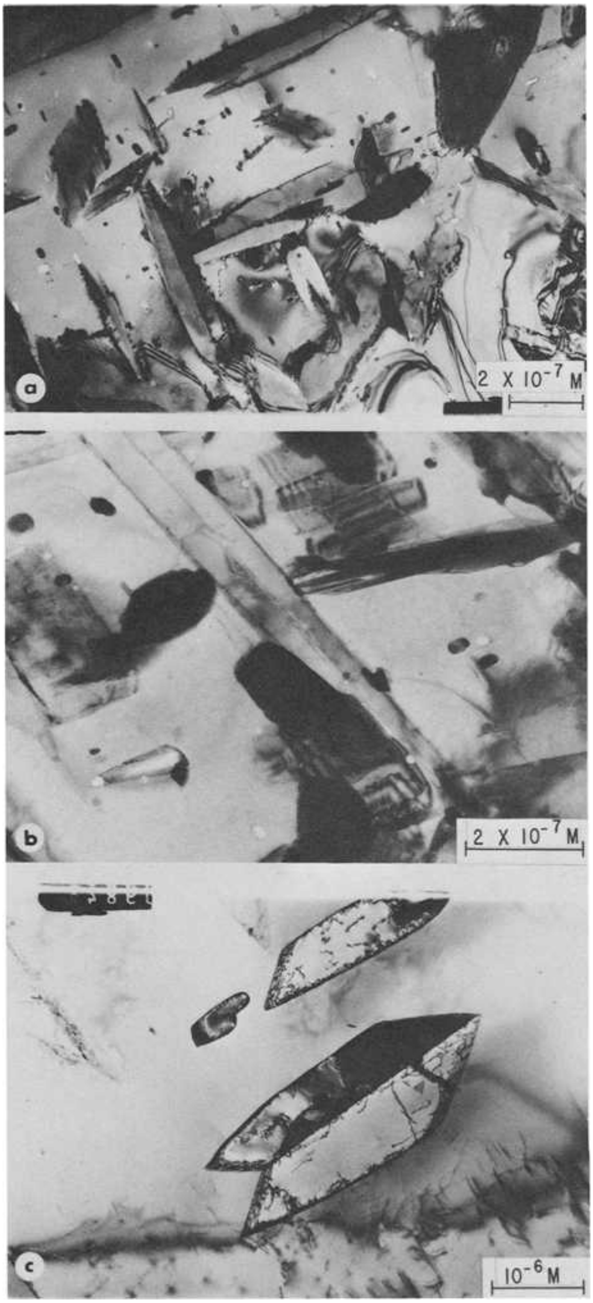

FIG. 6—*TEM of* γ_2 *in U50, (*a*) after 100 h 621°C, (*b*) after 100 h at 621°C, and (*c*) after 2 h at 800°C.*

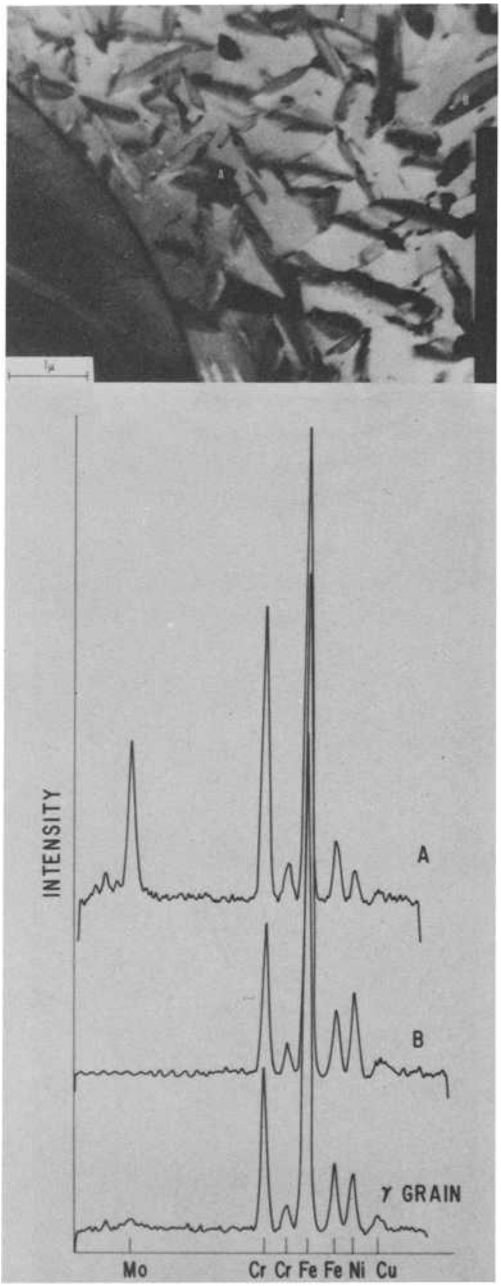

FIG. 7—*Scanning transmission micrograph showing the structure of U50 after aging 100 h at 621°C. The X-ray spectra from a* χ *phase precipitate (A) and a* γ_2 *precipitate (B) are shown along with the spectra for a* γ *grain.*

The dark precipitate adjacent to the γ_2 in Figs. 6*a* and *b* has been identified from selected area diffraction as χ phase. This analysis has also been substantiated by X-ray fluorescence in a scanning transmission electron microscopy investigation. A scanning transmission electron micrograph is shown in Fig. 7. The X-ray fluorescence spectrum from the precipitate marked A is also shown. The identification of the particle as χ was determined following the technique of Weiss et al [*8*]. They determined that the molybdenum-to-chromium and the iron-to-chromium signal intensities are characteristic for different types of precipitates. The intensity ratios of the spectrum of Region A correspond to the χ phase. The signal from the γ_2 region (B in Fig. 7) was the same as that of the massive γ of the duplex structure. This further confirms the identification of the lath-like twinned phase as austenite. The resolution of the X-ray analysis was not sufficient to identify the nature of the very fine copper or γ_2 phase, so this technique could not be used to make the distinction between the two phases.

475°C Embrittlement (α')—The lowest temperature decomposition of the ferrite of U50 is that associated with the precipitation of α'. Hochmann et al [*3*] did not consider the structure of U50 below 600°C. The α' and 475°C embrittlement regions of Fig. 2 were drawn with the aid of the microscopy and impact data of this study.

The phenomenon of 475°C embrittlement results from the separation of the ferrite of Fe-Cr alloys into an iron-rich α phase and a chromium-rich α' phase. This can result from an eutectoid transformation of $\sigma \rightarrow \alpha + \alpha'$ or by the direct decomposition of α. The eutectoid decomposition is theoretically possible; but, it is kinetically limited and, in practice, is not observed. If one cools rapidly enough to avoid σ, then it has been proposed that a miscibility gap is present in the Fe-Cr system [*9*]. Inside

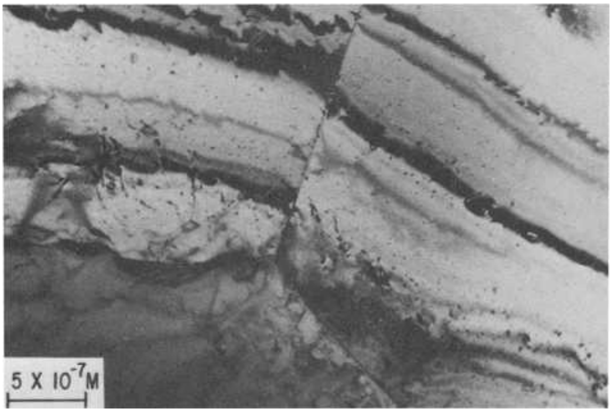

FIG. 8—*High-temperature precipitation of α' in U50 (after 2 h at 600°C). The γ grain is clear, only the α grains show α'.*

of this gap, there is a separation of α into iron- and chromium-rich phases. It has been shown [*10*] that, in the α of the U50, spinodal decomposition at 475°C produces iron- and chromium-rich regions and that α' forms from chromium-rich regions by 118 h. The same process, that is, spinodal decomposition leading to the end product α' phase, occurs in binary Fe-Cr alloys, but it takes about an order of magnitude longer for the α' phase to form than in the multicomponent ferrite of U50 [*10*].

The ferrite of U50 also differs from binary Fe-Cr alloys in that α' has been observed [*11*] to form at 600°C whereas in binary alloys with the same chromium content, 525°C appears to be about the upper limit for α' formation. The formation of α' at 600°C in the α of U50 is illustrated in Fig. 8. The α' precipitates are more widely spaced than those found at 475°C (see Fig. 9) and, as shall be discussed, are much less strengthening and embrittling. For this reason, the high-temperature α' precipitation has

FIG. 9—*Precipitation of α' in U50 after aging 474 h at 475°C. The α' is only present in the α grain and is not present in the two γ grains also shown in this figure.*

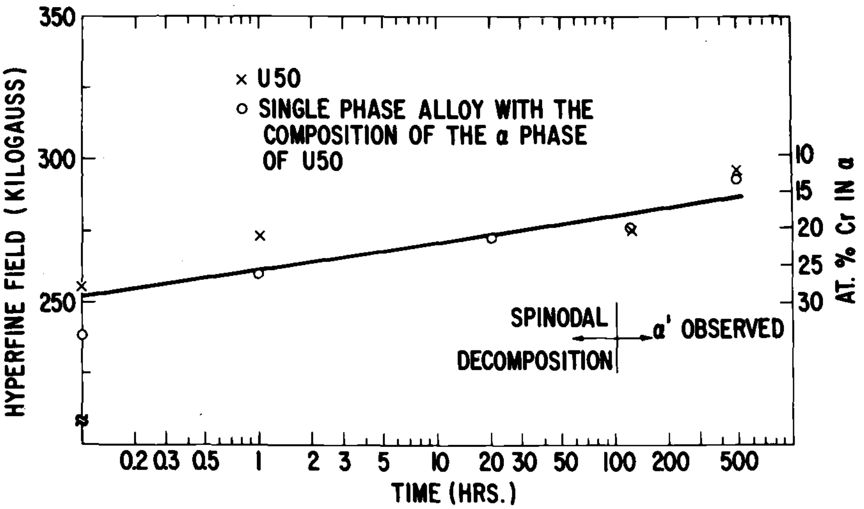

FIG. 10—*Variation in the hyperfine field as a function of aging time for U50 and a single-phase ferritic alloy with the composition of the α of U50.*

been distinguished in Fig. 2 from that occurring at about 475°C. This high-temperature α' is also metastable and disappears after longer aging times when other phases precipitate [*11*].

Both spherical [*12*] and plate [*12,13*] morphologies have been reported for α' in Fe-Cr alloys. The absence of streaking on the diffraction spots and a variation in the line of no contrast of the precipitates point to the precipitates being spherical in U50 after a long time 475°C aging treatment [*10*]. These precipitates are shown in Fig. 9. As can be seen, the α' is present only in the α and not the γ phase.

The phase separation and α' phase formation results in a reduction of the chromium level in the remaining α phase. The magnitude of the remaining chromium was estimated via Mössbauer spectroscopy [*10*]. The chromium level was estimated from the variations in the hyperfine field with aging time and is shown in Fig. 10. Figure 10 shows that aging at 475°C results in a depletion in chromium in the α as a result of spinodal decomposition and finally from the formation of the α' phase. Spinodal decomposition and the formation of α' thus not only strongly influence the mechanical properties of the α phase of U50 but can also influence the corrosion properties.

Relationship of Microstructure to Mechanical Properties

Annealed Unaged U50—Undirectional hot working of U50 gives rise to an anisotropic structure. This anisotropy is illustrated in Fig. 11. The microstructure shown in this figure was established by rolling at 1100 to

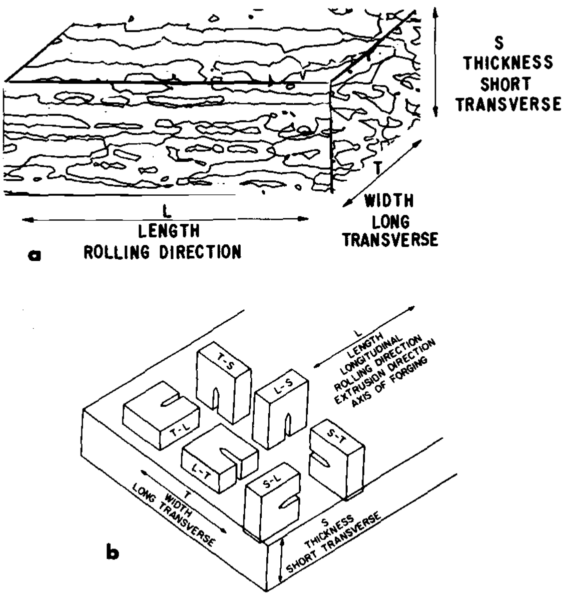

FIG. 11—(a) *Three-dimensional view of the standard U50 microstructure.* (b) *Types and nomenclature for Charpy specimens.*

1150°C and water quenching from 1150°C. Tension and Charpy specimens were cut from this plate. Two different orientations were studied in order to ascertain the influence of anisotropy on impact properties. LS specimens were oriented such that the fracture surface was normal to the L direction with the crack propagation in the S direction (see Fig. 11*b*). TL specimens were oriented such that the fracture surface was normal to the T direction, and the crack propagation was in the L direction. These orientations were chosen because fracture in the LS specimens cuts across the α and γ bands. In the TL specimens it is in the direction of the elongation of the bands. The effect of the microstructural anisotropy on the room-temperature Charpy energy is clearly shown in Table 3. The average ratio of the impact strength of the LS specimens to that of the TL specimens, heat treated in the same manner, was roughly 2.5. This same behavior was also noted in specimens embrittled by various supplementary heat treatments, but there is a greater spread in the ratio of the impact energies. This is shown in Table 4. The average ratio of the embrittled specimens is 2.5 ± 1 compared to 2.5 ± 0.1 for the unaged specimens.

A misleading impression of the impact behavior can be obtained if only one orientation is examined. The anisotropy must be kept in mind when considering impact data. Depending on the orientation of the microstructure relative to a fabricated part, it may be necessary to design with the lower TL impact values than with those of the LS specimens. For

TABLE 3—*Room-temperature Charpy energy for specimens in the standard condition (final heat treatment—1100 to 1150°C; Cv at room temperature ft·lb).*

Specimen No.	Cv (ft · lb)[a]		Remarks	LS/TL
	LS	TL		
20	240	. . .	Specimens were annealed 2 h at 1150°C. Plate rolled at 950°C.	2.6
10	. . .	91		
301	. . .	90	Plate rolled at 1100°C. No heat treatment of Charpy specimens.	2.4
326	218	. . .		
1003	. . .	75	Plate rolled at 1150°C. No heat treatment of Charpy specimens.	2.6
1020	193	. . .		
1002	. . .	98	As for Specimens 1003 and 1020 plus 2 h at 1150°C.	2.4
1004	. . .	98		
1021	240	. . .		
1022	205	. . .		
1044	240	. . .		

[a] 1 ft·lb = 1.356 J.

instance, the impact energy for a longitudinally propagating, through-wall crack (such as that caused by a hoop stress over load) would be measured by TL specimens where the microstructure is elongated in the tube axis direction (which would be the case for seamless drawn or extruded tubes).

Figure 2 and the Charpy data presented in this section show that U50 must be cooled past 950°C in less than 3 min to prevent the onset of σ phase embrittlement or variations in the amount of $M_{23}C_6$. Thus, cooling rate variations can result in variations in the toughness of specimens cooled from the 1100 to 1150°C annealing temperature. The relatively rapid kinetic of σ phase and $M_{23}C_6$ formation may make the achievement of the maximum toughness impossible in large section components. The influence of cooling rate is reflected in Table 3. Specimens 301, 326, 1003, and 1020 (see Table 3) were tested without any additional heat treatment

TABLE 4—*Variation of room-temperature Charpy energy with orientations for embrittled samples.*

Specimen	Cv (ft · lb)[a]		Aging Treatment	LS/TL
	LS	TL		
303	. . .	55	475°C, 2 h	2.5
334	140.0	. . .	475°C, 2 h	
313	. . .	43.5	475°C, 100 h	1.5
338	66.0	. . .	475°C, 100 h	
318	. . .	40.0	621°C, 40 h	1.6
329	64.0	. . .	621°C, 40 h	
319	. . .	13.5	621°C, 40 h + 475°C, 2 h	3.5
363	47.0	. . .	620°C, 40 h + 475°C, 2 h	

[a] 1 ft·lb = 1.356 J.

of the Charpy specimens. The plates from which these specimens were prepared were rolled at 1100 and 1150°C and then water quenched after a short soak at the process temperature. The impact energies were slightly lower than those of the Charpy specimens that had received an additional 1150°C anneal. This is especially true for Specimens 1003 and 1020. This behavior is probably caused by slower cooling rate of the plates compared to that of the less massive Charpy test specimens.

Tension specimens were made from the rolled plates used for the Charpy specimens. These tension specimens had 12.7 mm by 5 mm by 2.5 mm (0.5 in. by 0.2 in. by 0.1 in.) gage sections. They all had the 5 mm (0.2 in.) dimension taken through the plate. Some were oriented with the 12.7 mm (0.5 in.) length of the gage section in the rolling direction (denoted as L specimens), and some (T specimens) had the specimen length in the long transverse or width direction of the plate whose final thermal treatment was a water quench from 1100 to 1150°C. The tensile data are shown in Table 5. True stress-strain curves were constructed for several specimens and a strain hardening rate $n = \ln\sigma/\ln\epsilon = 0.20 \pm 0.02$ was measured. No tensile anisotropy was observed between L- and T-type specimens.

The tensile and impact properties of annealed U50, which are summarized in Tables 3 and 5, characterize this alloy as having moderate strength coupled with good ductility and moderate to excellent impact properties, depending upon orientation. However, these properties are degraded by the thermal treatments described in the following section.

Aged Specimens—The reduction in impact strength (of LS specimens) due to aging at temperatures of 550 to 900°C is shown in Fig. 12. Prior to the aging treatments, an 1100 to 1150°C anneal was employed if the plate fabrication procedures did not result in room-temperature Charpy energies of at least 200 ft · lb for the LS specimens.

Between 900°C and about 625°C, the embrittlement shown in Fig. 12 resulted primarily from the formation of σ phase. The stabilization of σ resulting from the molybdenum allows σ to form at 900°C, where the rate of embrittlement is quite rapid. σ phase can also form above 900°C; but,

TABLE 5—*Tensile results for specimens in the standard condition (final heat treatment, 1100 to 1150°C).*

Specimen No.	Orientation	σ_y[a](0.2%) ksi[b]	σ_{uts}[a], ksi	Uniform Elongation, %	$\Delta A/A_0$, %
23	L	56.0	92.0	26	80
54	T	55.0	95.5	27	74
1061	L	56.0	87.0	27	80

[a] Crosshead rate = 0.1 in./min.
[b] 1 ksi = 6.8948 MN/m^2.

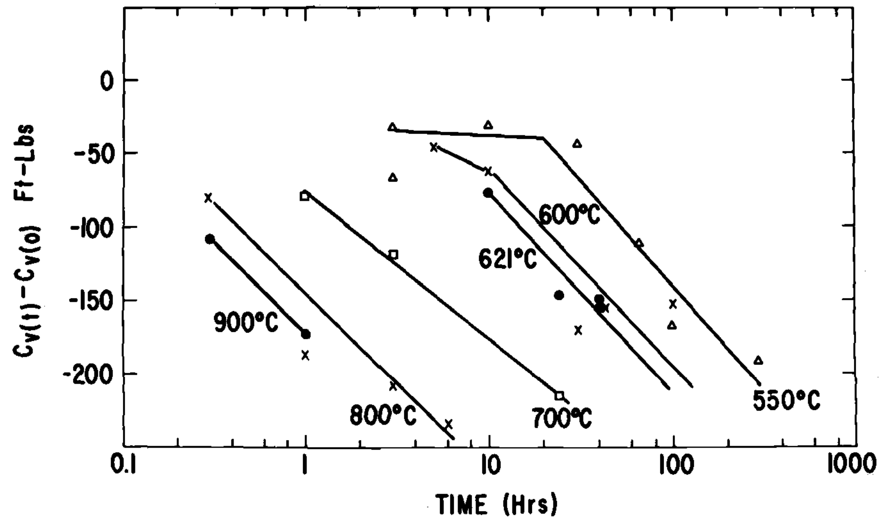

FIG. 12—*Drop in impact energy (measured at room temperature) as a function of time at different temperatures. 1 ft·lb = 1.356 J.*

owing to the typical C-curve kinetics exhibited by the precipitation, the rate of formation is lower than at 900°C.

No metallographic evidence of σ phase was found in specimens aged at below 600°C. Between 550 and 621°C, χ, γ_2, and $M_{23}C_6$ embrittlement are the probable causes of the observed reduction in impact energy. The results of aging at 500 to 550°C are shown in Fig. 13. Within experimental error, the behavior at all three temperatures is the same.

As has been noted, α' precipitation was observed in the range of 475 to 600°C (after 100 h at 475°C, 10 h at 525°C, and as little as 10 min at 600°C). The α' that forms at 600°C precipitates more rapidly than at 475°C, but it is much more coarsely spaced. The mean spacing between precipitates is about 5000 to 10 000 Å as compared to 100 to 250 Å for α' formed at 475°C. As expected from hardening models, this widely spaced α' cause much less of an influence on the mechanical properties. Aging 8 h at 600°C produces less than a 50 ft·lb decrease in impact energy. Further aging at 600°C will produce increased embrittlement, but this is due to the precipitation of other phases, in fact, there is evidence [*11*] that as these phases precipitate the α' goes into solution.

In contrast to the behavior at 500 to 600°C, there is considerable 475°C strengthening and embrittlement at lower temperatures. As has been described in the preceding section, the sequence of events at 475°C is that of a phase separation into iron- and chromium-rich regions, via spinodal decomposition, followed by the formation of the end product α' phase. The spinodal decomposition occurring in even 2 h at 475°C produces a significant alteration in mechanical properties. Further aging for about

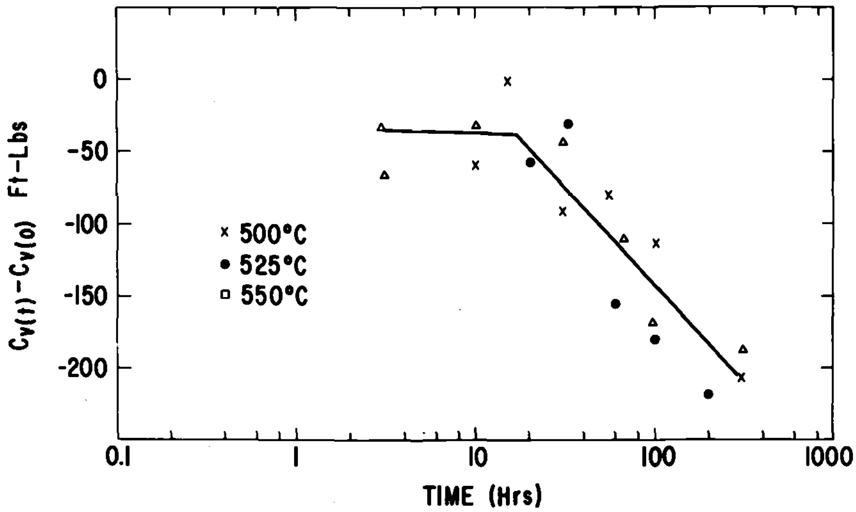

FIG. 13—*Drop in impact energy (measured at room temperature) as a function of aging time at 500, 525, and 550°C. 1 ft·lb = 1.356 J.*

24 h results in further spinodal decomposition [*10*] that produces further strengthening and embrittlement (see Table 4 and Fig. 14). Aging further to about 100 h, which now results in α' now being resolved in TEM, does not increase the strength but does increase the degree embrittlement.

The kinetics of 475°C embrittlement after aging at 475°C and below is clearly shown in the Charpy data of M. T. Wang [*14*]. His data have been replotted in Fig. 14. The results for Heats 84190 and 31302 are shown in this figure. Heat 31302 has a slightly higher ferrite content that, together with possible cooling rate variations, caused the initial room temperature Charpy energy of the mill-annealed specimens of this heat to be lower than that of specimens from Heat 84190. With the higher percent α, the influence of 475°C embrittlement of the α phase is generally greater for Heat 31302 than for Heat 84190 (the data for Heat 31302 are in most cases the lower of the two data points for each time at the four temperatures). The impact energy decrease caused by aging has been plotted so that the results from the two heats can more easily be compared. Data points gathered on the heat used in the present study are also displayed in Fig. 14. With the exception of the data obtained at 475°C after 100 h, all of the impact energy decrease is due to spinodal decomposition with no resolvable α' being present.

The results of Figs. 12, 13, and 14 have been used to construct Fig. 15. Each curve represents a given degree of embrittlement as measured by the room-temperature Charpy energy. It appears that the σ phase embrittlement can be separated from the embrittlement caused by χ, γ_2, or $M_{23}C_6$. The data of Fig. 15 probably represent five C-curves: one for

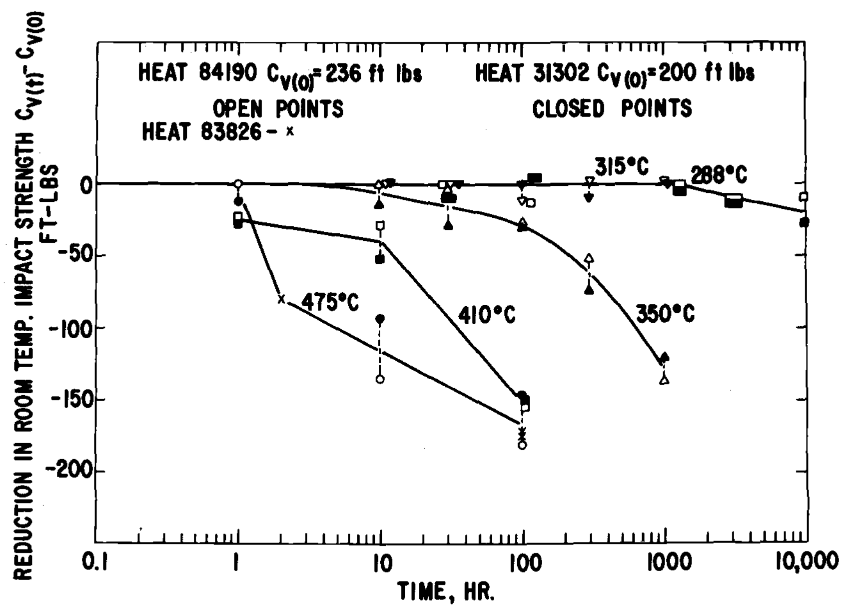

FIG. 14—*Drop in impact energy (measured at room temperature) as a function of aging time at 288 to 475°C. The data from Heats 84190 and 31302 are from the work of Wang (Ref 17). 1 ft·lb = 1.356 J.*

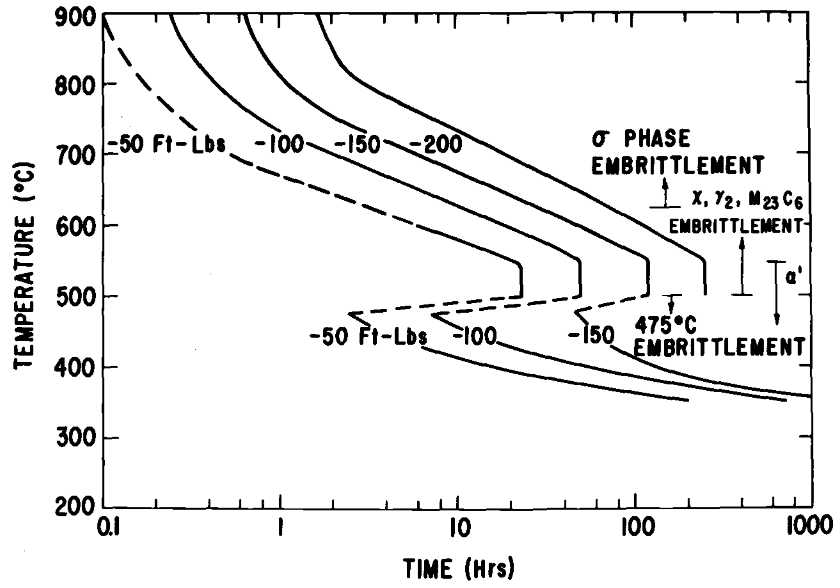

FIG. 15—*Temperature-time-relationship for a given decrease in Charpy energy. 1 ft·lb = 1.356 J.*

the σ phase; one each for χ, γ_2, or $M_{23}C_6$; and one for 475°C embrittlement. (The high-temperature α' produces less than a 50 ft · lb decrease in Charpy energy and has therefore not been included in this figure.) Unfortunately, the C-curves for the influence of χ, γ_2, or $M_{23}C_6$ are impossible to differentiate from each other and difficult to differentiate from that resulting from σ phase embrittlement.

The presence of the various embrittling phenomena limit the possible time-temperature regions where U50 can be heat treated or used. The annealing temperature has been set above 1000°C to avoid σ phase formation. Below 500°C, the time at temperature is limited by the phenomenon of 475°C embrittlement. Figure 15 clearly shows that the temperature region of 500 to 550°C is the optimum one in which to perform nitriding or stress relieving of U50. In this range, aging for as long as 20 h results in little or no embrittlement.

The influence on the tensile properties of aging at temperatures of 475 to 800°C is shown in Table 6. As can be seen, the high-temperature aging associated with σ phase formation does not increase σ_y or σ_{uts}. However, this brittle phase did reduce the uniform elongation and $\Delta A/A$. σ phase does not strengthen, it only embrittles.

The strain hardening exponent, n, is not altered when σ precipitates in the α. This is not surprising since the work hardening of duplex steels is determined primarily by the γ phase [*15*] that is unchanged by the aging treatment. The reduction in the uniform elongation and $\Delta A/A$ results from the σ induced brittleness of the α phase not by the normal necking of the γ.

In contrast to the behavior when σ precipitates, spinodal decomposition and α' precipitation at 475°C and below produce considerable strengthening (the beginning of which can be seen after 2 h at 475°C). The α' that forms, or spinodal decomposition leading up to it, does not act as a brittle phase. The uniform elongation and $\Delta A/A$ are only slightly reduced by aging at 475°C, even after aging 100 h where α' is noted. The high strain rate notched performance is however reduced as witnessed by the drop in impact strength with aging at 475°C, but this is compensated for by increased strength. Short-time aging at 475°C can be a useful strengthening procedure. Two hours aging at 475°C raises the yield strength to about 517.5 MN/m^2 (75 ksi) while retaining a room temperature impact strength of 190 J (140 ft · lb).

Localized Corrosion Properties

Figure 16 summarizes the results of the pitting potential measurements obtained on U50 as a function of aging treatment. The as-annealed and quenched material possessed good pitting resistance. Its pitting potential ranged from a low of 600 mV to a value above 700 mV. Transpassivity occurred at potentials above 900 mV. When pitting occurred during

TABLE 6—*Tensile results.*

Specimen No.	Orientation	$\sigma_y{}^a$(0.2%) ksi[b]	$\sigma_{uts}{}^a$, ksi	Uniform Elongation, %	$\Delta A/A$, %	Plate Rolling Temperature, °C	Anneal, °C	Age
23	L	56.0	91.5	26	80	950	1150, 2 h	none
28	L	53.0	98.5	17	35	950	1150, 2 h	800, 6 h
30	L	60.5	102.0	18	60	950	1150, 2 h	621, 40 h
54	T	55.0	95.5	27	74	950	1150, 2 h	none
55	T	50.5	101.0	13	20	950	1150, 2 h	800, 6 h
56	T	68.5	113.5	21	67	950	none	475, 2 h
30	L	60.5	102.0	18	60	950	1150, 2 h	621, 40 h
404	L	60.0	102.5	9	21	1100	none	700, 24 h
405	L	80.0	110.5	27	78	1100	none	475, 2 h
470	T	79.2	121.0	24	63	1100	none	475, 24 h
471	T	72.9	125	24	61	1100	none	475, 100 h
472	T	71.0	130	21	57	1100	none	475, 500 h
1061	L	56.0	87.0	27	80	1150	none	none
1062	L	84.8	111.0	24	75	1150	1150, 2 h	475, 24 h
1063	L	86.2	116.0	22	71	1150	1150, 2 h	475, 100 h
1064	L	81.4	120	15	68	1150	1150, 2 h	475, 500 h

[a] Crosshead = 0.1 in./min.
[b] 1 ksi = 6.8948 MN/m^2.

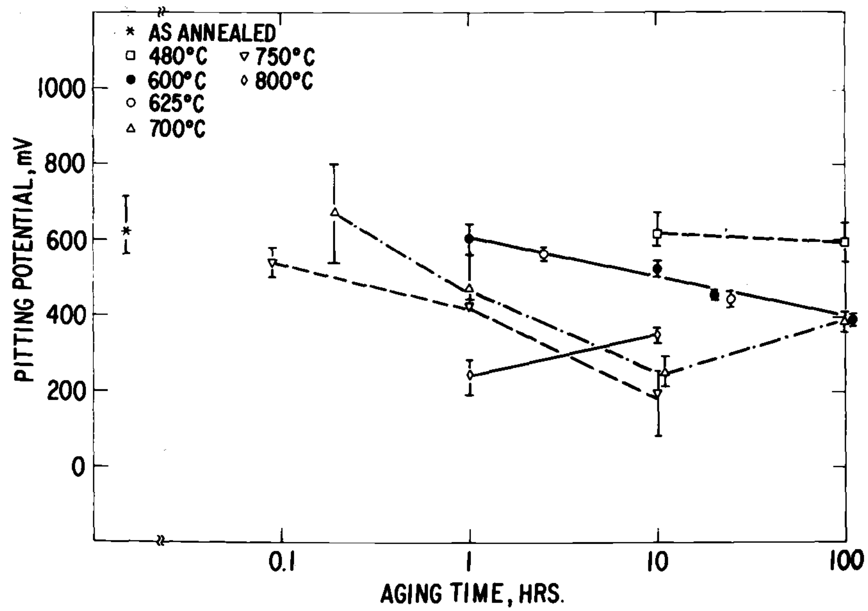

FIG. 16—*Effect of aging treatment on the pitting potential in 0.1NHCl of duplex U50.*

polarization, pits appeared to initiate at or near the austenite-ferrite phase boundary and then propagated into the austenite phase, leaving the ferrite phase relatively unattacked as illustrated in Fig. 17. In tests where pitting occurred, the pit density was very low, <5 pit/cm^2.

Aging specimens at 480°C for times up to 100 h produced no change in

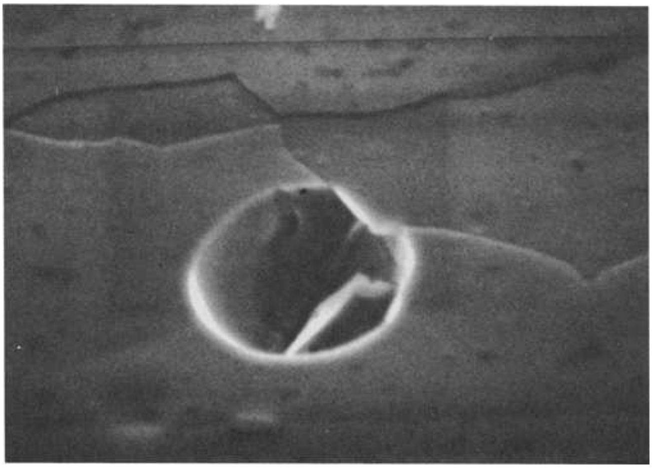

FIG. 17—*Scanning electron micrograph illustrating pit formation in the austenite phase at the austenite-ferrite interface in as-annealed U50 (original magnification ×5000).*

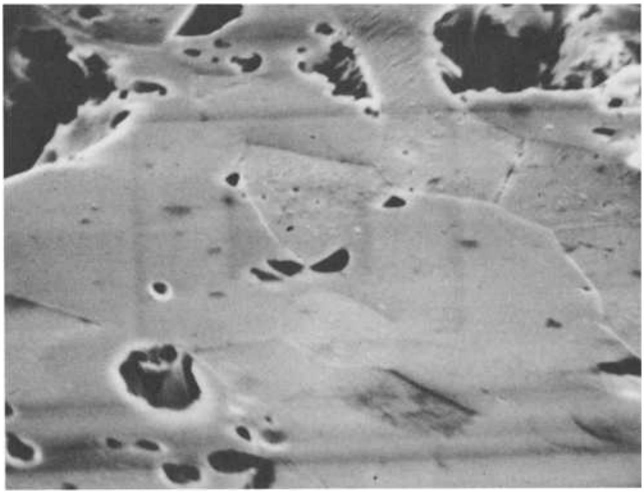

FIG. 18—*Scanning electron micrograph illustrating extensive pitting within the austenite phase of U50 aged for 10 h at 600°C (original magnification ×3000).*

pitting behavior. Following testing, a few (<5 pits/cm^2) large pits could be found in the samples just as in the case for the as-annealed material. Also, the pits appeared to have initiated at or near austenite-ferrite boundaries and propagated preferentially through the austenite phase leaving the ferrite relatively unattacked. As was the case for the as-annealed material, the pitting potential of samples aged at 480°C ranged from a low value of 600 mV.

Aging at 600°C for 1 h had little effect on the pitting potential. Pits again initiated at or near the austenite-ferrite interface and propagated preferentially through the austenite phase. However, aging for 10 h at 600°C resulted in a 60-mV drop in pitting potential. During testing, a very large number of small pits formed within the austenite phase as shown in Fig. 18. The pits initiated in the austenite both along the austenite-ferrite interface and within the austenite phase well away from the austenite-ferrite interface. Again, the pits do not propagate into the ferrite phase. After aging for 20 h or more at 600°C, the decomposition of the ferrite phase is quite apparent. However, as shown in Fig. 19, pitting again is confined to the austenite grains. Pits initiate in the austenite phase, both at the austenite-ferrite interface as well as away from the interface. They then propagate preferentially through the austenite phase. The pitting potential decreased continuously with aging time at 600°C.

Material aged at 700°C for 0.2 h behaved similarly to as-annealed samples. Some specimens did not pit during testing while others exhibited a very low pit density with pits initiating at potentials above 600 mV. Samples aged for 1 h at 700°C behaved much the same as material aged for 10 h or more at 600°C. A large pit density occurred and pits initiated at the

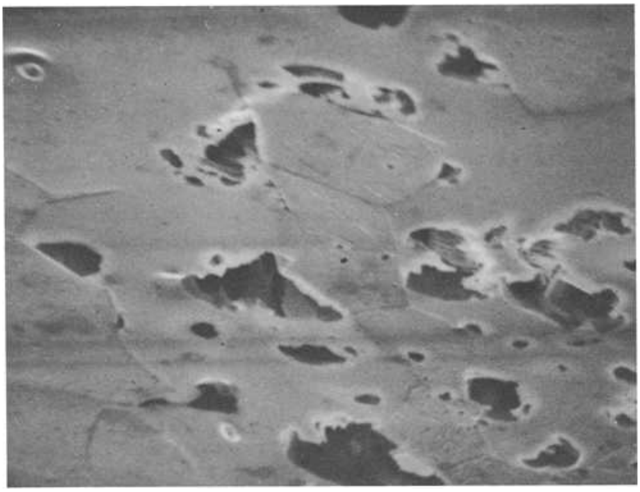

FIG. 19—*Scanning electron micrograph illustrating extensive pitting within the austenite phase of U50 aged for 20 h at 600°C (original magnification ×3000).*

austenite-ferrite interfaces as well as within the austenite and propagated into the austenite. As illustrated in Fig. 20, aging for 10 h at 700°C resulted in a large number of pits initiating within the ferrite phase in addition to those forming inside the austenite phase at and away from the austenite-ferrite interface.

Specimens aged at 750°C for 1 h behaved like samples aged at 600°C for ten or more hours. Specimens aged at 750°C for five or more hours and

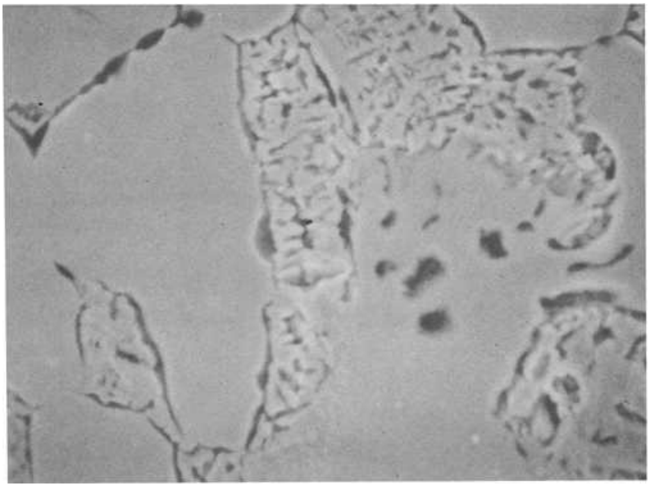

FIG. 20—*Scanning electron micrograph showing pits initiating within the former all-ferritic regions as well as inside the austenite phase at and away from the austenite-ferrite interface. Specimen was aged at 700°C for 10 h (original magnification ×3000).*

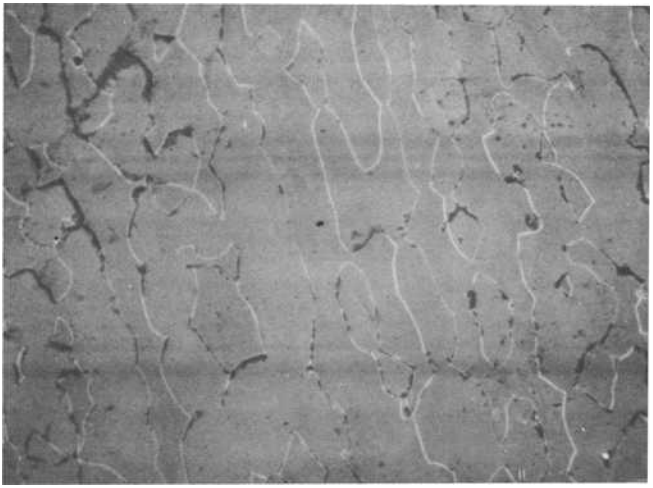

FIG. 21—*Surface appearance of as-annealed U50 following 72 h immersion in ASTM A 262-75 Practice (original magnification ×700).*

800°C for one or more hours also exhibited a very large pit density, but now pits were also forming inside the ferrite phase. In brief, their behavior was identical to that for samples aged at 700°C for 10 h.

The results of the corrosion tests conducted in accordance to ASTM 272–75 Practice E are best presented by viewing the appearance of the samples following testing. Figures 21 through 25 depict the appearance of selected samples following the 72-h immersion period in ASTM A262–75

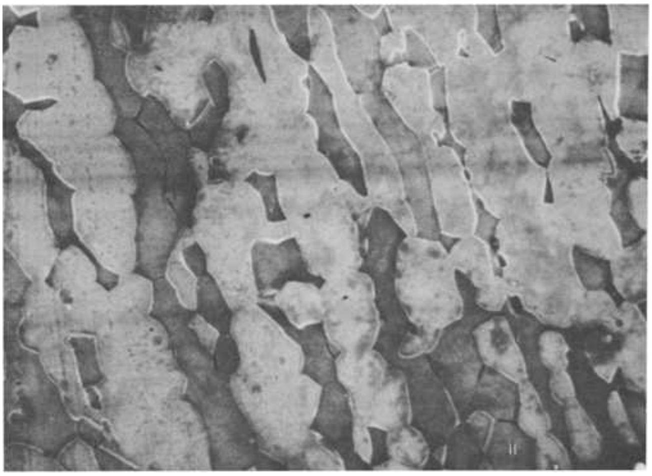

FIG. 22—*Surface appearance of U50 aged for 10 h at 480°C and immersed in ASTM A 262—75 Practice E for 72 h. Note enhanced corrosion attack of ferrite (original magnification ×700).*

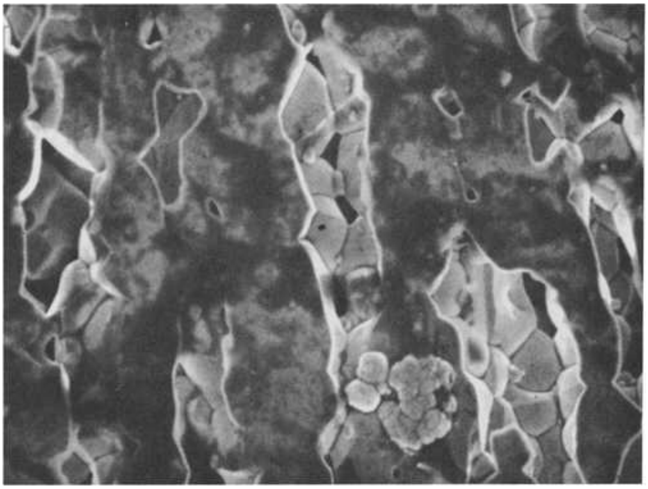

FIG. 23—*Surface appearance of U50 aged for 100 h at 480°C and immersed in ASTM A 262-75 Practice E for 72 h. Ferrite grains have completely dissolved (original magnification ×1000).*

Practice E. Figures 21 through 23 illustrate the increased rate of attack of the ferrite phase resulting from increasing aging times at 480°C. There was little difference in the rate of attack of the austenite and ferrite phases in the sample quenched from 1150°C (Fig. 21). In the sample subsequently aged for 10 h at 480°C, the ferrite phase was more rapidly attacked than

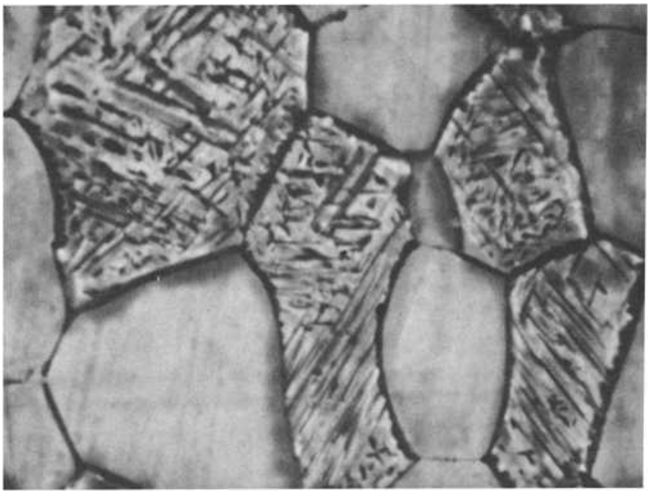

FIG. 24—*Surface appearance of U50 aged at 600°C for 24 h and immersed in ASTM A 262—75 Practice E for 72 h. Note accelerated attack of ferrite-ferrite grain boundaries and Widmanstatten austenite (original magnification ×3000).*

the austenite phase as shown in Fig. 22. Figure 23 indicates that following a 100-h age at 480°C, the ferrite phase was completely dissolved during the ASTM A 262–75 Practice E test. The austenite-ferrite boundaries of all samples aged at 600°C, 700°C, and 800°C were etched. However, there was no intergranular penetration down these boundaries. For all aging times examined, treatments at 600°C, 700°C, and 800° resulted in a broad corrosion attack of ferrite-ferrite grain boundaries, as illustrated in Fig. 24. It appeared as though austenite had formed along the ferrite grain boundaries and this austenite was preferentially attacked. The penetration into the sample down the former ferrite grain boundaries was less than one grain diameter. Samples aged for 10 h or more at 600°C, 700°C, or 750°C, or 7 h at 800°C exhibited preferential corrosion attack of some phase within the former all-ferrite regions. As shown in Fig. 24, the austenite that formed within the ferrite phase was preferentially corroded at a higher rate. On samples aged for longer than 10 h at 700 to 800°C, a significant fraction of the ferrite phase transformed to γ and σ. As shown in Fig. 25, this γ phase was preferentially attacked in ASTM A 262–75 Practice E.

Relationship of Localized Corrosion Properties to Microstructure

High-purity ferrous-base alloys with iron-nickel-chromium-molybdenum contents similar to that of U50 have been shown to be immune to pitting in aqueous chloride-ion containing media at ambient conditions. [*16*] Consequently, pits in the as-annealed samples of U50

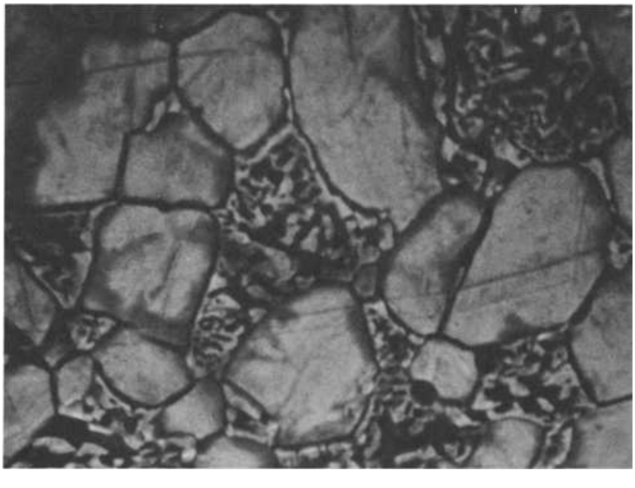

FIG. 25—*Surface appearance of U50 aged at 750°C for 10 h and immersed in ASTM A 262–75 Practice E for 72 h. Austenite (γ_2) formed within the ferritic grains is preferentially corroded (original magnification ×2000).*

probably initiated at soluble inclusions such as manganese sulfide, as has been observed for Type 316 stainless steel [*17*].

Previous investigators have demonstrated that chromium additions exert a strong effect on the passivation behavior of ferrous alloys [*18,19*] and molybdenum additions have a strong effect on the pitting resistance of ferrous alloys [*20–22*]. In other words, chromium additions enhance the formation of a passive film whereas molybdenum additions enhance the resistance of the passive film to breakdown. To be sure, chromium additions also play a role, although not as large as molybdenum's, in determining the resistance of the passive film to breakdown as higher chromium-containing alloys are more resistant to pitting than lower chromium content alloys [*23*]. The influence of aging treatment on the pitting behavior of U50 in 0.1 N HCl and its corrosion behavior in ASTM A262–75 Practice E is a consequence of these separate effects of chromium and molybdenum. Aging at 480°C results in the spinodal decomposition of the ferrite phase into chromium-rich ferrite and iron-rich ferrite. As shown in Fig. 10 and Ref *10* the chromium content of the α remaining when α' forms, approaches 12 percent. The α' contains 80 percent chromium [*12,13,24,25*]. The low chromium α phase in the material aged for 100 h at 480°C evidently has a Flade potential more noble than its corrosion potential in the ASTM A 262–75 Practice E test. The latter is 93 mV, the potential of the Cu/Cu^{++} couple. Consequently, the α phase actively dissolves away while the remainder of the sample exists in the passive state. A network of unattacked α' does not remain in the sample because the α' particles are so finely divided throughout the α that they simply fall into the solution during the dissolution of the α phase. The lack of influence of aging treatments at 480°C on the pitting behavior of U50 can be explained by assuming that molybdenum does not preferentially partition between the α and α' phases. Then one can postulate that the molybdenum present in the α phase more than compensates for the loss of chromium and the pitting resistance of the α phase is maintained. Although the chromium depletion of the phase may make it more difficult for it to passivate, once passivation has occurred, the presence of the molybdenum prevents breakdown of passivity.

Aging 2 h at 600°C has been shown to result in some widely dispersed α' but no other phases. This α' has *not* altered the pitting behavior or corrosion in ASTM A 262–75 Practice E. This is not surprising since the amount of α' formed is much less than is formed at 475°C. The chromium content of the α' is probably still about 80 percent so, owing to the low α' content, the chromium depletion does not drop the chromium level below the critical value required for passivity, and no attack is thus noted in ASTM A 262–75 Practice E.

Aging for 10 h at 600°C results in the precipitation of $M_{23}C_6$ along the austenite-ferrite boundary and within the austenite phase. Coincident with this precipitation reaction was a significant decrease in pitting resistance. Pits initiated within the austenite phase both at the austenite-ferrite interface, as well as away from the interface. Presumably, the pits initiated in the chromium depleted zones formed adjacent to the carbides. The pits propagated preferentially into the austenite phase and left the ferrite phase relatively unattacked because of the higher chromium and molybdenum contents of the ferrite phase. The monotonic decrease in pitting potential with aging time at 600°C could result from the gradual incorporation of molybdenum into the carbide resulting in a molybdenum depletion and enhanced susceptibility of the matrix to pitting or else could result from the molybdenum depletion accompanying precipitation of χ phase. Very little localized corrosion occurred in the ASTM A 262–75 Practice E test as a result of aging at 600°C, indicating that the chromium depletion caused by the $M_{23}C_6$ precipitation was not very widespread. Aging at 700°C, 750°C, and 800°C eventually results in the decomposition of the ferrite phase into austenite (γ_2) and σ. γ_2 is depleted both in chromium and molybdenum. This results in the massive initiation of pits within the former all-ferrite regions. The chromium depletion of γ_2 is responsible for its enhanced dissolution during ASTM A 262–75 Practice E testing.

It is worth emphasizing the resistance of U50 to intergranular corrosion attack following aging treatments that result in precipitation of $M_{23}C_6$. In a separate investigation, this resistance to intergranular corrosion was shown to be associated with the presence of ferrite phase [*26*]. If the alloy is first austenitized prior to aging, it becomes highly susceptible to intergranular corrosion. The mechanism whereby duplex U50 is resistant to intergranular corrosion is probably the same as that determined for duplex Type 308 stainless steel [*27*]. Namely, $M_{23}C_6$ precipitation occurs most heavily along austenite-ferrite boundaries. Most of the metal atoms in the carbide are supplied by the ferrite phase because of the higher diffusivity in the body centered cubic (bcc) structure than in the face centered cubic (fcc) structure. The carbon is primarily supplied by the austenite phase because of its greater carbon content. The early and rapid precipitation of $M_{23}C_6$ (made possible by the high diffusivity within the ferrite) along austenite-ferrite boundaries depletes the austenite of carbon and prevents extensive $M_{23}C_6$ precipitation within the austenite phase and precludes the possibility of intergranular corrosion along austenite grain boundaries. Since most of the metal atoms in the carbide come from the ferrite phase the chromium-depleted zone in the austenite phase adjacent to the carbide is relatively small and quickly replenished, preventing any significant corrosion attack along the austenite side of the austenite-ferrite interface. Since local equilibrium can be presumed to exist at the matrix-carbide interface [*28*], the greater chromium content of the ferrite phase results in a higher chromium content in the matrix at the matrix-carbide interface [29]. This effect combined with the more rapid diffusivity within the ferrite phase results in a not-very-severe chromium-depleted zone. Thus, the ferrite side of the austenite-ferrite interface is not susceptible to intergranular corrosion attack.

General Discussion and Conclusions

Properly heat treated, U50 possesses an excellent balance of mechanical and corrosion properties. The alloy is, however, not stable and many phases can precipitate in addition to the α and γ that are initially present in this duplex alloy.

The most harmful phase to precipitate is σ. σ phase reduces the toughness without any beneficial strengthening. The chromium and molybdenum depletion of the α resulting from the precipitation of the chromium- and molybdenum-rich σ resulted in massive pit initiation in the pitting test.

The precipitation of γ_2 and χ are less harmful to the mechanical properties than is σ phase precipitation. The precipitation of these phases also results in pit initiation either through a chromium and molybdenum depletion in the case of the χ or by the low chromium and molybdenum level of the γ_2.

Carbide precipitation can also give rise to chromium depletion, but the lack of attack in ASTM A 262–75 Practice E points to the depletion not being too severe. The duplex nature of the U50 provides protection against sensitization due to $M_{23}C_6$ precipitation. This protection is believed to stem primarily from a rapid replenishment of the chromium due to rapid chromium diffusion in the α phase and the high chromium content of the γ.

Aging at about 475°C results in strengthening with a concurrent drop in impact energy. The phase separation associated with this process gives rise to chromium depletion in the α. This resulted in α dissolution in the ASTM A 262–75 Practice E test but, owing to the presence of the molybdenum, the pitting resistance of the α was not adversely affected.

Duplex alloys possess a fascinating complexity of microstructural features. This complexity provides a challenge to the metallurgist. It should also make a designer very cautious. Improper heat treating, processing variations, and elevated temperature excursions can alter the properties. The possibility of the unintentional precipitation of any of the phases discussed in this report may cause serious problems.

References

[1] Hayden, H. W. and Floreen, S., *Metallurgical Transactions*, Vol. 1, 1970, pp. 1955–1959.

[2] Gray, R. J., *IMS Proceedings 1971*, pp. 141–160.

[3] Hochmann, J., Desestret, A., Jolly, P., and Mayoud, R., Metaux Corrosion Industries, Vol. 591–592, 1974, pp. 390–423.

[4] Hall, E. O. and Algie, S. H., *Metallurgical Reviews,* Vol. 11, 1966, pp. 61–88.

[5] Kasper, J. S., *Acta Metallurgica,* Vol. 2, 1954, pp. 456–461.

[6] Smith, C. J. E., Ruckman, J. C., and Lawrence, C. D., *Metals and Materials,* Vol. 7, 1973, pp. 234–240.

[7] Speich, G. R. and Oriani, R. A., *Transactions,* American Institute of Mining, Metallurgical, and Petroleum Engineers, Vol. 233, 1965, pp. 623–631.

[8] Weiss, B., Hughes, C. W., and Stickler, R., *Prak. T. Metall.,* Vol. 8, 1971, pp. 528–541.

[9] Williams, R. D., *Transactions,* American Institute of Mining, Metallurgical, and Petroleum Engineers, Vol. 212, 1958, pp. 497–502.

[10] Solomon, H. D. and Levinson, L. M., *Acta Metallurgica,* Vol. 26, 1978.

[11] Solomon, H. D. and Koch, E., to be published.

[12] Lagneborg, R., *Transactions,* American Society of Metals, Vol. 60, 1967, pp. 67–78.

[13] Blackburn, M. J. and Nutting, J., *Journal,* Iron and Steel Institute, Vol. 202, 1964, pp. 610–613.

[14] Wang, M. T., private communication.

[15] Floreen, S. and Hayden, H. W., *Transactions,* American Society of Metals, Vol. 61, 1968, pp. 489–499.

[16] Lizlovs, E. A. and Bond, A. P., *Journal,* Electrochemical Society, Vol. 116, 1969, p. 574.

[17] Eklund, G., *Journal,* Electrochemical Society, Vol. 121, 1974, p. 467.

[18] Flade, F., *Zeitschrift Physikchem.,* Vol. 76, 1911, p. 513.

[19] Rocha, H. J. and Lennartz, C., *Archiv. Eisenhuttenwessen,* Vol. 26, 1955, p. 117.

[20] Lizlovs, E. A. and Bond, A. P., *Journal,* Electrochemical Society, Vol. 122, 1975, p. 719.

[21] Bond, A. P., *Journal,* Electrochemical Society, Vol. 120, 1973, p. 603.

[22] Bond, A. P. and Lizlovs, E. A., *Journal,* Electrochemical Society, Vol. 115, 1968, p. 1130.

[23] Horvath, J. and Uhlig, H. H., *Journal,* Electrochemical Society, Vol. 115, 1968 p. 791.

[24] Fisher, R. M., Dulis, E. J., and Carrol, K. G., *Transactions,* American Institute of Mining, Metallurgical, and Petroleum Engineers, Vol. 197, 1953, pp. 690–695.

[25] Williams, R. O. and Paxton, H. W., *Journal,* Iron and Steel Institute, Vol. 185, 1975, pp. 358–374.

[26] Devine, T. M. and Solomon, H. D., to be published.

[27] Devine, T. M., "The Mechanism of Intergranular Corrosion in Two Phase Austenitic—Ferritic Stainless Steels," Corrosion 78, Houston, Tex., 9 March 1978.

[28] Strawstrom, C. and Hillert, M., *Journal,* Iron and Steel Institute, Vol. 207, 1969, p. 77.

[29] Tedmon, C. S., Vermilyea, D. A., and Rosolowski, J. H., *Journal,* Electrochemical Society, Vol. 118, 1971, p. 192.

STP672-EB/Jul. 1979

Discussion—Stainless Steels Session

Relationship Between Microstructure and Properties in Stainless Steels by F. B. Pickering

Question: Dr. H. D. Solomon[1]—You mentioned one of the main problems that occurs in ferritic stainless steels, namely, that grain growth tends to be very very rapid. Do you have any suggestions as to how these steels can be processed in such a way as to keep as fine a grain as possible?

Answer: Dr. Pickering—I think there are two ways at least for grain refining the ferrite stainless steels. In this context, I am referring to the fully ferritic steels that contain no austenite, because the presence of austenite at high temperatures can result in a refinement of the ferrite grain size. However, in fully ferritic steels, the conventional way to grain refine or inhibit grain growth is to introduce second phase particles that pin the ferrite grain boundaries. Such additions as titanium and niobium may be used, to form Ti(CN) and Nb(CN) particles, and I have evidence that under appropriate conditions these additions may prevent excessive grain coarsening until temperatures above 1200°C. The effect does, however, depend on the interstitial content, the grain coarsening temperature being lower with smaller interstitial contents. In this respect, one may express some minor concern when it is suggested that ultra-low interstitial contents are used because one wonders whether there will be sufficient carbo-nitrides formed to give adequate grain growth inhibition. Whilst the very low interstitial contents may be very desirable for corrosion resistance, toughness, and formability, there is always the possibility that, for example, the toughness advantage conferred by the low interstitial content may be more than offset by grain coarsening.

A second possible method of refining the ferrite grain size is by controlled processing, more specifically low rolling finishing temperatures. I believe this is being investigated, but I think there may be some problems because these ferritic steels recover rapidly to produce recovery type substructures. This lowers appreciably the driving force for recrystallization by reducing the stored energy, and so recrystallization is much retarded. In fact, many as-rolled materials show recovered rather than

---

[1] General Electric Co., Schenectady, N. Y.

recrystallized microstructures. In this respect, certain alloying elements may retard recovery and so cause recrystallization to be more rapid, due to the retention of more stored energy. If such alloying elements also can produce second phase particles that inhibit grain growth, so much the better. In the absence of grain growth inhibition, then, there is always the danger that any refined grain size produced by controlled processing would be very susceptible to coarsening during subsequent heating; that is, during welding.

Question: Dr. Solomon—There is literature information, work specifically by Angle, that would lead one to believe that for Type 304 stainless steel with 0.08 carbon, the M_d temperature is perhaps as low as room temperature, perhaps only 25°C. And my experience is that it may be a bit higher. I wonder if you could comment on that?

Answer: Dr. Pickering—The M_s and thus the M_d temperature depends very much on the composition, the less alloyed the Type 304, the higher the M_s and M_d. M_d also depends on the amount of strain applied, increasing with increasing strain. My experience is that with Types 301 and 304 steels, the M_d temperature at true strains of up to about 0.4 was usually lower than 100°C, and we never observed an M_d of 250°C. However, in very pure metals one might expect somewhat higher M_d temperatures. In atomic energy application, I believe there is quite a lot of evidence that the M_s temperature is increased by irradiation. Whether the M_s is raised as far as normal radiation temperatures, so that martensite is formed actually during irradiation, is, I think, very questionable. The irradiation-induced martensite, so called, I think, formed during cooling irradiated material back to room temperature.

Question: G. Bodine[2]—I'd like to make a comment regarding the ferritic materials. A few years ago, I made an interesting observation on the 26-1 (E-Brite) composition in which I got into an area that I felt was maybe way too deep. This relates to strain rate effects and their influence on the transition temperature, and I had a series of 26-1 (E-Brite) materials that when subjected to the conventional modes of evaluating, the transition looked very ductile, and so forth.

In fact, the same piece of material in different conditions exhibited good ductility, even on impact drop weight testing. But when I got into ultra-high strain rate evaluation, we had a completely new ball game.

This, I believe and would suggest, would be an interesting field for microstructure correlation. When we employed explosive deformation, one could take the same materials that were all essentially ductile, by conventional means, and separate them into two piles: one like glass and one remaining ductile. Some of the preliminary work I did inferred that

---

[2] Combustion Engineering, Chattanooga, Tenn.

there's a whole new ball game in evaluating some of the subtle characteristics of these ferritic stainless steels.

Answer: Dr. Pickering—Whilst I have never been concerned with explosive forming, I can appreciate that the very high strain rate, coupled with the shock-wave effect, would lead to ferritic stainless steels of the 26-1 type behaving in a brittle manner. May I suggest that this could be due to two effects. The first is the increase in the yield or flow stress at very high strain rates such that the cleavage fracture stress is exceeded and the ductile-brittle transition temperature is markedly raised. Hence, the transition temperature could be above room temperature, and the material could be very brittle. I think increasing ferrite grain size and the presence of elements that raise the transition temperature would aggravate this effect.

The second feature is the propensity of fully ferrite structures to mechanical twinning at high strain rates, and I believe that elements such as chromium, molybdenum, silicon etc. increase the mechanical twinning tendency. In ferrite, twinning (or rather intersecting twins) can readily nucleate a cleavage crack and thus initiate brittle cleavage fracture. I also believe that twinning is a very common form of deformation during explosive forming. Both these effects may contribute to the extreme brittleness in some explosively formed ferrite stainless steels, particularly if the grain size was coarse.

Question: L. Thompson[3]—Would you please comment on the relative effectiveness of strain-induced HCP epsilon martensite as opposed to BCC alpha martensite as related to the strain hardening observed in unstable austenitic stainless steels?

Answer: Dr. Pickering—Our experience has been that epsilon martensite contributed virtually nothing to strain-induced plasticity, at least compared with transformation to alpha martensite. I believe there is evidence in the literature to confirm this. In the stainless steels we examined, where the stacking fault energy was low, the formation of epsilon martensite was quickly followed by alpha martensite, and it was the latter that produced to the improved stretch formability of the unstable austenite stainless steels.

Possibilities for Microstructural Control During Hot Working of Austenitic Stainless Steels by B. Ahlblom and W. Roberts

Question: Dr. Solomon—Have you looked at the influence of delta ferrite in steels that have been particularly balanced to have some delta

---

[3] General Atomic Co., San Diego, Calif.

ferrite at the working temperatures? Do you see any differences between the dynamic, metadynamic, and static recrystallization.

Answer: Dr. Ahlblom—The only material we studied where delta ferrite is present, was Type 304 steel in the cast condition and, in this condition, recrystallization is much slower than for wrought material. However, this is mainly as a consequence of grain size differences rather than the presence of δ-ferrite.

Question: W. Dwyer[4]—Have you looked at dynamic recrystallization in the ferritic stainless steels? In particular, have you looked at a stabilized ferritic, something with high titanium? This would prevent any transformation. And, if not, do you have any feel for it?

Answer: Dr. Ahlblom—No! The problem with ferritic steels is that it is not very likely that they will recrystallize dynamically, because dynamic recovery is so rapid that the driving force never becomes sufficiently high for recrystallization during deformation.

Microstructural and Microchemical Studies in Weld Sensitized Austenitic Stainless Steels by P. Rao

Question: J. H. Steele, Jr.[5]—I have a question on sensitization and the relationship of the chromium depletion layer to the corrosion. If you make the premise that continuity of this depleted zone is necessary, it seems to me you have to look at it in terms of the spacing of the carbides and when continuity of this depleted zone exists. Is anybody doing any work in that specific area?

Answer: Dr. P. Rao—Yes. There are a number of models. One of our theoretical chemists, Dr. Mesmer, has been working on this to actually have models that really look at weld sensitization as opposed to thermal sensitization. There are some diffusion models to give you some idea of the critical spacing.

There is also another aspect of this to consider. If you look at very light sensitization, conditions that don't give rise to cracking, where you have very very small amounts of carbide formation, what you find is that you do not have a continuous average carbide distribution but rather some grain boundary segments that contain carbide while other grain boundary segments are completely free. So it's not only a question of the behavior between the individual carbides, but what fraction of the grain boundaries have any carbides in them at all. What you find is, if you look at something like an oxalic acid test and try to quantify it, you can get into a

---

[4] AC Spark Plug Div., GMC, Flint, Mich.

[5] Armco Corp., Middletown, Ohio.

situation where you get perhaps only 10 percent of grain boundaries having any carbides in them at all, although they may be moderately closely spaced, the other 90 percent of the grain boundaries are clear. There's a lack of continuity in this case, because only certain segments will be attached. You might get continuity along a single grain boundary, between two triple points—but then you go off to between other triple points and its completely clear. So you won't get attack in a modified Strauss test, for instance.

Question: R. Anderson[6]—Dr. Rao, in a presentation about a year ago, you had indicated that by longer times at sensitization temperatures that you could get a dampening out of this chromium depletion gradient. Could you comment on this in relation to other properties?

Answer: Dr. Rao—This has been observed in the alloy Armco Nitronic 50 or XM19 in which we see this phenomenon occurring quite readily. And what you observe and what has been measured is that with very long periods of time, you will still see the carbides present but you get a chromium replenishment, a healing effect.

In other words, the carbide is still present, but at long periods of time the chromium begins to build up again. So if you looked at a time-temperature sensitization curve, the diagram is skewed over. At very short times, there is no sensitization at a given temperature; at intermediate time, there is sensitization; and at long times, there is none.

And we have in fact observed this where we do see carbides, but then the chromium levels come back up again. And I refer you to the model of Stawstrom and Hillert that I think is the best explanation for why this occurs and it relates in fact to change in the chromium activity and the carbon activity as you begin to get carbide precipitation. In fact, you will get replenishment with long aging times at temperature.

Question: R. Anderson—Chromium carbide or other carbide?

Answer: Dr. Rao—No, it's still chromium carbide. And, in fact, Stawstrom and Hillert say that you still get carbides precipitating, but, in fact, the activity of the carbon and activity of the chromium is changing, and you keep the chromium level high at very long times.

Question: Dr. R. Simpson[7]—Obviously, the tendency to form the carbides is dependent on how fast you cool through the temperature range for sensitization. And the types of welds that I looked at are much heavier in section than the pipe welds. Therefore, it's a balance of heat input and the way in which the heat is conducted away, so welding parameters and

---

[6] Universal Cyclops Specialty Steel, Bridgeville, Pa.

[7] Westinghouse Electric Research & Development Center, Pittsburgh, Pa.

things like the thickness of the part being welded as well as the geometry make a big difference.

I'm interested, based on a question you asked me, do you ever find that you find chromium depletion in cases where you would not metallographically see carbides?

Answer: Dr. Rao—Generally, you can pick the carbides up metallographically. It depends upon what techniques you use. We often use oxalic acid.

We generally believe metallography is sufficient, although in some cases if you have a very small carbide fraction, let's say 10 or 20 percent of the grain boundaries containing carbides, it can be difficult to pick it up and you may need TEM in order to see it. But it is there and you can observe it optically, but it sometimes gets to be difficult.

Question: C. Matthews[8]—We use a lot of Type 304 stainless steel, and we find that with a given cooling rate that there's quite a difference in the susceptibility to sensitization between these different heats. And we've been unable to determine why this difference occurs. Do you have any information on that?

Answer: Dr. Rao—I won't answer that question, I'll leave that to the next speaker; that's an area in which he's been involved in working with this heat-to-heat variation. I have observed the same type of thing he's going to talk about. Sometimes pipes come in actually sensitized in the mill before we ever weld them. These pipes are then very severely sensitized by the subsequent welding process.

Correlation of Sensitization with Thermomechanical History of Type 304 Stainless Steel Pipe Joint by Y. G. Nakagawa, T. Kawamoto, M. Fukagawa, and Y. Saiga

Question: Dr. Solomon—I have one quick question. You mentioned the effect of 6 percent strain on continuous cooling sensitization. Did you look at lower levels of strain?

Answer: Dr. Y. Nakagawa—No, not yet, because that depends on the accuracy of the experiment, and in our set-up, 6 percent is the minimum strain with fair accuracy. But we have tried lower strain levels roughly estimated to be 4 and 3 percent, and we did observe the sensitization enhancement.

Comment: Dr. Solomon—I just want to make a quick comment. I have done similar experiments, and I find that in one heat that I looked at, there is very little effect on sensitization of straining (5 percent or less)

---

[8] Superior Tube Co., Norristown, Pa.

and at high strains there was a fairly large effect as you've shown here, but that if you went from 5 percent to even as high as 25 percent, it seemed to saturate. So I think there's a question of getting some more information at the very low strain levels. Also, there may be some heat-to-heat variability and interplay in these effects.

Question: D. Allen[9]—We've come across problems with probably smaller pipes than you are talking about. But, after you have solution treated them, there are often several operations that are known, certainly in Type 304, to accelerate or produce sensitization. Things like straightening and grinding, especially grinding of welds. Do you have any comments on this? And also, are the same effects in Types 304L and 316L?

Answer: Dr. Nakagawa—I agree with you. Our recent results for Type 304 indicate that those production and fabrication processes strongly influence sensitization of materials as well as initiation of cracking.

It seems to me that Types 316L and 304L are quite immune to these surface treatments. The best way to pick up the alternate material is to find material that is immune to any variability of heat treatments and fabricating the piping system, and these L-grade materials seem to have a great margin to them.

Microstructures Versus Properties of 29-4 Ferritic Stainless Steel by G. Aggen, H. E. Deverell, and T. J. Nichol

Question: Dr. Solomon—You made a comment about limiting the amount of copper. Have you ever done an experiment on heats containing higher amounts of copper? Specifically, do you know how the high copper might affect 475°C (885°F) embrittlement?

Answer: Dr. G. Aggen—We have not looked at the effects of copper on 475°C embrittlement. Your data, I believe, indicates copper accelerates the reaction?

Question: Dr. Solomon—There is some Climax Molybdenum work that dealt with a variety of different elements and their effects on 475°C (885°F) embrittlement. They didn't specifically do copper; they did do molybdenum, for instance.

Answer: Dr. Aggen—Which indicated that in some cases it (molybdenum) had no effect, and, in other cases, it accelerated embrittlement.

There are data in the literature indicating that cobalt and aluminum may slow 475°C (885°F) embrittlement, but even there, the data are inclusive. It may depend upon the level of alloying addition.

---

[9] General Electric Co., Wilmington, N. C.

Effect of Heat Treatment and Microstructure on the Mechanical and Corrosion Properties of a Precipitation Hardenable Stainless Steel by T. Kosa and A. DeBold

Question: B. Loescher[10]—I'd like to know if you have tested your material in the aged condition, say at 1125 or 1150°F, followed by a simulated service use at 750 or 800°F, and if so, did you find any adverse effect on notch toughness?

Answer: Dr. T. Kosa—For Custom 450 aged at 1150°F, exposure to temperatures of 700 and 800°F for times up to 3000 h decreases Charpy V-notch impact strength somewhat, but increases notch tensile strength and smooth tensile strength.

Question: Dr. Solomon—Why did you look at $MgCl_2$? That's an environment in which one might expect to see transgranular cracking in Type 304. Is there any specific reason why you chose that?

Answer: Dr. Kosa—We were trying to compare Custom 450 with Type 304, since the alloy was developed to have corrosion resistance similar to Type 304. (Type 304 was tested and was inferior to Custom 450 aged at 1150°F (894 K).)

Microstructure and Related Material Characteristics of Some Duplex Austenitic-Ferritic Alloys with Less Than 40 Percent Ferrite by G. C. Bodine, Jr., and C. H. Sump

Question: Dr. B. Wilde[11]—I noticed you didn't try any silicon variations, or at least you didn't discuss it on the board there. Is there any reason for this, say perhaps processing difficulties?

Answer: G. Bodine—You just introduced something interesting. As you and I know, we're doing work on some of the alloys that you have developed. Currently, we're doing work on duplex alloys ranging from 3.5Si to 4.5Si with essentially an 18-8 base. The stress corrosion cracking resistance on these materials is exceptional, but, first of all, we have found that these alloys can be processed from centrifugal castings by direct cold reductions. This is gratifying.

We haven't been able to crack either one of these alloys in $MgCl_2$ yet, and I understand that you have had some pretty good results in your testing. So as far as the silicon additives, this is current work. One thing—on one of the 3.5Si alloys, the ferrite is only around 4 or 5 percent; this might have an attraction for elevated temperature properties over and above the 4.5Si alloy.

[10] Dow Chemical Co., Midland, Mich.

[11] U. S. Steel Corp., Research Center, Monroeville, Pa.

Question: Dr. Wilde—Are you doing any high-temperature water tests in the sensitized condition? Because this is the area where we have found these duplex steels to be outstanding?

Answer: G. Bodine—Yes—we have done some work previously at Battelle. But we didn't have, let's say, spectacular results, although we did have very encouraging results correlating with some of the other work.

Influence of Microstructure on the Mechanical Properties and Localized Corrosion of a Duplex Stainless Steel by H. D. Solomon and T. M. Devine

Question: Dr. G. Aggen[12]—I think there's some evidence that in the micro-duplex, there might be a galvanic effect too, which prevents stress corrosion.

I think Climax Molybdenum has done some work on ferritics welded with all austenitic filler. They can't crack that in $MgCl_2$.

The main question I wanted to ask you is how good is your evidence that you are seeing alpha prime above say about 550°C? Could that be some other phase such as gamma, for example?

Answer: Dr. Solomon—That is a very good point. Our evidence rests on the fact that while we observe the precipitate, we observe no extra diffraction spots, and we can light up the precipitate in dark field using a matrix alpha spot.

Now, when we go to 700°C, we also observe a very fine precipitation, but here we did observe extra spots. So I think at 700°C, you can get microstructures that look identical to those seen at 475°C, that is, a very very fine precipitation—but here we have extra diffraction spots and we believe that those may be due to a very fine sigma phase precipitate.

When you get austenite present, it's pretty easy to see it because you have an extra set of austenite spots coming out pretty clearly.

Closing Comments: Dr. F. B. Pickering—It would be invidious of me to comment specifically on the various papers presented in this session, particularly as they still have to be studied in their finalized textural form. However, there are several points that arise on listening to the general trend of the papers and of the discussions that ensued. The first is that perhaps we should be a little concerned at the ingenious alloy developments that have taken place over the years, which employed complex metallurgical phenomena, and moreover, often used several such phenomena conjointly to achieve quite outstanding combinations of properties. Many of these developments have posed almost insuperable problems of control, and so have not be exploited widely and indeed have

---

[12] Allegheny-Ludlum, Brackenridge, Pa.

often been abandoned without effective commercial exploitation. Much metallurgical effort has therefore been ineffectively used, although one must admit that these developments have often contributed greatly to our general metallurgical understanding. It seems however, that we need to show great care in pursuing developments that are so difficult to control, because in the present climate of economic stringency, developments that are believed to be academic and too difficult to control, lead to a loss of creditability in metallurgical research.

Secondly, there has, over the past few years, been a marked improvement in our appreciation of structure-property relationships, particularly in a quantitative sense. Much still remains to be done in this respect to further improve our understanding, but we must be sure that the knowledge we have already gained is applied to the optimization of steel properties, and particularly to ensure that the optimum properties are reliably produced. Consistency in producing the optimum properties is absolutely essential.

Thirdly, perhaps we should not try to reach a complete understanding of structure-property relationships before we branch out into even more productive avenues of research. We need now, I would suggest, to become microstructural engineers and to begin to develop microstructural profiles for particular property requirements but, especially, to show how these profiles may be achieved by variation and control of the processing conditions. It seems to me that it is essential for metallurgists to now devote even more effort to quantifying the relationships between processing parameters and microstructure so that we can predict the processing conditions by which a particular microstructural profile, and hence property combination, may be achieved. This should first be aimed at developing ideas or models that relate such effects at temperature, strain, strain rate, holding time, quality of stress and strain, cooling rate, transformation temperature, etc., to the microstructure that is developed. Such ideas are under development in high-strength low-alloy steels; why not in stainless and other types of steels?

Finally, I submit that we need to do much more work on the quantification of user properties with structure and processing. These are the *abilities* of steels, such as weldability, machinability, formability, corrodability, etc. The relationships between processing microstructure and these user abilities should be our prime objectives in order to ensure that at a time when raw materials and energy conservation is becoming so important, every last advantage is squeezed from the materials we used. This perhaps should be the ultimate aim of microstructural control, and aspects of the subject might well form the basis of future MiCon meetings.

High-Temperature Alloys

Summary—High-Temperature Alloys Session

The third and the last session of MiCon 78 was devoted to the high-temperature alloys.

The keynote address, ''Microstructural Objectives for High Temperature Alloys in Advanced Energy Systems'' was delivered by Sims of the General Electric Co. Sims reviews a few advanced energy systems, in a general way, for those who are not involved in such developments. Then he addresses himself to the question, What role will superalloys play in these energy systems? He identifies potential applications and problems for superalloys and discusses the conditions that must be withstood, properties that will be required, and then discusses the ideal microstructures that one may find.

The advanced energy systems covered by Sims include coal liquifaction, coal gasification and pressurized fluid beds, and nuclear systems including liquid metal fast breeder reactors (LMFBR) and high-temperature gas reactors (HTGR). Sims discusses each of these energy systems individually and describes the major categories or superalloy *families* that will find applications therein.

Sims correlates these families or categories of materials pictorially and identifies the *power system,* draws out from these the major *critical system components,* leads to the *superalloy family* that might be used and then specifies *alloy* composition *examples.*

In keeping with the theme of the conference, Sims identifies ideal microstructures for superalloys utilizing the various *families/categories* as the basis for specific alloy microstructural examples.

The next three papers following the keynote address dealt with conventionally produced superalloys—melting, forging and processing, and the physical metallurgy. Emphasis again was on optimization of properties via microstructural control.

Lherbier of Universal Cyclops Specialty Steel Division points out through several examples the overriding importance of melting and casting a high quality starting material in his paper on ''Melting of Superalloys.''

Melting of superalloys is the initial, and perhaps the most important, step in the production of materials used in critical high-temperature applications. Increasing demands for high quality superalloys with specific requirements dictate various combinations of primary melting, refining, and secondary remelting operations.

Various combinations of melting processes can be used to obtain a desired chemistry not only in terms of the primary elements, but also for residual and tramp elements. Product forms frequently dictate a combination of melting processes that give importance to the shape of the ingot. Additionally, it is frequently important to choose melting combinations that achieve ingot structure control for optimum primary phase distribution, cleanliness or hot workability, or all.

Lherbier describes the various melting techniques: VOD, AOD, VAR, ESR, EBR, VIM and EBM, and shows how the development of these melting techniques has resulted in cost effective methods of producing high quality superalloys. He concludes that the choice of a melting sequence for the production of superalloys is dependent upon the quality and cost of the final product. He emphasizes that no amount of highly sophisticated hot or cold work, heat treatment, etc., can produce today's required quality level without a proper composition or structure in the cast ingot.

"Physical Metallurgy and Effects of Process Variables on Microstructure of Wrought Superalloys" was given by Muzyka of Carpenter Technology Corporation. Utilizing nickel-, nickel-iron, and iron-base superalloys with an austenitic matrix as examples, Muzyka shows how the property goals in these alloys, for various applications, can be achieved by proper selection of process parameters with respect to phase relationships.

Muzyka first classifies the family of the so-called heat resistant alloys, and describes the effect of each individual alloying element and presents a concise review of physical metallurgy. These will be found to be very useful by a design engineer who is not quite involved in development of these systems.

Muzyka describes how an excellent combination of tensile and creep rupture properties was accomplished by varying the forging reduction, temperature, and solution heat treatment. The phases responsible for the property latitude capability provided by *structure control* are described for the families of superalloys. The phase solvus temperatures are correlated with the alloying elements.

Muzyka then goes on to enumerate a series of steps that can be applied to any processing of superalloys, and shows the beneficial results obtained by application of the same in a number of superalloys, for example, Pyromet CTX-1, Alloy 706, etc. To keep the superalloy metallurgist honest, Muzyka also describes how structure control can be disadvantageous.

Various other thermomechanical processes associated with structure control are described with a brief discussion of physical metallurgy of powder superalloys.

Optimization of microstructure and concomitant properties of this important family of alloys via thermomechanical processes is described in the concluding paper in the morning session, "Forging and Processing of High-Temperature Alloys" by DeRidder and Koch of Ladish Co. In their paper, DeRidder and Koch describe how the performance upgrading of superalloys can be achieved via analysis of the microstructure, as affected by various processing parameters. They review the parameters affecting the material quality and the current state of the art of forging cast material. The parameters covered include ingot characteristics, ingot conversion, closed die forging process, etc.

The authors describe the carbide severity rating system developed at Ladish for dendritic segregation or banding in the case of billets. Using metallography and microprobe analysis, DeRidder and Koch show how thermal homogenization treatments can be utilized to reduce the dendritic segregation. They point up the shortcoming of this approach, if not properly controlled, resulting in incipient melting and loss of forgeability and mechanical properties. DeRidder and Koch further describe the ingot conversion practice in terms of an intermediate thermomechanical step in obtaining the best possible microstructure, before the metal is committed to a sequence of final closed die forging. They discuss the three important parameters, that of temperature, percent reduction, and the strain rate, associated with the closed die processing of superalloys.

In the last few years, there has been a thrust toward development of powder metallurgy (P/M) technique to process superalloys for improved properties and cost advantage through near net shape approaches. Bartos of the General Electric Co. presents an excellent review of this aspect of superalloy metallurgy in his paper "Review of Superalloy Powder Metallurgy Processing for Aircraft Gas Turbine Applications."

The high costs of processing today's high-strength superalloys, such as René 95, combined with the spiraling cost of raw materials, have shifted the emphasis trends in materials technology. The transition has been from technologies to maximize high performance at minimum engine weight to concerted efforts on increased reliability and cost improvement. The inherent forging difficulties associated with cast and wrought René 95 provided the impetus for the cost reduction programs.

Using René 95 as an illustration, Bartos describes how the development and application of advanced P/M technology provided the significant breakthrough in reducing the finish part costs. Various processing techniques, hot die forging, hot isostatic pressing (HIP), and forge and hipping as related to P/M are discussed. Advances made in as-HIP P/M technology are illustrated by cost savings achieved in manufacture of complex jet engine shaft components. The input material savings inherent in the configurational flexibility of P/M processing, combined with elimination of many fabrication steps, have culminated in as much as 80 percent cost reduction in some components.

Bartos also describes some of the potential problem areas associated with P/M, namely, defects in form of porosity and foreign particulates. These problem areas pose some unique quality control challenges to the superalloy metallurgist.

The last three papers were devoted to application of these materials.

Larson and Jenkins of Eaton Corporation review a few applications of nickel- and cobalt-base superalloys in "Application of Superalloys in Internal Combustion Engine Exhaust Valves." The authors show how these materials have played a significant role in the successful design of the exhaust valves to meet durability objectives.

Larson and Jenkins describe the two basic types of reciprocating engines that use poppet type exhaust valves. Exhaust valves, their design parameters, and metallurgical characteristics of high-temperature valve head materials are discussed in detail.

The authors point up that while most of these alloys were originally adapted from other applications, such as aerospace industry, their chemical makeup, heat treatments, and subsequent microstructural requirements have usually been modified to meet the specific needs of valve applications. To illustrate the factors governing the selection of appropriate alloys, Larson and Jenkins discuss four case studies in which tendency towards failure was eliminated by application of one of the superalloys. They conclude their paper by listing the future development opportunities for a superalloy metallurgist.

Deye and Couts of AiResearch Mfg. Co. and Wyman-Gordon Co., respectively, collaborated on a paper "Super Waspaloy Microstructure and Properties." Super Waspaloy is a compositional (lower carbon and higher titanium plus aluminum) and processing derivative of the widely-used nickel-base alloy, Waspaloy.

The new alloy evolved from the processing work carried out by one of the authors (Couts) in which the effect of lower forging temperature on the phase equilibria and properties of Waspaloy was studied.

Deye and Couts compare the tensile, low cycle fatigue, and creep rupture properties of Super Waspaloy forgings with the same of Waspaloy. They further discuss the microstructural differences. The authors show that the mechanical properties can be correlated with the physical metallurgy of the alloy and, as a result, the microstructure can be used as an effective quality control check.

Mankins and Wenschhof of Huntington Alloys, Inc. presented a paper on "Microstructure and Mechanical Properties of INCOLOY Alloy 800 After 14 Years of Service as a Catalyst Tube in a Steam-Methane

Reformer." The catalyst tube was removed for examination after 14 years of satisfactory service and the authors catalog the fine microstructural changes that took place during service in the temperature range of 540 to 815°C (1000 to 1500°F).

Additionally, room temperature tensile and stress rupture properties were carried out and correlated with the fine structure. Strength increase without any adverse ductility effect is attributed to precipitation of $Cr_{23}C_6$. Small quantity of discrete, blocky particles of sigma phase found in one section of the tube was ascertained to be innocuous.

The application papers, although limited in nature, since they dealt with specific alloys, did contribute to the general theme of the conference. The authors clearly showed that by utilizing the microstructural control, optimum properties of a material can be accomplished.

G. N. Maniar

Research and Development Center
Carpenter Technology Corp.,
Reading, Pa., session chairman.

C. T. Sims[1]

Microstructural Objectives for High-Temperature Alloys in Advanced Energy Systems

---

REFERENCE: Sims, C. T. "**Microstructural Objectives for High-Temperature Alloys in Advanced Energy Systems,**" *MiCon 78: Optimization of Processing, Properties, and Service Performance Through Microstructural Control., ASTM STP 672,* Halle Abrams, G. N. Maniar, D. A. Nail, and H. D. Solomon, Eds., American Society for Testing and Materials, 1979, pp. 480–513.

ABSTRACT: This paper reviews six advanced systems in a broad fashion helpful in orientation of engineering and technical personnel not directly involved in such developments. These are coal utilization systems including coal liquefaction, coal gasification and pressurized fluid beds, nuclear systems including liquid metal fast breeder reactors (LMFBR), and high-temperature gas reactors (HTGR). In concert with these systems, yet cross-functioning, superalloy technologies are discussed for combined-cycle electrical plants and high-temperature heat exchangers. Then potential applications and problems for superalloys in the systems, are identified, drawing from this base examples that might typically be applied, utilizing these to discuss ideal microstructures one may find.

KEY WORDS: steels, microstructure, superalloys, power systems

The objective of this paper is twofold. First, to review certain advanced energy systems in a broad fashion helpful in orientation of engineering and technical personnel not directly involved in such developments. Second, it is to identify potential applications and problems for superalloys in the systems, drawing from this base examples that might typically be applied, then utilizing these to discuss ideal microstructures one may find.

More specifically, it is intended here to cover coal utilization systems including coal liquefaction, coal gasification and pressurized fluid beds, nuclear systems including liquid metal fast breeder reactors (LMFBR), and high-temperature gas reactors (HTGR). In concert with these systems, yet cross-functioning, superalloy technologies are discussed for combined-cycle electrical plants.

---

[1] Manager, Advanced Materials Programs, Gas Turbine Division, General Electric Co., Schenectady, N. Y. 12345.

Energy Systems

Coal Utilization Processes

The U.S. Department of Energy (DOE) has identified a "National Plan" to assure this country sufficient energy. In the overall sense, the idea is to survive the next 20 to 30 years until the breeder reactor, nuclear fusion and conceivable solar energy can be brought into fruition and to create relatively unlimited energy sources. Obviously then, a heavy burden falls on the utilization of coal in this major intermediate period. Processes for generation of electrical energy from coal become vital.

For instance, projections for the use of coal during the period 1975 to 2000 envision an almost three-fold increase, to a total of about 50×10^{15} Btu[2] equivalent. One-third of this, about 14×10^{15} Btu is expected to be in the form of synthetic oil and gas from coal, almost exactly the same as the total energy drawn from coal in 1972.

All of the processes related to the use of coal for energy can be classified [*1*][3] into *coal conversion processes* and *coal combustion processes*. The former refers only to the *conversion* of solid coal into fuel to be used in other physical forms, obviously either gas or oil. In the latter case, the processes are ones in which the coal is essentially completely *combusted*, and the *gas stream* from the combustion process is directly utilized in power generation.

Four coal utilization processes will be discussed later. The first two, coal liquefaction and gasification are *conversion* processes; the others, conventional combined cycle plants and fluid bed combustion are *combustion* processes. Magnetohydrodynamics (MHD), a fifth process, is not covered here because of its limited potential for superalloy utilization.

The conversion of coal has intrigued man for generations. Coal is composed of a very complex high-molecular-weight polymer solid, with an average composition of about $CH_{0.8}$. However, it is chemically *dirty* and difficult to use as a solid. Accordingly, it is desirable to convert coal into liquid or gaseous components. The general idea is to increase the hydrogen-to-carbon ratio to generate more useful and cleaner fluid products, causing less atmospheric contamination. As the hydrogen to carbon (H/C) ratio increases, heavy oils are first generated, then fuel oils, and then petroleum distillates, reaching H/C levels of about $CH_{1.5}$. Around this point, liquefaction has occurred. One can say the ultimate product would be gaseous methane, CH_4, but in coal gasification processes the products range through many lower ratios also. Potentially, the

---

[2] 1 Btu = 1.055×10^3 J. For general clarity, contemporary units are retained prime in some instances.

[3] The italic numbers in brackets refer to the list of references appended to this paper.

product has markets as chemical feedstock, in transportation, and electric power generation.

Table 1 identifies many liquefaction and gasification processes as we know the technology now, but many changes can be expected in the process.

COAL GASIFICATION—Coal is heated and reacted to be converted into a usable gas, which goes into pipelines or directly to nearby process plants. Gasifier systems generate *low-Btu* or *high-Btu* gas. A low-Btu gasifier (such as the well-developed Lurgi) for a producer gas (110 to 150 Btu-ft^3) system is shown in highly simplified version with a combined cycle in Fig. 1. It uses counter-current flow of coal and gases, lock hoppers to control coal feeding and ash removal, and dust, sulfur, and alkali are removed at low temperatures. In most low-Btu systems, the gas is cooled and cleaned following gasification, so that the effluent gas will be relatively noncorrosive. Low-Btu systems will probably be the first to evolve commercially, and in the developmental sense, "third generation" systems are coming up.

High-Btu gas systems (200 Btu/ft^3 or more) are also fashionable. DOE and the American Gas Association (AGA) have a large joint effort to produce pipeline quality gas. The processes supported are Institute of Gas Technology (IGT) Hygas, Consol CO_2 Acceptor, Bituminous Coal Research (BCR) Bigas, and the Bureau of Mines Synthane process. The Bigas Process, which operates at relatively high temperatures, uses a coal-water slurry as feed. In the gasifier, steam and recycled char react with the fuel coal at 7 MPa (1000 psi) and in temperature ranges from 900 to 1600°C (1700 to 3000°F) to generate a gas composed mainly of H_2, CO, CH_4, CO_2, and H_2O. High-Btu systems generate gas that is readily combustible to high temperatures and thus, leads directly to more efficient gas turbines, although the gas may be more corrosive.

Other major differences also exist between coal gasification schemes. For instance, the *type* of bed is very significant. The Lurgi and General Electric (GE) gas systems use a fixed bed; Westinghouse and IGT use a fluid bed; and the Koppers-Totzek and Pittsburg-Midway systems feature suspension bed. Fisher-Tropsch uses a molten bed. Don't forget that simple fixed-bed gasifiers have been industrial equipment for 150 years!

The problems—Coal gasification is a technology involving many developing systems, so it is difficult to nail down neatly the materials problems involved. Figure 2 is an attempt to corral the various coal gasification systems into a series of major process steps to use as a roadmap for consideration of materials applications and needs [2].

The map, Fig. 1, is divided into three major segments. From the top, Coal Preparation and Handling involves processes conducted at moderate ambients; major problems expected are erosion, wear, and abrasion.

Skipping to the bottom, it turns out that the steps below Heat Recovery

TABLE 1—*Selected coal conversion processes.*

Process Name	Sponsor/Owner	Gasification	Liquification	Status/Remarks
Bigas	Bituminous Coal Research, Inc.	✓	✓	120 T/day plant in construction
CO_2 Acceptor	Consolidated Coal Co.	✓	. . .	40 T/day pilot plant operating
Gegas	General Electric	✓	. . .	pilot plant operating
Koppers-Totzek	Heinrich Koppers	✓	. . .	15 plants operating
Lurgi	Lurgi Minrealöl Technik	✓	. . .	14 world wide plants
Synthane	U.S. Bureau of Mines	✓	. . .	pilot plant operating
Coalcon	Union Carbide/ Chemical Construction Co.	✓	✓	pilot plant operating
Congas	Consortion	✓	✓	synthetic crude oil
Fischer-Tropsch	H.W. Kellog & others	✓	✓	gas, gasoline, and other products
Hygas	Institute of Gas Technology	✓	✓	75 T/day pilot plant operating
Toscoal	Oil Shale Co.	✓	✓	25 T/day pilot plant operating
Coed	FMC Co.	. . .	✓	synthetic crude
H-Coal	Hydrocarbon Research Inc.	. . .	✓	synthetic crude
SRC	Pittsburg-Midway Coal Co.	. . .	✓	synthetic fuel oil

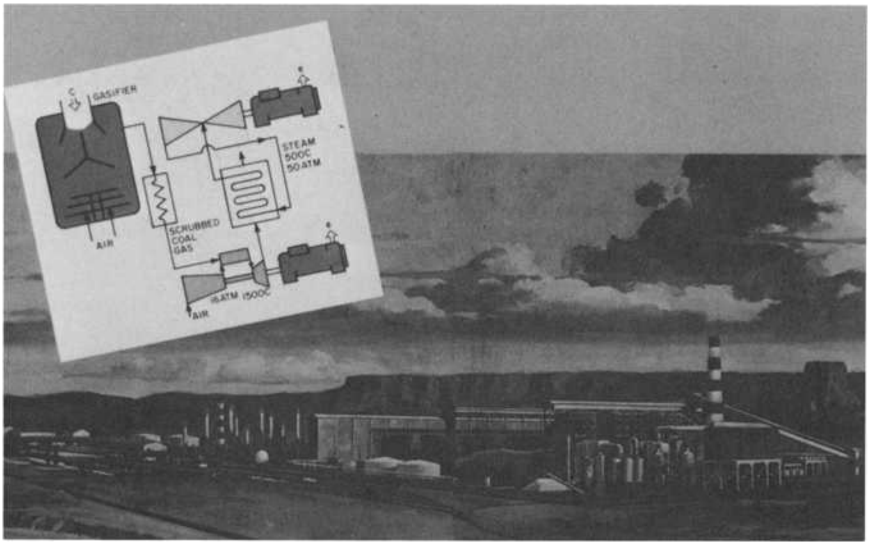

FIG. 1—*Coal gasification with combined cycle (first U. S. commercial gasification plant, near Farmington, N. M.: Fluor Corp.).*

are quite well-known to the contemporary chemical processes industries. The non-superalloy materials needed should be available from current practice, although the great component *size* may be a problem.

It is in the Coal Pretreatment, Coal Gasification, and Gas Quench steps and their appendage processes where materials will see extremes of environmental attack, and where superalloys may be needed.

In Coal Pretreatment, the problems relate principally to heating the coal and reactants to near-reaction temperatures through heat exchange with the reaction products of gasification. Hot erosion and abrasion from the feed coal and corrosion from the after-products of gasification will be heavy. For the sake of brevity, these problems are not detailed here, but will be—at least in the corrosion sense—similar to those discussed in Gas Quench.

Depending on the specific process, Coal Gasification will operate to over 1200°C (2000°F) and at 10 atm pressure. A gasifier will be an extremely large vessel or vessel group, into which the coal flows and is reacted to produce gas.

First, there will be significant erosion effects from the abrasive solid coal being injected and erosion from the solid ash ultimately produced. However, it is from the coal gas product that the greatest problems generate. In addition to relatively clean hydrogen and carbon-containing gases, with high intrinsic energy of combustion produced, many undesirable species including sulfides, sulfites, sulfates, ammonias, cyanides, volatilized oils, phenols, and our old trace-element enemies potassium,

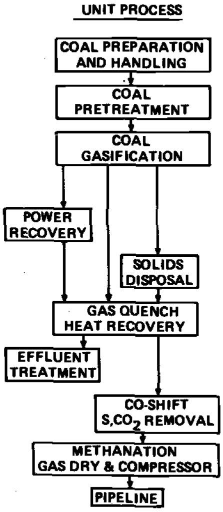

UNIT PROCESS	EQUIPMENT	PROBLEMS
COAL PREPARATION AND HANDLING	CONVEYORS, BINS, HOPPERS,CRUSHERS, SLURRY, HANDLING.	EROSION, WEAR, WET CORROSION (COAL).
COAL PRETREATMENT	PREHEATER, QUENCH SYSTEMS, HX, HOT SOLIDS HANDLING.	EROSION, WEAR, WET AND HOT CORROSION, (COAL, STEAM, GASES).
COAL GASIFICATION	MULTISTAGE PRESSURIZED CYCLONES, SOLIDS CONVEYING AND EDUCTING, GRIDS, CONTROL VALVES, LET-DOWN VALVES.	LARGE SIZE, EROSION, AND ASH FUSION, HOT AND CONDENSATE CORROSION. (H_2S, H_2, CO_2, NH_3, ORGANICS Na, K, FLUXES, SALTS, SLAGS).
POWER RECOVERY	DUCTING, GAS TURBINES.	HIGH-TEMPERATURE, HOT CORROSION (CORRODING GASES).
SOLIDS DISPOSAL	LOCK HOPPERS, PUMPS.	EROSION, WEAR, WET CORROSION. (ASH, TAR, CHAR, Na, FLUXES, SALTS, SLAGS).
GAS QUENCH HEAT RECOVERY	PRESSURE CHOKE, ORIFICE, HX.	HOT CORROSION, EROSION (CORROSIVE GASES, CONDENSATES).
EFFLUENT TREATMENT	CONTAINERS, CONDENSERS,REACTORS.	CORROSION.
CO-SHIFT S,CO_2 REMOVAL	CONDENSERS, REACTORS.	CORROSION.
METHANATION GAS DRY & COMPRESSOR	REACTORS, DRYERS, COMPRESSORS.	CORROSION.

FIG. 2—*Equipment and material problems characteristic of coal gasification processes.*

sodium, vanadium, and lead will occur. The incredible corrosion potential is obvious! Further, from this gaseous melange, liquids with high corrosion potential will condense on cooler parts of the system. The departing ash, in addition to being erosive, will be composed of oxides, sulfates, other inorganics and organics, and alkali metal concentrates. It is not overly apprehensive to note the systems may be reducing or oxidizing or *both* in different places. And this is all at high pressures.

In this matrix, it is very important to understand that only a *few ppm* of elements such as sodium, potassium, vanadium, and lead can initiate a severe reaction. Current specifications for heavy oil (which has many similarities) burned in gas turbines identify a limit of 1.0 ppm for sodium plus potassium.

Another problem is expected to be the huge size. Vessels or shells for the gasifier will be over 65 m high. They must meet Section VII of the ASME pressure vessel code. Obviously, such systems are so large that costly superalloys cannot be used. Instead, a growing solution is to use ceramic linings somewhat as used in blast furnaces, although gaseous corrodents will still penetrate and raise hob with the metallic support structures. Another technique to control corrosion is to waterjacket the vessels, creating a *cold wall* system. However, while the latter approach will avoid high-temperature gaseous corrosion, it will lead to low-temperature corrosion from condensation on the wall.

Even though these huge reactor vessels may be constructed of strong fabricable low-alloy materials utilizing ceramic linings or water cooling for protection, it is inevitable that other components within the system must withstand the full force of the corrosive media without protection. Solids separation cyclones, dip legs, solids, transfer piping, valves, instrument probes, refractory wall anchors, and stirring mechanisms all require high strength and fabricability and face extremes of temperature and corrosion attack. It is in some of these components that superalloys will find applications. Their high-temperature strength, structural stability, and corrosion resistance will be requisite.

Following the coal gasification operation itself, further corrosion problems are expected in Gas Quench and Heat Power Recovery components. For instance, in the Battelle and the Consol processes, gas turbine power will be generated from gas streams at 750°C (1500°F) and 1.5 MPa (1500 psi). In addition to carryover of corrosive species from gasification, SO_2 will be present in quantity. With sodium or potassium present, classic aggressive alkali sulfates will form. Thus, again we are brought back to the continuing problem of identifying materials with corrosion resistance. Also, one cannot ignore the high potential for erosion and for fouling on ducting separators, valves, gas turbine parts, and the like. For a more detailed breakdown of the corrosion, erosion, and fouling phenomena, the reader is referred to the discussion of the pressurized fluid bed process.

Wherever a hot gas stream is directed to heat recovery, the *gasification gas side* of the heat exchanger will be subject to all of these problems also. Temperatures can range up to 1000°C (1800°F) and pressure to ~70 atm (70 bar). The heat exchangers will be large, and the piping must be strong corrosion-resistant alloys; fabricability and weldability are obviously essential. The *leaner* superalloys may find application here as heat exchanger (HX) piping.

In many gasification systems, the coal gas will be water-quenched to allow removal of sulfur and other corrosion contaminants. During cooling, of course, a variety of liquids will condense; again, the potential for severe corrosion attack is generated.

Superalloy application—Superalloys will be found at least in the equipment listed and in the mill product types identified. Principal equipment types include: heat exchangers, pressure let-down valves, instrumentation, gas ducting, control valves, cyclones, and gas turbine hot stages (in power recovery). General form/type of superalloy required are tubing, small forged parts, fabricable sheet, and investment castings.

COAL LIQUEFACTION—Coal liquefaction, like coal gasification is far from new. In fact, coal liquefaction generated most of Germany's aviation gasoline near the end of World War II. Perhaps the most well-known early process was the Fischer-Tropsch, but many others exist (Table 1). A Fischer-Tropsch process plant producing gas, liquid fuels, methanol, and ammonia is operating in Sasolburg, South Africa. U.S. interest began in the 1950's; that interest is now vital.

Liquefaction of coal can be classified into about four processes:

pyrolysis, where coal is heated under reducing conditions (and often high pressure) to convert the solid to a gas, tar, and a char; *solvent extraction,* involving use of a hydrogenerated solvent to drive hydrogen into the carbon compounds in the coal; *indirect liquefaction,* where the coal is gasified but the gas is then purified and reacted with other products to generate a liquid; and *hydroliquefaction,* where coal is reacted with hydrogen-rich super-heated steam at high temperature and pressure so that a variety of liquids such as gasoline or methanol are produced.

In any case, the overall idea is to increase the hydrogen-to-carbon ratio (add hydrogen), often with the use of a catalyst. DOE feels that H-Coal, the SRC (solvent-refined coal) process, and a donor solvent process will be those reaching *third generation* development in the 1980's [*3*]. Plants will have general appearances much like gasification plants (Fig. 1).

Most coal liquefaction processes appear to be conducted at temperatures and pressures where the corrosion and strength requirements identify that stainless steels could do the job for typical plant construction needs. All processes "go" at less than 550°C (1000°F), except for the COED variation of pyrolysis where temperatures of 625°C (1150°F) are reached and where char conversion occurs at about 1000°C (1800°F).

Like coal gasification, however, coal liquefaction plants will include very large vessels and reactors. Thus, the *size* of the component is significant metallurgically, although this may not be of concern in superalloy application. Where unreacted coal itself is part of the processing cycle, erosion, abrasion, and corrosion problems are certain to generate similar to those in coal gasification.

The problems—Major materials problems will be found in components that handle coal-liquid slurrys, in pressure let-down valves, and general service valves, as well as transfer piping, hangers, and of course, hot components in equipment utilizing the product, such as auto engines and gas turbines. The problems will surface as hot corrosion, stress corrosion, carburization, and other surface attack characteristic of highly corrosive/erosive media.

Superalloy application—The use of superalloys in coal liquefaction itself will probably be modest because most of the proposed systems have low temperature operating characteristics. For instance, the solvent extraction, indirect liquefaction, and hydroliquefaction processes operate at 480°C (900°F) maximum. However, the pyrolysis process operates to 600°C (1100°F) with char gasification to 1000°C (1800°F).

Thus, stainless steels will do many of the tough jobs, although some may require alloys like Inconel 800 and HK-40. Superalloys, of course, will be utilized in the steam turbine-gas turbine combined cycle plant, as discussed separately later. The components could be either wrought or cast, depending on part complexity and economics.

In summary the principal equipment types include: fasteners, let-down valves, instrumentation, gas ducting, control valves, and gas turbine hot stages (in power recovery). General form/type of superalloy required are tubing, small forged parts, fabricable sheet and small investment castings.

PRESSURIZED FLUID BED COMBUSTION—"The most efficient way to utilize coal is by its direct combustion. Processes to permit combustion in fluidized bed boilers have a high potential payoff and will be pursued." is a statement from DOE [*1*]. Thus, the fluid bed combustor (FBC) represents a major potential method for energy conversion.

In the FBC, coal is burned in a fluid bed, under pressure (PFBC) or not (AFBC), to produce a hot gas stream that can drive gas turbines directly; boiler tubes criss-cross within and immediately above the fluid bed for steam generation. The hot high-pressure gases are never cooled and drive the gas turbine directly, so no loss of sensible heat occurs! However, this also means the gas is not cleaned before use. A simplified flow diagram for a PFBC system is given in Fig. 3. Atmospheric fluid beds are also of interest, but not discussed here for brevity.

It is presently believed that PFBC's will operate with bed temperatures up to about 950°C (1700°F), and will be fed by coal mixed with dolomite to control sulfur emission. Combustion will take place at about 10 to 15 atm (1 to 1.5 MPa). Systems will be designed for about 200 000 h life. However, to avoid use of intermediate heat exchangers, the hot gases pass directly from the combustion zone through several stages of filtration, and then to the gas turbine. AFBC's will be somewhat similar, but will not contain a gas turbine.

The fluid bed has high vertical thermal conductivity so combustion of the fluidized coal buttons occurs uniformly and quietly. Efficient combustion of the gases released by the coal also occurs, and these bubbles of "flue" gas help mixing in the bed. The dolomite (limestone) in the bed reacts with sulfur from the coal to form SO_1 and ash. NO_x emission is claimed relatively low. Design must minimize carryover of particulate fine by the escaping flue gas; steam boiler-tube geometry throughout the bed affects this significantly.

Additionally, it appears that in the bed the steam tubes become coated with a thin enamel-like layer of oxide, which may offer some corrosion protection. Importantly, the temperature of combustion is held to below coal ash fusion point (this will be discussed later), a significant benefit. However, despite the promise of FBC systems, it is this author's opinion that the FBC gas stream has more potential to destroy construction materials than in any other energy system operating below 1200°C (2000°F) under oxidizing condition. Some details are described following.

The problems—The potential of the atmosphere generated from the fluid bed to erode, corrode, and foul boiler tubes, ducting, filtration systems, and the gas turbine is the most significant problem in PFBC systems. Hot stage components of the gas turbine will be particularly

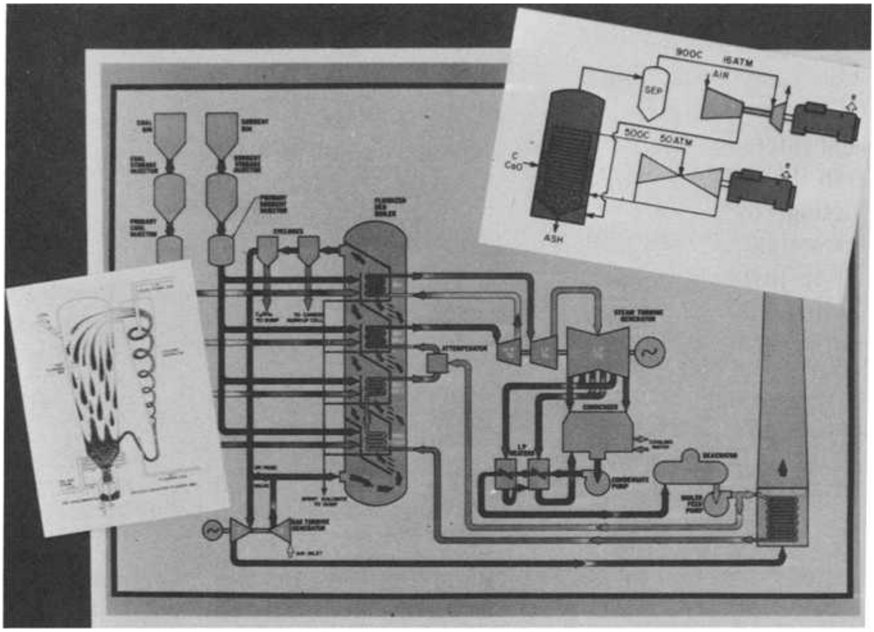

FIG. 3—*Pressurized fluid bed combustion power plant with gas and steam turbine combined cycle.*

susceptible. The gas will carry particulate ash/dust as well as a variety of vaporized aggressive chemical species, such as vaporous components of sodium and potassium. These impact or condense on alloys in the hot gas path and on critical gas turbine parts to cause hot corrosion, erosion, and fouling. All of these problems have been experienced in studies of gas streams from directly combusted powdered coal and from burning of residual fuels [*4*].

Experience in industrial turbines has shown that *hot corrosion* can be controlled to reasonable levels if sodium and potassium (the most aggressive commonly-found contaminants) do not exceed about 1.0 ppm in an oil fuel, (which is about 0.2 ppm in the gas stream) depending upon the air-to-fuel ratio. However, analysis of PFB gas streams show sodium plus potassium contents over 100 times these levels. Thus, there is far more sodium plus potassium in this type of system than the minimum needed to initiate hot corrosion; further, it is now believed that sodium plus potassium creates a much more aggressive atmosphere than sodium alone. In addition, it has recently been observed that the dolomite utilized to absorb sulfur may also be a very significant source of trouble [*5*]. Unacceptable hot corrosion will occur in gases from fluid bed combustors unless (*a*) sodium plus potassium contaminants in the combustion products are reduced more than two orders of magnitude and the effects of calcium from dolomite be neutralized, or (*b*) much more hot-corrosion-resistant materials than presently available can be brought into service, or both.

Erosion effects are also feared. In coal FBC, the gas stream will entrain a considerable volume of hard particulate matter (both ash and inorganics) from the combusted coal. This could cause direct surface metal loss on ducting, cyclones, other separators, and hot-stage gas turbine parts downstream.

For instance, the Locomotive Development Committee of BCR, studied a directly coal-fired gas turbine from 1949 to 1959. Catastrophic erosion of the trailing edges and bases of rotor blades at 1400 to 1700°C (2500 to 3000°F) occurred [*6*]. Shape and arrangement of airfoils were then changed to direct the ash towards the casing, instead of the root of the rotor blades. Titanium carbide wearstrips were installed at key locations. These changes resulted in a significant reduction of erosion, but the results were still far from satisfactory for the long-time service essential for power generation use.

In order to minimize such erosion problems from direct combustion of coal, a comprehensive approach involving parts design, materials tolerance, and filtration must be considered, to control gas velocity, avoid particulate flow concentrations, and utilize highly effective filtration systems. Material studies must consider control of the fluid bed to minimize emission, testing and evaluation of materials to resist the attack, and application of materials protection techniques, such as cladding, coating, and hard surfacing.

However, erosion experience so far in PFBC is a small bright spot [*4*]. Only slight erosion-related attack has been observed on components in the gas stream. *Conventional* combustion of coal in the range of 1400 to 1700°C (2500 to 3000°F) yields flue dust particles that are melted and sintered to round, hard, apparently glassy particles; obviously, these would cause severe erosion damage when impacting metallic compounds.

However, in FBC the temperature in the fluid bed is maintained below 900°C (1700°F). The fly ash does not form hard spheres. Instead, the particles appear to be low-density agglomerates of a very friable nature (Fig. 4). When impacting, the particles themselves may break up, sharply reducing damage to the impacted component. The possibilities of erosion damage on turbine hardware and other components appear reduced greatly and may be insignificant! However, since very effective particulate filtration will still be needed to prevent fouling and hot corrosion, even further improvement in the erosion situation can be expected.

Fouling is a severe problem. Coal is a particularly prolific source of fly ash, so in the FBC, uncontrolled fouling can be expected in a relatively short time. The dolomite/coal reaction creates additional fouling ash. In

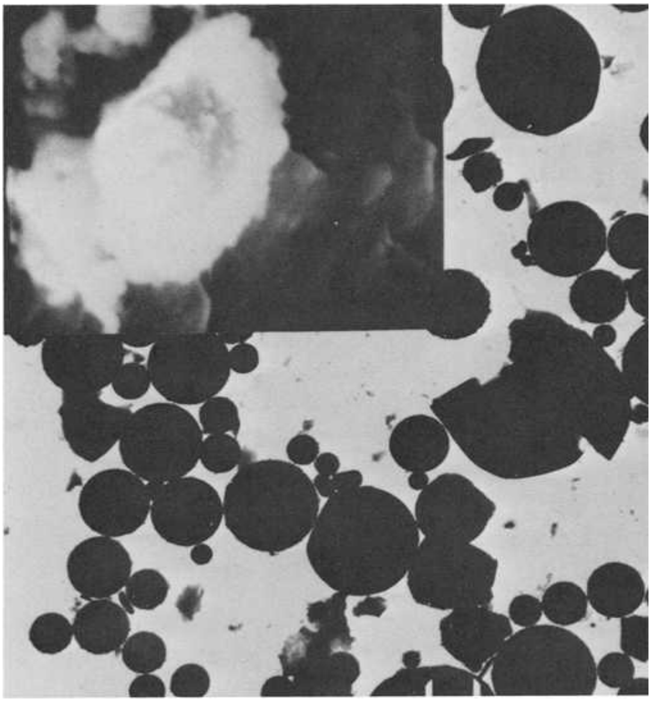

FIG. 4—*Scanning electron micrograph of fly-ash (original magnification ×10 000):* (background) *from direct combustion of coal, and* (upper left) *from FBC gas stream.*

one program [*1*], fouling occurred in less than 50 h on a nozzle cascade, and other fluid bed experiments have found similar effects. Turbine output and efficiency are reduced, and cleaning techniques become mandatory. In addition, destructive effects will occur on other gas-stream containment and treatment components. Critical effects and results to date can be summarized as follows: (*a*) sodium and potassium appear to be a main cause of deposit formation, and calcium in coal ash increases rates of deposition; (*b*) deposits usually promulgate corrosion of the host alloy; (*c*) to date, no information exists that identifies that the construction alloy effects the fouling process itself significantly; and (*d*) cleaning of deposits from hot-stage parts may be possible by water-washing, thermal shock, and injection of nutshells.

Thus, coal burned in FBC will certainly generate gas-stream particulate matter that will cause serious turbine fouling, even below 900°C (1700°F). Cleaning techniques to remove the deposits must be developed.

Superalloy application—In PFBC systems, one can expect to find superalloys applied in approximately the following pattern. Principal equipment types include: gas turbines, boiler tubes, valves, separators and cyclones, and ducting, elbows, etc. General form/type of superalloy required are tubing, investment castings, sheet and plate, coatings and claddings, and large forgings.

Combined Cycles—A *combined cycle* is merely a steam turbine and a gas turbine combined. However, the gas turbine acts as a *topping cycle* to the steam turbine system, raising the critical upper combined-cycle temperature and increasing efficiency significantly. The plant also has low first cost. Importantly, steam/gas turbines operating in combined cycles will be integrated as the major rotating electrical-generating equipment operating from both moderately-advanced and distant sources of energy such as coal gasifications, fluid bed combustion, certain types of reactors, and conventional boilers. Thus, while discussed separately, combined steam turbine/gas turbine cycles will usually be found integrated with many other systems, such as those just covered. For simplicity, superalloys for gas turbines designed for significantly increased operating temperatures are covered here.

As fuel costs have increased, combined cycles have become of interest to utilities for operation at 2000 to 5000 h per year (*mid-range*). In these cycles, a contemporary industrial gas turbine combined with an exhaust heat recovery steam system with the modest non-reheat steam conditions of, say 6 MPa/480°C, (850 psig/900°F) about 42 percent overall plant efficiencies are attainable; the incremental capacity from the bottoming steam system is approximately half of the gas turbine, and is attained with no additional fuel. This high efficiency advantage plus relatively low cost for the combined cycle plant (about $225/kW) make combined cycles attractive for base-load service. Further, the exhaust heat from the gas turbine, instead of being rejected into the air, is used to raise steam to help drive the steam turbines. In effect, this use of a gas turbine improves its share of the efficiency load markedly. In fact, fuel economy is so good that combined cycle owning costs (28 mils/kWh) compare favorably with modern steam plants (39 mils/kWh) and thus have become attractive for base load application as well [*1*]. At 1600°C (2900°F) fuel cost savings of 25 percent might be possible.

A typical combined cycle with the two major components—a steam turbine and a gas turbine—are shown in Fig. 5. Combined cycle steam plants are not new; in fact, the 234-MW Oklahoma Gas and Electric plant was installed in 1959, and dozens of combined cycle plants are working throughout the world today. Net plant efficiencies of 44 percent are being forecast for the 1980's with advances in the gas turbine the critical contributing factor. Plant sizes up to 600 MW are possible.

The problem—However, combined cycle plants are not yet really *advanced* in the sense intended here. The challenge comes when designers, metallurgists, and manufacturers will attempt to build combined-cycle plants that show net plant efficiencies in the range of 50 to 55

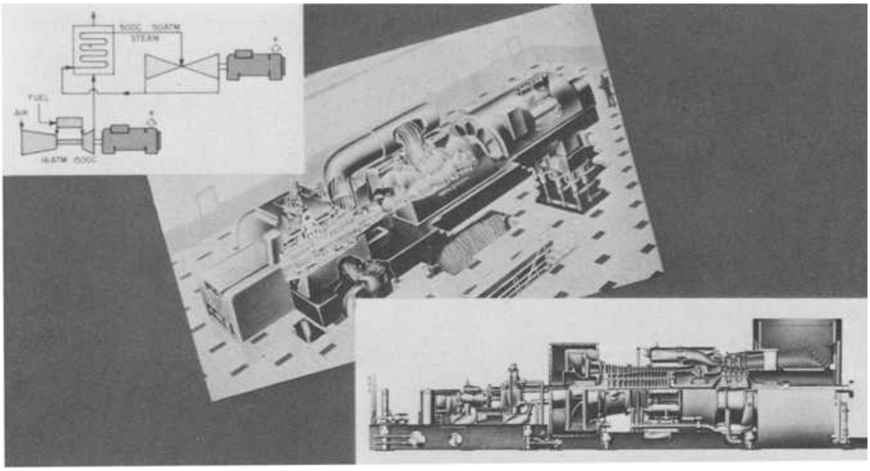

FIG. 5—*GE MS 7001 gas turbine and 3600 rpm steam turbine generator as utilized in combined cycle electric power plant.*

percent. The gas stream must reach about 1600°C (2900°F) or more, and lives of 100 K h or more must be attained. Without question, no contemporary gas turbine remotely can survive under these conditions. Further, while generalized predictions often assume that the fuel to be burned is a natural gas or clean oil, it is now clear only that future fuels for the gas turbine will be *different,* often heavy, contaminant-laden oils or combustion or conversion products from coal, with as yet unevaluated contaminant effects.

To meet the challenges of very high temperature for gas turbines, technology appears to divide into three categories: (1) air cooling; (2) water cooling; and (3) very-high-temperature materials, such as ceramics.

Air cooling is well known and technology well advanced. Superalloys can live in gas streams that are much hotter than normally survivable by cooling the metal with air from the compressor bypassed into the turbine section. This technology is becoming complex and for industrial turbines as gas stream temperatures increase, increasing amounts of cooling air will be required; eventually, so much is required that efficiency of the system drops, even though temperature and output continues climbing. Practically, this appears around 1400°C (2550°F).

Superalloys used will be similar to those we know now, but more strength and improved oxidation and corrosion resistance are needed. Improved compositions will yield some advance, and directional solidification and eutectics will get in the game. However, the size of industrial gas turbine parts is so great that use of the latter will be severely limited. Single crystals, perhaps used in aircraft engines, will not be used at all.

Thus, in a sense, we might say the picture is clear; superalloys improved will be used for this service; 1400°C (2550°F) or so will be the limit.

Water cooling is the next step. The large DOE High-Temperature Turbine Technology Program (HTTT) takes this approach as its main thrust [7]. Water cooling really opens such a large new door that design considerations immediately reach towards gas temperatures of about 1600°C (2900°F), since the "hot" gas turbine nozzle and diaphragms economically can be cooled to operate at very moderate temperatures indeed, such as about 550°C (1000°F). If so, it might appear superalloys might not even be necessary, except for the following considerations:

(*a*) *Surface Stability*—The fuels generating these high-temperature gas streams may very well be highly corrosive. Therefore, the materials servicing at 550 to 600°C (1020 to 1110°F) still require corrosion resistance, and superalloy claddings with high alloy content have such resistance.

(*b*) *Support Structures*—While the very hottest parts will be water cooled, downstream buckets and nozzles and components such as diaphragms, supports, exhaust structures, and combustion systems will be operated with superalloys just as now, and they will have to demonstrate the usual necessary strength and surface stability.

Very-high-temperature ceramic materials are under intensive study also. The current effort to apply them to gas turbine hot stages has consumed more financial support than any other major materials development effort we have seen. Some do appear to have the strength and durability potential to operate up to about 1600°C, although successful design and acceptable materials are a long way from being proven.

At their best, ceramics are expected to just sit there and take it. Then, as the designer backs away from the searing 1600°C (2900°F) gas stream, the materials that support the ceramics must be defined. This is a difficult task, since structural ceramics have high thermal conductivity, and are chemically reactive with metals.

Thus, while the first echelon of mechanical support will probably be ceramics also, design must allow attachment to metal eventually. Once again, the characteristic strength and surface stability of superalloys will be needed here, even though they now do not have the honor of facing the gas stream itself. In this application, the superalloys must demonstrate long-life chemical stability in contact with ceramics, a real problem!

Superalloy application—The principal equipment types include gas turbine components: buckets, nozzles, combustion liners, wheels, transition sections, support members, and hot gas ducting. General form/type of superalloy required are forgings, plate and sheet; and investment castings.

Nuclear Systems

Liquid Metal Fast Breeder Reactor (LMFBR)—While the specifics of predictions concerning the systems from which we will obtain energy vary from year to year, one consensus appears to vary little. This is that nuclear energy will shoulder a greater portion of the electric power load as time goes on. While current political activities are clouding the technology issues, most responsible engineers feel that LMFBR's eventually will be the principal energy-generating nuclear plants; on this assumption, they are covered briefly here.

An LMFBR system is shown in Fig. 6. A fast breeder reactor is *kind of a catalytic nuclear burner* that consumes U_{238} or Th_{232} so that the Pu_{239} or U_{233} catalysts are more than self-regenerating. The LMFBR's will be the most economical systems, because of their capability to produce (*breed*) more fissile material than consumed. Further, in addition to production of direct electric energy, the additional plutonium and uranium will be available for thermal reactors (LWR's and HTGR's) to use. Even more, they will be fueled with depleted uranium from the tailings built up from enrichment needed for LWR's running at present. Plutonium being held from LWR's will also be used. LMFBR's will be more thermally efficient than LWR's.

Major technical features of LMFBR's, of course, are that liquid sodium is used as the primary coolant. The fuel elements will be some form of uranium or plutonium oxides clad with stainless steels or higher alloys. Most systems visualized show an intermediate heat exchanger between the reactor and the steam generator. Currently concepted systems then identify typical steam turbine-generator sets to make power. Reactor temperatures are not high enough to make gas turbine introduction into combined cycles possible. However, *gas cooled* breeders (not discussed

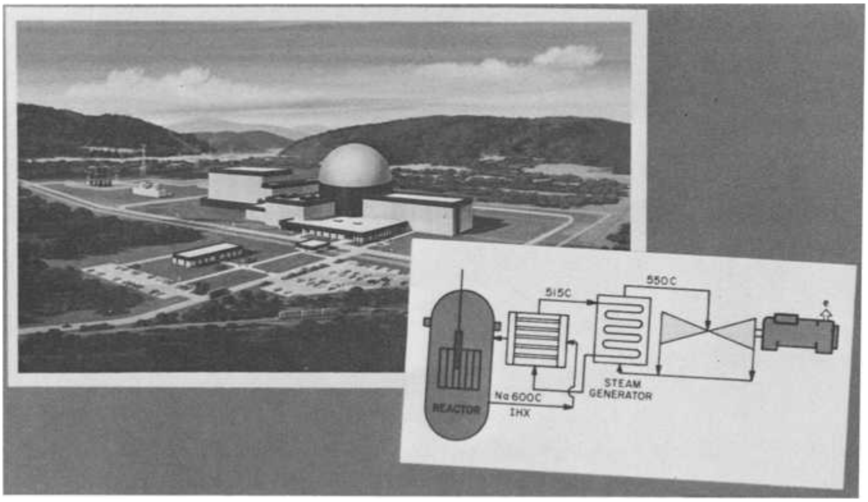

FIG. 6—*Liquid metal fast breeder reactor (Courtesy Clinch River Nuclear Plant).*

here) also are being studied; steam or gas turbines might take off power directly. Temperatures will probably hold below about 550°C (1020°F).

The promise of these reactor systems is regarded as far more viable by Europeans than Americans. Despite operation of the first liquid metal cooled reactor (by eight years), the U. S. will have only about 8 percent of the world's demonstration or commercial LMFBR's by 1984. The major U. S. effort is in the Clinch River Breeder Reactor (CRBRP), a prototype plant of 975 MS_{Th} (380 MW_e) power, the future of which is deep in limbo.

The problem—The action of an LMFBR is the plutonium or uranium fuel material or both contained in a metal cladding or sheeting. These fuel elements and their interrelated structure are all supported in a large moving bath (5 to 8 m/s) of liquid sodium, (the heat exchange medium) and operated in a neutron flux of $\sim 10^{15}$ n/cm^2-s. In the general sense, the major problems can be summarized as follows: (*a*) the core materials must have corrosion resistance to the liquid sodium heat exchange medium, (*b*) the core materials must resist damage from fission-generated fast neutrons, and (*c*) there must be mechanical strength and corrosion resistance in the structural members in order to provide support in the fuel and assure a compact ductile core.

Thus, a strong, fabricable, and corrosion-resistant alloy is needed, with high thermal conductivity, alloy structural stability, and strength up to 800°C (1300°F)—and obviously resistance to neutron damage. Nuclear engineers originally chose cold-worked stainless steels. However, as technology for the LMFBR has developed, a number of more specific materials problems have become evident.

First, it was found fast neutrons generate significant radiation damage in most of the materials considered for fuel cladding use. This includes classical radiation hardening, probably due to small defect clusters, void formation with associated dislocation networks from high doses of fast and helium bubble formation due to (n-α) transmutations. Attacking from within, perhaps swelling from void formation is the most concerning and serious phenomena (Fig. 7), since it results in metal distortion and possibly an unworkable core. To combat this, early plans were to utilize heavily cold-worked stainless steel for the claddings. This provides strength, of course, but it also was claimed expected neutron damage would keep the cold work *locked in* to the metal structure. However, results of radiation experiments finished several years ago showed that while this technique would be useful for modest periods of time, in the long run fast neutron flux results in severe void generation and reduction in strength properties.

It is now generally believed that all commercial austenitic alloys are subject to some degree of void swelling in a fast neutral flux. Since swelling is directly proportional to dose, any neutron flux gradient in the core will cause differential swelling. The problem is acute in fuel

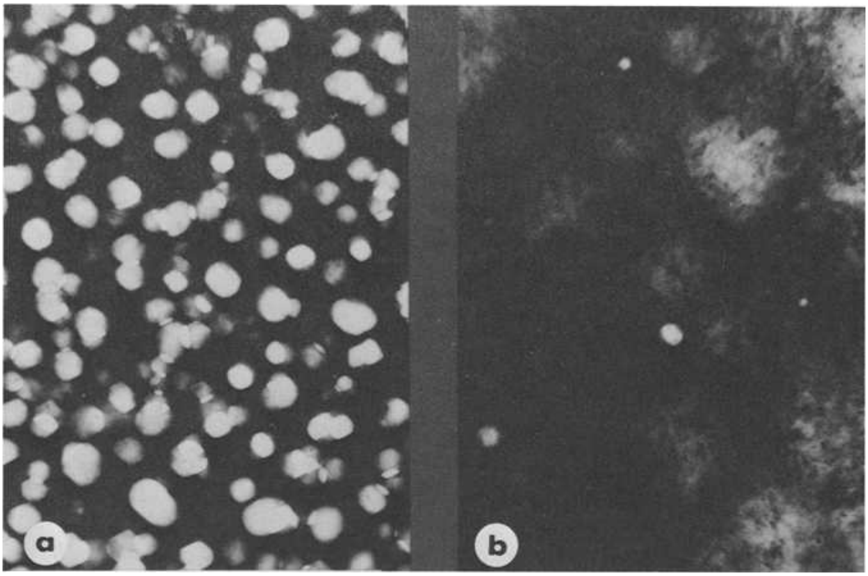

FIG. 7—*LMFBR cladding alloys showing voids generated by bombardment with 5 MeV nickel ions at 625°C damage lever, −140 displacements per atom. (Original magnification ×75 000):* (a) *Type 316 stainless steel, and* (b) *PE-16 alloy. (Courtesy Johnston and Turkalo).*

assemblies in which the radial flux gradient produces differential swelling across a single assembly, causing outward bow from the core center. This has prompted modification in design of the reactor core [*1*].

Two such modifications are currently being considered: a *constricted* core and an *unrestricted* core. In the latter, assemblies are supported only from the bottom and are free to bow. It is estimated that such a design can accommodate no more than 0.35 percent swelling for good service. In a contricted core, assemblies are firmly supported at both top and bottom. Thus, restrained from bowing, the assemblies are designed to withstand as much as 5 percent swelling. Use of Type 316 stainless steel was considered acceptable for the U. S. demonstration LMFBR (CRBR) that utilizes a constricted core. However, the amount of swelling encountered at high fluences precludes use of Type 316 stainless steel for long-time commercial plants.

In development of the unrestricted core concept, the United Kingdom Atomic Energy Authority (UKAEA) is exploiting the greater strength and swelling resistance of superalloys like Nimonic PE-16. The English also believe that cold-worked PE-16 will retain its strength throughout irradiation and that the strengthening γ' will be merely redistributed.

Obviously, LMFBR designs generate materials requirements that approach the limits of austenitic stainless steels. For longer lifetimes and higher operating temperatures, requirements are higher. Further, gains in efficiency can be achieved through use of materials with both higher strength and greater dimensional stability than stainless; this also permits reductions in the structural metal in the core. Recent advances in study of radiation damage attest to the attractive swelling behavior of high nickel superalloys. Reduced swelling in austenitic systems has been clearly shown to be a function of nickel content [*8*], and the basic relation to austenitic systems is obvious (Fig. 7). Though neutron absorption of nickel alloys is greater than for stainlesses, the reduced volume of structurals needed more than compensates for the reduced breeding ratio. Thus, for the longer range and improved performance, superalloys offer considerable potential as LMFBR construction materials. Coating of alloys for nuclear service, long ignored, should be given much more attention; coatings are workhorses in jet engines, where safety is of prime consideration.

Superalloy applications—LMFBR's will require superalloys of the principal component type in the plate or rod-type reactor fuel element. The superalloy equipment form/types include sheet, plate, tubing, and cast structural members.

HIGH TEMPERATURE GAS REACTORS—The high-temperature gas-cooled reactor (HTGR, or HTR, as in Europe) is a concept embracing a nuclear core of graphitic construction with uranium and thorium compound activation. The heat transfer fluid is helium. Application of the HTGR can be to supply heat for electric power generation or for an industrial process (Fig. 8). These reactors are of two general types, a *prismatic* type and the *pebble bed* (illustrated).

Prototype or demonstration plants designed to raise steam for electric power generation include the 40 MW Peach Bottom reactor of Philadelphia Electric Company, and the 300 MW Fort St. Vrain plant of the Public Service of Colorado. Both are characterized by a prismatic reactor core of graphite right hexagons; the blocks of graphite contain fissionable UO_2 in pellet form, and channels in which high pressure helium is heated then flows to heat exchangers to generate steam.

Technologically competitive, an experimental pebble-bed HTR plant of about 8 MW is operated at Jülich, Germany, by KFA (Kernforschungsalage Jülich); a commercial version, the 300 MW THTR, is being built at Oberhausen. A pebble-bed really is a large graphite hopper filled with 6-cm graphite balls containing particulate UO_2 fuel, with helium coolant passing through the bed. It is particularly well-fitted for process heat applications. The Jülich reactor has operated up to almost 1000°C (1800°F).

Present steam plants operate at about 700°C (1300°F). Application of superalloys is modest, principally in the turbine-like circulators for the helium, which use stainless steels or intermediate-temperature iron-nickel

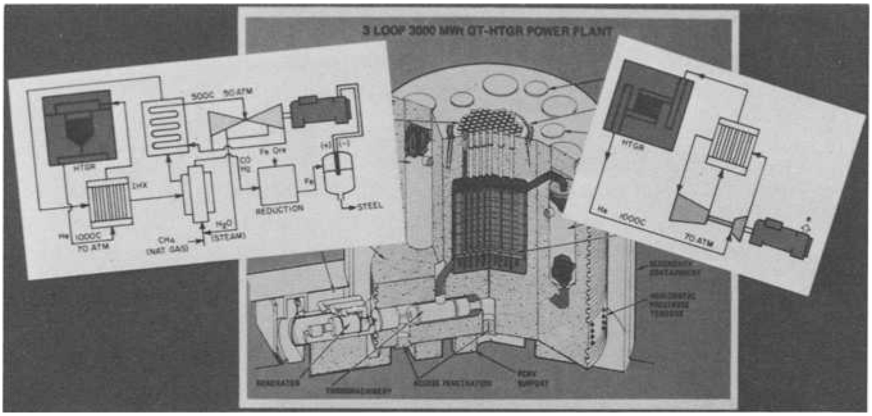

FIG. 8—*HTGR for direct cycle electric power plant* (right) *and for process heat steelmaking* (left).

alloys. However, the potential of HTGR's is to generate helium temperatures to the 1000 to 1200°C (1800 to 2200°F) range. This leads to the concept of *direct cycle,* wherein helium (at 70 atm) drives gas turbines integrated directly into the system as electric generators. Process versions of HTGR's use hot helium temperatures to conduct chemical reactions such as the reforming gas reaction or the reduction of iron ore, to provide heat for steelmaking, to gasify lignite (coal) to methane or synthetic gas, or (ultimately) to crack water for hydrogen generation, vital to German national energy plans. Bear in mind these reactors are virtual *concrete mountains* in the sizes to 1100 MW_e envisioned. Component lives of about 250 000 h are planned (the designers hope!)

The problem—In contrast to normal oxidizing gas streams, the opportunity to design components for helium (an inert gas) should appear a delight. However, it was found early on that *impurities* in the helium can cause surface interaction problems with construction materials, and with time this has been demonstrated to be a very significant problem.

While the helium atom itself is obviously nonreactive, the helium atmosphere (often called HTR-He) contains contaminants. Typical levels of these contaminants (in parts per million) are:

H_2	H_2O	CO	CO_2	CH_4	N_2
10–200	0.5–1.0	5–20	0.5–1.0	1.0–30	5–15

Under high pressure and temperature, these contaminants cause *at least* two deleterious effects in steels, stainless steels, and austenitic superalloys (the obvious construction materials) (1) localized surface reaction with selected elements from the alloy, leading to thin or patchy surface oxidation, internal oxidation, and ultimately to surface cracking; and (2) internal carburization of reactive components from the alloy.

In normal high-temperature oxidation service these effects, or something like them, often occur. However, the significant factor in helium is that P_{O_2} is so low that insufficient (if any) protective oxide film forms on the metal, allowing internal oxidation and carburization reactions to proceed into the alloy as fast as diffusion will allow, so it can be faster than in normal oxidative service.

The effect of these gas/metal reactions on mechanical properties is serious. Extensive surface/internal oxidation leads to cracking and hence to loss of rupture, creep, and low cycle fatigue (LCF) properties (Fig. 9). Some alloys show a 25 percent reduction in stress capability, depending on severity of the atmosphere studied; strength reductions have been found in N-80A, N-115, IN-102, Hastelloy X, IN-625, and Incoloy 800. Temperatures of about 700 to 900°C (1300 to 1650°F) are the worst. It is of less concern at low-to-intermediate temperatures where 12Cr steels, Cr-Mo-V steels, and carbon steels are used. However, regardless of alloy, it is probable that little deleterious effect will be encountered below 430°C (800°F).

Recently, Graham [6] has reported that over about 1000°C (1800°F) oxidation reaction essentially ceased on AISI Type 321 stainless steel, really to be expected from oxide stability thermodynamics. Therefore, an *upper* temperature limit also appears to exist. However, carburization can still occur.

Incoloy 800 illustrates classic effects from HTR-He with relatively high

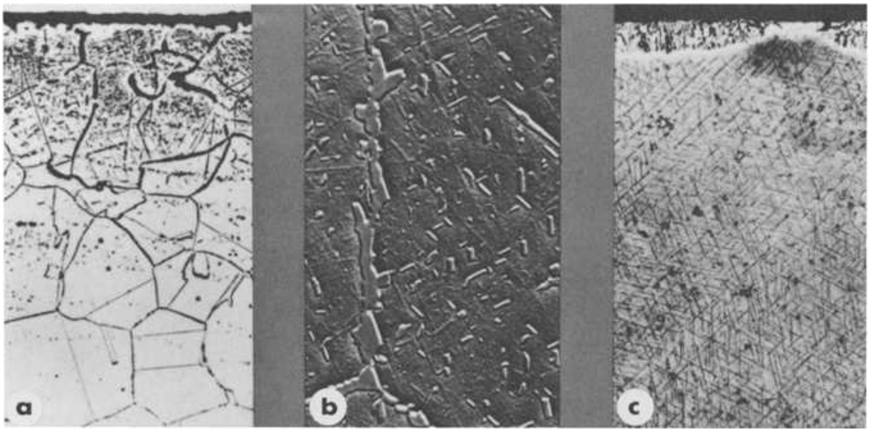

FIG. 9—*Microstructural effects in superalloys from exposure in HTR helium.* (a) *Incoloy 800 after 5000 h at 750°C (original magnification ×250),* (b) *Hastelloy X after 5000 h at 5 ksi at 750°C (original magnification ×10 000), and* (c) *Nimonic 115 exposed in HTR-He (original magnification ×250).*

oxidation potential (Fig. 9*a*). Exposure at 750°C (1380°F) at 42 N/mm^2 (about 8 ksi) for 5000 h to 2 percent strain generated uniform oxide scale and grain boundary oxide intrusions. Carburization and an intragranular plate-like precipitate to a depth of several grains develop simultaneously. Hastelloy X (Fig. 9*b*) was exposed at 750°C (1380°F) for 5000 h. A thin surface scale developed with minimal oxide intrusions. However, the precipitate decoration of $M_{23}C_6$ along grain boundaries shows here clearly. Tentative estimate of the load/temperature limit for a significant life (~10 000 h) more by this author suggests something like 70 MPa (10 ksi) at 700°C (~1300°F) in Dragon-type HTR helium test atmospheres might be expected. Nimonic 115 exposed by Dragon Project at about 800°C (1470°F) in a very *wet* atmosphere is shown in Fig. 9*c*. The oxide batch underlayed with oxide-filled metal and alloy-depleted areas is typical. The interior shows a continuous network of plate-like $M_{23}C_6$. Even in this relatively wet high-oxygen atmosphere, extensive carburization occurred. Obviously, various effects of the individual gas contaminants are critical. If HTR-He is reducing or very *dry*, then carburization and related reducing effects occur; if it is oxidizing or wet, then internal oxidation can be severe. Neither type of attack is exclusive of the other.

Superalloy applications—It can be expected that superalloys will see service in HTGR's somewhat on the following lines. Principal equipment types include: gas turbines, heat exchangers, circulators, and large diameter ducting. General form/type superalloy required are investment castings; sheet, plate, and tubing; and large forgings.

Superalloys in Energy Systems

A great portion of future energy generation systems will need superalloys as we know them now, as well as improved versions. Superalloys will be used in (at least) advanced gas turbines, coal combustion and conversion systems, liquid-metal fast-breeder reactors, and HTGR electric power and energy generating systems. These will be critical applications, but is also certain that superalloys will find many applications in lesser applications.

Thus, we will find at least the following major categories or superalloy "families" in demand: (*a*) investment cast superalloy parts, (*b*) superalloy wrought products, (*c*) large cast superalloy bodies, (*d*) large forged superalloy bodies, (*e*) directionally solidified (DS) or eutectic superalloy parts; and (*f*) oxide-dispersion-strengthened (ODS) products.

A major purpose of this paper is to attempt to identify ideal microstructures for superalloys in advanced power systems, discussed in the first part of this document. Hence, we will utilize the preceding families as the basis for specific alloy microstructural examples.

To attempt to correlate and collate the whole, Fig. 10 has been

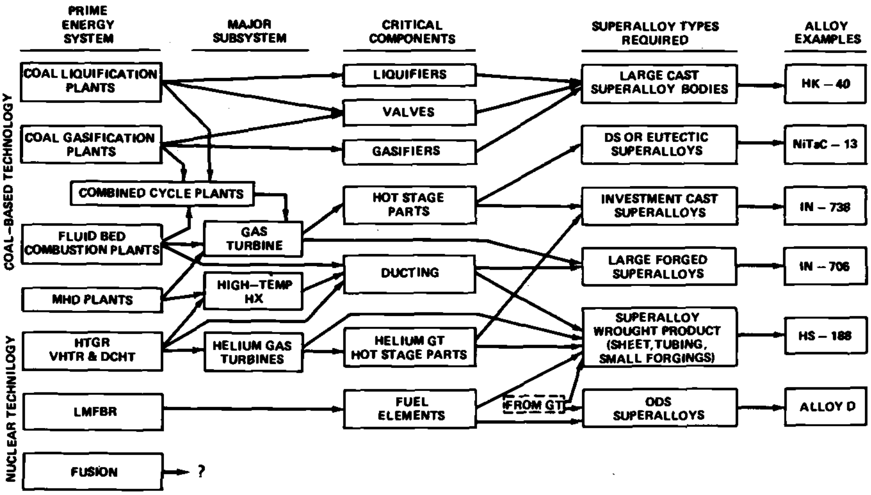

FIG. 10—*An overview of the system type, equipment, and superalloy application in future power generation systems.*

developed. It (1) identifies the *power system,* (2) draws out from these the major *critical system components,* (3) leads to the *superalloy family* that might be used, and then (4) to specific *alloy* composition *examples.*

The alloy examples (compositions in Table 2) are discussed in the following sections.

Large Castings—HK-40

HK-40 is an iron-nickel (Fe-Ni) base superalloy of simple composition (Table 2), usually utilized as medium-to-large corrosion-resistant castings. It is normally formed by sand casting and centrifugal casting, has been widely used in the petrochemical field, and is now headed towards a workhorse future in the energy systems field.

First, gross grain structure (Fig. 11*a*) has a significant effect on soundness and properties. Thus, casting design can effect cooling rates, grain structure, and most importantly, dendrite arm spacing, all of which affect thermal fatigue. To avoid thermal fatigue problems, creep ductility should be maximized by maintaining a narrow range of dendrite arm space, regardless of grain size (Fig. 11*b*).

General strengthening is achieved by solid solution (Ni, Cr) and by copius precipitation of $M_{23}C_6$, up to almost 10 percent by volume (Fig. 11*c*). Thus, gross structural control of carbide distribution is essential, related to casting design and heat treatment. The carbides enter and interact with virtually all aspects of mechanical behavior (Fig. 11*d*).

HK-40 type alloys are ripe for further improvement. In a recent

TABLE 2—*Composition of superalloy materials.*

Superalloy	Ni	Co	Cr	Fe	Al	Ti	Mo	W	Cb	Ta	Re	B	Zr	C	Other
HK-40	20	. . .	24	balance	. . .	. . .	. . .	. . .	. . .	. . .	. . .	. . .	. . .	0.45	. . .
NiTaC-13	balance	3	4	. . .	5	. . .	. . .	3.1	. . .	8.1	6.3	. . .	. . .	0.54	5.4V
IN-738	balance	8.5	16.0	. . .	3.4	3.4	1.7	2.6	0.9	1.7	. . .	0.01	0.02	0.11	. . .
HS-188	22	39	22	1.5	. . .	. . .	. . .	14	. . .	. . .	. . .	. . .	. . .	0.1	0.8La
Alloy D	balance	. . .	15	. . .	4.5	2.5	2	4	. . .	2	. . .	0.1	0.15	0.05	2.5 v/o Y_2O_3
IN-706	40	. . .	16	balance	0.3	1.6	. . .	. . .	3	. . .	. . .	0.004	. . .	0.35	. . .

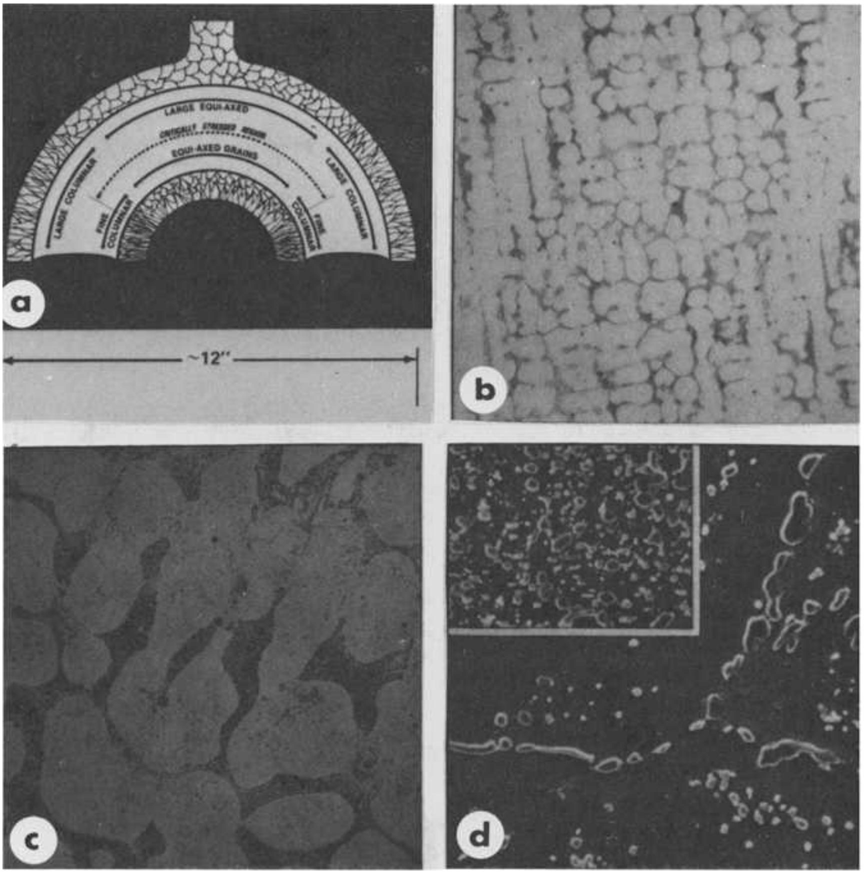

FIG. 11—*Large cast superalloy HK-40. Microstructures from castings designed and serviced in the petrochemical industries* [9]. (a) *Sketched microstructural design for petrochemical return, optimized for service;* (b) *as-centrifugally cast; both columnar and cellular* $M_{23}C_6$ *carbides present (original magnification ×100);* (c) *as-centrifugally cast; heavy eutectic* $M_{23}C_6$ *dominates with matrix* $M_{23}C_6$ *also precipitated (original magnification ×400);* (d) *following 3000 h service at 1000°C (1800°F); conventional and grain boundary* $M_{23}C_6$*; upper left shows high* $M_{23}C_6$ *density near a failure (original magnification ×750).*

study [*10*] of columbium additions, about one fourth of the carbide was converted to CbC. This alloy showed a two times to three times creep life improvement with very little rupture ductility degradation. Incoloy 800 has been modified similarly for HTGR service; more such improvements can be expected.

Critical structural features include (*a*) macro grain structure fitted to casting design, (*b*) narrow dendrite arm spacing to minimize thermal fatigue, and (*c*) controlled distribution of $M_{23}C_6$.

Eutectic Superalloys—NiTaC-13

Directional solidification of eutectic alloy compositions can lead to a natural composite system that is reinforced fibers of one of the components in the system. Leading examples of such systems go by the names CoTaC, NiTaC, and γ-γ'-δ; the former are cobalt or nickel base alloys strengthened by tantalum carbide (TaC), the latter a coprecipitation of coherent phases in the Ni-Al-Ti-Cb systems.

The γ-γ'-δ type system, while showing excellent longitudinal strengthening has nil transverse ductility, creating a reliability problem. CoTaC systems become chemically unstable when thermally exposed for long times at service temperatures, developing transverse striations on the TaC fibers leading to a lowering of properties. Thus, NiTaC appears at present to have the most promising future. The alloy NiTaC-13 is discussed in the next paragraph.

The NiTaC system is unique. While strengthening TaC fibers are relatively stable, the matrix is composed of an alloy similar to that of the complex polymorphic superalloys. This creates a strong transverse grain boundary, as in conventional superalloys. Thus, the advantages of both macro strengthening (the fibers) and micro strengthening (from proper grain boundary condition) are present. Importantly, it has recently become clear that superalloy failures in hot gas path turbine service are more due to low cycle or thermal fatigue than to creep, tensile, or high-cycle fatigue. The NiTaC structure is almost ideal to resist LCF.

Figure 12*a* shows the longitudinal alignment generated by a properly solidified bucket, with the juncture between vane and root section shown at upper left. Figures 12*b* and *c* show the two major microstructural features needed: the long needle-like fibers with clean closely-bonded interface with the matrice (but no reaction), and grain boundries well-decorated with a relatively continuous layer of γ' and creep-strengthened with $M_{23}C_6$ carbides. Not only does this type of grain boundary retain high-temperature toughness and ductility, but it is very effective in generating dislocations to provide ductility for the whole alloy.

Figure 12*d* shows an interesting negative feature. Without careful composition control, NiTaC can be σ-prone, a feature obviously to be avoided. This picture shows small platelets of σ growing coherently from the MC carbon.

Critical structural features include (*a*) uniformly dispersed fibers aligned in the major stress direction, (*b*) structural stability between fibers and alloy matrix, (*c*) well-developed tough grain boundary, and (*d*) uniform fine dispersion of γ'.

Investment Castings—IN-738

Nickel-base investment-cast alloys are the strongest widely-used high-temperature alloys, serviceable up to about 95 percent of their melting

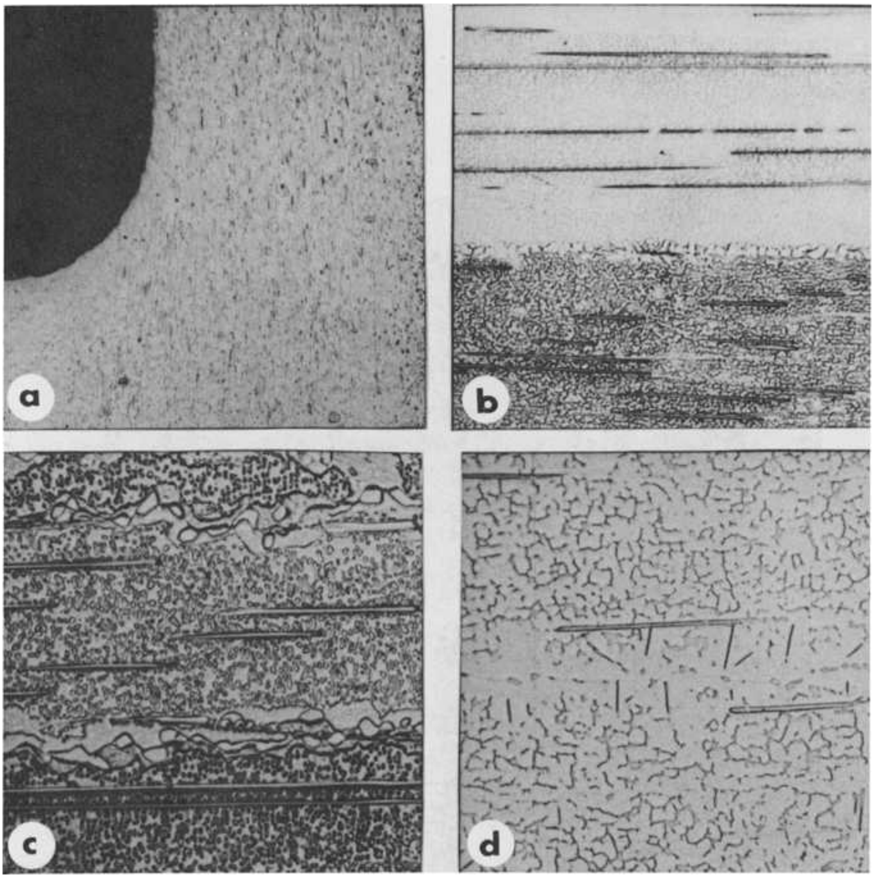

FIG. 12—*Eutectic alloy NiTaC-13. Microstructures from a directionally solidified gas turbine bucket* [10]. (a) *Strengthening TaC fibers at the bucket vane to root juncture (original magnification ×24);* (b) *TaC fibers and grain boundary (original magnification ×500);* (c) *TaC fibers, γ' and grain boundaries in matured alloy (original magnification ×1000);* (d) *sigma plates growing from TaC fibers (original magnification ×1000).*

point. Industry uses both nickel (very high strength) and cobalt (moderate strength, high corrosion resistance) alloys. Undoubtedly, they represent the most complex alloy development and technology of all alloy systems. IN-738, chosen as an example here, is in present production for buckets for dozens of industrial gas turbines. However, it has a microstructure expected to be characteristic of many future alloys, such as IN-792, GTD-111, and others yet undeveloped.

IN-738 is vacuum cast for rotating parts up to 23 kg (50 lb) weight. It is usually heat treated 1125°C (2050°F) (2 h/semi-solution) plus 850°C (1550°F) (24 h/aging). Figure 13*a* is a cross section from a large bucket,

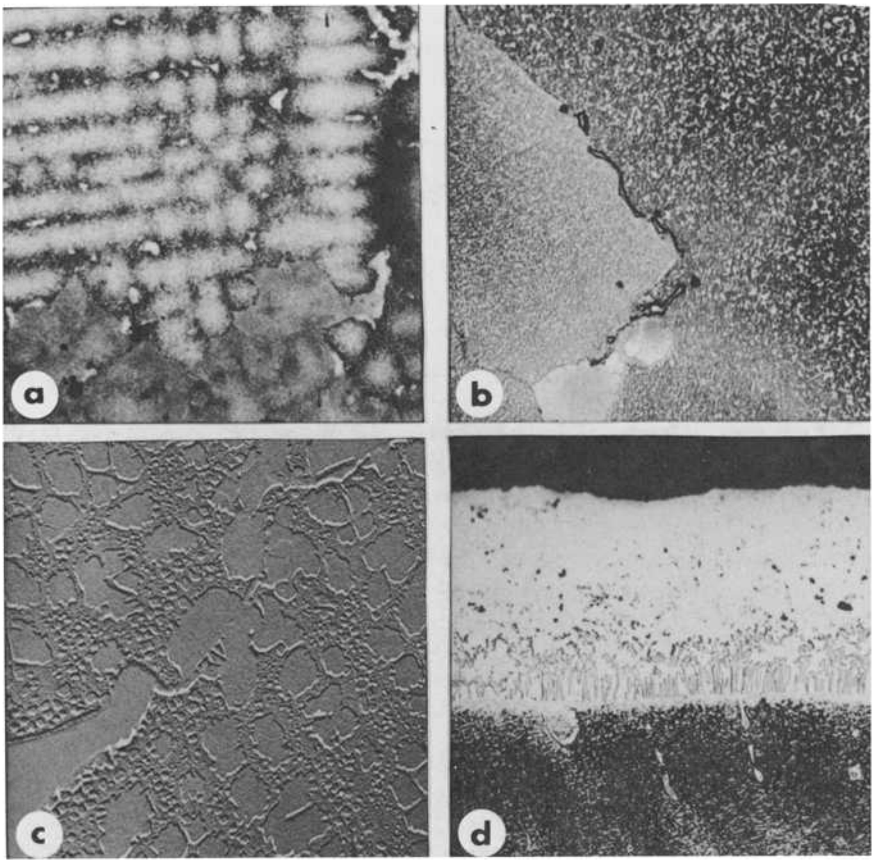

FIG. 13—*Cast superalloy IN-738. Microstructures from a large cast bucket solutioned at 1125°C (2050°F) and aged at 850°C (1550°F)* [11]. (a) *Section of investment casting showing dendritic structure and primary γ' islands (original magnification ×50);* (b) *grain boundary structure with carbides, γ' dispersion, and primary γ' (original magnification ×500);* (c) *γ' development and carbides along a grain boundary (original magnification ×10 000);* (d) *P + CrAl coating applied on IN-738 for gas turbine service (original magnification ×500).*

showing the heavy dendritic structure characteristic of these large castings. This coring, caused by segregating of solutioned refractory metal elements, is responsible for a large portion of the high-temperature creep-rupture strength. However, the major strengthener is γ', the fine particles in Fig. 13*b*. γ' is illustrated in more detail; the large particles are related to creep strengthening and the *fine* ones to tensile properties. The γ' interacts with moving dislocations, slowing them, and is cut by them.

Grain boundaries (Fig. 13*b* and *c*) are often jagged, contain a few dispersed $M_{23}C_6$ carbides, and intercept large MC carbides and eutectic *islands* of excess γ' precipitated from the melt. The MC acts as a source of carbon, slowly dissolving in service to maintain a controlled level of $M_{23}C_6$-M_6C type carbides, which also interract with dislocations. Unlike other recent alloys, the grain boundary is now encased in a layer of γ'. Ductility of the alloy system is probably close to minimum acceptable level, while strength is close to a maximum. The limiting mechanical property in service is usually low-cycle fatigue, and the limiting chemical property is hot corrosion. However, the overall chemical composition must be controlled at the melter's shop by PHACOMP calculative techniques to prevent formation of deleterious plate-like σ or μ phases, which provide easy fracture paths and rob the alloy of strengthening elements.

Referring to surface stability, Fig. 13*d* shows a familiar sight, the superalloy with a surface coating to protect it from oxidation and hot corrosion. In this case, the coating is RT-22, high in aluminum and chromium with a platinum underlayer. The major phase in such coatings is usually NiAl with interaction products at the mating/diffusion interface.

Critical structural features include (*a*) large grains, demonstrating obvious dendrite arms; (*b*) uniform distribution of about 50 to 200Å γ' with relatively fine interspersed 10Å γ' precipitate particles; (*c*) few scattered blocky MC carbide particles; both grain and grain-boundary located $M_{23}C_6$/M_6C-type carbide particles; and (*d*) *absence* of plate-like phases.

Large Forgings—Alloy IN-706

IN-706 is an Fe-Ni base superalloy designed to possess high strength concommitant with good forgability and machineability for service at about 650°C (1200°F). Prime use is for large wheels for gas turbines [*12*], hot ducting for helium turbines, and other large forged shapes such as for hot gas manifolds are in its long-range potential. While possessing a significant future, IN-706 is also a leading example of contemporary forging alloys and is often termed "the poor man's" *IN-718*. Ingots up to about 12 000 lb (5400 kg) have been melted and forged to wheels of about 2.1336×10^{-4} mm (7 ft) in diameter by the electroflux melting process (Fig. 14*a*).

Figure 14*b* shows the fine general grain size that is desirable and can be obtained, providing proper forging practice and minimal solution temperatures (not much over 900°C (1650°F)) are maintained during heat treatment. Fine grain size of this nature generates the best 650 to 1200°F/100 000 psi (350 to 650°C/7000 MPa) strength. Details of this structure (Fig. 14*c*) show one size of very fine γ' precipitate and a grain boundary decorated by globular bar-type mixed orthohombic Ni_3Cb and hexagonal Ni_3Ti phases; a small amount of $M_{23}C_6$ and Laves has also been found in these locations.

However, if (Fig. 14*d*) the higher solution temperatures originally

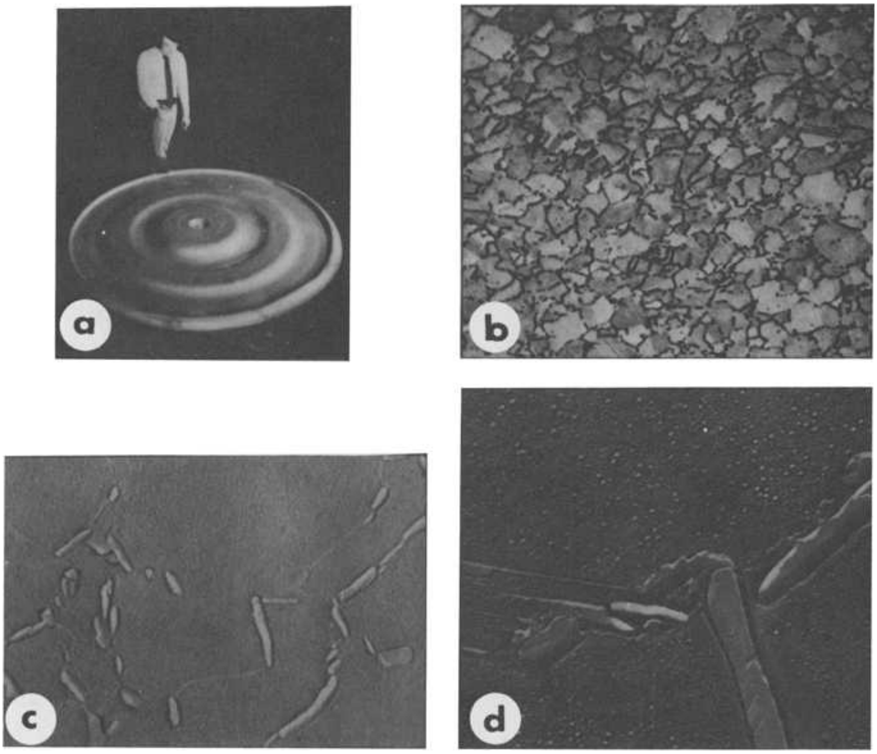

FIG. 14—*Forging alloy IN-706. Preferred microstructures for optimized 650°C/7000 MPa (1200°F/100 000 psi) properties* [13]. (a) *Seven-foot IN-706 industrial gas turbine wheel* [14]; (b) *optimized microstructure following rupture testing solutioned at 900°C (1650°F) and aged at 750°C (1350°F) and 600°C (1100°F) (original magnification ×500);* (c) *same as* (b), *note uniform* γ' *and globular phases (original magnification ×4250);* (d) *microstructure following rupture testing, solutioned at 1000°C (1800°F), aged at 850°C (1550°F), 2200°C (1325°F), and 625°C (1150°F) (original magnification ×8000).*

recommended for the alloy are used (1000°C (1800°F)), all of these phases generate to a less desirable form. The γ' precipitates in duplex sizes and is depleted near grain boundaries. The Ni_3Cb/Ni_3Ti appears at grain boundaries as large plate-like phases and even extends into formation of cellular blocks. This structure [*15*] produces lessened strength at 650°C (1200°F), so the lower solution treatment plus appropriate ages is preferred. Thus, conditions identified to generate the structures shown in Figs. 14*b* and *c* are advised.

These suggestions, of course, are for ideal conditions. Obviously, in fabrication of large wheels or other realistic parts for equipment, severe restraints on abilities to quench and heat treat as desired often arise, so the fine structure shown is presented as a goal.

Critical structural features include (*a*) fine, uniform grain size; (*b*) fine, well-dispersed uniform γ'; (*c*) minimal precipitation of γ' at grain boundaries; and (*d*) uniform globular Ni_3Cb/Ni_3Ti precipitation at grain boundaries.

Wrought Sheet Alloys—Alloy HS-188

This category is intended to cover wrought products utilized, for example, as sheet or plate for gas turbine combustion service and as pipe or tubing, particularly for high-temperature intermediate heat exchangers. HS-188 is a typical example of this class, which includes the reliable Hastelloy X, IN-671, and others. Obviously, such alloys depend heavily upon the fabrication technology utilized in their reduction to sheet or final thickness, as well as their chemistry and heat treatment to yield serviceable properties.

HS-188 is a cobalt-nickel-base alloy strengthened by solid solution and classic carbide precipitation. As a wrought alloy, ideal microstructures will be closer to the forged wheel alloys such as IN-708, than to investment cast alloys such as X-40. Dominant features can be expected to be grain and carbide particles size and shape [*16*].

Figure 15*a* and *b* give a feeling for appropriate grain size and uniformity in the process and annealed condition. Fine-grain twinned structures with precipitated carbides are the rule. The carbides are dispersed both throughout the structure and at grain boundaries. Under stressed long-time exposure, the grain size increases a little, twins from processing gradually disappear and new carbides are generated at the grain boundaries and along prior twinning lines and stacking fault lines. In the annealed condition, the carbides are M_6C, but after longer service, $M_{23}C_6$, and perhaps a little Laves, will also develop.

These features are seen in Fig. 15, where $M_{23}C_6$-laced grain boundaries are obvious. Figure 15*c* generates a feeling for the effect of these carbides in strengthening. These hard particles lock in with grain boundaries and stacking faults to restrict movement, tie up structural features, and to generate dislocations in the process (not shown) [*17*]. This, together with tungsten solutioning strengthening, constitutes the principal strengthening effects in such sheet alloys.

Critical structural features include (*a*) fine uniform grain size (twins can be expected); and (*b*) fine well-distributed carbides with minimal reaction tendencies.

Oxide Dispersion Strengthened (ODS) Superalloys—Alloy D

ODS alloys have become well-known since the advent of TD nickel and TD nichrome, wrought alloys strengthened by very fine particles of thoria. It has been the objective of metallurgists for a number of years to attempt to combine such oxide particle strengthening with classic γ'

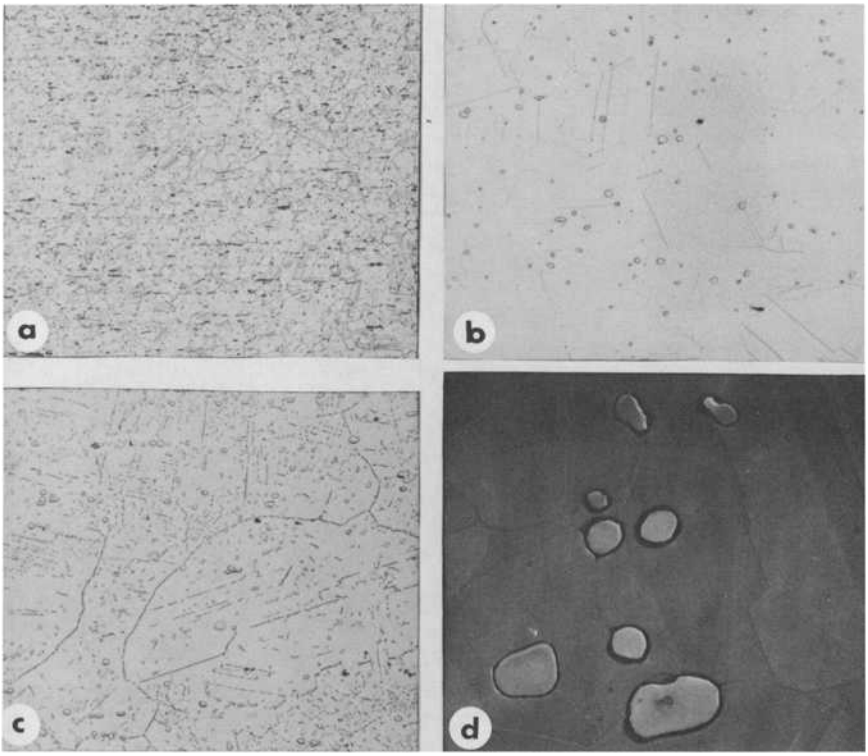

FIG. 15—*Wrought sheet alloy HS-188 showing optional microstructures for worked and annealed and serviced conditions* [16]. (a) *Fabricated to sheet and annealed (original magnification ×100);* (b) *fabricated to sheet and annealed (original magnification ×500);* (c) *fabricated and annealed plus 2000 h at 950°C (1700°F) (original magnification ×500);* (d) *fabricated to sheet and annealed (original magnification ×4000).*

strengthening. The most successful has come from the International Nickel Company in their *mechanical alloying* process.

In mechanical alloying, elemental powders are chosen to create a superalloy composition, plus an oxide for dispersion. The whole is ballmilled, creating a fine oxide particle dispersion in the metal matrix, then canned, extruded, and heat treated. Such alloys are invariably a wrought product, and now several are being considered by industry, such as IN-853. INCO has now identified a composition called *Alloy D* (with yttria dispersion) that appears to be the strongest alloy in rupture at 1100°C (2000°F) yet established.

Figure 16*a* shows Alloy D extruded bar following zone annealing [*18*]. Grains are extremely elongated, with aspect ratios of from 10:1 to 100:1. Interestingly, this is the same structure produced in tungsten wire by swaging and wire drawing for nearly 75 years. The alloy was extruded

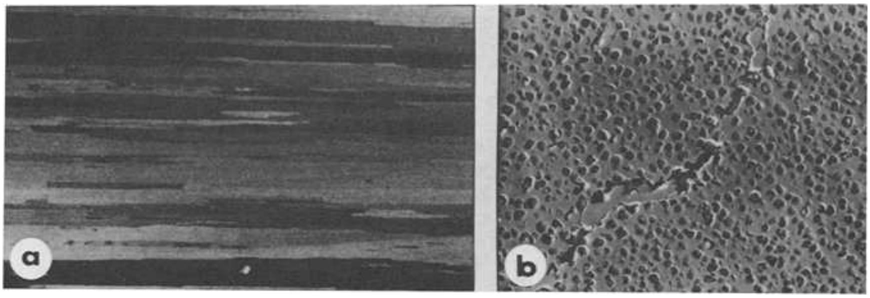

FIG. 16—*Advanced mechanical Alloy D combining ODS and γ' strengthening* [18]. *(a) Extruded bar following zone annealing (original magnification ×10), and (b) γ' particles and Y_2O_3 particles around a grain boundary containing carbides (original magnification ×11 500).*

20:1 at 1050°C (1900°F) and the zone annealed at 1350°C (2250°F) at 2.7 in./h to generate the elongated structure. Heat treatment was 0.5 h at 2250°F (1400°C)/ac plus 2 h 1750°F (950°C)/ac plus 24 h 1550°F (845°C)/ac.

Grain boundaries (Fig. 16*b*) have a few carbide particles and a moderate agglomeration (although not continuous) of γ'. The γ' is spherical, best for strength generation. Very fine Y_2O_3 (actually $Y_2O_3 \cdot Al_2O_3$) particles can be seen *within* the γ' particles. The great mechanical energy of the process has created fully alloyed particles from unalloyed powders and is the key to ODS technology.

Critical structural features include (*a*) highly elongated grain structure in the fabrication direction; (*b*) fine uniformly-dispersed γ' particles, preferably spherical in nature; and (*c*) 200 to 400 Å Y_2O_3 particles dispersed with the γ'.

Conclusion

Superalloys will be utilized in advanced technology systems where their unusual combinations of strength and surface stability will be of benefit. However, in some applications, corrosion will be so fierce that special procedures or protection will be essential. Despite the complexities of superalloy metallurgy, it is possible to correlate and collate their structures into several classes, which can then be related to major alloy type and ultimately into specific application.

References

[1] Sims, C. T., *Journal of Metals*, Vol. 28, Dec. 1976, p. 7.
[2] McNab, A. J., *Chemical Engineering Progress*, Vol. 71, No. 11, Nov. 1975, pp. 51–57.
[3] Batchelor, J. and Jones, W., "ERDA Liquefaction Program," Conference on Materials for Coal Conversion, Gaithersburg, Md., 11–13 Oct. 1977.
[4] Junge, R. et al, "Locomotive Development Committee Coal-Fired Turbine Blade Erosion Study," General Electric Report No. DF-59-GTD-32, 18 Dec. 1959.

[5] Stringer, J. S., "Corrosion-Erosion in Fluidized Bed Combustion," ERDA Conference on Materials for Coal Conversion and Utilization, U. S. Bureau of Standards, 11–13 Oct. 1977.
[6] Graham et al, Gas Cooled Reactor Symposium, Julich, Germany, Oct. 1975.
[7] Caruvana, A. et al, "Evaluation of a Water-Cooled Gas Turbine Combined Cycle Plant," ASME Gas Turbine Division Meeting, American Society of Mechanical Engineers, London, April 1977.
[8] Johnston, W. G. et al, *Journal of Nuclear Materials*, Vol. 54, 1974, pp. 24–40.
[9] Woulds, M., personal communication.
[*10*] Solomon, H., personal communication.
[*11*] Wood, J. and Lindblad, N., personal communication.
[*12*] Johnson, A. M. and Fritz, K. E., personal communication.
[*13*] Maniar, G., personal communication.
[*14*] Woodford, D. A. and Gigliotti, M., personal communication.
[*15*] Moll, J. H. et al, *Metallurgical Transactions*, Vol. 2, Aug. 1971, pp. 2143–2151 and 2153–2160.
[*16*] Herchenroder, R. E., personal communication.
[*17*] Sims, C. T., *The Superalloys*, Wiley Interscience, New York, 1972.
[*18*] Kim, Y. C., personal communication.

L. W. Lherbier[1]

Melting of Superalloys

REFERENCE: Lherbier, L. W., "**Melting of Superalloys,**" *MiCon 78: Optimization of Processing, Properties, and Service Performance Through Microstructural Control, ASTM STP 672,* Halle Abrams, G. N. Maniar, D. A. Nail, and H. D. Solomon, Eds., American Society for Testing and Materials, 1979, pp. 514–525.

ABSTRACT: Melting of superalloys is the initial, and perhaps most important, step in the production of materials used in critical high-temperature applications. Increasing demand for high-quality superalloys with specific characteristics has resulted in various combinations of primary, melting, refining, and secondary remelting operations. Specific characteristics of each of these process operations are used to produce superalloys that meet customer quality requirements for (1) chemistry, (2) product form, and (3) structural uniformity.

Various combinations of melting processes can be used to obtain a desired primary chemistry not only in terms of the primary elements, but also for residual and tramp elements. Product forms frequently dictate a combination of melting processes that give importance to the shape of ingots, the end product of superalloy melting processes. Additionally, it is frequently important to choose melting combinations that achieve ingot structure control for optimum primary phase distribution, cleanliness or hot workability, or both.

KEY WORDS: steels, microstructure, superalloys, melting, vacuum induction melting, argon oxygen decarburization, vacuum arc remelting, electric furnace melting, vacuum degassing, vacuum oxygen decarburization, election beam melting, electroslag remelting

In most analyses of superalloy developments throughout the past 20 years, attention is usually focused on the end product—gas turbines, ever growing in size and efficiency. The increase in efficiency has been due to both materials and design advances. The increase in high-temperature properties of materials generally referred to as iron, cobalt, and nickel superalloys has been astounding. Most everyone, and especially those directly involved with the manufacture and use of superalloys, will attest to the importance of alloy development efforts during the past two decades. However, fewer of us accept and even less recognize the fact that achievements in the gas turbine industry would not have

---

[1] Manager, Powder Metallurgy, Universal-Cyclops Specialty Steel Division, Bridgeville, Pa. 15017.

occurred except for the concurrent development of special melting methods that made possible the manufacture of superalloys for use in products that we so much take for granted today. In view of this situation, it seems appropriate to partially modify generally held views concerning superalloys and point up through several examples the overriding importance of melting and casting a high-quality starting material.

Definition of Superalloy

Superalloy is a generic term that can be applied to a wide variety of materials. To help narrow the focus of this effort concerning melting processes of commercial significance, I would initially like to define superalloys as a group of iron-, nickel-, or cobalt-base alloys, which provide useful strength capabilities at temperatures exceeding 426°C (800°F). Additionally, these alloys generally exhibit excellent oxidation resistance at service temperatures. Examples of commercial significance that fit this definition are listed in Table 1.

In addition to the nominal composition for the various alloys, Table 1 also groups the alloys listed by classifying them as to structure: austenitic and martensitic. The austenitic and martensitic groups are further broken down into specific types that are determined by some characteristic of that material: composition, strength, strengthening mechanism, etc. In the austenitic category, Type I precipitation hardening materials are typically the *nickel*-base alloys, characterized by gamma prime strengthening and carbide precipitation. The Type II precipitation hardening austenitic materials are typically the *iron-nickel* alloys also strengthened by gamma prime, Ni_3Cb, or Ni_3Ti precipitation. The Type II materials contain carbides and are prone to precipitation of intermetallic compounds such as Laves and Mu phases. Both the Type I and Type II materials are used for structural parts whose primary function is to supply strength at elevated temperatures. Generally speaking, the Type II materials are used up to 648°C (1200°F) while the Type I materials have a higher temperature capability approaching 760°C (1400°F). The Type III solid solution strengthened materials in the austenitic category are *nickel*- or *cobalt*-base alloys or both whose strengthening is achieved by solid solution hardening and carbide precipitation. Much of this material is fabricated from sheet into structural parts that require extremely good oxidation resistance. As such, these materials can generally be used at temperatures up to 926°C (1700°F) but at reduced strength levels.

The three types of materials listed in the martensitic stainless category are all *iron*-base materials and are generally employed at a temperature ranging from 426 to 538°C (800 to 1000°F). The Type I straight chromium material is the basic composition used to obtain adequate strength and nominal oxidation characteristics at minimum cost. The Type II

TABLE 1—*Classification of commercial high-temperature materials.*

Alloy Category	Examples	Chemical Analyses, percent by weight											
		C	Fe	Ni	Co	Cr	Mo	W	Cb	Al	Ti	B	Other
Austenitic													
Type I —precipitation hardening	Waspaloy	0.04	1.0	balance	14.0	19.0	4.3	. . .	. . .	1.3	3.0	0.005	0.06 Zr
(nickel base)	Astroloy	0.04	1.0	balance	18.5	15.0	5.2	. . .	. . .	4.3	3.5	0.030	. . .
Type II —precipitation hardening	UT[a] 718	0.05	19.5	52.0	. . .	18.0	3.0	. . .	5.2	0.5	1.0	0.003	. . .
(iron-nickel base)	UT 901	0.03	36.5	42.0	. . .	13.0	5.5	. . .	. . .	0.3	2.9	0.015	. . .
	A-286	0.05	balance	25.0	. . .	14.0	1.3	. . .	. . .	0.2	2.1	0.005	0.25 V
Type III—solid solution hardened	UT HX	0.07	18.5	balance	2.0	21.0	9.0	0.5	. . .	. . .	. . .	0.004	. . .
(nickel and cobalt)	UT 188	0.09	2.0	22.0	balance	22.0	. . .	14.0	. . .	. . .	. . .	0.005	0.05 La
Martensitic Stainless													
Type I —straight chromium	403	0.12	balance	0.5	. . .	12.0	. . .	. . .	. . .	. . .	. . .	. . .	. . .
Type II —chromium-molybdenum	422	0.22	balance	0.8	. . .	12.0	1.0	1.0	. . .	. . .	. . .	. . .	0.25 V
	Jethete M152	0.14	balance	2.7	. . .	12.0	1.8	. . .	. . .	. . .	. . .	. . .	0.30 V
Type III—precipitation hardening	UT 355	0.12	balance	4.3	. . .	15.5	2.8	. . .	. . .	. . .	. . .	. . .	0.10 N

[a] UT = Unitemp (Universal-Cyclops trademark).

chromium modified alloys achieve higher strength levels through the addition of molybdenum or some other solid solution hardening element or both for a modest increase in cost. The Type III precipitation hardening martensitic materials increase strength even further by altering the composition so as to provide precipitation hardening in conjunction with transformation hardening. Additionally, this material, because of higher chromium and molybdenum contents, generally exhibits higher oxidation resistance than the other two types in the martensitic alloy category. It should be further pointed up that all of the examples listed in Table 1 involve wrought superalloys and represent the bulk of the production of these materials in this country.

Factors Affecting Superalloy Performance

In analyzing the superalloys listed in Table 1, it should come as no surprise that their characteristics in service depend primarily on their chemical composition. As such, it is imperative that one uses a melting procedure to obtain the right balance of primary elements in these materials. However, it must be remembered that the characteristics imparted by the primary element composition can be significantly affected by other factors, such as residual gases, inclusions, and other impurities, which may be metallic or nonmetallic in nature. The effect of sulfur on elevated temperature ductility is well recognized as is the effect of inclusions on fatigue strength. Even the presence of minute quantities of various metallic elements can significantly affect superalloy properties. The beneficial effect of boron on stress rupture and creep was reported long ago. There can be negative effects also as shown by Fig. 1, which illustrates the harm bismuth has on the rupture properties of an iron-nickel (Fe-Ni) (Unitemp 718) superalloy.

Furthermore, desired characteristics in superalloys are not obtained by chemical composition alone, and it is recognized that the other major factor to be considered during initial production is the solidification structure. In many instances, the final properties are determined by the original cast structure, that is, grain size, phase distribution, and the degree and amount of cast structure defects. One very important aspect of structure involves the ability of the cast product to be satisfactorily hot or cold worked into a usable shape. The importance of structure and surface in altering the hot workability of a cobalt-base alloy is illustrated in Fig. 2. It must be recognized that chemistry changes occurring during melting operations aimed at improving structure can also influence hot workability. Recognition of the importance of both composition and structure has consequently resulted in the specialty steel industry developing advanced technology utilizing various combinations of melting and refining techniques to produce material capable of meeting quality requirements at the lowest possible cost.

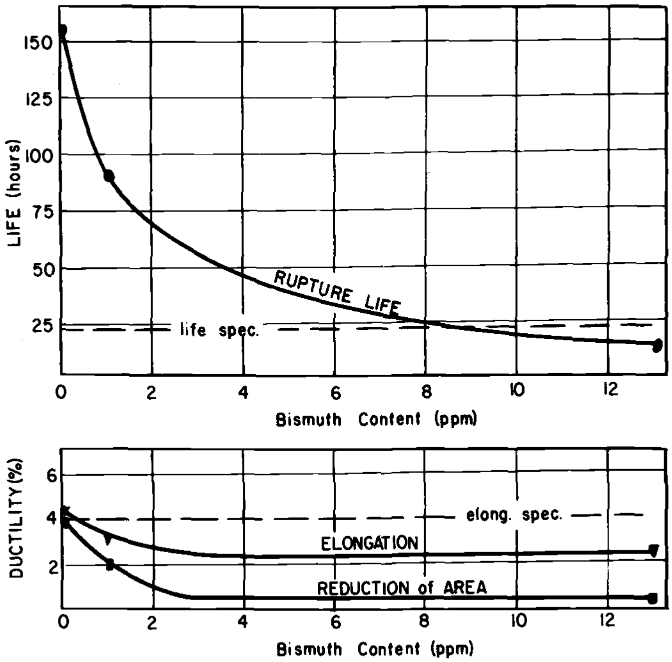

FIG. 1—*Effect of bismuth on 649°C/689 MPa stress rupture properties of an Fe-Ni superalloy.*

Melting Techniques

If we could design an ideal melting process for the production of high-quality superalloys, it would be necessary to have the following attributes: (1) it must have the capability of using all varieties of scrap and virgin raw materials; (2) it must be amenable to absolute control of chemistry with high recovery of all alloying elements; (3) it must be both flexible and adaptable to the production of all types of alloys, regardless of class; (4) it must be totally controllable from the standpoint of efficient refining reactions, and the solidification sequence; (5) it must be completely free from all sources of contamination from the standpoint of gases, impurities, and nonmetallic inclusions; and (6) it must be capable of high productivity at low operating cost.

It should be readily apparent that it is impossible to combine all of these requirements into a single melting unit. Rather, the melting of superalloys can be best understood by dividing the sequence into three separate categories as illustrated in Fig. 3. First, is the primary melting processes, which essentially makes the alloys from pure metals, ferro alloys, revert, and scrap material. Refining processes fall into the second category and can involve separate units or can be accomplished in the primary melting

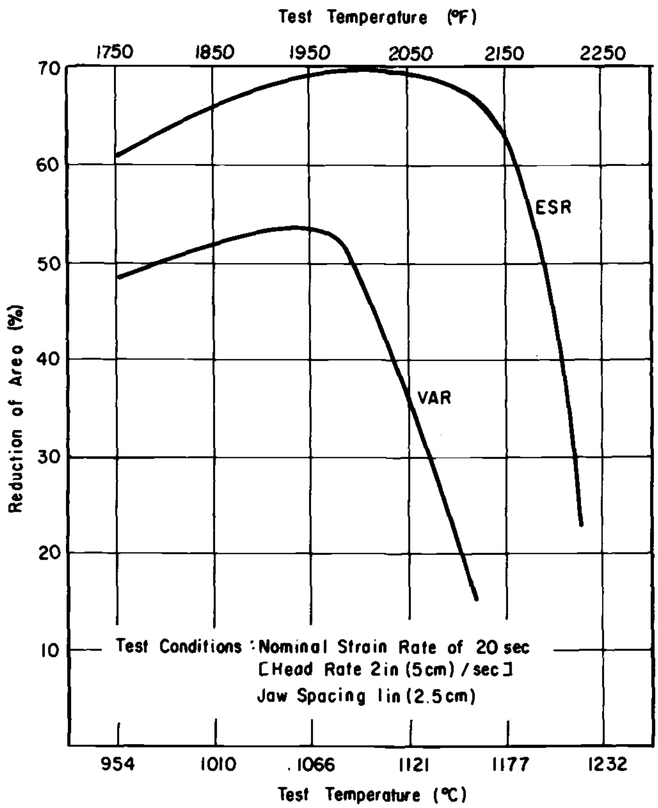

FIG. 2—*Effect of remelt practice on the Gleeble hot ductility values for a cobalt-base superalloy.*

equipment to obtain specified requirements in terms of gas content, impurity removal, alloy recovery, etc. The third category involves the secondary melting processes where primary emphasis is placed on solidification control to produce ingots of high structural integrity and also to obtain additional specific purification aims without introducting undesirable contamination from either refractories or the atmosphere. Although there are many variations within these three categories of primary melting processes, refining processes, and secondary melting processes, this effort will discuss only those of significant commercial importance for today's production of superalloys.

Primary Melting Processes

The basic electric arc furnace (EFM) was the first large-scale primary production unit for the melting of superalloys in this country. The

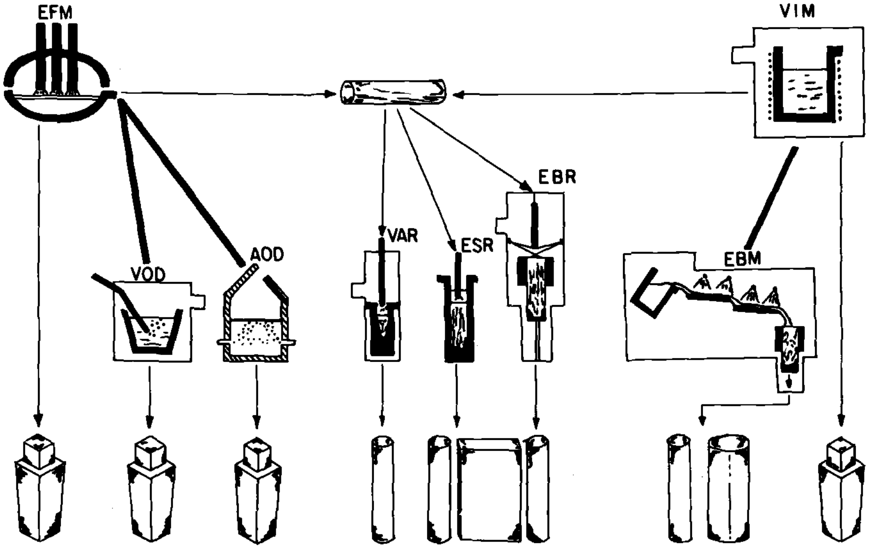

FIG. 3—*Advanced melting and refining technology for superalloys.*

procedure involves charging of solid scrap, virgin raw materials, ferro alloys, or all three within a refractory lined shell and melting in an air environment via the generation of heat resulting from an electric arc between graphite electrodes and the charge. Slags are added for refining purposes and the impurities removed as gases or as liquid slag. Generally, gaseous oxygen is used to lower the carbon, hydrogen, and nitrogen contents of the melt. The molten metal is generally cast into ingots for processing to various mill products or into electrodes for remelting to obtain further refinement and improved ingot structure. Principal advantages of the electric furnace include a wide flexibility in charge material (chemistry and shape), good temperature control, a fluid reactive slag for metallurgical refining, slag reactions adaptable to particular needs, and, perhaps most important of all, high productivity at low cost. Disadvantages include the presence of the refractories, ambient air, slag, and generally a lack of good stirring that leads to longer refining times and poor melt homogenization. However, years of experience have enabled producers to develop basic arc melting practices for high-temperature alloys by carefully tailoring the procedures of the equipment to meet specific material requirements.

The secondary primary melting process of commercial significance is vacuum induction melting (VIM). This process developed from a laboratory curiosity in the 1950's to a process that is today the dominant method of producing superalloys that must meet consistently stringent material specifications. The procedure involves charging solid scrap, virgin raw materials, ferro alloys, or all three into a refractory-lined crucible under vacuum and then generating the heat required for melting via eddy currents induced within the charge. In view of the reduced pressure during the melting process, some impurities are removed as gases and there is generally no contamination from air or slag or both. The refined molten metal is cast under vacuum into ingots for processing to mill products or into electrodes for melting to obtain further refinement and improvement in ingot structure.

The vacuum induction melting process is quite flexible and provides the best control over the entire melt chemistry, in terms of primary elements, beneficial trace elements, and harmful impurities. In fact, the reproducibility of chemical composition from heat to heat approaches for a number of elements the accuracy limits of present analytical techniques. The high degree of flexibility is made possible by induction stirring and the vacuum environment that allows the entire system to be treated in a thermodynamic sense. Control of the pressure in this process results in strong degassing, good carbon deoxidation, and highly favorable reaction kinetics. A significant advantage of the process, induction stirring, allows melt homogenization, complete control over refining times, and excellent temperature control during all phases of the operation. A major disadvantage is that it requires relatively good charge materials and cannot handle some of the charge materials used in the electric furnace. Other disadvantages are the potential reaction of the molten alloy with the refractory lining and the loss of high vapor pressure alloying elements. Consequently, the cost of production via vacuum induction melting is somehwat higher than electric furnace melting.

Refining Processes

Three basic refining processes have been applied to superalloys melted initially by the electric furnace process. Vacuum degassing (VD) was introduced as the first stage of up-grading the quality of electric furnace product. In this refining process, molten metal is degassed in a separate vessel by exposure to pressures substantially below atmospheric. Under these conditions, dissolved gases such as carbon monoxide, hydrogen, and nitrogen are reduced. Efficiency is increased by stirring the molten metal so as to maximize the exposure of the entire bath to the vacuum/metal interface. Some of the more sophisticated facilities have been equipped with graphite electrodes or induction coils to reheat the molten metal during or following the degassing operation. This refining process was soon followed by more complex metallurgical technologies involving carbon deoxidation and compositional adjustments under vacuum.

Degassing developments led to the vacuum oxygen decarburization process (VOD) in which stainless and superalloys could be treated in specially designed equipment under closely controlled conditions. In this refining process molten metal from the electric furnace containing relatively high levels of carbon and chromium is decarburized under vacuum by lancing with oxygen. Under these conditions, it is possible to remove carbon with minimal oxidation of chromium. This permits the use of a lower cost high-carbon-containing raw materials (especially chromium) in the production of some superalloys. Efficiency is greatly increased by stirring the molten metal during decarburization using argon or induction stirring or both. Dissolved gases are reduced during exposure to pressures below atmospheric.

The latest refining process to be adopted by the industry is argon/oxygen decarburization technique (AOD). Duplex processing combining the electric furnace and the AOD process marks a new era in specialty steelmaking whereby an alloy and scrap charge is melted in the basic electric furnace to the melt in composition, transferred to a slag-free argon/oxygen reactor, decarburized, the resulting slag reduced to recover chromium, etc., a new slag added for desulfurization, if required, and the material refined to a final high-quality product. The molten metal is usually decarburized by the injection of argon and oxygen. The argon/oxygen mixture is injected through separate tuyeres or nozzles, and the ratio of argon to oxygen is increased as refining or decarburization occurs. Slag metal reactions such as the reduction of chromium and desulfurization, if necessary, are enhanced by stirring with pure argon after the desired carbon level has been achieved. Injection of argon also promotes the removal of other dissolved gases.

The AOD process has received wide acceptance rapidly because of its simplicity and flexibility of operation, its easy control and reproducibility, and its superior quality over conventional electric furnace practices. This process can be termed as one of revolutionary significance in specialty steelmaking and offers unlimited potential for the production of nickel-base and other superalloys requiring low-carbon contents and nominal reactive element contents. This process permits the use of lower cost high-carbon ferrochrome and other less expensive raw materials in the production of many alloys. The simple construction of the AOD vessel makes it relatively free of maintenance or operating problems. The high consumption of argon has been partially reduced by the substitution of nitrogen in the early stage of decarburization. Admittedly, most of the AOD activity currently involves stainless steels, however, there are a number of firms using the process of corrosion-resistant and high-temperature nickel-base alloys.

The only refining process that has been applied to vacuum induction melted materials has been the electron beam technique (EBM). Although not commercially viable at the present time, it does seem appropriate to discuss the technique because a large unit was built and put into operation for several years. In the electron beam refining process, molten metal from the vacuum induction furnace is further refined by passing it through a very hard vacuum in a water-cooled copper trough during which it is heated locally to very high temperatures by electron beam guns. The refining efficiency is extremely high due to the combination of the hard vacuum and the intense localized heating. During this part of the process, there is no contamination from the air, slag, or crucible. The refined molten metal is continuously cast under vacuum for processing to mill products or for remelting to obtain an improved ingot structure.

Remelting Processes

It soon became apparent in the early days of vacuum induction melting that the achievement of closely controlled chemical composition in terms of both primary and residual elements was not sufficient to meet the quality requirements demanded by many applications, specifically those in the gas turbine industry. This situation resulted in the development of the remelting processes with the primary goal of further refining the molten metal from gases, nonmetallic and metallic impurities, and the production of larger ingots of uniform composition with dense homogeneous structures free of metallurgical defects.

The first remelting process developed on the commercial basis was the vacuum arc remelting process (VAR) in the late 1950's. Figure 4*a* illustrates the basic characteristics of the process. As-cast electric furnace

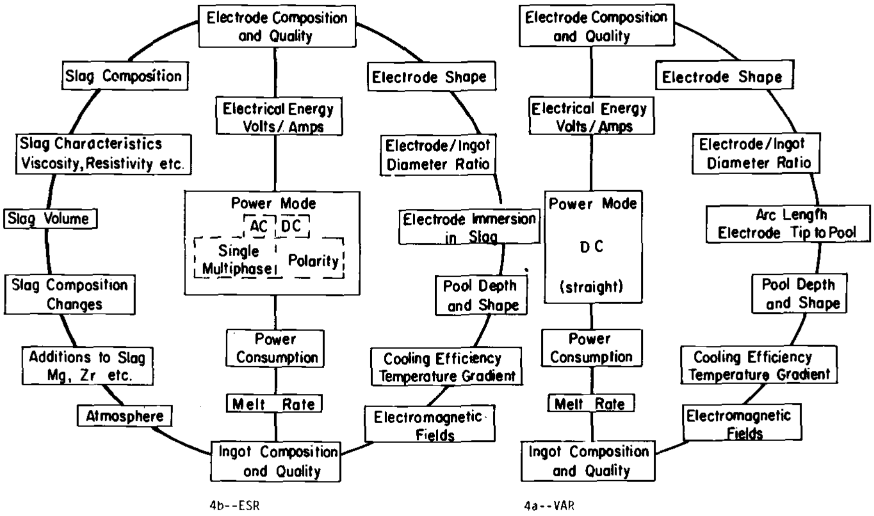

FIG. 4—*A comparison of electroslag and vacuum are remelting process characteristics.*

melted or vacuum induction melted electrodes are progressively remelted and solidified in water-cooled copper mold under vacuum by an electric arc generated between the electrode and the molten metal above the solidifying ingot. Some refining occurs by removal of impurities in gaseous form, and there is no further contamination from air, slag, or refractory. The progressively solidified ingot is completely homogeneous and free of shrinkage defects and can be processed directly to mill products. The process grew rapidly in the 1960's and found wide acceptance in this country for the production of superalloys. The process is the most important and dominant remelting process in the production of double-vacuum melted advanced superalloys, which must meet the specifications for most critical applications. A large number of widely different alloys of almost any composition can be remelted and improved by the vacuum arc remelting process.

Although developed many years ago, the electroslag remelting process (ESR) did not find wide use in this country until the mid-1960's. Characteristics of this process are also illustrated in Fig. 4*b*. In this process, as-cast electric furnace melted, or vacuum induction melted electrodes are progressively remelted and solidified in a water-cooled copper mold under a blanket of molten flux to electric current passing between the electrode and the solidifying ingot. Refining occurs as molten metal passes through the flux and impurities are removed as gas or by reaction with the flux to form slag. The progressively solidified ingot is completely homogeneous and free of shrinkage defects and can then be processed directly to mill products. The process has experienced very rapid growth in the last ten years for the production of a wide variety of materials and in particular many nickel- and cobalt-base alloys.

The electroslag process compliments vacuum arc remelt in several areas and, in others, it is an alternative process in competition with the highly perfected vacuum arc remelting technology. Nevertheless, each of the two remelting processes have their own particular characteristics as illustrated in Fig. 4 and should, therefore, be considered as complimentary to one another rather than competitive. An advantage of the electroslag process includes the production of shaped ingots and slabs with high aspect ratios. It also allows greater tolerance in the selection of remelting parameters owing to the favorable thermal effects of the flux bath by providing uniform heat distribution over the pool and reducing thermal gradients. Minor disadvantages include the problem of chemistry control in certain alloys attributable to mildly oxidizing conditions of the liquid flux. Flux compositional changes also need close attention because of possible control problems with certain highly reactive elements in the remelted material.

A third and much less significant remelting process is the electron beam remelting (EBR) technique. In this process, as-cast electric furnace melted or vacuum induction melted electrodes are progressively remelted and solidified under a very hard vacuum. Melting occurs from heat generated in the electrode due to the inpingement of high-energy electrons from electron beam guns. Refining efficiency is extremely high due to the vacuum and the intense heat generated by the bombarding electrons. Impurities are removed in gaseous form and there is no contamination from air, slag, or refractory. However, higher costs and insufficient quality improvements of this process have prevented it from becoming of great commercial significance at this point in time.

Summary

Development of the various melting processes by the specialty steel industry has resulted in cost effective methods of producing high-quality superalloys. Ultimately, the choice of a melting sequence for the production of these materials is dependent upon the quality and cost of the final product. Consequently, primary, refining, and remelted processes are used in a variety of combinations to produce ingots capable of being fabricated into reliable, cost effective products. The importance of melting in the overall sequence from raw material to end product cannot be overemphasized. No amount of highly sophisticated hot or cold processing, heat treatment, etc., can produce today's required quality level without a proper composition or structure in the cast ingot.

D. R. Muzyka[1]

Physical Metallurgy and Effects of Process Variables on the Microstructure of Wrought Superalloys

---

REFERENCE: Muzyka, D. R., "**Physical Metallurgy and Effects of Process Variables on the Microstructure of Wrought Superalloys,**" *MiCon 78: Optimization of Processing, Properties, and Service Performance Through Microstructural Control, ASTM STP 672,* Halle Abrams, G. N. Maniar, D. A. Nail, and H. D. Solomon, Eds., American Society for Testing and Materials, 1979, pp. 526–546.

ABSTRACT: Wrought superalloys that are capable of high strengths at room and elevated temperatures are characterized by complex alloy compositions and phase relationships. Alloy composition establishes which phases will occur, and composition control is critical to assure consistent phase boundary relationships. This presentation discusses the metallurgy of several important superalloys including: A-286, Alloy 901, Alloy 718, Waspaloy and René 95; and two new wrought superalloys, Pyromet CTX-1 and Pyromet 31. The achievement of property goals in these alloys, for various applications, is shown to be related to proper selection of process parameters with respect to phase relationships.

KEY WORDS: steels, microstructure, heat resistant alloys, precipitation hardening, phase diagrams, phase transformations, process variables

Superalloys refers to a group of high-strength, corrosion-resistant, high-temperature alloys, initially used in turbine-type machinery, but increasingly finding application in other areas such as in petrochemical equipment. The superalloys are generally divided into categories according to whether they are used as-cast or wrought and according to alloy base: nickel, cobalt, iron, or nickel-iron. Table 1 lists compositions of the important superalloys discussed in this paper.

Development of the superalloys began with the strengthening of the 80Ni-20Cr alloy base around 1930 [*1*][2]. The first practical nickel-base superalloy was Nimonic 80A. This alloy was air melted in relatively small

---

[1] Formerly, general manager, Distribution, now, division vice president, Technical, Carpenter Technology Corporation, Reading, Pa. 19603.

[2] The italic numbers in brackets refer to the list of references appended to this paper.

TABLE 1—*Composition of superalloys.*

Alloy	Composition, percent by weight										
	C	Cr	Ni	Fe	Co	Ti	Al	B	Mo	Cb	Others
Ni-Base											
Waspaloy[a]	0.05	19.5	balance	. . .	13.5	3.00	1.30	0.005	4.3	. . .	0.05Zr
Astroloy	0.05	15.0	balance	. . .	15.0	3.50	4.40	0.030	5.25	. . .	. . .
IN100	0.18	10.0	balance	. . .	15.0	5.00	5.50	0.015	3.0	. . .	1.0V, 0.05Zr
René 95[b]	0.15	14.0	balance	. . .	8.0	2.50	3.50	0.010	3.5	3.50	3.5W, 0.05Zr
Pyromet 31[c]	0.05	22.7	balance	15.0	. . .	2.30	1.30	0.005	2.0	0.85	. . .
Ni-Fe Base											
Alloy 901	0.05	13.5	42.7	34.0	. . .	2.5	0.25	0.015	6.1	. . .	. . .
Alloy 718	0.04	19.0	52.5	balance	. . .	0.90	0.50	0.005	3.05	5.30	. . .
Alloy 706	0.02	16.0	40.0	balance	. . .	1.70	0.30	0.004	. . .	2.75	. . .
Pyromet CTX-1	0.03	. . .	37.7	balance	16.0	1.75	1.00	0.008	. . .	3.00	. . .
Pyromet CTX-2	0.03	. . .	37.7	balance	16.0	1.75	1.00	0.008	. . .	3.00	0.75Hf
Fe Base											
A-286	0.05	15.0	26.0	balance	. . .	2.00	0.20	0.005	1.25	. . .	0.30V

[a] Waspaloy is a registered trademark of United Technologies Corp.
[b] René is a registered trademark of General Electric Corp.
[c] Pyromet is a registered trademark of Carpenter Technology Corp.

heats and forged into various turbosupercharger parts. Other alloys were used as-cast. Reportedly, the first of the cast alloys, a cobalt-base alloy, Vitallium, was originally developed for use in dental applications. It is generally agreed that advances of the jet engine and superalloys have closely paralleled each other since World War II. During the past four decades, a wide range of alloys have evolved, and today, various superalloys often comprise over 50 percent by weight of a contemporary jet engine.

In jet engines, the wrought superalloys are used primarily as compressor and turbine disks and blades, shafts, hubs, rings, bolts, spacers, and cases. The cast superalloys are often specified for turbine blades and vanes, and for various engine structural parts. Other applications for superalloys include: piston engine exhaust valves, turbosuperchargers, exhaust driven turbines, space vehicles, petrochemical equipment, hot work dies, and land-based power systems. Although superalloys were originally developed for use at gas turbine inlet temperatures (up to about 1093°C (2000°F)), more recently several superalloys have been adapted for chemical industry and petrochemical applications at temperatures as low as 204 to 316°C (400 to 600°F). This is because of a unique combination of mechanical properties and corrosion resistance exhibited by some alloys when given special processing sequences and heat treatments. Some superalloys are also gaining in favor for applications in nuclear reactors where their primary virtues include high strength, good stress corrosion cracking resistance, and, in one case, good swelling resistance in a fast neutron flux. A special group of superalloys recently developed for low expansion properties (with essentially zero chromium) has been found to be excellent in liquid hydrogen (−253°C (−422°F)) environment. One such alloy is Pyromet CTX-1.

It is significant to note that the superalloys have matured from a narrow group of alloys used only in creep and stress rupture limited applications, to a family of alloys capable of satisfying a wide range of applications from sub-zero temperatures to over 1093°C (2000°F). Increased knowledge of alloy systems—especially knowledge of structure/property relationships—has been the key to unlocking the potential of the superalloys to many unique new applications. The main ingredient in the realization of higher strength and ductility relationships in the temperature range below about 649°C (1200°F) has been processing, and, in particular, mechanical and thermal treatments.

Alloys of Interest

In order to limit the scope of this discussion, it is worthwhile to use experience to group alloys according to useful characteristics. As our title implies, we have chosen the wrought superalloys over the cast alloys. We will not discuss the so-called *heat resistant* alloys [2], such as Hastelloy X, that are strengthened only by solid solution effects. We will also refrain from discussing the cobalt-base alloys, such as Mar M 302, that are strengthened primarily by solid solution effects, but also by carbide precipitation. We will concentrate on the nickel-, nickel-iron-, and iron-base superalloys with an austenite matrix hardened by $\gamma'(Ni_3[Al,Ti])$ or $\gamma''(Ni_3Cb)$. This group of alloys is extensive and has probably received more study than any other group of complex alloys in the history of man.

Alloying Elements

The γ' strengthened superalloys really had two beginnings. The nickel-base superalloys, as just noted, evolved from the 80Ni-20Cr Nichrome alloy. The iron- and nickel-iron-base alloys, on the other hand, evolved from the stainless steels; the first iron-base superalloy being the German alloy Tinidur. The first significant American iron-base superalloy was A-286. In both groups of wrought superalloys nickel-base versus iron- and nickel-iron-base, most alloying elements play identical roles.

A brief but useful look at some of the most important elemental effects in superalloys can be provided by reviewing the evolution of the Nimonic[3] alloys [*1,3*]. The initial addition of titanium to the 80Ni-20Cr base provided some precipitation strengthening (Nimonic 80). This was followed by an aluminum addition that provided additional precipitation strength but also a more stable γ' (Nimonic 80A). Cobalt additions were found to increase the γ' solvus temperature (Nimonic 90), while molybdenum was determined to provide elevated temperature strength primarily due to solid solution effects (Nimonic 100).

The basis for any useful γ' strengthened superalloy is a properly balanced austenitic matrix. Major components are nickel and iron. Because most superalloys contain relatively little carbon and relatively large amounts of molybdenum and chromium, a minimum of about 25 percent nickel is necessary to maintain an austenitic matrix. Higher nickel contents usually provide higher useful temperature and improved stability with resultant higher cost. The solid solution strengtheners commonly added to superalloys include approximately: 10 to 25 percent chromium, 0 to 10 percent molybdenum, 0 to 6 percent titanium, 0 to 6 percent aluminum, and 0 to 5 percent columbium. In most cases, the nickel-base matrix has greater tolerance than the iron-base matrix to the larger percentages of these additions, before detrimental phases occur. Tungsten can be used in place of molybdenum, and tantalum in place of columbium.

Although as just noted, titanium, aluminum, and columbium serve as solid solution strengtheners in superalloys, their main function is to

---

[3] Registered trademark of International Nickel Limited.

combine with nickel from the alloy matrix to form the γ' or γ'' strengthening precipitates that provide the main strength of precipitation hardened superalloys.

Oxidation resistance is provided to the superalloys primarily by chromium and aluminum. Other elements provide various complex effects. For example, boron and zirconium are often added to improve workability and stress rupture properties. Carbon is added as a deoxidant and to act in concert with certain carbide formers, such as titanium, chromium, columbium, vanadium, zirconium, etc., to form various beneficial carbides. Recently, much interest has developed in utilizing hafnium as an alloying agent to provide elevated temperature ductility, although the exact mechanism appears to be controversial.

It must be noted that this view of elemental effects is necessarily cursory, and the reader is referred to Decker [*4*] and Sims [*5,6*] for more complete reviews.

Physical Metallurgy

The wrought superalloys are strengthened by three basic mechanisms: solid solution, precipitation, and special effects caused by boron and zirconium. The matrix of all of these alloys is face centered cubic (fcc) austenite containing nickel (and iron if applicable) and various percentages of the added alloying elements. Decker [*4*] has ranked the solid solution strengthening potency of the alloying elements in a *typical* nickel-base alloy as follows: aluminum, tungsten, molybdenum, chromium, iron, vanadium, titanium, and cobalt (from most to least potent). Irvine et al [*7*] have shown that the most potent solid solution strengtheners in nickel-iron alloys include the interstitial elements carbon, nitrogen, and boron.

The primary strength of superalloys is provided by the γ' or γ'' precipitate. In nickel-base alloys, aluminum and to some degree titanium combine with nickel to form the A_3B type compound ordered, fcc γ'. In the iron-base and nickel-iron-base superalloys, titanium, columbium, and, to a lesser degree, aluminum combine with nickel to form ordered fcc γ' or ordered body centered tetragonal (bct) γ''. Titanium is the main γ' forming element in γ' strengthened iron-base (such as A-286) and nickel-iron-base superalloys (such as Alloy 901), while columbium is the primary γ'' forming element in γ'' strengthened nickel-iron base superalloys (such as Alloy 718).

Many useful aspects of the physical metallurgy of any alloy system are revealed by metallographic studies. Figures 1 and 2 show typical microstructures for Waspaloy and Alloy 718, respectively. The microstructure of Waspaloy can be considered to be typical of wrought nickel-base superalloys and certain titanium strengthened iron- and nickel-iron-base superalloys. The microstructure of the Alloy 718 is typical of nickel-iron-base

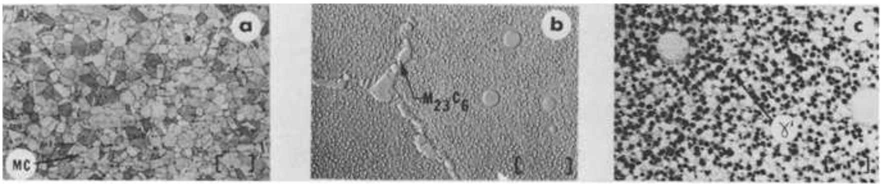

FIG. 1—*Microstructure of Waspaloy, a typical nickel-base superalloy strengthened by γ': heat treated 1010°C (1850°F), 4 h, oil-quenched plus 843°C (1550°F), 4 h, air cooled plus 760°C (1400°F), 16 h, air cooled.* (a) *Light micrograph (scalemark = 100 μm),* (b) *replica electron micrograph (scalemark = 1 μm), and* (c) *extraction electron micrograph (scalemark = 0.5 μm).*

superalloys that contain significant additions of columbium, such as Alloy 706 and Pyromet CTX-1.

The γ' in many of the leaner wrought nickel-base superalloys and in all known iron-base and nickel-iron-base superalloys is spherical as can be seen in Fig. 1 for Waspaloy. This indicates low lattice misfit between the γ and γ'. Other wrought nickel-base superalloys containing larger amounts of titanium and aluminum, such as Astroloy, will more likely form cuboidal γ', indicating higher misfit. Decker [*4*] provides an extended discussion of the effects of γ' morphology, etc. on strength of nickel-base alloys. Figure 3 shows one example of the effects of optimizing γ' particle size and distribution on the properties of Waspaloy. In the example given, stress rupture life is increased by an order of magnitude by optimizing the volume fraction of fine γ'. The γ' particle size and distribution was varied by varying the solution treating temperature and the stabilization aging time and temperature. The nickel-iron-base alloys containing columbium such as Alloy 718, form platelet γ'', Fig. 2. The γ'' provides excellent strength potential to about 650°C (1200°F).

Properly alloyed wrought nickel-base superalloys form no phases other than the γ matrix, the γ' strengthening precipitate, and the various carbides as seen in Fig. 1 for Waspaloy. The iron-base and nickel-iron-base alloys, on the other hand, are all prone to some degree to the

FIG. 2—*Microstructure of Alloy 718, a typical nickel-iron-base superalloy strengthened by γ'': heat treated 955°C (1750°F), 1 h, air cooled plus 720°C (1325°F), 8 h, cooled at 55°C (100°F) per hour to 620°C (1150°F), 8 h, air cooled.* (a) *Light micrograph (scalemark = 100 μm),* (b) *replica electron micrograph (scalemark = 1 μm), and* (c) *extraction electron micrograph (scalemark = 0.5 μm).*

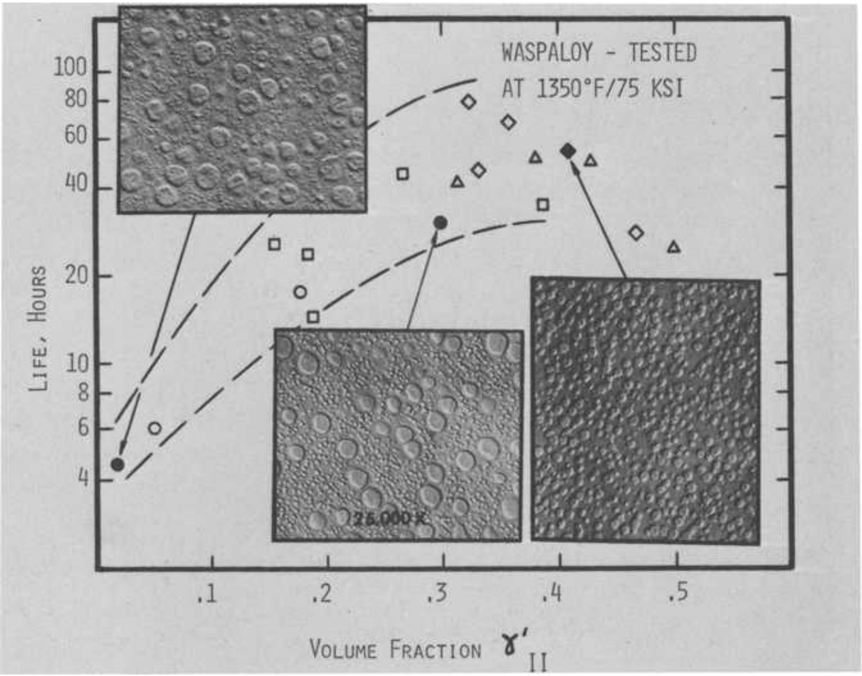

FIG. 3—*Effect of optimizing* γ' *particle size and distribution on stress rupture properties of Waspaloy.* γ_{II}' *refers to the* γ' *having a particle size of 200 to 400 Å that is formed during stabilization aging.*

formation of *third phases* such as hexagonal close packed (HCP)Ni_3Ti (η) and orthorhombic Ni_3Cb (δ) or both. Iron-base alloys, such as A-286, and titanium-rich nickel-iron-base alloys, such as Alloy 901, can form η, while columbium-rich Alloy 718 forms δ. Figure 2 shows the desirable globular morphology of this third phase in this type alloy.

All superalloys are prone to varying degrees to the formation of the various carbides: MC (M = Ti,Cb, etc.), M_6C (M = Mo,W), or $M_{23}C_6$ (M = Cr). The MC form upon solidification of alloys containing large amounts of titanium, columbium, hafnium, etc., and are usually seen as idiomorphic particles in interdendritic areas (Figs. 1 and 2). The M_6C form in like manner in alloys containing large amounts of molybdenum, tungsten, or both. The MC and M_6C serve to provide some barrier to grain growth in the various alloys as shown, for example, in Fig. 4 for Astroloy. $M_{23}C_6$ formation and morphologies have been controversial. It is generally agreed that the globular morphology shown in Fig. 1 for Waspaloy is beneficial. However, Decker [*4*] has shown that MC decomposition in the 900 to 1000°C (1652 to 1832°F) range can result in a continuous $M_{23}C_6$ grain boundary film that deteriorates ductility. A fine cellular form of

$M_{23}C_6$ is formed in A-286 by improper processing and can cause stress rupture notch sensitivity [9].

Evolution of Wrought Superalloy Processing

It is the availability of the various precipitating phases in the wrought superalloys that makes them so versatile with regard to property capability. In the early days, all wrought superalloys were forged from and solution heat treated at temperatures well in excess of the γ' solvus temperature. The high temperature solution treating step dissolved all γ', annealed the matrix, and promoted some grain growth. Typical grain size achieved was ASTM 3 or coarser. This was followed by one or more aging treatments that promoted controlled γ' and carbide precipitation. Optimum creep and stress rupture properties above about 760°C (1400°F) were achieved.

As the jet engine matured, there was an ever-increasing need for increased strength and reliability in forged superalloy parts, especially turbine and compressor disks. The forging industry met the task and in conjunction with alloy producers developed the necessary understanding and procedures to provide the required engine parts. As an example, it was found that careful control of forging furnace temperatures, slightly above recrystallization temperatures, provided an opportunity to produce grain sizes of ASTM 5 to 6. Modified heat treatments including lowered solutioning temperatures were required to maintain the fine grain structures. For some alloys, modified aging sequences were also necessary. A

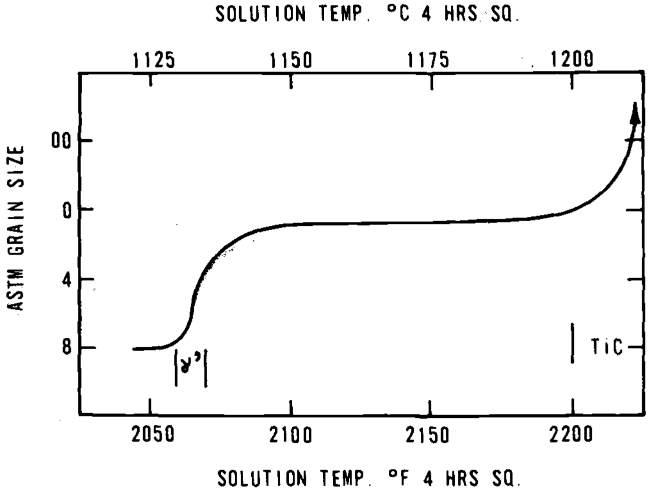

FIG. 4—*Grain size response in wrought Astroloy (after Ref 8). γ' and TiC solvus temperatures are marked. Grain coarsening accompanies solutioning of γ' as well as TiC.*

series of process refinements for the various wrought superalloys led to capability to produce excellent combinations of tensile, fatigue, and creep rupture properties in these alloys from 538 to 760°C (1000 to 1400°F), or even lower.

Waspaloy was one of the first alloys to receive attention. Studies of forging reduction, forging temperatures, and solution heat treating temperatures were performed [*10*]. It was found that starting forging at 1120°C (~2050°F) and finishing below about 1010°C (1850°F) produced a fine equiaxed ASTM 5 to 6 grain size. When this was followed by 1010°C (~1850°F) solution treatment plus a typical aging treatment: 843°C (1550°F), 4 h, air cooled + 760°C (1400°F), 16 h, air cooled; an excellent combination of tensile and creep rupture properties to about 732°C (1350°F) was produced. Table 2 shows some data on property improvements in Waspaloy achieved by process refinements [*11*].

The property latitude capability achieved by the forge shops was extended to other forms of the superalloys as well. For example, extremely high strength superalloy fasteners have evolved that provide outstanding combinations of strength and corrosion resistance at moderate temperatures. The extension of the processing latitude of superalloys has been the key to the extension of the usage of superalloys in many new applications.

Soon after these early developments, it was recognized [*12*] that the property capability latitude was provided by *structure control* effects by the various precipitating phases. For the nickel-base alloys—such as Waspaloy and René 95—γ' is the major structure controlling phase. For the important iron-base alloys such as A-286 and V-57, HCP Ni_3Ti (η) is the important structure controlling phase. The structure controlling phases vary among the nickel-iron base alloys—from HCP Ni_3Ti for alloys such as Alloy 901, to orthorhombic Ni_3Cb for Alloy 718, to mixtures of both Ni_3Ti and Ni_3Cb for the recently developed alloy, Pyromet CTX-1.

TABLE 2—*Property refinements in Waspaloy due to processing refinements (after Ref* 11*).*

	Room Temperature Yield Strength	
Year	MPa	ksi
1960	828.0	120
1961	862.5	125
1968	966.0	140
1972	1035.0	150
1977	1173.0	170

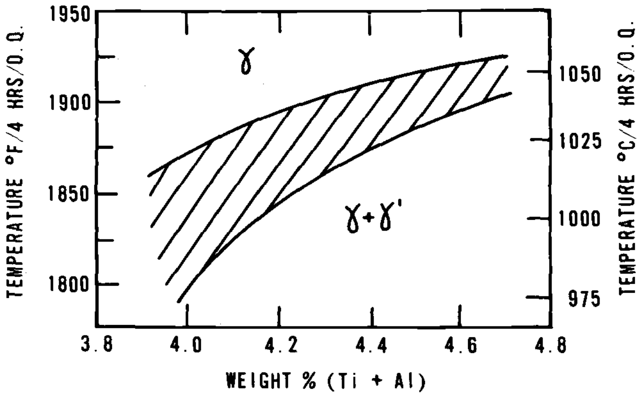

FIG. 5—*Phase relationships for Waspaloy (after Ref* 12).

Phase Relationships

In order to understand and to learn to better control the property capability of the various wrought superalloys, it was deemed necessary to establish phase solvus temperatures. It was also desired to learn how these relationships may vary with the slight chemistry variations that might occur among commercial heats. Some typical results are shown in Figs. 5, 6, and 7 as pseudo-binaries for Waspaloy, Alloy 901, and Alloy 718, respectively. This represents the range of effects usually noted.

It is possible to group alloys according to the phases that are utilized for structure control, as shown in Table 3. The working range is the temperature range over which the phase is useful to provide structure control effects. For all alloys, once this temperature range is exceeded the

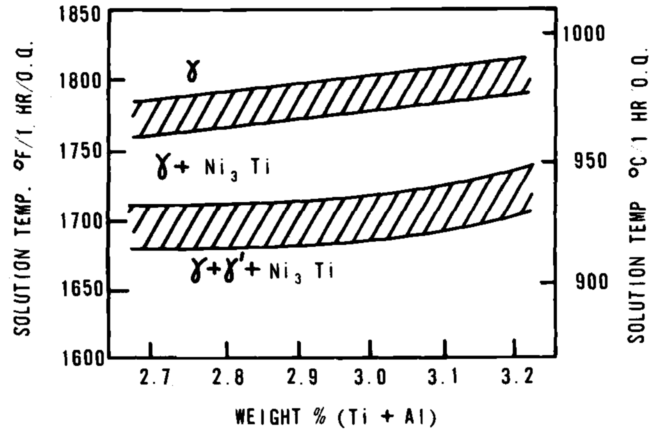

FIG. 6—*Phase relationship for Alloy 901 (after Ref* 13).

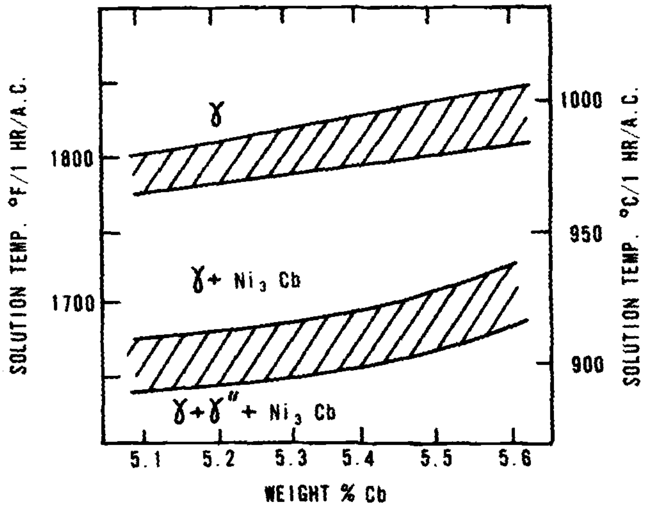

FIG. 7—*Phase relationship for Alloy 718 (after Ref 13).*

structure control phase goes into solution and loses its effect. For the nickel-base alloys below the working range, extensive precipitation of finer γ' begins and the alloy becomes too stiff to process. For the nickel-iron-base and iron-base alloys, temperatures below the working range cause γ' or γ'' to form—again leading to a matrix too stiff to process.

TABLE 3—*Structure control phases for various superalloys.*

Alloy	Phases for Structure Control	Working Range
Nickel-Base Superalloys		
Waspaloy	γ' ($Ni_3[Al,Ti]$)	954°C (1750°F) 1024°C (1875°F)
Astroloy	γ' ($Ni_3[Al,Ti]$)	1010°C (1850°F) 1121°C (2050°F)
IN-100	γ' ($Ni_3[Al,Ti]$)	1038°C (1900°F) 1177°C (2150°F)
René 95	γ' ($Ni_3[Al,Ti]$)	1024°C (1875°F) 1135°C (2075°F)
Nickel-Iron-Base Superalloys		
Alloy 901	η (Ni_3Ti)	940°C (1725°F) 995°C (1825°F)
Alloy 718	δ (Ni_3Cb)	915°C (1675°F) 995°C (1825°F)
Pyromet CTX-1	η (Ni_3Ti) or δ (Ni_3Cb) or both	855°C (1575°F) 915°C (1675°F)
Iron-Base Superalloy		
A-286	η (Ni_3Ti)	855°C (1575°F) 915°C (1675°F)

In virtually all nickel-base superalloys, the γ' solvus is critically controlled by the titanium plus aluminum content as shown in Fig. 5 for Waspaloy. That is, minor compositional changes of elements other than titanium plus aluminum have no significant effect on γ' phase boundary temperatures.

In the iron-base and nickel-iron-base superalloys strengthened primarily by titanium-rich γ', such as A-286 and Alloy 901, the titanium is the critical alloying element, as can be seen in Fig. 6. In the nickel-iron-base alloys strengthened primarily by columbium-rich γ'', such as Alloy 718, columbium content is critical, as is shown in Fig. 7. On the other hand, two newer nickel-iron-base superalloys containing relatively large amounts of columbium plus titanium, Alloy 706 and Pyromet CTX-1, have phase relationships heavily dependent on columbium plus titanium level [*12*,*14*].

Application of Principles

From the labors of the forgers and alloy producers, we have seen a series of principles evolve on the processing of wrought superalloys. These can be applied to any processing of superalloys, for example, to manufacture bars, wire, fasteners, sheet, plate, rings, etc., and include:

1. Know your application—what are its property requirements and property limitations: (a) creep, (b) creep rupture, (c) tensile, (d) low cycle fatigue, (e) high cycle fatigue, and (f) cyclic rupture (creep-fatigue interaction).
2. Know the alloy specified—is it nickel-base, iron-base, or nickel-iron-base? Does it form only γ', or is it prone to form other phases such as η, δ, etc.?
3. Know the important solvus temperatures for the alloy; γ', η, carbides, etc.
4. Know what microstructure will provide the best property response, or best combination of properties.
5. Utilize your experience with other alloys with similar phase relationships in designing your new process.

All of this may seem obvious, and yet, occasional problems with improperly processed superalloys can arise.

A recent example of process control is the achievement of notched stress rupture ductility in a new nickel-iron-base superalloy, Pyromet CTX-1, by *structure control* heat treating [*14*]. Initial development of the alloy utilized a heat treatment of 982°C (1800°F), 1 hr, air cooled + 718°C (1325°F), 8 h, cool 55°C (100°F)/h to 621°C (1150°F)/8 h/air cooled. Metallographic examination revealed equiaxed grains with extremely *clean* grain boundaries as shown in Fig. 8.

It was recalled from prior experience that a nickel-iron-base alloy of

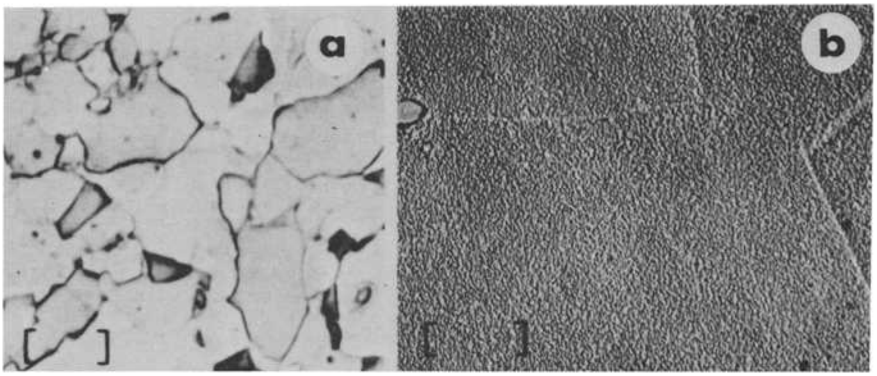

Scalemark indicates 20 μm Scalemark indicates 1 μm

FIG. 8—*Microstructure of notch sensitive Pyromet CTX-1 (after Ref* 14).

this type might be susceptible to stress rupture notch sensitivity if there were no globular particles along grain boundaries to prevent long-range grain boundary sliding. Phase studies, Fig. 9, revealed that the alloy was capable of forming HCP Ni_3Ti and orthorhombic Ni_3Cb (referred to as Ni_3 (Ti,Cb) for convenience). Thus, phases formed are similar to Alloy 706, an alloy that the author's laboratory had previously processed [*8,15,16*].

The studies [*14*] showed that if the Pyromet CTX-1, similar to Alloy 706, was forged such that the metal temperature dropped below the Ni_3 (Cb,Ti) solvus, about 871°C (1600°F), at finish, then a warm worked microstructure would result, Fig. 10. Then solution treating at 857°C (1575°F), 1 h, air cooled, between the γ' and Ni_3 (Cb,Ti) solvus temperatures produced a finished warm worked grain structure with grain boundaries decorated with Ni_3Ti and Ni_3Cb, Fig. 11. Properties for the notch sensitive and notch ductile conditions for Pyromet CTX-1 are

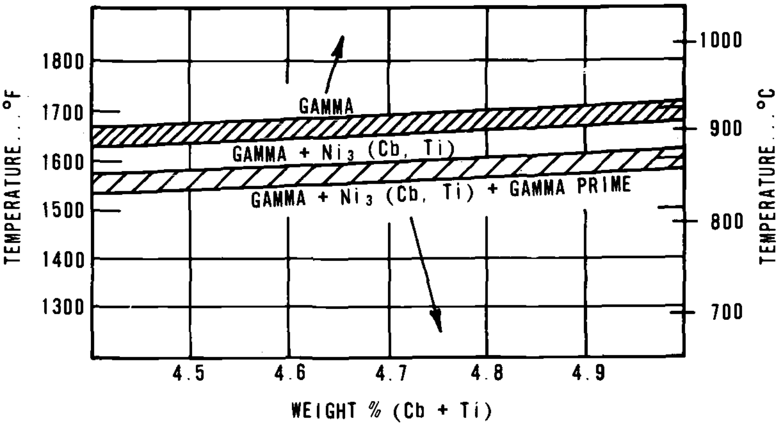

FIG. 9—*Phase relationship for Pyromet CTX-1 (after Ref* 14).

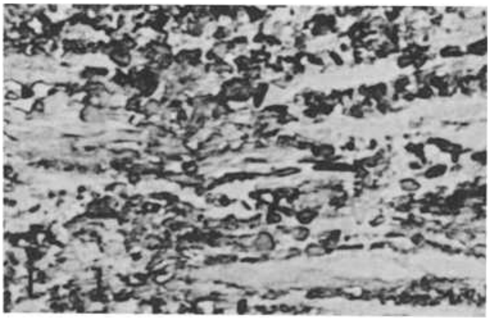

FIG. 10—*Microstructure of warm-worked Pyromet CTX-1 (after Ref* 14). *Scalemark indicates 20 μm.*

compared in Table 4. The advantages of the notch ductile condition are obvious.

There are cases, however, when structure control processings such as just described can be disadvantageous. One of these is in the application of Pyromet CTX-1 in jet engine rings. The relatively low hot-working temperatures required to produce the warm worked microstructure shown in Fig. 10 can result in directionality of properties. It was necessary then to find an alternative method to provide globular particles at grain boundaries to prevent long-range grain boundary sliding. Since processing variables had been exhausted, it was decided to try an alloy modification. The resultant alloy, Pyromet CTX-2 incorporates a 0.75 percent hafnium addition. Pyromet CTX-2 can be hot worked to a completely recrystallized microstructure, and in combination with a special heat treatment, is capable of providing notch ductile stress rupture properties, as shown in Table 4. However, due to the high cost of hafnium, the alloy is more expensive than Pyromet CTX-1.

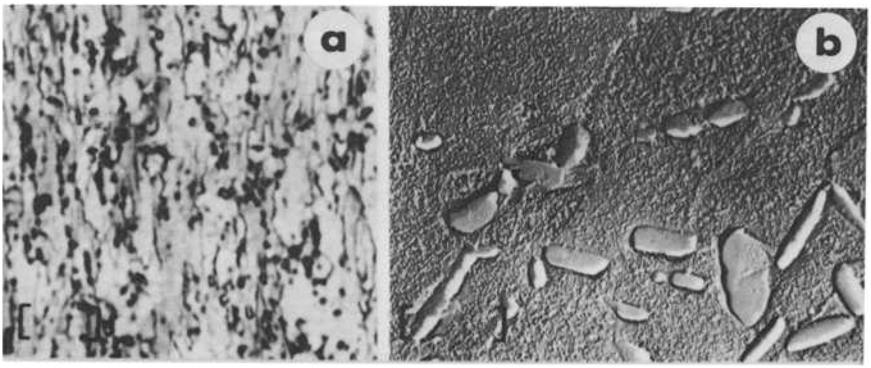

FIG. 11—*Microstructure of notch ductile Pyromet CTX-1 (after Ref* 14). (a) *Light micrograph (scalemark indicates 20 μm),* (b) *replica electron micrograph (scalemark indicates 1 μm).*

TABLE 4—*Typical properties of notch sensitive versus notch ductile Pyromet CTX-1 and Pyromet CTX-2.*

	20°C (70°F) Tensile				650°C (1200°F) Tensile				Combination Stress Rupture 650°C (1200°F/90 ksi)		
Alloy	0.2% Yield Strength, ksi	Ultimate Tensile Strength, ksi	Elongation, %	Reduction in Area, %	0.2% Yield Strength, ksi	Ultimate Tensile Strength, ksi	Elongation, %	Reduction in Area, %	Life, h	Elongation, %	Reduction in Area, %
CTX-1 Notch-sensitive Partially recrystallized	187	208	11	39	141	157	17	42	2	broke in notch	
CTX-1 Notch-ductile Warm worked structures	185	212	13	40	140	160	21	54	250	14.5	39.8
CTX-2 Fully recrystallized	155	194	19	56	124	173	16	47	180	7.4	10.8

In prior papers, the author has described several other processes that depend upon structure control principles. These include:

(*a*) Micrograin processing [*8*] where coarse (1 to 2 μm diameter) γ' particles are utilized in high γ' volume fraction nickel-base superalloys such as Astroloy, IN100, or René 95 to produce an ultra fine (5 to 10 μm diameter) austenite grain size—effectively rendering the alloy superplastic. This will be considered further below in the discussion of powder metallurgy (P/M) superalloys.

(*b*) Minigrain processing [*8*] that applies to nickel-iron-base superalloys such as Alloy 901 or Alloy 718, with phase relationships such as those shown in Figs. 6 and 7 (with wide temperature ranges separating γ' or γ'' and η or δ solvus temperatures and capability of forming large volume fractions of the η or δ). A dual process including forming a Widmanstatten array of the η or δ, warm working and a recrystallization heat treatment between the γ' or γ'' and η or δ solvus produces an extremely fine grain size (ASTM 12 to 13) and substantial improvements in low- and high-cycle fatigue strengths.

(*c*) Thermomechanical processing that can be applied to almost any alloy system. The author usually confines the term *thermomechanical* to those situations where the expressed intent is to use strain energy from the forming process to provide strength to the finish forged and heat treated part. Examples have been given for Waspaloy [*12*] where 20°C (70°F) 0.2 percent yield strength over 240 ksi was produced and René 95 [*8*] where 650°C (1200°F) 0.2 percent yield strength over 200 ksi was produced.

Many more examples of instances, in the maturing superalloy processing industry, where unusual combinations of properties have been developed by special processing sequences developed around knowledge of phase relationships could be given. Two papers [*10,11*] presented at a recent conference on Forging and Properties of Aerospace Materials in England provide additional information.

Powder Metallurgy Superalloys

Since about 1970, there has been a thrust toward development of P/M methods to process superalloys for improved properties and cost advantage through near net shape approaches. In the earliest successful work in this area, a modified version of IN100 alloy was manufactured into powder via inert gas atomization, contained under vacuum in a stainless steel container and then compacted to a solid billet by extrusion. By carefully controlling processing temperatures (below γ' solvus) an ultrafine grained structure is achieved (Fig. 12). Sections of the billet are then *gatorized*[4] or superplastically forged into turbine engine parts. The

[4] Gatorizing is a registered trademark of United Technologies Corp.

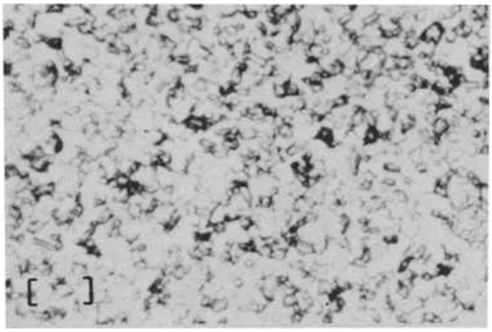

FIG. 12—*Microstructure of superplastic IN100. Scalemark indicates 10 μm.*

forgings are then heat treated and machined into finished parts. This has evolved into a commercial process with several companies capable of producing gatorized turbine engine hardware.

As in the case of Waspaloy, or other wrought nickel-base superalloys, the key to successful processing by this method is the achievement of a proper distribution of coarse γ'. Alloys with a high volume fraction of γ' such as IN100 and René 95 are readily capable of superplastic behavior, but alloys with lower volume fractions become marginal. As an example, Waspaloy (<25 volume percent γ' maximum available at gatorizing temperatures) is marginally superplastic. Due to low volume fractions of γ', Ni_3Ti or Ni_3Cb, and relatively low solvus temperatures for these phases in alloys such as A-286, Alloy 901, or Alloy 718, it is unlikely that any of the iron-base or nickel-iron-base alloys can be successfully superplastically forged.

Two other process routes for P/M superalloys have evolved: hot isostatically pressed (HIP) and HIP plus forge. Prime candidate alloys have been Astroloy and René 95. Although some controversy exists, it appears that approximately equivalent properties can be achieved by either method. In one case (as-HIP), the alloy is inert gas atomized into powder that is then placed in a pre-shaped container, evacuated, hot isostatically compacted, heat treated, and machined to finish. In the other (HIP plus forge), the sequence is interrupted after compaction, the part is usually machined all over, processed through a special forging sequence, heat treated, and machined. In both cases, an advantage over manufacture from ingot product is achieved by net-shape materials savings. Table 5 shows typical properties achieved by these methods.

One of the primary advantages of P/M superalloys has been the ability to achieve exceptionally good 538 to 649°C (1000 to 1200°F) fatigue properties through maintaining a fine grain size. For many applications, best properties have been associated with low HIP temperatures—below the γ' solvus. However, even in cases where HIP temperatures above the

TABLE 5—*Typical properties of HIP plus forged versus as-HIP powder metallurgy René 95 (after Ref* 17).

	2000°F/1 h/oil quenched + 1400°F/16 h/air cooled										
	Room Temperature Tensiles				650°C (1200°F) Tensiles				650°C (1200°F)/150 ksi/Stress-Rupture		
	Ultimate Tensile Strength	Yield Strength, 0.2%	Elongation, %	Reduction in Area, %	Ultimate Tensile Strength	Yield Strength, 0.2%	Elongation, %	Reduction in Area, %	Life, h	Elongation, %	Reduction in Area, %
HIP plus forged	250	195	18	20	215	175	12	12	150	3.5	N/A[a]
As-HIP	240	170	20	20	210	175	10	12	130	2.5	3.5

[a] N/A = not available.

γ' solvus are used, maximum achievable grain size in P/M superalloys appears to be a direct function of powder particle size. In conventional (ingot) wrought superalloys, it is well established that primary carbides (for example, TiC in Waspaloy) provide some practical limits to grain size depending upon carbon content. In P/M superalloys, the factors limiting achievable grain size are less well known.

Critical strain is the method that has been used to promote grain growth in P/M superalloys. In one case [*18*], elongated coarse grains were achieved by inducing critical strain in the finishing operations of a gatorizing process followed by recrystallization in a thermal gradient.

Pyromet 31

Relatively few new wrought superalloys have been introduced during the past five years. Almost all of the newer alloys have been designed with a single application in mind. One such alloy is Pyromet 31, developed for good sulfidation resistance. Sulfidation resistance is required in applications such as diesel engine exhaust valves that are operated in sulfur-rich fuels. Pyromet 31 was designed to replace Alloy X-750 that is susceptible to sulfidation attack.

With recent interest in nickel-base alloys for use in sulfur-rich sour gas well and oil well environments, Pyromet 31 is being evaluated as a modest cost candidate for use as *high strength* tubing [*19*]. Initially, studies were conducted to develop a heat treatment for the alloy that would produce a *minimum* room temperature 0.2 percent yield strength of about 689.5 Mn/m^2 (100 ksi) in combination with a *maximum* hardness of about 30 HRC. The selected heat treatment: 955°C (1750°F), 4 h, oil quenched, is slightly below the γ' solvus for the alloy: 1005 to 1010°C (1840 to 1850°F). This heat treatment, a *sub-solution* heat treatment, provides room temperature 0.2 percent yield strength of about 724 Mn/m^2 (105 ksi) and hardness of about 33 HRC.

Rice [*19*] has reported that sulfide stress cracking tests run in a sour brine solution (NACE test) and pitting/crevice corrosion tests run in a ferric chloride solution (ASTM Test for Pitting and Crevice Corrosion Resistance of Stainless Steels and Related Alloys by the Use of Ferric Chloride Solution G 48–76, Method B) show the alloy to be a viable candidate for sour gas/oil well service. Studies are continuing. It should be noted that if the alloy was subsequently age hardened at 650°C (1200°F) or above, substantially higher 0.2 percent yield strength and hardness would result. Service temperatures of about 233°C (450°F) for sour gas well applications are not expected to affect the alloy's properties.

Summary

From the 1930's to the mid-1960's, a wide range of superalloys evolved by various discoveries of unique effects of compositional changes on properties. Since the mid-1960's, processing has become more critical in permitting a wide range of property achievement in these alloys. In the wrought alloys, evolution of the following information on phase relationships has been critical in process design: identification of phases, determination of solvus temperatures, and effects of composition variations. These data exist for many contemporary alloys and may be found in the literature. Achievement of desired properties in new alloys can be simplified by comparing phase relationships with established alloys. Structure effects in P/M superalloys are partially explained on the same basis—but additional study is indicated. A new superalloy, Pyromet 31, originally designed for sulfidation resistance in applications such as diesel engine exhaust values, but being evaluated for sour gas well and oil well applications, is also discussed.

Acknowledgments

The author would like to acknowledge the Carpenter Technology Corporation for permission to publish this paper. Special thanks are extended to Sunil Widge for help in developing some of the figures and tables and for presenting the paper at MiCon.

References

[1] Betteridge, W., *The Nimonic Alloys*, Edward Arnold Ltd., London, 1959.
[2] Decker, R. F. and DeWitt, R. R., *Journal of Metals*, Vol. 17, No. 2, Feb. 1965, pp. 139–145.
[3] Sullivan, C. P. and Donachie, M. J., Jr., *Metals Engineering Quarterly*, Vol. 7, No. 1, Feb. 1967, pp. 36–45.
[4] Decker, R. F., Symposium on Steel Strengthening Mechanisms, Zurich, 1969, Climax Molybdenum Co., Greenwich, Conn., 1970, pp. 147–170.
[5] Sims, C. T., *Journal of Metals*, Vol. 18, No. 10, Oct. 1966, pp. 1119–1130.
[6] Sims, C. T. "Nickel Alloys—The Heart of the Gas Turbine Engines," ASME Report No. 70-GT-24, American Society of Mechanical Engineers, New York, 1970.
[7] Irvine, K. J., Llewellyn, D. T., and Pickering, F. B., *Journal*, Iron and Steel Institute, Vol. 199, Part 2, Oct. 1961, pp. 153–175.
[8] Muzyka, D. R. and Maniar, G. N. in *Metallography, ASTM STP 557*, American Society for Testing and Materials, Phila, Pa., 1974, pp. 198–219.
[9] Maniar, G. N. and James, H. M., *Transactions*, American Society for Metals, Vol. 57, March 1964, pp. 368–370.
[10] Wilkinson, N. A., *Metals Technology*, Vol. 4, Part 7, July 1977, pp. 346–359.
[11] Coyne, J. E., *Metals Technology*, Vol. 4, Part 7, July 1977, pp. 337–345.
[12] Muzyka, D. R., *Metals Engineering Quarterly*, Vol. 11, No. 4, Nov. 1971, pp. 12–20.
[13] Muzyka, D. R. in *The Superalloys*, C. T. Sims and W. C. Hagel, Eds., Wiley, New York, 1972, Chapter 4.
[14] Muzyka, D. R., Whitney C. R., and Schlosser, D. K., *Journal of Metals*, Vol. 27, No. 7, July 1975, pp. 11–15.
[15] Moll, J. H., Maniar, G. N., and Muzyka, D. R., *Metallurgical Transactions*, Vol. 2, No. 8, Aug. 1971, pp. 2143–2151.
[16] Moll, J. H., Maniar, G. N., and Muzyka, D. R., *Metallurgical Transactions*, Vol. 2, No. 8, Aug. 1971, pp. 2153–2160.
[17] Reichman, S., *International Journal of Powder Metallurgy and Powder Technology*, Vol. 11, No. 4, Oct. 1975, pp. 277–283.

[*18*] Allen, M. M., Miller, J. A., and Woodings, B. E., U.S. Patent No. 3,975,219. 17 Aug. 1976.

[*19*] Rice, P. W., "Evaluating Nickel Base and Stainless Alloys for Subsurface H_2S Service," ASME Report No. 77—Pet-16, The American Society of Mechanical Engineers, New York, 1977.

A. J. DeRidder[1] *and R. Koch*[1]

Forging and Processing of High-Temperature Alloys

REFERENCE: DeRidder, A. J. and Koch, R., "**Forging and Processing of High-Temperature Alloys,**" *MiCon 78: Optimization of Processing, Properties, and Service Performance Through Microstructural Control, ASTM STP 672,* Halle Abrams, G. N. Maniar, D. A. Nail, and H. D. Solomon, Eds., American Society for Testing and Materials, 1979, pp. 547–563.

ABSTRACT: Optimum properties of *superalloys* are derived from the interactions of the composition, thermomechanical deformation, and heat treatment. Nickel-base alloys contain a variety of elements in a large number of combinations to produce various desired effects. The general characteristics of any specific precipitation hardening heat-resisting alloy is determined by its composition. Microstructural variations in forging stock can further influence forging and heat treatment response. Specific alloy composition, as affected by heat treatment, is characterized by the time–temperature relationship to produce various phases and compounds. Chemical banding and carbide distribution, for example, contribute to directional property variations through differential response to heat treatment. Structural response relative to final property effects is also influenced by recrystallization brought about through use of selected thermomechanical processing parameters. Special controls are required under these circumstances to ensure satisfactory structural uniformity in forged components of complex configurations. These combined effects of composition, deformation, and heat treatment produce certain microstructures relating to the final desired properties.

KEY WORDS: steels, microstructure, high-temperature alloys, heat treatment, precipitation hardening

The interest in new high-temperature materials capable of performing at higher temperatures for the future generation of jet engines continues to be the object of intensified research. Of perhaps equal importance is the search for methods to upgrade the performance of high-temperature alloys currently used in jet engines. In many instances, the performance upgrading may be achieved through microstructural analysis. Historically, increased strength at higher temperatures has been obtained primarily by larger additions of age-hardening elements, primarily aluminum, titanium, and columbium (Table 1). A sobering consequence of the

---

[1] Manager, Aerospace Metallurgy, and supervisor, Advanced Metallurgy Section, Ladish Co., Cudahy, Wis. 53110.

TABLE 1—*Nominal chemical analysis for some high-temperature alloys.*

	Cr	Ni	Fe	Mo	Co	W	Cb	Ti	Al	Cb + Ti + Al
16-25-6	16	25	balance	6	. . .	. . .	. . .	. . .	. . .	. . .
Discaloy	13.5	26	balance	3	. . .	. . .	. . .	1.6	0.2	1.8
A286	15.0	26	balance	1.25	. . .	. . .	. . .	2.15	0.2	2.35
V57	14.75	27.0	balance	1.25	. . .	. . .	. . .	2.95	0.22	3.17
Inco 901	12.5	42.5	balance	5.75	. . .	. . .	. . .	2.85	0.25	3.10
Waspaloy	19.5	balance	1 max	4.25	13.5	. . .	. . .	3.00	1.40	4.40
René 41	19.0	balance	5 max	9.75	11.0	. . .	. . .	3.15	1.65	4.80
Alloy 718	19.0	52.5	balance	3.05	1 max	. . .	5.25	0.9	0.60	6.50
Astroloy	15.5	balance	0.5 max	5.25	17.0	. . .	. . .	3.30	4.50	7.90
René 95	14.0	balance	0.25 max	3.5	8.0	3.5	3.5	2.5	3.5	9.5
IN100	12.4	balance	0.2 max	3.20	18.5	0.05 max	0.02	4.33	5.0	9.35

higher hardener content to the forging industry was a tendency for reduced forgeability. Ultimately, the stage was reached where further increase in the age-hardening elements resulted in the complete loss of forgeability, as characterized by deep forging ruptures. The higher hardener content during ingot solidification of these alloys produced more pronounced dendritic segregation, voids, carbide networks, and brittle intermetallic particles contributing to crack initiation during hot forming. In recent years, powder metallurgy (P/M) techniques have been refined to permit fabrication of the more highly alloyed high-temperature alloys directly into usable shapes by hot isostatic pressing (HIP) or by forging of hot isostatically pressed preforms or extruded billets.

The intent of this paper is to review parameters affecting the material quality and current state of the art of forging conventionally melted material as well as P/M high-temperature alloys. These parameters include ingot and P/M characteristics, ingot conversion practices, closed die forging processes, and mechanical property performance optimization as recognized through microstructure analysis.

Ingot Characteristics

Specialty alloy producers have made many important contributions toward the manufacture of a more uniform product. A method for rating severity of carbide cleanliness in billets has been established and charts developed to provide a logical language of communication between producer and user leading to improved mechanical properties, primarily transverse tensile ductility and stress rupture notch ductility (Fig. 1). The acceptable limits within the charts will vary with the particular alloy and the intended application. Parts that must meet more stringent transverse tensile ductility requirements necessitate material with a better carbide rating. A maximum acceptable limit of S3, N3, C3, and M2 is necessary for Waspaloy to achieve the minimum transverse tensile ductility requirements at room temperature of 10 percent elongation and 12 percent reduction of area.

A severity rating system has also been established for dendritic segregation, or banding in forging billet stock, as revealed in samples electrolytically etched with 12 ml H_3PO_4, 47 ml H_2SO_4, and 41 ml HNO_3. The contrast between the dark and light dendrites is a semi-quantitative test for degree of dendritic segregation in ingots (Fig. 2). Microprobe analysis has shown a higher age-hardening element content in the darker areas versus the light areas, resulting in a greater concentration of thermally stable large gamma prime aging precipitate and carbide particles, as well as other less thermally stable intermetallic particles. The use of thermal homogenization treatments was introduced to diffuse dendritic segregation, primarily titanium and aluminum, and to improve mechanical

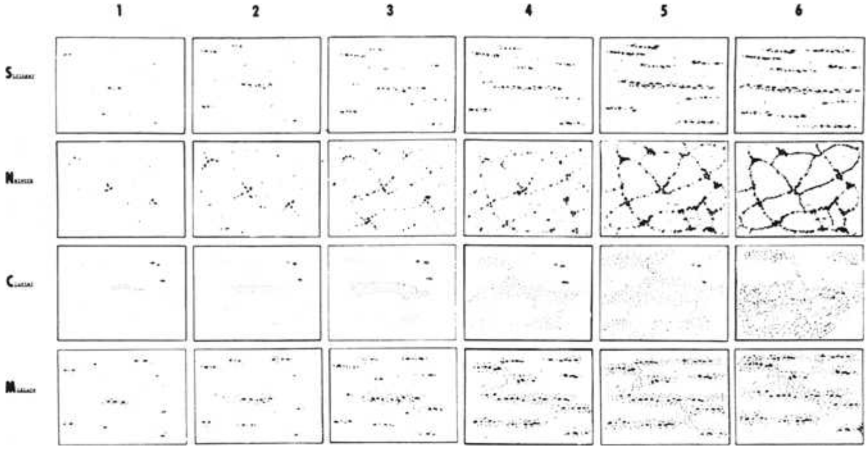

FIG. 1—*APML cleanliness classification of high-temperature alloys.*

property uniformity in the final product. Molybdenum is diffused at a far slower rate than either titanium or aluminum. The selection of the highest possible homogenization temperature, to shorten the homogenization time for energy conservation, is limited by incipient melting as observed in the microstructure (Fig. 3). Loss of forgeability and mechanical properties is evident even with the slightest amount of incipient melting (Fig. 4). At 1246°C (2225°F), incipient melting in Astroloy is present in the more segregated areas of the microstructure. When the homogenization temperature is further increased to 1232°C (2250°F), both incipient melting and porosity at grain boundary junctions are observed. Generally, any evidence of incipient melting is justifiable reason to scrap the material since reversal of this condition by hot deformation or heat treatment has been unsuccessful. Homogenization temperature for Waspaloy ingot ranges from 1177°C (2150°F) to 1204°C (2200°F) for 10 to 48 h depending on severity of alloy segregation and age-hardening element content. Examples of acceptable homogenized Inco 718 microstructure are found in Fig. 5. Transverse room-temperature tensile ductility improvement of

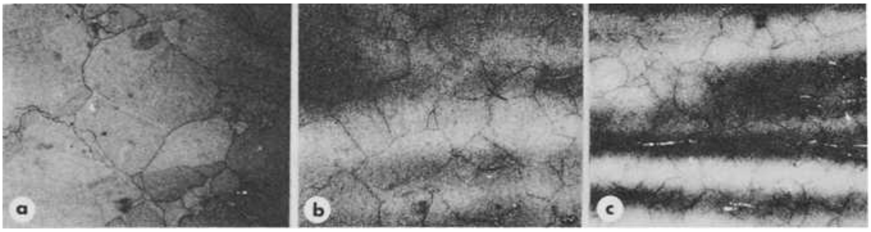

FIG. 2—*APML banding classification of Waspaloy 5Q6 (original magnification ×100): (*a*) acceptable, (*b*) metallic review, and (*c*) rejectable.*

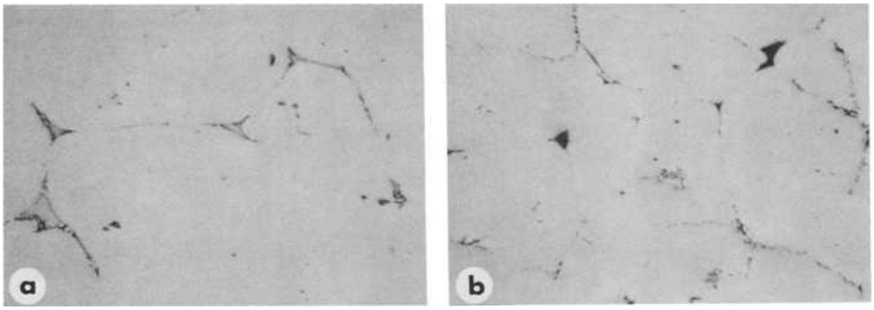

FIG. 3—*Astroloy* (a) *incipient melting at 1246°C (2225°F) and* (b) *incipient melting and voids at 1232°C (2250°F). (Original magnification ×100).*

9.1 to 11.5 percent elongation and 10.3 to 16.4 percent reduction of area was associated with homogenized Astroloy ingot material that had been upset forged to 8.9 cm (3.5 in.) thickness. Control tests were performed on unhomogenized ingot material similarly forged. Other beneficial effects have been associated with homogenization such as substantial reduction of Lave's phase in Inco 718 (Fig. 6). This particular phase was noted to initiate fine internal cracks during hot working evident only after nondestructive (NDT) testing of machined parts by penetrant inspection techniques (Fig. 7).

Alloys with higher hardener content as well as the larger ingot sizes are more prone to heavier dendritic segregation promoted by larger dendritic spacing, which allows segregation to occur in fewer but larger areas during solidification. The larger dendritic spacing also permits heavier concentration of thermally stable carbide and other intermetallic segregations.

A dendritic spacing of 0.39 mm (0.015 in.) or more generally indicates potential problems with René 95 or Astroloy. More rapid cooling practice during solidification of the ingot reduces dendritic spacing, but the

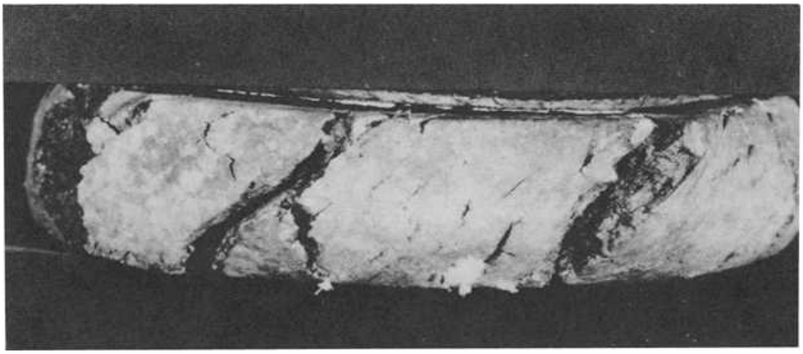

FIG. 4—*Gross ruptures due to incipient melting.*

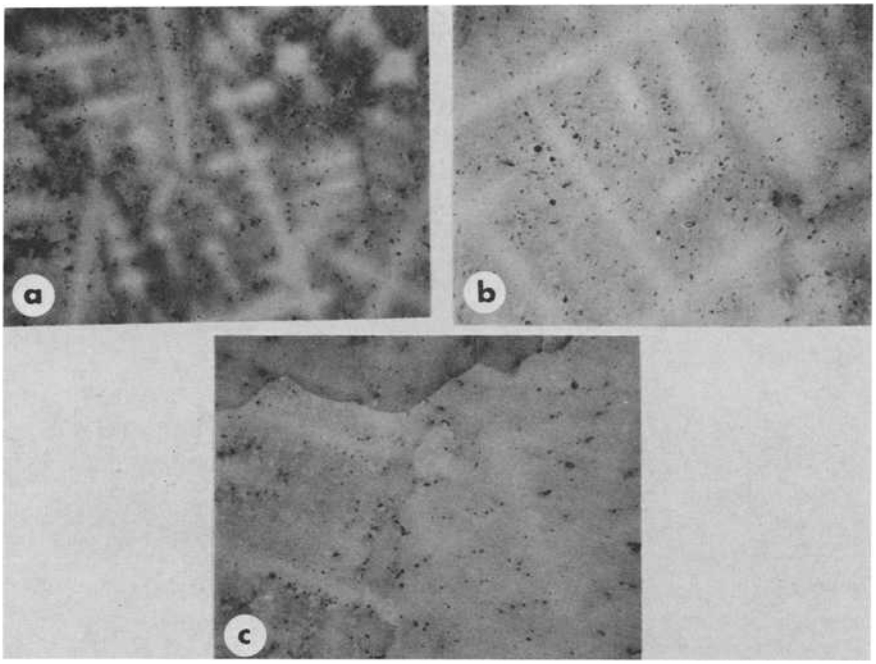

FIG. 5—*Progression of dendritic diffusion during homogenization (original magnification ×25):* (a) *moderate dendritic segregation, no homogenization;* (b) *light dendritic segregation, homogenized; and* (c) *very light dendritic segregation, homogenized.*

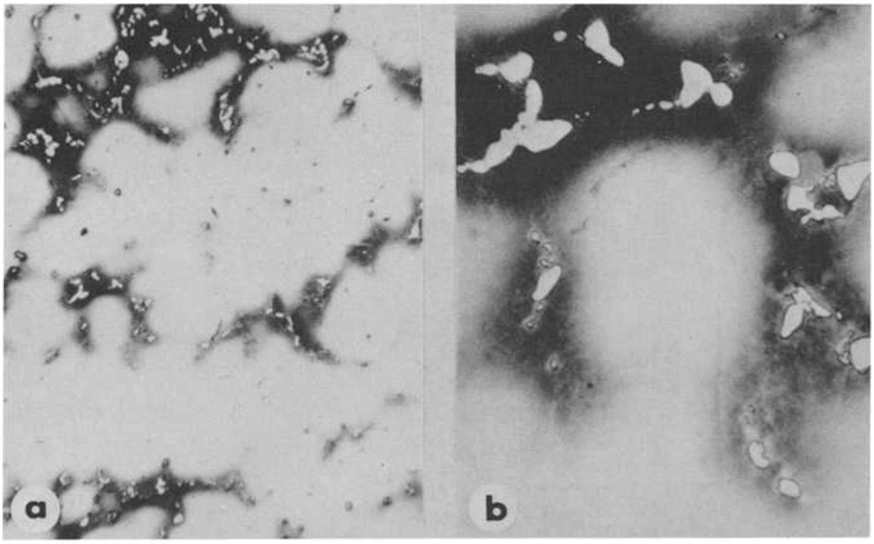

FIG. 6—*Dendritic segregation and Lave's phase* (a) *original magnification ×100 and* (b) *original magnification ×500.*

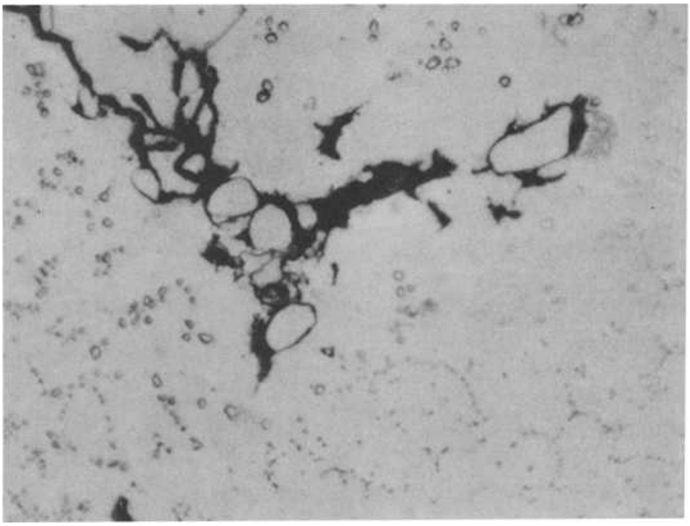

FIG. 7—*Internal microcracks initiating at Lave's phase particles during hot working (×500).*

benefits of more rapid cooling are compromised with the tendency for internal thermal stress cracking. It also appears that various stirring techniques prior to solidification of the ingot reduce segregation problems. Melting only small-size ingots may appear to be an obvious solution to the problem, but the economics of melting a 61 cm (24 in.) round ingot are much better on a cost per pound basis as compared to smaller-size ingots. Also, the forged part shape or size may dictate larger-size ingots.

Ingot Conversion into Billets

The ingot conversion practice, part of the total concept of thermomechanical processing procedure, is a most important intermediate step in obtaining the best possible microstructure before the material is committed to a sequence of final closed die forging. It is not merely a step to achieve desirable size billets. In some unusual cases, redundant work operations are necessary to provide the starting stock with additional uniformity and structural refinement where the particular final shape does not lend itself to adequate penetration during the finish forge operation. During conversion of the ingot to billet, the dendritic segregation is translated into parallel bands. Carbides and other related intermetallic networks are elongated into stringers.

Mechanical factors such as billet straightness, roundness, or localized surface nonuniformity can have a subtle but detectable effect on the final microstructure. For example, it is impossible to cut successive multiples from a crooked billet and obtain cut faces that are perpendicular to the longitudinal axis of the multiple. During upset forging of a non-square cut multiple, the upset progressively tips the piece in one direction causing an oval intermediate shape. The nonsymmetrical geometry of this intermediate shape affects the amount of progressive recrystallization and deformation in subsequent operations.

Good heat retention practice during the ingot drawdown is a substantial factor in obtaining a desirable uniform microstructure in the billet. Rapid transfer of the ingot from furnace to the drawdown press, as well as utilizing various techniques such as supplementary heat application during drawdown, is necessary to promote sufficient recrystallization during each successive pass across the dies (Fig. 8). Based on microprobe work, it appears that additional diffusion of the age-hardening elements is associated with recrystallization during ingot conversion. Mechanical factors such as cycling speed (which amounts to better heat retention), depth of pass, length of pass, die design, and tonnage of the drawdown press all contribute to good work penetration throughout the billet cross section.

In most cases, the initial ingot conversion operations are accomplished well above the gamma prime solvus temperature with the majority of the subsequent work completed below but still high enough to avoid excessive warm straining and unrecrystallized microstructure. The original ingot structure must be completely refined in billets to avoid carry-over into final forged shapes, particularly where complete work penetration during the final closed die forge sequence is impossible due to shape such as high coupling disks.

Occasional straightening of the billets is required prior to cooling to room temperature. Billets are usually either machined or swing ground to obtain a suitable surface for subsequent visual and ultrasonic inspection.

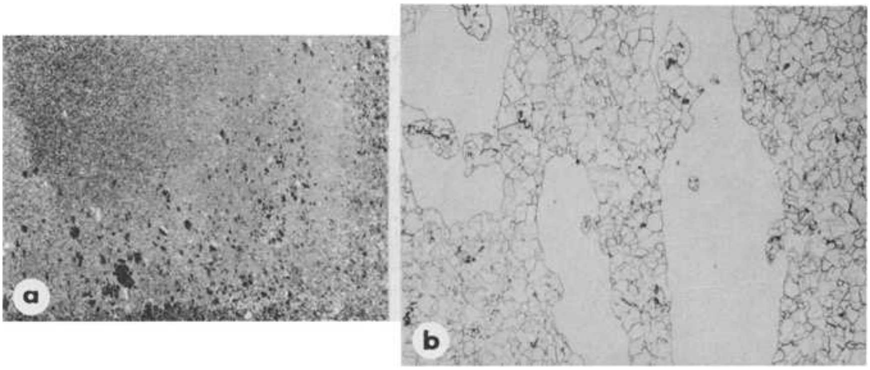

FIG. 8—*Waspaloy:* (a) *unrecrystallized coarse grains in billet (original magnification ×1), and* (b) *unrecrystallized coarse grains carried through into disk forging (original magnification ×100).*

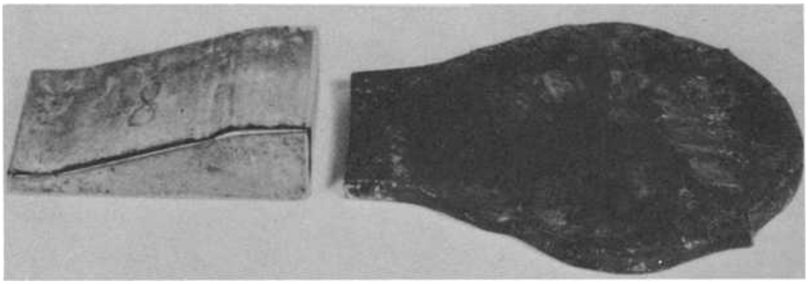

FIG. 9—*Wedge upset test.*

Localized burning during swing grinding will cause numerous slight localized surface ruptures during subsequent forging.

To some extent, the extent of grain refinement or grain size can be roughly estimated by ease of ultrasonic penetration.

Closed Die Processing

To achieve desired microstructure in the final part through closed die processing, three general parameters should be considered. The mechanical properties of the heat resistant alloys change significantly with relatively small differences in: (1) the forging temperature at any particular point, (2) how much the metal is moved at that temperature, and (3) how fast it is moved.

The closed die forging temperature selected is generally below the gamma prime solvus temperature in order to avoid excessive grain coarsening. Usually, the forging sequences are programmed to be completed over a falling temperature range. Approximately 80 percent of the metal reduction is scheduled in the recrystallization temperature range with the remaining 20 percent of work done at a lower temperature range in order to introduce a certain amount of warm working for added yield strength response. This is monitored with an optical pyrometer and the temperature recorded is judged against the approximate amount of metal reduction during forging. A wedge upset test was found to be a very useful tool to determine the amount of recrystallization or warm work or both associated with a particular temperature range (Fig. 9).

A very fast rate of metal movement during closed die forging will cause frictional heat build up, nonuniform recrystallized grain size, and mechanical property variations. Also, sensitivity for radial type ruptures increases both with forging rate or forging temperature (Fig. 10). For this reason, slow strain rates are preferred during the early closed die reductions for both Astroloy and René 95 alloys when the materials are less hot ductile. Again, as in the ingot conversion practice, good heat retention practice must be maintained. This includes rapid handling to

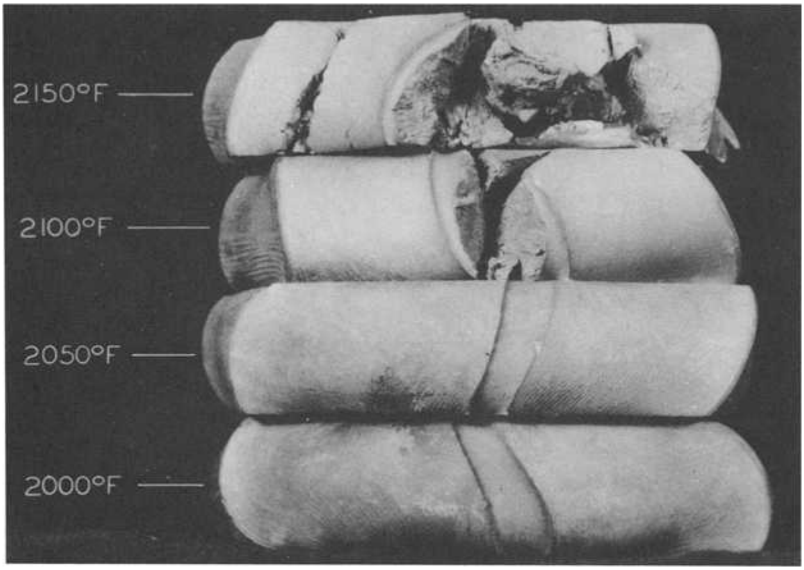

FIG. 10—*Inco 718 U-notch upset tests, 4 to 1 reduction; rupturing sensitivity associated with forging temperature (×0.3).*

avoid temperature loss from the furnace to the forging unit, and between various forging units when furnace heat restoration is not required. Rapid cooling or chilling of sharp outside radius corners must be avoided to prevent a phenomenon of chill cracking common to many high-temperature alloys (Fig. 11).

A sufficient amount of recrystallization is necessary in each of the closed die operations to achieve the desired grain size and reduce the effects of continuous grain boundary or twin boundary carbide networks that develop on stationary grain boundaries during heating and cooling (Fig. 12). This condition probably contributes more to mechanical property and other problems than any other single factor. Poor weldability, low-cycle fatigue properties, low hot strength, and stress rupture notch sensitivity are all associated with continuous grain boundary carbide networks. Heat treatment can do very little to correct this problem without creating equally undesirable mechanical property problems when higher solution treatments are used.

A long sought goal of producing improved high-temperature forgeable alloys has been achieved through advances in powder metal (P/M) technology. These advances have permitted the industry to take at least three general routes to produce hardware from P/M alloys. The first approach is to HIP, extrude, and creep form using the *gatorizing* process (Fig. 13). The second approach involves hot isothermal forging HIP preforms into near-net shapes. The third method involves machining

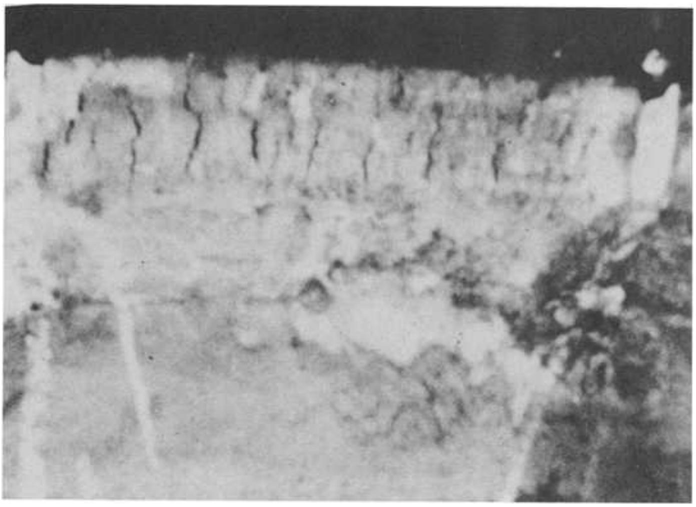

FIG. 11—*Chill cracks on inside diameter corner of rolled ring (Waspaloy arc cast and wrought) (×0.5).*

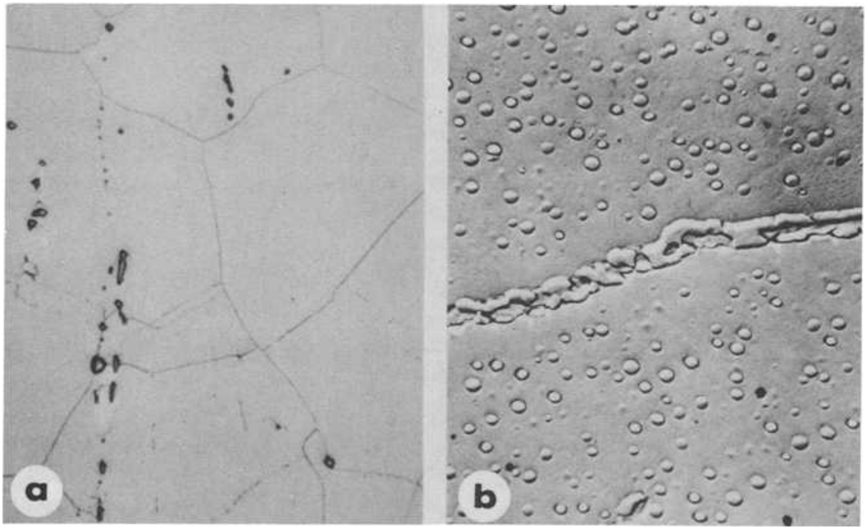

FIG. 12—*Waspaloy: continuous grain boundary network reduces forgeability, weldability, low-cycle fatigue, hot tensile yield strength, and stress rupture ductility;* (a) *optical micrograph and* (b) *electron micrograph.*

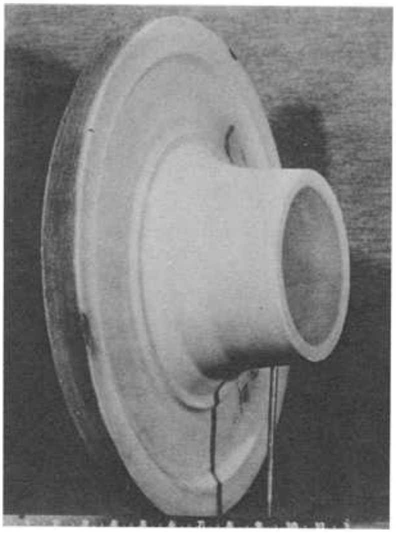

FIG. 13—*Typical gatorized IN100 turbine disk.*

hardware directly from the HIP shape. There is reason to believe that a new family of high-temperature alloys will be specifically developed to accomodate these P/M processes.

Concurrent with these achievements, the P/M industry has been periodically plagued with problems unique to powder. A number of sources have moved to solve these problems with considerable success. Many of the powder problems revolve around contamination that is either introduced prior to or during the atomization process, or accidentally introduced later during powder blending, handling, or as a result of protective container leaks. Routine metallographic examination performed on extruded consolidated IN100 material has established contamination in a variety of unsuspecting ways. As an example, chromium-rich particles surrounded by oxides were observed through routine optical reviews and identified through electron microprobe analysis. It was strongly suspected that the chromium contamination (Fig. 14), was due to an alloy melt addition that was already contaminated. The contaminated chromium addition was apparently small enough to flow through the atomizing nozzle with the liquid mix. Classification of the atomized particles by screening undoubtedly eliminated the larger particles. It was also determined that contamination of a different nature was introduced by decomposition of the melting crucible or the atomizing nozzle causing zirconium oxide or magnesium oxide particles to be uniformly dispersed throughout the powder blend (Fig. 15). Likewise, oxide contamination resulting from container leaks, due to poor welding practice, etc., caused

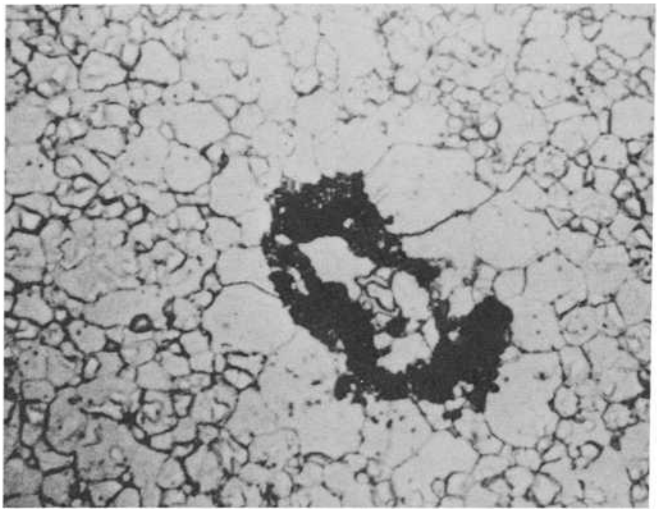

FIG. 14—*Chromium particle surrounded by oxide segregation (×100).*

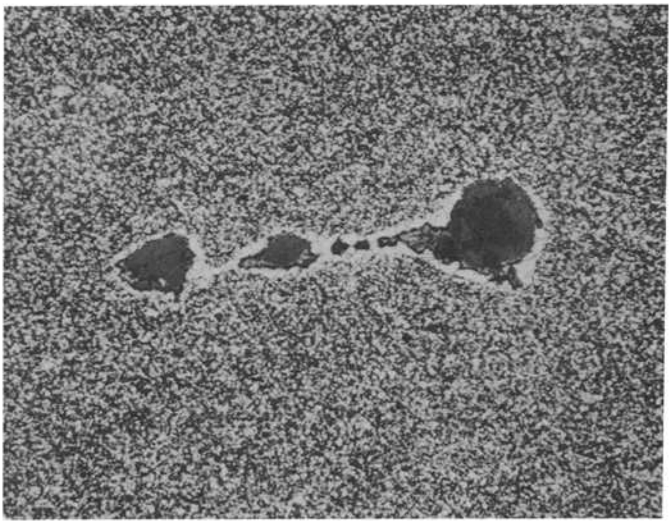

FIG. 15—*Zirconium oxide contamination (×100).*

TABLE 2—*Astroloy contamination in IN100 billet.*

Element	Contamination	Nominal IN100	Nominal Astroloy
Ti	3.35	4.25	3.5
Cr	15.30	10.0	15.0
Mo	4.90	3.0	5.0
Al	4.80	5.5	4.5

localized or general embrittlement of the P/M material causing poor hot formability and substandard mechanical property results (Fig. 16).

Good housekeeping in the form of cleanliness was a key factor in maintaining contamination-free powder blends. Insufficient cleaning of the storage and blending equipment did, in fact, produce contamination of IN100 with other high-temperature P/M alloys previously processed with the same equipment. Both René 95 and Astroloy powder agglomerates were randomly dispersed throughout the IN100 extruded material (Fig. 17 and Table 2). Apparently, the mechanical action of the P/M blender was not adequate to break these agglomerates into individual particles and were recognized as abnormal microstructure under the optical microscope.

A high percentage of P/M HIP preforms and extruded billets continue to show visual striations directly associated with alternate layers of coarse

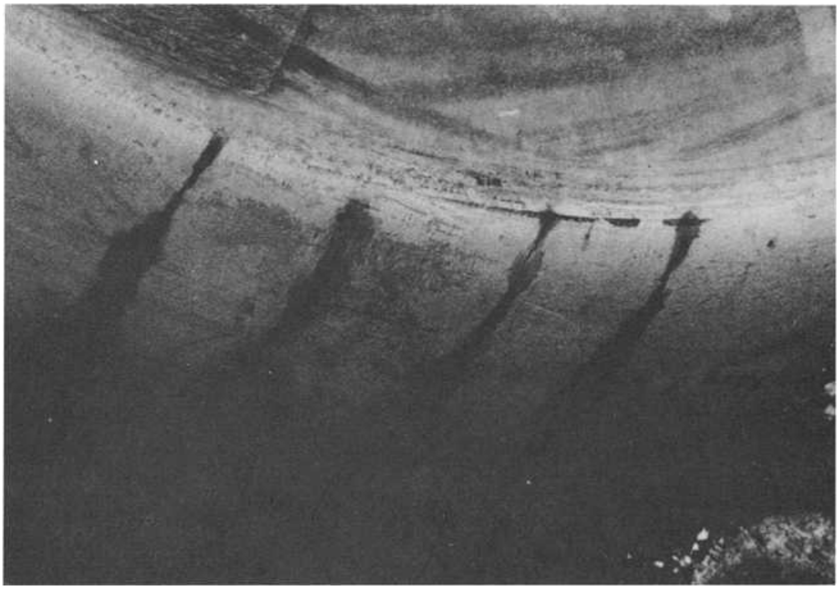

FIG. 16—*Forging ruptures due to oxygen contamination of preform surface.* (×0.5).

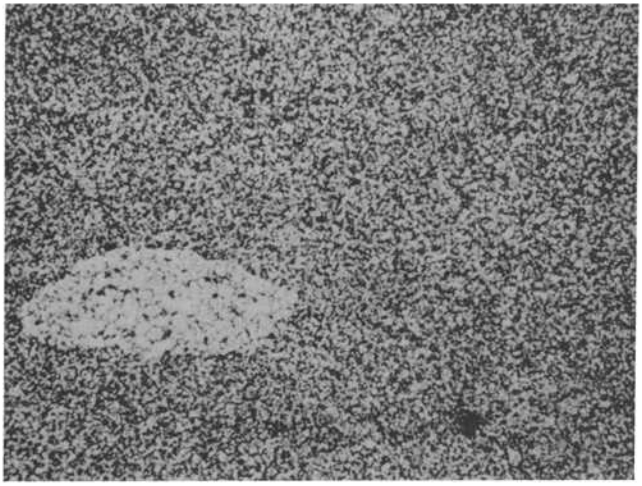

FIG. 17—*Electron microprobe analysis of Astroloy contamination in extruded IN100 billet (×100).*

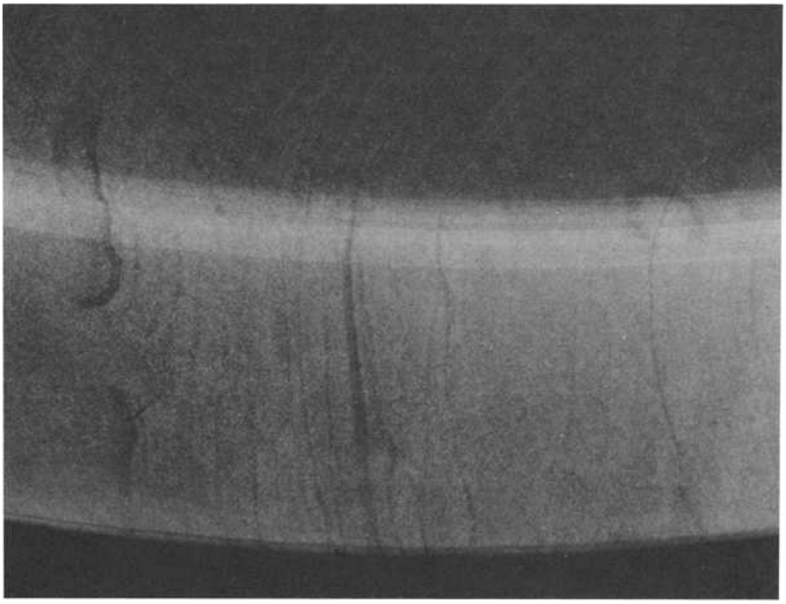

FIG. 18—*Powder particle size striations on HIP preform (P/M René 95) (×0.3).*

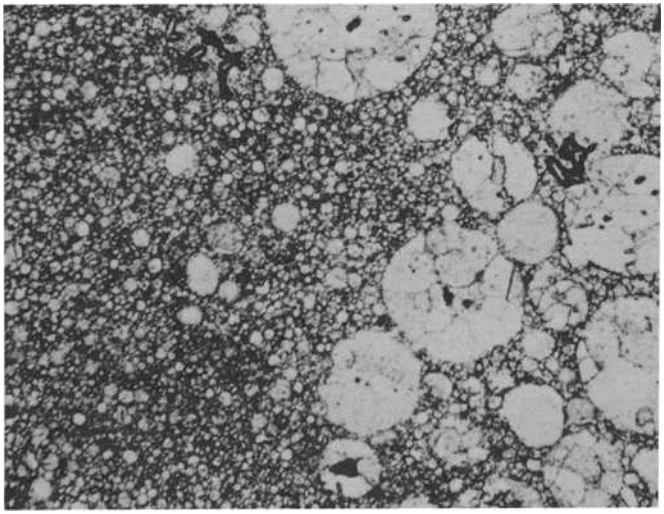

FIG. 19—*HIP René 95 powder particle separation during filling container (×100).*

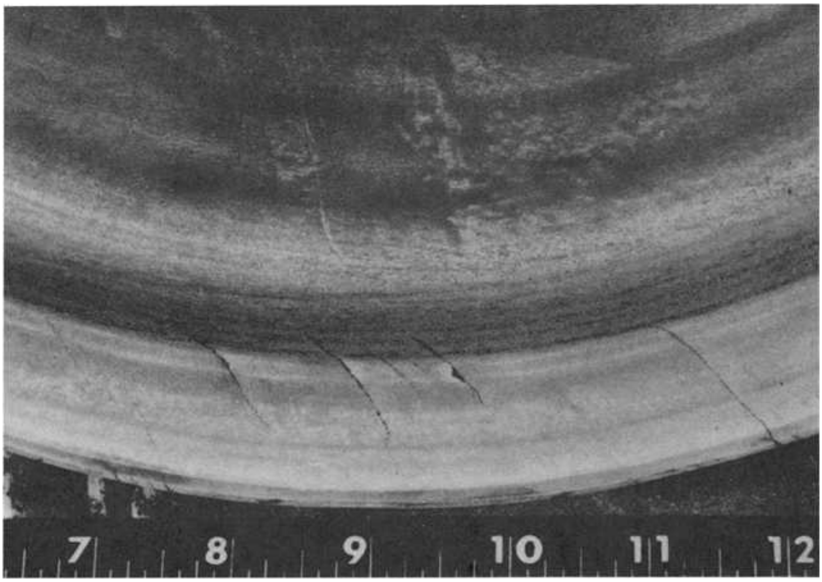

FIG. 20—*Ruptures formed during vacuum hot pressing due to powder particle size striations on HIP preform (P/M René 95) (×0.3).*

and fine powder particles. The uniformly mixed powder particles of different sizes reclassify themselves into layers due to mechanical vibration during filling of the HIP containers or repetitive shaking during subsequent transportation (Figs. 18 and 19). If sufficiently severe, the striated condition may cause localized rupturing during hot forming (Fig. 20). It is felt that hot forming is a type of built-in destructive test wherein parts containing severe microstructure nonuniformity will be readily identified and subject to rejection. Much progress has been made in producing quality high-temperature alloy powders, but there is still much work to be done. New P/M techniques combined with new forging techniques are needed to produce a better product.

A summary of material and processing characteristics indicates high quality assurance surveillance must be maintained from the raw material to the finished product. This approach would serve to avoid conditions that detract from performance and reliability.

Since most of these problems can be recognized through microstructural analysis, it is important to have a continuing program to exchange such microstructural information through a medium such as MiCon 78.

J. L. Bartos[1]

Review of Superalloy Powder Metallurgy Processing for Aircraft Gas Turbine Applications

REFERENCE: Bartos, J. L., "**Review of Superalloy Powder Metallurgy Processing for Aircraft Gas Turbine Applications,**" *MiCon 78: Optimization of Processing, Properties, and Service Performance Through Microstructural Control, ASTM STP 672,* Halle Abrams, G. N. Maniar, D. A. Nail, and H. D. Solomon, Eds., American Society for Testing and Materials, 1979, pp. 564–577.

ABSTRACT: Substantial increases in raw material and labor costs have provided the impetus for many diverse investigations aimed at reducing the manufacturing costs of aircraft gas turbine hardware. One of the most significant programs conducted at General Electric during the past decade involves application of powder metallurgy (P/M) processing technology to the fabrication of nickel-base superalloy rotating components. The evolution of P/M technology and its application to a high-strength superalloy, René 95, in a number of diverse aircraft engine components is described. Initial development concentrated on fabrication of P/M hardware by hot isostatic pressing (HIP) cylindrical powder preforms and forging in a conventional die system to an oversize shape. Subsequent refinement of this *HIP plus forge* process included HIP for shaped preforms followed by forging in an isothermal die system to a near net shape.

Emergence of a second P/M processing technology, designated *as-HIP,* in which the powder is simply HIP and heat treated, thus eliminating all secondary metalworking operations, is also reviewed. The technical advantages and constraints, along with the projected economic benefits of this new, highly promising P/M process, are analyzed and examples of its application to engine hardware presented. The future of P/M processing in the aircraft engine business, particularly as related to development of advanced superalloy materials, is also discussed.

KEY WORDS: steels, microstructure, nickel-base superalloy, powder metallurgy processing, hot isostatic pressing, cost reduction, isothermal forging

General Electric has had many years experience in the definition and fulfillment of goals for gas turbine materials. Achievement of these goals has occurred by either utilizing materials available in the marketplace or developing new alloys when the vendor offerings were not adequate. The demand for improved engine efficiency and thrust/weight ratio has

---

[1] Manager, Alloy Development, Aircraft Engine Group, General Electric Company, Cincinnati, Ohio 45215.

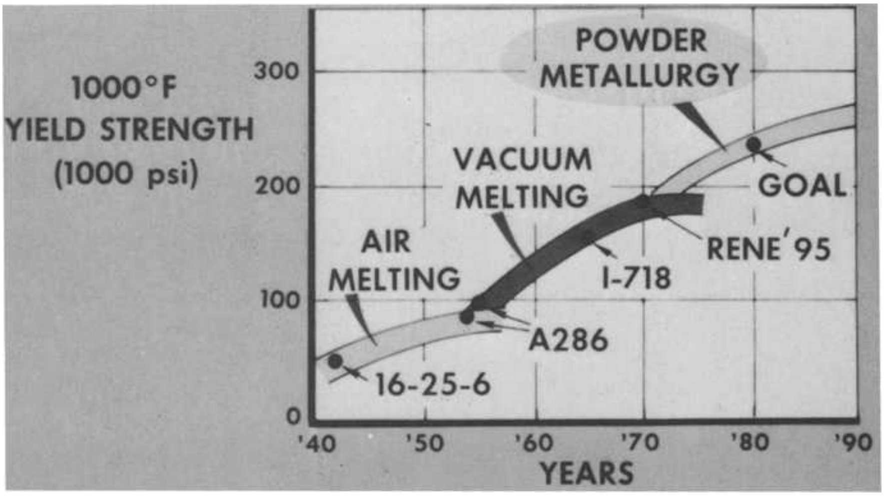

FIG. 1—*Progress in disk materials.*

resulted in a continuing development of higher strength alloys. Included in this group of alloys are aircraft engine rotor materials that have evolved from the high chromium steels and Timken alloys, through A286 and V57, René 41, Waspaloy, and up to the currently utilized Inconel 718, Astroloy, and René 95. A key to the development of higher strength alloys has been improvement in alloy processing technology. Figure 1 graphically depicts the strength benefits that accompanied new processing developments. The first gas turbine alloys were air melted, which placed a restriction on hardener content and thus on the strength level that could be attained. The advent of vacuum melting permitted significant increases in hardener content (principally gamma prime forming elements), leading to substantial improvements in mechanical properties. Table 1 illustrates the increase in hardener content and strength of turbine alloys from the early air melted compositions (A286) to the current high-strength vacuum melted superalloys.

René 95 Development

Of the wrought nickel-base superalloys used for aircraft turbine and compressor disks, shafts, rotating seals, and related parts, René 95 is by far the strongest of the commercially available alloys at temperatures up to 650°C (1200°F) as illustrated in Fig. 2. The alloy was developed in the late 1960's by General Electric under United States Air Force sponsorship [*1*].[2] To date, approximately 363 000 kg (800 000 lb) of double vacuum melted René 95 have been used by General Electric for application in various development and demonstrator engines.

---

[2] The italic numbers in brackets refer to the list of references appended to this paper.

TABLE 1—*Hardener content and strength of turbine alloys.*

Alloy	Hardener Content (Al+Ti+Cb), %	650°C (1200°F) 0.2% Yield Strength, MPa (ksi)
A286	2.4	689.4 (100)
V57	3.2	799.7 (116)
René 41	4.6	806.6 (117)
Inconel 718	6.7	930.7 (135)
Astroloy	7.5	930.7 (135)
René 95	9.5	1206.5 (175)

As would be expected, the exceptionally high strength of René 95 poses challenges to conventional methods of producing gas turbine hardware. The original René 95 alloy development was performed using double vacuum melting with vacuum arc remelting as the final step. Forging and heat treating procedures were developed to produce a unique microstructure, often referred to as the *necklace* structure. This structure consists of large (ASTM 3–7) warm worked grains surrounded by a necklace of fine (ASTM 8–12) recrystallized grains. Attainment of this microstructure is required in cast plus wrought René 95 to achieve the desired balance of strength and ductility in the alloy.

As a consequence of the extremely high strength of René 95, components made by conventional process technology are more expensive than similar parts produced from the weaker Inconel 718 alloy. The higher cost of conventional cast plus wrought René 95 components is a direct reflection of the large quantity of input material and the complex forging procedure required to fabricate engine parts. Figure 3, for instance,

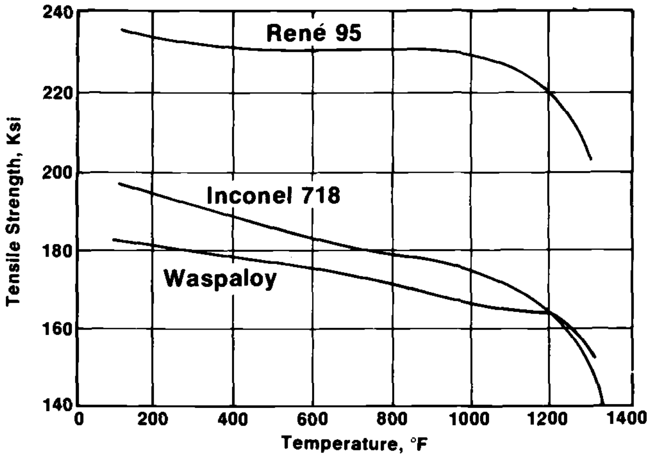

FIG. 2—*Tensile strength: René 95 versus other disk alloys.*

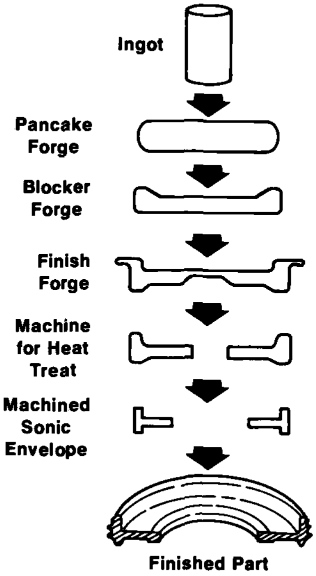

FIG. 3—*Typical processing sequence for cast and wrought René 95 disk; input/output weight ratio = 19:1.*

illustrates a typical example of the multiple forging steps, machining operations, and the rectilinear ultrasonic inspection envelope required to produce a compressor disk. Note that the finish part weight amounts to only about 5 percent of the input weight.

Powder Metallurgy Processing

The high cost of processing today's high-strength alloys such as René 95, coupled with the spiraling cost of raw materials, have shifted the emphasis trends in materials technology at General Electric. In the past 15 years, emphasis has transitioned from technologies to maximize high performance at minimun engine weight to concentrated efforts on cost improvement and increased reliability. This trend, illustrated in Fig. 4, is exemplified by developments since 1970 in René 95 technology.

The inherent forging difficulties encountered with conventional cast plus wrought René 95, along with the poor raw material conversion ratios (ratio of input to finished part weights) provided the impetus for initiation of cost reduction programs. The most significant breakthrough in reducing the costs of René 95 rotating parts was the development and application of advanced powder metallurgy (P/M) technology. The basic thrust of the P/M approach was aimed at decreasing the number of working operations and improving material utilization to ultimately reduce finish part costs.

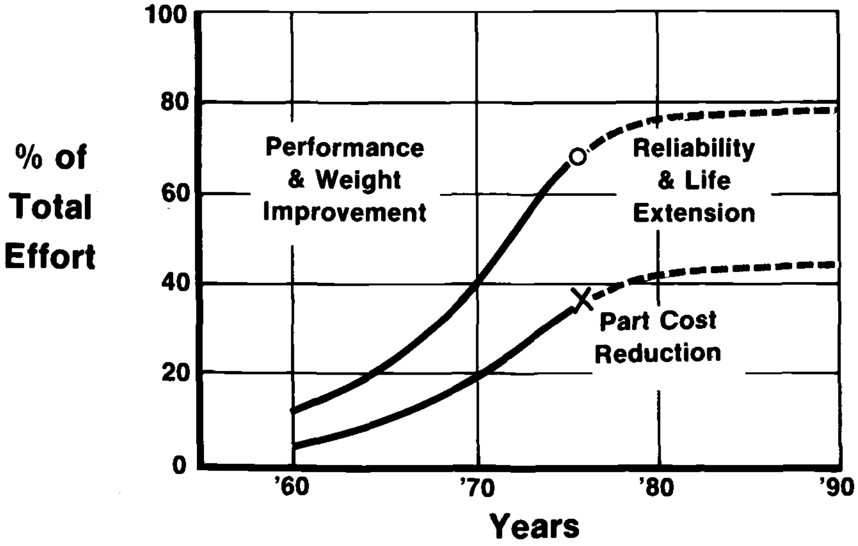

FIG. 4—*Material and process development trends.*

The René 95 composition shown in Table 2 is uniquely suited to P/M processing. A number of other commercially available superalloys have been processed utilizing P/M technology. However, in many cases an undesirable product resulted due to formation of a brittle carbide network on the surfaces of powder particles. This problem is avoided in René 95 [*2*] through the balance between carbon content, M_6C carbide formers (tungsten and molybdenum), and MC carbide formers (columbium and titanium). Suppression of this carbide network formation is considered a prerequisite for a viable P/M alloy.

The development of industrial capabilities to produce high purity superalloy powders by inert gas atomization and consolidate them to full

TABLE 2—*Chemical composition of P/M René 95.*

Element	Percent	Element	Percent
Carbon	0.04–0.09	Columbium	3.30–3.70
Manganese	0.15 max	Zirconium	0.03–0.07
Silicon	0.20 max	Titanium	2.30–2.70
Sulfur	0.015 max	Aluminum	3.30–3.70
Phosphorus	0.015 max	Boron	0.006–0.015
Chromium	12.00–14.00	Tungsten	3.30–3.70
Cobalt	7.00–9.00	Oxygen	0.015 max
Molybdenum	3.30–3.70	Nitrogen	0.005 max
Iron	0.50 max	Hydrogen	0.001 max
Tantalum	0.20 max	Nickel	remainder

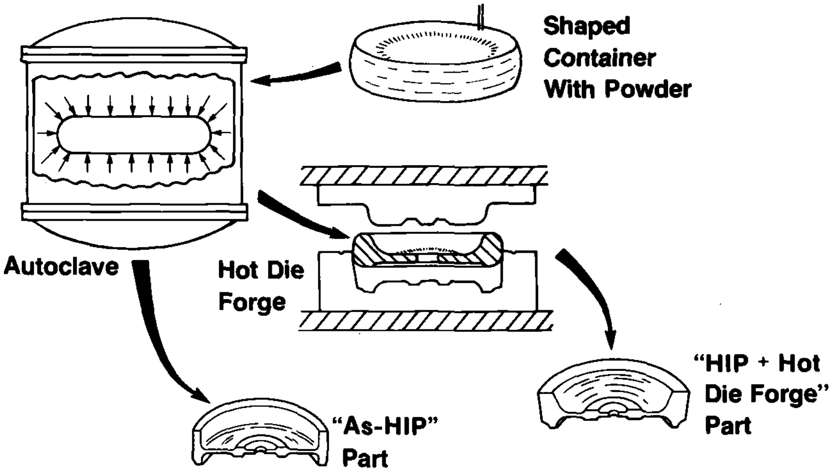

FIG. 5—*Powder metallurgy René 95 processing.*

density by hot isostatic pressing (HIP) provided the basis for initiation of P/M cost reduction programs at General Electric in 1971. Early efforts consisted of consolidating P/M preforms by HIP and applying conventional or *hot die* forging techniques to produce a HIP plus forge P/M product. More recent efforts have concentrated on development of the as-HIP P/M process, which completely eliminates all metalworking operations after HIP consolidation. A schematic description of the two processes is presented in Fig. 5.

HIP plus Forge P/M René 95

The first P/M René 95 components produced by General Electric were fabricated by forging a fully dense HIP preform on standard *cold* dies using techniques developed for conventional cast plus wrought parts [*3*]. The improved microstructural homogenity of the P/M preforms relative to conventional ingot product, as shown in Fig. 6, permitted a substantial reduction in the number of forging steps required to produce the desired forge shape. This advantage, combined with the configurational flexibility offered by P/M preforms, resulted in a higher strength, more uniform forging that could be produced at somewhat lower cost than the cast plus wrought product. The success of the HIP plus cold die forge process, exemplified by the turbine disks shown in Fig. 7, led to accumulation of considerable engine test time and the first production engine commitments for P/M hardware at General Electric.

The outstanding accomplishments of the P/M René 95 HIP plus cold die forge development programs, coupled with rapidly rising raw material costs, led to refinement and further cost reduction efforts. The develop-

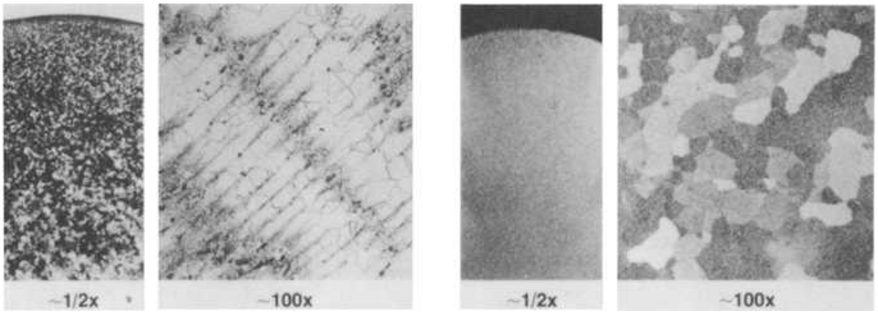

FIG. 6—*René 95 homogeneity; fusion metallurgy* (left) *versus powder metallurgy* (right).

ment of hot die forging capabilities at Wyman Gordon Company and Ladish Company [*4*] permitted further improvements in material utilization ratios by minimizing the surface chilling effect inherent in the conventional cold die system. This innovation allowed a reduction in the protective material envelope around the forging, thus reducing input material requirements significantly. In addition, advances in shaped P/M preform technology eliminated large quantities of unnecessary input material. These improvements are graphically illustrated in Fig. 8 on a typical engine disk component produced by cold and hot die techniques. A typical HIP plus hot die forged component, shown in Fig. 9, depicts the configurational detailing and minimization of forging flash material waste possible with the process. Studies to further reduce preform input weights and forging envelope thickness are continuing in an effort to extract the maximum cost reduction from the HIP plus hot die forge process.

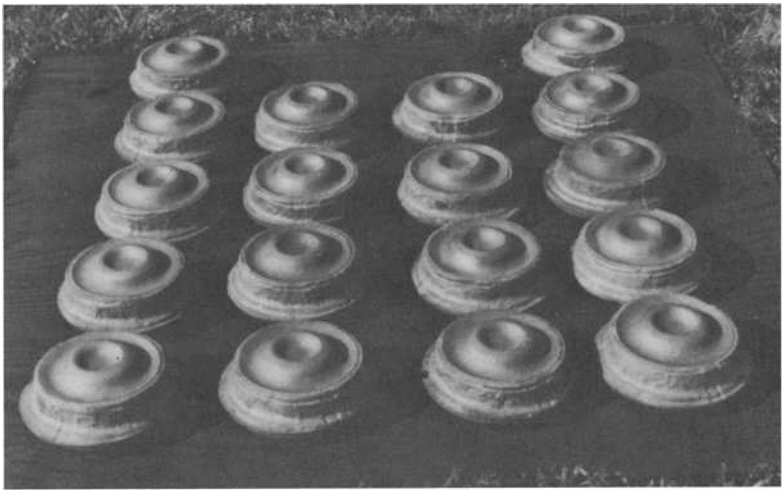

FIG. 7—*HIP and cold die forged P/M René 95 disk components.*

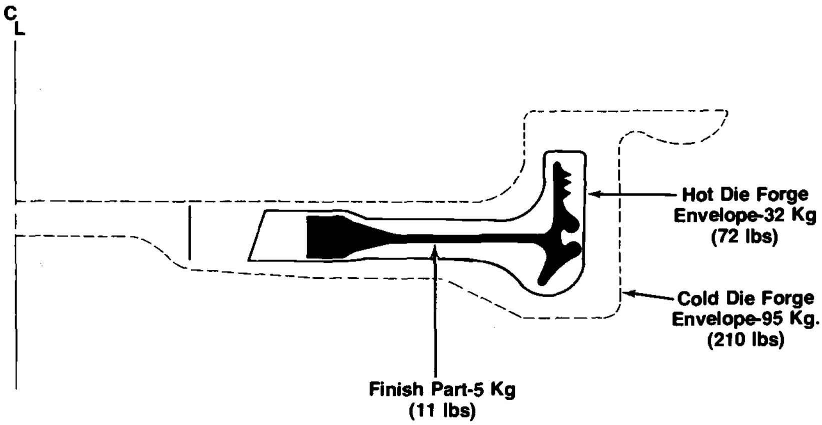

FIG. 8—*Forging envelopes for typical disk component.*

As-HIP P/M René 95

Development of the P/M forging preform technology, including the ability to fabricate components to 100 percent density, paved the way for further cost reductions from P/M processing. Initial studies of P/M preforms indicated that mechanical properties competitive with those achieved in forged products could be attained in HIP plus heat treated (as-HIP) René 95 components. Elimination of the forging operation in the P/M René 95 manufacturing process was projected to provide a substantial cost reduction relative to the HIP plus forge process. As an example, the cost reduction potential of a selected group of René 95 parts [5] is

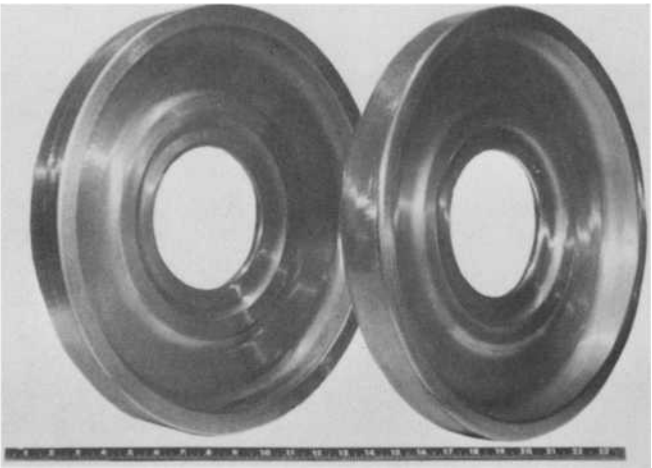

FIG. 9—*Hot die forged P/M René 95 disk component.*

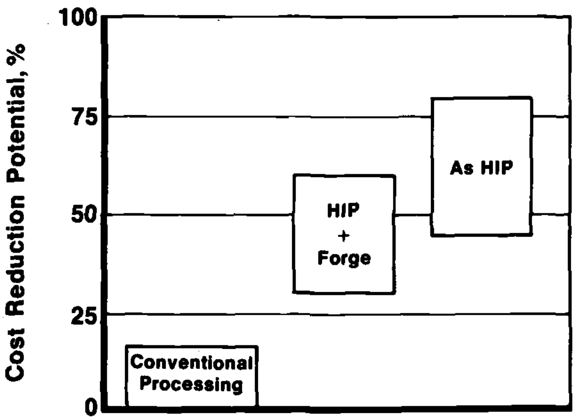

FIG. 10—*Cost reduction potential for a selected group of René 95 parts.*

shown in Fig. 10. Additional cost reductions of up to 50 percent are forecast through substitution of as-HIP processing for HIP plus forge techniques.

This discovery led to initiation of a development program at General Electric in 1973 to define processing parameters required to produce the desired mechanical property levels in as-HIP material. Basic HIP and heat treat parameters were developed [6] and the first as-HIP René 95 hardware, as shown in Fig. 11, was produced in 1975. Following extensive mechanical property evaluation, component testing, and actual engine testing, the process was accepted for production of rotating engine hardware in 1977.

One of the unique features of the as-HIP process is the mechanical property flexibility relative to conventional forged or rolled René 95 products. Strength levels in wrought products produced from either cast ingot or powder preforms are dictated primarily by the thickness of the component, that is, strength decreases as section thickness increases. Very little flexibility is possible, since it is difficult to control the amount of warm work retained in complex shaped forgings. On the other hand, properties in as-HIP products are determined primarily by the heat treatment parameters, with cooling rate from the second phase (γ') solvus being most influential. By altering this cooling rate in different section thicknesses using various quench media, a wide variety of strength levels can be achieved. This is illustrated in Fig. 12, which depicts experimentally determined cooling rates attained in various section size parts as a function of quench media. Resultant properties are dictated by the cooling rates. Thus, strength levels can be specified, within limits, in as-HIP components merely by selecting the proper quench medium.

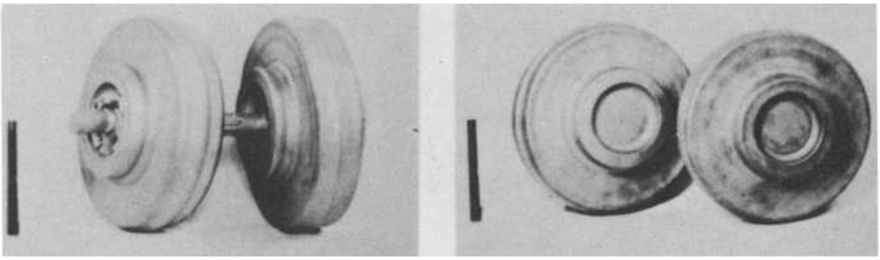

FIG. 11—*As-HIP René 95 disk components.*

Further development of the shape-making technology required to fabricate complex, near net shape engine parts is continuing in an effort to provide additional cost reduction potential to the as-HIP process. The most striking examples of the raw materials and cost reduction capability of the as-HIP process are associated with the manufacture of complex engine shaft components. A typical shaft processing sequence comparing the conventional cast plus wrought and as-HIP technologies is presented in Fig. 13. The configurational flexibility of P/M processing permits an input material savings of approximately 156 kg (approximately 350 lb). The savings, combined with the elimination of many fabrication steps, is projected to produce an 80 percent cost reduction over conventional fabrication methods. An excellent example of the near net shape capability to produce complex shaft components is shown in Fig. 14. These full-scale parts were produced by Crucible Materials Research Center for General Electric. Mechanical properties of shafts processed by both

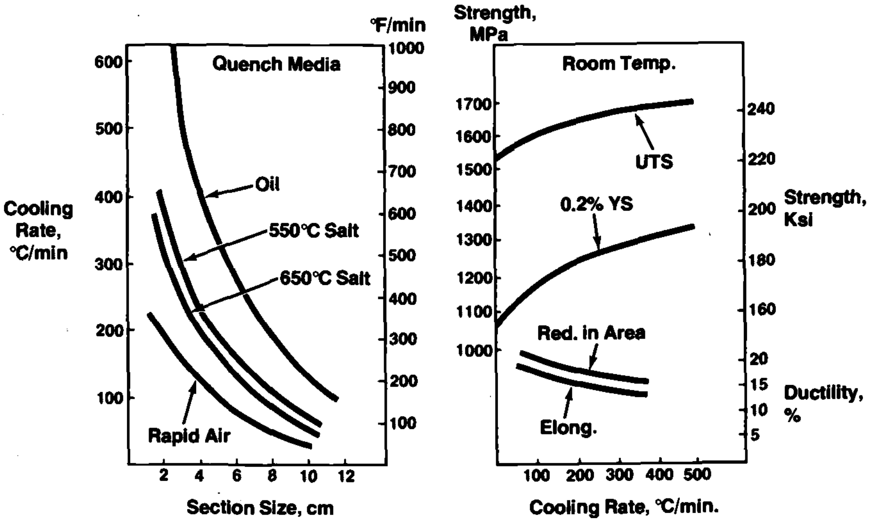

FIG. 12—*Heat treatment flexibility of as-HIP process.*

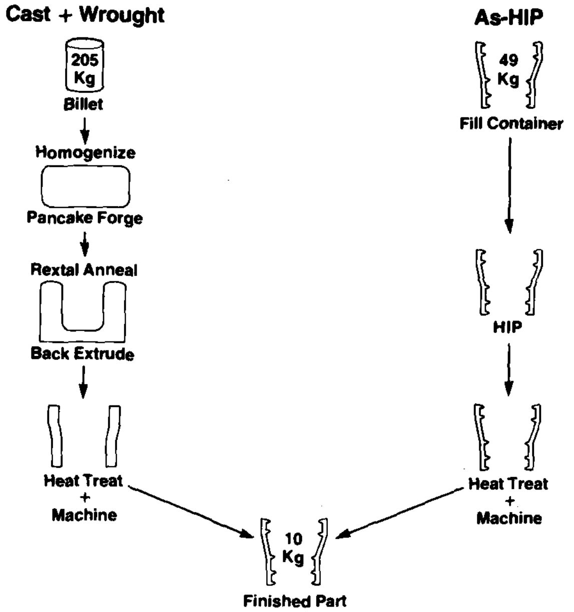

FIG. 13—*Fabrication processes for typical shaft component.*

as-HIP and conventional cast plus forging methods, presented in Fig. 15, indicate the fully comparable or superior strength levels obtained in the as-HIP product.

Powder Metallurgy Concerns

The spectacular progress achieved in P/M technology during the past ten years has also uncovered a number of potential problem areas that could have a detrimental effect on future applications in the aircraft gas turbine industry. A prime concern in all P/M products, especially when highly stressed components are involved, is the size and frequency of defects present due to powder production and handling techniques. In inert gas atomized powders, these defects are characterized into two broad categories: porosity and foreign particles.

Porosity is formed in P/M products as a result of entrapped argon gas. Argon may be entrapped between particles or inside hollow particles. Since the gas is inert, subsequent heating causes bubbles to form, producing pores up to 50 μm (0.002 in.) in diameter. Foreign particles included in the compacted P/M product are primarily nonmetallic oxides originating from either the atomization process or subsequent handling. These oxides, identified using several inspection techniques, are generally very small (less than 250 μm (0.01 in.) diameter). The potential degrading

FIG. 14—*Near net shape as-HIP René 95 shaft component.*

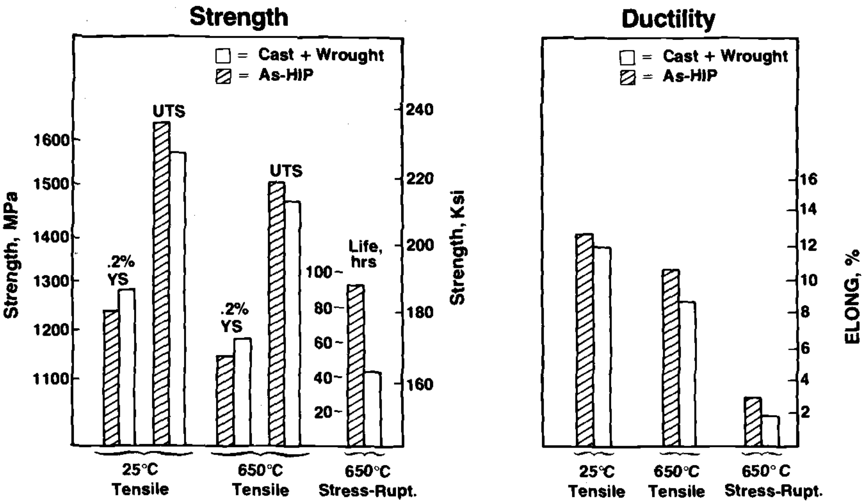

FIG. 15—*Mechanical properties of typical shaft component.*

effect of these defects on mechanical properties of critical rotating hardware is a source of continuing concern in the aircraft engine industry.

Achievement of substantial raw materials and cost savings in P/M parts is dependent to a large extent on the production of near net shape components. Information on the reliability, reproducibility, and product yields associated with processes capable of making complex shapes is just now being accumulated. Results in this area must be positive to justify continued investment in P/M technology.

Powder products present new quality control challenges that must be successfully met and solved. Inspection of complex, contoured near net shape parts must be completed economically, reliably, and at higher sensitivity levels than heretofore attempted in production environments. Advances in ultrasonic inspection and surface inspection techniques are required to assure even higher quality levels in P/M components than currently attained in conventional cast plus wrought parts.

Substantial efforts in all the aforementioned problem areas are underway, with significant progress already accomplished. Through the combined efforts of powder producers and users, these and future undefined technical problems must be solved before high-strength P/M components can be applied with the same confidence associated with conventional cast plus wrought products.

Future Applications

The significant technical difficulties associated with processing highly alloyed nickel-base superalloy compositions by conventional cast plus wrought techniques essentially dictates the application of P/M technology to future advanced aircraft engine alloys. This fact is exemplified by the development of AF115 [7], an advanced P/M disk alloy designed to operate at temperatures up to 760°C (1400°F).

AF115 was developed by General Electric under Air Force sponsorship to take advantage of the compositional freedoms afforded by P/M processing. The alloy chemistry was designed to avoid the carbide segregation problem inherent in other superalloys such as IN100. Although HIP and heat treatment parameters do not resemble those specified for as-HIP René 95, AF115 will benefit from the powder processing and near net shape advances of the past ten years.

Beyond alloys such as AF115 lie a myriad of new developments fostered by the compositional and configurational flexibility of P/M processing. The achievement of unique mechanical property levels in specified component locations appears feasible through the use of two or more powder compositions or the application of different processing techniques in each area. Blending of powders or mixing with selected forms of other alloys to make *composite* P/M parts provides an opportunity to develop unique mechanical properties beyond the capability of homogeneous materials.

Concluding Remarks

The past ten years have witnessed the evolution of powder metallurgy processing from a technology suitable for making small, simple, low-strength, sintered parts to a point where large, complex, ultra-high-strength critical rotating aircraft engine hardware can be produced with mechanical properties equivalent to those of conventional forged components. Emergence of the HIP plus hot die forging process, followed by development of the as-HIP process in the last four years have presented new opportunities for substantial raw material and component cost reductions. The future of P/M technology in the gas turbine industry is limited only by currently unresolved concerns over quality and cost. Based on the progress made to date, there is every indication that the industries involved will overcome all remaining technical challenges and bring superalloy P/M processing to full production status.

References

[1] Wukusick, C. S. and Smashey, R. W., "Ultra High Strength Superalloys," Technical Report AFML-TR-68-214, Air Force Materials Laboratory, Dayton, Ohio, 1968.

[2] Allen, R. E., Bartos, J. L., and Aldred, P., U.S. Patent Number 3,890,816, 24 June 1975.

[3] Bartos, J. L., Allen, R. E., Moll, J. H., Thompson, V. R., and Morris, C. A., "Development of Hot Isostatically Pressed and Forged Powder Metallurgy René 95 for Turbine Disk Application," SAE paper 740862 presented at National Aerospace Engineering and Manufacturing Meeting, San Diego, Calif., Oct. 1974.

[4] Deridder, A. J., Hayes, A. F., Koch, R. W., and Radovich, J. F., "Deformation Processing of Superalloy Hot Isostatic Press Preforms," paper presented at 106th AIME Annual Meeting, American Institute of Mining, Metallurgical, and Petroleum Engineers, Atlanta, Ga., March 1977.

[5] Arnold, D. B., "René 95 Powder Metallurgy Opportunities for Gas Turbine Applications," AGARD Conference Proceedings No. 200 on Advanced Fabrication Techniques in Powder Metallurgy and Their Economic Implications, Hanford House, London, 1976.

[6] Bartos, J. L. and Mathur, P. S., "Development of Hot Isostatically Pressed (As-HIP) Powder Metallurgy René 95 Turbine Hardware," *Superalloys: Metallurgy and Manufacture, Proceedings,* Third International Symposium, B. H. Kear, D. R. Muzyka, J. K. Tien, and S. T. Wlodek, Eds., Claitor, Baton Rouge, 1976, pp. 495–509.

[7] Bartos, J. L., "Development of a Very High Strength Disk Alloy for 1400°F Service," Technical Report AFML-TR-74-187, Air Force Materials Laboratory, Dayton, Ohio, 1974.

J. M. Larson[1] *and L. F. Jenkins*[1]

Application of Superalloys in Internal Combustion Engine Exhaust Valves

REFERENCE: Larson, J. M. and Jenkins, L. F., "**Application of Superalloys in Internal Combustion Engine Exhaust Valves,**" *MiCon 78: Optimization of Processing, Properties, and Service Performance Through Microstructural Control, ASTM STP 672*, Halle Abrams, G. N. Maniar, D. A. Nail, and H. D. Solomon, Eds., American Society for Testing and Materials, 1979, pp. 578–600.

ABSTRACT: The high-temperature and pressure conditions in some spark-ignited and heavy-duty diesel engines have necessitated the application of superalloy exhaust valve materials to meet long-term durability requirements. This penetration of superalloys is because of their excellent tensile, creep, and fatigue strengths, in combination with adequate oxidation resistance and forgeability. These attributes of the superalloys are discussed in conjunction with problems associated with manufacturing and alloy limitations. A strong emphasis is placed on field requirements versus material capabilities.

KEY WORDS: steels, microstructure, valves, poppets, engines, superalloys

There is significant usage of nickel- and cobalt-base superalloys as internal combustion engine exhaust valves. Their use has become widespread over the past decade as a result of increasing demands made on valves through steadily increasing stress levels or operating temperatures or both. Changes in fuels and lubricants have also created the need for improved corrosion resistance in many applications.

This paper will describe the application of superalloys in representative cases, indicating the performance needs that the superalloys have satisfied. While most of these alloys were originally adapted from other applications such as the aerospace industry, their chemical makeup, heat treatments, and subsequent microstructural requirements have usually been modified to meet manufacturing and service needs of specific valve application requirements.

---

[1] Chief engineer, Materials and Basic Processes, and chief engineer, Valve Gear Products, respectively, Eaton Corporation, Engine Components Div., Battle Creek, Mich. 49016.

Background

Types of Engines

There are two basic types of reciprocating engines that use poppet type exhaust valves.

1. Spark-ignited engines in which the fuel-air mixture is ignited in the combustion chamber by an electrical spark. This type of engine burns a wide variety of fuels, such as gasoline, propane, alcohols, and methane.
2. Compression-ignition (diesel) engines that operate on several different types of fuel oils that, when injected into compressed air, ignite spontaneously. One category of this type of engine provides for direct fuel-injection into the combustion chamber while a second category features injection into a precombustion chamber where combustion is started and subsequently propagates into the main chamber.

The exposure of exhaust valves to combustion gas temperatures and pressures, and under some circumstances dynamic loading conditions, can vary significantly from one engine type to another. The fuels and lubricants contain several residual elements as well as additives that are introduced into the engine exhaust valve environment. These varying conditions determine the material from which the valve must be manufactured.

Description of Exhaust Valves

The poppet type exhaust valves used in most reciprocating engines can be divided into three sections; the head, stem, and stem tip (illustrated in Fig. 1). Exhaust valves usually have a composite structure consisting of two or more materials. The head and a portion of the stem leading from the head consists of a high-temperature, high-strength, and corrosion-resistant alloy such as an austenitic stainless steel or a superalloy listed in Table 1. The sealing surface of the valve seat often consists of a weld overlay material such as the cobalt-base, high-temperature alloy, Stellite #6, also listed in Table 1. The remainder of the stem including the valve tip often consists of a hardenable martensitic steel welded to the high-temperature heat-resistant alloy of the head end of the valve. The portion of the valve of primary interest in this paper is the valve head end.

Metallurgical Characteristics of High-Temperature Valve Head Materials

Historically and in principle, nickel-base superalloys have been used for exhaust valve applications only when the less expensive iron-base stainless valve steel would not provide sufficient high-temperature strength or corrosion resistance or both, for a given application. The even more costly cobalt-base alloys, such as Stellite #6, were resorted to only

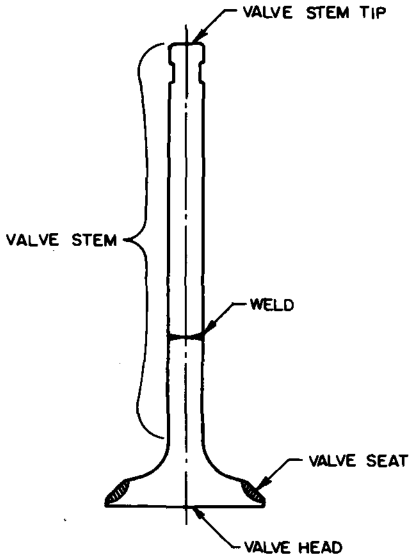

FIG. 1—*Sketch of a seat faced exhaust valve from a four-cycle spark-ignited engine.*

when no other available material would provide adequate corrosion resistance and fatigue strength in the head section and the required corrosion resistance or hot hardness, or both, on valve seating surfaces. The iron- and nickel-base alloys derive their high-temperature corrosion resistance primarily from the presence of substantial amounts of chromium in the alloy matrix. The chromium, when present in effective amounts for preventing corrosion, forms an impermeable adherent film of chromium oxide on the alloy surface resisting further corrosive attack.

The austenitic iron- and nickel-base alloys achieve their high-temperature mechanical properties by mechanisms such as: precipitation hardening, solid solution strengthening of the alloy matrix, and carbide/carbonitride precipitation strengthening of grain boundaries. The desired properties of both types of alloys are developed by similar heat-treatment sequences usually involving solution treatment to dissolve strengthening constituents, followed by aging heat treatments to precipitate phases in morphologies and distributions that will produce the desired mechanical properties. To a limited extent, the properties of both types of alloys can be optimized for a given application by modifications in the heat treatments.

The superior high-temperature strength of nickel-base superalloys is primarily attributable to the characteristics of the precipitation hardening mechanism that these alloys exhibit. Namely, it is the precipitation of a very finely dispersed stable and ordered intermetallic phase, Ni_3

TABLE 1—*Nominal compositions of typical alloys used in the manufacture of exhaust valves for reciprocating engines.*

Alloy Type	Alloy Designation	C	Mn	P	S	Si	Cr	Ni	N	Co	Al	Ti	Fe	Nb and Ta	W	Mo
Iron base	Silchrome 10[a]	0.38	1.0	. . .	0.030	3.0	9.0	8.0	. . .	. . .	. . .	. . .	balance	. . .	. . .	. . .
	21-2N[a]	0.55	8.3	0.05	0.07	0.15	21.0	2.2	0.30	. . .	. . .	. . .	balance	. . .	. . .	. . .
	21-4N[a]	0.53	9.0	0.03	0.07	0.15	21.0	3.75	0.42	. . .	. . .	. . .	balance	. . .	. . .	. . .
	21-21N[a]	0.20	1.3	0.03	0.03	1.0	21.0	11.5	0.20	. . .	. . .	. . .	balance	. . .	. . .	. . .
	N-155[a]	0.10	1.5	0.03	0.03	0.50	21.3	20.0	0.15	20.0	. . .	. . .	balance	1.0	2.5	3.0
	VMS-513[b]	0.08	11.0	. . .	. . .	0.06	27.0	39.0	. . .	. . .	1.0	2.5	balance	. . .	. . .	. . .
	EMS-235[a]	0.33	2.1	0.040	0.030	0.75	23.0	8.0	0.34	. . .	. . .	. . .	balance	. . .	. . .	. . .
Nickel base	Inconel 751[a]	0.05	0.060	. . .	0.015	0.30	15.0	balance	. . .	0.7	0.70	2.5	7.0	1.0	. . .	. . .
	Nimonic 80A[a]	0.05	1.0	. . .	. . .	0.60	20.0	balance	. . .	2.0	1.2	2.5	5.0	. . .	. . .	. . .
	Pyromet 31[d]	0.04	0.20	0.015	0.015	0.2	22.7	55.5	. . .	. . .	1.3	2.3	balance	0.85Nb	0.005B	2.0
	Inconel 671[e]	2.04	. . .	. . .	. . .	. . .	60.16	37.8	. . .	. . .	. . .	. . .	. . .	. . .	. . .	. . .
Cobalt base	Stellite 6[c]	1.2	0.5	. . .	. . .	1.1	28.0	3.00	. . .	balance	. . .	. . .	3.0	. . .	4.5	1.0
(valve seat hard facing)	CoCrAlY[f]	. . .	. . .	. . .	. . .	. . .	28.7	. . .	. . .	balance	6.30		(also 0.90Y)		. . .	. . .

---

[a] SAE Information Report, Engine Poppet Valve Materials, SAE J775a.

[b] Nehrenberg, A. E. et al, *Metals Progress*, Nov. 1974, pp. 67–70.

[c] Eaton Corporation material specification—tradename of Cabot Corp.

[d] Carpenter Technology data.

[e] Inco Data.

[f] Pratt and Whitney data.

(Al,Ti;Nb) commonly referred to as gamma prime [*1–3*][2] in a tough oxidation-resistant matrix composed mostly of nickel and chromium. The typical microstructural appearance of the gamma prime phase and the grain boundary strengthening carbides in nickel-base superalloys used as valve materials is illustrated in Fig. 2*a*. In contrast, the austenitic iron-base valve steels are strengthened by the precipitation of carbides and carbonitride phases in the matrix and at grain boundaries as shown in Fig. 2*b*. These precipitates are not as stable at high temperatures as the precipitates that provide the strengthening in the nickel-base alloys. The details of the precipitation strengthening mechanisms in austenitic alloys have been studied and reported elsewhere and will not be discussed here [*4*].

Description of Exhaust Valve Design Parameters

Operating Temperatures

The operating temperature profile of the exhaust valve is dependent upon the type of engine. Figure 3 shows typical temperature profiles observed for exhaust valves in spark-ignition and compression-ignition engines. The absolute operating temperature levels are dependent upon numerous engine operating parameters. However, the spark-ignition engine exhaust valves generally experience higher operating temperatures, in particular along the valve stem below the valve head. The high exhaust valve stem temperature experienced in spark-ignition engines is the result of its inherently higher exhaust gas temperatures.

Imposed Stress Level

The mechanical and thermal stresses imposed on the valve are also dependent upon the engine type. The following is a description of the most significant sources of applied stress during engine operation and the observed typical failure modes when the valve material selected lacks sufficient strength to withstand the stresses applied under the operating conditions.

Radial Tensile Stresses—Radial tensile stresses are developed in the fillet of the valve as the result of the combustion pressure acting on the top surface of the head. Figure 4 represents a typical stress distribution in the fillet of a direct fuel-injection diesel engine exhaust valve. This high stress level and the characteristic rapid pressure rise in this type of a diesel engine, can result in a chordal fatigue failure (Fig. 5) nucleating in the fillet at the location of maximum tensile stress.

The exhaust valves in precombustion chamber diesel and spark-ignited

---

[2] The italic numbers in brackets refer to the list of references appended to this paper.

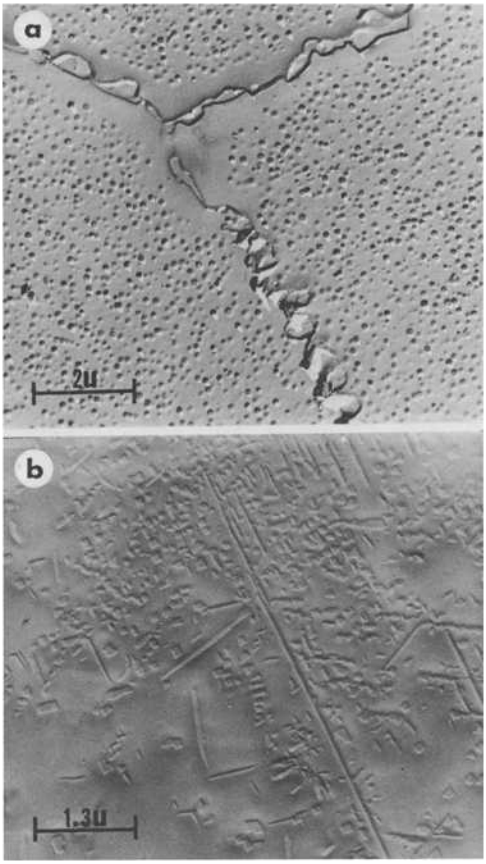

FIG. 2—(a) *Microstructure of typical nickel-base superalloy, Inconel Alloy 751, used for exhaust valve applications. Gamma prime particles are dispersed in the matrix and* $M_{23}C_6$ *outlines grain boundaries.* (b) *Microstructure of typical iron-base alloy, Alloy 21-4N, used for exhaust valve applications. Needle shaped particles are* $M_{23}C_6$ *and* M_xN.

engines experience similar stress distributions in the fillet, however, the magnitudes of the fillet stresses are usually significantly lower than in the exhaust valves of direct fuel-injection diesel engines. In addition, the rate of combustion chamber pressure rise is more moderate and accordingly, when valve failures do occur in these engines, they are often the result of creep deformation of the valve head as shown in Fig. 6. Note the upper valve has been virtually creep deformed into the exhaust port.

Longitudinal Tensile Stresses—Longitudinal tensile stresses, which are usually maximum at the junction of the head and stem of the valve, are the result of the valve seating event. Under normal operating conditions, these stress levels are very low regardless of the engine type. If, for any reason, the seating velocities significantly exceed the design level,

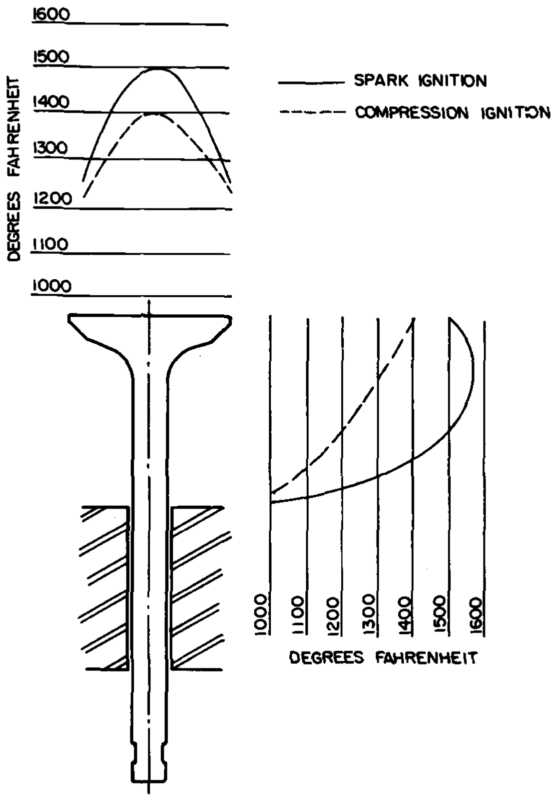

FIG. 3—*Typical temperature profiles of exhaust valves under normal operating conditions.*

breakage would be expected at the junction of the head and stem as shown in Fig. 7. Figure 8 shows a typical view of the fatigue fracture revealing the point of crack initiation and subsequent propagation.

Tangential Tensile Stresses—Tangential tensile stresses at the outer rim and seat of the valve are produced by a thermal gradient that normally exists between the center and the periphery of the valve head. These stresses are produced by differential thermal expansion between the hot center of the valve head and the cooler outer rim and valve seat face. These stresses, in conjunction with the mechanical stresses from engine operation, can initiate radial cracking at the valve seat or outer rim of the valve head. Figure 9 shows a typical example of this type of failure.

Corrosive Environment

Exhaust valves run in a number of different chemical environments depending on the makeup of the fuels and lubricants used in the engine.

Alloys must be selected so as to resist oxidation or corrosion, or both, in the specific environments of the various types of engines. Lack of adequate corrosion resistance can result in:

(*a*) pitting, intergranular attack, and excessive material loss on engine valves. The pitting and intergranular attack can initiate a crack in the exhaust valve seat (Fig. 10). Excessive material loss in the valve fillet or combustion chamber surface of the heat will ultimately result in fatigue failures (See Figs. 11 and 12). These corrosion problems have been related to the presence of lead oxides (PbO) and their interaction with surface oxides.

(*b*) stress corrosion cracking (Fig. 13) in austenitic valve steels. In spark-ignited engines, it has been associated with acidic condensates containing bromine or chlorine or both. In the case of diesel

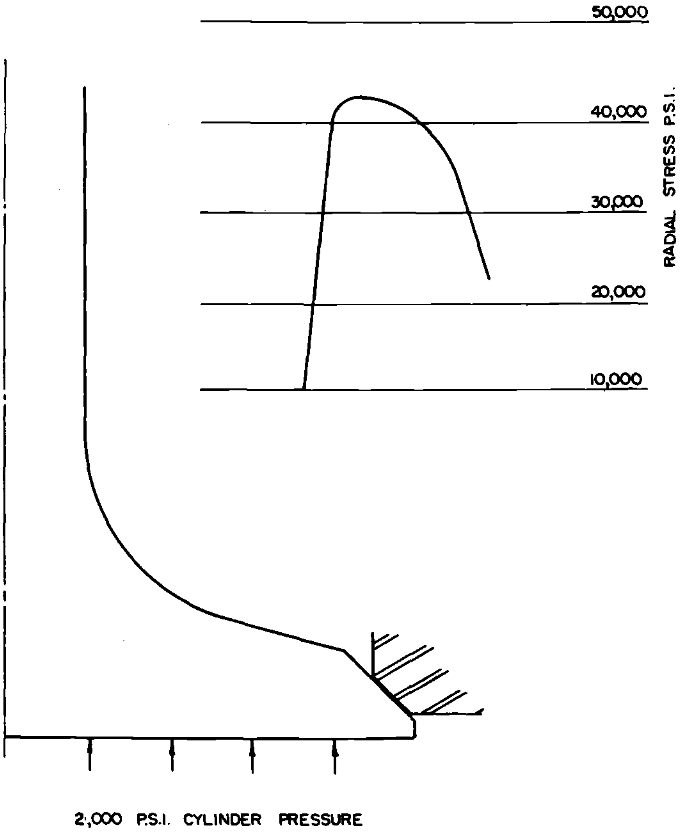

FIG. 4—*Typical stress distribution in exhaust valve fillet of a direct fuel-injection diesel engine.*

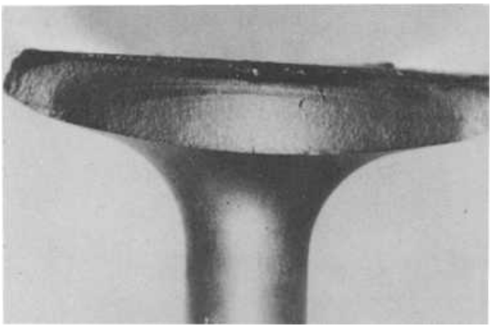

FIG. 5—*Typical chordal fatigue failure of engine valve. Note initiation occurs in fillet and propagates to top surface of valve head.*

engines, the corrodant is an acidic solution (pH 2–3) containing sulfur and carbonate compounds [*5*].

(*c*) corrosion attack of the seat face (Fig. 14) preventing proper valve seating related to lead ozide, sulfidation, or V_2O_5 corrosion. This type of attack ultimately results in a path for hot gases to literally erode away the base material commonly denoted as *guttering*.

Valve Seat Face to Cylinder Seat Interfaces

Attention must be given to the seating surface of the exhaust valve. Any significant deterioration of this surface will prevent proper sealing and will lead to loss of compression. The importance of corrosion resistance has

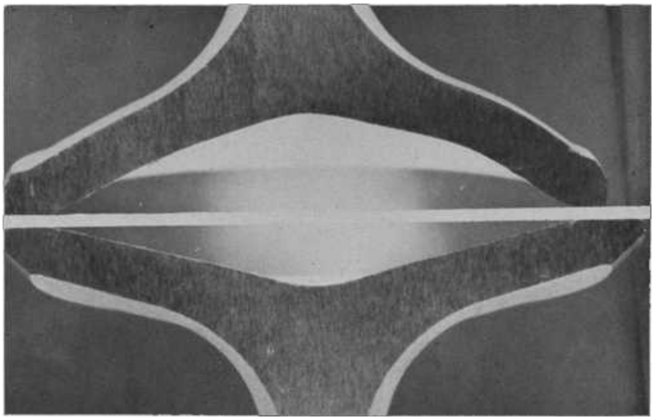

FIG. 6—*Comparison of valve head profiles showing the amount of deformation resulting from creep under combustion chamber pressure.*

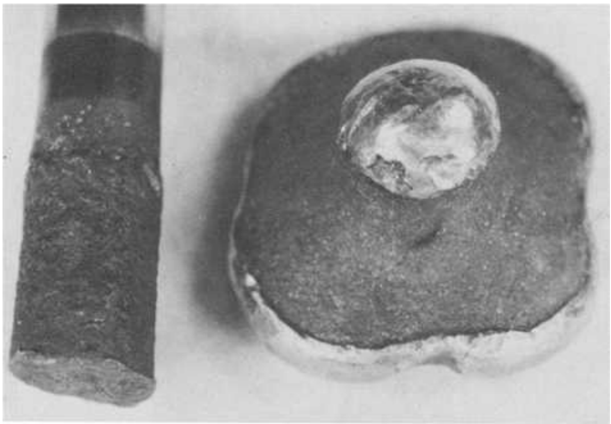

FIG. 7—*Typical fatigue failure at head-stem junction caused by excessive seating velocity.*

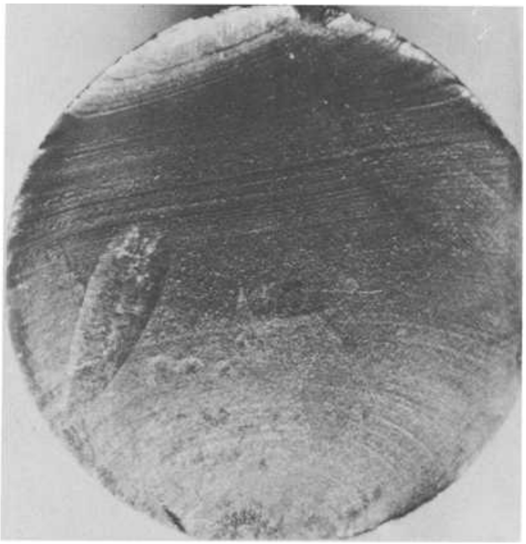

FIG. 8—*Fatigue fracture surface at valve head-stem junction. Note fatigue striations eminating from fatigue fracture initiation site at 6 o'clock position.*

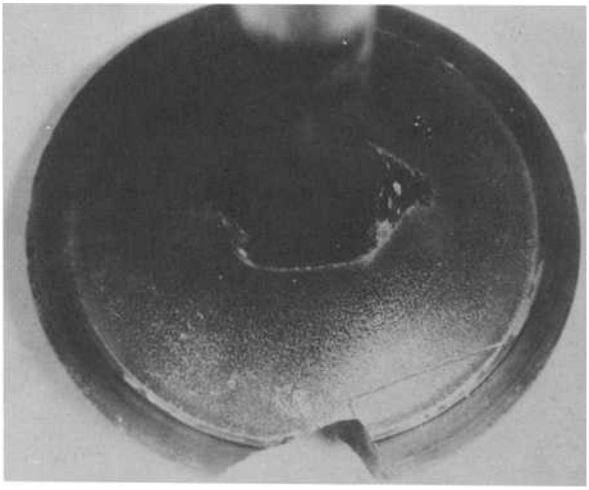

FIG. 9—*Typical view of radial cracking of exhaust valve seat and rim.*

FIG. 10—*Radial crack in the seat of an exhaust valve. Radial cracks can lead to catastrophic valve failure by* guttering *of the valve seat or by fracture of the valve head.*

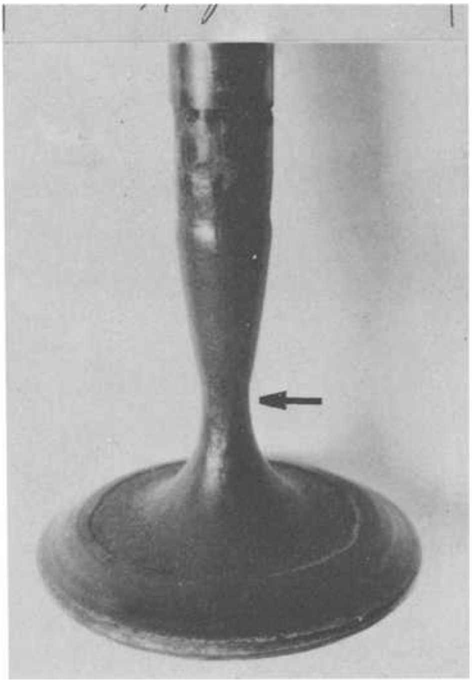

FIG. 11—*An exhaust valve from a four-cycle spark-ignited engine that exhibits severe PbO corrosion and metal loss at head-stem junction (arrow).*

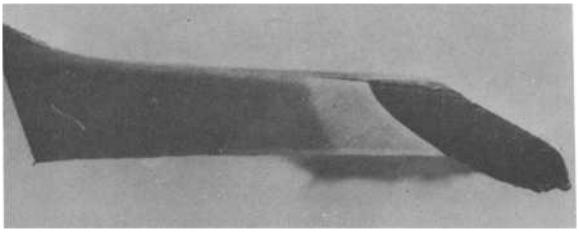

FIG. 12—*Radial cross section of valve head exhibiting excessive loss of material due to PbO corrosion on portion of the valve that faces combustion chamber.*

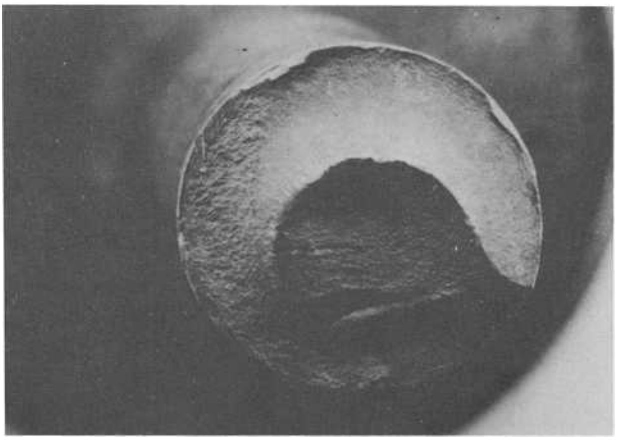

FIG. 13—*Stress corrosion cracking of valve stem of Type 21-4N stainless steel.*

already been mentioned. In addition, the valve material must have sufficient hot hardness to minimize susceptibility to two other failure modes, namely abrasive wear as shown in Fig. 15 and deposit indentation as shown in Fig. 16.

Application of Superalloys–Specific Examples

In order to illustrate factors governing the selection of appropriate alloys for exhaust valve applications, four specific cases will be examined in which tendencies towards failure were eliminated by changing from iron-base austenitic alloys to one of the superalloys. The complex

FIG. 14—*Typical view of valve seat* guttering *resulting from improper seating of valve seat.*

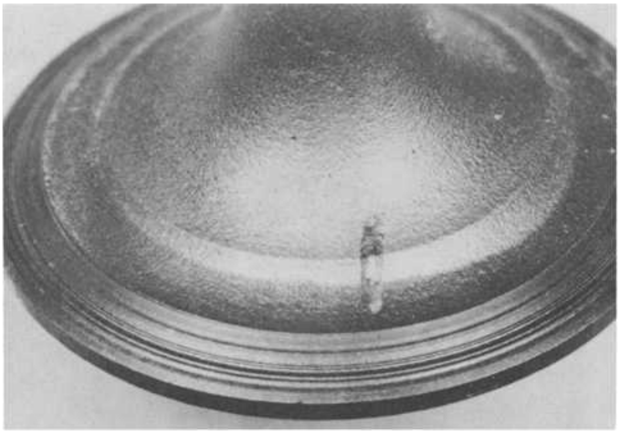

FIG. 15—*Typical appearance of excessive abrasive wear on a valve seat.*

interplay of the design parameters that bear on the selection of both the materials and their processing is illustrated.

Case 1

This involves an exhaust valve in a four-cycle spark-ignited engine operating on leaded fuel. In the original valve design, the materials selected consisted of an iron-base chromium-manganese austenitic alloy, Type 21-4N, as the base material, with the cobalt-base hardfacing alloy, Stellite #6, as a welded overlay on the valve seat. Type 21-4N has excellent hot strength and has the best lead oxide corrosion resistance of all the iron-base austenitic valve materials. In the present application, accelerated corrosive attack was observed at the junction of the valve head and stem as shown in Fig. 12. This region corresponds to the area of

FIG. 16—*Typical appearance of deposit indentation on a valve seat.*

maximum valve stem temperature in a spark-ignited engine exhaust valve, as illustrated in Fig. 3. The loss of a cross sectional area at the head-stem junction ultimately leads to a fatigue failure and breakage.

Examination of the corrosion mechanism using scanning electron microscopy (SEM) in conjunction with energy dispersive X-ray analysis (EDX) indicated that the scale on the severely corroded stem surface was rich in lead. The presence of lead in the scale strongly suggests that lead oxide in the scale had combined with other surface oxides or salts, or both, to form low melting slags that result in the catastrophic attack. A cross section through the corroded surface is shown in Fig. 17, with preferential attack at grain boundaries evident. The results of the EDX analysis of the scale are shown in Fig. 18.

To solve this problem, a comparison was made of the lead oxide corrosion resistance of Type 21-4N with that of several other high-temperature materials. As shown in Table 2, the nickel-base alloy, Nimonic 80A, should provide superior lead oxide corrosion resistance to Type 21-4N. Thus, Type 21-4N was replaced with Nimonic 80A as the valve head and adjacent stem base material that effectively eliminated the excessive valve stem corrosion and ultimate valve breakage.

Case 2

This case involves an exhaust valve designed for a four-cycle, direct fuel-injected diesel engine. The original design employed a base material of Type 21-12N, an iron-based chromium-nickel austenitic stainless steel alloy, with a Stellite #6 welded overlay on the seat. As engine output requirements were increased over a period of years subsequent to the

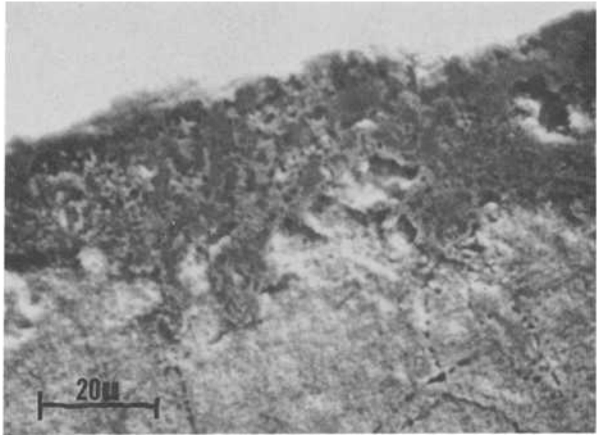

FIG. 17—*Cross section of severely corroded area of valve stem shown in Fig. 11*

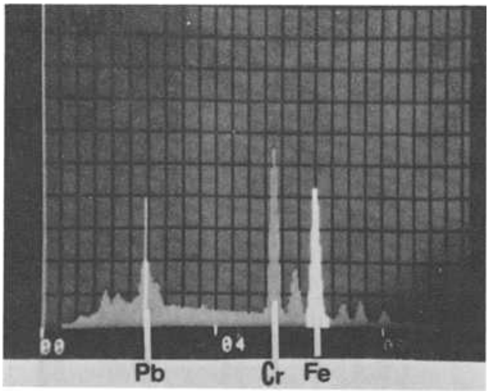

FIG. 18—*Energy dispersive X-ray spectra observed in oxide layer shown in Fig. 10.*

original valve design, combustion pressures also were increased, resulting in higher radial tensile stresses in the fillet of the valves as illustrated in Fig. 4. The result was a chordal fatigue-type failure similar to that illustrated in Fig. 5. A comparison of the high-temperature fatigue strengths of Type 21-12N and several other high-temperature alloys is given in Table 3. Since Inconel 751 has superior high-temperature fatigue strength compared to Type 21-12N and appeared to meet the other valve requirements, it was tested in this application. Engine operation showed no evidence of chordal fatigue problems and this material replaced Type 21-12N for this production part.

Case 3

This deals with a complex valve problem involving creep, fatigue, and corrosion in a two-cycle direct-injection engine. The original design

TABLE 2—*Resistance to molten lead-oxide corrosion of typical exhaust valve material*[a]

Alloy Type	Alloy Designation	Weight loss per hour, g/dm^2[b]
Iron base	Silchrome 10	31.0
	21-4N	20.5
	EMS-235	16.2
Nickel base	Inconel 751	12.0
	Nimonic 80A	6.4

[a] Armco Steel Corporation test results.

[b] Crucible tests performed by submerging specimens in molten lead-oxide (PbO) bath at 913°C (1675°F) for 1 h.

TABLE 3—*Fatigue strength of typical exhaust valve materials at 760°C (1400°F).*

Alloy Type	Alloy Designation	Stress to Produce Failure in 10^8 Cycles, kpsi (MPa)[a]
Iron base	21-4N	30 (205)[b]
	21-12N	21 (145)[b]
	N-155	41 (275)[c,d]
	EMS-235	27.5 (185)[b]
Nickel base	Inconel 751	50[e]
	Nimonic 80A	45[e]

[a] Rotating beam test.

[b] Armco Steel Corporation test results.

[c] Aged 50 hours at 649°C (1200°F).

[d] Determined from Larson-Miller parameter data.

[e] Eaton Corporation test results.

contained a head material of N-155, a chromium-nickel-cobalt alloy (see Table 1 for composition). The material was used in the as-forged condition to provide a fine-grained cold-worked microstructure to avoid excessive deposit indentations on the seating face (refer to Fig. 16), however, as the engine outputs were gradually upgraded, both creep and chordal fatigue failures (refer to Figs. 5 and 6) began to appear. Alloy N-155 was replaced with Inconel 751, because N-155 could not be solution treated for improved hot strength without causing the deposit indentation problems. Tables 3 and 4 illustrate the superior fatigue and creep strength, respectively, of Inconel 751 in the solution-treated and double-aged condition over Alloy N-155. Inconel 751 also has increased hot hardness that avoids any significant deposit indentation problems. Recently, however, an increasing number of failures of the valve were reported due to corrosive attack and ultimate guttering of the seat face of the Inconel 751 (refer to Fig. 3). This attack was identified as sulfidation.

An example of Inconel 751 sulfidation attack near the valve seat is shown in Fig. 19. From the EDX spectra shown in Figs. 20 and 21, it was apparent that the Inconel 751 surface was rich not only in chromium oxide but also phosphorous, calcium, zinc, and sulfur. The first three elements are believed to have come from the decomposition of additives in the lubricants, and sulfur is a significant impurity in the diesel fuel oil. The predominant constituent in this film is $CaSO_4$ and this compound in conjunction with carbon has resulted in severe sulfidation attack [6] culminating in a failure by guttering. Note in Fig. 19 the dark constituents below the surface; these have been identified as chromium- and nickel-rich sulfides. Also note that the grain boundaries are attacked more heavily than the matrix.

To make the seat of the Inconel 751 valve more resistant to sulfidation, a Stellite #6 hard facing was applied. This approach was based on the

TABLE 4—*Creep strength of typical exhaust valve materials at 732°C (1350°F).*

Alloy Type	Alloy Designation	Creep Strength, kpsi (MPa)[a]
Iron base	Silchrome 10	14-16 (95–110)[b]
	21-4N	18–20 (125–140)[b]
	N-155	24 (165)[b]
	EMS-235	29 (197)[c]
Nickel base	Inconel 751	48 (330)[b]

[a] Stress to produce 1 percent elongation in 100 h at 732°C (1350°F).
[b] Armco Steel Corporation test results.
[c] Determined from Larson-Miller parameter data.

generally accepted rule that cobalt-base alloys like Stellite #6 exhibit superior sulfidation resistance compared to nickel-base alloys [7]. This is believed to be primarily due to the fact the cobalt sulfides have a higher melting point than nickel sulfides and, thus, catastrophic hot corrosion in cobalt alloys occurs at a higher temperature than in nickel-base materials. Service history data has shown that the Stellite #6 facing was indeed more resistant to guttering as a result of sulfidation than Inconel 751.

Case 4

This deals with a combined creep and corrosion problem in an exhaust valve from a four-cycle prechamber diesel engine. The original valve incorporated Silchrome #10, a chromium-nickel austenitic alloy (see Table 1 for composition) as the head material with a Stellite #6 seat

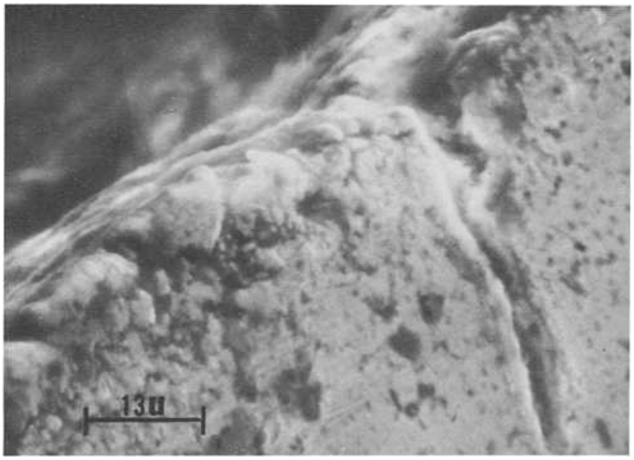

FIG. 19—*Cross section through Inconel 751 exhaust valve that guttered as a result of sulfidation.*

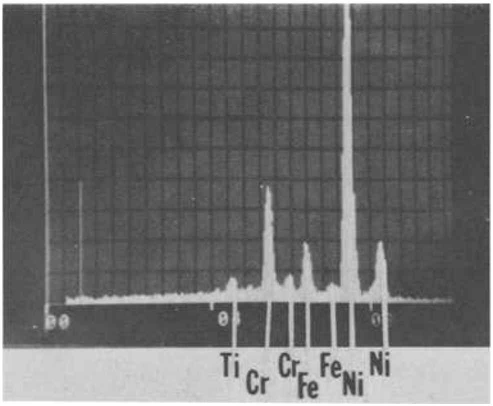

FIG. 20—*EDX analysis of Inconel 751 below the guttered surface. Note that only the elements of the base material are present.*

weldment. In highly turbocharged versions of the engine, the primary failure mode was one of creep (refer to Fig. 6). In addition, an unacceptable rate of corrosive attack occurred throughout the fillet area of the Silchrome #10 material in high-sulfur fuel applications. In this instance, the creep problem could not be solved by the use of a nickel-base alloy such as Inconel 751 because of it's even poorer sulfidation resistance than Silchrome #10 (refer to Table 5). To avoid this potential sulfidation problem and to solve the creep problem as well, the entire valve head had to be made from Stellite #6.

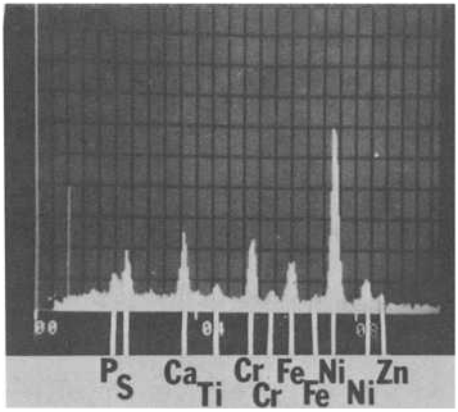

FIG. 21—*EDX analysis of the guttered surface of the Inconel 751. Note that phosphorous, sulfur, calcium, and zinc are present in addition to the base material elements.*

TABLE 5—*Resistance to sulfidation attack of typical exhaust valve material.*

Alloy Type	Alloy Designation	Weight loss per hour, g/dm²[a]
Iron base	Silchrome 10[b]	0.672
Nickel base	Inconel 751[b]	10.655

[a] Test performed by immersion of sample in molten salt consisting of 90% Na_2SO_4-10% NaCl at 927°C (1700°F).

[b] Carpenter Steel Corp. test data.

Development Opportunities for the Future

In most heavy-duty engine applications, superalloys have performed adequately and consistent with the design expectations. It is necessary, however, to emphasize the importance of maintaining a close surveillance on the performance of valves in various applications. Such a periodic review of the material behavior is necessary to enable a search for new materials that may be easier to fabricate and more cost effective than the production material in current use. To illustrate this point, four specific areas of concern are described in which modifications to present superalloys or the introduction of new alloys are under consideration.

1. As described in the last example, a strength and sulfidation problem was solved with the use of a Stellite #6 valve head. If a nickel-base alloy could have been used, this would have resulted in a much more cost effective solution. A new superalloy, Pyromet 31 (see Table 1 for composition), has been designed with improved sulfidation resistance to solve this problem. The expectation of improvement is based on examining the two materials after exposure to a Na_2SO_4-NaCl molten mixture at 927°C (1700°F) for 100 h. The Inconel 751 shows catastrophic attack while the Pyromet 31 is virtually untouched. The improved sulfidation resistance of Pyromet 31 is believed due to its higher chromium content. The new alloy has mechanical properties similar to Inconel 751, therefore, Pyromet 31 would appear to offer a more cost effective solution to sulfidation problems than Stellite #6 where the hot strength of superalloys are required.

2. Very recently, there have been attempts to run diesel engines on residual fuels containing high levels of vanadium and sulfur. This has resulted in premature seat guttering failures even with the cobalt-base Stellite #6 seat material. Figure 22 shows a cross section through the seat of a severely corroded valve. From the EDX spectrum in Fig. 23, it can be seen that the corrosion products are rich in vanadium and chromium. These elements are believed to combine with other oxides and sulfides on the alloy surface to form low melting phases that literally flux away the protective Cr_2O_3 scale and thus expose the base material to catastrophic

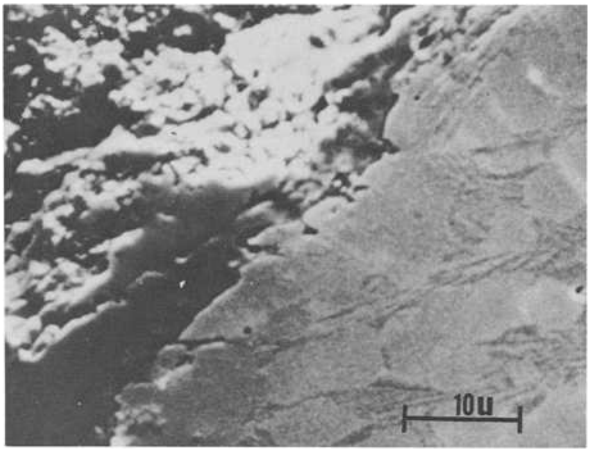

FIG. 22—*Cross section of severely corroded exhaust valve exposed to vanadium-rich fuel combustion products.*

oxidation attack. A development program is now underway to evaluate alloys similar to the Inconel 671 and CoCrAlY types (see Table 1 for compositions) for application as a seat weldment where resistance to vandaium pentoxide attack is required.

3. Over the past few years, there has been an increasing concern over the cost and availability of certain strategic alloying elements such as nickel, cobalt, tungsten, etc. With the increasing trend towards heavy usage of superalloys in the construction of valves, several approaches are being investigated to minimize the dependence on these metals wherever feasible. One important example is the significant usage of Stellite #6 that

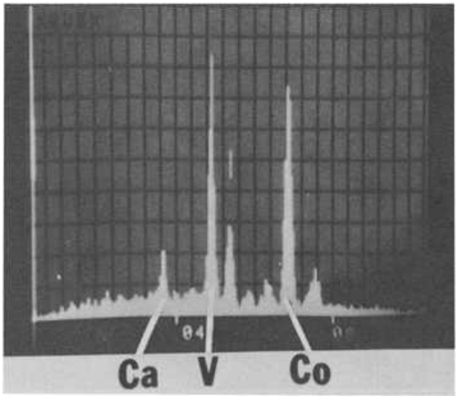

FIG. 23—*Energy dispersive X-ray spectra of vanadium-rich oxide scale in Fig. 22.*

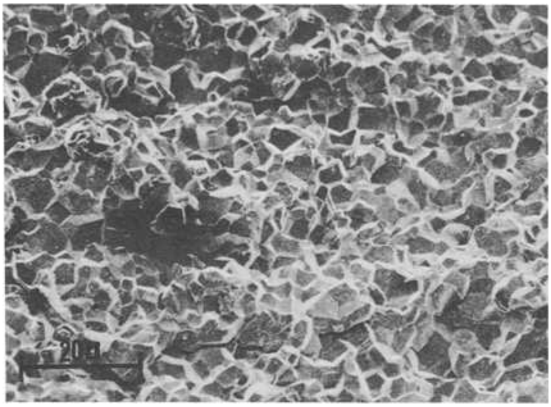

FIG. 24—*Strain age cracking in Nimonic 80A valve stems.*

is high in cobalt and tungsten content. It is expected that an alloy will be developed involving a substitution for these elements by less strategic ones and still retain the excellent high-temperature properties of the Stellite #6.

4. Of equal importance to an alloy's end use properties is its resistance to manufacturing or fabrication oriented problems. An example of this is the concern over susceptibility to strain age cracking in nickel-base alloys. This phenomenon occurs because of internal stress gradients created during valve manufacturer in conjunction with a volume decrease that occurs during aging; that is, gamma prime precipitation. Strain aging sometimes produces intergranular transverse cracks in the valve stem (see Fig. 24) that may initiate and propagate during the aging heat treatment or during engine operation. While the control of the manufacturing operations to minimize internal residual stresses is obviously important, an added safety factor can be introduced by more careful specification of the alloying elements and the heat treat sequences for the nickel-base alloys. A development program is being conducted to define those parameters of material processing and alloy composition that must be controlled to minimize incidents of strain age cracking in exhaust valves.

Conclusions

The application of nickel- and cobalt-base superalloys has played an important role in the successful design of exhaust valves to meet durability objectives in virtually all types of reciprocating internal-combustion engines. A careful examination and evaluation of the operating environment will continue to be necessary to assure that the proper alloy selection can be made to meet the individual engineering and cost requirements of each application. The engine valve is, and will continue to be a dynamic product, presenting ever changing demands on the alloy system in use. In this regard, this paper could be considered a progress report on the evolution of the usage of superalloys in the automotive industry.

Acknowledgments

The authors wish to acknowledge the efforts of all persons that contributed to this paper. We also wish to give special thanks to Don Cole, Don Johnson, and Simon Narasimhan for their helpful comments.

References

[1] Betteridge, W. and Heslop, J., *The Nimonic Alloys*, Crane, Russak, & Co., New York, 1974.
[2] Decker, R. F., "Strengthening Mechanisms in Nickel Base Superalloys," presented at the Steel Strengthening Mechanisms Symposium, Zurich, Switzerland, 5–6 May 1969.
[3] Symond, C. H., *Journal*, Australian Institute of Metals, Vol. 16, No. 1, Feb. 1971, pp. 1–15.
[4] Kasak, A., Hsiao, C. M., and Dulis, E. J. in *Proceedings*, American Society for Testing and Materials, Vol. 59, 1959, pp. 786–803.
[5] Jenkins, L. F. and Larson, J. M., "The Development of a New Austenitic Stainless Steel Exhaust Valve Material," SAE No. 780245, presented at the Society of Automotive Engineers, Detroit, 1 March 1978.
[6] Clark, G. C., "Sulfidation Corrosion of Nickel-Base Exhaust Valves," Society of Automotive Engineers.
[7] Sim, C. T. and Hagel, W., *The Superalloys*, Wiley, New York, 1970.

D. J. Deye[1] *and W. H. Couts*[2]

Super Waspaloy Microstructure and Properties

REFERENCE: Deye, D. J. and Couts, W. H., "**Super Waspaloy Microstructure and Properties,**" *MiCon 78: Optimization of Processing, Properties, and Service Performance Through Microstructural Control, ASTM STP 672,* Halle Abrams, G. N. Maniar, D. A. Nail, and H. D. Solomon, Eds., American Society for Testing and Materials, 1979, pp. 601–615.

ABSTRACT: Waspaloy is currently one of the more widely used alloys for turbine disk applications in the aerospace industry. However, higher engine performance demands by aircraft engine manufacturers have resulted in a number of approaches by material suppliers to upgrade the alloy. These approaches range from simple compositional modifications to a combination of chemistry modifications coupled with thermal mechanical processing. One such approach resulted in what is now commonly referred to as Super Waspaloy.

Tension, low-cycle fatigue, and creep rupture tests of Waspaloy and Super Waspaloy forgings were conducted from room temperature to 1089 K (1500°F), after which material properties were reviewed and correlated with the disk microstructure.

KEY WORDS: steels, microstructure, Waspaloy, Super Waspaloy, closed die forging, physical metallurgy, tension tests, creep rupture, low-cycle fatigue

The ever-increasing drive to improve the thrust and efficiency of gas turbine engines, mainly through an increase in turbine inlet temperature, places a greater demand on the blade, vane, and disk materials selected for application in the turbine section. Disk development has progressed chiefly by metallurgical means, with emphasis on compositional and processing technology. However, one method used to extend disk life is disk face cooling wherein cooling air is directed on the disk surface. Although this reduces the requirements for high-temperature creep-rupture properties, it places greater emphasis on tensile and low-cycle fatigue properties because of increased thermal gradients.

---

[1] Metallurgist, Materials Applications Group, AiResearch Manufacturing Company of Arizona, Phoenix, Ariz. 85010.

[2] Manager, Research and Development, Wyman Gordon Co., North Grafton, Mass. 01536.

Waspaloy is currently one of the more widely used wrought nickel-base alloys for turbine disk applications. Mechanical properties such as tensile, low-cycle fatigue, and creep are extremely important and are highly dependent upon the thermal processing that takes place during forging and subsequent heat treatment of the disk. It has been shown that processing for optimum tensile and low-cycle fatigue properties can result in lower creep properties due to variations in grain size and metallurgical structure. Therefore, forging procedures coupled with solution heat treatments must be carefully selected to obtain the needed balance of these properties. It becomes a matter of obtaining the best tensile and low-cycle fatigue properties while not sacrificing creep properties to the extent that the alloy becomes creep limited.

One such alloy that has shown a balance of properties is Super Waspaloy, a compositional and processing derivative of Waspaloy. This alloy has evolved from the processing work of Couts and Radavich reported in 1964 [*1*],[3] in which the effect of lower forge temperature on the phase equilibria and properties of Waspaloy was studied. Since this time, various sources, notably Car Tech personnel [*2–4*], evaluated the effect of lower carbon and higher titanium and aluminum contents on the mechanical properties of Waspaloy. It is the combination of these approaches, modified forging procedures and compositional changes, that has resulted in what is now known as Super Waspaloy.

This paper compares the tensile, low-cycle fatigue, and creep rupture properties of Super Waspaloy forgings with the properties of typical forged Waspaloy and correlates the properties with the disk microstructure.

Processing

Production Waspaloy disk forgings are currently hammer-forged in two steps: block and finish. However, both operations are performed at temperatures significantly above the γ' solvus. Forgings are subsequently heat treated as follows: (*a*) solution treat at 1278 K (1840°F) for 4 h followed by an oil quench; (*b*) stabilization at 1116 K (1550°F) for 4 h and air cool; and (*c*) age at 1033 K (1400°F) for 16 h and air cool.

Super Waspaloy billet material, 10 cm (4 in.) in diameter, was procured from Teledyne Allvac and hammer-forged by Reisner Metals, Inc. The chemistry of the Teledyne Allvac Super Waspaloy heat is compared with the standard Waspaloy heat in Table 1. Five disk forgings (Fig. 1) were made in the following manner: (*a*) billets were heated to a temperature above the γ' solvus, held at temperature approximately 1 h, and air cooled; (*b*) billets were reheated to 1297 K (1875°F), which should be

---

[3] The numbers in brackets refer to the list of references appended to this paper.

TABLE 1—*Waspaloy and Super Waspaloy chemistry.*

Element	Waspaloy	Super Waspaloy
Carbon	0.048	0.024[a]
Sulfur	0.001	0.002
Manganese	0.02	0.10
Silicon	0.05	0.07
Chromium	19.70	19.13
Molybdenum	4.25	4.18
Cobalt	13.90	13.68
Titanium	3.02	3.13[a]
Aluminum	1.24	1.46*a*
Aluminum + titanium	4.26	4.59[a]
Boron	0.005	0.007
Zirconium	0.06	0.06
Iron	0.96	0.26
Copper	0.03	0.03
Phosphorus	0.008	0.008
Nickel	balance	balance

[a] Major differences.

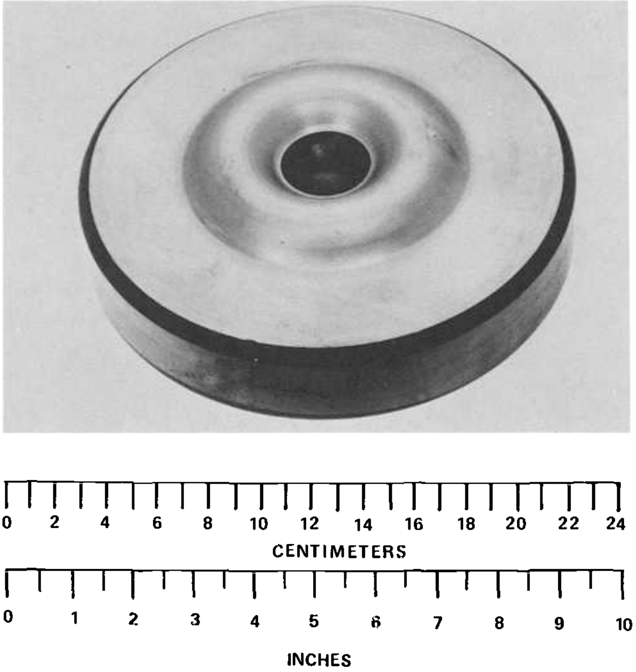

FIG. 1—*Super Waspaloy disk forging.*

below the γ' solvus temperature, and forged in a blocker die; and (*c*) forgings were reheated to 1283 K (1850°F) and finish forged.

The initial annealing cycle above the γ' solvus temperature was employed to completely recrystallize the large nonrecrystallized grains that were present in the billet.

The die sequence was designed to produce a uniform cross-sectional reduction of approximately 40 percent during finish forging. However, in a conventional forging, the die sequence is designed to produce a uniform reduction in cross-section of 10 to 25 percent during the finish operation. Forgings were heat treated at 1278 K (1840°F) for 4 h followed by the same stabilization and aging cycle that Waspaloy receives.

Tension, low-cycle fatigue, and creep-rupture specimens, machined from these forgings, as shown in Fig. 2, were tested and compared with typical forged Waspaloy data.

Results and Discussion

Mechanical Properties

Tensile properties generated from specimens machined from Super Waspaloy forgings were established at room temperature, 811 K (1000°F), and 950 K (1250°F). The average tensile properties are compared with typical Waspaloy tensile properties in Table 2. This shows a significant strength improvement for Super Waspaloy of 103 to 108 MPa (15 to 20 ksi) at each of the temperatures tested. In addition, the ductility of Super Waspaloy appears to be equivalent to if not better than Waspaloy.

Low-cycle fatigue testing was performed at room temperature, 811 and 950 K (1000 and 1250°F) at 1- and 2-percent strain using completely reversed push-pull strain control loading ($A = \infty$, 20 cpm). Neuber parameter[4] versus cycles-to-failure for both Super Waspaloy and Waspaloy at the three test temperatures are shown in Figs. 3, 4, and 5. These plots illustrate the improved low-cycle fatigue properties of Super Waspaloy over the entire temperature range. A similar improvement in the cycles-to-crack-initiation was also observed.

Creep-rupture testing performed in the 894 to 1089 K (1150 to 1500°F) temperature range has shown that the properties of Super Waspaloy are comparable to Waspaloy at the lower Larson-Miller parameters that represent lower-temperature, higher-stress testing conditions. At higher

---

[4] Neuber parameter = $(\Delta\sigma_{Nf/2} \cdot E \cdot \Delta\epsilon_t)^{1/2}$
where:

$\Delta\sigma_{Nf/2}$ = stress range required to achieve the desired strain range at the specimen half-life ksi;
E = elastic modulus; and
$\Delta\epsilon_t$ = total strain range, in./in.

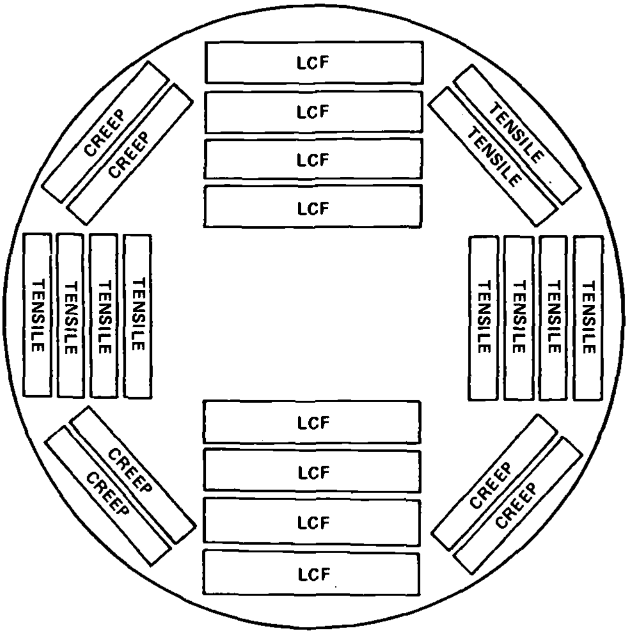

FIG. 2—*Specimen location in Super Waspaloy forging.*

TABLE 2—*Typical tensile properties of Super Waspaloy versus Waspaloy.*

Material	0.2% Yield Strength, MPa (ksi)	Ultimate Strength, MPa (ksi)	Elongation, %	Reduction of Area, %
Room temperature				
Super Waspaloy	1110 (161.1)	1460 (212.0)	22.5	37.7
Waspaloy	965 (140.0)	1340 (194.0)	23.0	27.5
811 K (1000°F)				
Super Waspaloy	1010 (145.9)	1370 (198.6)	17.0	23.8
Waspaloy	896 (130.0)	1240 (180.0)	19.5	22.5
950 K (1250°F)				
Super Waspaloy	966 (140.1)	1170 (170.6)	30.3	47.0
Waspaloy	786 (114.0)	1030 (150.0)	18.7	21.5

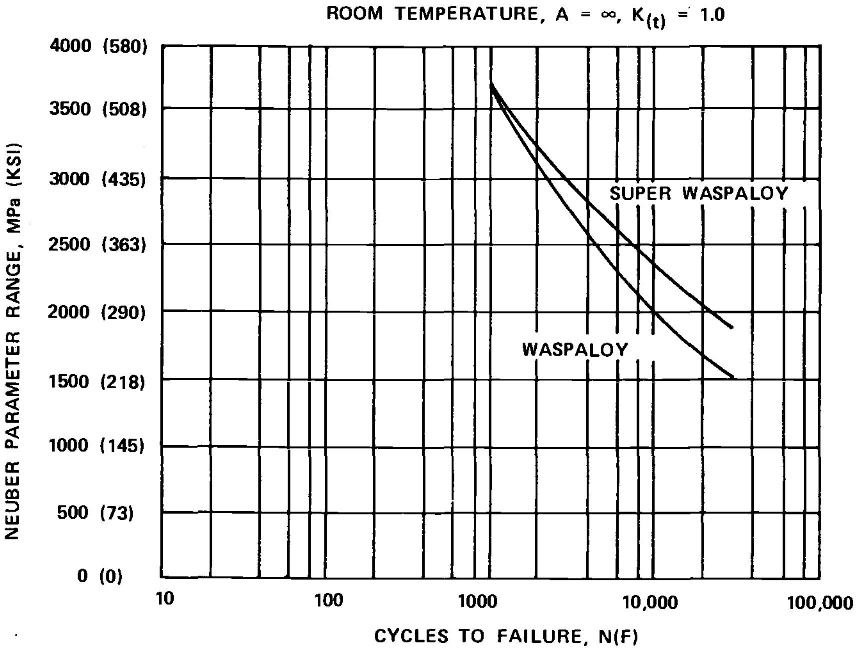

FIG. 3—*Comparison of the LCF properties of Super Waspaloy and Waspaloy forgings.*

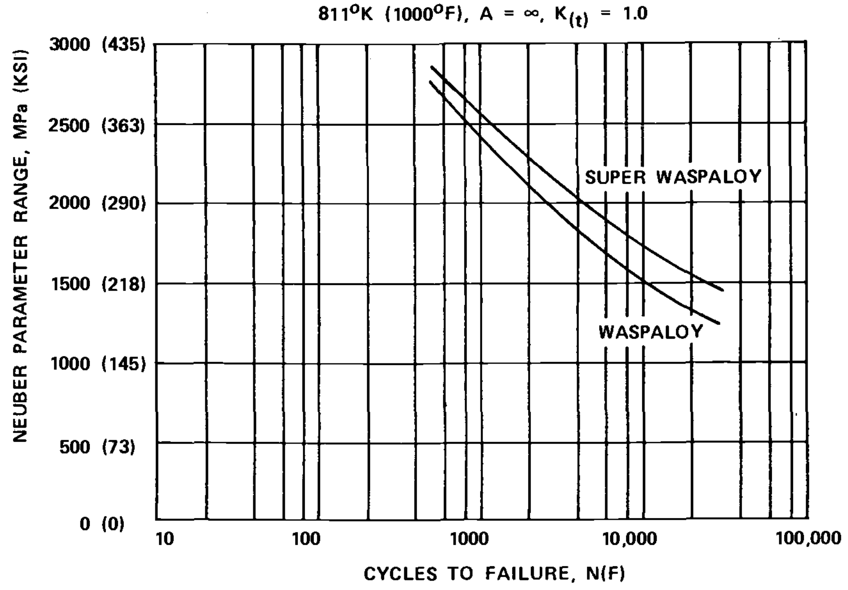

FIG. 4—*Comparison of the LCF properties of Super Waspaloy and Waspaloy forgings.*

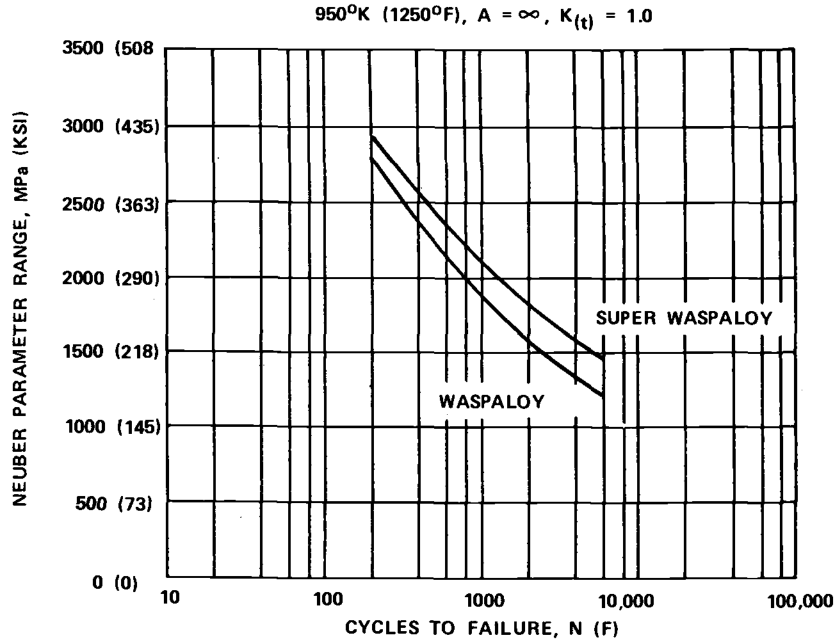

FIG. 5—*Comparison of the LCF properties of Super Waspaloy and Waspaloy forgings.*

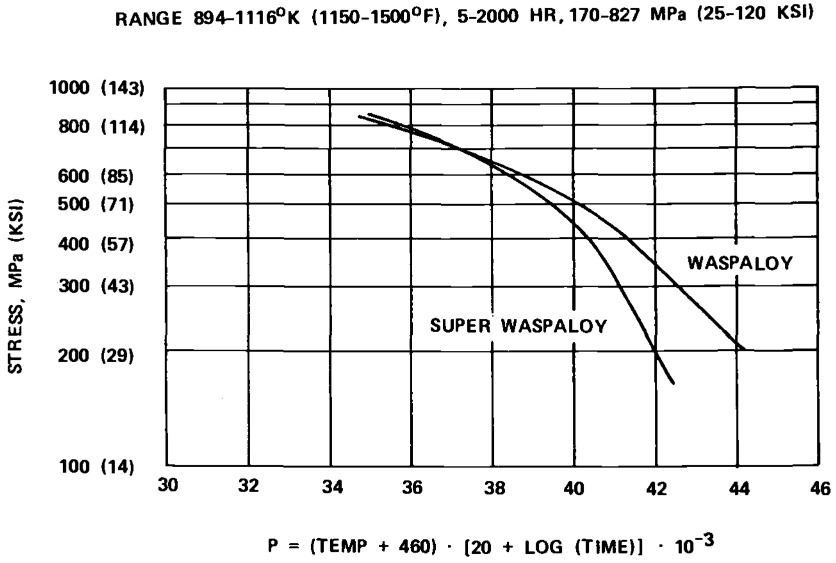

FIG. 6—*Stress rupture properties of Super Waspaloy versus Waspaloy.*

Larson-Miller parameters where test conditions represent higher temperatures and lower stresses, Super Waspaloy is inferior to Waspaloy (Fig. 6). This indicates that Super Waspaloy may be temperature limited. Thus, above a certain temperature, the reduced creep properties become the life limiting factor.

Physical Metallurgy

The physical metallurgy of Waspaloy has been well documented [*5,6*]. Forge temperatures are normally in the 1339 to 1442 K (1950 to 2100°F) temperature range, well above the γ' solvus. Consequently, the γ' is dissolved although some fine cooling γ' may form while cooling from the forge temperature. In addition, some of the MC-type carbides ((Ti,Mo) C) are either partially or totally dissolved at the forge temperature. This increases the carbon and titanium content of the solid solution matrix. Due to the absence of γ' and the reduced number of carbides, recrystallization is enhanced and the Waspaloy, as forged, has a fully recrystallized, equiaxed, fairly uniform grain structure.

The subsequent solution heat treat of Waspaloy will have little effect on grain size, but will precipitate and agglomerate some γ', particularly in the interdendritic areas. Depending upon the amount of carbon in solution, some $M_{23}C_6$ may be precipitated at the grain boundaries. Waspaloy will precipitate a second generation of γ' during the 1116 K (1550°F) stabilization age. In addition, more $M_{23}C_6$ will be precipitated at the grain boundaries. When properly processed, these carbides are discrete particles instead of continuous films. A fine γ' also forms during the 1033 K (1400°F) age. This structure is shown in Figs. 7 and 8.

Super Waspaloy has a different microstructural history. As a result of the lower carbon and higher titanium and aluminum contents, it will have a γ' solvus somewhat higher than Waspaloy and also fewer MC carbides. It is forged below the solvus with γ' present during the deformation. The presence of γ' inhibits grain growth and a much finer grain size results in the Super Waspaloy forgings (Fig. 9). Due to the reduced forging temperature, less MC carbides are dissolved and, therefore, less carbon is found in solid solution.

The heat treat is nominally the same for both alloys, but more of the larger γ' is observed in Super Waspaloy (Fig. 10). It is believed that this is caused by the richer chemistry of the Super Waspaloy. The Super Waspaloy also has some γ' particles that are significantly larger than any particles in Waspaloy. It is believed that these are the particles that are present during the forging cycle.

The finer γ', resulting from the 1116 and 1033 K (1550 and 1400°F) stabilization and age, appears similar in both Super Waspaloy and Waspaloy. The Super Waspaloy has almost no $M_{23}C_6$ precipitation at the

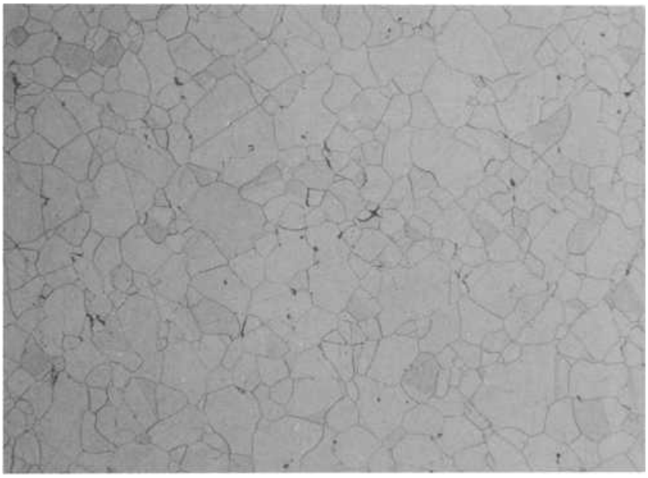

FIG. 7—*Optical micrograph of typical as-heat treated Waspaloy (ASTM grain size 4 to 6, original magnification ×100).*

boundaries due to the reduced carbon in solution at the end of the forging cycle (contrast with Figs. 8 and 10).

Selected samples of both Waspaloy and Super Waspaloy were examined with use of thin foil transmission electron microscopy (TEM). Due to the high magnification, the term *average field* is difficult to justify. It is believed that the grain boundary differences are best revealed in Figs. 8 and 10. Therefore, grain matrix was used as the basis for selection of the fields presented in Fig. 11.

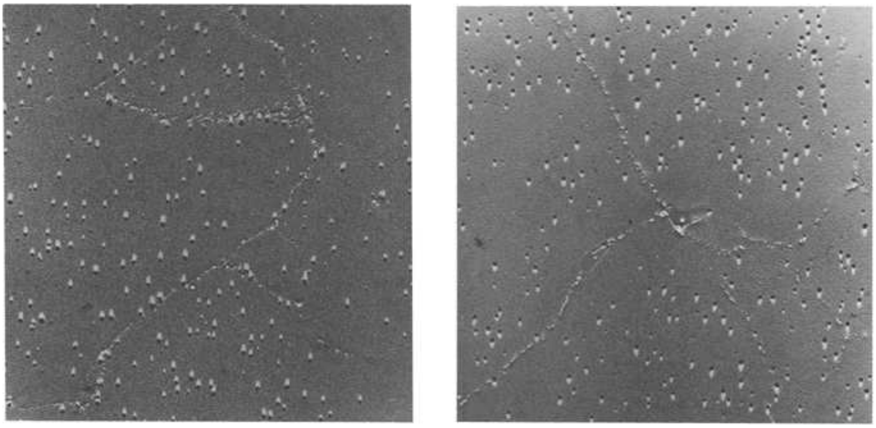

FIG. 8—*Electron micrograph showing typical Waspaloy structure (original magnification ×7000).*

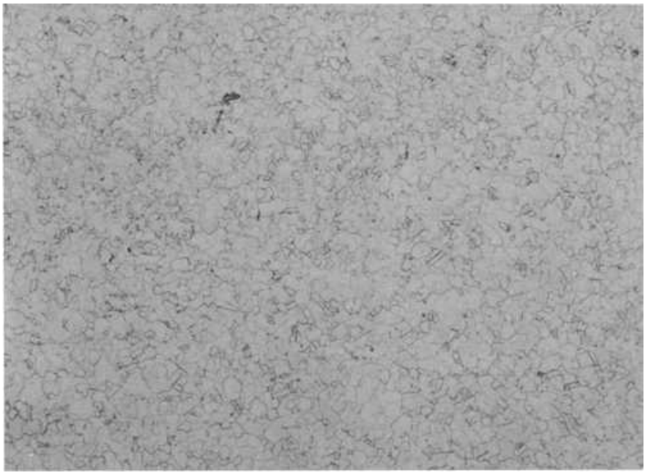

FIG. 9—*Optical micrograph of typical as-heat treated Super Waspaloy (ASTM grain size 8 to 10, original magnification ×100).*

As shown in Fig. 11*a*, the Waspaloy is very uniform. There are randomly scattered larger γ' spheroids and a background of fine γ'. Wavy dislocations are uniformly dispersed throughout the matrix. In contrast, the Super Waspaloy is much more complex. The upper left-hand corner of Fig. 11*b* shows a recrystallized area devoid of large γ'. The remainder of the field shows scattered γ' that correlate with the intermediate size γ' of Fig. 10. The matrix among these γ' has some bands of recrystallized

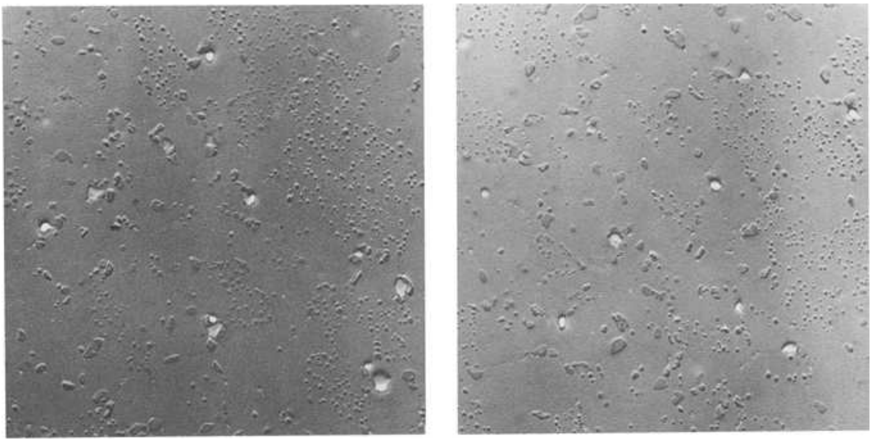

FIG. 10—*Electron micrograph showing typical Super Waspaloy structure (original magnification ×7000).*

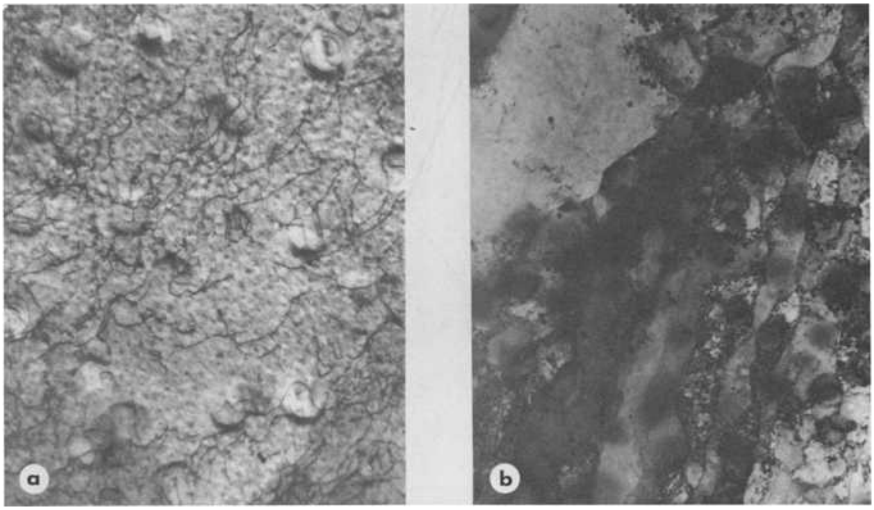

FIG. 11—*Thin foil transmission electron micrograph structures (original magnification ×40 000): (*a*) Waspaloy and (*b*) Super Waspaloy.*

material intermixed with the nonrecrystallized matrix. The field selected for Fig. 11*b* does not include any of the largest γ' shown in Fig. 10.

The fields presented suggest that the recrystallized regions of Super Waspaloy have fewer dislocations than regular Waspaloy and that the nonrecrystallized regions have more dislocations than regular Waspaloy. However, dislocation density is a difficult task to determine and work is continuing on the TEM evaluation.

The next objective was to seek a correlation between the microstructural differences just outlined and the corresponding mechanical properties and fracture surface appearance.

The tensile fracture mode of Super Waspaloy was completely transgranular at all test temperatures, whereas Waspaloy appears somewhat intergranular at room temperature and less intergranular at higher temperatures. The room temperature tensiles shown in Fig. 12 illustrate these variations.

Apparently tensile fracture, especially at room temperature, prefers to follow the distribution of $M_{23}C_6$, if present. Super Waspaloy is able to develop the full strength of the matrix, because the easy fracture path is missing.

Room-temperature low-cycle fatigue specimens showed similar fracture features for both Waspaloy and Super Waspaloy. However, at 950 K (1250°F), the low-cycle fatigue fracture path of Waspaloy (Fig. 13) shows some faceting. The Super Waspaloy in Fig. 14 appears to be free of

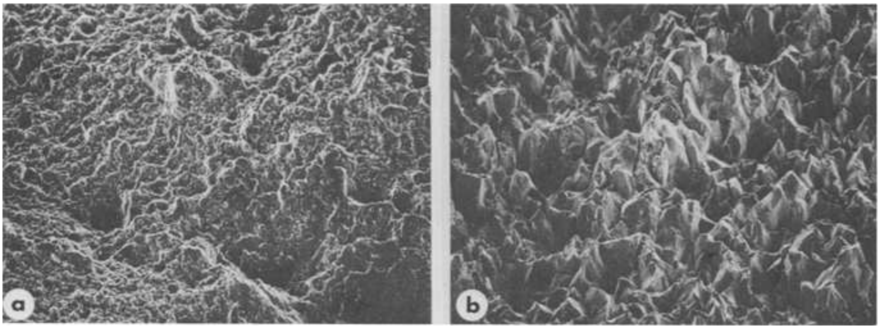

FIG. 12—*Room temperature tensile fracture specimens:* (a) *Super Waspaloy (original magnification ×250) and* (b) *Waspaloy (original magnification ×290).*

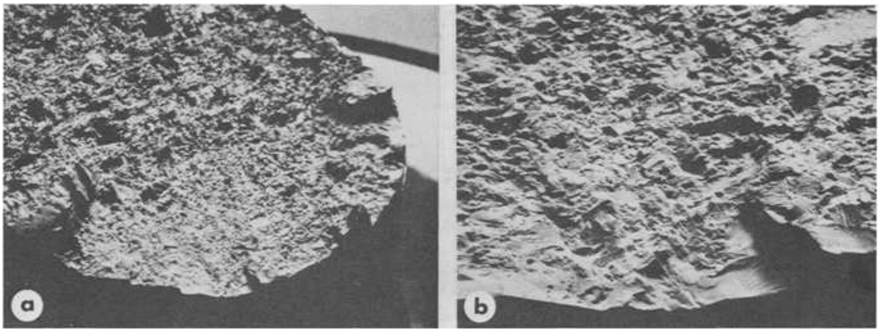

FIG. 13—*LCF fracture appearance of Waspaloy specimens at elevated temperature, 950 K (1250°F):* (a) *original magnification ×23 and* (b) *original magnification ×110.*

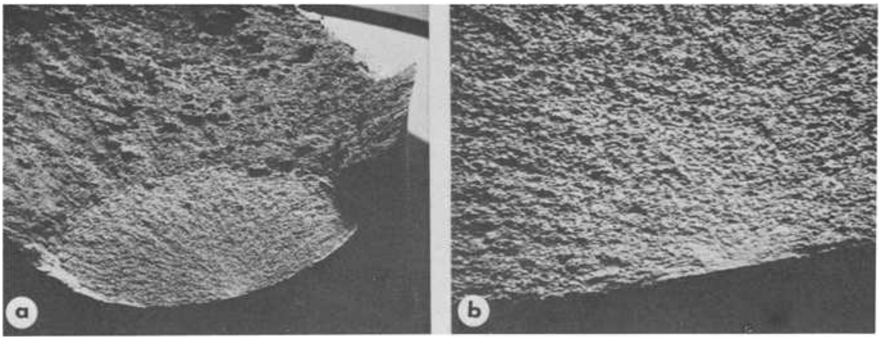

FIG. 14—*LCF fracture appearance of Super Waspaloy specimens at elevated temperature, 950 K (1250°F):* (a) *original magnification ×23 and* (b) *original magnification ×110.*

faceting . The absence of the $M_{23}C_6$ or the finer grain size of Super Waspaloy or both probably account for the improvement in low-cycle fatigue properties.

The fracture surfaces of Super Waspaloy and Waspaloy stress-rupture specimens were very similar at 894 K (1150°F) (Fig. 15), however, at 1089 K (1500°F), there is a dramatic difference. With Waspaloy there was massive secondary cracking/grain boundary separation present with little necking (Fig. 16). In Super Waspaloy, drastic necking occurred with few secondary cracks present on the surface (Fig. 17). These observations, and the stress rupture life, support the theory that the grain boundary carbides initiate cracks but at the same time also retard crack growth [7]. As the service temperature increases, discrete $M_{23}C_6$ precipitates become more helpful. But at lower temperatures where tensile and low-cycle fatigue govern, a reduction in the extent of $M_{23}C_6$ precipitation does not harm stress-rupture life.

Conclusions

Super Waspaloy offers a significant improvement in tensile and low-cycle fatigue properties over Waspaloy.

Stress rupture properties of Super Waspaloy are comparable to Waspaloy at lower temperature test conditions. At higher temperature test conditions, Super Waspaloy properties are significantly lower.

Mechanical properties can be correlated with the physical metallurgy of Super Waspaloy and, as a result, microstructure may provide an effective quality control check.

Acknowledgments

The authors would like to acknowledge Ed Hoeft, Reisner Metals Inc., for his work in developing the forging procedures for Super Waspaloy and

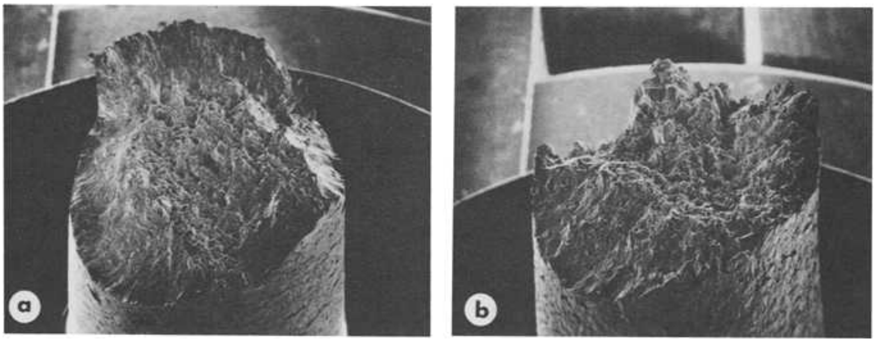

FIG. 15—*Creep rupture fracture specimens at elevated temperature, 894 K (1150°F) (original magnification ×20):* (a) *Super Waspaloy and* (b) *Waspaloy.*

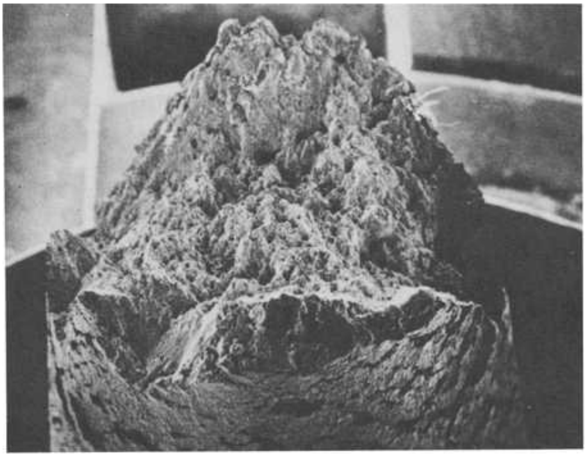

FIG. 16—*Creep rupture fracture of Waspaloy specimen tested at 1089 K (1500°F) (original magnification ×20).*

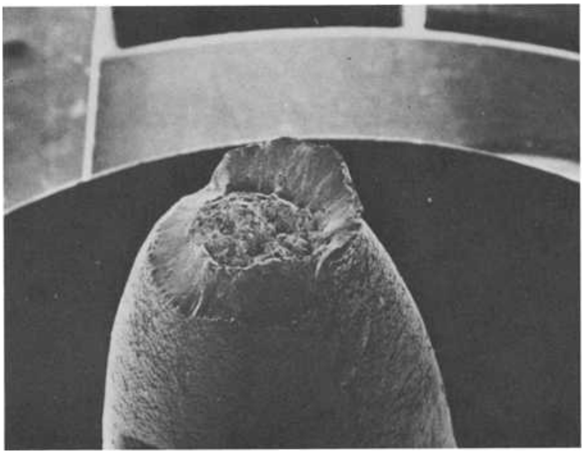

FIG. 17—*Creep rupture fracture of Super Waspaloy specimen tested at 1089 K (1500°F) (original magnification ×20).*

Wil Danesi, AiResearch, for his invaluable assistance and support. J. Radavich, Micro-Met, made the replica electron micrographs. R. Biederman, Worcester Poly Tech, made the transmission electron micrographs. Bill Nichols, Wyman Gordon, made the scanning electron micrographs.

The authors would also like to thank AiResearch, Wyman Gordon, and Reisner Metals for permission to publish the results.

References

[*1*] Radavich, J. F. and Couts, W. H., Jr., "Correlation of Forge Temperature and Phase Equilibria During Processing of a Nickel-Base Alloy," presented at AIME Symposium on Effect of Time, Temperature, and Service Conditions on Microconstituents and Stability of Superalloys, New York, American Institute of Mining, Metallurgical, and Petroleum Engineers, 19 Feb. 1964.

[*2*] Muzyka, D. R., Car Tech, Reading, Pa., personal communication.

[*3*] Rehrer, W. P., Muzyka, D. R., and Heydt, G. B., "Solution Treatment and Al + Ti Effects on the Structure and Tensile Properties of Waspaloy, *Journal of Metals,* Feb. 1970.

[*4*] Couts, W. H., Jr., "The Influence of Carbon Upon Cast Waspaloy," presented at SAE Annual Meeting, Paper No. 690100, Society of Automotive Engineers, Jan. 1969.

[*5*] Radavich, J. F. and Pennington, W. J., *Metal Progress,* Feb. 1961 pp. 94–97.

[*6*] Donachie, M. J., Pinkowich, A. A., Danesi, W. P., Radavich, J. F., and Couts, W. H., Jr., *Metallurgical Transactions,* Vol. 2, Sept. 1970, pp. 2623–2630.

[*7*] Rowe, J. P. and Freeman, J. W., "Relations Between Microstructure and Creep-Rupture Properties of Nickel-Base Alloys as Revealed by Overtemperature Exposures," NASA TND-1325, Sept. 1962.

W. L. Mankins[1] *and D. E. Wenschhof*[1]

Microstructure and Mechanical Properties of INCOLOY Alloy 800 After 14 Years of Service as a Catalyst Tube in a Steam-Methane Reformer

---

REFERENCE: Mankins, W. L. and Wenschhof, D. E., "**Microstructure and Mechanical Properties of INCOLOY Alloy 800 After 14 Years of Service as a Catalyst Tube in a Steam-Methane Reformer,**" *MiCon 78: Optimization of Processing, Properties, and Service Performance Through Microstructural Control, ASTM STP 672,* Halle Abrams, G. N. Maniar, D. A. Nail, and H. D. Solomon, Eds., American Society for Testing and Materials, 1979, pp. 616–632.

ABSTRACT: An INCOLOY Alloy 800 catalyst tube, which served satisfactorily in a steam-methane reformer for more than 14 years, was removed for examination. The tube had been heated to temperatures varying along its length from 540 to 815°C (1000 to 1500°F).

The deepest penetration of intergranular oxidation was only 0.33 mm (0.013 in.) on the outer surface.

Room-temperature tensile properties and stress-rupture properties improved significantly with the precipitation of carbides at higher temperatures and gamma prime at the lower temperatures. Gamma prime was the principal strengthening phase, and mechanical properties show that ductility was retained.

Rare, discrete, blocky particles of sigma phase found in one section of the tube were determined to be innocuous.

KEY WORDS: steel, microstructure, mechanical properties, tubing, strengthening

A goal of microstructural metallurgists is to have the opportunity to examine materials that have had long exposure to high temperatures in punishing environments. Such an opportunity was presented by the material examined in this study.

One INCOLOY[2] Alloy 800 tube was removed from service after satisfactorily performing as a catalyst tube in a commercial steam-methane reformer for more than 14 years. The tube provided material that

---

[1] Senior metallurgist and projects engineer, respectively, Huntington Alloys, Inc., Huntington, W. Va. 25720.

[2] Trademark for products of Huntington Alloys, Inc.

had been exposed to temperatures varying along its length from 540 to 815°C (1000 to 1500°F). Inside the catalyst-filled tube, methane and steam reacted to form carbon monoxide and hydrogen. The outside of the tube was exposed to combustion products from natural gas. Hoop stresses acted on the tube as the reaction took place.

The purposes of the study were to examine the environmental effects on the tube, to determine mechanical properties of the tube at various points along its length, and to correlate the test results with the microstructure of the material.

The use of specific alloys for long-time service at high temperatures is predicated on their ability to retain ductility. This study showed that the INCOLOY Alloy 800 tube retained its ductility and gained in strength at the same time. Significant strengthening resulted from the precipitation of gamma prime, Ni_3 (Al, Ti), where the service temperature was under 705°C (1300°F). A slight increase in strength in sections exposed to 815°C (1500°F) was caused by carbide precipitation.

Experimental Procedure

Samples for this investigation came from a single tube of INCOLOY Alloy 800, the chemical composition of which is given in Table 1. The 89 mm by 7.11 mm wall (3.5 in. by 0.280 in. wall) tube was placed in service in the as-extruded condition.

A schematic arrangement of the tube in the reformer is illustrated in Fig. 1. Approximate operating temperatures are shown at various elevations along the tube.

Short lengths were selected from near the inlet pigtail, from the center of the fire box, and at the outlet pigtail. Those locations provided samples that had been exposed to the wide range of operating temperatures. During its 14 years of service, the tube was cycled from ambient to operating temperature an estimated 20 times.

Samples 1 and 2 came from the top of the tube toward the inlet and near the support. Methane and steam entered at a temperature of 150 to 315°C (300 to 600°F), and the temperature at the top of the fire box was about 815°C (1500°F). Thus, the operating temperature at the point represented by Samples 1 and 2 was an estimated 540°C (1000°F).

TABLE 1—*Chemical composition, percent by weight, of samples studied.*

Carbon	0.05	Nickel	30.58
Manganese	0.74	Chromium	20.87
Sulfur	0.007	Aluminum	0.41
Silicon	0.41	Titanium	0.41
Copper	0.35	Iron	remainder

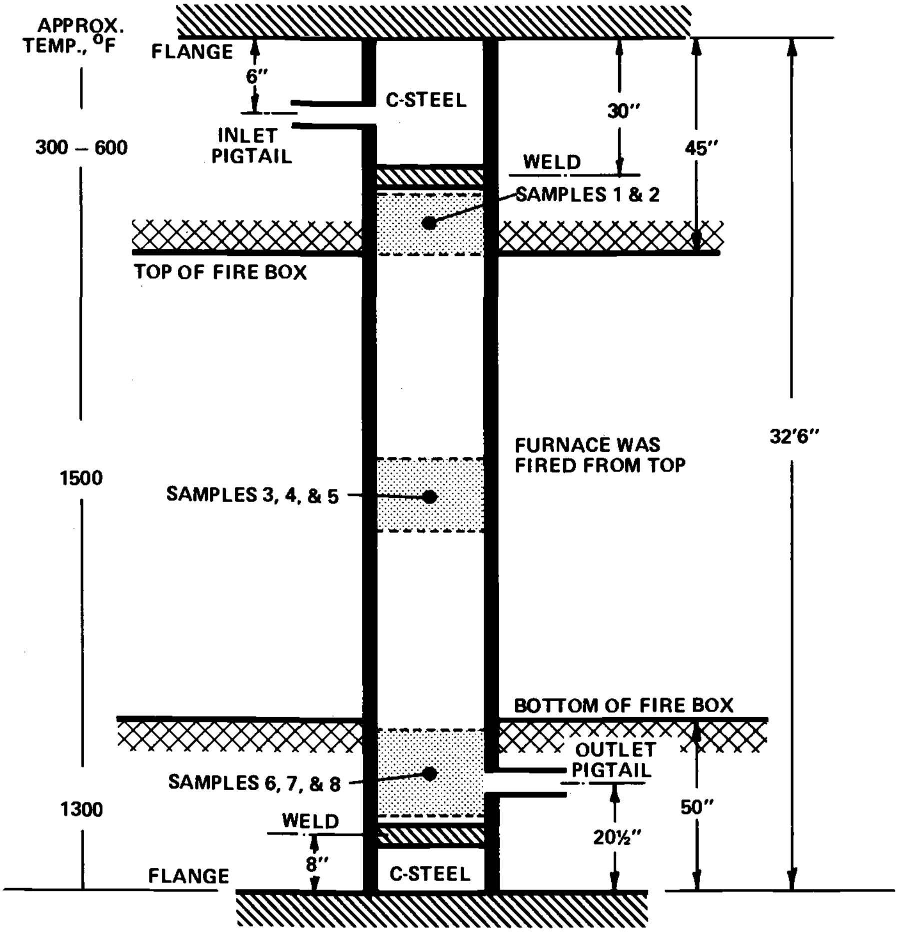

FIG. 1—*Schematic of reformer tube (not to scale).*

Samples 3, 4, and 5, from the central portion of the tube located near the middle of the firebox, typified a region maintained near 815°C (1500°F).

Samples 6, 7, and 8 were taken from the outlet area and included the outlet pigtail. The temperatures of the gases at the outlet were held close to 705°C (1300°F).

Tensile and stress-rupture specimens were cut from the wall of the tube in the longitudinal direction. The samples were subsize—3.18 mm diameter by 12.70 mm gage length (0.125 in. by 0.500 in. gage)—and measurements were determined from cross-head movement as recorded on charts.

The stress-rupture tests were conducted at a stress level slightly above that at which as-extruded tube would have 100-h rupture life. Typically, specimens showed 100-h life at 650°C and 159 MPa (1200°F and 23 000 psi).

Surface Examination

The oxides that formed on the outside surface of the tube were very thin. Surface discoloration varied along the length of the tube, but there was no indication that the serviceability of the tube was impaired.

A transverse metallographic mount was prepared from each section of tube and examined for oxide penetration. The greatest intergranular penetration of oxides occurred in the central section of the tube where temperatures were highest. Figure 2*a* illustrates the outside surface of that section, which was exposed at 815°C (1500°F), and the deepest oxidation of 0.33 mm (0.013 in.). The maximum intergranular penetration inside the tube was also found in the center portion. Figure 2*b* shows the interior oxidation that measured 0.20 mm (0.008 in.). The samples showed that more than 90 percent of the original 7.11-mm (0.280-in.) wall remained free from intergranular oxidation even at the highest temperatures.

The ends of the tube operated at lower temperatures and showed a maximum intergranular penetration of only 0.08 mm (0.003 in.).

Room-Temperature Tensile Results

Room-temperature tensile properties at various locations along the tube are shown in Table 2. Typical results for as-extruded and straightened tube are also included for comparison. The central portion of the tube showed about a 20 percent increase in yield strength while maintaining its original ultimate tensile strength and elongation. The reduction in area was somewhat lower but quite acceptable.

The ends of the tube showed the greatest change. Yield strengths increased by 130 to 172 MPa (20 000 to 25 000 psi), an increase of 55 to 70 percent over the typical values, while the tensile strength rose by 48 to 186 MPa (7000 to 27 000 psi), an improvement of 9 to 36 percent. The improved tensile properties were obtained without a loss in ductility, as shown by the similarity in elongation and reduction of area before and after exposure.

Microstructure

Microstructures of the tensile specimens from each tube section were studied to help explain the observed improvement in tensile properties. Phases were identified in residues extracted by either of two electrolytes. Table 3 shows the X-ray-diffraction data. Chromium carbide was the

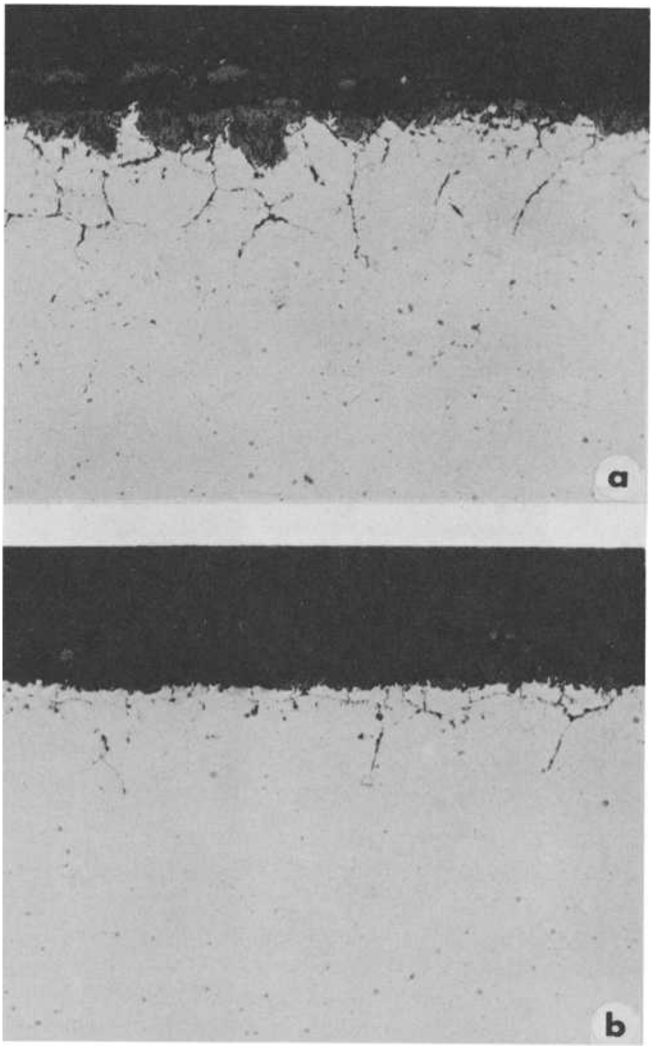

FIG. 2—(a) *Section at outside surface of tube center portion showing maximum intergranular penetration of about 0.33 mm (0.013 in.).* (b) *Section at inside surface of tube center portion showing maximum intergranular penetration of about 0.20 mm (0.008 in.). Original magnification ×100.*

predominant carbide, and its presence and amount could be correlated with service temperature.

Figure 3 typifies material from the inlet end of the tube. The incomplete grain boundaries demonstrate that there is very little grain-boundary precipitate. Yet, there is nothing visible in the microstructure to explain the increase in mechanical properties.

TABLE 2—*Effect of 120 000-h exposure on room-temperature tensile properties.*

Sample Location	Approximate Service Temperature		Yield Strength (0.2% Offset),		Tensile Strength,		Elongation, %	Reduction of Area, %	Hardness, Rb
	°F	°C	ksi	MPa	ksi	MPa			
1. Inlet	1000	540	61.8	426	98.6	680	42.6	63.0	90
2. Inlet	1000	540	67.5	465	102.7	708	38.0	40.2	90
3. Center	1500	815	41.2	284	76.3	526	36.8	59.3	72
4. Center	1500	815	43.8	302	76.5	527	36.8	48.8	76
5. Center	1500	815	42.3	291	75.6	521	35.6	53.4	72
6. Exit	1300	705	53.1	366	93.1	642	29.0	49.3	86
7. Exit	1300	705	55.7	384	93.5	645	28.0	48.7	86
8. Exit	1300	705	55.2	381	82.1	566	36.0	79.8	83
Typical properties, unexposed			35	241	75	517	33	65	. . .

TABLE 3—*Precipitated phases determined by X-ray diffraction of extracted residues.*[a]

Sample Location	Electrolyte: 10% HCl + Methanol				Electrolyte: H_3PO_4		
	$M_{23}C_6$	Ti(C,N)	σ	Volume % Extracted	Ti(C,N)	γ'	Volume % Extracted
1. Inlet	R	M	N	0.084	R	N	0.042
2. Inlet	R	M	N	0.126	R	N	0.053
3. Center	A	M	N	0.828	M	N	0.248
4. Center	A	M	N	0.629	M	N	0.218
5. Center	A	M	N	1.208	M	N	0.259
6. Exit	A	M	R	0.868	M	R	1.875
7. Exit	M	M	VR	0.675	M	R	1.864
8. Exit	R	M	N	0.343	R	N	0.016

[a] A=abundant, M=medium, R=rare, VR=very rare, N=none detected. Nickel-filtered copper radiation, 50 kV, 16 MA, 1.5-h exposure.

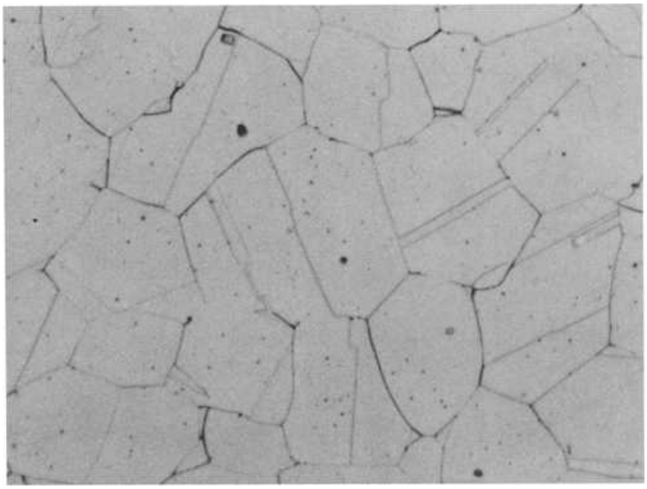

FIG. 3—*Typical microstructure near inlet end of tube. Material was exposed about 540°C (1000°F) for 120 000 h. Etchant: phosphoric acid electrolytic. Original magnification* ×500.

Figure 4 shows the microstructure of the central portion of the tube. The higher temperature, approximately 815°C (1500°F), resulted in the precipitation of numerous carbides, both in the grain boundaries and within the grains. The gain in yield strength shown by material from the central portion of the tube is attributable to the presence of carbides, which impede slip. Gamma prime could not form in that section of the tube, because the service temperature was above the solution point.

The outlet section of the tube presented interesting contrasts in microstructure. Figure 5 is a sketch of that short section of tube. At the outlet pigtail, Sample 7, the control temperature was about 705°C (1300°F). The portion near the burners, Sample 6, was perhaps 15 to 25°C (25 to 50°F) hotter. Below the pigtail, Sample 8, the tube was cooler, 650 to 690°C (1200 to 1275°F) because of heat transfer to the end plug, supports, and surroundings.

The microstructure at the sealed end, Fig. 6, is characterized by poorly defined grain boundaries and is similar to the structure at the inlet section of the tube. The phosphoric acid etch would have accented the grain boundaries if they had contained much chromium carbide. The photomicrograph shows some titanium carbonitride and fine chromium carbides within the grain.

The similarity of structures at the process end and at the pigtail is shown by Figs. 7 and 8. The structure near the firebox, Fig. 8, shows more extensive twinning indicative of a slightly higher operating temper-

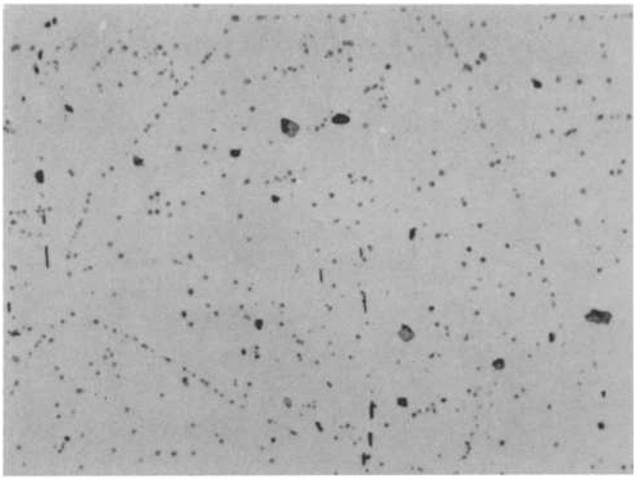

FIG. 4—*Typical microstructure near the center of tube. Exposure at 815°C (1500°F) resulted in precipitation of intergranular and intragranular carbides. Etchant: phosphoric acid electrolytic. Original magnification ×500.*

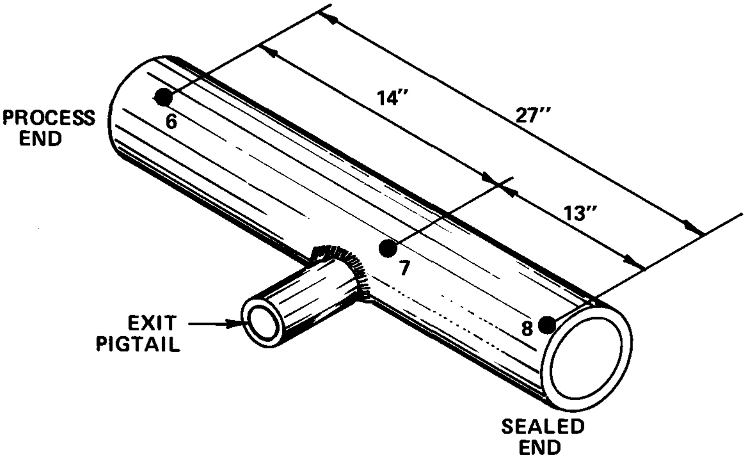

FIG. 5—*Exit portion of tube showing sample locations.*

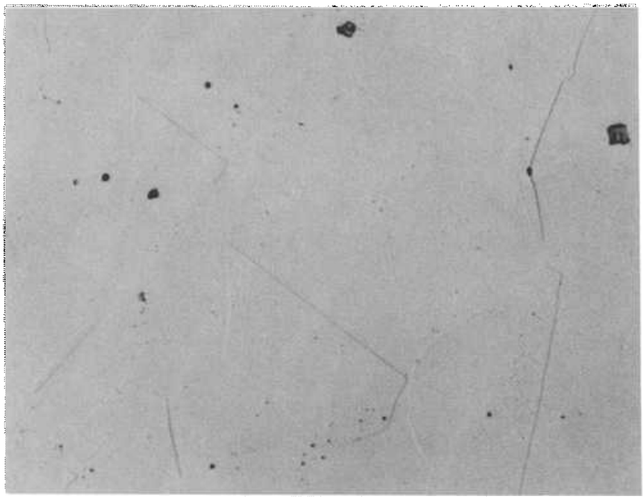

FIG. 6—*Microstructure at exit end of tube. Grain boundaries are not delineated. Etchant: phosphoric acid electrolytic. Original magnification ×500.*

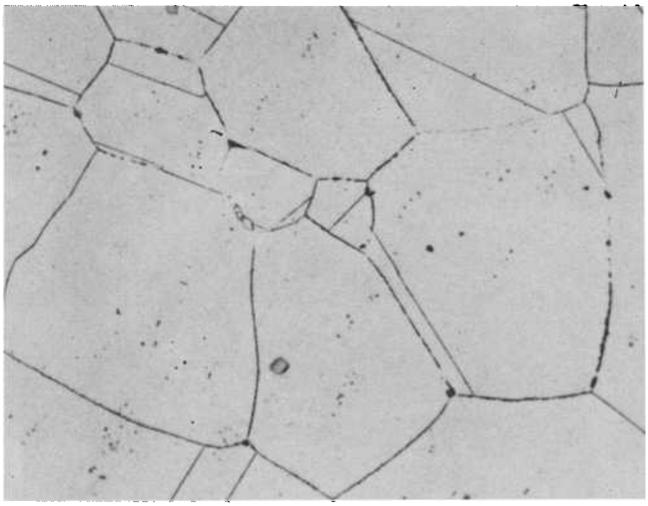

FIG. 7—*Well-defined grain boundaries at exit-pigtail area of tube. Coarse carbides are present within grains and grain boundaries. Etchant: phosphoric acid electrolytic. Original magnification ×100.*

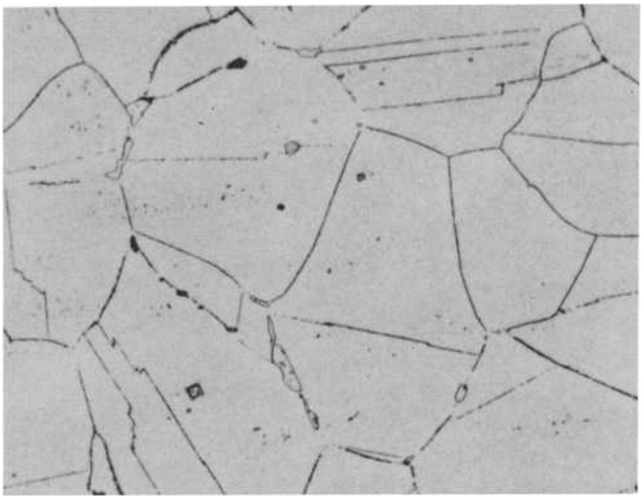

FIG. 8—*Blocky grain-boundary precipitate in area just above exit pigtail. Microstructure is similar to that in Fig. 7. Etchant: phosphoric acid electrolytic. Original magnification ×500.*

ature. The well-defined grain boundaries reveal the presence of fine chromium carbides.

A comparison of the microstructures at both ends of the tube with the structure at the center leads to the conclusion that strengthening at the tube ends cannot be attributed to carbide precipitation. The center had more carbides and showed only a slight increase in yield strength, whereas the ends exhibited significantly increased strength but contained few carbides.

A coarse, blocky precipitate is visible in the grain boundaries in Fig. 8. With the electron microprobe analyzer, many of the particles were found to be chromium carbides that had agglomerated during the long-time exposure. Some of the particles were identified as sigma phase.

The X-ray-diffraction results of Table 3 show the presence of gamma prime in two of the three samples from the outlet end. Gamma prime could explain strengthening at the outlet end, but an even greater increase in tensile properties occurred at the inlet end, where gamma prime was not found.

A trace of sigma phase was also found by X-ray diffraction. Mechanical properties showed the phase to be innocuous.

To characterize the gamma prime, extraction replicas for electron microscopy were prepared [*1*][3] from each outlet-section specimen. The

---

[3] The italic numbers in brackets refer to the list of references appended to this paper.

variation in particle size and a semi-quantitative assessment of volume percent are shown in Fig. 9. Volume percent was determined from particle count and average particle size. The particles were largest toward the firebox, slightly finer but more numerous at the pigtail, and very fine (and few in number as pointed out by arrows on the figure) near the sealed end. Note that even though a higher magnification was used, the gamma prime at the sealed end of the tube was barely resolvable. The particles were 100 to 150 Å in diameter; smaller particles would be difficult to detect.

These results explain strenghtening in two areas within the exit portion of the tube, but do not clearly show that gamma prime caused strengthening at either the sealed end or the inlet portion.

A computer model [2] was used to predict the phases and their amounts that would form in material having the composition of the Alloy 800 tube. Although the model relies on an equilibrium program and certain assumptions were made to obtain equilibrium constants, the predicted data were consistent with experimental results. Figure 10 compares experimental and predicted data. The computer program predicted the formation of gamma prime at service temperatures between 540 and 705°C (1000 and 1300°F), with increased gamma prime forming near the lower temperature. Although it could not be identified in samples that had seen service

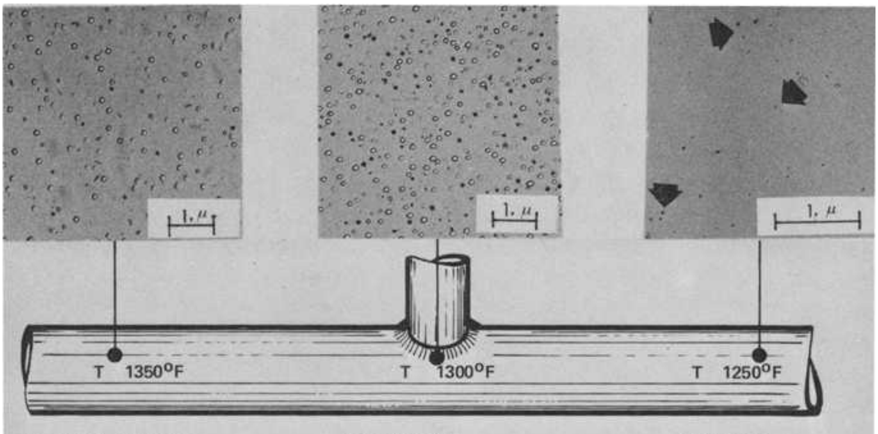

NEAREST FIREBOX	EXIT PIGTAIL	SEALED END
500 to 800 Å	PARTICLE SIZE 300 to 800 Å	100 to 150 Å
0.185%	VOLUME PERCENT 0.227%	UNDETERMINED

FIG. 9—*Gamma prime present in the three rupture-test specimens from the exit end of the tube. Original magnification, left to right: ×9200, ×9200, ×18 2000.*

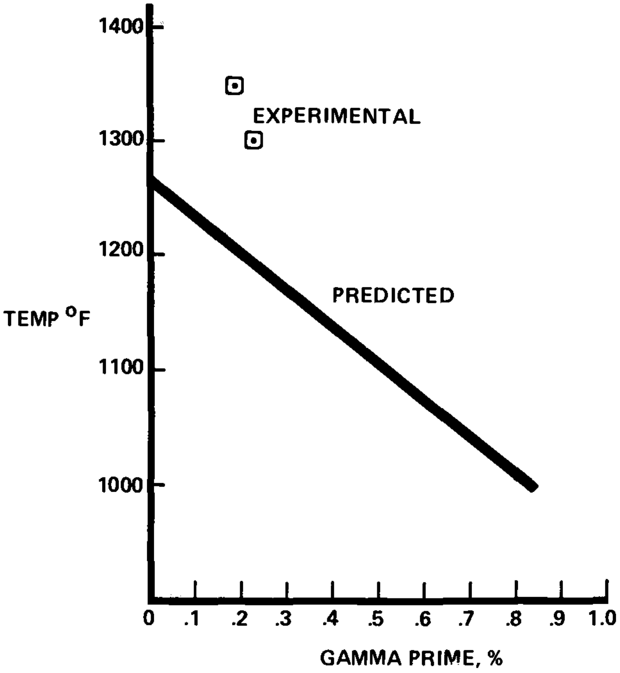

FIG. 10—*Percent gamma prime in INCOLOY Alloy 800 (0.41Al, 0.41Ti) as a function of temperature.*

at 540 to about 650°C (1000 to 1200°F), gamma prime could be presumed to have caused the increase in strength.

The only explanation, then, for the inability to extract gamma prime from residues or by extraction replicas is that the very fine particles were dissolved. Various techniques, including different electrolytes and mechanical separation, were tried to isolate the particles, but to no avail. The use of light etches to prepare samples for parlodion replication would be expected either to extract the particles or to dissolve them and leave their sites in relief for replication. However, the particles were not detected, presumably because they were so small that their impressions in the plastic were as fine as the grain in the photographic film or in the plastic itself.

Transmission electron microscopy of thin foils was not attempted because prior research by the authors as well as by others [*3*] has shown the impossibility of bright-field imaging of gamma prime particles less than 250 Å in diameter. Volin [*4*] did image fine gamma prime using high-resolution dark-field illumination, but particle size and amount could not be determined.

Conclusive identification of such small particles of gamma prime may at present exceed the capability of the science. The available information, however, leads to the deduction that the Alloy 800 tube was strengthened, without loss of ductility, by the precipitation of gamma prime particles of less than 100 Å in diameter.

Stress-Rupture Tests

Stress-rupture tests were conducted on samples from the three locations within the tube to reinforce the conclusions drawn from the tension tests. Tests were run at 650°C and 172 MPa (1200°F and 25 000 psi), conditions that should produce a rupture life of slightly less than 100 h in as-extruded tubing [5]. The test temperature was selected to represent the mid-range of the service temperatures and, more importantly, to encourage the growth of gamma prime, making it easier to resolve metallographically.

Table 4 contains the rupture-test results. The center of the tube, strengthened only by carbides, had the shortest rupture life—less than 100 h—as predicted. The ends of the tube, being strengthened as shown in tension-test results, had much longer rupture lives. The two samples from the outlet end that had shown a resolvable size of gamma-prime particle as removed from service had rupture lives of about 150 h. The ductility of the tube was maintained throughout its length.

The broken rupture-test samples from the inlet side of the tube, the central (firebox) section, and the section nearest the sealed end were examined further to explain the strengthening mechanism. Quantitative extractions for gamma prime were run on each sample, and X-ray-diffraction studies were conducted. Table 5 contains the results. Gamma

TABLE 4—*Stress-rupture properties at 649°C (1200°F) and 172 MPa (25 ksi) after 120 000-h exposure.*

Sample Location	Approximate Service Temperature		Rupture Life, h	Elongation, %	Reduction of Area, %
	°F	°C			
1. Inlet	1000	540	433.9[a]	23.2	26.0
2. Inlet	1000	540	434.2[a]	22.3	31.0
3. Center	1500	815	78.8	22.9	34.7
4. Center	1500	815	80.1	29.1	40.0
5. Center	1500	815	58.9	24.8	28.9
6. Exit	1300	705	150.0	45.1	34.8
7. Exit	1300	705	168.2	40.6	38.2
8. Exit	1300	705	383.3[b]	41.5	65.4

[a] Stress increased to 207 MPa at 335 h, to 241 MPa at 360 h, to 276 MPa at 385 h, to 310 MPa at 404 h, and to 345 MPa at 432 h.

[b] Stress increased to 207 MPa at 335 h and to 241 MPa at 360 h.

TABLE 5—*Gamma prime determinations on samples rupture-tested at 649°C (1200°F).*

Approximate Service Temperature		Rupture Life, h	% Residue Extracted	Gamma Prime Presence	Particle Size, Å
°F	°C				
1000	540	434.2	0.21	yes	70–90
1500	815	80.1	0.33	rare or doubtful	. . .
1200	650	383.3	0.16	yes	175–300

prime was present in the samples from the inlet and outlet sections of the tube, but its presence in the firebox sample was doubtful or rare. That the percentage of residue was highest in the firebox section could be attributed to carbides formed during service. Sample 4 had a rupture life of only 80 h, which is not sufficient time at 650°C (1200°F) to nucleate and grow gamma prime to a resolvable size in the alloy. Separation of extracted particles from the electrolyte was an arduous task for the samples rupture-tested at 650°C (1200°F), particularly in the sample from the inlet section of the tube. Both chemical and mechanical means were used to recover the fine residue from the colloidal solution.

Extraction replicas were prepared from the shoulders of the broken rupture-test samples. Selected-area electron diffraction verified that the particles were gamma prime. Figure 11 shows the size of the particles and provides a correlation with the mechanical properties. In Fig. 11*a*, the particles are 70 to 90 Å in diameter, the smallest particles observed. That sample also had the highest tensile properties and longest rupture life. Extrapolating backward from the large gamma-prime particles in samples rupture tested for 400 h at 650°C (1200°F) suggests that the particle size resulting from service at 540°C (1000°F) was smaller by an order of magnitude. Such an extremely fine particle at the low volume percent may explain the retention of good ductility.

The gamma-prime particles in the outlet section of tube grew larger during the 383-h rupture test. The 175- to 300-Å particles reflect the higher service temperature. The section near the plug originally believed to have been subjected to a temperature of near 705°C (1300°F) may actually have been nearer 650°C (1200°F). The particle size also supports the mechanical test results.

The clustering of gamma-prime particles seen in Fig. 11 results from their agglomeration during rinsing of the sample after etching. Thus, it would not be accurate to determine the volume percent present from the photomicrographs.

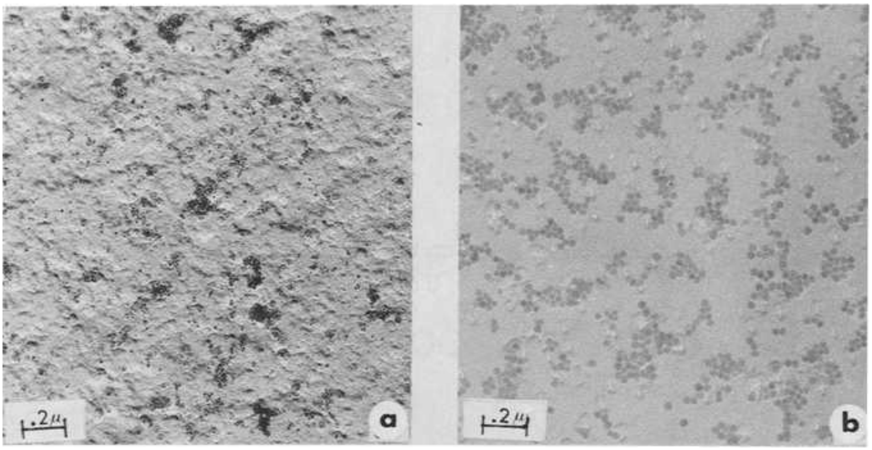

FIG. 11—*Gamma prime in samples rupture-tested at 649°C (1200°F) and 172 MPa (25 000 psi).* (a) *Inlet section of tube, exposed to service temperature of about 540°C (1000°F). Rupture life was 434.2 h. Particle size: 70 to 90 Å.* (b) *Exit section of tube near plug, exposed to service temperature of about 650°C (1200°F). Rupture life was 383.3 h. Particle size: 175 to 300 Å.*

Conclusions

The INCOLOY Alloy 800 tube showed only minimal environmental damage after 14 years of service as a catalyst tube in a steam-methane reformer. The maximum penetration of oxides was 0.33 mm (0.013 in.) on the outside surface while the most severe attack on the inside surface was only 0.20 mm (0.008 in.). Therefore, more than 90 percent of the 7.11-mm (0.280-in.) tube wall was unaffected by environmental attack.

The tube showed significant improvement in room-temperature tensile properties and in stress-rupture properties. The center of the tube, which was exposed to 815°C (1500°F), was strengthened by the precipitation of carbides, principally $Cr_{23}C_6$. The ends of the tube, operating at temperatures between 540 and 705°C (1000 and 1300°F), were strengthened in service by the precipitation of gamma prime.

The tube was not embrittled during its service. The room-temperature tensile ductility showed that the reduction in area in each test exceeded 40 percent. Stress-rupture tests at 650°C (1200°F) gave reductions in area of over 25 percent.

No embrittling effects were associated with any precipitates. Rare, discrete, blocky particles of sigma phase found in one section of the tube were innocuous. Gamma prime was the principal strengthening phase, and mechanical properties decisively showed that ductility was retained.

Acknowledgments

The authors appreciate the efforts of R. W. Guenther for assistance with X-ray diffraction studies, Dr. D. J. Cometto for the theoretical phase-prediction program, and A. A. Hesse for microprobe studies.

References

[1] *Metals Handbook,* Vol. 8, 8th ed., American Society for Metals, pp. 100–102.
[2] Cometto, D. J., unpublished research, Huntington Alloys, Inc., Huntington, W. Va.
[3] Nahm, H. and Moteff, J., *Metallurgical Transactions A,* Vol. 7A, Sept. 1976, pp. 1473–1477.
[4] Volin, T. E., unpublished research, Paul D. Merica Research Laboratory, Suffern, N.Y.
[5] *INCOLOY Alloys,* Huntington Alloys, Inc., Huntington, W. Va., 1973.

STP672-EB/Jul. 1979

Discussion—High-Temperature Alloys Session

Microstructural Objectives for High-Temperature Alloys in Advanced Energy Systems by C. T. Sims

Question: J. M. Leitnaker[1]—I'd like to thank you for your boost for the breeder reactor. You mentioned the swelling problem in Type 316 stainless steel and showed a particularly bad example of that problem.

I'd like to report that at least partial solution to that problem is a triumph of microstructural analysis in that if you remove the impurities from Type 316 stainless steel, the swelling goes up dramatically. The secret in controlling the swelling in the Type 316 is to selectively increase those impurities and by modifying the composition slightly of Type 316, raising the nickel a little bit, lowering the chromium a little bit, and also lowering the molybdenum and increasing the silicon that you can reduce the swelling to a very negligible amount comparable to PE 16. It's just a very recent result that has come out following the picture that you've shown and fits right in with the message that you have.

Answer: C. T. Sims—That's good to hear. If Type 316 is capable of doing the job as a fuel cladding material, that's going to be a lot easier than trying to use a higher-cost superalloy.

Question: F. Sczenzenie[2]—In discussing LMFBR, you mention claddings as a potential component. I think I know what you mean, but could you expound a little bit more on what components and what material systems you're talking about?

Answer: C. T. Sims—Ok, I'll try to be very general. In a reactor, of course, the heat comes from the uranium or thorium as a fissioning material. The material may be an oxide, metal, or other component, depending on reactor design. It must be contained some way in order to release the heat and still not react with the heat exchanger fluid that cools it. So all reactors, at least those I know of, have the active ingredient—the

---

[1] Oak Ridge Labs., Oak Ridge, Tenn.

[2] Special Metals Corp., New Hartford, N. Y.

uranium-containing material—in a sheath or cladding of some sort. It could be a pin, it could be a ball, it could be a coated particle, but most commonly and for the near future, it's as a clad body like a fuel plate. The plate might be about 3 to 5 in. wide, many feet long, and ¼ to ½ in. thick. It will contain a layer of the uranium-containing material. The fluid heat-exchange medium moves by the protecting alloy cladding, removing the heat. Thus, those fuel plates grow rather hot.

The pebble bed helium gas reactor is most interesting. The fuel elements are a 6-cm graphite ball, admixed with a coated UO_2 or other fissile particles containing carbon-coated UO_2 or other fissile particles distributed within it. That whole ball acts as the container. A metal sheathing is not needed.

Question: S. Banerji[3]—Would you care to comment a little bit about the single crystal materials that are being developed for turbine blades?

Answer: C. T. Sims—Single crystal blades are generated by directional solidification. First, there's an intermediate product—directionally solidified alloys—that are composed of alloys with grains that run directionally in the strength-needed direction. In a turbine bucket for instance, they are parallel to the major stress direction, and thus the lack of transverse grain boundaries sharply reduces the possibility of transgranular fractures. I understand some are now in service.

If then, as Pratt & Whitney has done, one develops a process for producing a single crystal part, not only will there be no horizontal or transverse grains to initiate and promulgate fracture, but no vertical ones will be present also. However, I keep hearing that this process is pretty expensive, and one wonders whether it can come through economically. Someone from Pratt & Whitney may want to comment on this.

Comment: R. King[4]—We have made a couple of engine sets of monocrystal blades in the new foundry in Middletown with that automated process, but I will agree at this point in time it's more expensive than the directionally solidified process.

Reply: C. T. Sims—Would you think that because it's expensive, that perhaps we'll see a day when single crystals will be in use as a part of the high-temperature part, bonded to it, where the single crystal is used to resist low-cycle fatigue, perhaps as a turbine blade leading or trailing edge?

Comment: R. King—I really don't have any comment on that. I don't think the technology is that far along. I think the monocrystal today is in

---

[3] Foote Mineral Co., Exton, Pa.

[4] Pratt & Whitney Aircraft, East Hartford, Conn.

the same category as the directionally solidified blade was, let's say, five or six years ago when it was in its infancy.

Comment: W. Jones[5]—I would like to add that the candidate alloys you've discussed are going to appear on energy conversion lists other than the ones you have discussed. Currently, in solar thermal boiler design and in geothermal hot rock drilling schemes, these kinds of alloys are again going to be considered. No matter which innovative energy scheme you consider, one will encounter less than desirable environments and high temperatures. The list of potential uses for these alloys then includes solar thermal, geothermal, fusion, coal, and fission energy conversion.

Answer: C. T. Sims—Thank you very much. That is a most appropriate comment, and I appreciate that you have made it. For this talk, I have just picked a few energy systems of a major type. Further, if I may, I would like to mention water-cooled turbines and ceramics.

The thought may have gone through your mind that in those kinds of systems we will be using no superalloys. Nothing could be further from the truth. All we will be doing is to move the then intermediate temperature problems further down in the gas turbine. For instance, if one were to conceive that one could develop a gas turbine with first-stage bucketing of a ceramic material, superalloys would then be used at their limits in the latter stages, because design would minimize the stages using ceramics.

Water cooling is the same circumstance. Superalloys will be needed in latter stages, and also to protect water-cooled interiors from corrosion. So superalloys are going to be here for a long time.

Melting of Superalloys by L. W. Lherbier

Question: F. Sczenzenie—You showed that arsenic, antimony, and tin remain stable under VIM melting. The levels didn't decrease. Could you comment on the ability of the various remelt processes to reduce those elements?

Answer: L. W. Lherbier—I think, basically, the remelting processes do not do much to reduce those elements either. There is a possibility they can be minimized in a remelting via electroslag. I just don't think there's been enough work done yet to define how much or even if they can be reduced to acceptable levels. We generally look at elements of that type as having to be controlled in the charge of raw materials.

Question: W. Mankins[6]—I would just like to reemphasize a comment

---

[5] Sandia Labs., Albuquerque, N. M.

[6] Huntington Alloys, Inc., Huntington, W. Va.

that you made concerning the tandem use of the electric arc furnace and the AOD furnace. I think that one of the benefits of this process is that both pieces of equipment are utilized for the purpose that they do best. The electric furnace is very efficient for melting, but it is not the most functional equipment for refining. Using the electric furnace—I don't know other's experiences—but having worked in our melt shop, I've always felt that there was a lot of *witchcraft* (melter's art) associated with electric furnace refining, watching melters read carbon tests, and perform other steps that seem to be shrouded in an aura of mysticism that challenged metallurgical explanation.

By contrast, transferring a heat to the AOD vessel for refining, the process adheres to metallurgical theory. Refining is being done in a device that is thermodynamically sound. The operator knows exactly how much oxygen is needed to blow the carbon to the level desired, and when it's completed, the metallurgist says lo and behold, it works just like the textbook says it would.

Answer: L. W. Lherbier—Not having worked as a melter, I can sympathize with your witchcraft, and I think it may apply to all melting techniques, not just the electric furnace. However, a computer calculation is not going to make a heat every time. In fact, when a heat does not final as forecast, the experience of the melting person is necessary to correct the failure.

Question: Dr. M. K. Koul[7]—I'd like to comment on this thing that everybody looks at, the AOD process as the solution for all problems. But one thing you have to see is that when you were making very high purity alloys, in the past, melters placed very very severe specifications on the raw materials they used. That is, raw materials like chromium, manganese, nickel, and other alloying elements.

Now, when you go to the AOD process, one of the incentives there is to go to low-cost material—high carbon chrome and things like that.

And for 15 cents a pound or 20 cents a pound, you are not going to get very high purity material as compared to electrolytic chrome or electrolytic manganese. So when you look at a process bringing in AOD, you should think about this, if you are going to get very high purity alloying elements with the AOD process combination with the electric furnace.

Answer: L. W. Lherbier—That's true. However, I think you have to recognize what the end application is, and what the customer requires. Customers are generally open to suggestions that potentially will reduce the cost of the metal that they're buying. And although for critical rotating parts you're locked in in many cases, if you present enough evidence,

---

[7] Foote Mineral Co., Exton, Pa.

they will give you a lot of deviation so that you can make some changes and perhaps go a lower cost route.

Comment: Dr. Koul—You see, in titanium alloys, for example, half of the load is taken away from the melters and producers by the raw material producers, so that the raw material producers supply a very pure material at high price. What I'm saying is that you cannot put similar specifications on the producers of low-cost ferro alloys. You are going to have to do everything in your shop. This should be kept in mind when you talk about very high purity materials.

Forging and Processing of High-Temperature Alloys by A. J. DeRidder and R. Koch

Question: Dr. R. Cremisio[8]—I think that we rarely get a chance to see such an excellent review, particularly on a new technology such as powder forging. I may have missed it, but I didn't see anything about argon entrapment. Does that mean this problem is pretty well licked?

Answer: R. Koch—I don't really have a lot on argon entrapment. I presume it would occur; I haven't recognized it as argon entrapment. We do see small voids. Much of the powder we see has a lot of very small voids in it, and apparently during a mechanical property test is they're at a limit of being small enough, they don't have a great impact on mechanical properties.

Review of Superalloy Powder Metallurgy Processing for Aircraft Gas Turbine Applications by J. L. Bartos

Question: F. Sczenzenie—In talking about your success on forging the as-HIP parts, you mentioned that you raised the gamma prime solvus. Would you explain that please?

Answer: Dr. Bartos—The gamma prime solvus of powder metallurgy René 95 is higher than in the conventional cast plus wrought version. The slight change in chemistry—reducing the carbon and chromium contents—raises the solvus in powder metallurgy René 95 to 2120 to 2150°F. This 25 to 50°F increase in solvus temperature relative to cast plus wrought René 95 permits a higher solution temperature in as-HIP that is largely responsible for the competitive property levels. However, the higher solvus has very little effect on the forged powder parts, since the solution temperature is much lower than that used on as-HIP parts.

Question: F. Sczenzenie—A second question. You mentioned that in order to control gas porosity, you were going to finer powder particle

---

[8] Materials Technology Associates, Clinton, N. Y.

sizes. I normally associate finer powder with higher specific surface and more potential for gas problems. Could you explain your rationale and what powder size ranges you're working in?

Answer: Dr. Bartos—Finer powders generally mean more surface area, which raises concerns about the oxygen and nitrogen contents. However, these interstitial levels are still at acceptably low levels in the finer mesh powder we've evaluated. On the other hand argon, the gas that causes porosity problems, doesn't react with powder surfaces, so the increased surface area of finer powders is not a concern. The major benefit relative to porosity levels derived from finer powders is the fact that most of the powder particles containing entrapped argon are eliminated. The nature of the argon atomization process results in a substantial number of hollow particles, primarily concentrated in the larger size range, which contain entrapped argon. This entrapped argon cannot be removed by evacuation and causes porosity in the HIP compact. By screening down to a finer particle size, many of these larger hollow particles are eliminated, thus reducing the overall quantity of argon contained in the compact. Both the number and size of argon pores are reduced substantially by utilizing a finer mesh powder. General Electric is currently evaluating the feasibility of using powders in the −100 to −150 mesh size range.

Question: M. Woulds[9]—I'm glad at last someone is recognizing powder metallurgy as its own production technique, and not something you can convert castings and forgings into. On that line, with your development of AF 115, is any work being done by you or anyone else in the field in going one step beyond, that is, taking an elemental phase dispersion type powder and blending? That is to say, taking gamma prime with a high hardener content and a matrix powder alloy and combining them; this way, one could have an alloy with high tungsten, that because of segregation in a VIM system could not be easily cast.

Answer: Dr. Bartos—We've never attempted to process René 95 in the manner you suggest. The technique you describe sounds like mechanical alloying, something we've never considered for superalloy rotating components like turbine disks. We've always felt the best way to achieve the desired high level of homogeneity is to use prealloyed powder production techniques. Homogeneity is going to be a problem when you try to mix a dozen or more different elements together to make a typical superalloy. On the other hand, prealloyed powders, in which every powder particle has essentially the same composition, are a much more efficient method of achieving homogeneity rather than relying on some exotic blending

---

[9] Certified Alloy Products, Long Beach, Calif.

technique to distribute all elements uniformly. We don't feel that blending techniques are really practical at this time.

Question: M. Woulds—What about two or three master alloys with different phases, rather than all the elements?

Answer: Dr. Bartos—We feel the same type of problem, inhomogeneity, would still be present, especially when different input master alloy particle sizes are involved. Mr. Koch showed you how powders segregate by particle size even though they're the same composition. The distribution of all elements by this mechanical mixing technique may lead back to the segregation present in cast plus wrought products—locally high concentrations of certain elements. Since homogeneity is one of the principal desirable features of powder metallurgy processing, pre-alloyed powder appears to us to be the best production technique at this time.

Question: M. Hart[10]—How do the cyclic rupture properties compare for the as-HIP microstructure versus the cast and wrought necklace microstructure.

Answer: Dr. Bartos—The cyclic rupture properties of as-HIP René 95 are essentially equivalent to those of the cast plus wrought product containing a duplex necklace microstructure. Mr. Koch showed that a fine-grained, fully recrystallized wrought structure yields lower cyclic rupture properties than the duplex necklace structure. The as-HIP structure is essentially fine grained, but it's not recrystallized in the same manner as the cast plus wrought product, and it also is given a different heat treatment. Apparently, the microstructure produced during HIP combined with the heat treatment results in improved cyclic rupture relative to that of the conventional forged fine grain product. Cyclic rupture is a property prone to fairly significant scatter, so slight differences may be hidden. We're still gathering data to evaluate this question but from what we've seen so far, there doesn't seem to be a great difference in the cyclic rupture properties of the three forms of René 95—as-HIP, HIP plus forge, or conventional necklace microstructure cast plus wrought.

Super Waspaloy Microstructure and Properties by D. J. Deye and W. H. Couts

Question: G. N. Maniar[11]—Is it mandatory that you keep the carbon low? Because it seems you refine the grain size by keeping gamma prime out to inhibit the grain size.

---

[10] Cameron Iron Works, Houston, Tex.

[11] Carpenter Technology Corp., Reading, Pa.

Answer: D. J. Deye—In order to develop the best tensile and low cycle fatigue properties, we feel that it is necessary to keep the carbon content low. We forged conventional chemistry Waspaloy using the same forging parameters that we used for Super Waspaloy and showed an improvement in the tensile and low cycle fatigue properties. However, it was not to the extent that we saw with Super Waspaloy.

Question: G. N. Maniar—Did you have to balance any elements such as titanium or boron when you lowered the carbon or did you keep them the same?

Answer: D. J. Deye—The titanium content was increased and the boron content range was tightened up.

Question: Kuang-Ho Chien[12]—What is the difference in stress rupture ductility between conventional Waspaloy and Super Waspaloy?

Answer: D. J. Deye—At the higher temperatures, the rupture ductility for Super Waspaloy was slightly higher than that for conventional Waspaloy. At the lower temperatures, that is 1350°F, the rupture ductilities were equivalent.

Microstructure and Mechanical Properties of INCOLOY Alloy 800 After 14 Years of Service as a Catalyst Tube in a Steam-Methane Reformer by W. L. Mankins and D. E. Wenschhof

Question: L. Thompson[13]—We've been working on the age-hardening in commercial heats of Alloy 800H ourselves. The investigation has been directed at five heats supplied by Huntington Alloys, and in the as-received condition, we find titanium carbides, titanium carbonitrides, and $M_{23}C_6$ type carbides all present in small amounts. We have aged these alloys at 538, 593, 649, 760, and 816°C (1000, 1100, 1200, 1400, and 1500°F) for times approaching 20 000 h. The maximum aging response was observed at 593 and 649°C (1100 and 1200°F) with the aging response at the other temperatures much lower.

The majority of the age-hardening was observed to occur within 500 to 1000 h of exposure. We have performed extensive transmission electron microscopy to look for the gamma-prime phase and other precipitating phases, as well as, extraction analyses similar to those that you've performed. We did not observe any gamma-prime precipitation within 1000 h of exposure. However, we have observed gamma-prime after aging 4000 to 8000 h. What we observe are small, spherical precipitates coherent with the matrix, with strain fields around the precipitates of the order of 100 Å in diameter. The precipitates themselves are not resolv-

---

[12] Cameron Iron Works, Houston, Tex.

[13] General Atomic Co., San Diego, Calif.

able, but, by the size of the strain fields, they are certainly much smaller and are probably of the order of 30 Å or so in diameter.

The only consistent observation we've made within the 500 to 1000 h exposure time period has been the precipitation of $M_{23}C_6$ carbides at the grain boundaries. At 649°C, (1200°F) they form a continuous network along the grain boundaries that could possibly inhibit slip transferral from one grain to the adjacent grains. No cross-slip has been observed for this alloy. At higher temperatures 760 and 816°C (1400 and 1500°F), we see the carbide present much as you did, as very large, discrete carbides, and at these temperatures no strong aging response was found. No gamma-prime precipitation has ever been observed to form at these higher temperatures in our lab.

At lower temperatures, the kinetics for the precipitation of $M_{23}C_6$ are retarded and the aging response is delayed. There is still, however, much work to be done in this alloy system, and the results that you present are very interesting.

I should also mention that I'm having four experimental heats melted at the Lawrence Berkeley Laboratory, through the University of California, with controlled variations in carbon, aluminum, and titanium, and hopefully some of the confusion will be cleared up within the next year.

Question: R. Anderson[14]—Do you think that this problem of the gamma-prime precipitates dissolving in your extraction electrolyte might be a similar reason for not finding gamma-prime in 718, where it's often been postulated and some people have said it's there, but it's difficult to show in extraction?

Answer: W. L. Mankins—I really believe it is. It's a good question and my own personal feeling is that you do extract it. Let's assume it's there. You extract it. It falls down to the bottom of your beaker and is simply chemically digested, particularly if it's real fine. So you go to look for it, and it isn't present.

Question: Dr. W. Jones—For the component that you discussed, was there any thermal fatigue superimposed on the low static loading during its life? In other words, was there any creep—fatigue history?

Answer: W. L. Mankins—I couldn't be specific about that, but creep damage was one of the things we did examine the tube for. In cutting it all apart, many more micros were made than were shown in this presentation—we did examine it for creep damage. It was very minimal or if there was creep damage, it was not sufficient that I was willing to say that it was observed.

---

[14] Universal Cyclops Specialty Steel, Bridgeville, Pa.

Question: Dr. W. Jones—In ferritic and austenitic stainless steels that we've been looking at, which were mechanically tested at 1100°F, we find that in creep-fatigue conditions very long hold times and therefore relatively few cycles at modest strain ranges, that we find there are enough vacancies generated during the fatigue cycles to greatly influence the kinetics of, in these cases, carbide precipitation. And it may be here, in this case, that if you have marginal phase stability, that if you happen to have the right high-temperature history and extra vacancies, that in some cases people will find the marginally stable gamma-prime primarily as a result of enhanced kinetics, while others may never see it.

Answer: W. L. Mankins—One comment on that. One of the ideas that gets batted around a little bit on this subject is that the observed strengthening may result from a pre-precipitation phenomena, such as GP zones or some other pre-precipitation occurrence.

Comment: L. Thompson—I'd like to emphasize one point that I glossed over earlier. That is that we saw two strengthening responses—one after a short aging time, up to about 1000 h, and then one after a longer period of time that seemed to be consistent with when we have observed gamma-prime precipitation. By far, the stronger of the two happened to coincide with the precipitation of $M_{23}C_6$ carbides at the grain boundaries. Some of this work is documented in a paper by R. E. Villagrana and his associates that will appear in *Metallurgical Transactions* in July 1978, while considerable other documentation has been made in General Atomic Company's Department of Energy quarterly progress reports for the Generic Technology Program.

Comment: D. J. Deye—You showed a pretty significant improvement after 120 000 h, but do you have any 200 000-h pipe data?

Index